

Combined gas engine-solid oxide fuel cell systems for marine power generation

Sapra, H.D.

DOI

[10.4233/uuid:12393b11-a4c3-4697-8757-2b2dbc1291ec](https://doi.org/10.4233/uuid:12393b11-a4c3-4697-8757-2b2dbc1291ec)

Publication date

2020

Document Version

Final published version

Citation (APA)

Sapra, H. D. (2020). *Combined gas engine-solid oxide fuel cell systems for marine power generation*. [Dissertation (TU Delft), Delft University of Technology]. <https://doi.org/10.4233/uuid:12393b11-a4c3-4697-8757-2b2dbc1291ec>

Important note

To cite this publication, please use the final published version (if applicable). Please check the document version above.

Copyright

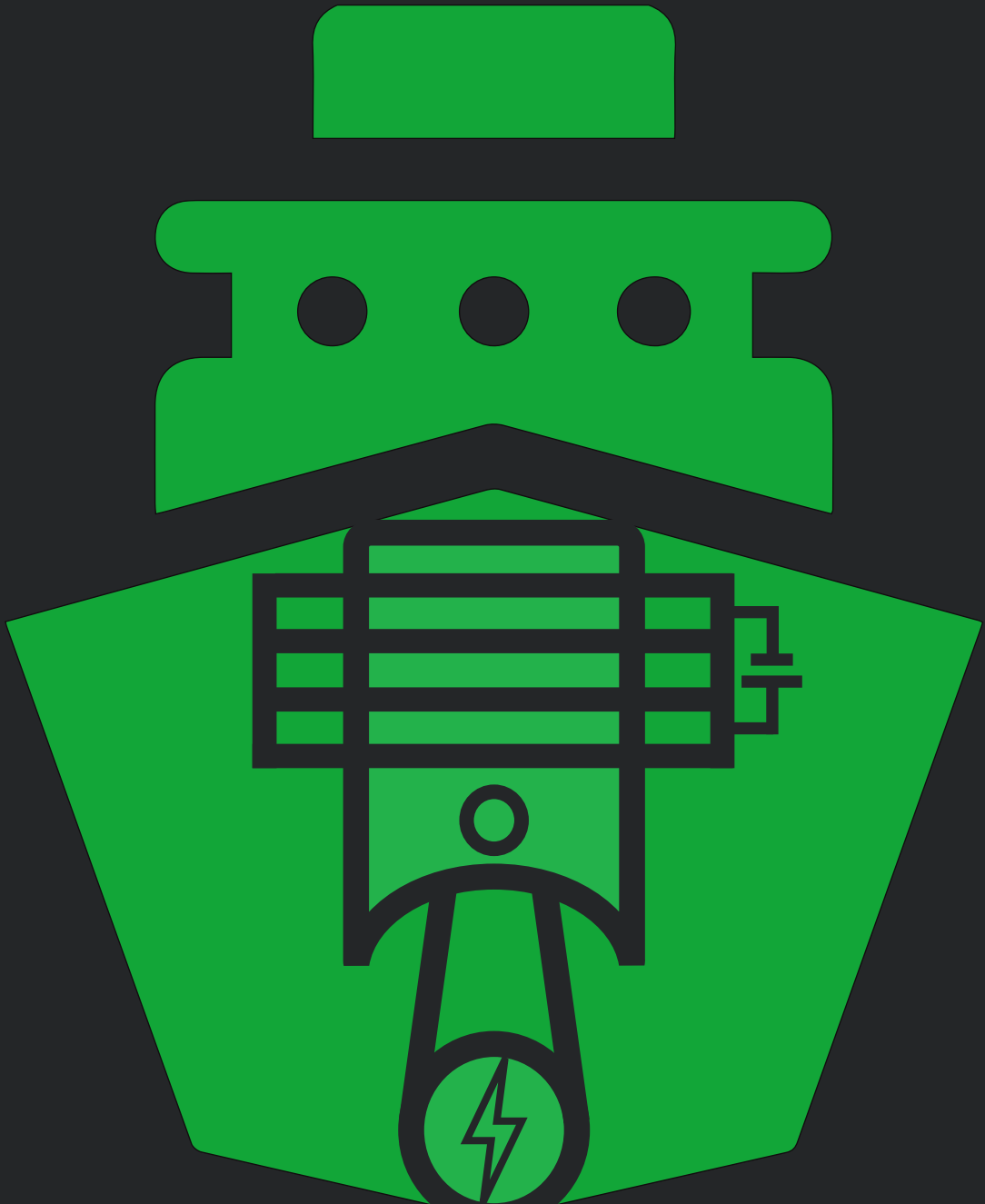
Other than for strictly personal use, it is not permitted to download, forward or distribute the text or part of it, without the consent of the author(s) and/or copyright holder(s), unless the work is under an open content license such as Creative Commons.

Takedown policy

Please contact us and provide details if you believe this document breaches copyrights. We will remove access to the work immediately and investigate your claim.

Combined Gas Engine- Solid Oxide Fuel Cell Systems for Marine Power Generation

Harsh Darshan Sapra



**COMBINED GAS ENGINE-SOLID OXIDE FUEL CELL
SYSTEMS FOR MARINE POWER GENERATION**

COMBINED GAS ENGINE-SOLID OXIDE FUEL CELL SYSTEMS FOR MARINE POWER GENERATION

Proefschrift

for the purpose of obtaining the degree of doctor
at Delft University of Technology,
by the authority of the Rector Magnificus prof. dr. ir. T.H.J.J. van der Hagen,
chair of the Board for Doctorates
to be defended publicly on
Wednesday 16 December 2020 at 15:00 o'clock

by

Harsh Darshan SAPRA

Master of Science in Mechanical Engineering,
Delft University of Technology, Delft, Netherlands,
born in Pune, India.

This dissertation has been approved by the promotor.

Composition of the doctoral committee:

Rector Magnificus,	chairperson
Prof. ir. J.J. Hopman,	Delft University of Technology, promotor
Dr. ir. P. de Vos,	Delft University of Technology, copromotor

Independent members:

Prof. dr. ir. D.J.E.M. Roekaerts,	Delft University of Technology
Prof. dr. ir. C.A. Ramirez,	Delft University of Technology
Prof. dr. ir. R. G. van de Ketterij,	Netherlands Defence Academy
Prof. dr. T. Jacobs,	Texas A&M University, United States of America

Other members:

Ir. K. Visser,	Delft University of Technology, daily supervisor
----------------	--

The research in this dissertation is part of the research programme '*GasDrive: Minimizing emissions and energy losses at sea with LNG combined prime movers, underwater exhausts and nano hull materials*' (project 14504) of the Netherlands Organisation for Scientific Research, domain Applied and Engineering Sciences (TTW).



Keywords: Solid oxide fuel cells, Internal combustion engines, Underwater exhaust systems, Marine power generation, Alternative fuels, System integration, Combustion, Experiments and Modelling and simulations

Printed by: Ipskamp printing, Enschede

Front & Back: Green SOFC-ICE Ship & Word Cloud by Harsh D. Sapra.
Ship icon adapted from the Noun Project, by Uswatun Hasanah.

Copyright © 2020 by Harsh D. Sapra

ISBN 978-94-6421-149-8

An electronic version of this dissertation is available at
<http://repository.tudelft.nl/>.

Somewhere, something incredible is waiting to be known.

Carl Sagan

CONTENTS

List of Figures	xi
List of Tables	xxi
Summary	xxv
1 Introduction	1
1.1 Current State of Shipping	1
1.2 Maritime Fuels	3
1.2.1 Biodiesel	4
1.2.2 Natural Gas	6
1.2.3 Hydrogen	6
1.2.4 Methanol	7
1.2.5 Dimethyl Ether	8
1.2.6 Ammonia	9
1.2.7 Summary: The Gas Age	10
1.3 GasDrive	11
1.3.1 The Why and How of SOFC-ICE Integration	13
1.3.2 The Role and Challenge of Underwater Exhaust	14
1.4 Short Literature Overview	15
1.5 Integrated System Variables	18
1.6 Problem Statement and Research Questions	19
1.7 Proposed Approach	20
1.8 Dissertation Outline	21
References	24
2 SOFC-ICE Integration Approach and Research Methodology	29
2.1 Introduction to SOFCs	29
2.2 SOFC Combined Cycles	32
2.2.1 Maritime perspective	36
2.3 Proposed SOFC-ICE Integration	37
2.4 Research Methodology	38
2.4.1 Research methodology for SOFC-ICE integration	39
2.4.2 Research methodology for back pressure effects	43
2.5 Conclusions	45
References	47

3	Zero-Dimensional SOFC Model	55
3.1	SOFC Model Introduction	55
3.2	SOFC single cell model outline and assumptions	56
3.3	Pre-reformer model	58
3.4	Single cell model equations	59
3.4.1	Equilibrium model for anode-off gas composition	59
3.4.2	Electrochemical model	60
3.4.3	Mass balance	62
3.4.4	Energy balance	63
3.5	SOFC cell-to-stack performance	65
3.6	SOFC Model Verification and Performance	65
3.7	Conclusions	72
	References	73
4	Experimental Investigations of SI Marine Engine Performance	75
4.1	Marine NG Engine Test Setup	76
4.2	Experiments on Hydrogen-Natural Gas Combustion	78
4.2.1	Experimentation Methodology for H ₂ -NG Combustion	78
4.2.2	Experimental Results for H ₂ -NG Combustion	79
4.3	Experiments on Carbon Dioxide-Natural Gas Combustion	89
4.3.1	Experimentation Methodology for CO ₂ -NG Combustion	89
4.3.2	Experimental Results for CO ₂ -NG Combustion	90
4.4	Conclusions	98
	References	99
5	Combustion Modelling of Anode-off Gas Constituents in a SI Marine Natural Gas Engine	101
5.1	Engine Modelling	102
5.2	Modelling Methodology for H ₂ -NG and CO ₂ -NG Combustion Characterization	106
5.3	Measurements to 0-D HRR model	107
5.3.1	Energy balance	107
5.3.2	Mass and composition balance	108
5.4	HRR Model to Combustion Characterization	110
5.4.1	HRR to Seiliger-based combustion characterization model	111
5.4.2	HRR to Wiebe-based combustion characterization model	113
5.5	H ₂ -NG Combustion Characterization Modelling Results	116
5.5.1	Characterization of H ₂ -NG combustion using Seiliger modelling	116
5.5.2	Characterization of H ₂ -NG combustion using Wiebe modelling	118
5.6	Comparison of Seiliger and double Wiebe function-based modelling for H ₂ -NG combustion characterization	120
5.6.1	Effects of different H ₂ -NG fuel blends and lean-burn operation	120
5.6.2	Effects of different H ₂ -NG fuel blends and engine loads	127

5.7	HRR Model Results for CO ₂ -NG fuel blends	131
5.8	CO ₂ -NG Combustion Characterization Modelling Results	134
5.8.1	Characterization of CO ₂ -NG combustion using Seiliger modelling.	134
5.8.2	Effects of CO ₂ -NG fuel blends with engine leaning.	135
5.8.3	Effects of different CO ₂ -NG fuel blends and engine loads	138
5.9	Conclusions.	140
	References	143
6	Mean Value Engine Model for SOFC-ICE Integration	149
6.1	AOG-NG Combustion Modelling	149
6.1.1	Parametrization of hydrogen-natural gas combustion	150
6.1.2	Parametrization of carbon dioxide-natural gas combustion	153
6.1.3	Anode-off gas and natural gas blend combustion	155
6.2	AOG-NG MVEM.	159
6.2.1	Initial estimation of manifold pressure.	161
6.2.2	Seiliger process, mass and composition balance model	163
6.2.3	Changing MAP, trapped temperature, mass and air-excess ratio	165
6.2.4	Turbocharger and exhaust receiver model	166
6.2.5	Emissions	169
6.3	AOG-NG MVEM validation and potential	170
6.4	Conclusion	172
	References	173
7	SOFC-ICE Integration	175
7.1	SOFC-ICE Integration Results.	176
7.2	Heat Integration	181
7.3	Load sharing, Engine Load Response and Unexplored Potential of SOFC-ICE Integration	185
7.3.1	Load sharing.	185
7.3.2	Load response of SOFC and ICE	189
7.3.3	Unexplored Potential of SOFC-ICE Integration.	197
7.4	Conclusions.	200
	References	202
8	Underwater Exhaust System and Marine Engine Performance	205
8.1	Investigations of Marine Diesel Engine Performance Against Static Back Pressure.	206
8.1.1	Methodology and test setup for static back pressure	206
8.1.2	Extended mean value engine model description	209
8.1.3	Discussion: Defining static back pressure limits	223
8.2	Experimental Investigations of Marine Diesel Engine Performance Against Dynamic Back Pressure	230
8.2.1	Methodology and test setup for dynamic back pressure	230
8.2.2	Results	235
8.2.3	Discussion: Fuel penalty.	244
8.3	Conclusion	247
	References	249

9	Conclusions and Future Research	253
9.1	Conclusions.	253
9.2	Contributions of the Thesis	262
9.3	Recommendations for Future Research	265
A	SOFC geometrical, physical and thermodynamic properties	269
	References	270
B	Variability in Performance Measurements and Combustion Modelling Results	271
B.1	Variability in Performance Measurements	271
B.2	Variability in Combustion Modelling Results	273
C	Additional Details of HRR, Seiliger and Wiebe Modelling	275
C.1	Impact of TDC Shift on Normalized Reaction Co-ordinate	275
C.2	Parameters Simulated by the Seiliger and Wiebe Modelling Approach	276
C.3	Derivation of Trapped Air-fraction	278
C.4	Derivation of Trapped Mixture Temperature for SI NG Engine with Zero Valve Overlap	279
C.5	Variations in Wiebe Shape Parameters	281
C.6	Effects of Spark-timing on the In-cylinder and Combustion Process	282
	References	284
D	In-cylinder Process for Composition 2 and 3	285
E	Example Efficiency Calculation for SOFC-ICE Integration	287
	Samenvatting	291
	Acknowledgements	295
	Curriculum Vitae	299
	List of Publications	301

LIST OF FIGURES

1.1	LNG-powered CMA CGM Jacques Saade container ship under construction [1]	1
1.2	NO _x (a) and SO _x (b) emissions from land-based sources and international shipping for 1990-2030 (as estimated by a 2015 study [10])	2
1.3	IMO TIER-III NO _x emission regulations setup in January 2016 [11]	2
1.4	Relative comparison of estimated energy densities, production capacity (a), price (b) and total CO ₂ emissions (c) of alternative maritime fuels. Calculations based on LHV, storage from [17–22], production capacity from [23–27] and fuel costs from [28–33]. The production capacities are calculated in Million Metric Tons (MMT), gravimetric energy density in MJkg ⁻¹ , volumetric energy density in MJL ⁻¹ and fuel costs in US \$/MJ of energy available from fuel. The CO ₂ emissions are in grams of equivalent carbon dioxide per kilometer (gCO ₂ -eqkm ⁻¹) [34]. For any quantity and type of greenhouse gas (mainly CO ₂ and CH ₄), CO ₂ -eq depicts the carbon dioxide, which would have an equivalent global warming impact. Side notes: The light green bar in (a) signifies the production capacity of NG while the dark green bar signifies the global liquefaction capacity of NG. The production capacity for LH ₂ in (a) is for only hydrogen, while its liquefaction capacity is expected to be lower. Similarly, the production capacity for LN _{H3} in (a) is for only ammonia, while its liquefaction capacity is expected to be lower. LH ₂ -(CH ₄) and LH ₂ -(H ₂ O) in (c) signify liquid hydrogen production from natural gas reforming and water electrolysis.	4
1.5	Summarized comparison of maritime fuels. Green: Very good, light green: good, orange: poor, red: very poor and NA: not applicable. The CO ₂ -eq emissions from biodiesel can vary based on production methods.	10
1.6	Schematic representation of GasDrive concept	12
1.7	Compatibility of solid oxide fuel cell and internal combustion engine. A green tick indicates an 'available attribute', red cross indicates a 'missing attribute' while an orange-brown tick indicates a 'bartered attribute' between SOFC and engine	13
1.8	A schematic representation of the conventional above-water exhaust system (from sideview) (a) and underwater exhaust system (from topview) (b)	15
1.9	Schematic representation of the dissertation outline	22
2.1	Schematic representation of a single SOFC cell	30
2.2	50 kWe Sunfire IT-SOFC stack for marine power generation [11]	31
2.3	Pressurised SOFC-GT combined cycle presented by van Biert et al. [10]	33
2.4	SOFC-ST combined cycle presented by van Biert et al. [10]	34

2.5	LHR-SOGTST system presented by Fyffe et al. [49]. C: Compressor, P: Pump, M: Mixer, 3WHX: Three-way heat exchanger, T: Turbine, CAB: Catalytic afterburner	36
2.6	System layout of the proposed SOFC-ICE integration for maritime applications. P.H.: Preheater, C.O.: Cooler, S.H. Superheater, Evap: Evaporator, Eco: Economiser. This subsection provides an overview of the system layout. The reader is directed to section 7.2 of Chapter 7 for a detailed description of the system and heat integration	38
2.7	Research methodology for SOFC-ICE integration	39
2.8	Pictures of test setup with the CAT G3508 SI NG engine	40
2.9	Research methodology to study the effects of static back pressure	43
2.10	Picture of test setup with the MAN4L2027 diesel engine	44
3.1	Schematic view of 3 single SOFC cells as part of a SOFC stack [7]	56
3.2	Single cell model schematics with three control volume: cathode-flow channel, PEN structure and anode-flow channel. The MSR, WGS and HOR 'ovals' mark the approximate locations of the heat source	57
3.3	i-V and PoD curve with cell losses at 1073 K for undepleted fully reformed mixture	66
3.4	i-V and PoD curves at 973, 1023 and 1073 K for undepleted fully reformed mixture	66
3.5	Current density vs cell voltage (a) and PEN temperature (b)	68
3.6	Pre-reforming ratio vs air-excess ratio (a) and cell voltage (b)	70
3.7	Fuel utilization vs cell voltage (a), PEN temperature (b) and efficiency (c)	71
4.1	Schematic representation of marine NG test engine setup	76
4.2	Cyclic variations in maximum in-cylinder pressure for the engine operating on only natural gas at 75 % (a), 50 % (b) and 25 % (c) load and NO _x emission of 500 mgN m ⁻³	80
4.3	Coefficient of variations in IMEP averaged for 145 consecutive cycles at 75 % (a), 50 % (b) and 25 % (c) engine loading for 0H ₂ -NG, 10H ₂ -NG, and 20H ₂ -NG fuel blends	81
4.4	Operating window at 75 %, 50 % and 25 % engine loading for 0H ₂ -NG (a), 10H ₂ -NG (b), and 20H ₂ -NG (c) fuel blends	82
4.5	Manifold pressure (a) and flame-propagation period (b) at 75 %, 50 % and 25 % engine loading for 0H ₂ -NG, 10H ₂ -NG, and 20H ₂ -NG fuel blends at 500 mgN m ⁻³ of NO _x	83
4.6	Maximum in-cylinder pressure at 75 %, 50 % and 25 % engine loading for 0H ₂ -NG, 10H ₂ -NG, and 20H ₂ -NG fuel blends at 500 mgN m ⁻³ of NO _x	84
4.7	Engine efficiency at 500 mgN m ⁻³ of NO _x (a) and engine efficiency for varying NO _x values (b) at 75 %, 50 % and 25 % engine loading for 0H ₂ -NG, 10H ₂ -NG, and 20H ₂ -NG fuel blends	85
4.8	Carbon monoxide (a) and unburnt hydrocarbon (b) emissions at 75 %, 50 % and 25 % engine loading for 0H ₂ -NG, 10H ₂ -NG, and 20H ₂ -NG fuel blends at 500 mgN m ⁻³ of NO _x	86

4.9	Combustion efficiency at 75 % (a), 50 % (b) and 25 % (c) engine loading for 0H ₂ -NG, 10H ₂ -NG, and 20H ₂ -NG fuel blends, and varying air-excess ratios	87
4.10	Effect of spark-timing on air-excess ratio (a) and maximum in-cylinder pressure (b) at 75 % engine loading for 10H ₂ -NG fuel blend and 500 mgNm ⁻³ of NO _x	88
4.11	Effect of spark-timing on engine efficiency at 75 % engine loading for 10H ₂ -NG fuel blend and 500 mgNm ⁻³ of NO _x	88
4.12	Engine efficiency at 75 %, 50 % and 25 % engine loading for CO ₂ -NG fuel blend and 500 mgNm ⁻³ of NO _x (a). Engine efficiency at 75 % engine loading for CO ₂ -NG blends and their corresponding ONG performance measurements (b)	90
4.13	Coefficient of variations in IMEP averaged for 145 consecutive cycles at 75 % (1), 50 % (b) and 25 % (c) engine loading for 10CO ₂ -NG and 20CO ₂ -NG fuel blends. Coefficient of variations in IMEP at 75 % engine loading for 05CO ₂ -NG, 10CO ₂ -NG and 15CO ₂ -NG fuel blends and their corresponding ONG performance measurements (d)	92
4.14	Operating window at 75 %, 50 % and 25 % engine loading for 10CO ₂ -NG (a) and 20CO ₂ -NG (b) fuel blends	93
4.15	Manifold pressure at 75 %, 50 % and 25 % engine loading for CO ₂ -NG fuel blend and 500 mgNm ⁻³ of NO _x (a). Manifold pressure at 75 % engine loading for CO ₂ -NG blends and their corresponding ONG performance measurements (b)	94
4.16	Maximum in-cylinder pressure at 75 %, 50 % and 25 % engine loading for CO ₂ -NG fuel blend and 500 mgNm ⁻³ of NO _x (a). Maximum in-cylinder pressure at 75 % engine loading for CO ₂ -NG blends and their corresponding ONG performance measurements (b)	95
4.17	Unburnt hydrocarbon emissions at 75 %, 50 % and 25 % engine loading for CO ₂ -NG fuel blend and 500 mgNm ⁻³ of NO _x (a). Unburnt hydrocarbon emissions at 75 % engine loading for CO ₂ -NG blends and their corresponding ONG performance measurements (b)	95
4.18	Carbon monoxide emissions at 75 %, 50 % and 25 % engine loading for CO ₂ -NG fuel blend and 500 mgNm ⁻³ of NO _x (a). Carbon monoxide emissions at 75 % engine loading for CO ₂ -NG blends and their corresponding ONG performance measurements (b)	96
4.19	Combustion efficiency at 75 %, 50 % and 25 % engine loading for CO ₂ -NG fuel blend and 500 mgNm ⁻³ of NO _x (a). Combustion efficiency at 75 % engine loading for CO ₂ -NG blends and their corresponding ONG performance measurements (b)	96
5.1	Development cycle of simulation model [44, 45]	105
5.2	Combustion modelling methodology	106
5.3	HRR model simulation of average in-cylinder temperature (a) and normalized reaction co-ordinate (b) for 10H ₂ -NG fuel blend at 375 kWe load and 500 mgNm ⁻³ NO _x	111

5.4	Definition of five-stage Seiliger process with in-cylinder pressure-volume diagram (a) and outline of combustion characterization procedure using the Seiliger process (b)	112
5.5	Outline of the combustion characterization procedure using Wiebe modelling	115
5.6	Comparison between measured and simulated (Wiebe) normalized reaction co-ordinate for 10H ₂ -NG fuel blend at 75 % engine load and 500 mgN m ⁻³ of NOx	115
5.7	Comparison between measured and simulated (Seiliger) in-cylinder pressure (a) and in-cylinder temperature (b) for 10H ₂ -NG fuel blend at 75 % engine load and 500 mgN m ⁻³ of NOx	117
5.8	Comparison between measured and simulated (Wiebe) in-cylinder pressure (a) and in-cylinder temperature (b) for 10H ₂ -NG fuel blend at 75 % engine load and 500 mgN m ⁻³ of NOx	119
5.9	Normal (a) and zoomed-in (b) in-cylinder pressure variations using the Seiliger-based characterization for different H-NG fuel blends (0H ₂ -NG, 10H ₂ -NG) and NOx values (500 mgN m ⁻³ , 250 mgN m ⁻³ of NOx) at 75 %	121
5.10	Normal (a) and zoomed-in (b) in-cylinder temperature variations using the Seiliger process characterization for different H ₂ -NG fuel blends (0H ₂ -NG, 10H ₂ -NG) and NOx values (500 mgN m ⁻³ , 250 mgN m ⁻³ of NOx) at 75 %	122
5.11	Normal (a) and zoomed-in (b) normalized reaction co-ordinate variations using the Wiebe modelling characterization for different H ₂ -NG fuel blends (0H ₂ -NG, 10H ₂ -NG) and NOx values (500 mgN m ⁻³ , 250 mgN m ⁻³ of NOx) at 75 %	125
5.12	Normal (a) and zoomed-in (b) non-dimensional combustion rate variations using the Wiebe modelling characterization for different H ₂ -NG fuel blends (0H ₂ -NG, 10H ₂ -NG) and NOx values (500 mgN m ⁻³ , 250 mgN m ⁻³ of NOx) at 75 %	126
5.13	In-cylinder pressure (a) and temperature (b) variations using Wiebe characterization process for different H ₂ -NG fuel blends (0H ₂ -NG, 10H ₂ -NG) and NOx values (500 mgN m ⁻³ , 250 mgN m ⁻³ of NOx) at 75 %	126
5.14	Three-dimensional surface representation of the delta in Seiliger parameters 'a', 'b' and 'c' as a function of the normalized natural gas fuel mass and the volumetric hydrogen percentage	128
5.15	Three-dimensional surface representation of the delta in Wiebe combustion shape parameters 'm ₁ ' (a), 'm ₂ ' (b), CD ₁ (c) and CD ₂ (d) as a function of the normalized natural gas fuel mass and the volumetric hydrogen percentage	130
5.16	HRR model simulation of normalized reaction co-ordinate for 20CO ₂ -NG fuel blend and ONG at 375 kWe load and 500 mgN m ⁻³ NOx	132
5.17	Flame-propagation period at 75 %, 50 % and 25 % engine loading for CO ₂ -NG fuel blends and 500 mgN m ⁻³ of NOx (a). Flame-propagation period at 75 % engine loading for CO ₂ -NG blends and their corresponding ONG performance measurements (b)	133

5.18	Delta in combustion duration for primary combustion at 75 %, 50 % and 25 % engine loading for CO ₂ -NG fuel blends and 500 mgNm ⁻³ of NO _x relative to their corresponding ONG performance simulations using the HRR model	133
5.19	Comparison between measured and simulated (Seiliger) in-cylinder pressure (a) and in-cylinder temperature (b) for 20CO ₂ -NG fuel blend at 50 % engine load and 500 mgNm ⁻³ of NO _x	135
5.20	In-cylinder pressure (a) and in-cylinder temperature (b) variations for 20CO ₂ -NG and 0CO ₂ -NG fuel blend at 50 % engine load and 500 mgNm ⁻³ of NO _x	136
5.21	In-cylinder pressure (a) and in-cylinder temperature (b) variations for 20CO ₂ -NG fuel blend at 50 % engine load and different NO _x values (500 mgNm ⁻³ , 200 mgNm ⁻³) of NO _x	137
5.22	Three-dimensional surface representation of the delta in Seiliger parameters 'a', 'b' and 'c' as a function of the normalized natural gas fuel mass and the volumetric carbon dioxide percentage	139
6.1	Comparison between measured and simulated in-cylinder pressure (a) and temperature (b) using the Seiliger process modelling approach for 20H ₂ -NG fuel blend at 75 %	153
6.2	Comparison between measured and simulated in-cylinder pressure (a) and temperature (b) using the Seiliger process modelling approach for 20CO ₂ -NG fuel blend at 50 % load	156
6.3	Comparison between measured and simulated in-cylinder pressure (a) and temperature (b) using the Seiliger process modelling approach for 15 %H ₂ -15 %CO ₂ -70 %NG fuel blend at 75 % load	158
6.4	Schematic representation of AOG-NG mean value engine model	159
6.5	Exhaust receiver temperature (a) and pressure before the throttle, manifold pressure and the air-excess ratio (b) for only natural gas, 20H ₂ -NG and 20CO ₂ -NG fuel blend at 100 % engine loading and 500 mgNm ⁻³	171
7.1	Simulated efficiencies (a) and power outputs (b) for SOFC-ICE integration at different current densities with total system power output of 750 kW	177
7.2	Simulated efficiencies (a) and power outputs (b) for SOFC-ICE integration at different pre-reforming ratios with total system power output of 750 kW	178
7.3	Simulated efficiencies of SOFC-ICE integration for different fuel utilizations at system power output of 750 kW. Appendix E provides an example of efficiency calculation of the SOFC-ICE integration for the test condition depicted with a dashed vertical line in the above figure corresponding to 80 % fuel utilization	180
7.4	Heat management for SOFC-ICE integration with 50-50 power split at 80 % fuel utilization and total power output of 750 kW. P.H.: Preheater, S.H. Superheater, C.O.: Condensor, EVA: Evaporator, ECO: Economiser	181
7.5	Simulated efficiencies (a) and emission reductions [%] of SOFC-ICE integration at different power splits with a total system power output of 750 kW. All emissions are calculated in gkW ⁻¹ h ⁻¹	187

7.6	0-D SOFC model verification in simulating dynamic response. Normalized SOFC voltage and PEN temperature response for change in current density from 5000 to 7000 A m^{-2} . The simulation output of the 0-D SOFC model is compared against results reported in [17]	189
7.7	Comparison between the dynamic response of SOFC (a) and ICE (b) for load change from 250 to 375 kWe. In (a) response of fuel cell voltage and AC power output have been plotted. ' i_r ' is the current density ramp rate measured in $\text{A m}^{-2} \text{ min}^{-1}$	191
7.8	Comparison between the dynamic response of ICE operating on only natural gas and 10 H_2 -NG blend for a load change from 250 to 375 kWe. O_2 % in exhaust and NOx in mg N m^{-3} at 5 % O_2 reference (a). Corresponding engine speed and power response (b)	193
7.9	Comparison between pressure before throttle response of ICE operating on only natural gas and 10 H_2 -NG blend for a load change from 250 to 375 kWe	194
7.10	Comparison between the knocking frequencies recorded for only natural gas and 10 H_2 -NG fuel blends (a); and only natural gas and 20 CO_2 -NG blends at 250 kWe load and 500 and 3000 mg N m^{-3} of NOx	195
7.11	Load sharing between the components for SOFC-ICE integration (a) Projected efficiency based on the FFb method (b) at different ships speeds	198
8.1	Research methodology to study the effects of static back pressure	206
8.2	Measurement setpoints along the propeller curve	207
8.3	Outline of test setup along with the butterfly valve and sensor placement	208
8.4	Extended mean value engine model [8, 9]	209
8.5	Measured turbine inlet pressure pulse	211
8.6	Simplified (Step function) turbine inlet pressure pulse [17]	211
8.7	Correction factors α and β as a function of the pulse factor suggested by Zinner, according to Stapersma [10, 17]	212
8.8	Discretization of measured turbine inlet pressure pulse at 340 kW and 981 rpm	213
8.9	Comparison between measured and simulated inlet receiver pressure (a), and air mass flow rate (b)	215
8.10	Comparison between measured and simulated inlet receiver temperature (a), and turbocharger speed (b)	216
8.11	Comparison between α , β values obtained from simulation (s) and values calculated from measurements (m)	217
8.12	Comparison between measured and simulated values of lowest turbine inlet pressure	218
8.13	Comparison between measured and simulated turbine inlet (a), and outlet temperatures (b)	219
8.14	Back pressure effect on turbocharger speed based on measurements (m) and simulations (s)	220
8.15	Back pressure effect inlet receiver pressure based on measurements (m) and simulations (s)	221

8.16 Back pressure effect on air mass-flow rate based on measurements (m) and simulations (s) 221

8.17 Back pressure effect on fuel consumption based on measurements (m) and simulations (s) 222

8.18 Back pressure effect on turbine inlet temperature based on measurements (m) and simulations(s) 223

8.19 Simulated load and engine rpm points (blue points) along with engine envelope (black line) 224

8.20 Static engine map with lines of constant air-excess ratio (a), and lines of constant charge pressure (b) for a 100 degree valve overlap constant pressure turbocharged engine 225

8.21 Static engine map with lines of constant exhaust valve temperature (a) and constant exhaust receiver temperature (b) for a 100 degree valve overlap constant pressure turbocharged engine 226

8.22 Back pressure effect on air-excess ratio (a) and exhaust valve temperature (b) of a constant pressure turbocharged engine with 100 degree valve overlap 227

8.23 Back pressure effect on air-excess ratio (a), and exhaust valve temperature (b) of a constant pressure turbocharged engine with 30 degree valve overlap 228

8.24 Comparison between inlet receiver pressure (a) and air mass-flow rate (b) delivered by a pulse turbocharger and constant pressure turbocharger with a 30 degree valve overlap engine 229

8.25 Back pressure effect on air-excess ratio (a) and exhaust valve temperature (b) of a pulse pressure turbocharged engine with 30 degree valve overlap . 230

8.26 Possible exhaust outlet positions relative to a sea wave (a) and a representation of the external back pressure wave corresponding to underwater exhaust system at position 2 (b) 232

8.27 Measurement setpoints along the propeller curve 233

8.28 Angle and time input of a sinusoidal waveform for the butterfly valve (a) and the corresponding back pressure wave produced (b) 234

8.29 Applied single back pressure wave of 0.45 mWC pressure amplitude with a 6 seconds wave period at 340 kW load 236

8.30 Measured effect on inlet receiver pressure due to the applied single back pressure wave of 0.45 mWC pressure amplitude with 6 seconds wave period at 340 kW load 236

8.31 Measured effect on turbine inlet temperature (a) and outlet temperature (b) due to the applied single back pressure wave of 0.45 mWC pressure amplitude with 6 seconds wave period at 340 kW load 237

8.32 Applied single back pressure wave (a) of 0.25 mWC pressure amplitude with 6 seconds wave period at 340 kW load and its effect on exhaust receiver temperature (b) 237

8.33 Measured maximum increase in exhaust receiver temperature due to a single back pressure wave of 0.25 mWC and 0.45 mWC pressure amplitude with 6 seconds wave period at varying engine loads along the propeller curve 238

8.34 Applied multiple back pressure wave (a) of 0.45 mWC pressure amplitude with 6 seconds wave period at 340 kW and its effect on exhaust receiver temperature (b)	239
8.35 Applied multiple back pressure wave (a) of 0.35 mWC pressure amplitude with 6 seconds wave period at 340 kW and its effect on exhaust receiver temperature (b)	240
8.36 Measured maximum increase in exhaust receiver temperature due to multiple back pressure wave of 0.35 mWC and 0.45 mWC pressure amplitude with 6 seconds wave period at varying engine loads along the propeller curve	240
8.37 Applied single back pressure wave (a) of 0.45 mWC pressure amplitude with 4 seconds wave period at 340 kW and its effect on exhaust receiver temperature (b)	241
8.38 Applied single back pressure wave (a) of 0.45 mWC pressure amplitude with 8 seconds wave period at 340 kW and its effect on exhaust receiver temperature (b)	241
8.39 Measured maximum increase in exhaust receiver temperature due to a single back pressure wave of 0.45 mWC pressure amplitude with 4 and 8 seconds wave period at varying engine loads along the propeller curve	242
8.40 Applied multiple back pressure wave (a) of 0.45 mWC pressure amplitude with 4 seconds wave period at 340 kW and its effect on exhaust receiver temperature (b)	243
8.41 Applied multiple back pressure wave (a) of 0.45 mWC pressure amplitude with 8 seconds wave period at 340 kW and its effect on exhaust receiver temperature (b)	243
8.42 Measured maximum increase in exhaust receiver temperature due to multiple back pressure waves of 0.45 mWC pressure amplitude with 4 and 8 seconds wave period at varying engine loads along the propeller curve . .	244
8.43 Measured maximum increase in exhaust receiver temperature due to static back pressure of 0.30 and 0.435 mWC pressure amplitude at varying engine loads along the propeller curve	245
8.44 Measured percentage increment in fuel flow due to static back pressure of 0.30 and 0.435 mWC pressure amplitude at varying engine loads along the propeller curve	246
B.1 Variability in repeated measurements of natural gas flowrate, manifold pressure and manifold temperature for the three test cases of ONG at 25 % load (a-c), 20H ₂ -NG at 50 % load (d-f) and 05CO ₂ -NG at 75 % load (g-i) at different NO _x emissions. Legend: (marker: o, linetype: dashed, colour: blue) represents mean value; (marker: plus, linetype: dashed, colour: red) represents +5 % deviation from mean; (marker: square, linetype: dashed, colour: black) represents -5 % deviation from mean; (marker: star, colour: blue) represents measurement set 1; (marker: star, colour: green) represents measurement set 2; (marker: star, colour: red) represents measurement set 3	272

B.2	Variability in repeated measurements of exhaust oxygen, carbon monoxide and unburnt hydrocarbons for the three test cases of ONG at 25 % load (a-c), 20H ₂ -NG at 50 % load (d-f) and 05CO ₂ -NG at 75 % load (g-i) at different NO _x emissions. Legend: (marker: o, linetype: dashed, colour: blue) represents mean value; (marker: plus, linetype: dashed, colour: red) represents +5 % deviation from mean; (marker: square, linetype: dashed, colour: black) represents -5 % deviation from mean; (marker: star, colour: blue) represents measurement set 1; (marker: star, colour: green) represents measurement set 2; (marker: star, colour: red) represents measurement set 3	273
C.1	Normalized reaction co-ordinate for 0H ₂ -NG fuel blend at 24°C CA bTDC spark-timing, 375 kWe engine loading and 500 mgN m ⁻³ NO _x with no TDC shift (a) and -0.9°C CA TDC shift	275
C.2	Non-dimensional combustion rate for increasing value of m ₂ (a) and m ₂ (b) while other Wiebe combustion parameters are fixed at value found for 10H ₂ -NG fuel blend, 500 mgN m ⁻³ NO _x at 75 % engine load	281
C.3	In-cylinder pressure (a) and temperature (b) variations using the Seiliger characterization process for different spark-timings and 10H ₂ -NG fuel blend, 500 mgN m ⁻³ NO _x at 75 % engine load	283
C.4	In-cylinder pressure (a) and temperature (b) variations using the Wiebe characterization process for different spark-timings and 10H ₂ -NG fuel blend, 500 mgN m ⁻³ NO _x at 75 % engine load	283
D.1	Comparison between measured and simulated in-cylinder pressure (a) and temperature (b) using the Seiliger process modelling approach for 12.65 %H ₂ -12.65 %CO ₂ -74.7 %NG fuel blend at 75 % engine load	285
D.2	Comparison between measured and simulated in-cylinder pressure (a) and temperature (b) using the Seiliger process modelling approach for 9.2 %H ₂ -17.5 %CO ₂ -73.3 %NG fuel blend at 75 % engine load	285

LIST OF TABLES

3.1	Comparison between simulated and reference [7] cell temperatures and anode-off gas composition [Volume %]	67
3.2	Effect of fuel utilization on anode-off gas compositions [Volume %]	71
4.1	Marine NG test engine specifications	77
4.2	Typical natural gas composition	77
4.3	Tested Hydrogen-Natural gas fuel blends	79
4.4	Experimentally tested CO ₂ -NG blends for varying NO _x values.	89
5.1	Seiliger parameters and polytropic exponents for 10H ₂ -NG fuel blend at 75 % engine load and 500 mgN m ⁻³ NO _x	117
5.2	Error between the Seiliger combustion characterization simulation and measured values of performance parameters for 10H ₂ -NG fuel blend at 75 % engine load and 500 mgN m ⁻³ NO _x	118
5.3	Combustion heat ratios for different H-NG fuel blends (0H ₂ -NG, 10H ₂ -NG) and NO _x values (500 mgN m ⁻³ , 250 mgN m ⁻³ of NO _x) at 75 % engine load	118
5.4	Seiliger parameters for different H ₂ -NG fuel blends (0H ₂ -NG, 10H ₂ -NG) and NO _x values (500 mgN m ⁻³ , 250 mgN m ⁻³ of NO _x) at 75 % engine load	118
5.5	Derived Wiebe parameters for 10H ₂ -NG fuel blend at 75 % engine load and 500 mgN m ⁻³ NO _x	119
5.6	Error between the simulated (Wiebe) and measured values of performance parameters for 10H ₂ -NG fuel blend at 75 % engine load and 500 mgN m ⁻³ NO _x	119
5.7	Wiebe parameters for different H ₂ -NG fuel blends (0H ₂ -NG, 10H ₂ -NG) and NO _x values (500 mgN m ⁻³ , 250 mgN m ⁻³ of NO _x) at 75 % engine load	120
5.8	Error percentages between the Seiliger combustion characterization simulation and measured values of performance parameters for different H ₂ -NG fuel blends (0H ₂ -NG, 10H ₂ -NG) and NO _x values (500 mgN m ⁻³ , 250 mgN m ⁻³ of NO _x) at 75 % engine load	122
5.9	Error percentages between the Wiebe-based combustion characterization simulation and measured values of performance parameters for different H ₂ -NG fuel blends (0H ₂ -NG, 10H ₂ -NG) and NO _x values (500 mgN m ⁻³ , 250 mgN m ⁻³ of NO _x) at 75 % engine load	125
5.10	Tested hydrogen blend percentages and engine loads	128
5.11	Error percentages between the Seiliger combustion characterization simulation and measured values of performance parameters for different 20H ₂ -NG fuel blends and 500 mgN m ⁻³ NO _x at 75 %, 50 % and 25 % engine load	129

5.12	Error percentages between the Seiliger combustion characterization simulation and measured values of performance parameters for different 20H ₂ -NG fuel blends and 500 mgN m ⁻³ NO _x at 75 %, 50 % and 25 % engine load	131
5.13	Seiliger parameters and polytropic exponents for 20CO ₂ -NG fuel blend at 50 % engine load and 500 mgN m ⁻³ NO _x	135
5.14	Error between the Seiliger combustion characterization simulation and measured values of performance parameters for 20CO ₂ -NG fuel blend at 50 % engine load and 500 mgN m ⁻³ NO _x	135
5.15	Delta in Seiliger parameters for 20CO ₂ -NG fuel blend relative to the corresponding ONG operating condition at 50 % engine load and 500 mgN m ⁻³ NO _x	136
5.16	Error percentages between the Seiliger-based combustion characterization simulation and measured values of performance parameters for 0CO ₂ -NG fuel blends at NO _x value of 500 mgN m ⁻³ and 20CO ₂ -NG fuel blend at NO _x value of (200 mgN m ⁻³ at 50 % engine load	137
5.17	Tested carbon dioxide blend percentages and engine loads	138
5.18	Error percentages between the Seiliger-based combustion characterization simulation and measured values of performance parameters for 10CO ₂ -NG fuel blend at NO _x value of 500 mgN m ⁻³ and different engine loads	139
6.1	Parametric regression equation coefficients for only natural gas fuel	151
6.2	Part I: Parametric regression equation coefficients for H ₂ -NG fuel blends	152
6.3	Part II: Parametric regression equation coefficients for H ₂ -NG fuel blends	152
6.4	Derived Seiliger parameters based on combustion parameterization for 20H ₂ -NG fuel blend and 500 mgN m ⁻³ NO _x at 75 % load	152
6.5	Error percentages between the predicted and measured values of performance parameters 20H ₂ -NG fuel blend and 500 mgN m ⁻³ NO _x at 75 % load	152
6.6	Part I: Parametric regression equation coefficients for CO ₂ -NG fuel blends	154
6.7	Part II: Parametric regression equation coefficients for CO ₂ -NG fuel blends	154
6.8	Derived Seiliger parameters based on combustion parametrization for 20CO ₂ -NG fuel blend and 500 mgN m ⁻³ NO _x at 50 % load	155
6.9	Error percentages between the predicted and measured values of performance parameters 20CO ₂ -NG fuel blend and 500 mgN m ⁻³ NO _x at 50 % load	155
6.10	Tested AOG-NG fuel blends for 500 mgN m ⁻³ of NO _x at 75 % load	156
6.11	Derived Seiliger parameters and natural gas fuel mass based on combustion parameterization for ONG fuel and the three anode-off gas and natural gas fuel compositions provided in Table 6.10 at 500 mgN m ⁻³ NO _x and 75 % load	157
6.12	Error percentages between the predicted and measured values of performance parameters for the three anode-off gas and natural gas fuel compositions provided in Table 6.10 at 500 mgN m ⁻³ NO _x and 75 % load	158

6.13 Simulated engine efficiency and error percentages between the simulated and measured values of performance parameters for the three anode-off gas and natural gas fuel compositions provided in Table 6.10 at 500 mgN m ⁻³ NOx and 75 % load	170
7.1 Flow-rates of hydrogen and carbon dioxide present in SOFC anode-off gas for different fuel utilizations	179
7.2 Blend percentages and flow-rates of hydrogen and carbon dioxide (from SOFC anode-off gas) directed into the engine for different fuel utilizations	179
7.3 Efficiency improvement for different fuel utilizations obtained from the SOFC-ICE integration compared to the standalone ONG marine engine performance at 750 kWe	180
7.4 Areas of different heat exchanging elements for SOFC-ICE integration with 50-50 power split at 80 % fuel utilization and total power output of 750 kWe	185
7.5 Tested power splits (SOFC-ICE) with corresponding anode-off gas flow-rates in m ³ h ⁻¹	186
7.6 Anode-off gas flow compositions and flow-rates corresponding to the AOG-NG engine for the three test cases with varying power splits	186
7.7 Integrated SOFC-ICE system efficiency improvement and reduction for the three test cases of varying power splits compared to the standalone ONG marine engine performance and standalone SOFC at 750 kWe power output	188
7.8 Gravimetric and volumetric densities of a standalone engine and SOFC-ICE integration for four power splits including the three power splits presented in Table 7.5 with the same rated power outputs of 750 kWe. PS = SOFC-ICE power split	188
7.9 Summary of effects of SOFC control parameters on the efficiency of the SOFC, integrated AOG-NG engine and the SOFC-ICE power plant	200
8.1 Engine specifications	207
8.2 Values of α and β calculated from the discretization pulse	214
8.3 Wave data of varying wave heights and wave periods obtained from NDBC [38]	231
8.4 Wave data for experimentally simulated single and multiple back pressure waves	232
A.1 Geometrical properties data of single SOFC cell [1]	269
A.2 Physical properties data of single SOFC cell [1]	269
A.3 Electrode properties data of single SOFC cell [1]	270
A.4 Fit functions of molar specific enthalpy for temperature 700-1500 K [2]	270
B.1 Percentage deviations in performance parameters simulated by the Seiliger and Wiebe combustion characterization models for a simulated deviation of +/-3.04 % in in-cylinder pressure measurements for 10H ₂ -NG fuel blend and 500 mgN m ⁻³ NOx values at 75 % engine load	274

C.1	Parameters simulated by the Seiliger and Wiebe modelling approach. A: Available, NA: Not Available, AwHRR: Available with HRR model	276
C.2	Part 1: Error percentages between the Wiebe combustion characterization simulation and measured values of crank angle resolved parameters for 20H ₂ -NG fuel blend and 500 mgN m ⁻³ NOx values at 75 % engine load . .	277
C.3	Part 2: Error percentages between the Wiebe combustion characterization simulation and measured values of crank angle resolved parameters for 20H ₂ -NG fuel blend and 500 mgN m ⁻³ NOx values at 75 % engine load . .	277
C.4	Part 1: Error percentages between the Seiliger combustion characterization simulation and measured values of crank angle resolved parameters for 20H ₂ -NG fuel blend and 500 mgN m ⁻³ NOx values at 75 % engine load	278
C.5	Part 2: Error percentages between the Seiliger combustion characterization simulation and measured values of crank angle resolved parameters for 20H ₂ -NG fuel blend and 500 mgN m ⁻³ NOx values at 75 % engine load	278

SUMMARY

Even now, in the midst of the global COVID-19 pandemic, the shipping industry has continued to move vital cargo such as food supplies, medicines and medical equipment; thus, proving ships to be indispensable for global trade, economy and healthcare. Furthermore, the increase in global trade demands coupled with the rise of containerization and intelligent process automation is driving international shipping to continuously expand. Driven by economics and technology, future ships are projected to get bigger and increasingly intelligent, however, there is an urgent need for greener ships with lower environmental impact, as state-of-the-art ships typically use cheap and polluting fuels in rather conventional diesel engines.

At present, ships are responsible for significant contributions to greenhouse gas (GHG) and other harmful emissions such as nitrogen oxides (NO_x), sulphur oxides (SO_x) and particulate matter (PM) causing serious health risks and even premature deaths due to air pollution. Therefore, significant improvements in energy efficiency and reduction of ship-to-air emissions are essential. To address these concerns, the International Maritime Organization (IMO) has set up strict regulations for air pollutant emissions from ships while aiming to reduce the total annual GHG emissions from ships by at least 50% by 2050 compared to the GHG emissions in 2008. These emission regulations are difficult to meet with current marine diesel engines operating on conventional marine fuels such as HFO (Heavy Fuel Oil), MDO (Marine Diesel Oil) and MGO (Marine Gas Oil). Therefore, the maritime scientific community, together with the maritime industry, is researching alternative fuels and propulsion systems that will help improve energy efficiency and reduce emissions.

In this dissertation, prospective alternative maritime fuels are reviewed with regards to their production capacity, fuel costs, storage, safety (toxicity), technical feasibility and environmental impact. Based on the analysis, natural gas (NG), at least in the short term, is established as a very good choice of maritime fuel; especially if methane or unburnt hydrocarbon (UHC) emissions can be mitigated. Therefore, this PhD dissertation explores system integration opportunities for enhanced power generation onboard NG-fuelled ships as part of the GasDrive project. GasDrive is a novel maritime power plant concept that proposes a serial integration of a solid oxide fuel cell (SOFC) and an internal combustion engine (ICE) with underwater exhaust (UWE) system to achieve high system efficiency with ultra-low emissions. The underwater expulsion of exhaust gases is to allow for zero direct emissions to the atmosphere (emissions still exist) with the possibility of drag reduction via exhaust gas lubrication. This research investigates the feasibility and potential of a novel SOFC-ICE integration concept for maritime applications. In addition to SOFC-ICE integration, another focus of this research is to provide a comprehensive understanding of high static and dynamic back pressure effects on marine engine performance due to underwater exhaust systems. GasDrive, and the research presented in this thesis on NG-fuelled energy conversion devices, aims to pave the way

for the next generation of extremely efficient power plants onboard ships, operating on alternative marine fuels.

In this research, the review of existing literature on SOFC combined cycles shows that SOFC-ICE integration is focused on the application of advanced engine combustion technologies operating as bottoming cycles to generate a small load share, which leads to a typical SOFC-ICE power split of about 85-15 %. Although this may be a promising approach for land-based systems for maximum efficiency operation, this integration approach can pose challenges for ships such as restricted dynamic capabilities and large space and weight requirements of marine power plants. Furthermore, the potential of SOFC-ICE integration for marine power generation has not yet been explored. Consequently, the current work proposes a novel approach of SOFC-ICE integration for maritime applications, which allows for relatively high-efficiency power generation while the SOFC anode-off gas (AOG) is blended with natural gas (NG) and combusted in a (conventional, commercially existing) marine spark-ignited (SI) engine for combined power generation. The objective of this research is to investigate the impact of SOFC-ICE integration and UAE on engine performance and quantify the operation of the integrated SOFC-ICE system for maritime applications to demonstrate feasibility, energy efficiency improvements and emission reductions compared to conventional marine NG engines.

In this PhD research, a combined literature, experimental and simulation-based approach is adopted for a qualitative and quantitative investigation of SOFC-ICE integration. To simulate the SOFC performance along with the corresponding anode-off gas flow-rates and compositions, a zero-dimensional (0-D) cell-to-stack modelling approach is developed, which has been verified with results in the literature. With the known anode-off gas composition, effects of anode-off gas combustion are studied experimentally on a turbocharged, marine spark-ignited NG engine. This experimental investigation is used to further develop a methodology to build in-cylinder combustion models capable of capturing the effects of anode-off gas combustion. The in-cylinder combustion model capable of simulating anode-off gas effects is further combined with a mean value engine model (MVEM) to analyse the integrated SOFC-ICE system. The experiments, developed MVEM and the 0-D SOFC model are used to study the effects of integrated system variables (ISVs) such as SOFC current density, SOFC fuel utilization, engine fuel composition, SOFC-ICE power splits, etc. on SOFC-ICE integration with respect to feasibility, energy efficiency and emissions. Similar to SOFC-ICE integration, the effects of static and dynamic back pressure (an ISV as well) due to underwater exhaust systems on marine engine performance are studied by combining engine experiments with an extended mean value engine model.

The main findings of the dissertation are that an efficiency improvement of about 8 % can be gained for a 67-33 power split between the SOFC and the ICE while producing a total power output of 750 kWe. At the same time, UHC (methane) and NO_x emissions can be reduced by about 43 % and 60 % in comparison to a conventional marine natural gas engine. Furthermore, carbon dioxide (CO₂) emissions can be reduced by 20.74 %. However, the 67-33 power split also accounted for space and weight increments of approximately two and a half times. For more realistic and dynamic maritime applications, promising improvements in efficiency of 5.2 %, UHC and NO_x reductions of about 30 % and CO₂ reductions of about 12 % can be achieved from a 33-67 SOFC-ICE power split

with comparatively much smaller increments in size and weight of 1.7 times compared to a conventional marine natural gas engine. This research shows that significant enhancements in efficiency and reductions in emissions can be attained by integrating the SOFC with commercially existing engine technology. SOFC-ICE integration has further unexplored potential to achieve unprecedented efficiency improvements at part load operation for marine power generation. Furthermore, the study concludes that in the proposed SOFC-ICE system for maritime applications, a power split that favours the ICE would significantly improve the dynamic capabilities of the combined system and that the possible, and regularly encountered, sudden and large load changes can be met by the ICE.

Besides SOFC-ICE integration, the research performed in this PhD project also focussed on the effects of static and dynamic back pressure due to underwater exhaust systems on marine engine performance. Using the experimentally validated and extended MVEM, engine smoke limit and thermal overloading are investigated to define boundaries of acceptable back pressures for an engine. Furthermore, the MVEM simulation results show that a combination of pulse turbocharger system and small valve overlap can significantly improve the back pressure handling capabilities of engines. Interestingly, this research finds that the effects of dynamic back pressure fluctuations are not as severe as those found during static back pressure measurements. Therefore, a marine engine may be able to handle much higher levels of dynamic back pressures when operating with underwater exhaust systems in higher sea-states. If the underwater exhaust gas lubrication indeed lowers the ship resistance, as intended from the GasDrive project, the required power to be installed onboard a ship can be lowered, which will help in further reducing the fuel consumption and the space and weight requirements of the integrated SOFC-ICE system.

1

INTRODUCTION

1.1. CURRENT STATE OF SHIPPING



Figure 1.1: LNG-powered CMA CGM Jacques Saade container ship under construction [1]

In 2019, the global merchant fleet consisted of approximately 96300 shipping vessels contributing to 80% of global trade by volume [2]. The total volume of cargo to be traded via sea in 2021 is estimated to be 12.5 billion tons at the current annual growth rate of about 4% [3, 4]. Increasing global trade demands coupled with the rise of containerization and intelligent process automation are driving international shipping to continuously expand. With increasing seaborne trade, ships are growing in size and their cargo-carrying capacity. Figure 1.1 shows the CMA CGM Jacques Saade container ship under construction, which is currently the largest liquified natural gas (LNG) powered container ship of the world with a carrying capacity of 23000 TEU and length equivalent to 4 football fields [1]. The increase in ship supply capacity is surpassing the growth in demand, thus, changing the market balance with improvements in freight rates and earnings along with reduced costs of traded commodities. . Further driven by economics

Parts of this chapter have been published in Applied Energy [5]

and technology, intelligent unmanned ships are poised to alter the future of shipping [6, 7]. Unmanned ships will further contribute to enormous financial savings by circumventing human errors, improving financial margins due to reduced wages and reducing fuel costs with lighter fuel storage or extra cargo capacity [8, 9]. Therefore, future ships are projected to get bigger and increasingly intelligent, however, the shipping evolution is a trifecta as there is an urgent need for greener ships with significant improvements in energy efficiency and ship emissions.

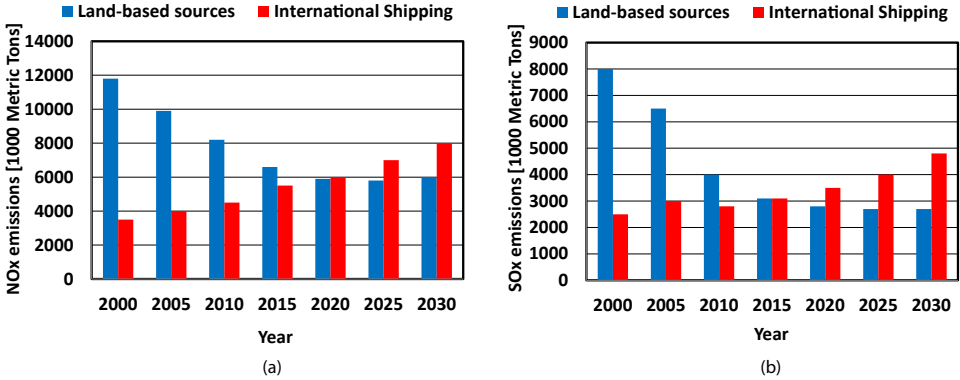


Figure 1.2: NOx (a) and SOx (b) emissions from land-based sources and international shipping for 1990-2030 (as estimated by a 2015 study [10])

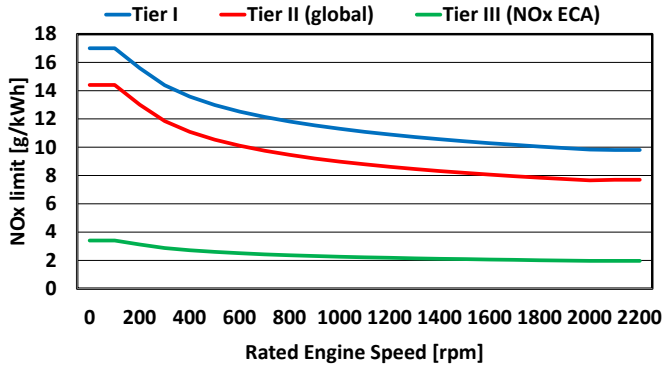


Figure 1.3: IMO TIER-III NOx emission regulations setup in January 2016 [11]

Ships are responsible for large portions of SOx and NOx emissions near coastal areas. As per a study in 2015 [10], by 2030, total NOx and SOx emissions from international trade ships around Europe were projected to surpass total land-based emissions from mobile and stationary power sources combined. Although a grim projection, ship emissions are expected to significantly reduce with the advent of strict emission regulations setup. However, the concerns related to ship emissions are of high consequence, since, in Europe alone, maritime emissions are estimated to be responsible for approximately 50,000 premature deaths per year due to air pollution [12]. In addition to NOx and SOx emissions, ships emit a significant amount of CO₂, unburnt hydrocarbon and black car-

bon (BC) emissions. It is estimated that CO₂ emissions from ships amount to about 3% of global CO₂ emissions while black carbon emissions from ships form about 2% of global BC emissions [13, 14]. Based on the 2016 emissions data provided by the International Maritime Organization, if the shipping industry were a country, it would be the sixth-largest emitter of CO₂ emissions with annual CO₂ emissions more than that of Germany [15]. CO₂ and BC emissions from ships not only contribute to but also accelerate global warming effects as ships operating close to the poles increase ice melting through black carbon depositions on ice and snow.

To address these concerns, the International Maritime Organization (IMO) has set up strict limits on ship emissions. Figure 1.3 shows the IMO Tier-III regulations for NO_x emissions which were applied from January 2016 in NO_x Emission Control Areas (ECAs). Similarly, by 2020, the sulfur content in maritime fuels will be globally restricted below 0.5%, which will help in drastically reducing SO_x emissions as they are directly linked to the sulphur content in fuel. Furthermore, IMO aims to reduce the total annual greenhouse gas (GHG) emissions from ships by at least 50% by 2050 compared to the GHG emissions in 2008 [16]. These emission regulations are difficult to meet with marine diesel engines operating on conventional marine fuels such as HFO (Heavy Fuel Oil), MDO (Marine Diesel Oil) and MGO (Marine Gas Oil). Therefore, the maritime industry is researching alternative fuels and propulsion devices that will help improve energy efficiency and reduce emissions to meet the strict emission regulations.

1.2. MARITIME FUELS

Over the past decades, technological advancements have helped reduce ship emissions and fuel consumption of the traditional marine diesel marine engines. However, the IMO Tier-III emission limits cannot be met by upgrading the diesel engines alone. Therefore, with the advent of strict emission regulations, the maritime industry is transitioning to cleaner and alternative fuels.

The choice of the future maritime fuel is governed by various parameters, of which the parameters considered most important are:

- Production capacity
- Fuel cost
- Storage
- Safety (assessed in terms of toxicity to humans)
- Technical feasibility (ease of employing a fuel in an energy conversion device)
- Environmental impact (assessed in terms of GHG or gCO₂-eqkm⁻¹ emissions)

Figure 1.4 compares the energy densities (including storage), current availability, cost estimates and carbon dioxide emissions of prospective maritime fuels relative to MGO. The fuel costs are calculated as US \$/MJ of energy available from fuel. The energy densities provided in Figure 1.4(a) include the weight and volume of the storage system. The production capacities of different fuels presented in Figure 1.4 are based on values found

for the period of 2018-2019. At the same time, the fuel costs are calculated based on data available for current production methods for the period of 2019-2020. This section summarizes the advantages and disadvantages/challenges associated with adopting each alternative fuel based on the above parameters.

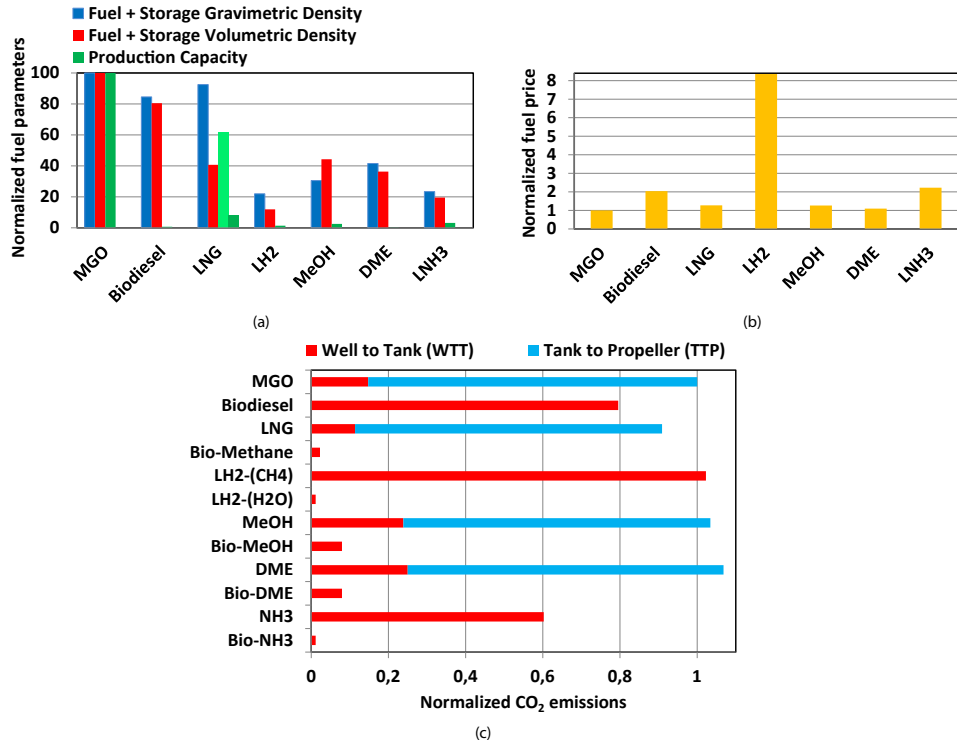


Figure 1.4: Relative comparison of estimated energy densities, production capacity (a), price (b) and total CO₂ emissions (c) of alternative maritime fuels. Calculations based on LHV, storage from [17–22], production capacity from [23–27] and fuel costs from [28–33]. The production capacities are calculated in Million Metric Tons (MMT), gravimetric energy density in MJkg⁻¹, volumetric energy density in MJL⁻¹ and fuel costs in US \$/MJ of energy available from fuel. The CO₂ emissions are in grams of equivalent carbon dioxide per kilometer (gCO₂-eqkm⁻¹) [34]. For any quantity and type of greenhouse gas (mainly CO₂ and CH₄), CO₂-eq depicts the carbon dioxide, which would have an equivalent global warming impact. Side notes: The light green bar in (a) signifies the production capacity of NG while the dark green bar signifies the global liquefaction capacity of NG. The production capacity for LH₂ in (a) is for only hydrogen, while its liquefaction capacity is expected to be lower. Similarly, the production capacity for LNH₃ in (a) is for only ammonia, while its liquefaction capacity is expected to be lower. LH₂-(CH₄) and LH₂-(H₂O) in (c) signify liquid hydrogen production from natural gas reforming and water electrolysis.

1.2.1. BIODIESEL

Diesel fuel produced from animal fats and vegetable oils is a renewable alternative to the conventional marine gas oil (MGO) or low sulphur diesel fuel oil.

- **Production capacity**

The present global production capacity of biodiesel is less than 1 % of MGO. The biggest challenge for the deployment of biodiesel or biofuel as a dominant marine fuel is the production capacity to be developed that will fulfil the requirements of the global maritime industry. It is estimated that to power the current global merchant fleet, the annual energy requirement is 7.3×10^{12} MJ [35]. To produce an equivalent amount of energy from biofuels derived from vegetable oils, a land area twice the size of United Kingdom is required [35]. This raises the moral and economical question of using the land for agriculture to fulfil the food production needs of the increasing world population. Increased competition for land between food and power production will affect food supply and prices. On the other hand, biofuel production from algae is a promising but nascent technology, which could ease the competition due to reduced landmass requirements. However, over the past decades biofuel production and government policies are majorly focused towards satisfying the road and air transport requirements further challenging the availability of biofuels for shipping
- **Fuel cost**

Biodiesel is the third most expensive alternative fuel.
- **Storage**

Besides being a renewable fuel, biodiesel has similar but lower gravimetric and volumetric energy densities compared to MGO.
- **Safety**

Biodiesel is safe to handle, store, and transport [36].
- **Technical feasibility**

Biodiesel can be combusted in marine diesel engines. It provides higher lubricity than conventional diesel fuel, thus, reducing engine wear with possible extension in life cycle. However, some drawbacks such as the adverse impact on fuel injection system due to high viscosity and density, deterioration of hoses and seals (natural rubber materials) and cold start may need further attention [37].

Biodiesel is not considered as a convenient fuel for fuel cells. Based on the type of fuel cell, various fuel processing steps may be needed to produce a sufficiently pure feed gas for the fuel cell [17].
- **Environmental impact**

Combustion of biodiesel leads to similar emissions as conventional diesel with some potential reductions in particulate matter [37]. Biodiesel, in general, produces higher NO_x emissions [38]. Furthermore, combustion of biodiesel produces no SO_x emissions due to absence of sulphur in fuel. Since biodiesel is produced from plant feedstock, CO₂ emissions released by the power plant to the atmosphere are not considered in total CO₂ emissions as seen from Figure 1.4(c). Figure 1.4 shows the equivalent CO₂ emissions for biodiesel produced from rapeseed oil. However, the total CO₂-eq emissions from biodiesel can drastically vary based on the production method [39]. Therefore, the total GHG emissions from biodiesel can be ultra-low or exceed those from LNG [39].

1.2.2. NATURAL GAS

- Production capacity

In early 2019, the global liquefaction capacity of natural gas (NG) was at 393 Million Metric Tons per Annum (MMTPA), which is higher than the production capacity of all the other alternative fuels [40]. Presently, natural gas has the highest production capacity compared to other alternative fuels.

- Fuel cost

Liquefied natural gas (LNG) is one of the most economical alternative fuels with costs similar to that of MGO.

- Storage

LNG is natural gas stored at -162°C (liquefaction temperature) in cryogenic tanks. Liquefaction of NG shrinks the gas to more than 600 times in volume. Therefore, liquefaction provides the highest energy density compared to other storage methods of natural gas, thus, making it the preferred choice for onboard fuel storage. LNG has the highest gravimetric energy density and third-highest volumetric energy density compared to other alternative fuels.

- Safety

LNG is a safe fuel [41, 42].

- Technical feasibility

An increasing LNG bunkering infrastructure, high energy density, low environmental impact, high production capacity and comparable fuel costs have enhanced the adoption of NG in dual-fuel and spark-ignited engines for maritime applications. Natural gas is also an ideal fuel for solid oxide fuel cells, which are a promising alternative to diesel engines for maritime applications.

- Environmental impact

CO_2 -eq emissions produced during lean-burn NG combustion are reduced by about 20%, with 90% reduction in NO_x emissions [43]. The total CO_2 -eq emissions due to LNG are currently lower than most of the alternative fuels while being lower than those from MGO as seen in Figure 1.4(c). Moreover, the production of bio-methane from biogas has the potential of drastically reducing GHG emissions [39].

Besides CO_2 and NO_x , emissions of SO_x and particulate matter are negligible or absent. However, combustion of natural gas leads to emissions of methane (methane slip), which has a higher global warming potential than carbon dioxide. Although there are no global emission regulations for methane, methane slip is identified as a challenge for large scale deployment of natural gas as a marine fuel [44].

1.2.3. HYDROGEN

- Production capacity

The current global hydrogen production capacity is close to (1.5%) of MGO.

- Fuel costs

Liquid hydrogen (LH_2) is drastically costlier than other alternative fuels.

- Storage

Hydrogen can be stored at high pressures of 350 or 700 bar. Additionally, it can be liquefied at -253°C and stored as liquid hydrogen in cryogenic tanks [19]. Compared to compressed hydrogen storage, liquid hydrogen has a higher energy density. However, its energy density is still the lowest compared to other alternative fuels as seen from Figure 1.4(a). The lowest energy density drastically increases its price per megajoule of available energy.

- Safety

Hydrogen is non-toxic and can be handled safely.

- Technical feasibility

Hydrogen is an ideal fuel for fuel cells, since the electrochemical oxidation kinetics are fast, even at low temperatures. Therefore, it can be used as a fuel in low and high-temperature polymer electrolyte membrane fuel cells (LT/HT-PEMFCs) without extensive pretreatment. Pure hydrogen used in PEMFCs can produce high-efficiency energy of (50% and higher) with only demineralised water as an emission. Natural gas can also be used as a hydrogen carrier in high-temperature solid oxide fuel cells (SOFCs), which have a much higher tolerance for impurities such as carbon monoxide and sulphur, unlike LT-PEMFCs. Hydrogen and fuel cells are very suitable for maritime applications because of advantages such as ultra-low or zero emissions, high energy efficiency, noiseless operation, modular design and good part load efficiencies. Hydrogen engines are also a promising prospect for the maritime industry due to ultra-low emissions under lean operating conditions along with the high reliability of low CAPEX engines.

- Environmental impact

Hydrogen is considered as the cleanest of alternative fuels. However, presently, it is mostly produced from natural gas via steam reforming, which contributes to excessively high CO_2 -eq emissions. The U.S Environmental Protection Agency estimated CO_2 emissions of 8.5 MMTPA for every 1 MMTPA of hydrogen produced from natural gas [45]. Alternatively and ideally, hydrogen can be also be produced from electrolysis of water, which produces almost no GHG emissions assuming renewable electricity production.

1.2.4. METHANOL

- Production capacity

Methanol is mostly produced from natural gas, by combining hydrogen and carbon dioxide. The production capacity of methanol is very low compared to MGO.

- Fuel cost

Methanol is an economical fuel for the amount of available energy due to the low overall cost of methanol, which is 1.414 \$/gallon compared to the 2.2 \$/gallon of MGO.

- Storage

The main advantage of methanol is that it is a liquid fuel at ambient pressure, thus, making storage and infrastructure adaptation relatively easier. However, its low gravimetric energy density is a disadvantage.

- **Safety**
Methanol is considered toxic in high concentrations. Liquid methanol can be absorbed through the skin or ingested in vapour form through the lungs [46].
- **Technical Feasibility**
Methanol (MeOH) is another alternative fuel that can be used in both fuel cells and engines for energy production. However, the performance of direct methanol fuel cells needs to be improved for widespread commercial acceptance [47]. On the other hand, methanol can be reformed and used as a hydrogen carrier in HT-PEMFCs [48]. Furthermore, MeOH can be also indirectly utilized in SOFCs for energy production, however, few studies have investigated MeOH performance in SOFCs [17]. Application of methanol in internal combustion engines (ICEs) is possible and is gathering significant research interest in the maritime industry [49]. However, methanol is corrosive to aluminium and iron parts used in engines.
- **Environmental impact**
Currently, methanol is mostly produced from natural gas, which leads to significantly high well to tank CO₂-eq emissions. Furthermore, the combustion of MeOH also contributes to high CO₂ emissions due to its low energy density. Therefore, the total CO₂ emissions of MeOH are higher than those of MGO. However, bio-methanol can significantly reduce the well to tank emissions while being considered as climate neutral [49]. SOx emissions from methanol are negligible. Moreover, MAN Diesel and Wärt-sillä have reported the NOx emissions from methanol combustion to be lower than the NOx emissions from diesel by 30 to 60 % respectively [49].

1.2.5. DIMETHYL ETHER

- **Production capacity**
The current production capacity of Dimethyl ether (DME) is the lowest amongst the different alternative fuel options, which hinders its prospects as a maritime fuel.
- **Fuel cost**
Contrary to this disadvantage of lowest production capacity, DME is an economical fuel to produce and deliver even more than diesel [50].
- **Storage**
DME is a liquid at a low pressure of 5 bar, similar to liquefied petroleum gas (LPG), which makes it relatively easier to store. However, DME has less than half the density of diesel fuel, thus, accounting for more than twice the weight and storage space compared to diesel fuel.
- **Safety**
DME is non-toxic.
- **Technical feasibility**
DME can be combined in an ICE for power generation onboard ships. To combust DME in diesel engines, modifications to the fuel system are required due to its low boiling point -24°C and low critical temperature of 127°C . Additionally, low density,

low lubricity and corrosiveness of DME are challenges that need further research for the economical application of DME in marine engines [35]. DME can be easily decomposed to methane, carbon monoxide and hydrogen at temperatures higher than 700°C for applications in high-temperature fuel cells. It can be used in SOFC systems designed for LPG without major modifications [51, 52].

- Environmental impact

DME combustion produces virtually no particular matter due to its lack of carbon-to-carbon bonds [53]. For the same injection quantity, NO_x production of DME is less compared to diesel combustion [54]. Like methanol, total CO₂-eq emissions per kilometer from DME are higher than that of ultra-low-sulfur diesel (USLD) fuel. [55] The higher total CO₂ emissions of DME could be attributed to the production of DME from natural gas or methanol and a similar energy density as methanol. DME can also be created from biomass feedstock as a renewable fuel, which would reduce its carbon footprint as seen from Figure 1.4(c).

1.2.6. AMMONIA

- Production capacity

The current production capacity of ammonia (NH₃) is very low compared to MGO, which needs to be expanded aggressively.

- Fuel cost

Cost of liquid ammonia (LNH₃) is the second-highest amongst the alternative fuels.

- Storage

Ammonia can be stored as a liquid at -33°C and atmospheric pressure or at slightly elevated pressures of 10 bar, which can ease storage requirements onboard ships. However, it has the second-lowest energy density, which is marginally higher than that of liquid hydrogen.

- Safety

Ammonia is a challenging fuel to handle due to its high toxicity [56].

- Technical feasibility

Ammonia is a hydronitrogen fuel rather than a hydrocarbon fuel such as natural gas or diesel. It can be combusted in an engine and used in a fuel cell for power generation with carbon-free emissions. However, ammonia combustion is unstable at low loads due to its low flame propagation speed. Therefore, the low combustion rate of ammonia is enhanced by blending it with combustion enhancing agents such as gasoline, diesel or hydrogen [56]. The combustion promoters are needed at low loads and/or high engine speeds. The required quantity of a combustion promotor can vary with load and speed fluctuations, thus, raising control challenges [57].

Ammonia is a hydrogen carrier with a higher energy density than any other hydrogen storage method. It can be cracked to release hydrogen for combustion enhancement inside engines or use in fuel cells. For use in PEMFCs, hydrogen has to be cracked externally; and traces of leftover ammonia can poison the anode catalyst

causing performance degradation [58]. On the other hand, it is possible to internally decompose ammonia in SOFCs due to operation at high temperatures; and it has not been shown to be poisonous to ceramic electrolytes utilized in SOFCs [59, 60]. Addition of combustion promoters and/or pretreatment devices for NH_3 cracking can increase system complexity and costs. However, the absence of carbon is a significant advantage, which has peaked the interest of researchers to test and improve the feasibility of ammonia in marine engines and fuel cells.

- Environmental impact

Ammonia combustion contributes to high NO_x emissions [56]. However, the NO_x emissions can be reduced with a Selective Catalytic Reducer (SCR), which requires ammonia for operation. SO_x emissions from ammonia are non-existent. If hydrogen is used as a combustion promoter, then ammonia combustion produces no CO_2 emissions. However, combustion of diesel with ammonia will lead to CO_2 emissions. Furthermore, ammonia is currently produced from hydrogen, which is produced from natural gas. Therefore, well to tank GHG emissions of ammonia are high. Based on current (non-renewable) production methods, ammonia has the lowest total CO_2 -eq emissions compared to other alternative fuels. Ammonia can be produced from renewable hydrogen, which would significantly reduce the total CO_2 emissions.

1.2.7. SUMMARY: THE GAS AGE

		MGO	Bio diesel	LNG	LH2	MeOH	DME	LNH3
Production capacity		●	●	●	●	●	●	●
Fuel cost		●	●	●	●	●	●	●
Gravimetric density		●	●	●	●	●	●	●
Volumetric density		●	●	●	●	●	●	●
Safety (Toxicity)		●	●	●	●	●	●	●
Technical feasibility		●	●	●	●	●	●	●
Env. impact	Current	●	NA	●	●	●	●	●
	Renewable	NA	●	●	●	●	●	●

Figure 1.5: Summarized comparison of maritime fuels. Green: Very good, light green: good, orange: poor, red: very poor and NA: not applicable. The CO_2 -eq emissions from biodiesel can vary based on production methods.

The above review of alternative maritime fuels has been summarized in Figure 1.5, which highlights the following key points. First, biodiesel has good energy density compared to other diesel substitutes, however, disadvantages such as extremely low availability, diesel-like emissions, high costs and competition with the global food supply chain in addition to other transportation modes hinder the potential of biodiesel fuel. Next, although methanol and DME are easy to store and economically favourable (DME),

challenges such as toxicity of methanol, currently limited production capacity and low energy densities restrict the global application of these fuels. All alternative fuels contribute to high GHG emissions based on current production methods. However, on a positive note, all of them have the potential of renewable production which can drastically reduce the GHG emissions.

Based on the current production method, hydrogen has the highest WTT CO₂-eq emissions and it is the costliest alternative fuel while Ammonia is possibly the most challenging fuel with high toxicity. Both hydrogen and ammonia, exhibit highly restricted availability with lowest energy densities. Natural gas currently poses the serious challenge of reducing GHG emissions linked to fugitive methane emissions. However, at present, natural gas is the only competitive alternative to marine diesel fuel with significant advantages over other alternative fuels such as highest production capacity, expanding infrastructure, lower costs, highest gravimetric energy density, non-toxicity, high technical feasibility, lower total CO₂ emissions and large reductions in SO_x, NO_x, and particulate matter. Therefore, although the development of alternative fuels is progressing, at this day and age, natural gas is the only feasible alternative to MGO.

Based on the above analysis and conclusive advantages over other alternative fuels, natural gas is established as a very good choice of maritime fuel. Therefore, this PhD dissertation explores system integration opportunities for enhanced propulsion of NG-fuelled ships as part of the GasDrive project. GasDrive is a Dutch national project funded in 2015 by the Netherlands Organisation for Scientific Research (NWO) under the Applied and Engineering Sciences (TTW) domain. GasDrive, and the research presented in this thesis on NG-fuelled energy conversion devices, aims to pave the way for the next generation of extremely efficient prime movers onboard ships, operating on alternative marine fuels, with ultra-low emissions.

1.3. GASDRIVE

In recent years, electrification and hybridisation of the marine powertrain is being widely investigated. At present, diesel engines operated in generator mode are the main source of electrical power generation in hybrid architectures. The onboard electricity requirements (auxiliary and propulsion) can also be met by fuel cells. Unlike the thermomechanical engines, fuel cells are electrochemical energy conversion devices capable of producing relatively higher efficiency electrical power with negligible or no NO_x production, vibrations and noise. Additionally, high modularity and good part load performance of fuel cells make them very attractive for maritime applications. The GasDrive project aims to develop a hybrid marine power generation system for NG fuelled ships by exploring system integration opportunities between a solid oxide fuel cell and an internal combustion engine. The title of the GasDrive project is as follows [61]:

GasDrive – Minimizing emissions and energy losses at sea with novel maritime fuels, combined prime movers, underwater exhausts and nano hull materials

GasDrive is a novel maritime power plant concept that proposes a serial integration of a SOFC and an internal combustion engine (ICE) with underwater exhaust (UWE) system to achieve high propulsion efficiency with ultra-low emissions. Figure 1.6 shows

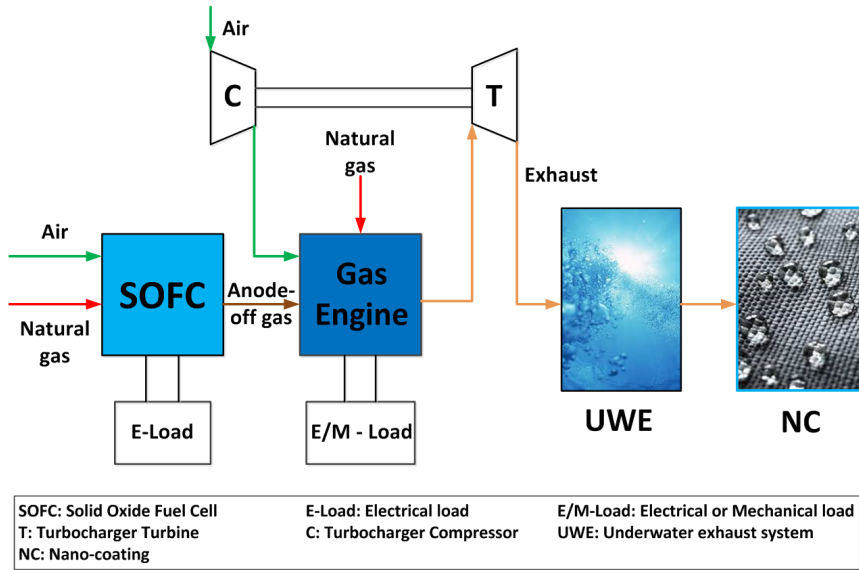


Figure 1.6: Schematic representation of GasDrive concept

the schematic representation of the GasDrive concept. As seen from Figure 1.6, the SOFC will provide electrical power, and the anode-off gas (gas at fuel cell exhaust) is used in the engine to deliver additional electrical or mechanical power as part of the electrical or hybrid power generation architecture. In the GasDrive concept, the exhaust gases are expelled below the waterline, which is captured by nano-hull coatings to reduce ship drag. Drag reduction is expected to further reduce fuel consumption due to depreciation in onboard power requirements. The GasDrive project proposal identified the following research challenge [61]:

Fully understanding the integration of the proposed innovations with one another is a significant challenge due to dynamic interactions between the individual components of the system. Therefore, in-depth knowledge of all components is required in order to study system feasibility and optimization of the system over entire operational profiles.

Motivated by the above challenge, the research performed in this PhD dissertation focusses on the performance integration of a solid oxide fuel cell and an internal combustion engine along with underwater exhaust system. PhD research on fundamental fuel cell performance to investigate reforming kinetics, and sulphur poisoning along with carbon-deposition is performed by Lindert van Biert and Jelle Stam of Delft University of Technology (TU Delft). The GasDrive work of Pim Bulle, of the University of Twente, aims to study the drag reduction possibilities by capturing the exhaust gases expelled under water using nano-hull coatings. Moreover, research of Yuzhu Wei, from the University of Wageningen, focusses on the effects of underwater exhaust on marine life. Lastly, Ali Haseltalab of TU Delft aims to develop control strategies for optimized energy management and power management of SOFC-ICE integration. In this manner, these

six research directions will address the complete scope of the GasDrive project.

1.3.1. THE WHY AND HOW OF SOFC-ICE INTEGRATION

Solid oxide fuel cells are high temperature (600°C to 1000°C) fuel cells with a negative oxygen ion-conducting solid electrolyte placed between an anode and cathode electrode. Unlike proton-exchange membrane or polymer electrolyte membrane fuel cells PEMFCs, the main advantage of SOFCs is the ability to readily use hydrocarbon fuels such as natural gas to generate electrical power with high efficiency. Standalone SOFCs have higher than 50% efficiency. They produce negligible NO_x emissions and mainly water at the anode along with ultra-low emissions of CO and significantly reduced emissions of CO₂ compared to marine diesel engines. The water produced at the anode can be utilized for reforming natural gas and/or to meet onboard water requirements. Furthermore, fuel cells are modular in design allowing for distributed power generation on ships. Thus, opening opportunities for optimized space utilization and enhanced reliability. These advantageous characteristics of SOFCs in addition to their ability to work with natural gas, make them well suited for NG fuelled ships.









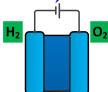







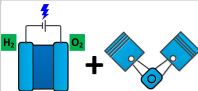







	Modular	Ultra-Low Emissions	Electrical Efficiency >50%	Net Water Production	High Power Density	High Dynamic Capabilities	Low CAPEX
							
							
							

Figure 1.7: Compatibility of solid oxide fuel cell and internal combustion engine. A green tick indicates an 'available attribute', red cross indicates a 'missing attribute' while an orange-brown tick indicates a 'bartered attribute' between SOFC and engine

However, SOFCs are bulky and heavy due to the excessive combined size of supplementary devices (Balance-of-Plant) such as pumps, blowers, combustor, etc. required for stable operation. The low power density of SOFCs poses a challenge due to stringent space and weight restrictions of ships. Furthermore, SOFCs also require considerably high capital expenditure compared to engines. The less favourable attributes of SOFCs such as low power density, limited dynamic capabilities and high CAPEX, presently, restrict the swift adoption of SOFC technology by the maritime industry. Interestingly, these unfavourable limitations of SOFCs are well compensated by reciprocating engines. Figure 1.7 reflects the compatibility of engines with solid oxide fuel cells.

A spark-ignited (SI) natural gas engine has 4 times the power density by weight and volume compared to SOFCs for a similar power output. In terms of cost comparisons,

an NG engine is far more economical than a state-of-the-art SOFC used for power generation. The dynamic load-taking capabilities of engines supplement and surpass those of SOFCs. The timescale for a load change by an engine is in the order of few tens of seconds, while SOFCs can take several hundred seconds to stabilize during a load change. In this manner, engines and SOFCs perfectly complement each other and, thus, an integration of these two energy conversion devices can be very attractive for the maritime industry. This potential of SOFC-ICE integration is identified and researched in this PhD thesis under the GasDrive umbrella.

In the proposed GasDrive power unit, the SOFC operates on natural gas to produce high-efficiency electrical power. The reaction processes at the anode of the fuel cell produce electrons in addition to the anode-off gas (AOG), i.e., a mixture of hydrogen, carbon monoxide, carbon dioxide and water vapour. After water condensation, this anode-off gas contains waste energy in the form of hydrogen and carbon monoxide, which can be combusted in an engine for additional power generation, thus, enhancing propulsion efficiency and system performance through integration. However, the presence of reactive hydrogen and carbon monoxide with inert carbon dioxide in the anode-off gas can significantly impact engine performance and even limit the potential of SOFC-ICE integration. Consequently, the overall challenge is to employ the optimal amount of anode-off gas for enhanced marine NG engine performance in addition to achieving high-efficiency SOFC operation for successful integration of the proposed SOFC-ICE power generation system. Therefore, there is a need for detailed and validated research to study and develop the SOFC-ICE integration for maritime applications, which forms the core of this PhD research. The need and novelty of the research presented in this dissertation are further warranted by the lack of investigations in existing literature on SOFC-ICE integration for maritime applications as the existing literature on SOFC combined cycles is limited and focussed towards distributed power generation.

1.3.2. THE ROLE AND CHALLENGE OF UNDERWATER EXHAUST

The GasDrive concept employs underwater expulsion of exhaust gases to allow for zero direct emissions to the atmosphere (emissions still exist) with the possibility of drag reduction via exhaust gas lubrication. The drag reduction could lead to further reduction in fuel consumption and carbon dioxide emissions. Underwater exhaust systems also provide various advantages such as space saving, and reduction in noise, exhaust gas odor and pollution on working decks. Other advantages of expelling underwater are reduced hotspot detection risks for naval ships and improved aesthetics of luxury ships due to the elimination of bulky and unappealing vertical exhaust funnels that pass through decks. These advantages of underwater exhaust (UWE) systems can be visualised from Figure 1.8, which compares the schematic representations of the conventional above-water (highlighted in blue) and the unconventional underwater exhaust system (highlighted in red) for ships.

Underwater expulsion of exhaust gases has many advantages, however, the water or the sea waves at the outlet of the submerged exhaust impose a high and fluctuating resistance or back pressure to the exhaust gas flow of the engine. This high and dynamic back pressure can reduce the operating limits of an engine, increase fuel consumption, increase thermal loading and also lead to exhaust smoke. For successful implementa-

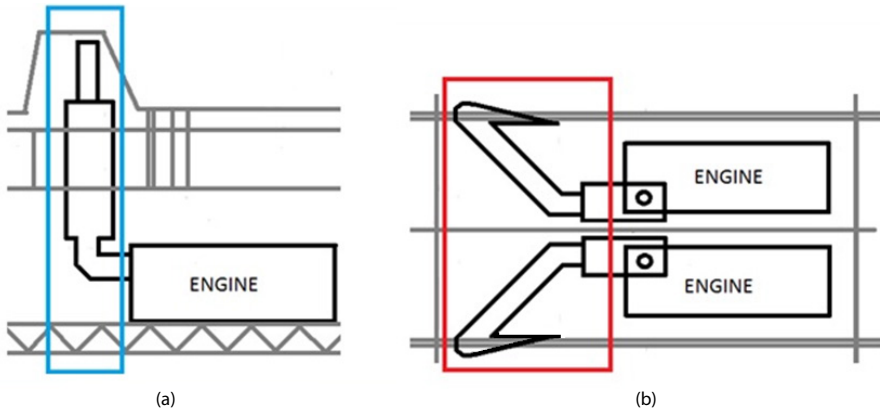


Figure 1.8: A schamtic representation of the conventional above-water exhaust system (from sideview) (a) and underwater exhaust system (from topview) (b)

tion of UWE to allow for gas lubrication in the GasDrive concept, it is crucial to quantitatively and qualitatively capture the effects of back pressure on marine engine operation. Therefore, in addition to SOFC-ICE integration, another focus of this research is to provide a comprehensive understanding of high static and dynamic back pressure effects on marine engine performance. In this dissertation, an experimental and simulation-based investigation is performed to study the marine diesel engine performance against static and dynamic back pressure due to underwater exhaust systems, which has been presented in Chapter 8.

1.4. SHORT LITERATURE OVERVIEW

In this dissertation, a literature survey has been presented for four different topics, namely, SOFC combined cycles, engine experiments with anode-off gas constituents, engine modelling and effects of static and dynamic back pressure on marine engine performance due to underwater exhaust systems. Although these topics are well integrated in GasDrive, they are independent topics that require an individual focus on existing literature followed by research on each topic. Therefore, the current literature on each topic has been covered in different chapters to provide a good progression of the storyline presented in this dissertation. In this section, a concise overview of each literature survey has been presented along with questions that remain unanswered and, thus, need further investigation.

- **SOFC combined cycles**

In recent years, a number of researchers have investigated SOFC combined cycles to capitalize on the enhanced efficiency and low emission SOFC operation [62–65]. For instance, SOFC-Gas turbine (GT) systems have been widely studied, which employ the SOFC for high-efficiency electrical power generation while the SOFC anode-off gas is combusted and expanded in a turbine for additional power output [66]. Similarly, SOFCs are combined with a steam turbine as SOFC anode-off gas is combusted to raise

the heat for high-pressure steam generation, which is expanded in the steam turbine (ST) to produce extra electrical power [67]. The SOFC-GT and SOFC-ST combined cycles promise high-efficiency power generation. An alternative high-efficiency SOFC combined power generation system is the integration of SOFC with a reciprocating internal combustion engine (ICE) [65].

The majority of SOFC combined cycles presented in current literature employ the GT/ST/ICE in the downstream of the fuel cell as a bottoming cycle, which consumes the unreacted fuel or SOFC anode-off gas to produce a small load share of the system power output. However, numerous challenges such as the poor part load performance, limited load transients, complex control management requirements complex architecture, high space and weight considerations, etc. can restrict the commonly investigated bottoming cycle approach for SOFC-ICE integration from a maritime perspective. Thus, raising questions pertaining to the suitability of the bottoming cycle approach for SOFC-ICE integration to generate power onboard ships. Chapter 2 of this dissertation presents a detailed literature analysis of the SOFC combined cycles discussed in current literature while highlighting the lack of knowledge and potential of SOFC-ICE integration for maritime applications.

The handful of studies on SOFC-ICE combined cycles in existing literature mainly employ advanced combustion engine technologies such as homogenous charge compression ignition (HCCI) or reactivity controlled compression ignition (RCCI) for combustion of anode-off gas to generate additional engine power [65, 68]. Chapter 2 presents the literature on SOFC-ICE integration with advanced combustion engine technology adopted as part of a bottoming cycle to achieve high efficiencies for distributed power generation. However, HCCI and RCCI engines are not commercially ready engine technologies with a number of combined challenges such as heat release control for stable combustion, extension of operating range, low exhaust temperatures requiring high turbocharger efficiencies and improvements in after-treatment systems to operate with the low exhaust temperatures. Therefore, the current work investigates SOFC integration with a commercially available, and conventional marine SI natural gas engine.

- [Engine experiments on AOG constituents](#)

Even though the effects of combusting SOFC anode-off gas in an advanced combustion technology engine have been experimentally studied by Choi et al. [68] and Chuahy et al. [65]. The effects of anode-off gas combustion on the performance of a marine SI natural gas engine will be significantly different due to differences in operation, engine design, combustion process, etc. Furthermore, the presence of reactive hydrogen and high percentages of carbon dioxide in AOG can significantly impact, even limit, the engine performance and SOFC-ICE integration. Therefore, questions pertaining to the impact of AOG constituents on the combustion process, combustion stability, efficiency, emissions, operating limits and performance of a marine SI NG engine need further research. Subsection 2.4.1 and subsection 2.4.1 of Chapter 2 cover the literature survey on experimental investigations of combusting anode-off gas constituents.

- [Engine modelling](#)

The combustion of anode-off gas constituents such as hydrogen and carbon dioxide in a marine SI NG engine can drastically affect various aspects of engine operation. While combustion modelling of hydrogen and carbon dioxide has been investigated before, mostly using CFD models, the literature on combustion characterization models of SOFC anode-off gas constituents, especially for the application of marine, lean-burn, SI NG engines is highly limited. Therefore, to study the impact of varying engine fuel compositions, there is a need for models that can capture the variations in the combustion and in-cylinder process due to different anode-off gas compositions from the SOFC in a marine SI NG engine.

In addition to the in-cylinder process, combusting anode-off gas of varying quality and quantity can also affect exhaust temperatures, turbocharging, heat integration with the SOFC, engine load response, efficiency and emissions. To study the impact of variables such as AOG quality and quantity, engine fuel composition, air-excess ratios and load-sharing, it is vital to develop engine models capable of capturing the details of the in-cylinder and combustion process while simulating the complete engine performance. Therefore, engine models are needed to investigate the potential of SOFC-ICE integration.

However, the choice of engine modelling approach can vary from detailed computational fluid dynamics (CFD) models to straight forward transfer function models depending on the required accuracy, amount of information and computational time required. Thus, raising the question pertaining to the choice of suitable modelling approach to quantify engine performance with anode-off gas effects and study system integration between the SOFC and the engine. Chapter 5 provides a detailed literature survey on engine modelling approaches to capture the combustion and engine performance with anode-off gas constituents.

- **Back pressure effects on marine engine operation**

After-treatment technologies are adopted in automobiles and ships to meet the strict emission regulations, which increase exhaust back pressure. Moreover, a new trend is to employ underwater exhaust systems onboard ships due to their various advantages such as space saving, noise reduction, improved working conditions on working decks, etc. Capitalizing on these advantages of UWE and more, the GasDrive concept employs them to allow for drag reduction via gas lubrication, which can help reduce on board fuel requirements. However, as explained earlier, water at exhaust outlet creates a flow resistance for the exhaust gases, which adds to the back pressure. High back pressure can have significant adverse effects on engine performance such as limiting engine operation, turbocharger damage due to thermal overloading, etc. A detailed discussion on the potential and challenge of underwater exhaust systems and existing literature on engine performance against back pressure has been presented in subsection 2.4.2 of Chapter 2.

While the effects of back pressure were recognized earlier, there is a lack of experimentally validated research on the performance limits of a turbocharged, marine engine against high static and fluctuating back pressure for the entire operating window. Furthermore, there is a need to identify the limits of acceptable back pressure along with methods to tackle high back pressure. Therefore, research questions pertaining

to quantified understanding of back pressure effects on marine engine operation are identified and researched in this dissertation.

1.5. INTEGRATED SYSTEM VARIABLES

In SOFC-ICE integration, numerous integrated system variables (ISVs) can impact the performance of each energy conversion device, system efficiency, overall emissions, system power density, response to load variations and system feasibility. For instance, the quality (composition) and quantity of anode-off gas are regarded as an ISV, which is significantly dependent on SOFC operation, and impacts the in-cylinder process, turbocharging, energy efficiency and even operating limits of the integrated engine. In this dissertation, the integrated system variables are divided into three different categories pertaining to SOFC operation, Engine operation, and System operation. The following integrated system variables (ISVs) are identified under the three different categories for SOFC-ICE and UWE integration:

1. SOFC operation

- Current density,
It is the current per unit cell area.
- Pre-reforming ratio,
It dictates the pre-conversion percentage of incoming methane fuel to hydrogen and carbon monoxide rich gas needed for fuel cell operation.
- Fuel utilization
It is the ratio of fuel or hydrogen consumed to the ratio of total hydrogen supplied.

2. Engine operation

- AOG quality and quantity
It is the composition and amount of anode-off gas available from the SOFC.
- Engine fuel composition
It is is composition of fuel entering the marine SI NG engine.
- Air-excess ratio
It is the fresh air mass entering the engine cylinder to the minimum amount of air required for combustion.
- Spark-timing
It dictates the timing at which a spark is provided to initiate ignition inside the engine cylinder.
- Back pressure
It is the resistance to exhaust gas flow felt by the engine at turbine outlet.

3. System operation

- Heat integration
For high-efficiency SOFC operation, the heat integration or heat balance of the SOFC needs to be maintained, ideally without external heat supply.

- Power-split between the SOFC and the ICE

The load-share (rated power output) of each energy conversion device gives the power-split between the SOFC and the ICE.

For successful SOFC-ICE integration, a combined system and component level investigation is necessary due to complex interactions between the integrated system variables and their impact on SOFC and engine operation in addition to the SOFC-ICE power plant performance.

1.6. PROBLEM STATEMENT AND RESEARCH QUESTIONS

Based on the above literature overview on SOFC-ICE integration and underwater exhaust systems, the following problem statement is formulated for this research:

Modern marine diesel engines operating on conventional marine fuels are unable to further reduce the adverse impact of ship emissions on the environment. Integration of a natural gas (NG)-fuelled solid oxide fuel cell (SOFC) and internal combustion engine (ICE) equipped with an underwater exhaust (UWE) can provide the opportunity for mitigating ship emissions and at the same time improve energy efficiency. However, numerous integrated system variables such as fuel utilization, engine fuel composition, load-sharing etc. can profoundly impact SOFC and ICE operation and, therefore, affect the feasibility and performance of the SOFC-ICE power plant. Moreover, presence of high and fluctuating back pressure due to an UWE can negatively impact engine operation and its performance limits.

Current literature on SOFC combined cycles for maritime applications is scarce while knowledge specifically pertaining to SOFC-ICE integration for marine power generation is currently next to non-existent. Furthermore, an experimentally validated and comprehensive understanding of high and dynamic back pressure effects on marine engine performance due to underwater exhaust systems is lacking.

Based on the above problem statement, the following main research question is derived:

What is the impact of SOFC-ICE integration and UWE on marine engine performance and how to quantify the operation of the integrated SOFC-ICE system for maritime applications to demonstrate feasibility, energy efficiency improvement and emission reduction?

The above problem statement and main research question lead to the following sub research questions, first questions on SOFC-ICE integration:

1. Is the bottoming cycle approach presented in existing literature, which has been reviewed in Chapter 2, the right way to approach SOFC-ICE integration for ships?
2. What is the detailed composition of anode-off gas, how does it vary with SOFC performance and how to model the compositions of anode-off gas based on SOFC performance?

3. What are the effects of combusting anode-off gas (constituents) on the performance, in-cylinder process, operating limits and emissions of a marine NG engine?
4. What simulation model can be used to quantify engine performance with anode-off gas effects and study system integration between the SOFC and the engine?
5. What are the effects of ISVs on SOFC and engine operation, and how do they impact the performance of the integrated SOFC-ICE power plant?
6. What is the optimal composition of anode-off gas based on engine performance, SOFC performance and SOFC-ICE integration?
7. How does the integrated SOFC-ICE power pack compare against a conventional marine engine for power generation in terms of efficiency, emissions and power density (gravimetric and volumetric)?
then on underwater exhaust system:
8. What are the quantitative effects of static back pressure on marine engine performance due to underwater exhaust system?
9. What are the quantitative effects of dynamic back pressure on marine engine performance due to underwater exhaust system?

1.7. PROPOSED APPROACH

In this Phd thesis, a combined literature, experimental and simulation-based approach is adopted for a qualitative and quantitative investigation of SOFC-ICE integration. Existing, limited literature studies on SOFC-ICE integration are mainly focussed towards land-based distributed power generation. The application of the system integration approach mainly presented in existing literature may not be suitable from a maritime perspective. Therefore, to answer Research Question 1, and identify the suitable engine integration approach for maritime applications, a literature review and qualitative analysis is performed.

To simulate the SOFC performance along with the corresponding anode-off gas flow-rates and compositions, a zero-dimensional cell-to-stack modelling approach is adopted based on literature data to answer Research Question 2. With the known anode-off gas composition and the fixed engine integration approach, effects of anode-off gas combustion are studied experimentally on a turbocharged, marine SI NG engine. This experimental investigation was used to further develop a methodology to build in-cylinder combustion models capable of capturing the effects of anode-off gas combustion. The experimental and simulation-based approach is used to answer Research Questions 3 and 4. In this step, two modelling approaches are investigated and compared in terms of their ability to capture the combustion and in-cylinder processes for varying fuel blends. The comparison led to a choice of one approach over the other based on the ability to capture in-cylinder process variations, simulation accuracy and compatibility with the system integration approach.

The in-cylinder combustion model capable of simulating anode-off gas effects is further combined with a mean value engine model (MVEM) to perform system integration.

The developed MVEM and 0-D SOFC model are further used to study the effects of ISVs on SOFC-ICE integration. The experimental and simulation-based approach adopted in this research is used to investigate the impact of different ISVs on SOFC performance, ICE performance and SOFC-ICE integration, thus providing insights to answer Research Questions 5. The effects of ISVs has been covered in Chapters 3, 4, 5, 6 and 7. The combination of the MVEM and 0-D SOFC model helped find the optimal anode-off gas compositions and flows based on the performance of the engine, SOFC and the integrated system, thus, answering 6. The developed simulation models are also used to investigate Research Question 7 and compare the performance of SOFC-ICE integration against a standalone conventional marine engine. Furthermore, individual effects of combusting hydrogen and carbon dioxide on the dynamics capabilities of the marine SI NG engine are discussed with the help of experiments, which provide further understanding of engine performance and, thus, help in completely answering Research Question 3.

Lastly, to study the effects of static and dynamic back pressure (ISV) due to underwater exhaust systems, and answer Research Questions 8 and 9, experiments are performed on a turbocharged, marine engine. By combining engine experiments with an extended mean value engine model, a conceptual basis for the engine smoke limit as well as for thermal overloading is investigated. A methodology applying the conceptual basis to define boundaries of acceptable back pressures is presented.

1.8. DISSERTATION OUTLINE

The outline of this PhD dissertation is depicted in Figure 1.9 and organised as follows:

- In Chapter 2, the SOFC technology is introduced and the existing literature on SOFC combined cycles is analysed and discussed in detail. Vital considerations for SOFC-ICE integration are discussed from a maritime perspective. Based on the literature study and qualitative analysis, a novel SOFC-ICE integration approach is proposed for marine power generation. Next, the chapter presents the detailed experimental and simulation-based research methodology employed to study SOFC-ICE integration and back pressure effects on marine engine performance. Additionally, the chapter covers previously published literature on hydrogen-natural gas combustion and carbon dioxide-natural gas combustion experiments to highlight the need and basis for the experiments performed in this research. Lastly, a literature survey of back pressure effects on engine performance has been presented in the chapter.
- In Chapter 3, a zero-dimensional SOFC single cell-to-stack model is described to simulate the performance of the fuel cell. The SOFC model is used to capture the impact of ISVs on fuel cell efficiency, anode-off gas composition, flow-rates and cell temperature profiles. The SOFC model is verified against data available from literature. Furthermore, the chapter discusses the variations in SOFC performance and anode-off gas compositions necessary for SOFC-ICE integration.
- In Chapter 4, experimental investigations of combusting individual anode-off constituents in a marine SI NG engine are presented. Effects of ISVs such as fuel composition, air-excess ratio and spark-timing on various engine parameters such as combustion duration, cyclic variations, engine operating limits, emissions and efficiency are

studied. The chapter also describes the detailed experimental setup and methodology employed to study anode-off gas combustion in a marine SI NG engine.

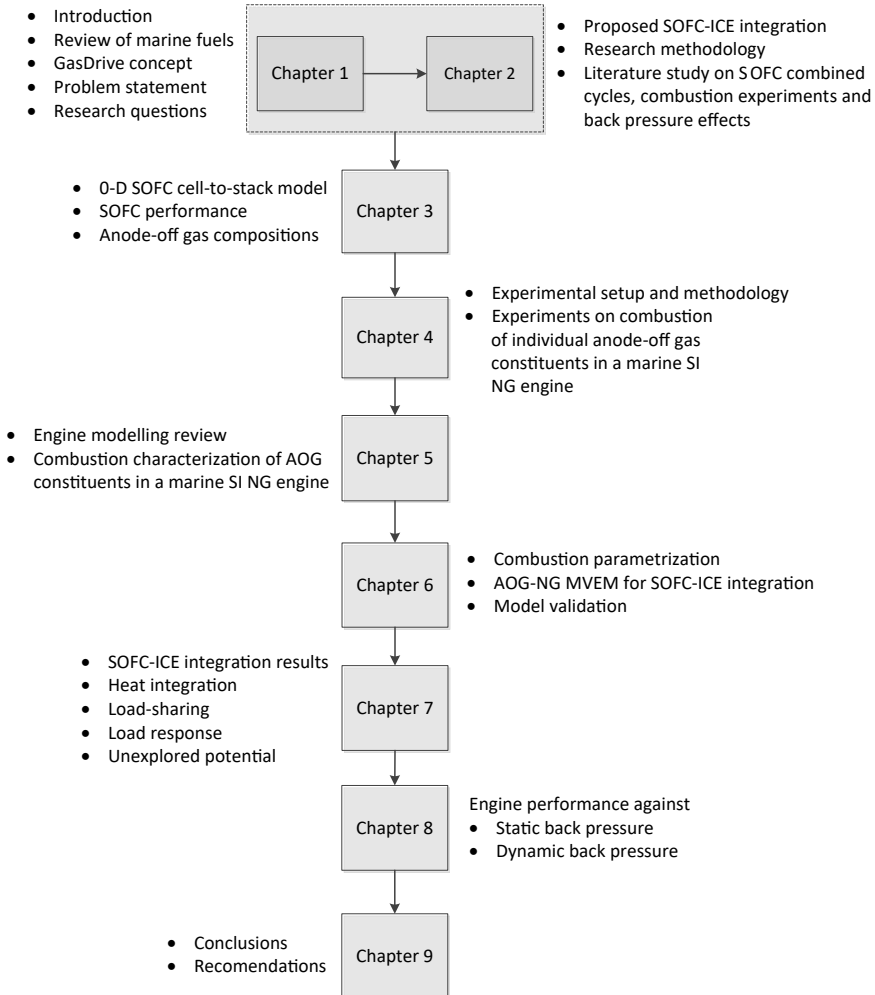


Figure 1.9: Schematic representation of the dissertation outline

- In Chapter 5, at first, a comprehensive literature review of engine modelling methodologies to capture the effects of hydrogen-natural gas and carbon dioxide-natural gas combustion are presented. After describing the reasoning for the chosen engine modelling methodology, the effects of hydrogen combustion in a marine SI NG engine are captured and studied by developing two combustion characterization modelling approaches based on engine measurements. The chapter provides a detailed comparison of the characterization methodology and the two modelling approaches in terms of their abilities to characterize and capture the effects of hydrogen addition, engine

leaning (lean-burn operation) and engine load variations on the combustion process. The comparative analysis showcases the superior applicability of one modelling approach over another for the research covered in this thesis. The selected modelling approach is also used to characterize and capture the effects of carbon dioxide combustion inside the marine NG engine. The model simulations presented in this chapter are used to gain a detailed understanding of the impacts of ISVs such as engine fuel composition (varying blends of anode-off gas constituents and natural gas), air-excess ratio (engine leaning), engine loading and spark-timings on the in-cylinder process of the marine lean-burn NG engine

- In Chapter 6, parametric equations derived to simulate the in-cylinder and combustion process for varying percentages of hydrogen and carbon dioxide addition are presented. The effects of combusting varying SOFC anode-off gas compositions on in-cylinder process of the marine NG engine are captured via model simulations and compared against engine measurements. Furthermore, a novel mean value engine model is developed and validated against engine measurements to simulate the complete integrated engine performance with varying compositions of AOG from the SOFC. The chapter also covers the impact of different fuel compositions (ISV) on engine performance and turbocharging, thus, presenting additional insights to answer Research Question 5.
- In Chapter 7, the results of SOFC-ICE integration are presented and the effects of ISVs such as current density, fuel utilization and pre-reforming ratio on the system efficiency and integration are discussed. Next, a SOFC-ICE heat integration analysis is performed for prescribed operating conditions. The chapter also covers an analysis of different power splits between the SOFC and the engine and their impact on system efficiency, power density and emissions. The integrated system performance is compared against that of a standalone conventional marine NG engine. Furthermore, the chapter provides a comparison of the load response of the SOFC and that of the ICE. It also provides insights into the impact of anode-off gas constituents on the load response of the marine SI NG with the help of experiments. Finally, the chapter concludes with a discussion on the unexplored potential of SOFC-ICE integration for future research.
- In Chapter 8 the impact of back pressure (ISV) due to underwater exhaust systems on marine engine performance is studied. An extended mean value engine model is used in union with engine experiments to understand the effects of static and dynamic back pressure on marine engine performance. The chapter also compares the performance capabilities of pulse and constant pressure turbocharged engines against high back pressure. Lastly, a conceptual methodology is proposed to define the boundaries of acceptable back pressures.
- Chapter 9 summarises the conclusions of this dissertation and presents recommendations for future work to expand on the research presented in this thesis.

REFERENCES

- [1] The CMA CGM JACQUES SAADE, the world's first 23,000 TEU powered by LNG. <https://cmacgm-group.com/en/launching-cmacgm-jacques-saad%C3%A9-world's-first-ultra-large-vessel-powered-by-lng>, 2019.
- [2] S.N. Sirimanne et al. Review of Maritime Transport 2019. Technical report, United Nations Conference on Trade and Development, 2019.
- [3] European Community Shipowner's Associations. Shipping and Global Trade: Towards an EU External Shipping Policy. Technical report, 2017.
- [4] J. Hoffmann et al. Review of Maritime Transport 2018. Technical report, United Nations Conference on Trade and Development, 2018.
- [5] H.D. Sapra et al. Integration of Solid Oxide Fuel Cell and Internal Combustion Engine for Maritime Applications. *Applied Energy*, 2020.
- [6] R.D. Geertsma. *Autonomous Control for Adaptive Ships with Hybrid Propulsion and Power Generation*. PhD thesis, Delft University of Technology, 2019.
- [7] A. Haseltalab. *Control for Autonomous All-Electric Ships: Integrating Maneuvering, Energy Management, and Power Generation Control*. PhD thesis, Delft University of Technology, 2019.
- [8] Lloyd's Register Group Limited, QinetiQ, and University of Strathclyde. Global Marine Trends 2030. Technical report, 2030.
- [9] DNV GL Technology Outlook 2025 – Digitalization and Innovation. <https://to2025/dnvgl.com/innovation-drivers/digitalization/>.
- [10] I. Komar and B. Lalić. Sea Transport Air Pollution. In Farhad Nejadkoorki, editor, *Current Air Quality Issues*. IntechOpen, 2015.
- [11] International Maritime Organization. MARPOL ANNEX VI and NTC 2008 with Guidelines for Implementation - Supplement. Technical report, 2015.
- [12] J. Brandt et al. Assessment of Past, Present and Future Health-cost Externalities of Air Pollution in Europe and the Contribution from International Ship Traffic Using the EVA Model System. *Atmospheric Chemistry and Physics*, 2013.
- [13] Energy Efficiency and the Reduction of GHG Emissions from Ships. <https://www.imo.org/en/MediaCentre/HotTopics/GHG/Pages/default.aspx>.
- [14] P. Aakko-Saksa. Black Carbon Measurements Using Different Marine fuels. In *CIMAC Congress*, 2016.
- [15] Z. Schlanger. If Shipping were a Country, It would be the World's Sixth-biggest Greenhouse Gas Emitter | World Economic Forum. <https://www.weforum.org/agenda/2018/04/if-shipping-were-a-country-it-would-be-the-world-s-sixth-biggest-greenhouse-gas-emitter>.
- [16] International Maritime Organization. Reduction of GHG emissions from ships - Third IMO GHG Study 2014 – Final Report. Technical report, 2014.
- [17] L. van Biert, M. Godjevac, K. Visser, and P.V. Aravind. A Review of Fuel Cell Systems for Maritime Applications. *Journal of Power Sources*, 2016.

- [18] R. Verbeek, M. Bolech, and H. den Uil. *Alternative Fuels for Sea Shipping*. Technical report, 2011.
- [19] S.M. Aceves et al. High-density Automotive Hydrogen Storage with Cryogenic Capable Pressure Vessels. *International Journal of Hydrogen Energy*, 2010.
- [20] Fuel Oil - Storage Tanks. https://www.engineeringtoolbox.com/fuel-oil-storage-tanks-dimensions-d_1585.html.
- [21] LNG Storage Vessels. www.ChartLNG.com, 2016.
- [22] R. Metkemeijer and P. Achard. Comparison of Ammonia and Methanol Applied Indirectly in a Hydrogen Fuel Cell. *International Journal of Hydrogen Energy*, 1994.
- [23] *OECD-FAO Agricultural Outlook 2018-2027*. 2018.
- [24] Oil – World Energy Outlook 2018 – Analysis. <https://www.iea.org/reports/world-energy-outlook-2018/oil#abstract>.
- [25] Gas – World Energy Outlook 2019. <https://www.iea.org/reports/world-energy-outlook-2019/gas#abstract>.
- [26] S. Satyapal. *Hydrogen and Fuel Cells Overview*. Technical report, US Department of Energy, 2017.
- [27] U.S. Geological Survey. *Nitrogen (Fixed)-Ammonia*. Technical report, 2013.
- [28] Global Average Bunker Price. <https://shipandbunker.com/prices/av/global/av-glb-global-average-bunker-price#MGO>.
- [29] U.S. Department of Energy. *Clean Cities Alternative Fuel Price Report*, April 2019. Technical report, 2019.
- [30] Nitrogen Leads Fall 2019 Fertilizer Prices Lower. <https://aei.ag/2019/10/14/nitrogen-leads-fall-2019-fertilizer-prices-lower/>, 2019.
- [31] Census and Economic Information Center. *China: Market Price: Monthly Avg: Organic Chemical Material: Dimethyl Ether: 99.0% or Above*. <https://www.ceicdata.com/en/china/china-petroleum-chemical-industry-association-petrochemical-price-organic-chemical-material/cn-market-price-monthly-avg-organic-chemical-material-dimethyl-ether-990-or-above>.
- [32] Methanex. *Methanex Monthly Average Regional Posted Contract Price History*. Technical report, 2020.
- [33] E. Connelly et al. *Current Status of Hydrogen Liquefaction Costs*. Technical report, Department of Energy, USA, 2019.
- [34] Maritime Knowledge Centre, TNO, and Delft University of Technology. *Final Report-Framework CO2 Reduction in Shipping*. Technical report, 2017.
- [35] Royal Academy of Engineering. *Future Ship Powering Options: Exploring Alternative Methods of Ship Propulsion*. Technical report, 2013.
- [36] U.S. Department of Energy. *Alternative Fuels Data Center: Biodiesel Benefits and Considerations*. https://afdc.energy.gov/fuels/biodiesel_benefits.html.
- [37] C.W. Mohd Noor, M.M. Noor, and R. Mamat. *Biodiesel as Alternative Fuel for Ma-*

- rine Diesel Engine Applications: A Review. *Renewable and Sustainable Energy Reviews*, 2018.
- [38] H. Chen, B. Xie, J. Ma, and Y. Chen. NO_x Emission of Biodiesel Compared to Diesel: Higher or Lower? *Applied Thermal Engineering*, 2018.
- [39] DNV GL. Maritime Assessment of Selected Alternative Fuels and Technologies. Technical report, 2019.
- [40] International Gas Union. 2019 World LNG Report. Technical report, 2019.
- [41] How Dangerous is LNG? <https://breakingenergy.com/2014/12/22/how-dangerous-is-lng/>, 2014.
- [42] Chapter 9 - LNG Safety and Security Aspects. In S. Mokhatab, J. Y. Mak, J. V. Valappil, and D. A. Wood, editors, *Handbook of Liquefied Natural Gas*. Gulf Professional Publishing, 2014.
- [43] G. Hellén. NO_x Emissions of LNG Operated Engines. In *CIMAC Circle @ Marintec*, 2015.
- [44] CIMAC Working Group 17. Methane and Formaldehyde Emissions of Gas Engines. In *CIMAC*, 2014.
- [45] U.S. Environmental Protection Agency. Technical Support Document for Hydrogen Production : Proposed Rule for Mandatory Reporting of Greenhouse Gases. Technical report, 2008.
- [46] Methanol Institute. Methanol Safe Handling Manual: 4th Edition. Technical report, 2017.
- [47] S.H. Seo and C.S. Lee. A Study on the Overall Efficiency of Direct Methanol Fuel Cell by Methanol Crossover Current. *Applied Energy*, 2010.
- [48] S.J. Andreasen, S.K. Kær, and S. Sahlin. Control and Experimental Characterization of a Methanol Reformer for a 350 W High Temperature Polymer Electrolyte Membrane Fuel Cell System. *International Journal of Hydrogen Energy*, 2013.
- [49] DNV GL. Methanol as Marine Fuel: Environmental Benefits, Technology Readiness, and Economic Feasibility. Technical report, 2016.
- [50] T.H. Fleisch, A. Basu, and R.A. Sills. Introduction and Advancement of a New Clean Global Fuel: The Status of DME Developments in China and Beyond. 2012.
- [51] K. Sato, Y. Tanaka, A. Negishi, and T. Kato. Dual Fuel Type Solid Oxide Fuel Cell Using Dimethyl Ether and Liquefied Petroleum Gas as Fuels. *Journal of Power Sources*, 2012.
- [52] C. Su, R. Ran, W. Wang, and Z. Shao. Coke Formation and Performance of an Intermediate-temperature Solid Oxide Fuel Cell Operating on Dimethyl Ether Fuel. *Journal of Power Sources*, 2011.
- [53] U.S. Department of Energy. Alternative Fuels Data Center: Dimethyl Ether. https://afdc.energy.gov/fuels/emerging_dme.html.
- [54] I.M. Youn, S.H. Park, H.G. Roh, and C.S. Lee. Investigation on the Fuel Spray and Emission Reduction Characteristics for Dimethyl Ether (DME) Fueled Multi-

- cylinder Diesel Engine with Common-rail Injection System. *Fuel Processing Technology*, 2011.
- [55] M. Matzen and Y. Demirel. Methanol and Dimethyl Ether from Renewable Hydrogen and Carbon dioxide: Alternative Fuels Production and Life-cycle Assessment. *Journal of Cleaner Production*, 2016.
- [56] A. Valera-Medina et al. Ammonia for Power. *Progress in Energy and Combustion Science*, 2018.
- [57] S.H. Crolius. Ammonia-powered Internal Combustion Engines - Ammonia Energy Association. <https://www.ammoniaenergy.org/articles/ammonia-powered-internal-combustion-engines/>, 2016.
- [58] R. Lan and S. Tao. Ammonia as a Suitable Fuel for Fuel Cells. *Frontiers in Energy Research*, 2014.
- [59] D. Cheddie. Ammonia as a Hydrogen Source for Fuel Cells: A Review. In *Hydrogen Energy - Challenges and Perspectives*. IntechOpen, 2012.
- [60] A. Wojcik, H. Middleton, I. Damopoulos, and J. van Herle. Ammonia as a Fuel in Solid Oxide Fuel Cells. *Journal of Power Sources*, 2003.
- [61] Delft University of Technology, University of Twente, and University of Wageningen. Project proposal: GasDrive: Minimizing Emissions and Energy Losses at Sea with LNG Combined Prime Movers, Underwater Exhausts and Nano Hull Materials. Technical report, 2015.
- [62] L. van Biert et al. A Thermodynamic Comparison of Solid Oxide Fuel Cell-Combined Cycles. *Journal of Power Sources*, 2018.
- [63] T.H. Lim et al. Operating Characteristics of a 5 kW Class Anode-supported Planar SOFC Stack for a Fuel Cell/Gas Turbine Hybrid System. *International Journal of Hydrogen Energy*, 2008.
- [64] S.J. McPhail et al. SOFC and MCFC: Commonalities and Opportunities for Integrated Research. *International Journal of Hydrogen Energy*, 2011.
- [65] E.D.F. Chuahy and S.L. Kokjohn. Solid Oxide Fuel Cell and Advanced Combustion Engine Combined Cycle: A Pathway to 70% Electrical Efficiency. *Applied Energy*, 2019.
- [66] A. Buonomano et al. Hybrid Solid Oxide Fuel Cells-Gas Turbine Systems for Combined Heat and Power: A Review. *Applied Energy*, 2015.
- [67] Y.M.A. Welaya, M. Mosleh, and N.R. Ammar. Thermodynamic Analysis of a Combined Solid Oxide Fuel Cell with a Steam Turbine Power Plant for Marine Applications. *Journal of Marine Science and Application*, 2014.
- [68] W. Choi et al. Experimental Study of Homogeneous Charge Compression Ignition Engine Operation Fuelled by Emulated Solid Oxide Fuel Cell Anode Off-Gas. *Applied Energy*, 2018.

2

SOFC-ICE INTEGRATION APPROACH AND RESEARCH METHODOLOGY

In this chapter, the proposed SOFC-ICE integration approach is introduced, followed by the methodology adopted for this PhD research. The chapter provides an introduction to solid oxide fuel cells along with a detailed literature analysis of the SOFC combined cycles discussed in current literature while highlighting the lack of knowledge and potential of SOFC-ICE integration for maritime applications. The chapter uses this detailed literature analysis of SOFC combined cycles to answer Research Question 1. Additionally, the chapter covers previously published literature on hydrogen-natural gas combustion and carbon dioxide-natural gas combustion experiments to highlight the need and basis for the experiments performed in this research. Lastly, a literature survey of back pressure effects on engine performance has been presented in this chapter.

2.1. INTRODUCTION TO SOFCs

Solid oxide fuel cells are electrochemical energy conversion devices in contrast to the traditional thermomechanical engines. These fuel cells produce electricity and heat from a gaseous or gasified fuel via an electrochemical reaction between the fuel and oxidant. Researchers have shown the potential of SOFCs to outperform traditional energy conversion devices in terms of efficiency. SOFCs are solid-state fuel cells with high operating temperature (600 – 1000 °C) [1]. The availability of high-temperature heat and steam allows for internal reforming of hydrocarbon fuels to hydrogen and carbon monoxide, thus, making them ideal for natural gas.

Figure 2.1 shows a schematic representation of a SOFC. The grey strip (B) on the left represents the anode electrode, which is a porous cermet made up of nickel and yttrium-

Parts of this chapter have been published in the ASME ICEF-2018 Conference [2], CIMAC World Congress 2019 [3], ASME ICEF-2019 Conference [4] and Applied Energy [5, 6].

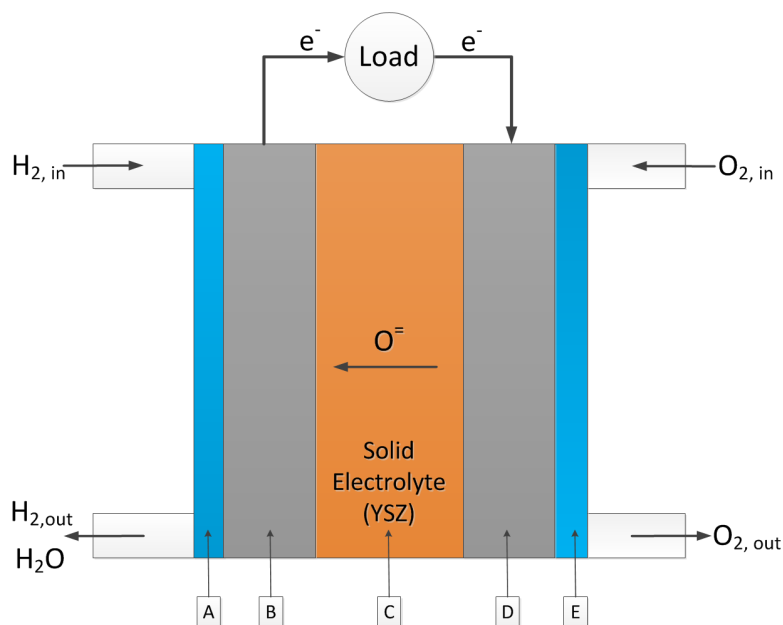


Figure 2.1: Schematic representation of a single SOFC cell

stabilized zirconia skeleton (NiO/8YSZ). The SOFC cathode (D) is also porous and made up of strontium-doped lanthanum ferrite (LCSF) or strontium-doped lanthanum manganite (LSM). The porosity of the electrodes is to support mass transport of gases taking part in the reactions. The anode and cathode are connected with an oxide ion conducting, ceramic solid electrolyte (C) in the middle. The solid composite of the positive electrode, electrolyte and negative electrode is referred to as the PEN structure. The anode and the cathode are connected to the anode-flow and cathode-flow channels signified by A and E in Figure 2.1.

The anode-flow channel carries the incoming fuel, i.e., natural gas plus H_2 and CO as partially reformed gas, in addition to the outgoing anode-off gas. The partially reformed gas entering the anode-flow channel also contains carbon dioxide and water vapour. Hydrogen obtained from reforming of natural gas diffuses in through the porous anode while oxygen enters from the cathode-flow channel that carries air. At the cathode side, oxygen reduces to form an oxide ion at the interface of the cathode, electrolyte and oxygen called the triple phase boundary (TPB). The oxide ion is then carried through the electrolyte to the anode side, where the hydrogen oxidation reaction takes place at the TPB of anode, electrolyte and gaseous fuel to release electrons and form water vapour. Similarly, carbon monoxide formed as a product of the methane steam reforming is also oxidized at the anode TPB to produce electrons and carbon dioxide. The generated electrons contribute to the circuit current, which on multiplication with the voltage across the cell produces the high-efficiency electrical power. The electrochemical reaction produces steam and heat, which are utilized for internal reforming of natural gas entering

the anode-flow channel after partial reforming in the pre-reformer. The outgoing gas at the anode mainly consists of unutilized hydrogen and carbon monoxide in addition to the water vapour and carbon dioxide formed during the electrochemical reaction. This outgoing gas at the anode leaves through the anode-flow channel at high temperatures and is referred to as the anode-off gas or anode-tail gas. Similarly, the oxygen-depleted air exits the cathode-flow channel at high temperatures. Detailed descriptions of the reactions and processes taking place inside a SOFC have been provided in Chapter 3.

Unlike SOFCs, the relatively low operating temperatures (65 °C to 200 °C) of PEMFCs create the need for a platinum catalyst at the anode to support the oxidation reaction [7]. The use of a platinum catalyst reduces the tolerance of PEM fuel cells to fuel impurities. For instance, carbon monoxide (CO) produced during reforming of hydrocarbon fuels is absorbed by the platinum, thus, blocking the catalytic surface for hydrogen oxidation, which adversely impacts cell performance [8]. Therefore, PEM fuel cells are suitable for operation with hydrogen fuel of ultra-high purity. Otherwise, they require extensive pre-treatment to filter out the impurities such as CO and sulphur, which reduce efficiency and power density while increasing costs and system complexity. On the other hand, SOFCs have enhanced tolerance due to higher operating temperatures with the potential of achieving electrical efficiencies greater than 55 % on natural gas reformat containing H₂ and CO [9, 10].

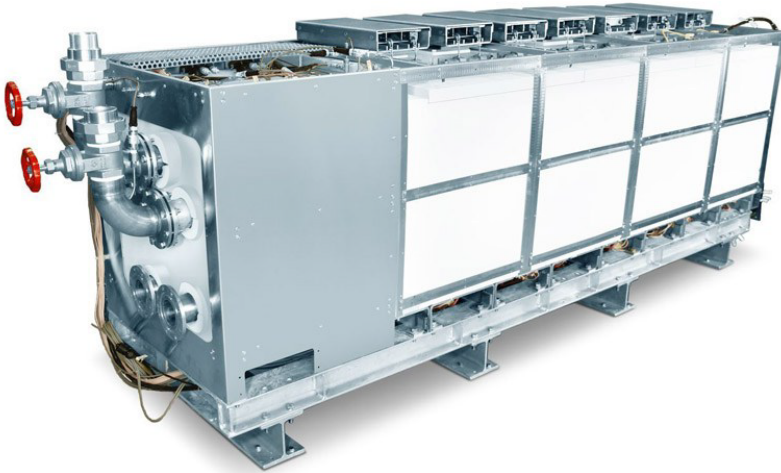


Figure 2.2: 50 kW Sunfire IT-SOFC stack for marine power generation [11]

Significant demonstrations of SOFC technology were performed by Siemens-Westinghouse in the '1990s' with a rated power output of 100 kW. The installed SOFCs were tubular, however, currently, SOFC manufacturers are focussed on planar design due to their relatively lower ohmic losses and low-cost fabrication methods [7]. Furthermore, research efforts have been directed towards lowering the fuel cell operating temperatures, due to numerous challenges with cell reliability, high-temperature materials and manufacturing costs. Presently, 'Intermediate Temperature' SOFCs (IT-SOFC), with operating temperatures ranging from 600 to 900 °C, are gaining enormous research interests [12]. The

IT-SOFCs have exhibited enhancements in efficiency and power density [13]. In case of SOFCs, high efficiency and absence of expansive high temperature combustion allow for drastic emission reductions with significantly lower CO₂ emissions and negligible emissions of nitrogen oxides (NO_x) and volatile organic compounds (VOCs) [14, 15]. Furthermore, SOFCs offer noiseless operation due to the absence of large moving parts such as a piston and connecting rod arrangement or turbine blades. Thus, attributes of high-efficiency power generation, ultra-low emissions and noise-less operation make SOFCs a promising power generation technology for maritime applications. Figure 2.2 shows the external layout of a 50 kWe SOFC stack commercially available for ocean-going vessels. The commercial 50 kWe IT-SOFC stack operates at 800 °C with an achievable electrical efficiency of 50 % [11].

2.2. SOFC COMBINED CYCLES

In recent years, solid oxide fuel cells have become the focus of numerous research investigations due to their promise of high efficiency, ultra-low emissions and noise-free operation [16]. However, their limited development state, low gravimetric and volumetric density, restricted transient capabilities and high costs have hindered their wide-spread adoption [10]. The load response of an SOFC can take several hundreds of seconds [17, 18]. To avoid high temperature gradients and thermal stresses, the start-up time of SOFCs can be greater than 10 minutes [19]. SOFCs are also an expensive technology with the unit cost of a state-of-the-art SOFC being approximately equal to 7000 \$kW⁻¹e [20]. Furthermore, current solid oxide fuel cells can be 4 times heavier and bulkier than a traditional internal combustion engine of similar power output, thus, challenging their successful industrialization.

To offset the challenges associated with SOFCs and capitalize on their enhanced efficiency operation, a number of researchers have investigated SOFC combined cycles [1, 16, 21, 22]. For instance, SOFC-Gas turbine (GT) systems have been widely studied, both computationally and experimentally [23]. In a SOFC-GT integrated system, the SOFC functions as a high-efficiency electrical power generation device while the combusted SOFC anode-off gas is expanded in a turbine for additional power generation as shown in Figure 2.3. Similarly, a number of studies have been focussed towards the development of SOFC-Steam turbine (ST) combined cycles employing heat from anode-off gas combustion for steam generation, which is expanded in a steam turbine for additional power generation. Figure 2.4 shows a SOFC-ST combined cycle as presented by van Biert et al. [10]. The extra power generated from turbines in SOFC combined cycles increases the electrical efficiency. Furthermore, SOFC-GT and SOFC-ST combined systems can allow for pressurised SOFC operation, which leads to further improvements in efficiency due to increased cell voltages [7, 10, 24].

The conventional SOFC-GT system employs a pressurized SOFC with a turbine matched to operate on combusted SOFC anode-tail gas. In this integration approach, the SOFC and GT operation is coupled, which hinders the system operation capabilities [25]. The coupled SOFC-GT system architecture was demonstrated by Siemens-Westinghouse and Mitsubishi Heavy industries with a 75 kWe micro GT [26, 27]. The reported system efficiency was greater than 50 %, however, a mismatch between the SOFC and GT resulted in GT power of only 20 to 30 kW. Few other experimental demonstrations by industries such

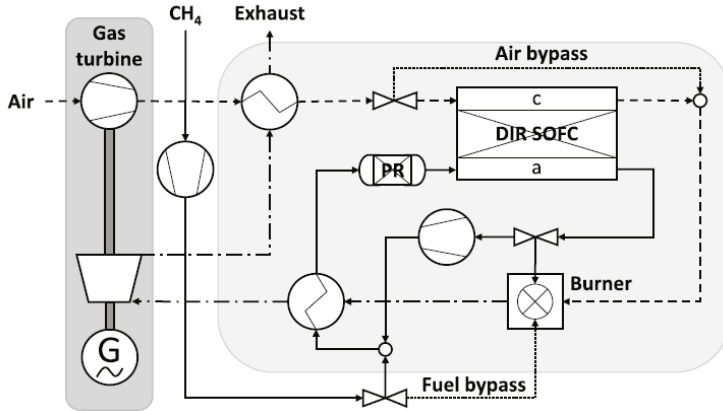


Figure 2.3: Pressurised SOFC-GT combined cycle presented by van Biert et al. [10]

as Rolls Royce, General Electric and Allison Engines have been reported for such systems due to high costs and complexities [25, 28]. However, a number of simulation-based investigations have been performed to study the potential and challenges of pressurised SOFC-GT systems. Model simulations have shown that SOFC-GT combined cycles have the potential of achieving high efficiencies ranging from 58.1 % to even 67.9 % for a 1.5 MW output with a pressure ratio of 7.8 [29, 30]. Similarly, Park et al. [31] reported efficiencies of 59.2 % and 61.6 % for an ambient and pressurised SOFC-gas turbine system, respectively. Although presented SOFC-GT systems have showcased high rated operation efficiencies, off-design and part load performance have been proven to be much less efficient. An efficiency drop from 60.6 % to 37.4 % was reported for part load operation at 57 % load by Chan et al. [32]. Thus, the matching of SOFC and GT for full load operation can lead to poor part load performance with complex control architecture requirement due to SOFC-GT coupling [28].

Another alternative SOFC combined power generation system is the integration of SOFC with a reciprocating engine. The better part load performance, better economics, robustness and simplified integration potential of engines compared to gas or steam turbines make engines highly suitable for integration with SOFCs. Additionally, as explained earlier SOFCs have poor transient and start-up capabilities with sudden load response leading to restricted life-cycle of the fuel cell. On the contrary, engines are known for their instant load-taking abilities, therefore, load fluctuations could be achieved by the engine in an integrated SOFC-ICE system. In the case of SOFC-GT and SOFC-ST integration, load transients can be challenging due to complex architecture and control management requirements caused by the coupling of the two systems [17, 28]. A de-coupled SOFC-ICE system can meet the instant load change by bypassing the fuel directly to the engine [28]. Additionally, in a combined cycle, engines have shown superior dynamic load response compared to gas turbines while operating at higher part load efficiencies [13, 33, 34]. Internal combustion engines are also less capital intensive than their gas turbine counterparts, thus, allowing for an economic SOFC combined cy-

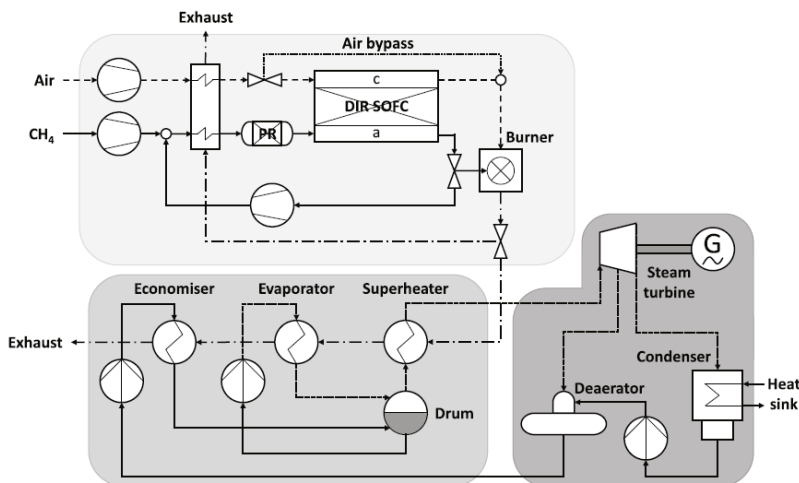


Figure 2.4: SOFC-ST combined cycle presented by van Biert et al. [10]

cle [35]. Moreover, system power and efficiency produced by a SOFC-ICE system will be less sensitive to ambient condition variations as engines are, in general, less sensitive to ambient conditions compared to gas turbines [28]. Therefore, an integrated SOFC-ICE system can be a promising power generation alternative.

Motivated by the above reasoning, researchers have investigated the integration of a SOFC with engines operating on different combustion strategies such as homogenous charge compression ignition (HCCI) [36, 37], reactivity controlled compression ignition (RCCI) [28] and spark-assisted ignition (SAI) [38]. For SOFC-HCCI engine integration, researchers have investigated the economic feasibility based on a thermo-economic analysis [35, 39]. Choi et al. demonstrated HCCI engine operation with a variety of anode-off gas compositions [40] and also researched the causes and impact of heat losses in an HCCI engine operating on SOFC anode-off gas [41]. HCCI is an advanced combustion technology that has shown to achieve high engine efficiencies with low NO_x emissions for a significantly diluted fuel charge of SOFC anode-off gas [42]. The SOFC-HCCI engine integration allows high-efficiency operation of SOFC while the SOFC anode-off gas is combusted in an HCCI engine allowing for high overall efficiency achievements [43, 44]. In a relatively recent study, Choi et al. investigated the design point performance of a 5 kWe SOFC-HCCI engine hybrid system with a system efficiency of 59% [45]. Similarly, Wu et al. analysed a SOFC-ICE hybrid system with a metal hydride reactor and an HCCI engine to showcase high overall system efficiency improvements [46]. However, there are numerous challenges associated with HCCI operation such as difficulties in controlling auto-ignition, limited operating range, difficulties in homogeneous charge preparation and controlling knock in addition to high emissions of unburnt hydrocarbons (UHC) and carbon monoxide (CO) [38, 47].

Next to HCCI combustion for SOFC-ICE integration, Chuahy et al. [28] proposed the RCCI technology, which uses the different chemical kinetic characteristics of diesel fuel

and SOFC anode-off gas for improved control over the combustion start, duration and heat release compared to HCCI combustion. The authors further explained that the direct injection of diesel or liquid fuel in large percentages can allow for a rapid increase in system loading, thus, de-coupling the engine from the SOFC. Chuahy et al. used a combination of engine simulations and experiments to show an optimised SOFC-ICE combined cycle operating on diesel as the parent fuel, and capable of achieving 70 % (LHV) electrical efficiency. The 70 % system efficiency was achieved for a system producing approximately 1 MWe power and a load share of approximately 85 %-15 % between the SOFC and engine. For high system efficiency, the engine was proposed to generate a much smaller fraction of additional power from the SOFC anode-off gas. Moreover, the current density of the cell was set to 2000 A m^{-2} to achieve SOFC efficiencies of about 60 % or higher [28]. Operating at such low current densities could allow for high-efficiency operation, however, the system size and weight can significantly increase as more cells are required to produce a given power output. The significant increment in space and weight requirements can be a limitation for the application of the power generation system onboard ships. In contrast to HCCI and RCCI strategies, Kim et al. experimentally showed the feasibility of SAI combustion technology [38] for SOFC-ICE integration and explained that compression ignition (CI) may not be a practical combustion strategy for anode off-gas (with high dilution) because it requires significant compression work per chemical energy delivery. Similarly, Ran et al. experimentally investigated the combustion of SOFC anode-off gas (without water vapour) in a SI engine for additional power generation [48].

Another intriguing approach of integrating an engine and SOFC is presented by Fyffe et al. [37, 49], which employs a low-heat rejection (LHR) compression ignition (CI) engine. LHR is an under-research engine technology that aims to increase engine efficiency by increasing in-cylinder temperatures through thermal barrier coating materials applied on chamber walls for high insulation [49, 50]. In the system proposed by Fyffe et al., the LHR produces work and very-high temperature exhaust gas to reform any remaining fuel (in the exhaust) and additional fuel to syngas for the SOFC. Furthermore, the SOFC is operated as part of GT-ST triple cycle to allow for high-efficiency system performance. This integration approach is called LHR-SOGTST cycles by the authors and has been shown in Figure 2.5. The authors state that the application of engine to produce work and syngas for the SOFC enables a quick-start approach for the integrated system while operating on a range of fuels, which is a vital consideration for marine power generation. Although the integration approach presented in Figure 2.5 led to a simulated LHV efficiency of 69.9 % based on exergy analysis, numerous aspects of the combined cycle need further investigations to confirm system feasibility. For instance, the simulated LHV efficiency of 69.9 % was achieved by assuming future advancements in turbocharging such as operating with turbine inlet temperatures of $1000 \text{ }^\circ\text{C}$ and increased polytropic efficiencies. However, these advancements in turbocharging are commercially unavailable. Furthermore, LHR engine technology is also commercially unavailable with challenges such as high NO_x emissions in addition to advanced lubrication and material requirements to sustain the high in-cylinder temperatures [50]. Lastly, the complexity of the proposed system architecture could pose additional challenges with respect to control, system size and weight requirements for implementation onboard ships, and therefore,

+/- 15 % even with instant primary fuel injection. A solution could be to integrate the SOFC with an over-capacity engine or a large battery pack for quick transients, however, such an integration would further reduce the gravimetric and volumetric density of the already heavy and large system. The power output of the integrated ICE could be increased by 25 to 50 % by turbocharging, however, the small load share of the ICE in the bottoming cycle approach would still restrict the transient capabilities for maritime applications [51]. Depending on ship operations such as manoeuvring, entering a port or sailing in harsh weathers, the dynamic load changes of a ship can be large and sudden [52, 53], thus, highlighting the challenge of dynamic load response associated with the existing SOFC-ICE combined cycles. The dynamic load response of the SOFC and the ICE are further discussed in subsection 7.3.2 of this thesis. In addition to ICE, smaller load shares were also found for gas and steam turbines in SOFC-GT and SOFC-ST combined cycles [13, 17, 24, 31]. Next to the challenge of dynamic response posed by the bottoming cycle approaches in literature, HCCI and RCCI are not commercially ready engine technologies for maritime applications with a number of combined challenges such as heat release control for stable combustion, extension of operating range, high UHC and CO and low exhaust temperatures requiring high turbocharger efficiencies and improvements in after-treatment systems [54].

The above literature highlights the application of SOFC-ICE integration with advanced combustion engine technology adopted as part of a bottoming cycle to achieve high efficiencies for distributed power generation. However, there is a lack of investigations on SOFC-ICE integration for maritime applications. Furthermore, the above discussion presents the challenges of implementing a SOFC-ICE bottoming cycle for maritime applications. Consequently, the current work proposes a novel approach of SOFC-ICE integration for maritime applications, which allows for high-efficiency power generation while the SOFC anode-off gas is blended with natural gas and combusted in a conventional spark-ignited, lean-burn, marine engine for additional power generation. Governed by SOFC and system performance, variations in blend percentages of anode-off gas and natural gas fuel require the engine to operate on flexible anode-off gas-natural gas (AOG-NG) fuel blends for power generation rather than operating as a bottoming cycle working on only anode-off gas.

2.3. PROPOSED SOFC-ICE INTEGRATION

Figure 2.6 shows the system architecture of the proposed SOFC-ICE integration for marine power generation operating on natural gas as parent fuel. In the proposed system, the SOFC operation on natural gas (methane) with an integrated pre-reformer is aimed at producing high-efficiency electrical power. The reaction processes at the anode of the fuel cell lead to the production of electrons along with the anode-off gas, which is a mixture of hydrogen, carbon monoxide, carbon dioxide and water vapour. As seen from Figure 2.6, the water vapour from the anode-off gas is condensed out in the cooler (C.O.). The preheaters P.H.1 and P.H.2 are used to preheat the incoming fuel and air. Engine exhaust and anode-off gas are together used to superheat the steam required for SOFC operation. AOG from the SOFC contains energy in the form of hydrogen and carbon monoxide, which can be combusted in a marine natural gas engine for additional power generation, thus, enhancing efficiency and system performance through integra-

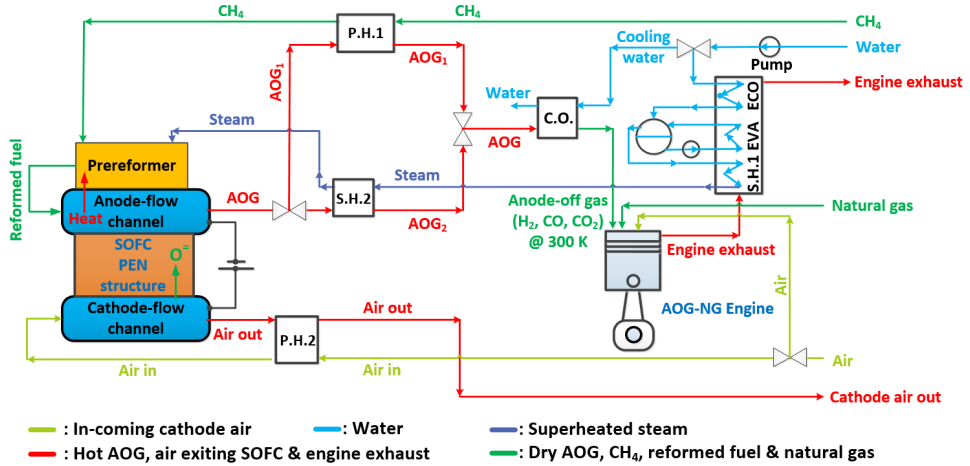


Figure 2.6: System layout of the proposed SOFC-ICE integration for maritime applications. P.H.: Preheater, C.O.: Cooler, S.H. Superheater, Evap: Evaporator, Eco: Economiser. This subsection provides an overview of the system layout. The reader is directed to section 7.2 of Chapter 7 for a detailed description of the system and heat integration

tion. The system integration approach aims at blending the SOFC AOG with natural gas to produce the engine power. However, the reactive hydrogen and high percentages of carbon dioxide in AOG can significantly impact, even limit, the engine performance and, thus, the SOFC-ICE integration. Therefore, it is vital to study the SOFC performance, its impact on anode-off gas flow and composition, and the effects of varying anode-of gas and natural gas fuel blends on marine engine performance. The overall challenge is to employ the optimal amount of anode-off gas for enhanced marine NG engine performance in addition to achieving high-efficiency SOFC operation for successful integration of the novel SOFC-ICE power plant proposed for power generation onboard ships. Therefore, the objective of this research is to investigate the impact of SOFC-ICE integration (and UWE) on marine engine performance and quantify the operation of the integrated SOFC-ICE system for maritime applications to demonstrate feasibility, energy efficiency improvements and emission reductions compared to conventional marine engines.

2.4. RESEARCH METHODOLOGY

Research performed in this PhD dissertation is divided into two parts. First and the primary part is focussed on investigating SOFC-ICE integration for marine power generation while the secondary part covers the study of static and dynamic back pressure on marine engine performance due to underwater exhaust systems. The fundamental research approach adopted for both parts of this dissertation is the same and can be compared by observing Figure 2.7 and Figure 2.9. For both, SOFC-ICE integration and static back pressure effects, engine experiments are used as a basis to understand the underlying phenomena. Then, the experiments are further used as building blocks to develop

and calibrate engine simulations models capable of capturing engine performance for different test conditions such as varying anode-off gas compositions, varying air-excess ratios, load variations, static back pressure variations, different types of turbocharging, etc. The forthcoming subsections present the research methodologies adopted for each part, while the detailed descriptions of the experimental test setups and experimental methodologies have been covered in Chapter 4 and Chapter 8.

2.4.1. RESEARCH METHODOLOGY FOR SOFC-ICE INTEGRATION

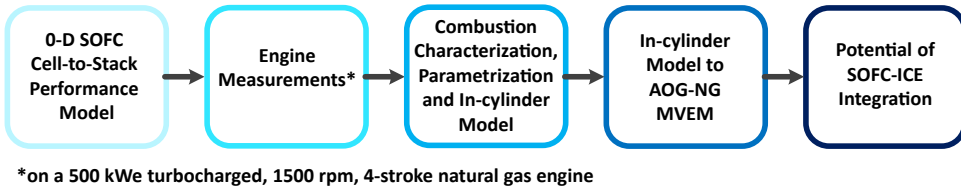


Figure 2.7: Research methodology for SOFC-ICE integration

The integration of a SOFC and engine is investigated for maritime applications by combining model simulations with engine experiments. Figure 2.7 shows the five-step approach employed for this research. In the first step, a 0-D SOFC fuel cell-to-stack model was adopted to simulate the performance of the fuel cell. The model is adopted to simulate a planar, anode-supported, intermediate temperature SOFC cell in addition to a pre-reformer. The SOFC stack performance is extrapolated from the single cell model, which is based on a 0-D electrochemical, equilibrium and energy conservation model. The SOFC model is used to capture the impact of ISVs such as current density, fuel utilization and pre-reforming ratio on fuel cell efficiency, anode-off gas composition, flow-rates and cell temperature profiles. Performance parameters such as fuel cell efficiency, anode-off gas quality and quantity are necessary to investigate the potential of the fuel cell and engine integration. The quantity and quality of anode-off gas dictate the performance of the engine and, thus, also of the GasDrive power generation system. Additionally, the determination of cell temperatures is vital to maintain and understand the required heat balance during system integration as seen in Figure 2.6. The SOFC cell model is developed with and verified against the well-documented cell model by Aguiar et al. [12].

Based on the proposed integration approach, the blend of SOFC anode-off gas and natural gas is combusted in a marine NG engine to produce additional power as seen in Figure 2.6. In the second step of this study, the effects of combusting anode-off gas constituents blended with natural gas were studied experimentally. For this purpose, experiments were performed on a 500 kW, eight-cylinder, turbocharged spark-ignited natural gas engine. Figure 2.8 shows the pictures of the test setup and the CAT G3508 SI NG engine used to study the effects of anode-off gas and natural gas combustion. Chapter 4 provides the engine specifications, test setup and experimentation methodology.

As seen from Figure 2.6, water vapour from the SOFC is condensed out before the anode-off gas is directed into the engine. Additionally, the effects of carbon monoxide on engine performance were not considered at this stage of the research. Chapter 4 pro-

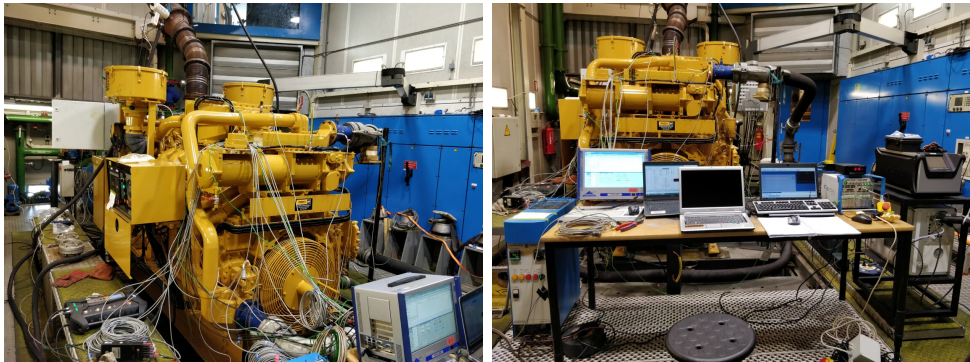


Figure 2.8: Pictures of test setup with the CAT G3508 SI NG engine

vides the complete reasoning for the exclusion of CO effects and condensation of water vapour. To understand and capture the effects of combusting anode-off gas and natural gas fuel blends, effects of combusting only hydrogen and carbon dioxide with natural gas were first studied, experimentally. Subsection 2.4.1 and subsection 2.4.1 cover the existing literature on hydrogen-natural gas and carbon dioxide-natural gas combustion experiments. These literature studies highlight the need and basis for the experiments performed in this PhD research.

After performing the engine experiments, simulations based on these engine measurements were used to capture engine performance to study the impact of ISVs such as AOG quality and quantity, engine fuel composition, air-excess ratios, spark-timing and power-split (load-sharing). In order to develop a holistic engine model capable of capturing the performance of the AOG-NG engine, a detailed modelling approach was adopted. At first, combustion characterization models were developed based on engine measurements for different blends of anode-off gas constituents and natural gas. Therefore, the in-cylinder pressure and crank angle measurements were used as the inputs for the 0-D, single zone H_2 -NG Heat Release Rate (HRR) model. This model was used to describe the detailed heat release process in the zero valve overlap, lean-burn test engine for combustion of different H_2 -NG fuel mixtures at varying engine loads and air-excess ratios (NO_x emissions). Further, various outputs of the HRR model were used to develop two 0-D combustion characterization models capable of capturing the effects of hydrogen-natural combustion. The first model employed the first-principle, thermodynamic 5-stage Seiliger process modelling to characterize the H_2 -NG combustion process, while in the second model a double Wiebe function was used in a 0-D, single zone model to capture the combustion at every crank angle. In this step, various Seiliger and Wiebe combustion parameters were used to define and characterize the H_2 -NG combustion process for different H_2 -NG blends, loads and air-excess ratios (engine leaning). Next, both the combustion characterization models were compared in their capabilities to capture the changes in the combustion process due to hydrogen addition, load variations and engine leaning (lean-burn operation). The comparison yielded the superior capabilities and applicability of one combustion characterization approach over the other. The superior characterization modelling approach was further extended and ap-

plied to model the in-cylinder process for different blends of carbon dioxide and natural gas.

Based on the computed combustion parameters, parametric equations were derived to simulate the in-cylinder process for varying anode-off gas and natural gas fuel blends that could not be experimentally tested. Next, the in-cylinder model was combined with a mean value engine modelling (MVEM) approach to capture the complete AOG-NG engine performance for different blends of anode-off gas and natural gas. The developed in-cylinder modelling approach and the MVEM were validated against engine measurements. In the final step, the developed MVEM (for the AOG-NG engine) in combination with the SOFC model was employed to investigate the potential of SOFC-ICE integration for different current densities, pre-reforming ratios, fuel utilizations and load sharing strategies. The variables used to evaluate system performance are efficiency and emissions along with space and weight considerations. Additionally, for high-efficiency SOFC operation, the heat balance of the SOFC needs to be maintained ideally without external power supply. For this purpose, heat integration between the SOFC and the engine is investigated to present a balance-of-plant (BoP) system for SOFC-ICE integration. Lastly, the effects of anode-off gas constituents on the dynamic load response of the marine NG engine are discussed based on engine measurements supplemented with MVEM simulations.

PREVIOUS LITERATURE ON HYDROGEN-NATURAL GAS COMBUSTION EXPERIMENTS

With the advent of IMO TIER-III regulations, the maritime industry is adopting natural gas as an alternative fuel to reduce ship emissions [55, 56]. Natural gas prominently contains methane, which being the lightest hydrocarbon directly decreases CO₂ emissions. Additionally, the absence of sulphur in natural gas helps eliminate SO_x emissions. Researchers have found that natural gas combustion can reduce NO_x emission due to low in-cylinder temperatures when burning at a high air-excess ratio [57, 58]. The capabilities of natural gas to reduce NO_x, SO_x and CO₂ emissions prove natural gas to be a very promising maritime fuel. However, combustion of natural gas is unstable and produces high cyclic variations at lean air-to-fuel ratios causing engine misfire [59]. Moreover, natural gas engines are also restricted at low air-excess ratios by knock [59], therefore, limiting the operating window between knock and misfire limits. This limits the load-taking capabilities of marine spark-ignited natural gas engines, which restricts their implementation to generator applications [60].

Blending natural gas with a high flame speed fuel like hydrogen can increase the combustion rate. Increasing combustion rate has been shown to reduce cycle-to-cycle variations [61, 62]. Researchers in the automotive field have shown that cyclic variations can be decreased by replacing a small amount of natural gas with hydrogen [63]. Hydrogen and natural gas blending has shown to increase thermal efficiency and operation limits in automobile engines [64–66]. Hydrogen addition in automobile engines also increased NO_x emissions, which have to be restricted below emission regulations [63]. Therefore, hydrogen addition in automobile natural gas engines has been studied [66–68]. However, as the engine load or BMEP increases the operating window between knock and misfire decreases in modern marine engines as they operate at BMEP of 30 bar [69, 70]. Moreover, the emission regulations for automotive and marine natural

gas engines are different. This will change the performance capabilities and the operating limits of marine natural gas engines as they operate with different blends of hydrogen and natural gas. Therefore, it is crucial to qualitatively and quantitatively understand the effects of engine loading along with hydrogen addition in marine natural gas engines.

Previous literature shows a gap in the research on the performance of marine natural gas engines operating at varying engine loads and hydrogen addition percentages. Therefore, the objective of the experimental investigation performed in this PhD is to capture and understand the performance variations in marine hydrogen-natural gas engines due to variations in engine load, spark-timing and hydrogen addition for development of SOFC-ICE integration. The performance of these engines is analysed by studying the effects of hydrogen addition on cycle-to-cycle variations (combustion stability), engine operating limits, thermal efficiency and engine emissions, thus, accounting for maritime emission regulations. Chapter 4 presents the hydrogen-natural gas experiments performed during this research.

PREVIOUS LITERATURE ON CARBON DIOXIDE-NATURAL GAS COMBUSTION EXPERIMENTS

In addition to hydrogen, SOFC anode-off gas can contain high percentages of carbon dioxide as discussed in Chapter 3. Carbon dioxide is a non-combustible constituent of anode-off gas with a higher specific heat capacity compared to air [71]. High carbon dioxide content could counter adversely impact engine performance and SOFC-ICE integration.

Multiple researchers have studied the effects of adding carbon dioxide to diesel and/or natural gas in SI and compression ignition (CI) engines [72, 73]. The effects of adding or increasing carbon dioxide percentage in biogas, diesel or natural gas fuel are often understood as representative of the effects of exhaust gas recirculation (EGR) in engines [74]. In EGR, a portion of, high specific heat capacity, exhaust gas containing inert elements such as carbon dioxide and nitrogen, besides water vapour and others, are rerouted back into the engine cylinders [75]. In existing literature, carbon dioxide addition or EGR have been proven to be promising solutions for reduction of in-cylinder temperatures and, hence, NO_x emissions due to the high absorption heat capacity of the gases [71, 73, 74]. Besides NO_x reduction, studies have shown some adverse impacts of carbon dioxide concentration in biogas, natural gas and/or diesel-fuelled engines.

Porpatham et al. performed experiments to study the effects of increasing methane percentages in biogas on engine performance [76]. The authors modified a diesel engine for SI operation at constant speed. The results showed that high CO₂ percentages adversely impact engine efficiency. Similarly, Henham and Makkar studied the combustion of varying compositions of biogas in a dual-fuel diesel engine [77]. Mixtures varying from 100 % natural gas to 40-60 natural gas-carbon dioxide blends were tested experimentally by the authors. For 58 % gasoil substitution with natural gas, the efficiency decreased from 28.2 % to 26.2 % with increasing CO₂ content in the gas mixture.

A study on the effects of CH₄, H₂ and CO₂ mixtures on the performance of SI engine was performed by Chuayboon et al. [78]. The authors showed that for CO₂ volumetric percentage of 39.12 %, the engine brake power output was lower by 22.5 % compared to that for 20.44 % of CO₂. For the same test condition, the hydrogen percentage was simultaneously decreased from 9.85 to 7.54 % respectively. All the experiments were performed at a constant throttle opening of 14 % [78]. Furthermore, a study by Park et al.

showed that the mixing of CO₂ with natural gas-hydrogen blends in a 213 kW SI engine caused unburnt hydrocarbons and CO emissions to increase at constant air-excess ratios [74]. The increments in UHC and CO emissions were attributed to higher quenching caused by the relatively lower flame proliferation speed of the diluted mixture.

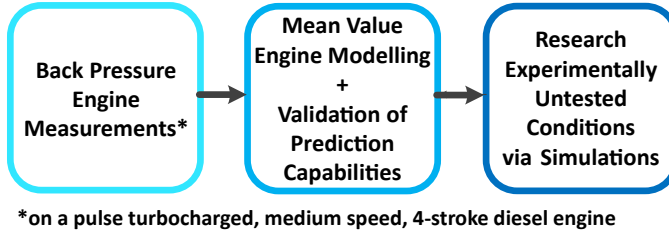


Figure 2.9: Research methodology to study the effects of static back pressure

Current literature on CO₂ addition to fuel mixtures showed that high percentages of carbon dioxide could lead to the reduction of engine brake power and efficiency while increasing UHC and CO emissions. Therefore, the adverse effects of high CO₂ content in SOFC anode-off gas on engine performance can be quite significant. The effects of CO₂ addition have not been studied in a marine SI lean-burn engine for compositions dictated by SOFC anode-off gas. Like hydrogen, carbon dioxide also has an effect on NO_x formation and emissions, which will change the performance capabilities and the operating limits of marine natural gas engines as they operate with different blends of carbon dioxide and natural gas. For this reason, it is vital to understand the impact of carbon dioxide from anode-off gas on the in-cylinder and combustion process along with the complete marine engine performance. Therefore, the impact of CO₂-NG fuel blends on cyclic variations, engine operating limits, in-cylinder process, emissions, and thermal efficiency are experimentally studied and presented in Chapter 4, which form a crucial step in the potential investigation of SOFC-ICE integration.

2.4.2. RESEARCH METHODOLOGY FOR BACK PRESSURE EFFECTS

As explained in Chapter 1, in addition to SOFC-ICE integration, another focus of this research is to provide a comprehensive understanding of high static and dynamic back pressure effects on marine engine performance due to underwater exhaust systems. In this part of the research, first, engine model simulations along with experiments on a pulse turbocharged, medium speed, and 4-stroke diesel engine are used as tools to study the effects of static back pressure on engine performance. Figure 2.9 shows the basic approach followed for this research while Figure 2.10 shows the MAN4L2027 test engine. An extended mean value engine model (Ex-MVEM) is adopted to simulate engine performance against externally applied high static back pressure, which could not be studied experimentally. In this dissertation, the engine model adopted to study the static back pressure effects is referred to as the Ex-MVEM in order to distinguish it from the MVEM developed to capture the performance of the AOG-NG engine for SOFC-ICE integration. The Ex-MVEM can be understood as an extension of the AOG-NG MVEM as explained in Chapter 8. A detailed description of the experimental setup, experimenta-

tion methodology and engine modelling to study back pressure effects have been covered in Chapter 8. The effects of dynamic back pressure on marine engine performance due to underwater exhaust systems are experimentally studied on the same test engine by controlling an electronic butterfly valve installed in the downstream of the turbine outlet. The next subsection discusses the existing literature on the effects of static and dynamic back pressure on engine performance. This literature study highlights the need and basis for the experiments performed in this PhD.

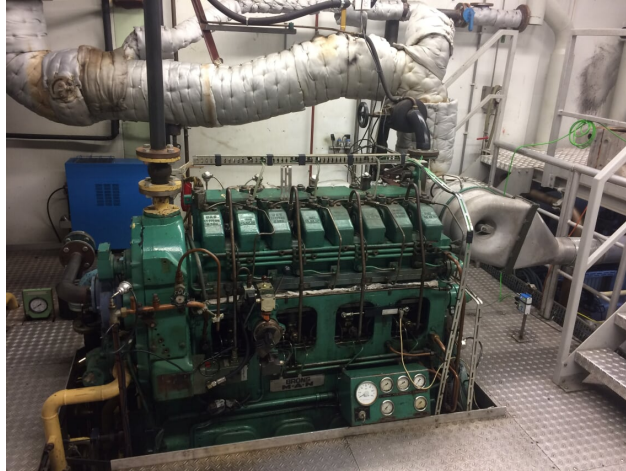


Figure 2.10: Picture of test setup with the MAN4L2027 diesel engine

PREVIOUS LITERATURE ON BACK PRESSURE EFFECTS

For a given mechanical loading, back pressure is known to increase engine thermal loading and also fuel consumption. In extreme cases, a diesel engine can also start smoking due to incomplete combustion, caused by lack of sufficient combustion-air inside the cylinder. Although back pressure effects on engine performance have been recognised before, few studies address the consequences of marine engines running against high static and fluctuating back pressure, especially due to underwater exhausts systems.

For instance, researchers such as Joardder et al. [79] and Cong et al. [80] experimentally investigated the performance and emissions of naturally aspirated compression ignition (C.I.) engines against back pressure. However, effects of back pressure on a naturally aspirated engine will be different from the effects on a turbocharged engine due to the difference in air-intake, fuel-intake, inlet receiver pressures, exhaust receiver temperatures, etc. Mittal et al. [81] conducted experiments on a 4-stroke turbocharged diesel engine against a maximum static back-pressure of 25 mbar at low loads. He observed that the brake specific fuel consumption (bsfc) increased at light loads, while the changes at high load were inconsequential. He also found that the NO_x emissions reduced at all operating loads, whereas soot and particulate matter (PM) emissions increased with an increase in back pressure. However, a marine engine operating with an underwater exhaust system could be exposed to much higher back pressures than 25 mbar (or 0.25

mWC) [82]. Michos et al. [83] investigated the performance of advanced turbocharging techniques to curtail the effects of high back pressure using engine model simulations, however, experimental validation of the simulation results was not provided. Furthermore, the authors studied the performance only at full-load and rated engine speed. In [84], Burnete et al. studied the effects of back pressure on engine power, torque and exhaust gas opacity of a diesel engine for generator applications. Lastly, Mahabadipour et al. [85] characterized the effect of back pressure on exhaust exergy in a diesel engine. Besides these studies, some patents discussed the implementation of marine underwater exhaust [86–88]. Two studies describing the effects of exhaust system design on the performance of a naturally aspirated SI engine for automotive applications were also found [89, 90].

Although limited, all the above-mentioned studies analysed engine performance against static back pressure. Only a few researchers have investigated the effects of dynamic back pressure on engine performance. For example, Tauzia et al. [91] used model simulations to provide a general understanding of the effects of dynamic back pressure due to a partially submerged exhaust on the performance of a marine diesel engine. Although the effects of 600 mbar (or 6 mWC) back pressure amplitude were studied, a validated and quantitative analysis of back pressure effects on a real engine was not provided. Hield used the Ricardo Wave engine model simulations to study the effects of dynamic back pressure on a submarine diesel engine [92] and recommended the need for experiments to validate the research results before they can be relied upon. In a similar study, Ed Swain [93] studied the application of variable geometry turbine (VGT) turbocharging for a diesel-electric submarine.

The above literature study highlights a lack of experimentally validated research on qualitative and quantitative effects of static and dynamic back pressure on marine diesel and natural gas engine performance and their operating limits due to underwater exhaust systems. Although the GasDrive project proposes the integration of a natural gas engine with an underwater exhaust system, in this dissertation, the impact of back pressure due to an underwater exhaust is studied on a marine diesel engine. This study lays the foundation for future research to investigate marine natural gas engine performance against static and dynamic back pressure.

The initial focus of this study is to provide an in-depth understanding of static back pressure effects on marine diesel engine performance at different engine loads and speeds with the help of engine experiments and engine model simulations. Chapter 8 presents a methodology to apply a conceptual model of smoke and thermal overload to define a ceiling for acceptable back pressures that could be adopted in practice for any engine. The study also investigates the capabilities of different turbocharger configurations along with different engine valve overlap settings to tackle high back pressures. Lastly, the dissertation covers an experimental investigation of marine diesel engine performance against dynamic back pressure of varying amplitudes and time periods due to an underwater exhaust system operating in different sea-states.

2.5. CONCLUSIONS

In this chapter, an overview of SOFC technology and SOFC combined cycles in current literature has been provided. A detailed discussion of the advantages and shortcomings

of the SOFC combined cycles has been covered, in addition to a qualitative analysis of the combined cycles from a maritime perspective. The chapter also presents the adopted research methodology. Additionally, the chapter covers previously published literature on hydrogen-natural gas combustion and carbon dioxide-natural gas combustion experiments to highlight the need and basis for the experiments performed in this research. Lastly, a literature survey of back pressure effects on engine performance has been presented in this chapter. The following concluding remarks are noted from the discussions presented in this chapter:

- The literature study showed that existing studies on SOFC-ICE integration and combined cycles are mainly focussed towards land-based distributed power generation with advanced combustion engine technology and turbines employed as part of a SOFC bottoming cycle. Furthermore, numerous challenges of implementing SOFC-ICE bottoming cycle for maritime applications have been debated. By discussing and analysing the shortcomings of the existing SOFC-ICE integration approach in literature, with respect to the necessary considerations for power generation onboard ships, a novel SOFC and AOG-NG Engine integration approach for maritime applications has been proposed, which answers Research Question 1.
- The objective of the research performed in this dissertation is to investigate the impact of SOFC-ICE integration and UWE on marine engine performance and quantify the operation of the integrated SOFC-ICE system for maritime applications to demonstrate feasibility, energy efficiency improvements and emission reductions compared to conventional marine engines.
- The research performed in this PhD dissertation is divided into two parts. First, and the primary part, is focussed on investigating SOFC-ICE integration for marine power generation while the secondary part covers the study of static and dynamic back pressure on marine engine performance due to underwater exhaust systems. The fundamental research approach adopted for both parts of this dissertation is the same. For both, SOFC-ICE integration and static back pressure effects, engine experiments have been used as a basis to understand the underlying phenomena. Then, the experiments are further utilized as building blocks to develop and calibrate engine simulations models capable of capturing engine performance for different test conditions such as varying anode-off gas compositions, varying air-excess ratios, load variations, static back pressure variations, different types of turbocharging, etc.
- A 0-D SOFC modelling approach has been adopted to simulate SOFC performance. The SOFC model is used to capture the impact of ISVs such as current density, fuel utilization and pre-reforming ratio on fuel cell efficiency, anode-off gas composition, flow-rates and cell temperature profiles. Performance parameters such as fuel cell efficiency, anode-off gas quality and quantity are necessary to investigate the potential of the fuel cell and engine integration.
- In this research, the effects of combusting anode-off gas constituents blended with natural gas in a marine engine have been studied experimentally and through engine model simulations. For this purpose, experiments have been performed on a 500 kW_e, eight-cylinder, turbocharged spark-ignited natural gas engine.

- Previous literature on hydrogen-natural combustion experiments showed a gap in the research on the performance of marine natural gas engines operating at varying engine loads and hydrogen addition percentages. Therefore, the objective of the experimental investigation performed in this PhD is to capture and understand the performance variations in marine hydrogen-natural gas engines due to variations in engine load, spark-timing and hydrogen addition for development of SOFC-ICE integration. The performance of these engines has been analysed by studying the effects of hydrogen addition on cycle-to-cycle variations (combustion stability), engine operating limits, thermal efficiency and engine emissions, thus, accounting for maritime emission regulations.
- Current literature on CO₂ addition to fuel mixtures showed that high percentages of carbon dioxide could lead to the reduction of engine brake power and efficiency while increasing UHC and CO emissions. Therefore, the adverse effects of high CO₂ content in SOFC anode-off gas on engine performance can be quite significant. The effects of CO₂ addition have not been studied in a marine SI lean-burn engine for compositions dictated by SOFC anode-off gas. Therefore, the impact of CO₂-NG fuel blends on cyclic variations, engine operating limits, in-cylinder process, emissions, and thermal efficiency have been experimentally studied in this PhD research.
- For the secondary part of the research performed in this PhD dissertation, engine model simulations along with experiments on a pulse turbocharged, medium speed, and 4-stroke diesel engine have been used as tools to study the effects of back pressure on engine performance.
- The literature study on back pressure effects highlighted a lack of experimentally validated research on qualitative and quantitative effects of static and dynamic back pressure on marine diesel and natural gas engine performance and their operating limits due to underwater exhaust systems. Although the GasDrive project proposes the integration of a natural gas engine with an underwater exhaust system, in this dissertation, the effects of back pressure due to an underwater exhaust have been studied on a marine diesel engine.

In the next chapter, a 0-D SOFC cell-to-stack performance model has been presented to simulate the impact of SOFC operating conditions on output parameters such as fuel cell efficiency, anode-off gas compositions, flow-rates, etc.

REFERENCES

- [1] S.J. McPhail et al. SOFC and MCFC: Commonalities and Opportunities for Integrated Research. *International Journal of Hydrogen Energy*, 2011.
- [2] H.D. Sapra et al. Experimental Investigations of Hydrogen-Natural Gas Engines for Maritime Applications. In *ASME Internal Combustion Engine Fall Technical Conference*, 2018.
- [3] H.D. Sapra et al. Experimental Investigations of Performance Variations in Marine Hydrogen-Natural Gas Engines. In *CIMAC*, 2019.

- [4] H.D. Sapra et al. Experimental Investigations of Marine Diesel Engine Performance Against Dynamic Back Pressure at Varying Sea-States Due to Underwater Exhaust Systems. In *ASME Internal Combustion Engine Fall Technical Conference*, 2019.
- [5] H.D. Sapra et al. Experimental and Simulation-Based Investigations of Marine Diesel Engine Performance Against Static Back Pressure. *Applied Energy*, 2017.
- [6] H.D. Sapra et al. Integration of Solid Oxide Fuel Cell and Internal Combustion Engine for Maritime Applications. *Applied Energy*, 2020.
- [7] J. Larminie and A. Dicks. *Fuel Cell Systems Explained, Second Edition*.
- [8] P.J.H. Wingelaar, M.P.A. Geers, J.L. Duarte, and M.A.M. Hendrix. CO-Tolerant Operation of Platinum-Loaded PEM Fuel Cells. In *IEEE International Symposium on Industrial Electronics*, 2007.
- [9] G. Sattler. Fuel Cells Going On-Board. *Journal of Power Sources*, 2000.
- [10] L. van Biert, M. Godjevac, K. Visser, and P.V. Aravind. A Review of Fuel Cell Systems for Maritime Applications. *Journal of Power Sources*, 2016.
- [11] Sunfire Supplies ThyssenKrupp Marine Systems with 50 kW SOFC. <https://www.sunfire.de/en/company/news/detail/sunfire-supplies-thyssenkrupp-marine-systems-with-50-kw-sofc-20>.
- [12] P. Aguiar, C.S. Adjiman, and N.P. Brandon. Anode-Supported Intermediate Temperature Direct Internal Reforming Solid Oxide Fuel Cell. I: Model-Based Steady-State Performance. *Journal of Power Sources*, 2004.
- [13] S. Campanari et al. Predicting the Ultimate Potential of Natural Gas SOFC Power Cycles with CO₂ Capture – Part A: Methodology and Reference Cases. *Journal of Power Sources*, 2016.
- [14] Energy Server ES5-300 kW Data Sheet. <https://www.bloomenergy.com/datasheets/energy-server-es5-300kw>.
- [15] Birch Tree Capital New Energy Opportunities, La Capra Associates. Report on Delmarva Power's Application for Approval of a New Electrical Tariff Applicable to Proposed Bloom Energy Fuel Cell Project. Technical report, 2011.
- [16] F. Ramadhani, M.A. Hussain, and H. Mokhlis. A Comprehensive Review and Technical Guideline for Optimal Design and Operations of Fuel Cell-Based Cogeneration Systems. *Processes*, 2019.
- [17] A. Salogni and P. Colonna. Modeling of Solid Oxide Fuel Cells for Dynamic Simulations of Integrated Systems. *Applied Thermal Engineering*, 2010.
- [18] S. Kang and K.Y. Ahn. Dynamic Modeling of Solid Oxide Fuel Cell and Engine Hybrid System for Distributed Power Generation. *Applied Energy*, 2017.
- [19] A.M. Beney. Investigation into the Heat Up Time for Solid Oxide Fuel Cells in Automotive Applications, 2018.
- [20] Bloom Box Costs \$12.50 per Watt. <https://www.wired.com/2011/01/bloom-box-cost/>.
- [21] T.H. Lim et al. Operating Characteristics of a 5 kW Class Anode-Supported Planar

- SOFC Stack for a Fuel Cell/Gas Turbine Hybrid System. *International Journal of Hydrogen Energy*, 2008.
- [22] F. Baldi, L. Wang, M. Pérez-Fortes, and F. Maréchal. A Cogeneration System Based on Solid Oxide and Proton Exchange Membrane Fuel Cells with Hybrid Storage for Off-Grid Applications. *Frontiers in Energy Research*, 2019.
- [23] X. Zhang et al. A Review of Integration Strategies for Solid Oxide Fuel Cells. *Journal of Power Sources*, 2010.
- [24] Y.M.A. Welaya, M. Mosleh, and N.R. Ammar. Energy Analysis of a Combined Solid Oxide Fuel Cell with a Steam Turbine Power Plant for Marine Applications. *Journal of Marine Science & Application*, 2014.
- [25] A. Buonomano et al. Hybrid Solid Oxide Fuel Cells-Gas Turbine Systems for Combined Heat and Power: A Review. *Applied Energy*, 2015.
- [26] Y. Kobayashi et al. Recent Progress of SOFC Combined Cycle System with Segmented-In-Series Tubular Type Cell Stack at MHI. *ECS Transactions*, 2013.
- [27] M. Nishiura et al. Development of SOFC-Micro Gas Turbine Combined Cycle System. *ECS Transactions*, 2007.
- [28] F.D.F. Chuahy and S.L. Kokjohn. Solid Oxide Fuel Cell and Advanced Combustion Engine Combined Cycle: A Pathway to 70% Electrical Efficiency. *Applied Energy*, 2019.
- [29] L. van Biert et al. A Thermodynamic Comparison of Solid Oxide Fuel Cell-Combined Cycles. *Journal of Power Sources*, 2018.
- [30] S.H. Chan, H.K. Ho, and Y. Tian. Modelling of Simple Hybrid Solid Oxide Fuel Cell and Gas Turbine Power Plant. *Journal of Power Sources*, 2002.
- [31] S.K. Park and T.S. Kim. Comparison Between Pressurized Design and Ambient Pressure Design of Hybrid Solid Oxide Fuel Cell-Gas Turbine Systems. *Journal of Power Sources*, 2006.
- [32] S.H. Chan, H.K. Ho, and Y. Tian. Modelling for Part-Load Operation of Solid Oxide Fuel Cell-Gas Turbine Hybrid Power Plant. *Journal of Power Sources*, 2003.
- [33] Combustion Engine vs Gas Turbine-Part Load Efficiency and Flexibility. <https://www.wartsila.com/energy/learn-more/technical-comparisons/combustion-engine-vs-gas-turbine-part-load-efficiency-and-flexibility>.
- [34] Combustion Engine vs Gas Turbine-Startup Time. <https://www.wartsila.com/energy/learn-more/technical-comparisons/combustion-engine-vs-gas-turbine-startup-time>.
- [35] S.H. Park, Y.D. Lee, and K.Y. Ahn. Performance Analysis of an SOFC/HCCI Engine Hybrid System: System Simulation and Thermo-Economic Comparison. *International Journal of Hydrogen Energy*, 2014.
- [36] Y.D. Lee, K.Y. Ahn, T. Morosuk, and G. Tsatsaronis. Exergetic and Exergoeconomic Evaluation of an SOFC-Engine Hybrid Power Generation System. *Energy*, 2018.

- [37] C. Edwards, J. Fyffe, M. Donohue, and C. Regalbuto. Exploration of a Fuel Cell/Internal Combustion Engine Combined Cycle for High Efficiency Power Generation (A GCEP Exploratory Project). 2013.
- [38] J. Kim et al. Analysis on the Operating Performance of 5-kW Class Solid Oxide Fuel Cell-Internal Combustion Engine Hybrid System Using Spark-Assisted Ignition. *Applied Energy*, 2020.
- [39] P. Zhu et al. High-Efficiency Conversion of Natural Gas Fuel to Power by an Integrated Dystem of SOFC, HCCI Engine, and Waste Heat Recovery: Thermodynamic and Thermo-Economic Analyses. *Fuel*, 2020.
- [40] W. Choi et al. Experimental Study of Homogeneous Charge Compression Ignition Engine Operation Fuelled by Emulated Solid Oxide Fuel Cell Anode Off-Gas. *Applied Energy*, 2018.
- [41] W. Choi and H.H. Song. Composition-Considered Woschni Heat Transfer Correlation: Findings from the Analysis of Over-Expected Engine Heat Losses in a Solid Oxide Fuel Cell-Internal Combustion Engine Hybrid System. *Energy*, 2020.
- [42] P.W. Bessonette et al. Effects of Fuel Property Changes on Heavy-Duty HCCI Combustion. In *SAE Technical Paper*, 2007.
- [43] J.E. Dec, Y. Yang, and N. Dronniou. Boosted HCCI-Controlling Pressure-Rise Rates for Performance Improvements Using Partial Fuel Stratification with Conventional Gasoline. *International Journal of Engines*, 2011.
- [44] S.L. Kokjohn, R.M. Hanson, D.A. Splitter, and R.D. Reitz. Experiments and modeling of dual-fuel hcci and pcci combustion using in-cylinder fuel blending. *International Journal of Engines*, 2010.
- [45] W. Choi, J. Kim, Y. Kim, and H.H. Song. Solid Oxide Fuel Cell Operation in a Solid Oxide Fuel Cell-Internal Combustion Engine Hybrid System and the Design Point Performance of the Hybrid System. *Applied Energy*, 2019.
- [46] Z. Wu et al. Performance Analysis of a Novel SOFC-HCCI Engine Hybrid System Coupled with Metal Hydride Reactor for H₂ Addition by Waste Heat Recovery. *Energy Conversion and Management*, 2019.
- [47] V.D. Chaudhari and D. Deshmukh. Challenges in Charge Preparation and Combustion in Homogeneous Charge Compression Ignition Engines with Biodiesel: A Review. *Energy Reports*, 2019.
- [48] Z. Ran, D. Assanis, D. Hariharan, and S. Mamalis. Experimental Study of Spark-Ignition Combustion Using the Anode Off-Gas from a Solid Oxide Fuel Cell. In *SAE Technical Papers*, 2020.
- [49] J.R. Fyffe, M.A. Donohue, M.C. Regalbuto, and C.F. Edwards. Mixed Combustion-Electrochemical Energy Conversion for High-Efficiency, Transportation-Scale Engines. *International Journal of Engine Research*, 2017.
- [50] C.A. Amann. Promises and Challenges of the Low-Heat-Rejection Diesel. *Journal of Engineering for Gas Turbines and Power*, 1988.
- [51] J. Hartman. *Turbocharging Performance Handbook*. Motorbooks, 2007.

- [52] C. Sui, E. Song, D. Stapersma, and Y. Ding. Mean Value Modelling of Diesel Engine Combustion Based on Parameterized Finite Stage Cylinder Process. *Ocean Engineering*, 2017.
- [53] B. Taskar, K.K. Yum, S. Steen, and E. Pedersen. The Effect of Waves on Engine-Propeller Dynamics and Propulsion Performance of Ships. *Ocean Engineering*, 2016.
- [54] R.D. Reitz and G. Duraisamy. Review of High Efficiency and Clean Reactivity Controlled Compression Ignition (RCCI) Combustion in Internal Combustion Engines. *Progress in Energy and Combustion Science*, 2015.
- [55] T. Korakianitis, A.M. Namasivayam, and R.J. Crookes. Natural-Gas Fueled Spark-Ignition (SI) and Compression-Ignition (CI) Engine Performance and Emissions. *Progress in Energy and Combustion Science*, 2011.
- [56] H. Thomson, J.J. Corbett, and J.J. Winebrake. Natural Gas as a Marine Fuel. *Energy Policy*, 2015.
- [57] H.M. Cho and B.Q. He. Spark Ignition Natural Gas Engines-A Review. *Energy Conversion and Management*, 2007.
- [58] G.A. Karim, I. Wierzba, and Y. Al-Alousi. Methane-Hydrogen Mixtures as Fuels. *International Journal of Hydrogen Energy*, 1996.
- [59] J.B. Heywood. *Internal Combustion Engine Fundamentals*. McGraw-Hill Series in Mechanical Engineering, 1988.
- [60] CIMAC Working Group 17. Transient Response Behaviour of Gas Engines. In *CIMAC*, 2011.
- [61] F. Ma and Y. Wang. Study on the Extension of Lean Operation Limit Through Hydrogen Enrichment in a Natural Gas Spark-Ignition Engine. *International Journal of Hydrogen Energy*, 2008.
- [62] J.C. Keck, J.B. Heywood, and G. Noske. Early Flame Development and Burning Rates in Spark Ignition Engines and Their Cyclic Variability. In *SAE Technical Paper*, 1987.
- [63] R.K. Mehra et al. Progress in Hydrogen Enriched Compressed Natural Gas (HCNG) Internal Combustion Engines - A Comprehensive Review. *Renewable and Sustainable Energy Reviews*, 2017.
- [64] F. Ma et al. Effects of Hydrogen Addition on Cycle-By-Cycle Variations in a Lean Burn Natural Gas Spark-Ignition Engine. *International Journal of Hydrogen Energy*, 2008.
- [65] F. Ma et al. Experimental Study on Thermal Efficiency and Emission Characteristics of a Lean Burn Hydrogen Enriched Natural Gas Engine. *International Journal of Hydrogen Energy*, 2007.
- [66] C.G. Bauer and T.W. Forest. Effect of Hydrogen Addition on the Performance of Methane-Fueled Vehicles. Part II: Driving Cycle Simulations. *International Journal of Hydrogen Energy*, 2001.
- [67] M.A. Escalante Soberanis and A.M. Fernandez. A Review on the Technical Adap-

- tations for Internal Combustion Engines to Operate with Gas/Hydrogen Mixtures. *International Journal of Hydrogen Energy*, 2010.
- [68] S. Verma and L.M. Das. Spark Advance Modelling of Hydrogen- Fuelled Spark Ignition Engines using Combustion Descriptors. *Journal of Engineering for Gas Turbines and Power*, 2018.
- [69] L. Xiang, E. Song, and Y. Ding. A Two-Zone Combustion Model for Knocking Prediction of Marine Natural Gas SI Engines. *Energies*, 2018.
- [70] K. Packham. Lean-Burn Engine Technology Increases Efficiency, Reduces NOx Emissions (White paper). 2007.
- [71] W. Li, Z. Liu, Z. Wang, and Y. Xu. Experimental Investigation of the Thermal and Diluent Effects of EGR Components on Combustion and NOx Emissions of a Turbocharged Natural Gas SI Engine. *Energy Conversion and Management*, 2014.
- [72] A.B. Wasu, A.R.A. Aziz, and M.R. Heikal. The Effect of Carbon Dioxide Content-Natural Gas on the Performance Characteristics of Engines: A Review. *Journal of Applied Sciences*, 2012.
- [73] J. Huang and R.J. Crookes. Assessment of Simulated Biogas as a Fuel for the Spark Ignition Engine. *Fuel*, 1998.
- [74] C. Park, S. Won, C. Kim, and Y. Choi. Effect of Mixing Carbon Dioxide with Natural Gas-Hydrogen Blends on Combustion in Heavy-Duty Spark Ignition Engine. *Fuel*, 2012.
- [75] E. Hu et al. Experimental Study on Combustion Characteristics of a Spark-Ignition Engine Fueled with Natural Gas-Hydrogen Blends Combining with EGR. *International Journal of Hydrogen Energy*, 2009.
- [76] E. Porpatham, A. Ramesh, and B. Nagalingam. Effect of Swirl on the Performance and Combustion of a Biogas Fuelled Spark Ignition Engine. *Energy Conversion and Management*, 2013.
- [77] A. Henham and M.K. Makkar. Combustion of Simulated Biogas in a Dual-Fuel Diesel Engine. *Energy Conversion and Management*, 1998.
- [78] S. Chuayboon et al. Effects of CH₄, H₂ and CO₂ Mixtures on SI Gas Engine. *Energy Procedia*, 2014.
- [79] M.U.H. Joardder, M.S. Uddin, and M.M. Roy. Effect of Engine Backpressure on the Performance and Emissions of a CI Engine. 2011.
- [80] S. Cong, C.P. Garner, and G.P. Mctaggart-Cowan. The Effects of Exhaust Back Pressure on Conventional and Low-Temperature Diesel Combustion. *Proceedings of the Institution of Mechanical Engineers, Part D: Journal of Automobile Engineering*, 2011.
- [81] M. Mittal, R. Donahue, and P. Winnie. Evaluating the Influence of Exhaust Back Pressure on Performance and Exhaust Emissions Characteristics of a Multicylinder, Turbocharged, and Aftercooled Diesel Engine. *Journal of Energy Resources Technology*, 2015.
- [82] H.D. Sapra. Study of Effects on Diesel Engine Performance due to varying Back

- Pressure for an Underwater Exhaust System. Master's thesis, Delft University of Technology, 2015.
- [83] C.N. Michos, S. Lion, I. Vlaskos, and R. Taccani. Analysis of the Backpressure Effect of an Organic Rankine Cycle (ORC) Evaporator on the Exhaust Line of a Turbocharged Heavy Duty Diesel Power Generator for Marine Applications. *Energy Conversion and Management*, 2017.
- [84] N. Burnete, D. Moldovanu, D. Baldean, and L. Kocsis. Studies Regarding the Influence of Exhaust Backpressure on the Performances of a Compression Ignited Engine. In *Proceedings of the European Automotive Congress*, 2015.
- [85] H. Mahabadipour et al. Characterization of the Effect of Exhaust Back Pressure on Crank Angle-Resolved Exhaust Exergy in a Diesel Engine. In *ASME Internal Combustion Engine Fall Technical Conference*, 2019.
- [86] W. Woods and D. Woods. Submerged Exhaust Discharge for Marine Vessel, 2010.
- [87] P. Hoquet, D. Leducq, R. Mattout, and P. Sagnes. Underwater Exhaust Device for the Internal Combustion Engine of a Vessel, 1993.
- [88] H.C. Nelson and W.H. Mullins. Under-Water Exhaust for Launches, 1908.
- [89] J.A. Bolt, S.P. Bergin, and F.J. Vesper. The Influence of the Exhaust Back Pressure of a Piston Engine on Air Consumption, Performance, and Emissions. In *SAE Technical Paper*, 1973.
- [90] T.G. Adams. Effect of Exhaust System Design on Engine Performance. In *SAE Technical Paper*, 1980.
- [91] X. Tauzia, P. Chessé, and A. Maiboom. Simulation Study of a Ship's Engine Behaviour Running with a Periodically Immersed Exhaust. *Proceedings of the Institution of Mechanical Engineers, Part M: Journal of Engineering for the Maritime Environment*, 2008.
- [92] P. Hield. The Effect of Back Pressure on the Operation of a Diesel Engine. Technical report, Defence Science and Technology Organisation, 2011.
- [93] E. Swain. Turbocharging the Submarine Diesel Engine. *Mechatronics*, 1994.

3

ZERO-DIMENSIONAL SOFC MODEL

In this chapter, a SOFC single cell-to-stack model is described to simulate the performance of the fuel cell. The SOFC model is used to capture the impact of ISVs on fuel cell efficiency, anode-off gas composition, flow-rates and cell temperature profiles. The SOFC model is verified against data available from literature. Furthermore, the chapter discusses the variations in SOFC performance and anode-off gas compositions necessary for SOFC-ICE integration. In this manner, the chapter provides insights for answering Research Question 2 and partially answering Research Question 5.

3.1. SOFC MODEL INTRODUCTION

Numerous researchers have presented SOFC performance models, which can vary in terms of their PEN structure (electrolyte or electrode supported), cell geometry (monolithic, tubular or planar) and flow arrangements (co, counter or cross-flow) [1, 2]. They also range from zero-dimensional (0-D) to three-dimensional (3-D) models, thus, varying in their degree of complexity, details and computational effort required [3, 4]. For the purpose of research presented in this dissertation, system-level modelling capable of computing the polarization curves, fuel cell efficiency, anode-off gas compositions and flow rates is sufficient [5]. Therefore, in this research, SOFC stack performance is extrapolated from a single cell model, which is based on a 0-D electrochemical and equilibrium model. The IT-SOFC single cell model adopted for this research is a 0-D, planar cell model with co-flow configuration as shown in Figure 3.1.

Figure 3.1 shows the combination of 5 layers forming a unit or single SOFC cell consisting of a PEN structure, anode-flow (af) channel for fuel, cathode-flow channel for air and the interconnects adjacent to each electrode. A single SOFC cell is unable to generate a useful voltage as it generates a marginal voltage (V) of about 0.7 V. For this reason,

Parts of this chapter have been published in Applied Energy [6].

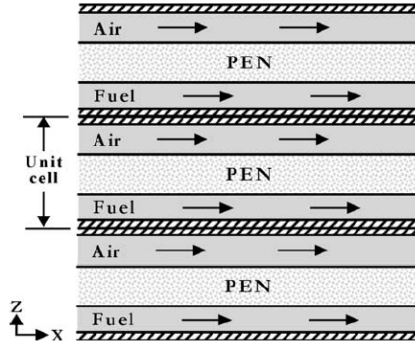


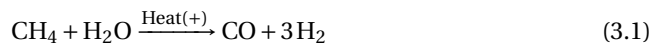
Figure 3.1: Schematic view of 3 single SOFC cells as part of a SOFC stack [7]

numerous electrochemical cells are connected to form a SOFC stack for power generation. Therefore, SOFC models are generally based on a single cell and then expanded to capture the SOFC stack performance. The same approach is adopted in this dissertation to simulate the SOFC stack performance for SOFC-ICE integration.

3.2. SOFC SINGLE CELL MODEL OUTLINE AND ASSUMPTIONS

The single cell model presented in this research uses the incoming fuel rate or fuel utilization (ratio of fuel consumed to fuel supplied), current density, air-excess ratio and methane pre-reforming ratio as inputs to compute the cell performance. The model can be solved with incoming fuel flow rate as an input or as an anti-causal model that uses fuel utilization as an input. Under real operating conditions, the incoming fuel flow rate is controlled to dictate the required fuel utilization. Based on the inputs, the cell model solves an electrochemical model, anode-off gas composition and mass and energy balance solver to compute cell voltage, anode-off gas composition, anode-off gas flow rates, polarization or current-voltage (i-V) curve, cell power, efficiency and temperature curves. The SOFC single cell model is based on cell geometry and material data presented in [7]. The reference cell data is for a planar, anode-supported and co-flow IT-SOFC. Appendix A provides the relevant cell geometry and material data.

In order to model SOFC cell operation, various physical phenomena need to be taken into consideration. Figure 3.2 provides the model schematics of the single SOFC cell comprising of three control volumes and various physical phenomenon. The anode, electrolyte and the cathode are combined to form the PEN structure, which is assumed as one control volume. The anode-flow channel forms another control volume, which accommodates the methane steam reforming (MSR) and water-gas shift (WGS) reaction to form the hydrogen needed for the electrochemical oxidation process. The MSR and WGS reactions are given by equation 3.1 and equation 3.2, respectively. The MSR reaction is endothermic, while the WGS reaction is moderately exothermic.



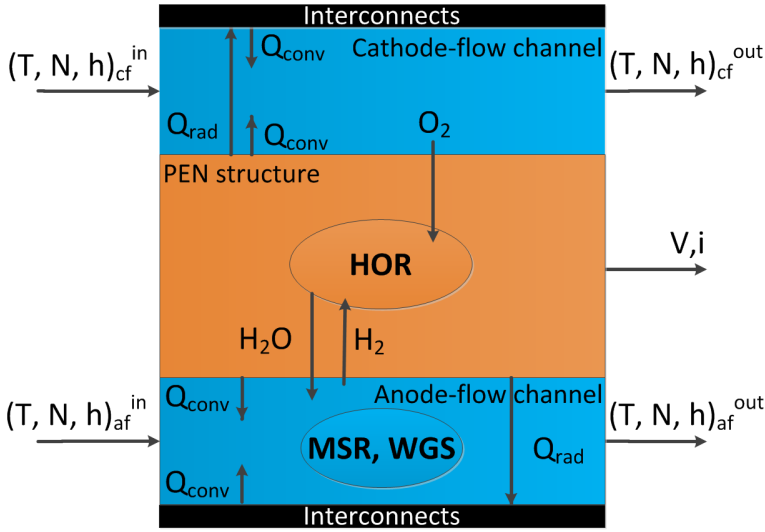
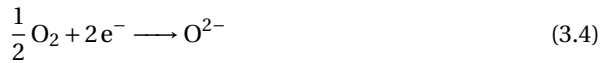
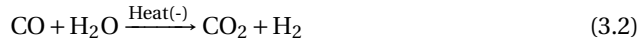


Figure 3.2: Single cell model schematics with three control volume: cathode-flow channel, PEN structure and anode-flow channel. The MSR, WGS and HOR 'ovals' mark the approximate locations of the heat source



To avoid the risk of carbon deposition on the anode surface along with large temperature gradients, the modelled SOFC operates with a methane pre-reformer. A pre-reformer partially pre-reforms a fixed percentage of methane to hydrogen and carbon monoxide. Inside the pre-reformer, the steam required for the MSR and WGS reactions is controlled to maintain a steam-to-carbon (S/C) ratio of 2 or more [8]. From the pre-reformer outlet, the partially reformed methane gas mixture is supplied to the anode-flow channel. Remaining methane undergoes direct internal reforming in the anode-flow channel to produce hydrogen [7] as explained earlier. The hydrogen diffuses into the PEN structure through the anode and further participates in the hydrogen oxidation reaction (HOR) to produce steam, heat and electrons as given by equation 3.3 and shown in Figure 3.2. Therefore, the HOR reaction and the corresponding heat release is assumed to take place within the PEN structure. Equation 3.4 shows the oxygen reduction at the cathode, as oxygen combines with electrons to form oxygen ions. The oxide ion diffuses into the PEN structure through the porous cathode and combines with hydrogen to complete the hydrogen oxidation reaction. The amount of hydrogen consumed in the reaction is dictated by the fuel-utilization factor. Thus, the combination of MSR, WGS and HOR reactions form the anode-off gas or anode-tail gas, which consists of CH_4 , H_2O , H_2 , CO and CO_2 as it exits the cell at high temperatures through the anode-flow channel.

Following the above-described schematics, the proceeding sections present the equations adopted to capture various physical phenomena in the single cell model and pre-reformer model. The presented pre-reformer and SOFC model operate under the following main assumptions and considerations.

- The SOFC model operates on natural gas with 100 % methane [7, 9]. In reality, natural gas can contain small percentages of sulphur, which can poison the anode and reduce the catalytic activity [10, 11]. Therefore, SOFCs operating on natural gas require a sulphur removal system. However, for system-level modelling and dynamic modelling, this effect can be neglected [4, 12].
- All gases in the SOFC follow the ideal gas law due to operation at high temperatures (higher than 1000 K) and ambient pressure.
- Pressure differences along the anode-flow and cathode-flow channels are assumed to be insignificant.
- The electrochemical oxidation of CO is neglected. Electrochemical reaction of CO is 2 - 5 times slower than that of hydrogen, therefore, carbon monoxide is considered to be consumed via the water-gas-shift reaction (WGS) [13].
- Pre-reformer is integrated with the SOFC to allow for indirect internal reforming. The heat for maintaining the reforming reactions is taken from the SOFC, therefore, the pre-reformer operates at the same temperature as the SOFC.
- Methane is completely reformed via indirect internal reforming (pre-reformer) and direct internal reforming.
- The MSR and WGS reactions are assumed to be fast enough to achieve chemical equilibrium [5].
- Adiabatic boundary conditions are assumed for the stack, i.e., heat loss to the surroundings is neglected. This assumption is further discussed in section 3.6.

3.3. PRE-REFORMER MODEL

The model uses a prescribed methane pre-reforming ratio (PRR) to control the percentage of methane being pre-reformed. The relation between the molar flow-rate of methane exiting the pre-reformer (pre,out) and the molar flow rate of methane entering the pre-reformer (pre,in) is given by equation 3.5, where REF is the pre-reformer conversion factor. During pre-reforming, the required amount of steam is dictated by the prescribed steam-to-carbon ratio. The pre-reformer model numerically solves equation 3.5, the molar balances of hydrogen, carbon and oxygen elements along with the WGS equilibrium equation to compute the flows of the five outgoing species, namely, H₂, H₂O, CH₄, CO and CO₂. Equations 3.6, 3.7 and 3.8 give the element balance for hydrogen (H), carbon (C) and oxygen (O). The pre-reformer model is adopted from [14].

$$\text{REF} = 1 - \text{PRR} = \frac{\dot{N}_{\text{CH}_4}^{\text{pre,out}}}{\dot{N}_{\text{CH}_4}^{\text{pre,in}}} \quad (3.5)$$

$$4\dot{N}_{\text{CH}_4}^{\text{pre,out}} + 2\dot{N}_{\text{H}_2}^{\text{pre,out}} + 2\dot{N}_{\text{H}_2\text{O}}^{\text{pre,out}} - 4\dot{N}_{\text{CH}_4}^{\text{pre,in}} - 2\dot{N}_{\text{H}_2\text{O}}^{\text{pre,in}} - 2\dot{N}_{\text{H}_2}^{\text{pre,in}} = 0 \quad (3.6)$$

$$\dot{N}_{\text{CH}_4}^{\text{pre,out}} + \dot{N}_{\text{CO}}^{\text{pre,out}} + \dot{N}_{\text{CO}_2}^{\text{pre,out}} - \dot{N}_{\text{CH}_4}^{\text{pre,in}} - \dot{N}_{\text{CO}}^{\text{pre,in}} - \dot{N}_{\text{CO}_2}^{\text{pre,in}} = 0 \quad (3.7)$$

$$\dot{N}_{\text{H}_2\text{O}}^{\text{pre,out}} + \dot{N}_{\text{CO}}^{\text{pre,out}} + 2\dot{N}_{\text{CO}_2}^{\text{pre,out}} - \dot{N}_{\text{H}_2\text{O}}^{\text{pre,in}} - \dot{N}_{\text{CO}}^{\text{pre,in}} - 2\dot{N}_{\text{CO}_2}^{\text{pre,in}} = 0 \quad (3.8)$$

$$K_{\text{eq,WGS}} = \frac{\dot{N}_{\text{H}_2}^{\text{pre,out}} \cdot \dot{N}_{\text{CO}_2}^{\text{pre,out}}}{\dot{N}_{\text{H}_2\text{O}}^{\text{pre,out}} \cdot \dot{N}_{\text{CO}}^{\text{pre,out}}} \quad (3.9)$$

where, the equilibrium constant ' $K_{\text{eq,WGS}}$ ' is computed by equation 3.10 [15]. $K_{\text{eq,WGS}}$ depends on the change in Gibbs free energy and can be written as a function of the PEN temperature.

$$K_{\text{eq,WGS}} = \exp\left(\frac{4276}{T_{\text{PEN}}} - 3.961\right) \quad (3.10)$$

The modelled pre-reformer simulates indirect internal reforming, thus, the heat (Q_{pre}), in W, required to maintain the reactions in the pre-reformer is obtained from the SOFC and calculated by equation 3.11. ' T_{pre} ' in K is the operating temperature of the pre-reformer, which is equal to the initial operating temperature of the SOFC and 'j' is each species participating in the reactions, namely, H_2 , H_2O , CH_4 , CO and CO_2 .

$$Q_{\text{pre}} = \sum_j \dot{N}_j^{\text{pre,in}} \cdot h(T_{\text{pre}})_j - \sum_j \dot{N}_j^{\text{pre,out}} \cdot h(T_{\text{pre}})_j \quad (3.11)$$

where, 'h' is the molar specific enthalpy in J mol^{-1} .

In real systems, indirect internal reforming of methane is performed by reformers positioned in close thermal contact with the stack [16]. In this SOFC model, the total heat required for pre-reforming the methane flow entering the stack is discretized. Therefore, the pre-reformer model is solved with the single cell model to account for the heat required for indirect internal reforming of the methane flow corresponding to each cell.

In this manner, the pre-reformer computes the composition of the outgoing partially reformed methane gas based on the pre-defined pre-reforming ratio, steam-to-carbon ratio, methane molar flow rate entering the pre-reformer and operating temperature.

3.4. SINGLE CELL MODEL EQUATIONS

3.4.1. EQUILIBRIUM MODEL FOR ANODE-OFF GAS COMPOSITION

The partially reformed methane gas flows from the pre-reformer into the anode-flow channel. The remaining methane gas is completely reformed via the MSR and WGS reaction taking place directly on the anode with nickel acting as the catalyst. Hydrogen diffuses into the PEN structure, where the hydrogen oxidation reaction is assumed to take place. The water-vapour and heat formed during the hydrogen oxidation reaction diffuse back into the anode channel, where they take part in the direct internal reforming process. Therefore, the MSR, WGS and the HOR reactions dictate the composition of the anode-off gas. To compute the anode-off gas composition, the MSR and WGS reactions are assumed to be fast enough to achieve chemical equilibrium. The following four equations are solved simultaneously for chemical equilibrium.

$$p_{\text{H}_2} \cdot p_{\text{CO}_2} = K_{\text{eq,WGS}} \cdot p_{\text{H}_2} \cdot p_{\text{CO}_2} \quad (3.12)$$

$$2(p_{\text{H}_2} + p_{\text{H}_2\text{O}}) = \frac{\text{H}}{\text{C}} \cdot (p_{\text{CO}_2} + p_{\text{CO}}) \quad (3.13)$$

$$2p_{\text{CO}_2} + p_{\text{CO}} + p_{\text{H}_2\text{O}} = \frac{\text{O}}{\text{C}} \cdot (p_{\text{CO}_2} + p_{\text{CO}}) \quad (3.14)$$

$$p_{\text{H}_2} + p_{\text{H}_2\text{O}} + p_{\text{CO}} + p_{\text{CO}_2} = 1 \quad (3.15)$$

In equations 3.12 to 3.15, 'p' represents the partial pressure of each species in Pa. Equation 3.12 solves for the WGS equilibrium while equation 3.13 and 3.14 solve for the conservation of elements H, C and O in the form of H/C and O/C ratios, respectively [17]. The equilibrium constant for the WGS reaction is estimated by using equation 3.10, which is a function of the temperature. Equation 3.15 fixes the sum of all partial pressures to be 1. Ratios H/C and O/C in equation 3.13 and equation 3.13 are computed as a function of fuel utilization (U_f) and S/C ratio. Fuel utilization is the ratio of fuel or hydrogen consumed to the ratio of total hydrogen supplied. U_f is calculated using equation 3.16 [18], and it directly impacts the electrical efficiency of the fuel cell and also the anode-off gas composition.

$$U_f = \frac{i \cdot A_{\text{act}}}{2 \cdot F \cdot (4y_{\text{CH}_4}^{\text{in}} + y_{\text{H}_2}^{\text{in}} + y_{\text{CO}}^{\text{in}}) \cdot \dot{N}_{\text{af}}^{\text{in}}} \quad (3.16)$$

where, 'y' is the molar fraction of CH_4 , H_2 and CO , ' $\dot{N}_{\text{af}}^{\text{in}}$ ' in mols^{-1} represents the molar flow rate entering the anode-flow (af) channel from the pre-reformer, 'i' is the current density in A m^{-2} , 'F' is Faraday's constant (96485 C mol^{-1}) and ' A_{act} ' is the active cell area in m^2 . The active area of the cell is a multiple of active cell length and active cell width in (m).

In this manner, equations 3.12 to 3.15 are solved as a function of cell temperature, fuel utilization and S/C ratio at every time step to determine the molar fractions of the four species present in anode-off gas, namely, H_2O , H_2 , CO and CO_2 . CH_4 is assumed to be completely reformed and converted to H_2 in the anode-flow channel.

3.4.2. ELECTROCHEMICAL MODEL

When current is drawn, the cell produces a potential difference after accounting for all irreversibilities or losses, which is called as the operating cell voltage (V_{cell}) in V. The multiple of current density and cell voltage is equal to the amount of power produced by the cell per unit active cell area, and is referred to as the power density (PoD) in W m^{-2} . Equation 3.17 is used to compute the cell power density.

$$\text{PoD} = i \cdot V_{\text{cell}} \quad (3.17)$$

The operating cell voltage is equal to the open-circuit voltage (E) minus the various cell losses as shown in equation 3.18. The open-circuit voltage is calculated by using the Nernst equation, which accounts for the reactivity of the products and reactant as shown in equation 3.19. E is also called the 'Nernst voltage' and is the reversible cell voltage that would exist at a given PEN temperature and pressure [16]. The SOFC is considered to be operating at an ambient pressure of 100 000 Pa. The logarithmic term in equation 3.19 captures the changes in the chemical driving force due to changes in temperature and

compositions as the values of partial pressures used in equation 3.19 are an average of the incoming and outgoing partial pressures in the anode-flow channel.

$$V_{\text{cell}} = E - \Delta V_{\text{act}} - \Delta V_{\text{conc}} - \Delta V_{\text{ohm}} \quad (3.18)$$

$$E = E^0 + \frac{R \cdot T_{\text{PEN}}}{2F} \cdot \ln\left(\frac{P_{\text{H}_2} \cdot P_{\text{O}_2}^{0.5}}{P_{\text{H}_2\text{O}}}\right) \quad (3.19)$$

where, 'E⁰' is the open-circuit voltage at standard pressure. It is the maximum theoretical open-circuit voltage of the cell, and can be computed from the change in Gibbs free energy of hydrogen oxidation and Faraday's constant [16]. 'R' is the universal gas constant in J mol⁻¹ K⁻¹.

After deriving the value of 'E', the operating cell voltage is computed from equation 3.18, which accounts for the activation, concentration and ohmic losses. The proceeding subsections provide a discussion on each voltage loss.

ACTIVATION LOSSES

Activation loss or activation potential accounts for the slow kinetics of the reactions taking place on the surface of the electrodes. A proportion of the open-circuit voltage is needed to drive the chemical reaction. The activation loss is estimated for each electrode and depends on their individual exchange current density (*i*₀) as shown in equation 3.20 [19]. The exchange current densities of each electrode are calculated from equation 3.21 and equation 3.22 [18].

$$\Delta V_{\text{act}} = \frac{R \cdot T_{\text{PEN}}}{F} \sinh^{-1}\left(\frac{i}{2i_{0,a}}\right) + \frac{R \cdot T_{\text{PEN}}}{F} \sinh^{-1}\left(\frac{i}{2i_{0,c}}\right) \quad (3.20)$$

$$i_{0,a} = \frac{R \cdot T_{\text{PEN}}}{2F} \cdot k_a \cdot \exp\left(\frac{-E_{a,a}}{R \cdot T_{\text{PEN}}}\right) \quad (3.21)$$

$$i_{0,c} = \frac{R \cdot T_{\text{PEN}}}{2F} \cdot k_c \cdot \exp\left(\frac{-E_{a,c}}{R \cdot T_{\text{PEN}}}\right) \quad (3.22)$$

where, 'k_a' and 'k_c' are pre-exponential coefficients in Ω m⁻² while 'E_{a,a}' and 'E_{a,c}' represent the activation energy for the anode and the cathode measured in J mol⁻¹.

CONCENTRATION LOSSES

Mass transport or concentration losses result from the changes in concentration of reactants at the triple-phase boundary as the fuel is consumed. In this model, hydrogen and water vapour are assumed to diffuse in and out of the PEN structure from the anode through pores. Similarly, oxygen is assumed to diffuse into PEN structure from the cathode. Concentration losses are modelled by using equations 3.23 to 3.26 [7]. Equations 3.24 to 3.26 are relations between the partial pressures of H₂, H₂O and O₂ at the TPB and current density, which are required to calculate the concentration losses [7].

$$\Delta V_{\text{conc}} = \frac{R \cdot T_{\text{PEN}}}{2F} \cdot \ln\left(\frac{P_{\text{H}_2\text{O,TPB}} \cdot P_{\text{H}_2,\text{af}}}{P_{\text{H}_2\text{O,af}} \cdot P_{\text{H}_2,\text{TPB}}}\right) + \frac{R \cdot T_{\text{PEN}}}{4F} \cdot \ln\left(\frac{P_{\text{O}_2,\text{cf}}}{P_{\text{O}_2,\text{TPB}}}\right) \quad (3.23)$$

$$p_{H_2,TPB} = p_{H_2,af} - \frac{R \cdot T_{PEN} \cdot \tau_{anode}}{2F \cdot D_{eff,anode}} \cdot i \quad (3.24)$$

$$p_{H_2O,TPB} = p_{H_2O,af} - \frac{R \cdot T_{PEN} \tau_{anode}}{2F \cdot D_{eff,anode}} \cdot i \quad (3.25)$$

$$p_{O_2,TPB} = p_{cf} - (p_{cf} - p_{O_2,cf}) - \exp\left(\frac{RT_{PEN} \tau_{anode}}{4F \cdot D_{eff,cathode} \cdot p_{cf}} \cdot i\right) \quad (3.26)$$

where, ' τ_{anode} ' and ' $\tau_{cathode}$ ' are the thickness of each electrode in m while ' $D_{eff,anode}$ ' represents the average effective diffusivity coefficient in the anode, and ' $D_{eff,cathode}$ ' represents the oxygen effective diffusivity coefficient in the cathode. The diffusivities are measured in $m^2 s^{-1}$.

OHMIC LOSSES

Ohmic loss is resistance to the flow of electrons and ions through the electrodes, interconnects and electrolytes. Voltage drop due to ohmic losses is proportional to current density as given by equation 3.27

$$\Delta V_{ohm} = i \cdot R_{ohm} \quad (3.27)$$

where,

$$R_{ohm} = \frac{\tau_{anode}}{\sigma_{anode}} + \frac{\tau_{cathode}}{\sigma_{cathode}} + \frac{\tau_{electrolyte}}{\sigma_{electrolyte}} \quad (3.28)$$

' R_{ohm} ' is the combination of electronic and ionic resistances within the cell and ' σ ' represents the electrical conductivity of the anode, cathode and electrolyte in $\Omega^{-1} m^{-1}$.

This concludes the discussion on the electrochemical model adopted in this research. After solving the electrochemical model, the mass and energy balance are computed.

3.4.3. MASS BALANCE

The mass balance inside the anode-flow and cathode-flow (cf) channel is given by equation 3.29 and equation 3.30, respectively. The transfer of oxygen ions from the cathode to anode side accounts for the changes in flow rates as oxygen takes part in the hydrogen oxidation reaction, thus, forming water-vapour that moves through the anode-flow channel.

$$\dot{m}_{af}^{out} = \dot{m}_{af}^{in} + \dot{m}_{O_2}^{in} \quad (3.29)$$

$$\dot{m}_{cf}^{out} = \dot{m}_{cf}^{in} - \dot{m}_{O_2}^{out} \quad (3.30)$$

where,

$$\dot{m}_{O_2}^{in} = \dot{m}_{O_2}^{out} = \frac{1}{4F} \cdot M_{O_2} \quad (3.31)$$

The outgoing anode and cathode molar flow rates can be calculated from the mass flow rates by using equation 3.32

$$\dot{N} = \frac{\dot{m}_{out}}{\sum_j y_j^{out} \cdot M_j} \quad (3.32)$$

In equation 3.32, 'j' represents the species present in anode and cathode-flow. The mole fractions (y) of the species present in the anode-flow account for the computed

anode-off gas compositions as explained in subsection 3.4.1. To compute the mole fractions of oxygen and nitrogen in outgoing cathode-flow, concentration balance is solved for each species as given by equation 3.33 and 3.34 [7], respectively.

$$\frac{dC_{O_2}}{dt} = \frac{u_{cf}}{L} \cdot (C_{O_2}^{in} - C_{O_2}^{out}) - \frac{1}{2} \cdot \frac{1}{H_{cf}} \cdot r_{HOR} \quad (3.33)$$

$$\frac{dC_{N_2}}{dt} = \frac{u_{cf}}{L} \cdot (C_{N_2}^{in} - C_{N_2}^{out}) \quad (3.34)$$

where, 'C' is species concentration measured in mol m^{-3} , ' u_{cf} ' is the velocity of cathode-flow calculated from the ideal gas equation. 'L' and ' H_{cf} ' are the length of the cell and the height of the cathode channel in m. ' r_{HOR} ' is the reaction rate of the hydrogen oxidation reaction given by equation 3.35 [16].

$$r_{HOR} = \frac{i}{2F} \quad (3.35)$$

After calculating the molar flow rates for each species in the cathode and anode-flow channel, the volumetric flow rates ($\text{m}^3 \text{s}^{-1}$) can be calculated using the ideal gas equation. The total flow of the incoming air is controlled with the air-excess ratio given by equation 3.36 [7]. The air-excess ratio can be controlled to keep the difference between outlet and inlet temperatures of the channels within 100 K, which can help avoid thermal stressing across the cell [20].

$$\lambda = \frac{x_{O_2}^{in} \cdot \dot{N}_{cf}^{in}}{i \cdot A_{act} / 4F} \quad (3.36)$$

3.4.4. ENERGY BALANCE

During SOFC operation, energy is exchanged in the form of heat, chemical energy and electrical energy. To determine the cell operating temperatures, energy balance is solved for the anode-flow channel, cathode-flow channel, PEN structure and the interconnect in the following manner.

ENERGY BALANCE: ANODE-FLOW CHANNEL

Inside the anode-flow channel, the temperature evolution of the anode-flow is dependent on the reforming reaction, water-gas shift reaction, energies of the incoming and outgoing flows along with the heat transfer from PEN structure and the interconnects. Equation 3.37 solves the energy balance to determine the temperature of the anode-flow (T_{af}) in K [18].

$$\frac{dT_{af}}{dt} = \frac{\sum_j \dot{N}_j^{in} \cdot h_{j,af}^{in} - \sum_j \dot{N}_j^{out} \cdot h_{j,af}^{out} + \dot{Q}_{PEN-af}^{conv} + \dot{Q}_{ICa-af}^{conv} - A_{act} \cdot r_{HOR} \cdot (h_{H_2} - h_{H_2O})}{N_{af} \cdot c_{p,af}} \quad (3.37)$$

where, ' j ' \in (CH_4 , H_2O , H_2 , CO , CO_2), ' $c_{p,af}$ ' is the isobaric molar specific heat capacity of the anode-flow in $\text{J mol}^{-1} \text{K}^{-1}$, ' $h_{j,af}$ ' is the molar specific enthalpy (J mol^{-1}) of each species in anode-flow, which is estimated from first order polynomials of temperature presented in Table A.4 of Appendix A [14].

In equation 3.37, first two terms on the right-hand side account for the energy fluxes of the incoming and outgoing flows. These energy fluxes also take into account the heat release during the water-gas shift reaction and the heat absorption during the methane steam reforming reaction taking place inside the anode-flow channel. ' \dot{Q}^{conv} ' terms on the right-hand side of equation 3.37 represent the convective heat transfer rate in W from the PEN structure and the interconnect (ICa) to the anode-flow. The convective heat transfers to anode-flow channel can be seen in Figure 3.2. The last term represents enthalpy associated with the hydrogen oxidation reaction [18].

ENERGY BALANCE: CATHODE-FLOW CHANNEL

The cathode air flow temperature (T_{cf}) is estimated by solving the energy balance given in equation 3.38. For the energy balance, energies carried by the incoming and outgoing cathode air flows and heat transfer from the PEN structure and the interconnect (ICc) to the cathode flow are taken into account. The enthalpy flux associated with oxygen flow through the cathode into the PEN structure is also taken into account and is given by the last term of equation 3.38.

$$\frac{dT_{\text{cf}}}{dt} = \frac{\sum_j \dot{N}_j^{\text{in}} \cdot h_{j,\text{cf}}^{\text{in}} - \sum_j \dot{N}_j^{\text{out}} \cdot h_{j,\text{cf}}^{\text{out}} + \dot{Q}_{\text{PEN-cf}}^{\text{conv}} + \dot{Q}_{\text{ICc-cf}}^{\text{conv}} - 0.5 \cdot A_{\text{act}} \cdot r_{\text{HOR}} \cdot h_{\text{O}_2}}{N_{\text{cf}} \cdot c_{p,\text{cf}}} \quad (3.38)$$

where, ' j ' \in (O_2 , N_2).

ENERGY BALANCE: PEN STRUCTURE

The PEN structure accommodates the hydrogen oxidation reaction as it encompasses the anode, cathode and the electrolyte. Inside the PEN structure, heat is released due to the hydrogen oxidation reaction as the hydrogen from the anode and the oxygen ions from the cathode react. The reaction produces electrons and water vapour as by-products, thus, producing the electrical power while water vapour diffuses into the anode-flow channel. Equation 3.39 gives the energy balance solved to determine the PEN temperature (T_{PEN}). The heat released within the PEN structure is transferred to the anode and cathode-flow channels via convection while the interconnects receive the heat through radiation (\dot{Q}^{rad}), which is estimated from [18]. In this cell model, radiative heat transfer is considered due to high operating temperatures [7], however, researchers have shown that radiation may be neglected in the energy balance for SOFCs [21].

$$\frac{dT_{\text{PEN}}}{dt} = \frac{A_{\text{act}} \cdot r_{\text{HOR}} \cdot (h_{\text{H}_2} + 0.5 \cdot h_{\text{O}_2} - h_{\text{H}_2\text{O}}) - i \cdot V_{\text{cell}} \cdot A_{\text{act}}}{m_{\text{PEN}} \cdot c_{p,\text{PEN}}} - \frac{\dot{Q}_{\text{PEN-af}}^{\text{conv}} - \dot{Q}_{\text{PEN-cf}}^{\text{conv}} - \dot{Q}_{\text{PEN-ICa}}^{\text{rad}} - \dot{Q}_{\text{PEN-ICc}}^{\text{rad}}}{m_{\text{PEN}} \cdot c_{p,\text{PEN}}} \quad (3.39)$$

where, ' m_{PEN} ' is the mass of the PEN structure in kg while ' $c_{p,\text{PEN}}$ ' is the specific heat of the PEN material in $\text{J kg}^{-1} \text{K}^{-1}$

ENERGY BALANCE: INTERCONNECTS

The interconnect simply takes part in heat transfer with the flow channels and PEN structure via convection and radiation as shown in equation 3.40. Additionally, heat for

pre-reforming is transferred to the integrated pre-reformer from the interconnect.

$$\frac{dT_{IC}}{dt} = \frac{\dot{Q}_{PEN-ICa}^{rad} + \dot{Q}_{PEN-ICc}^{rad} - \dot{Q}_{ICa-af}^{conv} - \dot{Q}_{ICc-cf}^{rad} - \dot{Q}_{pre}}{m_{IC} \cdot c_{p,IC}} \quad (3.40)$$

where, ' m_{IC} ' is the mass of the interconnect in kg while ' $c_{p,IC}$ ' is the specific heat of the interconnect material in $J kg^{-1} K^{-1}$.

3.5. SOFC CELL-TO-STACK PERFORMANCE

Based on above-described model, single cell performance is extrapolated to estimate the stack performance. The SOFC stack consists of a number of cells (n_{cells}) with uniform performance. Therefore, the SOFC (DC) stack power is estimated by using the equation 3.41

$$P_{SOFC,DC} = n_{cells} \cdot i \cdot V_{cell} \cdot A_{act} \quad (3.41)$$

For the purpose of integration with the engine (AC), DC to AC conversion losses are considered by applying a conversion efficiency ($\eta_{DC/AC}$). Additionally, 5 % auxiliary losses (P_{aux}) are added as parasitic power losses for the Balance of Plant (BoP) system. Therefore, the total useful power produced by the SOFC is given by equation 3.42

$$P_{SOFC,AC} = (P_{SOFC,DC} \cdot \eta_{DC/AC}) - P_{aux} \quad (3.42)$$

After calculating the total SOFC power ($P_{SOFC,AC}$), SOFC efficiency is estimated by applying the following equation 3.43.

$$\eta_{SOFC} = \frac{P_{SOFC,AC}}{\dot{N}_{CH_4}^{in} \cdot LHV_{CH_4}} \quad (3.43)$$

where, ' $\dot{N}_{CH_4}^{in}$ ' is the molar flow rate of incoming hydrogen while ' LHV_{CH_4} ' is the lower heating value of methane, which is equal to $802.6 \times 10^3 \text{ kJ mol}^{-1}$ [22].

3.6. SOFC MODEL VERIFICATION AND PERFORMANCE

For the purpose of verification, SOFC cell model outputs are compared against the cell performance data provided by Aguiar et al. [7]. The electrochemical cell model is used to compute cell voltages and power density (PoD) curves against current density (i) for an undepleted fully reformed fuel mixture. Figure 3.3 shows the current density-voltage (i - V) curves predicted by the electrochemical model for cell operating temperature of 1073 K. Activation, concentration and ohmic cell voltage losses have also been plotted and compared against data provided by Aguiar et al. As seen from Figure 3.3, the open-circuit voltage, cathode activation potential, cathode concentration potential loss and ohmic losses match well with the literature data. However, there are small deviations between the reference and simulated anode activation loss, which is transferred to a marginal deviation in the computed cell voltage (V_{cell}).

Figure 3.3 also depicts the comparison between the simulated and reference power density at 1073 K. The computed power density compares well with the reference model, however, deviations arise after PoD of 10000 Am^{-2} . This divergence in PoD after 10000 Am^{-2}

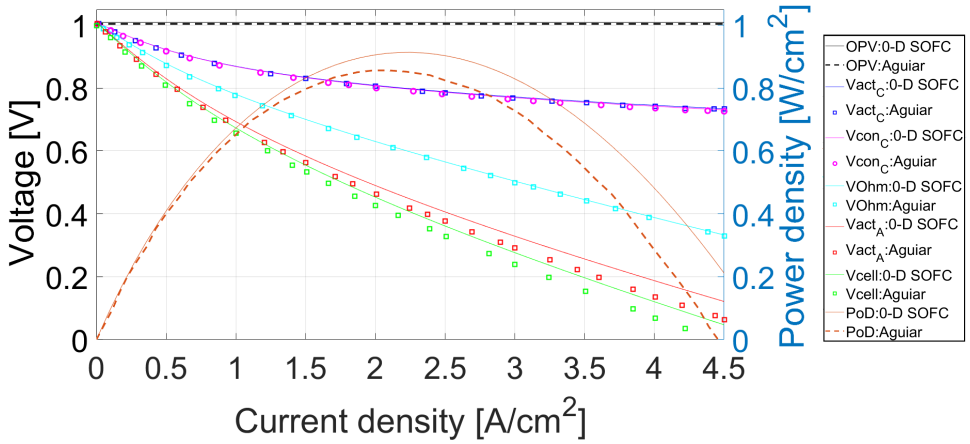


Figure 3.3: i-V and PoD curve with cell losses at 1073 K for undepleted fully reformed mixture

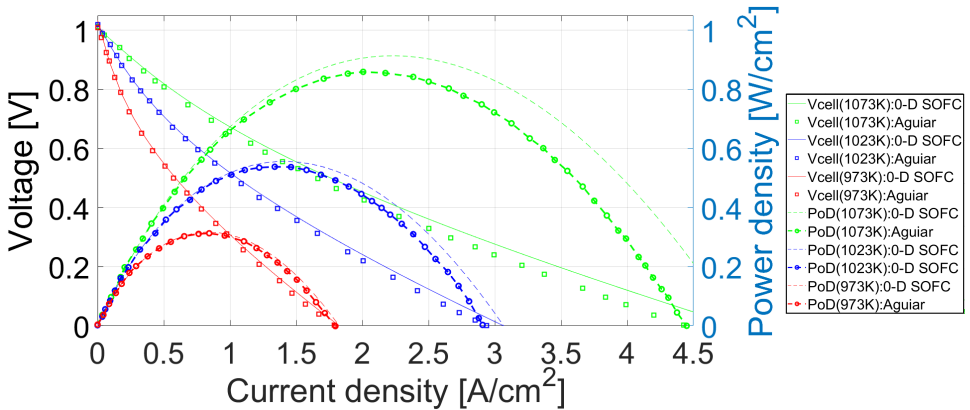


Figure 3.4: i-V and PoD curves at 973, 1023 and 1073 K for undepleted fully reformed mixture

are due to the deviations in the anode-activation loss, which also leads to a difference in estimation of operating cell voltage. The difference in anode-activation loss could be attributed to the difference in equations used in the cell model and the 1-D model by Aguiar et al. The 1-D model developed by Aguiar uses the Butler-Volmer equation to calculate the activation loss [7]. However, the current cell model employs the hyperbolic sine approximation shown in equation 3.20, which represents the combined anode and cathode activation losses. The combined hyperbolic sine approximation is a widely employed method to calculate the loss in activation potential. Norren and Hoffman made a comparison of various approximations and recommended the hyperbolic sine approximation due to its superior accuracy over the majority of operating current densities [23].

To avoid large deviations in the estimation of cell voltage, the current density values assumed in this study for SOFC performance analysis are kept below 10000 A m^{-2} . The

deviations at high current densities are also evident at operating temperatures of 973 K and 1023 K, as seen in Figure 3.4. The cell voltage and power density increase with increased cell temperature due to lower potential losses and improved reaction kinetics. The electrochemical model verification affirms the voltage and power density prediction capabilities of the cell model, which are essential for computing the fuel cell efficiency as given by equation 3.43. Additionally, anode-off composition and cell temperatures computed by the cell model are compared against the verification data presented in [7].

To test the cell performance against reference data, the following cell input conditions are modelled. Air and fuel inlet temperatures are at 1023 K, while the operating pressure is ambient (100 kPa). Current density is maintained at 5000 Am^{-2} , fuel utilization at 75 % and air-excess ratio at 8.5. The incoming composition for the anode-flow channel is obtained as a result of 10 % pre-reforming with S/C ratio of 2. Table 3.1 shows the simulated cell temperatures and anode-off gas composition in comparison to the reference model for the above-mentioned input conditions. As seen in Table 3.1, the cell temperatures and anode-off gas composition are within small deviations of the reference data. Additionally, as shown by Aguiar et al. CH_4 is fully consumed in the anode-flow channel, thus, supporting the earlier assumption of complete methane conversion made in this research.

The deviations in cell performance prediction shown in Table 3.1 could be attributed to the difference in modelling approach of 0-D versus the 1-D model by Aguiar et al. Although the 1-D modelling approach can be more accurate in simulating cell performance compared to a 0-D model, the higher level models require much more computational effort [14, 18]. Therefore, for the SOFC-ICE system integration research presented in this dissertation, a 0-D SOFC model capable of capturing the polarization curves, cell temperatures, anode-off gas compositions and flow rates with good accuracy is found to be acceptable. For future research and improved accuracy in cell performance prediction, calibration of the 0-D SOFC model with experiments in addition to development of higher level SOFC models is recommended.

Based on the reference cell geometry from Aguiar, the cell length used for the above model verification is 40 cm. However, the commonly applied and technologically relevant planar cells are square in shape with an accepted size of $10 \times 10 \text{ cm}^2$. Furthermore,

Table 3.1: Comparison between simulated and reference [7] cell temperatures and anode-off gas composition [Volume %]

Parameter	1-D model[7]	0-D model	Deviation [%]
T_{PEN} [K]	1134	1096.2	3.33
T_{IC} [K]	1120	1095.3	2.21
T_{af} [K]	1128	1092.5	3.15
T_{cf} [K]	1108	1090.7	1.56
CH_4 [%]	0	0	0
H_2O [%]	65	64.16	1.3
H_2 [%]	15	15.84	-5.63
CO [%]	4	4.16	-3.9
CO_2 [%]	16	15.84	0.97

in an extended research paper by Aguiar et al., the $10 \times 40 \text{ cm}^2$ single cell was modelled as four series cells of $10 \times 10 \text{ cm}^2$ [20]. Therefore, after verifying the model against literature data from Aguiar, the cell length is fixed at 10 cm for all the SOFC simulations. The change in cell length correlates to change in power produced per cell, which is reduced by 4 times since the cell voltage and, hence, power density change marginally while the cell area is reduced. Therefore, to produce the same power output from the SOFC stack the number of cells are simply increased by 4 times.

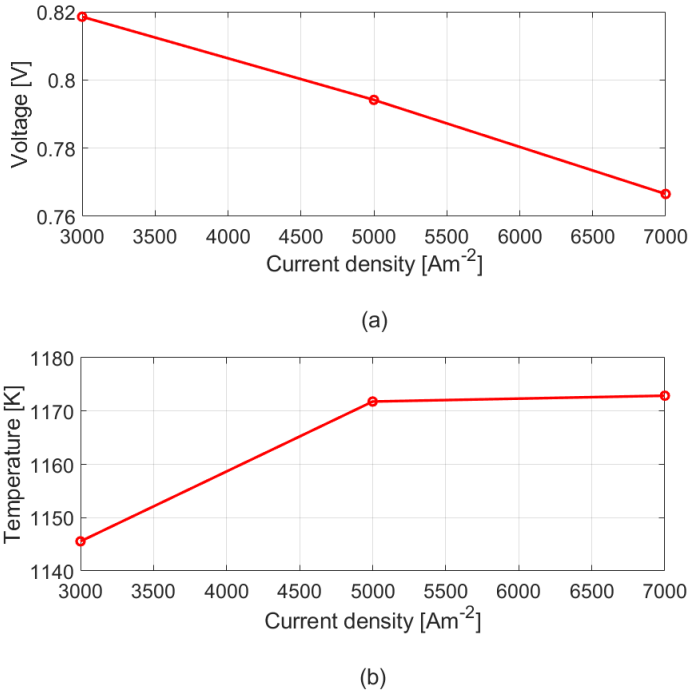


Figure 3.5: Current density vs cell voltage (a) and PEN temperature (b)

Control parameters such as current density, pre-reforming ratio and fuel utilization impact SOFC performance. These control parameters are regarded as integrated system variables and have been introduced in section 1.5 of Chapter 1. To understand the effect of these integrated systems variables on SOFC performance, a sensitivity study is performed. In this study, each control parameter is changed while the remaining parameters are kept constant. Unless mentioned, the fixed control and input parameter values for this sensitivity study are as follows. As shown earlier, higher cell temperature can provide higher cell voltage, which improves cell efficiency. Therefore, from this point onwards fuel and air inlet temperatures (initial cell temperature) are kept at 1073 K for all steady-state performance investigations presented in this research. The operating pressure is ambient (100 kPa); current density in the 0-D model is maintained at 5000 A m^{-2} , fuel utilization at 75% and S/C ratio at 2. The air-excess ratio is controlled by a PI controller to keep the inlet and outlet temperatures of the cell within 100 K for this and all the

proceeding investigations in this research. This is done to maintain a thermal gradient of 10 Kcm^{-1} and avoid thermal stresses due to large temperature gradients. Furthermore, pre-reformer is operated at a pre-reforming ratio of 0.3, where the reaction heat is taken from the SOFC. The number of cells in the stack is assumed to be 11000.

The cell voltage almost linearly reduces as current density increases from $3000 - 7000 \text{ Am}^{-2}$ as seen from Figure 3.5(a). At 5000 Am^{-2} , the cell voltage was found to be just below 0.8 V. This value of cell voltage is similar to the values found in literature for cells operating at 1073 K and 5000 Am^{-2} [5, 24]. However, as explained earlier the cell voltage calculated by the 0-D SOFC cell-to-stack performance model can deviate from reference due to the choice of modelling approach, equations and even assumptions. For instance, the current SOFC model assumes adiabatic boundary conditions for the stack, however, heat loss from the stack could reduce cell temperatures. Therefore, it is possible that the 0-D SOFC model could be slightly overestimating the cell temperatures. Although the stack is insulated under real operating conditions to avoid the cooling-out of stack [25], the reduction in cell temperature due to some heat loss could reduce the cell voltage. The reduction in cell voltage will cause the power output to reduce and, thus, adversely impact the fuel cell efficiency. Therefore, it is vital to understand that even though the 0-D SOFC model satisfactorily simulates the fuel cell performance for this investigation, there is a scope for deviation in voltage prediction, which can impact cell output and efficiency.

As seen in Figure 3.3 and Figure 3.4, the increase in current density results in large ohmic and activation losses. Therefore, SOFC efficiency increases at lower current densities and lower loads, which is contradictory to engines. Part load efficiency of engines is lower than the efficiency at rated power. Contrary to voltage, increasing current density at constant fuel utilization leads to high PEN temperatures. Higher PEN temperatures are a result of increased heat release during the hydrogen oxidation of more incoming hydrogen at higher current densities. However, at high current densities, the temperatures are controlled by increasing the air-excess ratio as explained earlier. The increment in PEN temperature due to current density and their control is evident from Figure 3.5(b), which limits the temperature value below 1173 K.

Contrary to current density, increasing methane pre-reforming ratio results in somewhat lower PEN temperatures. Additional pre-reforming through internal indirect reforming results in more heat extraction from the SOFC to sustain the pre-reforming reactions. The reduction in heat present in the cell helps reduce the amount of air needed to cool the cells, thus, reducing the air-excess ratio. Figure 3.6(a) shows the lower air-excess ratio values simulated for high pre-reforming ratios. In Figure 3.6(b), the cell voltage shows an increase with increasing pre-reforming ratios due to higher open-circuit voltage and lower concentration and activation losses.

Changes in fuel utilization affect the cell performance, the anode-off gas compositions and flow-rates. Variations in anode-off gas flow affect the performance of the engine in SOFC-ICE integration. Figure 3.7(a) and Figure 3.7(c) show the changes in cell voltages and standalone SOFC efficiency due to different fuel utilizations. As the fuel utilization increases, the Nernst or open-circuit voltage decreases with increase in concentration losses [26]. At the same time, increments in temperature due to fuel utilization seen in Figure 3.7(b) reduce the resistance and activation losses. The delicate bal-

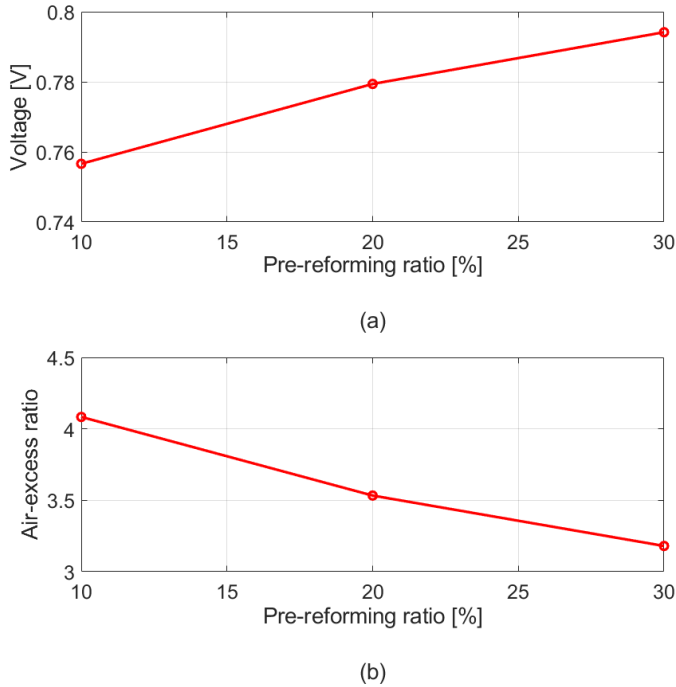


Figure 3.6: Pre-reforming ratio vs air-excess ratio (a) and cell voltage (b)

ance between these two phenomena dictates the cell losses and the open-circuit voltage, which impacts the operating cell voltage given by equation 3.18. The competing effects between the two phenomena resulted in maximum voltage at 70 % fuel utilization while the voltage reduced at higher fuel utilizations.

At high fuel utilizations and constant current density, the cell voltage decreases, however, the fuel intake reduces. Therefore, at high fuel utilizations, the efficiency of the cell increased while more and more hydrogen is consumed in the oxidation process, thus, leaving small percentages of left-over hydrogen in the anode-off gas. On comparing with literature [27, 28], it was found that the 0-D SOFC model could be overpredicting the voltages by a small margin at high fuel utilizations. In other words, the drop in cell voltage due to increasing fuel utilization could be somewhat higher. Based on the earlier explanation, a higher drop in cell voltage at high fuel utilization will result in a lower power output and a lower improvement in cell efficiency.

Although increasing fuel utilization showed improvements in efficiency, operation at high fuel utilizations is restricted because a much higher contribution of concentration polarization and a high risk of fuel starvation is observed. Researchers have shown that local oxidations of the cells due to fuel starvation can be found irrespective of the applied fuel and current density, which adversely affect the lifetime of the cell [29]. For this reason, fuel utilization is kept below 85 % for all following investigations presented in this research. On the other hand, low fuel utilization can significantly reduce SOFC efficiency

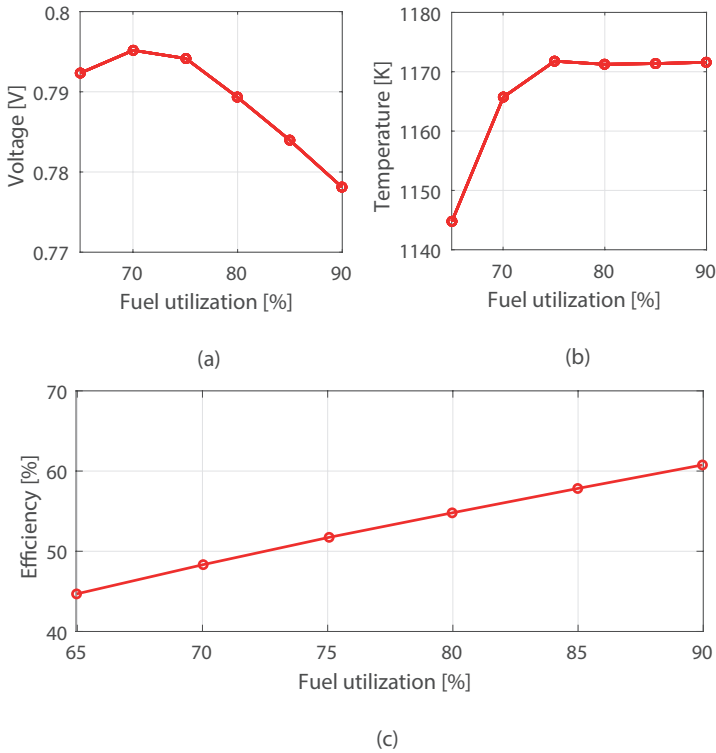


Figure 3.7: Fuel utilization vs cell voltage (a), PEN temperature (b) and efficiency (c)

as shown in Figure 3.7(c). As fuel utilization decreases, higher percentages of hydrogen and carbon monoxide are available in the anode-off gas relative to water vapour and carbon dioxide. Table 3.2 shows the anode-off gas compositions and flow-rates for fuel utilizations varying from 70 % to 85 %.

Table 3.2: Effect of fuel utilization on anode-off gas compositions [Volume %]

Fuel Utilizations	70 %	75 %	80 %	85 %
H ₂ O [%]	61.71	64.88	67.89	70.95
H ₂ [%]	18.29	15.12	12.11	9.05
CO [%]	5.69	4.83	3.91	2.96
CO ₂ [%]	14.31	15.17	16.09	17.04
CO ₂ /H ₂	0.783	1	1.33	1.88

As seen in Table 3.2, water-vapour forms the largest constituent of anode-off gas. Volumetric percentage of CO is small compared to the percentages of H₂ and CO₂. Furthermore, the amount of CO further decreases at higher fuel utilizations. The percentage of hydrogen relative to the percentage of carbon dioxide is more at 70% U_f, with equal

amounts at 75% U_f . At higher fuel utilizations, carbon dioxide increases in comparison to hydrogen reaching a carbon dioxide-to-hydrogen ratio of about 1.88. For SOFC-ICE integration, anode-off gas compositions presented in Table 3.2 are directed from the SOFC to combust in the marine natural gas engine.

3.7. CONCLUSIONS

In this chapter, a 0-D SOFC single cell-to-stack performance model has been presented. The SOFC cell model simulates an anode-supported, intermediate temperature, co-flow and planar cell with an integrated pre-reformer. The 0-D model consists of a pre-reformer model, an equilibrium model for anode-off gas composition and an electrochemical model in addition to a mass and energy balance solver to compute cell voltage, anode-off gas composition, anode-off gas flow rates, polarization or current-voltage (i-V) curve, cell power, efficiency and temperature curves. The SOFC stack performance is extrapolated from a single cell model. The developed 0-D SOFC cell-to-stack performance model has been used to solve Research Question 2. The model has been also used to study the effects of ISVs on SOFC performance and, thus, provide a partial answer to Research Question 5. The following concluding remarks are noted from the discussions presented in this chapter:

- The SOFC cell model has been verified against cell performance data obtained from Aguiar et al. The 0-D SOFC model satisfactorily simulates the fuel cell performance for this investigation, however, there is a scope for deviation in voltage prediction, which can impact cell output and efficiency. The simulated cell voltage can deviate from reference due to the choice of modelling approach, equations and even assumptions.
- Increasing current density at constant fuel utilization leads to high PEN temperatures and reduced cell voltages. The sensitivity study shows that SOFC voltage and efficiency increase at low current densities and low load operation, which is contradictory to engine operation. The cell voltage increased with increasing pre-reforming ratio. However, operation at high fuel utilizations reduced cell voltage while efficiency increased.
- The SOFC model is also capable of computing the quality (composition) and quantity of anode-off gas for different fuel utilizations. The largest constituent of anode-off gas was found to be water-vapour while percentages of carbon monoxide were estimated to be the smallest. The volumetric percentage of hydrogen and carbon dioxide were found to equal at 75% fuel utilization. A lower value of fuel utilization resulted in a higher amount of hydrogen and a higher value of fuel utilization showed an increase in percentage of carbon dioxide. Thus, the SOFC model can be used to study the impact on the quality and quantity of anode-off gas, which will dictate the engine performance for SOFC-ICE integration. In this manner, the 0-D SOFC cell-to-stack performance model has been adopted to answer Research Question 2.

Based on the SOFC performance analysis presented in this chapter, the following fuel cell parameters are considered as performance boundaries for all the proceeding investigations in this dissertation. The operating pressure of the SOFC is maintained at 100 kPa, fuel and air inlet temperature (initial cell temperature) are kept at 1073 K, S/C ratio

is fixed at 2 and fuel utilization is kept below 85 %. In the next chapter, the effects of combusting SOFC anode-off gas constituents in a marine engine are studied experimentally to support the development of SOFC-ICE integration.

REFERENCES

- [1] S.G. Neophytides. The Reversed Flow Operation of a Crossflow Solid Oxide Fuel Cell Monolith. *Chemical Engineering Science*, 1999.
- [2] S. Nagata, A. Momma, T. Kato, and Y. Kasuga. Numerical Analysis of Output Characteristics of Tubular SOFC With Internal Reformer. *Journal of Power Sources*, 2001.
- [3] D. Marra, C. Pianese, P. Polverino, and M. Sorrentino. Models for Solid Oxide Fuel Cell Systems: Exploitation of Models Hierarchy for Industrial Design of Control and Diagnosis Strategies, 2016.
- [4] L. van Biert, M. Godjevac, K. Visser, and P.V. Aravind. Dynamic Modelling of a Direct Internal Reforming Solid Oxide Fuel Cell Stack Based on Single Cell Experiments. *Applied Energy*, 2019.
- [5] F.D.F. Chuahy and S.L. Kokjohn. Solid Oxide Fuel Cell and Advanced Combustion Engine Combined Cycle: A Pathway to 70% Electrical Efficiency. *Applied Energy*, 2019.
- [6] H.D. Sapra et al. Integration of Solid Oxide Fuel Cell and Internal Combustion Engine for Maritime Applications. *Applied Energy*, 2020.
- [7] P. Aguiar, C.S. Adjiman, and N.P. Brandon. Anode-Supported Intermediate Temperature Direct Internal Reforming Solid Oxide Fuel Cell. I: Model-Based Steady-State Performance. *Journal of Power Sources*, 2004.
- [8] S. Campanari et al. Predicting the Ultimate Potential of Natural Gas SOFC Power Cycles with CO₂ Capture – Part A: Methodology and Reference Cases. *Journal of Power Sources*, 2016.
- [9] M. Azzopardi. Dynamic Modelling Implementation for a Multi-Purpose 1-D Planar SOFC: Gaining Insight Behaviour into an Intermediate Temperature SOFC, 2017.
- [10] D. Papurello et al. Sulfur Poisoning in Ni-Anode Solid Oxide Fuel Cells (SOFCs): Deactivation in Single Cells and a Stack. *Chemical Engineering Journal*, 2016.
- [11] P.J. de Wild, R.G. Nyqvist, F.A. de Bruijn, and E.R. Stobbe. Removal of Sulphur-Containing Odorants from Fuel Gases for Fuel Cell-Based Combined Heat and Power Applications. *Journal of Power Sources*, 2006.
- [12] L. van Biert et al. A Thermodynamic Comparison of Solid Oxide Fuel Cell-Combined Cycles. *Journal of Power Sources*, 2018.
- [13] Y. Matsuzaki and I. Yasuda. Electrochemical Oxidation of H₂ and CO in a H₂-H₂O-CO-CO₂ System at the Interface of a Ni-YSZ Cermet Electrode and YSZ Electrolyte. *Journal of the Electrochemical Society*, 2000.
- [14] J.W. Reurings. A Modeling Study to Investigate Performance of SOFC-ICE Hybrid Systems for Marine Applications. Master's thesis, Delft University of Technology, 2019.

- [15] H. Xi, J. Sun, and V. Tsourapas. A Control Oriented Low Order Dynamic Model for Planar SOFC Using Minimum Gibbs Free Energy Method. *Journal of Power Sources*, 2007.
- [16] J. Larminie and A. Dicks. *Fuel Cell Systems Explained*. John Wiley & Sons Ltd, 2003.
- [17] E.J. Weinberg. Explicit Equations for the Calculation, by Successive Approximations, of Equilibrium Gas Compositions at High Temperatures: The Hydrogen+Carbon+Oxygen and the Hydrogen+Carbon+Oxygen+Nitrogen Systems without Solid Carbon Formation. In *Proceedings of the Royal Society of London. Series A, Mathematical and Physical Sciences*. Royal Society, 1957.
- [18] A. Salogni and P. Colonna. Modeling of Solid Oxide Fuel Cells for Dynamic Simulations of Integrated Systems. *Applied Thermal Engineering*, 2010.
- [19] V.M. Janardhanan and O. Deutschmann. Modeling of Solid-Oxide Fuel Cells. *Z. Phys. Chem*, 2007.
- [20] P. Aguiar, C.S. Adjiman, and N.P. Brandon. Anode-Supported Intermediate-Temperature Direct Internal Reforming Solid Oxide Fuel Cell: II. Model-Based Dynamic Performance and Control. *Journal of Power Sources*, 2005.
- [21] H. Mahcene et al. Radiation Phenomenon in Electrodes/Electrolyte Interface of Solid Oxide Fuel Cells. *Energy Procedia*, 2014.
- [22] S. Perry, R.H. Perry, D.W. Green, and J.O. Maloney. *Perry's Chemical Engineers' Handbook*. 2000.
- [23] D.A. Noren and M.A. Hoffman. Clarifying the Butler-Volmer Equation and Related Approximations for Calculating Activation Losses in Solid Oxide Fuel Cell Models. *Journal of Power Sources*, 2005.
- [24] F. Zhao and A.V. Virkar. Dependence of Polarization in Anode-Supported Solid Oxide Fuel Cells on Various Cell Parameters. *Journal of Power Sources*, 2005.
- [25] E. Achenbach. Three-Dimensional and Time-Dependent Simulation of a Planar Solid Oxide Fuel Cell Stack. *Journal of Power Sources*, 1994.
- [26] Inc EG&G Technical Services. *Fuel Cell Handbook (Seventh Edition)*. 2004.
- [27] J.S. Szmyd et al. The Effect of Applied Control Strategy on the Current-Voltage Correlation of a Solid Oxide Fuel Cell Stack during Dynamic Operation. *Archives of thermodynamics*, 2014.
- [28] J.H. Hirschenhofer, D.B. Stauffer, R.R. Engleman, and M.G. Klett. *Fuel Cell Handbook, Fourth Edition*. 1998.
- [29] Q. Fang et al. SOFC Stack Performance Under High Fuel Utilization. *International Journal of Hydrogen Energy*, 2015.

4

EXPERIMENTAL INVESTIGATIONS OF SI MARINE ENGINE PERFORMANCE

To integrate the SOFC with the engine for marine power generation, anode-off gas generated from the SOFC is blended with natural gas and combusted in a lean-burn SI marine engine. In this integration approach, water-vapour in the anode-off gas is condensed out because SI natural gas engines can experience ignition and combustion instability problems with water vapour intake [1]. The removal of moisture creates a flexible mixture of producer gas containing high percentages of hydrogen and carbon dioxide with smaller percentages of carbon monoxide as seen in Table 3.2. In the dry anode-off gas, hydrogen and carbon monoxide are combustible products while carbon dioxide is non-combustible, which can adversely impact the engine performance and integration with the SOFC. Operating the SOFC at different fuel utilizations and loads can provide a tailored anode-off gas quality and quantity, which can be blended with natural gas and combusted in the engine to meet the required power demand onboard a ship.

To investigate the potential of SOFC-ICE integration in terms of efficiency, emissions and load-sharing, effects of combusting anode-off gas and natural gas blends in the SI engine need to be understood. For this reason, the effects of combusting blends of individual constituents of anode-off gas and natural gas are studied experimentally in this chapter. The effects of ISVs such as engine fuel composition (varying blends of anode-off gas constituents and natural gas), air-excess ratio and spark-timing are studied experimentally. This chapter covers the effects of these ISVs on engine efficiency, operating limits, emissions, etc, thus, partially answering Research Question 3 and 5. The chapter also covers a detailed description of the engine test setup and the experimentation methodology.

Parts of this chapter have been published in the ASME ICEF-2018 Conference [2] and CIMAC World Congress 2019 [3].

In the next chapter, the engine experiments are used as building blocks for simulation models that can help capture and understand the in-cylinder and combustion process in a marine engine operating on hydrogen-natural gas (H₂-NG) and carbon dioxide-natural gas (CO₂-NG) fuel blends. Next, by combining this understanding of the effects of each constituent, combustion and engine performance with different anode-off gas and natural gas blends is analysed in the following chapters. In this research, the effects of carbon monoxide on the combustion process and engine performance are not considered. Section 4.3.2 details the reasoning for neglecting the effects of carbon monoxide in this phase of the research.

4.1. MARINE NG ENGINE TEST SETUP

As explained earlier in the research methodology described in Chapter 2, experiments were performed on a 500 kW_e, lean-burn and turbocharged marine SI natural gas engine to study the effects of combusting blends of anode-off constituents (hydrogen and carbon dioxide) with natural gas. The zero valve overlap test engine was connected to a

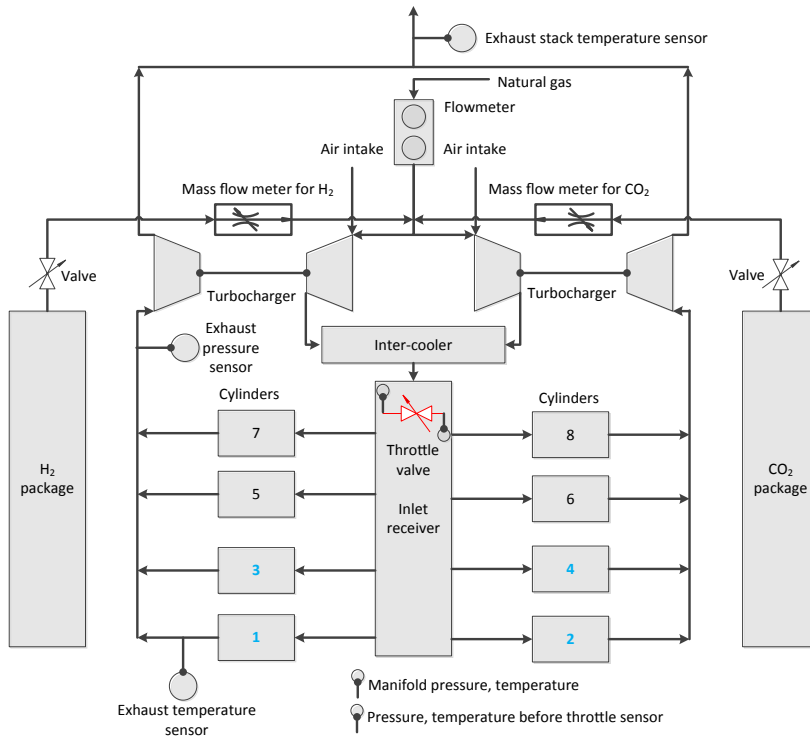


Figure 4.1: Schematic representation of marine NG test engine setup

generator to apply the load at 1500 rpm. Engine measurements were performed at varying engine loads of 75 %, 50 % and 25 % at rated rpm. To study the effects of hydrogen and carbon dioxide addition based on SOFC anode-off gas, natural gas was replaced by dif-

Table 4.1: Marine NG test engine specifications

Parameters	Value/Unit
Number of Cylinders	8
Bore	0.17 m
Stroke	0.19 m
Rated speed	1500 rpm
Rated power	500 kWe
Compression ratio	12:1
Boost pressure	2.2 bar
Spark-timing	24°CA BTDC
Inlet Valve Open (IO)	8.7°CA ATDC
Exhaust Valve Open (EO)	20.1°CA BBDC
Inlet Valve Close (IC)	21.5°CA ABDC
Exhaust Valve Close (EC)	11.8°CA BTDC

ferent percentages of hydrogen and carbon dioxide, by volume. The tested engine blends have been presented in subsection 4.2.1, and subsection 4.3.1 of this chapter and in subsection 6.1.3 of Chapter 6. Additionally, experiments were also performed at different values of air-excess ratio to control the NO_x emissions for each combination of fuel blend and engine load. For this purpose, engine performance was first measured at a fixed load point and NO_x value, and then the engine was leaned, by increasing the air-intake (air-excess ratio) via manual control, to a lower value of NO_x measured in mgN m⁻³ (at 5% reference oxygen). In this manner, engine performance for a fixed fuel blend and load was measured at different NO_x values till misfire. For only natural gas (ONG) fuel and 500 mgN m⁻³ of NO_x at 75% load, the value of air-excess ratio was higher than 1.6 and increased with engine leaning, thus, representing the lean-burn operation [4].

Table 4.2: Typical natural gas composition

Constituents	Vol. [%]
Methane	80.58
Ethane	3.80
Propane	0.69
I-Butane	0.122
N-Butane	0.131
I-Pentane	0.0348
N-Pentane	0.031
NeoPentane	0.00481
N-Hexane	0.009
Nitrogen	13.1
Carbon dioxide	1.46
Hydrogen	0.01
Helium	0.0418

Natural gas flow was injected in the engine before the turbocharger and measured using a flowmeter. Natural gas for the engine testing was available through the Dutch gas connection. Table 4.2 shows the typical composition of the incoming natural gas flow obtained through gas composition analysis. It is vital to note that the natural gas composition can vary, which may also impact engine performance as will be discussed in section 4.3.2. The natural gas composition shown in Table 4.2 was used for all the engine experimental analysis and model simulations presented in this dissertation.

Hydrogen and carbon dioxide stored in pressurized bottles were injected in the natural gas line before the turbocharger, and the flow of blended gases was controlled via a mass flow controller. During these experiments, temperatures, pressures, and flow rates were measured at different locations within the test setup, which have been depicted in Figure 4.1. Additionally, engine emissions such as nitrogen oxides, carbon monoxide, unburnt hydrocarbons (methane) and oxygen percentage were measured for each test condition. A schematic representation of the test setup including the hydrogen and carbon dioxide addition setup has been presented in Figure 4.1. Cylinders 1, 2, 3 and 4 were equipped with a water-cooled Kistler 7061B sensors for in-cylinder pressure measurements. The sensors were flushed in each cylinder head to record a clean pressure signal. The in-cylinder pressure data was continuously measured in sets of 145 consecutive cycles at each measurement point using the Kistler Ki-Box measurement unit [5]. The average in-cylinder pressure and crank angle measurements were used as a starting point for the combustion characterization process and models used in the third step of the research methodology as shown in Figure 2.7 of Chapter 2. Additional details of the experimentation methodology for hydrogen-natural gas and carbon dioxide-natural gas combustion have been presented in section 4.2.1 and section 4.3.2. Furthermore, Appendix B discusses the variability or uncertainty in the measurements of different performance parameters.

4.2. EXPERIMENTS ON HYDROGEN-NATURAL GAS COMBUSTION

This section describes the experimentation methodology for hydrogen-natural gas combustion and the corresponding experimental results.

4.2.1. EXPERIMENTATION METHODOLOGY FOR H₂-NG COMBUSTION

The experiments of hydrogen addition were performed keeping in mind the emission regulations by measuring engine performance against different values of NO_x emissions. This is a critical part of the methodology since hydrogen can increase the thermal efficiency of the engine while drastically increasing NO_x emissions beyond the emission regulation limit [2]. To have a clear discussion on the effects of hydrogen addition at different engine loads, the engine performance should be compared at the same NO_x values. Following this methodology, engine performance was first measured at a fixed load point and a fixed NO_x value. After this measurement, the engine was leaned to a lower value of NO_x, measured in mgN m⁻³ (at 5% reference oxygen), by manually controlling and increasing the air-intake (air-excess ratio). The performance of the engine at a fixed load point was measured at each step of different NO_x value varying from 3000 mgN m⁻³ of NO_x till the engine misfired. This procedure was followed for each hydrogen-natural

gas blend ratio given in Table 4.3. Thus, at each load point, engine performance was recorded for each hydrogen-natural gas blend ratio from 3000 mgN m⁻³ of NOx till engine misfire. Hydrogen-natural gas combustion was tested at 75 %, 50 % and 25 % engine loading and rated speed of 1500 rpm.

Table 4.3: Tested Hydrogen-Natural gas fuel blends

Fuel blends	Natural Gas [Vol. %]	Hydrogen [Vol. %]
0H ₂ -NG	100	0
05H ₂ -NG	95	5
10H ₂ -NG	90	10
20H ₂ -NG	80	20

The point of engine misfire depicts the leaning limit of the engine operating window. For these experiments, the definition of engine misfire is based on the magnitude of variation in indicated mean effective pressure (IMEP). The magnitude of variation in IMEP was calculated by using Equation 4.1.

$$\text{COV}_{\text{IMEP}} = \frac{\sigma_{\text{IMEP}}}{\text{IMEP}_{\text{mean}}} \quad (4.1)$$

The coefficient of variations in IMEP (COV_{IMEP}) is defined as the standard deviation of IMEP (σ_{IMEP}) divided by its mean value ($\text{IMEP}_{\text{mean}}$) for 145 consecutive cycles at each measurement point [6]. The engine was considered to be misfiring if the COV_{IMEP} crossed 10 % for even one cycle out of the recorded 145 cycles. This is because a COV above 10 % is considered as a poor driving condition by a driver in the automotive industry [6]. The COV_{IMEP} is a measure of cyclic variations exhibited by an engine at a measurement point.

All the results presented in this chapter are at the 500 mgN m⁻³ (at 5 % reference oxygen) unless the results are presented at varying air-excess ratios. The 500 mgN m⁻³ of NOx measurement was close to the NOx IMO TIER-III limit of this engine, which is equal to 2.08 gkW⁻¹ h [2]. For this reason, the 500 mgN m⁻³ of NOx was considered as the representative NOx limit of the engine.

Following the above-described methodology, engine performance was studied for varying blends of hydrogen-natural gas ratios at different engine loads and NOx values.

4.2.2. EXPERIMENTAL RESULTS FOR H₂-NG COMBUSTION

To study the variations in the performance of marine hydrogen-natural gas engines, effects of ISVs or control parameters such as engine load, spark-timing, air-excess ratio and hydrogen percentage were investigated experimentally. In this section, experimental results for three gas fuel blends of 0H₂-NG, 10H₂-NG, and 20H₂-NG at engine loadings of 75 % (375 kWe), 50 % (250 kWe) and 25 % load (125 kWe) have been studied. Except for section 4.2.2, engine performance results in all the sections have been presented at a spark-timing of 24 degrees before Top Dead Center (bTDC). Variations in the performance of marine hydrogen-natural gas engines have been discussed by understanding the variations in combustion and performance parameters such as combustion duration

maximum in-cylinder pressure, operating window, engine efficiency and emissions. Effects of spark-timing on the operating window and brake thermal efficiency of hydrogen-natural gas engines have also been covered.

EFFECT OF HYDROGEN ADDITION AND ENGINE LOADING ON CYCLIC VARIATIONS AND OPERATING WINDOW

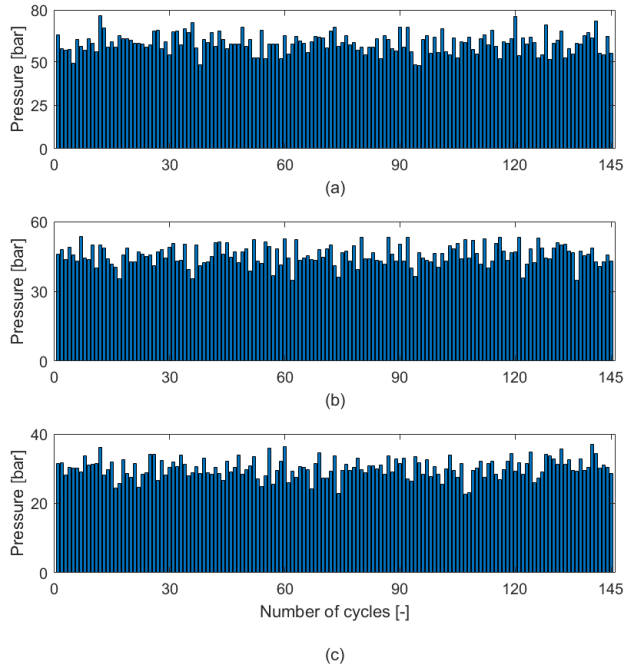


Figure 4.2: Cyclic variations in maximum in-cylinder pressure for the engine operating on only natural gas at 75 % (a), 50 % (b) and 25 % (c) load and NO_x emission of 500 mgN m⁻³

The flame velocity of natural gas is 0.38 m/s close to stoichiometric conditions, whereas that of hydrogen can be about 2.5 m/sec [7, 8]. The low flame velocity of natural gas makes the combustion rate of natural gas slow inducing combustion instability. At higher air-excess ratios during turbocharging, dilution of air-fuel mixture further reduces overall combustion rate. This decreasing combustion rate in natural gas engines induces in-cylinder pressure fluctuations during each combustion cycle. These in-cylinder pressure fluctuations during each combustion cycle are called cycle-to-cycle or cyclic variations. Figure 4.2 shows the cyclic variations in maximum in-cylinder pressure for 145 consecutive cycles at 75 %, 50 % and 25 % engine loading and the same NO_x emission of 500 mgN m⁻³. As seen in Figure 4.2, each cycle has a different value of maximum pressure at a constant engine loading. In addition to maximum pressure, cyclic variations impact the in-cylinder process and output, which is quantified by calculating the variations in COV_{IMEP} and have been presented in Figure 4.3.

As mentioned in the experimentation methodology section, measurements were performed at constant NO_x values by controlling the engine air-excess ratio. It is evident

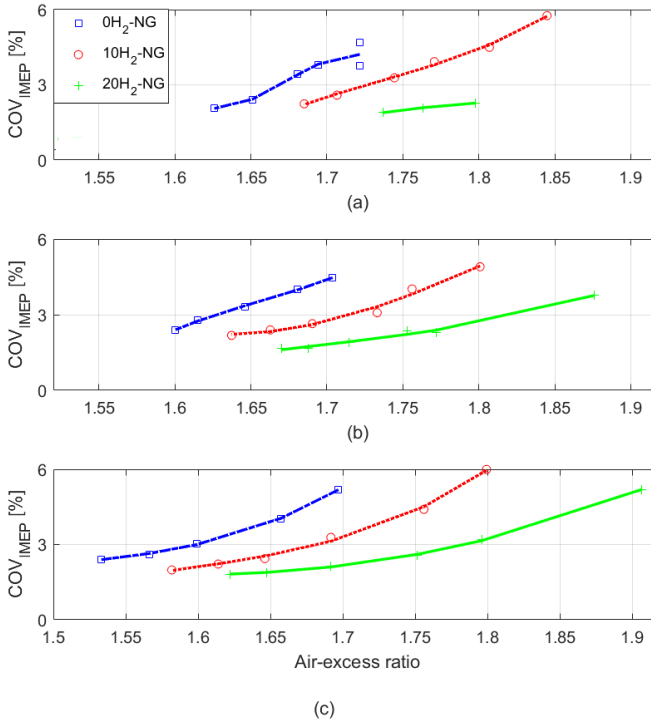


Figure 4.3: Coefficient of variations in IMEP averaged for 145 consecutive cycles at 75 % (a), 50 % (b) and 25 % (c) engine loading for 0H₂-NG, 10H₂-NG, and 20H₂-NG fuel blends

from Figure 4.3 that to achieve the same NO_x emission at higher loads, the engine settles at a higher value of air-excess ratio controlling the in-cylinder temperature and, hence, the NO_x emission. Variations in IMEP remain approximately the same at different engine loads, however, they decrease with increasing hydrogen percentage at each load. This decrease in cyclic variations is due to the increase in mixture combustion rate due to hydrogen addition. Keck and Heywood have also shown that cyclic variations can be reduced with increased combustion rate [9]. The decrease in cyclic variations and an increase in combustion rate can be attributed to the eight times higher flame velocity of hydrogen and lower ignition energy compared to natural gas [10]. Therefore, hydrogen improves combustion stability and allows for engine leaning to higher air-excess ratios.

Figure 4.3 also shows that at higher air-excess ratios the value of COV_{IMEP} increases drastically indicating the engine misfire limit. This misfire limit defines the lean operation limit of the operating window of the engine. In the direction of rich air-excess ratio, the operating window of the engine is restricted by the IMO TIER-III NO_x limit. Therefore, the operating window of the natural gas engine is restricted between the NO_x limit and misfire or lean operation limit as shown in Figure 4.4(a). Figure 4.4 shows the operating window of the hydrogen-natural gas engines at increasing power outputs and hydrogen percentages. The orange region marks the region of high NO_x emissions be-

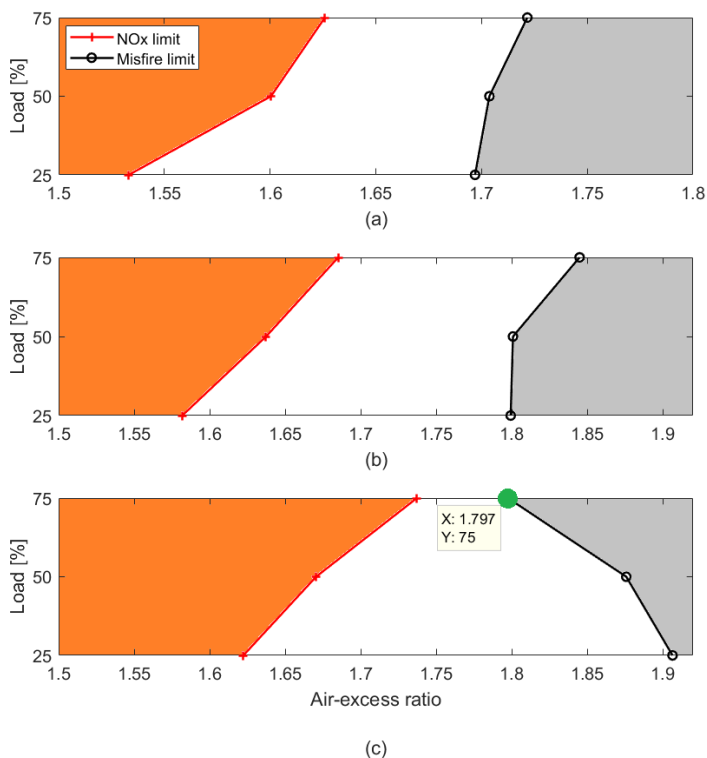


Figure 4.4: Operating window at 75 %, 50 % and 25 % engine loading for 0H₂-NG (a), 10H₂-NG (b), and 20H₂-NG (c) fuel blends

yond the NO_x limit in red, while the black line indicates the misfire limit. The region between the red line and the black line marks the window of acceptable operation.

Figure 4.4 shows that at higher engine loading the NO_x limit shifts towards relatively high air-excess ratios reducing the operating window. Figure 4.4 also shows that increment in hydrogen percentage has the same effect on NO_x limit as it shifts towards even higher air-excess ratios. To operate at same NO_x emissions, the engine needs more air with hydrogen to control the increasing in-cylinder temperatures due to higher flame speeds of hydrogen. As explained earlier, hydrogen induces combustion stability allowing the engine to operate at higher air-excess ratios and pushing the misfire limit at all engine loads as shown in Figure 4.4(b) and Figure 4.4(c). Thus, hydrogen expands the earlier restricted operating window by improving the leaning capabilities, which allows for stable and efficient operation at lower NO_x values. In Figure 4.4(c), although at 75 % load the operating window is depicted to be reduced, it is vital to note that the operating point of air-excess ratio of 1.797 at 75 % load in Figure 4.4(c) (highlighted in green) does not represent the misfire limit for the 20H₂-NG engine. This is because at this measurement point the engine reached its turbocharging capacity, i.e., it was not possible to lean out the engine anymore below 300 mgN m⁻³ of NO_x towards the misfire limit,

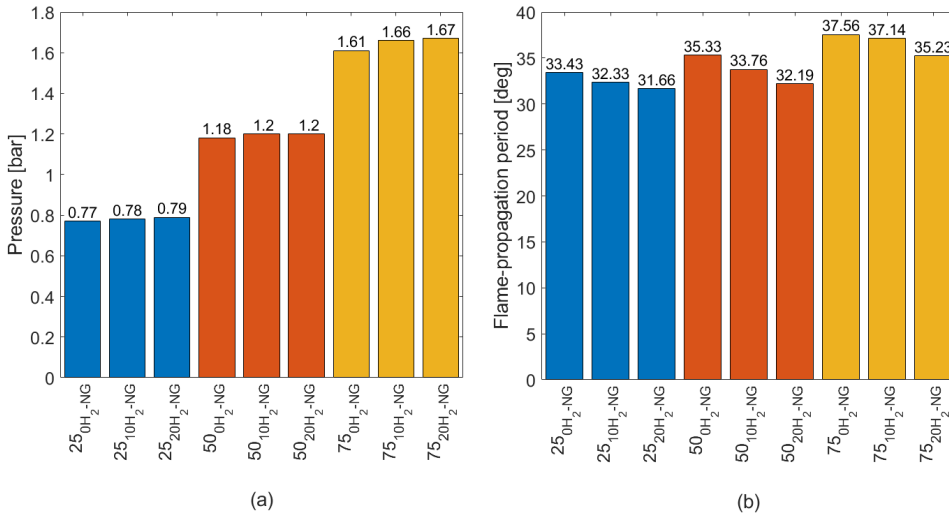


Figure 4.5: Manifold pressure (a) and flame-propagation period (b) at 75%, 50% and 25% engine loading for 0H₂-NG, 10H₂-NG, and 20H₂-NG fuel blends at 500 mgN m⁻³ of NOx

which generally lies close to or even below 100 mgN m⁻³ of NOx. This turbocharger limit reached at 75% load, 20% hydrogen addition and 24 degree spark-timing can also be seen in Figure 4.3(a), where only three measurement points are depicted instead of 5 or 6 points at each engine load and hydrogen percentage. Testing of hydrogen addition with leaning at rated engine load was also restricted due to this turbocharger limit, therefore, it can be concluded that marine hydrogen-natural gas engines may require larger turbochargers than only natural gas engines.

In summary, increasing engine loading reduces the operating window, whereas increasing hydrogen percentage in fuel expands the operating window by improving the leaning capabilities of the engine. With hydrogen blending marine hydrogen-natural gas engines could operate at high loads with a wider operating window and better leaning capabilities, thus, allowing stable and efficient operation at reduced emissions.

EFFECT OF HYDROGEN ADDITION AND ENGINE LOADING ON COMBUSTION, EFFICIENCY AND EMISSIONS

To understand the variations in the combustion process inside marine natural gas engines, combustion and performance parameters at different engine loading and hydrogen percentages will be presented at the same NOx value of 500 mgN m⁻³ (at 5% oxygen) unless mentioned otherwise. In this section, combustion and performance parameters such as manifold pressure, combustion duration, peak cylinder pressure, thermal efficiency and engine emissions will be discussed.

In the previous section, it was established that increasing hydrogen percentage and engine loading require the engine to operate at higher air-excess ratios. This increase in air-excess ratios increases the manifold air pressure (MAP) as shown in Figure 4.5(a). Higher MAP may lead to a reduction in pumping losses and residual gas trapped from

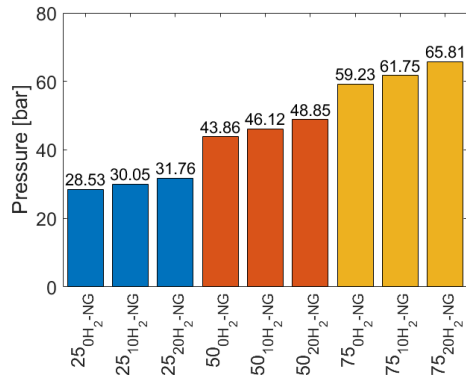


Figure 4.6: Maximum in-cylinder pressure at 75 %, 50 % and 25 % engine loading for 0H₂-NG, 10H₂-NG, and 20H₂-NG fuel blends at 500 mg N m⁻³ of NO_x

the previous cycle. Quader showed that as airflow (MAP) increases the residual gases trapped inside the cylinder reduce non-linearly [11]. This decrease in residual gases due to increasing air flow reduces as air flow increases more. The reduction in residual gases due to increasing MAP caused by an increase in load and/or hydrogen percentage affects the combustion duration. Residual gases play the same role as exhaust gas recirculation (EGR) and increase the combustion duration by decreasing flame speed. Therefore, reduction in residual gas with increasing MAP can help reduce combustion duration. On the other hand, the increase in MAP directly relates to the increase in the air-excess ratio or incoming air, which slows down combustion and increases the combustion duration due to dilution of the air-fuel mixture. Additionally, the increase in hydrogen percentage speeds up the combustion rate and reduces the combustion duration. Therefore, there is a complex interplay between the effect of air, residual gas, natural gas and hydrogen that decides the final combustion rate inside the cylinder.

The ultimate effect of engine loading is to increase the combustion duration while adding hydrogen decreases combustion duration as shown in Figure 4.5(b). The combustion duration between 10 % and 90 % mass-burn fraction shown in Figure 4.6(b) is regarded as the flame-propagation period [6]. The flame-propagation period shown in Figure 4.5(b) is obtained from the Kistler Ki-Box measurement analyser [5], which provides a crude estimation based on the first law of thermodynamics method. The method used by the Ki-Box provides insights on the relative changes in the combustion process due to hydrogen blending, however, it does not account for several effects such as heat loss inside the cylinder, the impact of trapped residual gases in the zero valve overlap engine, in-cylinder temperature evolution, etc. For accurate combustion characterization of different fuel blends, a detailed heat release rate model is required, which will be discussed in the next chapter.

Simultaneous to the effect on combustion duration, engine loading also increases the maximum cylinder pressure (p_{\max}). Additionally, p_{\max} increases with increasing hydrogen percentage due to higher flame speed and reduced combustion duration. Figure 4.6 presents the effects of engine loading and hydrogen addition on maximum cylin-

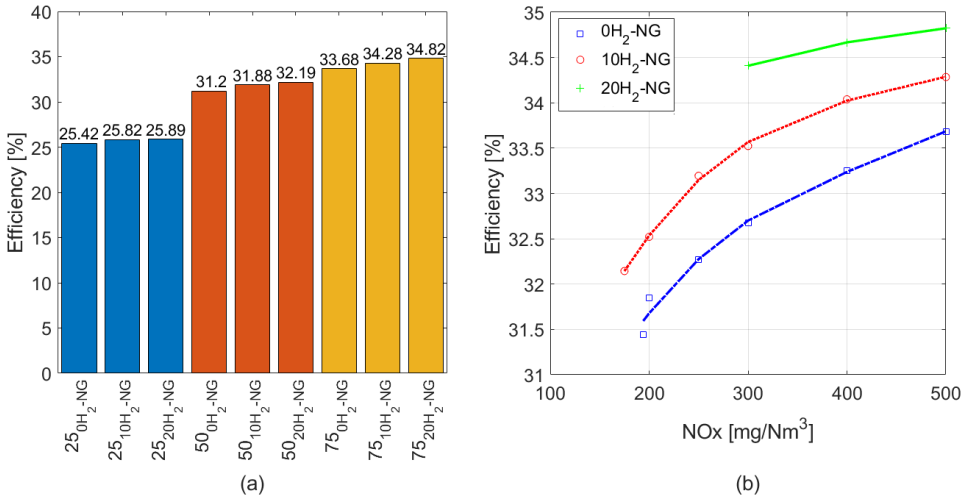


Figure 4.7: Engine efficiency at 500 mgNm^{-3} of NOx (a) and engine efficiency for varying NOx values (b) at 75%, 50% and 25% engine loading for 0H₂-NG, 10H₂-NG, and 20H₂-NG fuel blends

der pressure. Interestingly, as the engine load increases, the increase in p_{max} due to increasing hydrogen percentage also increases. In other words, the increase in p_{max} at 25% load between 0H₂-NG and 20H₂-NG engine is 3.23 bar, which increases to 4.99 bar and 6.58 bar at 50% and 25% load, respectively. This increase in p_{max} with increasing load and hydrogen percentage directly correlates to increase in thermodynamic efficiency [12]. An increase in thermodynamic efficiency points towards an increase in thermal efficiency of the engine as they are directly correlated [12].

Figure 4.7(a) shows that as the engine load increases, the increment in thermal efficiency due to 20% hydrogen addition also increases. The improvement in thermal efficiency increases from 0.47% at 25% load to 1.16% at 75% load for 20H₂-NG fuel blend. Based on this understanding, it may be possible to achieve higher efficiency improvements due to hydrogen addition at higher engine loads as shown in Figure 4.7(a). This could be particularly beneficial for marine hydrogen-natural gas engines as marine engines operate at high engine loading and, based on the above discussion, may gain higher increments in efficiency improvements due to hydrogen addition.

The potential of efficiency improvement due to hydrogen addition becomes even more evident during lean-burn operation. Figure 4.7(b) shows the thermal efficiency for hydrogen addition at 75% load and engine leaning with different NOx values. Hydrogen addition leads to much higher improvements in engine efficiency compared to only natural gas performance at leaner air-excess ratios and lower NOx emissions. For instance, at 300 mgNm^{-3} of NOx, engine operation with 20 percent hydrogen addition is more efficient than engine operation with only natural gas at 500 mgNm^{-3} of NOx. Thus, hydrogen has a prominent effect on engine performance during lean operating conditions. Based on the above discussions, blending hydrogen with natural gas would lead to extension of the operating window and allow engine operation at much lower val-

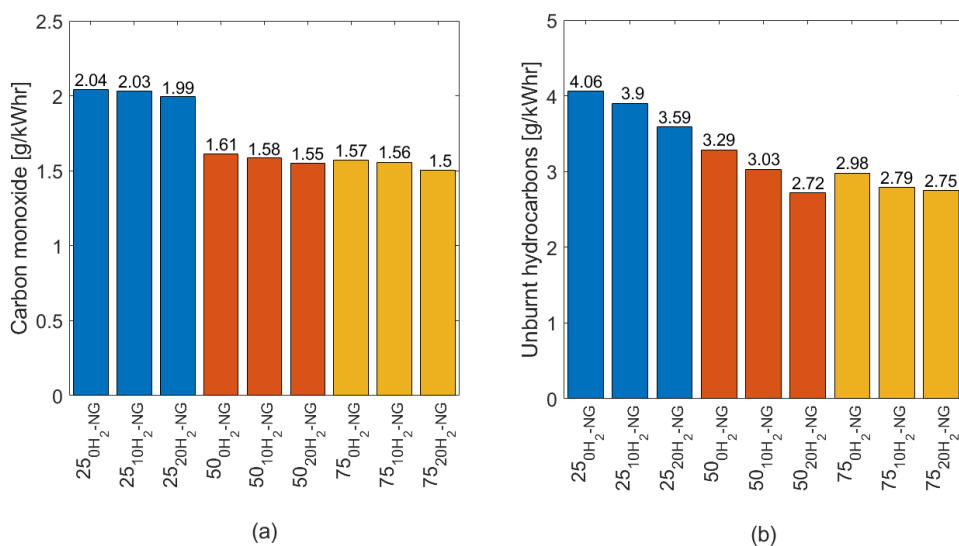


Figure 4.8: Carbon monoxide (a) and unburnt hydrocarbon (b) emissions at 75 %, 50 % and 25 % engine loading for 0H₂-NG, 10H₂-NG, and 20H₂-NG fuel blends at 500 mgN m⁻³ of NOx

ues of NOx emissions with higher engine efficiencies. This can be advantageous for the GasDrive power plant, which can use the waste hydrogen from the SOFC anode-off gas for engine operation at high loads with reduced emissions and efficiency improvements.

In addition to improving engine efficiency and leaning capabilities of the engine, hydrogen also impacts engine emissions. Figure 4.8 and Figure 4.8 shows the carbon monoxide and unburnt hydrocarbon emissions at increasing engine loads and hydrogen percentages. As seen in Figure 4.8(a), specific carbon monoxide emissions increase with decreasing load. The increase in CO emissions is drastic at 25 % load due to an excessive increase in specific fuel consumption. On the other hand, hydrogen decreases carbon monoxide emissions, however, by small margins. Engine load and hydrogen addition have the same effect on unburnt hydrocarbon (UHC) emissions, which in general increase with decreasing load and decrease with increasing hydrogen percentage. One reason for the reduction in CO and UHC emissions is the direct replacement of methane, a carbon-based fuel, with hydrogen. The second reason could be enhanced combustion efficiency due to hydrogen addition.

In addition to the reduction in unburnt hydrocarbons, the zero valve overlap of the engine contributes to the reduction in methane slip. During scavenging, a valve overlap can help reduce residual gases and induce fresh charge into the cylinder. In a premixed air-fuel mixture, a small portion of the fresh fuel charge can slip through from the inlet to the exhaust port during the valve overlap period. Therefore, a zero valve overlap restricts the slippage of fresh charge containing unburnt fuel or methane [13].

In addition to CO and UHC emissions, hydrogen addition also impacts combustion efficiency. Figure 4.9 shows the combustion efficiency or conversion percentage of carbon from fuel to carbon dioxide. Equation 4.2 gives the formula used for calculation of

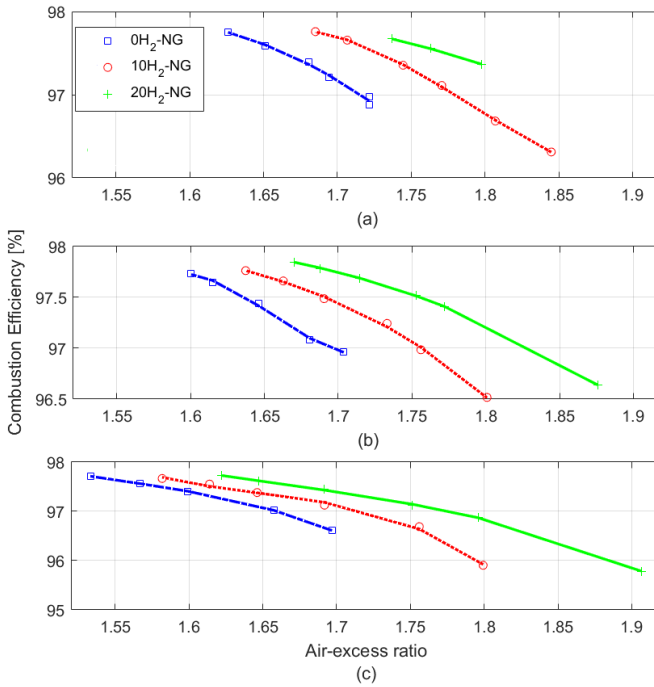


Figure 4.9: Combustion efficiency at 75 % (a), 50 % (b) and 25 % (c) engine loading for 0H₂-NG, 10H₂-NG, and 20H₂-NG fuel blends, and varying air-excess ratios

combustion efficiency based on carbon forming carbon monoxide (C_{CO}), carbon from UHC (C_{UHC}) and carbon in incoming fuel (C_{fuel}), all measured in kgkg^{-1} of fuel.

$$\eta_{\text{comb}} = \left(1 - \frac{C_{CO} + C_{UHC}}{C_{\text{fuel}}}\right) \cdot 100 \quad (4.2)$$

As seen from Figure 4.9, the 20H₂-NG blend has a higher rate of conversion to carbon dioxide at constant air-excess ratios, even though the incoming carbon from the fuel reduces due to hydrogen addition. The improvement in combustion efficiency due to hydrogen addition is evident at constant air-excess ratios. However, hydrogen addition at constant NO_x values does not show much improvements in combustion efficiency, thus, indicating that the reduction in UHC at constant NO_x emissions may be mainly due to replacement of natural gas by hydrogen.

EFFECT OF SPARK-TIMING WITH HYDROGEN ADDITION ON AIR-EXCESS RATIO AND EFFICIENCY

Besides engine load, spark-timing also affects the operating window and engine efficiency. Changes in spark-timing lead to changes in in-cylinder pressures and temperatures, thus altering the engine operating limits and engine efficiency. As explained earlier, the increase in air intake during leaning can reduce combustion speed. This reduces the rate of in-cylinder pressure rise shifting the cylinder pressure peak far into

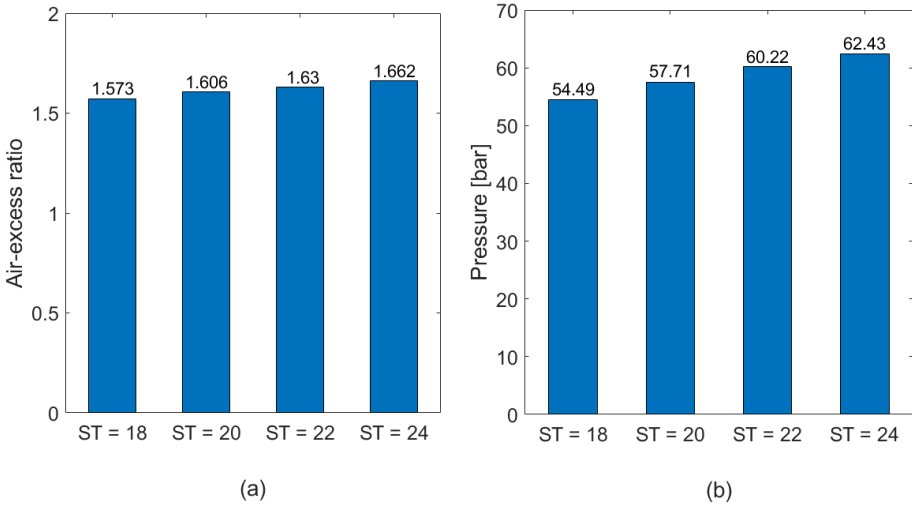


Figure 4.10: Effect of spark-timing on air-excess ratio (a) and maximum in-cylinder pressure (b) at 75% engine loading for 10H₂-NG fuel blend and 500 mgNm⁻³ of NO_x

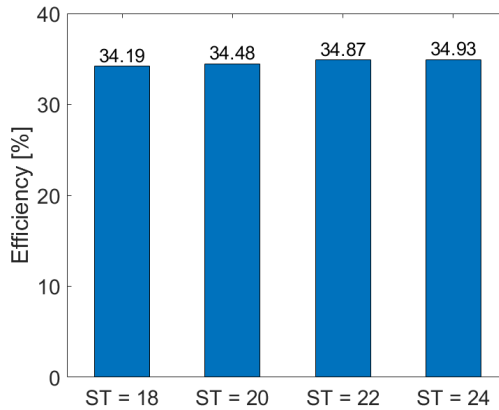


Figure 4.11: Effect of spark-timing on engine efficiency at 75% engine loading for 10H₂-NG fuel blend and 500 mgNm⁻³ of NO_x

the expansion stroke, which can make combustion unstable and lead to loss of power due to extended combustion duration [13]. To counter this effect during engine leaning, spark-timing is advanced [10]. On the other hand, the addition of hydrogen increases the combustion rate and also the rate of pressure rise, which moves the in-cylinder pressure peak more towards the TDC or the compression stroke. Increasing hydrogen percentage shortens the ignition delay and can cause large increments in in-cylinder pressure and temperature around the end of the compression stroke if the spark-timing is too advanced. Therefore, the power loss may increase to overcome this high in-cylinder pressure [13]. To avoid this large increment in in-cylinder pressures, temperatures and NO_x

emissions, ignition timing may need to be postponed or retarded. In totality, it is vital to optimise ignition timing in a marine hydrogen-natural gas engine as it plays a crucial role in modulating the combustion process inside the cylinder.

Figure 4.10(a) shows the variations in the air-excess ratio at 75 % load, 10 % hydrogen addition and NO_x value of 500 mgNm⁻³ as spark-timing is advanced from 18 degrees bTDC to 24 degrees bTDC. As seen in Figure 4.10(a), the engine needs more air to produce the same amount of NO_x emissions as the spark-timing is advanced. Additionally, Figure 4.10(b) presents the increasing trend of p_{max} as ignition timing is advanced. The increase in maximum in-cylinder pressure with advanced ignition timing leads to increased thermal efficiency as depicted in Figure 4.11.

Therefore, advancing ignition timing can help increase the engine efficiency of lean-burn marine hydrogen-natural gas engines. However, it is vital to note that at advanced spark-timing of 24 degrees bTDC a hydrogen-natural gas engine can reach its turbocharger limit before reaching the misfire limit, which highly reduces the operating window and its leaning capabilities as shown in Figure 4.4. Therefore, to achieve efficiency improvements with reduced emissions due to engine leaning at high loads and advanced spark-timing the turbocharging capacity should be increased.

4.3. EXPERIMENTS ON CARBON DIOXIDE-NATURAL GAS COMBUSTION

This section describes the experimentation methodology for carbon dioxide-natural gas combustion and the corresponding experimental results.

4.3.1. EXPERIMENTATION METHODOLOGY FOR CO₂-NG COMBUSTION

Similar to hydrogen, experiments were performed on the same 500 kW_e, lean-burn, zero valve overlap turbocharged SI marine engine to understand the effects of carbon dioxide and natural gas fuel blends on the combustion process and engine performance. As shown in Figure 4.1, carbon dioxide from pressurized bottles was injected through a mass flow controller before the turbocharger in different percentages and blended with natural gas. Table 4.4 shows the different CO₂-NG blends and operating conditions tested. For 5CO₂-NG blends, measurements were performed for 400, 500 and 1000 mgNm⁻³ of NO_x at all loads while others blends were tested till engine misfire.

Table 4.4: Experimentally tested CO₂-NG blends for varying NO_x values.

Engine Load [%]	CO ₂ -NG Blends	NO _x [mgNm ⁻³]
75	05, 10, 15CO ₂ -NG	(400 - 1000), 500 to misfire
50	05, 10, 20CO ₂ -NG	(400 - 1000), 500 to misfire
25	05, 10, 20CO ₂ -NG	(400 - 1000), 500 to misfire

Like hydrogen, experiments for different CO₂-NG blends were also performed at different values of constant NO_x emissions by controlling the air-intake. The general experimentation methodology followed for studying the effects of CO₂-NG blends was the same as that provided in section 4.2.1 for hydrogen-natural gas blends. However, one

change was made in the experimentation methodology for CO₂-NG blends, which has been discussed in subsection 4.3.2.

4.3.2. EXPERIMENTAL RESULTS FOR CO₂-NG COMBUSTION

In this section, experimental results for three gas fuel blends of 05CO₂-NG, 10CO₂-NG, and 15 or 20CO₂-NG at engine loadings of 75 % (375 kWe), 50 % (250 kWe) and 25 % load (125 kWe) have been studied. Engine performance results have been presented at a fixed spark-timing of 24 degrees bTDC in all the following sections. All the results are presented at 500 mgNm⁻³ of NO_x unless mentioned otherwise. Variations in the performance of the marine engine due to carbon dioxide addition have been discussed by understanding the variations in efficiency, operating window, cyclic variations and emissions.

4

CHALLENGES AND CONSIDERATIONS DURING CO₂-NG COMBUSTION EXPERIMENTS

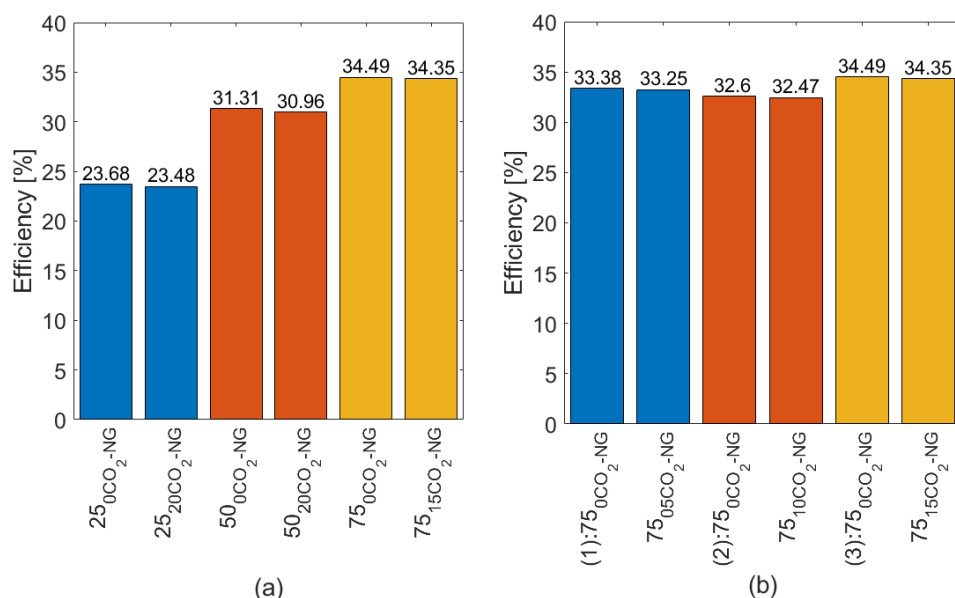


Figure 4.12: Engine efficiency at 75 %, 50 % and 25 % engine loading for CO₂-NG fuel blend and 500 mgNm⁻³ of NO_x (a). Engine efficiency at 75 % engine loading for CO₂-NG blends and their corresponding ONG performance measurements (b)

The experiments to study the effects of carbon dioxide addition in the lean-burn test engine were performed separately from the earlier discussed hydrogen addition experiments. During the CO₂-NG combustion experiments, the engine showed minor but important variations in engine performance. These variations made it difficult to initially compare and understand the CO₂-NG measurements relative to H₂-NG measurements. This section presents a discussion on these variations and the change in experimentation methodology during CO₂-NG combustion experiments through experimental results.

Figure 4.12(a) shows that at all loads engine efficiency consistently decreases due to CO₂ addition for constant NO_x of 500 mgN m⁻³. Addition of CO₂ activates the throttle control for adjustment in total air-fuel charge while the natural gas intake is increased by the engine to maintain the same power output, thus, avoiding engine power reduction or derating. The carbon dioxide flow is simultaneously controlled with increasing natural gas flow to sustain the required CO₂ blending percentage. Increment in natural gas flow with same power output leads to depreciation of engine efficiency.

Although the efficiency clearly decreased with increasing CO₂ at all loads, the engine efficiency of 34.35 % for 15CO₂-NG fuel blend at 75 % load was found to be higher than the efficiency found for 10H₂-NG fuel blend at 75 % load as seen from Figure 4.7(a). This finding of CO₂-NG fuel blends leading to better efficiency compared to H₂-NG fuel blends for the same power output and operating conditions is unlikely and a contradiction to the underlying physical phenomenon. The efficiency for H₂-NG fuel blend should be higher as hydrogen is a combustible gas while CO₂ is inert, thus, requiring more natural gas intake for the same power output. Therefore, compared to the corresponding ONG performance shown in Figure 4.12(a) the efficiency due to CO₂ addition clearly decreases.

The clarification for the above discrepancy can be attained by comparing the engine efficiency for ONG or 0CO₂-NG fuel blend at 75 % load and the corresponding efficiency for ONG or 0H₂-NG fuel blend at 75 % provided in Figure 4.12(a). It is evident that during CO₂-NG experiments the engine showed better efficiency for ONG performance and same operating conditions. Thus, even though the efficiency decreased with CO₂ addition as expected, it seemed to be higher than that found for H₂-NG fuel blends.

It is evident from the above discussion that engine performance showed minor but important fluctuations during CO₂-NG experiments. These fluctuations could be due to changes in natural gas quality and the corresponding impact on engine control and performance. Due to the fluctuations, an additional step was added in the experimentation methodology to understand and capture the variations in engine performance due to CO₂ blending. In the additional step, corresponding ONG performance measurements were performed for every CO₂-NG fuel blend and operating condition. This step of additional measurements proved to be crucial because engine performance also showed some fluctuations when performing repeated measurements of ONG performance corresponding to different CO₂-NG blends as shown in Figure 4.12(b) for 75 %. For all CO₂-NG fuel blends, the engine efficiency decreased relative to corresponding ONG performances, which is an expected outcome. However, the engine efficiency fluctuated for all the three corresponding ONG operating conditions at 75 % engine load. The engine efficiency for ONG operating condition ((3):75₀CO₂-NG) corresponding to the 15CO₂-NG fuel blend was found to be the highest as seen from Figure 4.12 (b). Therefore, although the efficiency with 15 % CO₂ blending dropped relative to the corresponding ONG performance, it was higher than that found for 05CO₂-NG and 10CO₂-NG fuel blend, which is unexpected. This indicated that the natural variability in engine operation was found to be larger than the variations in engine performance due to the addition of CO₂.

Based on the above discussion and to avoid misinterpretation of results, the effects of CO₂ addition were understood and modelled as deviations from their corresponding ONG performance for the same engine operating conditions. Engine performance due

to CO₂ addition relative to the corresponding ONG performance matches with the existing literature and underlying physical principles.

EFFECT OF CARBON DIOXIDE ADDITION AND ENGINE LOADING ON CYCLIC VARIATIONS AND OPERATING WINDOW

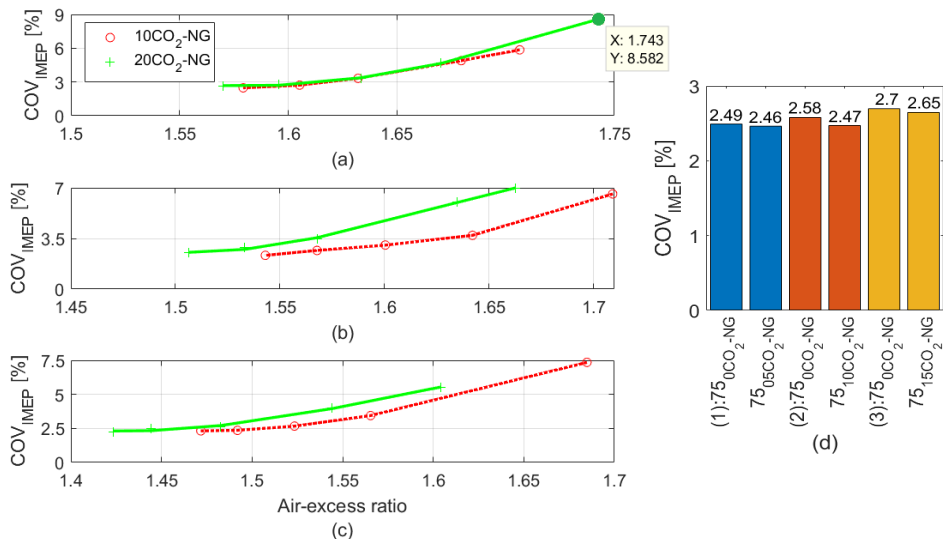


Figure 4.13: Coefficient of variations in IMEP averaged for 145 consecutive cycles at 75 % (1), 50 % (b) and 25 % (c) engine loading for 10CO₂-NG and 20CO₂-NG fuel blends. Coefficient of variations in IMEP at 75 % engine loading for 05CO₂-NG, 10CO₂-NG and 15CO₂-NG fuel blends and their corresponding ONG performance measurements (d)

Blending of carbon dioxide with the incoming natural gas flow can have a significant impact on the cyclic variations. Figure 4.13(a-c) shows the coefficient of variations in IMEP for two CO₂-NG blends and different engine loads. At 75 % load, the cyclic variations do not show any significant variations with increments in CO₂ blending percentage. At lower loads and same air-excess ratios, the adverse effect of CO₂ on cyclic variations becomes more evident. Addition of CO₂ leads to absorption of combustion heat due to the high specific heat capacity and slow down of the combustion process. Therefore, contrary to hydrogen, CO₂ can reduce the combustion rate, which increases cyclic variations and decreases combustion stability. The reduced combustion stability is evident at lean air-excess ratios as the values of COV_{IMEP} reach close to 9 % due to CO₂ addition when nearing misfire. With CO₂ addition, the measurements indicate much higher values of COV_{IMEP} compared to the values depicted in Figure 4.3 for H₂-NG blends. The decrease in combustion stability due to increasing CO₂ percentage reduces the leaning capabilities of the engine, thus, generally leading to engine misfire at lower air-excess ratios.

Although the cyclic variations increased due to CO₂ addition when compared at constant air-excess ratios, the values of COV_{IMEP} for constant NO_x values were found to be similar or marginally lower for higher CO₂-NG fuel blends. This trend of similar or

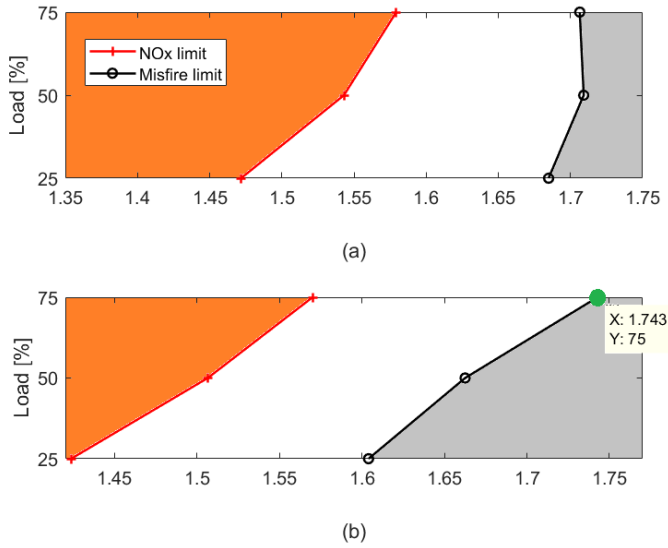


Figure 4.14: Operating window at 75 %, 50 % and 25 % engine loading for 10CO₂-NG (a) and 20CO₂-NG (b) fuel blends

lower COV_{IMEP} at higher values of CO₂-NG fuel blends was found for values close to 500 mgNm⁻³ of NO_x corresponding to the relatively rich air-excess ratios. Figure 4.13(d) shows the decrease in COV_{IMEP} at 75 % load for 05CO₂-NG, 10CO₂-NG and 15CO₂-NG fuel blends compared to the corresponding ONG performance measurements. The similar or lower values of COV_{IMEP} indicate no depreciation or even improvement in combustion stability for higher CO₂-NG fuel blends at constant NO_x emissions. This finding will be further discussed by studying the variations in other engine parameters and also via modelling in the next chapter.

The engine experiments to study the effects of combusting H₂-NG and CO₂-NG blends were conducted at constant values of NO_x emissions. To produce the same power output and the same amount of NO_x with increasing CO₂ addition, the natural gas flow and the air-to-fuel ratio were controlled. As explained in the preceding subsection, the natural gas flow increased with CO₂ addition. However, the presence of non-combustible CO₂ in the fuel blend leads to lower air-intake relative to the fuel-intake to attain the same NO_x value. Therefore, the engine operation at the same NO_x value becomes increasingly rich with increasing CO₂ fuel blend percentage. Figure 4.14 depicts the lower air-excess ratios corresponding to the NO_x and misfire limits for higher CO₂ content. The green point in Figure 4.13(a) and Figure 4.14(b) for 75 % engine load represents engine performance for 15CO₂-NG fuel blend, while the remaining operating points in the figures correspond to 20CO₂-NG blend.

Based on the above discussion, CO₂ addition led to engine operation at rich air-to-fuel ratios for same NO_x emissions, which is contrary to the effect of hydrogen addition. Additionally, CO₂ blending reduced combustion stability for constant air-excess ratios

while hydrogen addition enhanced combustion stability.

EFFECT OF CARBON DIOXIDE ADDITION AND ENGINE LOADING ON COMBUSTION AND EMISSIONS

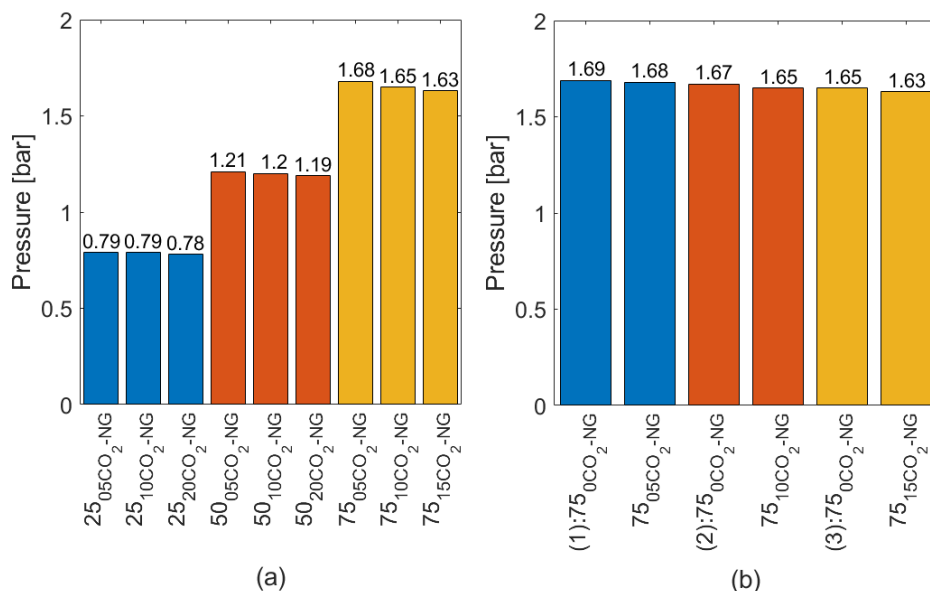


Figure 4.15: Manifold pressure at 75 %, 50 % and 25 % engine loading for CO₂-NG fuel blend and 500 mg N m⁻³ of NOx (a). Manifold pressure at 75 % engine loading for CO₂-NG blends and their corresponding ONG performance measurements (b)

In the previous subsection, it was shown that carbon dioxide blending requires the engine to operate at lower air-excess ratios. The reduction in air-excess ratio causes the manifold pressure (pressure after throttle) to reduce with increasing carbon dioxide blend percentage as shown in Figure 4.15. As explained earlier, the effects of carbon dioxide addition are understood relative to their corresponding ONG performance measurements. For this purpose, Figure 4.15(b) also shows the decrease in manifold pressure with addition of carbon dioxide relative to the corresponding ONG performance measurements. Increase in CO₂ content decreases the air-to-fuel ratio and also impacts the trapped residual gases as the total trapped mass at the time of inlet valve closing reduces with reduced trapped pressure. While CO₂ addition and the presence of trapped residual gases will slow down the combustion rate, the decrease in air-excess or the rich air-to-fuel ratio will increase the combustion rate. Thus, there is a complex interaction between carbon dioxide, air, natural gas and the residual gases that will dictate the combustion duration inside the cylinder. The impact of CO₂ addition on the combustion duration will be discussed in the next chapter with the help of heat release rate and combustion characterization modelling.

In general, increase in CO₂ content would decrease in-cylinder pressures due to decreased rate of pressure rise and combustion. However, CO₂ blending with natural gas

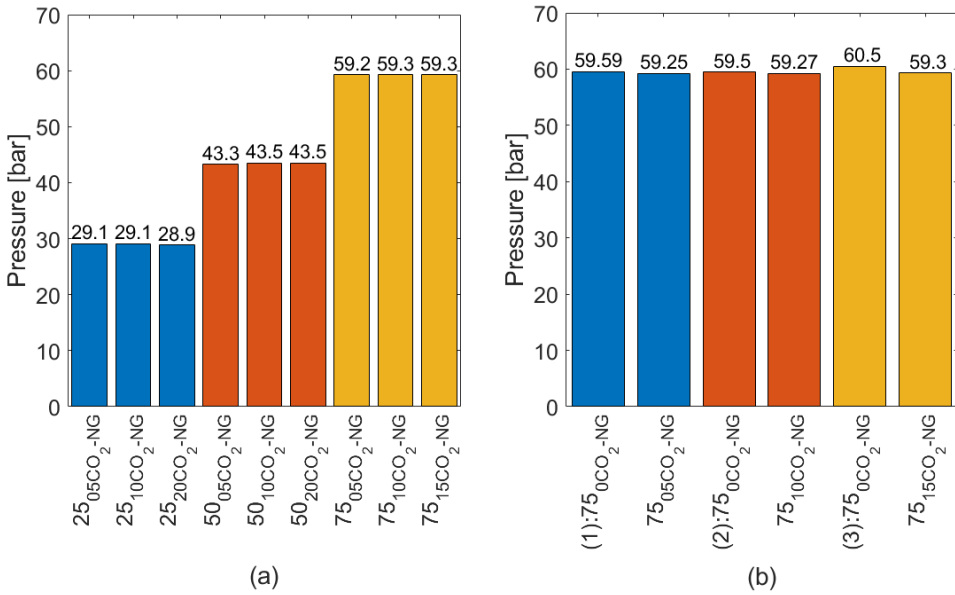


Figure 4.16: Maximum in-cylinder pressure at 75 %, 50 % and 25 % engine loading for CO₂-NG fuel blend and 500 mgNm⁻³ of NO_x (a). Maximum in-cylinder pressure at 75 % engine loading for CO₂-NG blends and their corresponding ONG performance measurements (b)

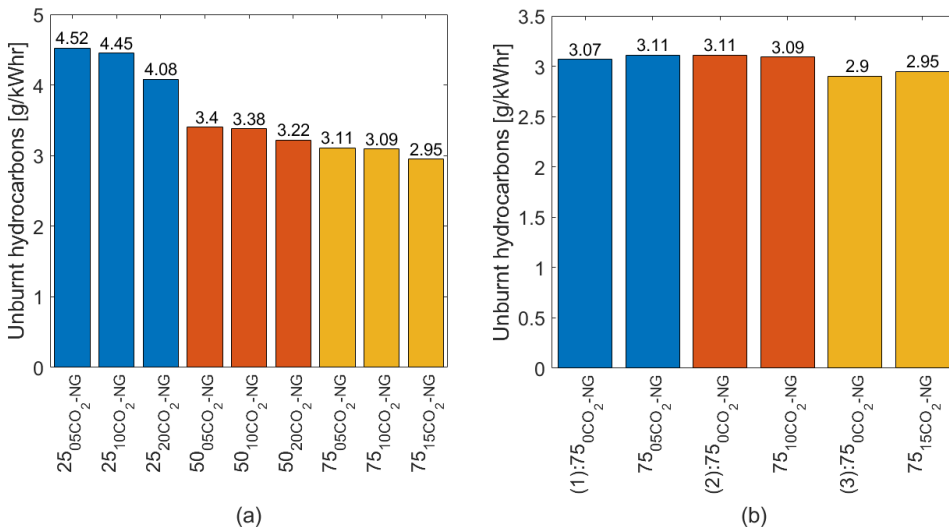


Figure 4.17: Unburnt hydrocarbon emissions at 75 %, 50 % and 25 % engine loading for CO₂-NG fuel blend and 500 mgNm⁻³ of NO_x (a). Unburnt hydrocarbon emissions at 75 % engine loading for CO₂-NG blends and their corresponding ONG performance measurements (b)

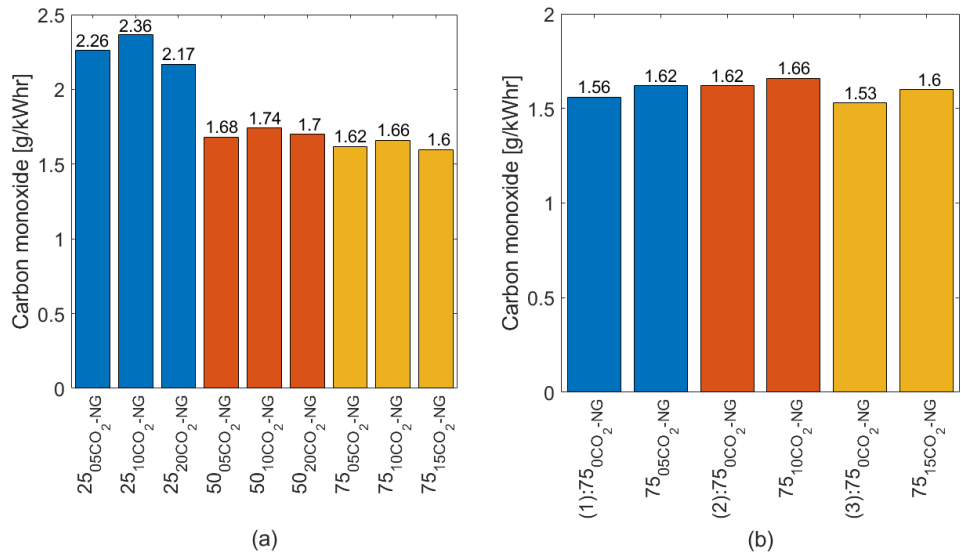


Figure 4.18: Carbon monoxide emissions at 75 %, 50 % and 25 % engine loading for CO₂-NG fuel blend and 500 mg N m⁻³ of NOx (a). Carbon monoxide emissions at 75 % engine loading for CO₂-NG blends and their corresponding ONG performance measurements (b)

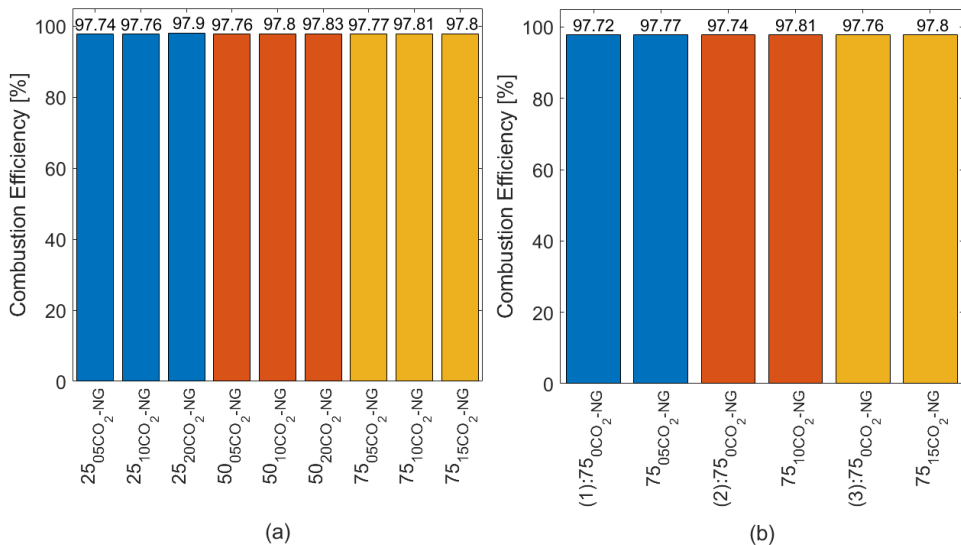


Figure 4.19: Combustion efficiency at 75 %, 50 % and 25 % engine loading for CO₂-NG fuel blend and 500 mg N m⁻³ of NOx (a). Combustion efficiency at 75 % engine loading for CO₂-NG blends and their corresponding ONG performance measurements (b)

did not cause any significant decrease in maximum in-cylinder pressure as seen in Figure 4.16. In this research, the richening of air-to-fuel ratio for engine operation at constant NOx showed a profound effect in countering the decrease in combustion rate and combustion stability due to CO₂ addition. The countering effect of rich air-to-fuel ratio on the combustion rate will be further discussed in the next chapter. Thus, the adverse effects of CO₂ addition could be suppressed by controlling the engine operation for same NOx operation.

Confirming the positive impact of air-fuel enrichment, Bauer and Wachtmeister found that engine operation for 30 and 50CO₂-NG fuel blends at same NOx emissions showcased a higher heat release compared to only NG performance [14]. They also showed that the enrichment of air-to-fuel ratio with CO₂ blending and constant NOx operation led to lower formaldehyde and unburnt hydrocarbon emissions. Small reductions in unburnt hydrocarbons with CO₂ blending were also found in the present research at different engine loadings as seen from Figure 4.17. However, the decrease was not found for all CO₂-NG fuel blends when compared against their corresponding ONG performance measurements, which is evident from Figure 4.17(b). From the above discussion, it can be concluded that the richening of air-to-fuel ratio due to constant NOx operation allows for no significant increase in unburnt hydrocarbons due to CO₂ addition and could even contribute to reductions of UHC emissions. Bauer et al. also found that formaldehyde emissions reduced more effectively at retarded spark-timings with CO₂ blending, which could help in the reduction of methane and formaldehyde emissions from SI NG engines.

After unburnt hydrocarbons, the impact of different CO₂-NG fuel blends on carbon monoxide emissions was unclear as seen from Figure 4.18(a). The carbon monoxide emissions increased for 10CO₂-NG fuel blends and then decreased for higher CO₂-NG fuel blends at all engine loadings. However, carbon dioxide blending showed a general trend of increasing carbon monoxide emissions relative to the corresponding ONG performance measurements as seen in Figure 4.18(b). Interestingly, carbon dioxide addition provided small improvements in combustion efficiency at constant NOx emissions. The improvements in combustion efficiency are evident for increasing CO₂-NG fuel blends and also relative to the corresponding ONG performance measurements as seen from Figure 4.19. This enhancement in combustion can be attributed to the counter effect provided by enriched air-to-fuel ratio, which also has a positive impact on unburnt hydrocarbons.

In this manner, the individual effects of adding hydrogen and carbon dioxide as constituents of SOFC anode-off gas on engine performance are studied in this research. These individual effects of both the anode-off gas constituents are further studied and captured via in-cylinder process modelling in the next chapter. As mentioned earlier, the effects of carbon monoxide from the anode-off gas were not taken into consideration in this phase of research, and the reasons are as follows:

- The percentage of CO in anode-off gas is small compared to the percentages of hydrogen and carbon dioxide.
- The CO percentage reduces even further in the AOG-NG fuel blends studied in this research. Although the volumetric lower heating value of CO is slightly higher than

that of hydrogen [15], the energy input of the engine due to CO addition for the AOG-NG blends tested in this research increases by only 1.2% compared to when CO is not considered. Therefore, the relatively smaller percentages of CO could support the combustion process and contribute to the engine efficiency like hydrogen, however, for the AOG-NG blends tested in this research, the impact would be non-significant. Refer to chapter 6 and Chapter 7 for the AOG-NG blends tested in this research.

- The effects of CO should be considered in future when testing higher blend percentages of AOG to account for the possible positive impact on SOFC-ICE integration.

4.4. CONCLUSIONS

In this chapter, the effects of combusting anode-off gas constituents in a zero valve overlap, lean-burn, turbocharged marine SI natural gas engine have been studied experimentally. For the SOFC-ICE integration approach presented in this dissertation, water-vapour in the anode-off gas is condensed before combusting the AOG in a marine natural gas engine for additional power generation. Furthermore, the effects of carbon monoxide from anode-off gas have not been considered in this research. Hydrogen and carbon dioxide are the main constituents of anode-off gas investigated in this research for combustion in an ICE. The research results presented in this chapter help in partially answering Research Question 3 and 5. The following concluding remarks are noted from the discussions presented in this chapter:

- The experimental results showed that increasing engine loading reduces the operating window, whereas increasing hydrogen percentage in fuel expands the operating window by improving the leaning capabilities of the engine. With hydrogen blending marine hydrogen-natural gas engines could operate at high loads with a wider operating window and better leaning capabilities, thus, allowing stable and efficient operation at reduced NO_x emissions.
- Addition of hydrogen improved engine efficiency while reducing carbon monoxide and unburnt hydrocarbon emissions. Blending hydrogen with natural gas also led to improvements in combustion efficiency at constant air-excess ratios. However, hydrogen addition at constant NO_x values did not show much improvements in combustion efficiency, thus, indicating that the reduction in UHC at constant NO_x emissions may be mainly due to replacement of natural gas by hydrogen.
- Furthermore, the experimental investigation concluded that advancing ignition timing can help increase the engine efficiency of lean-burn marine hydrogen-natural gas engines. However, it is vital to note that at advanced spark-timings of 24 degrees bTDC a hydrogen-natural gas engine can reach its turbocharger limit before reaching the misfire limit, which highly reduces the operating window and its leaning capabilities.
- Experiments to understand the marine engine performance on carbon dioxide and natural gas fuel blends were found to be challenging due to minor but important fluctuations in engine performance. Therefore, the effects of CO₂ addition in this research are understood and modelled as deviations from their corresponding ONG performance for the same engine operating conditions.

- Carbon dioxide blending reduced engine efficiency, however, the addition of CO₂ indicated no depreciation or even improvement in combustion stability for higher CO₂-NG fuel blends at constant NO_x emissions. This finding will be further discussed by studying the variations in other engine parameters and also via modelling in the next chapter.
- Addition of CO₂ with constant NO_x operation led to reduction of air-excess ratio, thus, indicating richening of the air-fuel mixture. In this research, the richening of air-to-fuel ratio for engine operation at constant NO_x showed a profound effect in countering the decrease in combustion rate and combustion stability due to CO₂ addition. The countering effect of rich air-to-fuel ratio on the combustion rate will be further discussed in the next chapter. Thus, the adverse effects of CO₂ addition could be suppressed by controlling the engine operation for same NO_x operation.
- Interestingly, carbon dioxide addition provided small improvements in combustion efficiency at constant NO_x emissions. This enhancement in combustion can be attributed to the counter effect provided by enriched air-to-fuel ratio, which also has a positive impact on unburnt hydrocarbons as small reductions in unburnt hydrocarbons with CO₂ blending were found in the present research at different engine loadings.

In this manner, experimental investigations have been performed to study the effects of combusting individual constituents of SOFC anode-off gas (hydrogen and carbon dioxide) in a marine natural gas engine and, thus, partially answering Research Question 3. The experimental study also helped in understanding the effects of ISVs such as engine fuel composition (varying blends of anode-off gas constituents and natural gas), air-excess ratio, spark-timing and engine loadings on marine engine performance, thus, providing insights to partially answer Research Question 5.

The engine experiments discussed in this chapter are used as a building block to develop combustion characterization models that will help capture the combustion and in-cylinder process for different H₂-NG and CO₂-NG fuel blends, engine loading and engine leaning. The individual effects of both the anode-off gas constituents are further studied and captured via combustion and in-cylinder process modelling in the next chapter.

REFERENCES

- [1] H. Arruga et al. Effect of Intake Manifold Water Injection on a Natural Gas Spark Ignition Engine: An Experimental Study. In *IOP Conference Series: Materials Science and Engineering*, 2017.
- [2] H.D. Sapra et al. Experimental Investigations of Hydrogen-Natural Gas Engines for Maritime Applications. In *ASME Internal Combustion Fall Technical Conference*, 2018.
- [3] H.D. Sapra et al. Experimental Investigations of Performance Variations in Marine Hydrogen-Natural Gas Engines. In *CIMAC*, 2019.

- [4] K. Packham. Lean-Burn Engine Technology Increases Efficiency, Reduces NOx Emissions (White paper). 2007.
- [5] KiBox To Go | Kistler. <https://www.kistler.com/en/products/systems/kibox-to-go/>.
- [6] J.B. Heywood. *Internal Combustion Engine Fundamentals*. McGraw-Hill Series in Mechanical Engineering, 1988.
- [7] P. Dirrenberger et al. Measurements of Laminar Flame Velocity of Components of Natural Gas. *Energy & Fuels*, 2011.
- [8] A. E. Dahoe. Laminar Burning Velocities of Hydrogen-Air Mixtures from Closed Vessel Gas Explosions. *Journal of Loss Prevention in the Process Industries*, 2005.
- [9] J.C. Keck, J.B. Heywood, and G. Noske. Early Flame Development and Burning Rates in Spark Ignition Engines and Their Cyclic Variability. In *International Congress and Exposition*. SAE Technical Paper Series, 1987.
- [10] F. Ma and Y. Wang. Study on the Extension of Lean Operation Limit through Hydrogen Enrichment in a Natural Gas Spark-Ignition Engine. *International Journal of Hydrogen Energy*, 2008.
- [11] A.A. Quader. Lean Combustion and the Misfire Limit in Spark Ignition Engines. In *International Automobile Engineering and Manufacturing Meeting*. SAE International, 1974.
- [12] H.K. Woud and D. Stapersma. *Design of Propulsion and Electric Power Generation Systems*. Institute of Marine Engineering, Science and Technology, 2002.
- [13] E. Hu et al. Experimental Study on Combustion Characteristics of a Spark-Ignition Engine Fueled with Natural Gas-Hydrogen Blends Combining with EGR. *International Journal of Hydrogen Energy*, 2009.
- [14] M. Bauer and W. Georg. Formation of Formaldehyde in Lean-Burn Gas Engines. In *CIMAC*, 2010.
- [15] L. Waldheim and T. Nilsson. Heating Value of Gases from Biomass Gasification. Technical report, 2001.

5

COMBUSTION MODELLING OF ANODE-OFF GAS CONSTITUENTS IN A SI MARINE NATURAL GAS ENGINE

In this research, engine experiments are combined with simulation models to gain a better understanding of the combustion, in-cylinder process and the performance of the AOG-NG engine operating on different fuel blends of SOFC anode-off gas and natural gas. The developed simulation models are further used to study the potential of the integrated SOFC-ICE power plant. For this reason, in this chapter, the effects of individual constituents of anode-off gas on the combustion and in-cylinder process are studied by developing simulation models.

The current chapter is initiated by discussing different engine modelling approaches that have been presented in existing literature to capture H₂-NG and CO₂-NG combustion effects. Next, a methodology is presented to characterize the combustion process for H₂-NG and CO₂-NG fuel blends based on engine experiments. This chapter also provides a comprehensive analysis comparing two different modelling approaches (Seiliger and Wiebe) to capture the combustion and in-cylinder process. Based on the comparison of the capabilities of the two modelling approaches, one modelling approach is chosen for further research in this dissertation. Effects of H₂ addition, CO₂ addition, engine leaning and engine loading are captured and understood by using the developed combustion characterization simulation models. Characterization of the combustion process will be followed by the parametrization process, which is used to capture the in-cylinder process for varying anode-off gas and natural gas fuel blends for SOFC-ICE integration. The parametrization of the combustion process to simulate the effects of

Parts of this chapter have been published in Energy Conversion and Management [1] and Applied Energy [2]. Topics discussed in sections 5.1 to 5.6 are based on publication [1].

AOG-NG fuel blends on the combustion and in-cylinder process along with the complete engine performance will be covered in the next chapter.

In this chapter, the developed simulation models help in understanding the impact of AOG constituents on the in-cylinder process, thus, providing an answer to Research Question 3. Additionally, Research Question 4, which raises questions pertaining to the suitable choice of simulation models to quantify engine performance with AOG constituents for SOFC-ICE integration, is partially answered in this chapter. The combustion and in-cylinder process models developed in this chapter in combination with the holistic engine model developed in the next chapter form the complete solution to Research Question 4. Additionally, the model simulations presented in this chapter are used to gain a detailed understanding of the impacts of ISVs such as engine fuel composition (varying blends of anode-off gas constituents and natural gas), air-excess ratio (engine leaning), engine loading and spark-timings on the in-cylinder process of the marine lean-burn NG engine, thus, providing insights to answer Research Question 5.

5.1. ENGINE MODELLING

The development of engine technology is extensively supported by model simulations. Models can help improve engine design, understanding of in-cylinder chemical and physical processes, their overall performance and transient capabilities [3–6]. The choice of engine modelling approach can vary from detailed computational fluid dynamics (CFD) models to straight forward transfer function models depending on the required accuracy, amount of information and computational time required. The specific choice of CFD models helps to acquire detailed process information with a high degree of model complexity and computational time [7–9]. Numerous CFD studies have been conducted to study the performance and combustion of diesel, alternative and blended fuels such as H₂-NG, methane diluted with CO₂, methanol and DME [10–13].

Followed by CFD models, in terms of complexity, are one-dimensional and quasi-dimensional thermodynamic models [14–16]. In addition to multiple dimensions, the combustion process can be studied as single-zone, two-zone and multi-zone combustion models. In single-zone models, the working fluid undergoing the combustion process is assumed to be lumped into a single thermodynamic control volume [17, 18]. On the other hand, the working fluid is split between a burned and an unburned thermodynamic control volume (or zone) in a two-zone model and several zones in a multi-zone model [19]. Although multi-dimensional models provide detailed predictions of the combustion process, zero-dimensional (0-D) thermodynamic models are often applied due to their ability to capture the in-cylinder combustion process with reduced computational effort as they are relatively simpler [20, 21]. 0-D combustion models are practical as they provide quick and helpful results to study engine performance, however, the simulation results may have reduced accuracy and details.

A 0-D model by definition has no spatial resolution and does not provide any information on the dynamics of fluid within the process. A commonly adopted approach for 0-D combustion models is to employ the empirical Wiebe model to simulate the fuel mass-burn rate and compute the combustion energy released. The combustion process can be represented by single or multiple Wiebe functions, which are mathematically defined by single or multiple Wiebe coefficients for combustion efficiency, shape factor

and combustion duration [22, 23]. In SI natural gas engines, the combustion is divided into three phases of flame development, propagation and termination, which have different combustion rates [24]. For instance, the flame termination phase is very slow as compared to the other two phases.

A single Wiebe function with three coefficients can struggle in precisely capturing all the three combustion phases with different alternative fuels, fuel blends, injection strategies and lean operating conditions. Based on this understanding, Yildiz et al. [20] compared the capabilities of single and double Wiebe functions to reproduce the experimental in-cylinder pressures and gross indicated mean effective pressure (GIMEP) for methane and hydrogen-methane blends in a 500 cc SI engine. They concluded that double Wiebe functions fitted better than the single-Wiebe functions, however, discussions on the capabilities of double Wiebe function to simulate in-cylinder temperatures, combustion heat and work at varying engine loads and lean operating conditions were not provided. Furthermore, Liu et. al. [25] showed that the standard single Wiebe function was unable to predict the mass-burn fraction in a single-cylinder diesel engine converted to a natural gas SI engine. However, a modified double Wiebe function for the slower burning process inside the squish region performed better. They also concluded that such a condition-dependent double Wiebe model is limited to the operating conditions used for determining the model parameters.

Most of the studies employing Wiebe modelling for gaseous fuel combustion are focussed on automotive or small scale engines [26–28]. In NG engines, the stability of the combustion process affects the operating window between knock and misfire limits as shown in the previous chapter. Furthermore, the operating window of marine NG engines reduces as the brake mean effective pressure (BMEP) scales upwards [29]. Marine engines also operate at lower engine speeds, thus, increasing the combustion process time. Additionally, marine engines have less heat loss due to the larger combustion chamber volume to surface area ratio compared to automotive engines. The lower heat loss in marine engines has a direct impact on the combustion heat, work in-cylinder pressures and temperatures. Therefore, the performance and combustion within a marine SI NG engine can vary from that of an automobile engine. However, it is unclear if the scaling effects in marine lean-burn SI engines for H₂-NG and CO₂-NG combustion are captured using Wiebe or the zero-dimensional modelling approach.

Other than Wiebe functions, another approach that could be adopted for 0-D combustion models is the Seiliger process modelling approach. Like Wiebe in 0-D combustion models, a Seiliger process model also does not provide any spatial or fluid dynamic related information. Seiliger cycle is a variation of the thermodynamic dual cycle used to define the in-cylinder processes [30, 31]. The Seiliger process uses finite, discretised stages to describe the in-cylinder process out of which three stages divided into isochoric, isobaric and isothermal processes are used to capture the combustion process [31]. Therefore, Seiliger is a first-principle, thermodynamic approach to capture the in-cylinder and combustion process compared to the semi-empirical Wiebe functions [22].

Additionally, the Wiebe modelling approach provides an estimation of the combustion and in-cylinder process per crank angle, while Seiliger discretises the same process into finite stages and estimates in-cylinder information at all the critical points using the Seiliger combustion parameters [31]. Therefore, Seiliger cannot provide informa-

tion pertaining to crank-angle events such as CA10, CA50, CA90 and maximum rate of pressure rise, unlike the Wiebe modelling approach. However, the Seiliger modelling approach provides sufficient details of the in-cylinder and combustion process that can be captured with low computational effort. This makes the Seiliger modelling approach in combination with mean value engine models (MVEMs) ideal for studying load variations, system integration, control strategies, voyage simulations and smart maintenance of ships. MVEMs capture the average engine performance over one operating cycle (or engine revolution) by dividing the engine process into various discretized processes such as inflow, combustion, blowdown, outflow, turbocharging, etc. [32]. For each of these processes, mean values of mass flow, temperature, composition, pressure and work are calculated in an MVEM to simulate the complete engine performance. Sui et.al. fitted the Seiliger cycle for diesel combustion in an MVEM [33, 34]. Similarly, Georgescu et. al. adopted the Seiliger cycle for a dual-fuel natural gas engine to study the dynamic behaviour based on MVEM simulations [35, 36]. Skogtjarn [37] used the Seiliger cycle for estimation of exhaust gas temperatures in diesel engines. Appendix C.2 lists all the parameters that can be estimated using the Wiebe and Seiliger modelling approach.

In comparison to H₂-NG combustion, studies on performance and combustion modelling of CO₂-NG fuel blends are limited in current literature. Slefarski studied the combustion of premixed methane flames with carbon dioxide dilution for pressurized combustion systems using experiments and model simulations [16]. The author performed calculations with a 1-D numerical code to estimate the harmful emissions of NO_x and CO for CO₂-methane blend ratios ranging from 0:100 to 30:70. The study found that the NO_x emissions reduced with CO₂ dilution while CO emissions increased as a result of thermal dissociation. Next to this, a CFD simulation study performed by Hadeef et al. also concluded that dilution with CO₂ leads to a reduction of radical species concentrations and reduction of maximum flame temperatures causing the NO emissions to decrease [11]. A numerical simulation study by Guo and Smallwood showed that the reduction of the radical H caused by CO₂ addition in ethylene/air flames led to suppression of soot formation [38].

Furthermore, Bagheri et al. used detailed kinetic mechanisms to analyse and discuss the experimental results for validation of CO₂ and H₂O dilution in a lean methane-hydrogen system [39]. The authors concluded that both H₂O and CO₂ reduced system reactivity and laminar flame speeds. The decrease in laminar flame speed due to CO₂ and H₂O dilution in oxy-fuel CH₄/O₂ flames was also found by Mazas et al. based on experiments and numerical simulations [40]. Other than these fundamental studies on flame properties and emissions in combustion systems with CO₂ dilution, a very few researches have investigated the performance of CO₂-NG fuel blends inside engines. Furthermore, some investigations have focussed on the modelling of the effect of EGR in gas and diesel engines [41, 42]. Swain and Shrestha performed a CFD simulation to analyse the performance of a SI engine fuelled by landfill gas with up to 60 % CO₂ addition [43]. The researchers found that the efficiency decreased by about 4.2 % with reduction in power output for a 50/50 fuel/diluent (CO₂) ratio, which was representative of typical landfill gas composition. Lastly, Carrera et al. conducted a numerical study on the combustion process of biogas in a SI engine with 40 percent carbon dioxide content [27].

To study the potential of SOFC-ICE integration, it is vital to capture the variations in

the in-cylinder and combustion process due to addition of anode-off gas constituents. 0-D combustion models can provide sufficient details of the in-cylinder and combustion process while providing the opportunity to combine them with open-cycle MVEMs to simulate the entire performance of the engine for SOFC-ICE integration. Therefore, in this research, a 0-D modelling approach is chosen to capture the combustion of blending anode-off gas constituents (H_2 and CO_2) in an SI lean-burn marine natural gas engine. However, in the current literature, Seiliger process modelling has been mainly limited to capturing diesel combustion as part of system-level investigations. There is a lack of comprehensive investigations on the capabilities of Seiliger process modelling in capturing combustion of gaseous fuels such as H_2 -NG and CO_2 -NG fuel blends. Furthermore, the above literature survey of Wiebe-based modelling highlights that the Wiebe function coefficients and their capabilities to capture combustion vary with operating conditions, combustion modes, type of fuel and fuel blends. It also indicates limited literature on a comprehensive analysis of the capabilities of a double Wiebe function in capturing lean-burn combustion of hydrogen-natural gas blends in a marine SI engine. Additionally, there is no literature that compares the capabilities of these two modelling approaches in capturing the lean-burn H_2 -NG combustion process. Furthermore, there is a knowledge gap in existing literature pertaining to modelling the impacts of CO_2 dilution on the combustion process in a marine engine. Therefore, there is a need for research on combustion characterization and 0-D modelling of CO_2 -NG fuel blends in a marine SI engine, which is also vital for SOFC-ICE integration.

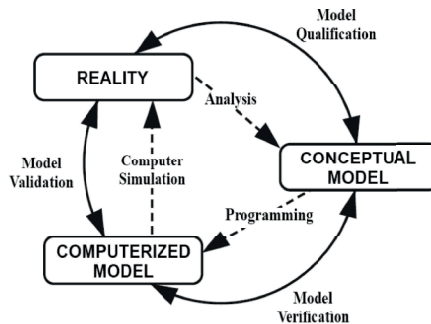


Figure 5.1: Development cycle of simulation model [44, 45]

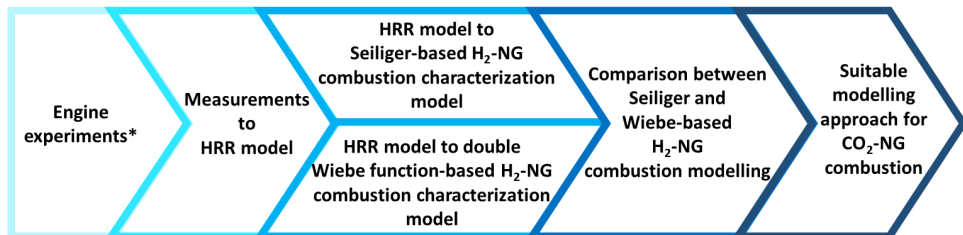
Based on the above limitations in existing literature, the capabilities of the first-principle Seiliger-based and semi-empirical double Wiebe function-based modelling approaches in capturing H_2 -NG combustion are first compared in this chapter. The model results are studied and compared for different H_2 -NG fuel blends, engine loads and engine leaning (lean-burn operation). The two modelling approaches are studied to capture H_2 -NG combustion in the lean-burn (air-excess ratio higher than 1.6) marine SI natural gas engine. Based on the enhanced capabilities of one modelling approach over another, a modelling approach is chosen to capture and study the variations in in-cylinder and combustion process for CO_2 -NG fuel blends. For this research, the simulation model development cycle depicted in Figure 5.1 is followed. The mathematical (conceptual) combustion models, programmed in Matlab/Simulink, are developed and calibrated by

analysis of engine measurements (reality) for the development of high-quality models.

5.2. MODELLING METHODOLOGY FOR H₂-NG AND CO₂-NG COMBUSTION CHARACTERIZATION

To simulate and study the in-cylinder and combustion process due to blending of anode-off gas constituents in a SI marine engine, a five-step modelling methodology is followed. Figure 5.2 shows the five-step combustion modelling methodology followed for this study. After completing the first step of H₂-NG and CO₂-NG engine performance experiments described in the previous chapter, the Heat Release Rate (HRR) model was derived. Since the heat release cannot be directly measured and is integral to the development of the Seiliger and Wiebe-based combustion models, the in-cylinder pressure and crank angle measurements were used as the inputs for the 0-D, single zone heat release rate model. This model was used to describe the detailed heat release process in the zero valve overlap lean-burn test engine for combustion of different H₂-NG and CO₂-NG fuel mixtures at varying engine loads and air-excess ratios (NO_x emissions).

In the third step, various outputs of the HRR model were used to develop two 0-D combustion characterization models capable of capturing the effects of hydrogen-natural gas and carbon dioxide-natural gas combustion. The first model employed the first-principle, thermodynamic 5-stage Seiliger process modelling to characterize the H₂-NG combustion process, while in the second model a double Wiebe function was used in a 0-D, single zone model to capture the combustion at every crank angle. In this step, various Seiliger and Wiebe combustion parameters were used to define and characterize the H₂-NG combustion process for different H₂-NG blends, loads and engine leaning.



*on a 500 kW turbocharged, 1500 rpm, 4-stroke natural gas engine

Figure 5.2: Combustion modelling methodology

Next, both the combustion characterization models were compared in their capabilities to capture the changes in the combustion process due to hydrogen addition, load variations and engine leaning (lean-burn operation). In this step, one approach is found more suitable over another to further study the combustion anode-off gas and natural gas fuel blends. In the last step, the suitable and chosen modelling approach is further adopted to characterize and study the combustion of CO₂-NG fuel blends. In the next chapter, the characterization will be followed by parametrization of H₂-NG and CO₂-NG combustion based on the chosen modelling approach to simulate different blends

of anode-off gas and natural gas fuel blends for SOFC-ICE integration. In this manner, 0-D combustion models were developed to study and capture the H₂-NG and CO₂-NG combustion process in a marine lean-burn SI engine based on engine measurements. In this research, all the simulation and modelling results are presented at spark-timing of 24°CA bTDC and 500 mgN m⁻³ of NO_x value (at 5 % reference oxygen), unless mentioned otherwise. During experiments, the measurements with different hydrogen and carbon dioxide percentages were restricted to the maximum load set-point of 75 % load.

5.3. MEASUREMENTS TO 0-D HRR MODEL

To study the heat release and combustion process of H₂-NG and CO₂-NG fuel blends, a single-zone, 0-D, thermodynamic heat release rate (HRR) model has been developed. The building blocks for this heat release rate model are in-cylinder pressure and crank angle measurements obtained from engine measurements described in the previous chapter. The heat release rate model is the first step towards the characterization of hydrogen-natural gas combustion using the Seiliger and double Wiebe function-based modelling approach based on engine measurements.

The experimental test engine has a zero valve overlap as shown in Table 4.1. The absence of valve overlap leads to large amounts of trapped residual gas, which has an impact on the trapped mass, in-cylinder temperature and even heat release. Therefore, it is important to calculate the trapped residual gas. This subsection discusses the heat release rate model while using the engine measurement to account for the amount of trapped residual gas and the impact on the in-cylinder combustion process. The developed HRR model has been adopted from the HRR model used for diesel combustion [46].

5.3.1. ENERGY BALANCE

The 0-D HRR model for H₂-NG and CO₂-NG fuel blends solves the mass, composition and energy balance at every crank angle starting with the trapped condition within the cylinder at the closing of the inlet valve. The first law of thermodynamics is used to compute the combustion reaction rate (CRR) provided in equation 5.1. The term $u_{\text{comb-fuel}}$ is the effective heat of combustion and depicts the fuel energy. It is dependent on temperature, composition of the gas fuel blend and also the properties of fuel, air and combustion gas [47]. For diesel combustion, the effective heat of combustion value would also include the heat loss due to fuel evaporation [46], however, this evaporation heat loss is disregarded in case of gaseous hydrogen-natural gas and carbon dioxide-natural gas combustion.

$$\text{CRR} = \frac{\dot{U} + \dot{W} + \dot{Q}_{\text{loss}}}{u_{\text{comb,fuel}}} = \frac{m \cdot c_v \cdot \frac{dT}{dt} + p \cdot \frac{dV}{dt} + \dot{Q}_{\text{loss}}}{u_{\text{comb,fuel}}} \quad (5.1)$$

where, ' \dot{U} ' is internal energy in kJ s⁻¹, ' \dot{W} ' is work in kJ s⁻¹, ' \dot{Q}_{loss} ' is the heat loss in kJ s⁻¹, ' $\frac{dV}{dt}$ ' is the rate of volume change, ' m ' is the in-cylinder mass in kg and ' c_v ' is the specific heat at constant volume in kJ kg⁻¹.

In equation 5.1, the pressure (p) is obtained from the in-cylinder pressure measurements, while the rate of volume change is calculated as a function of crank-angle [47].

The heat loss to the walls, piston crown and cylinder head is estimated by using the Woschni heat loss formulation for the heat transfer coefficient [46]. The trapped in-cylinder mixture is assumed to be an ideal gas with uniform temperature and pressure within the cylinder [24]. The HRR model uses the ideal gas law to compute the average in-cylinder mixture temperature (T) during the cycle from the in-cylinder pressure measurement, volume, in-cylinder mass (m) and the mixture gas constant. Since this average in-cylinder temperature is calculated based on measured variables in the HRR model, it is referred to as the measured in-cylinder temperature for all the subsequent sections in this chapter. For the temperature estimation, the in-cylinder mass is calculated from the mass balance, while the in-cylinder mixture gas constant (R_{mixture}) is computed from the composition balance of the air (x_{air}), combustion gas (x_{cg}) and fuel (x_{fuel}) along with their properties as given by equation 5.2.

$$R_{\text{mixture}} = x_{\text{air}} \cdot R_{\text{air}} + x_{\text{sg}} \cdot R_{\text{sg}} + x_{\text{fuel}} \cdot R_{\text{fuel}} \quad (5.2)$$

Similar to the gas constant, the specific heat at constant pressure of the mixture is a summation of the in-cylinder composition and the corresponding specific heats of each in-cylinder component (air, combustion gas and fuel). The gas constant is subtracted from the specific heat at constant pressure to obtain the specific heat at constant volume, which is required for internal energy.

5

5.3.2. MASS AND COMPOSITION BALANCE

In the test engine, the air and natural gas enter the cylinder as a premixed mixture and combine with the residual gas from the previous cycle. Therefore, the total mass of in-cylinder mixture (m) at any moment within the closed cylinder is a sum of the mass of air (m_{air}), mass of combustion gas (m_{cg}) and the mass of fuel (m_{f}). The mass of fuel burnt at every crank angle is given by the reaction co-ordinate (RCO), which is obtained by integrating the CRR as given by equation 5.3. Division of RCO by the initial or trapped fuel mass ($m_{\text{f,t}}$) gives the normalized reaction co-ordinate (RCO_{norm}), which is the fuel mass-burn fraction that monotonously increases from zero to 1. Using the RCO, trapped in-cylinder mass (m_{t}), trapped air fraction ($m_{\text{air,t}}$), trapped residual gas fraction ($m_{\text{rg,t}}$) and the stoichiometric air-to-fuel ratio (σ), the model solves the following mass balance at every crank angle to compute the mass of each in-cylinder component.

$$m_{\text{f}} = \text{RCO} = \int \text{CRR} \quad (5.3)$$

$$m_{\text{air}} = x_{\text{air}} \cdot m_{\text{t}} - m_{\text{f}} \cdot \sigma \quad (5.4)$$

$$m_{\text{cg}} = x_{\text{rg,t}} \cdot m_{\text{t}} - m_{\text{f}} \cdot (\sigma + 1) \quad (5.5)$$

$$m = m_{\text{air}} + m_{\text{cg}} + m_{\text{f}} \quad (5.6)$$

The computed mass of each component is used to calculate the corresponding mass fractions (x) and the in-cylinder composition. Equations 5.7 to 5.10 give the composition balance inside the cylinder.

$$x_{\text{air}} = \frac{m_{\text{air}}}{m} \quad (5.7)$$

$$x_{\text{cg}} = \frac{m_{\text{cg}}}{m} \quad (5.8)$$

$$x_{\text{f}} = \frac{m_{\text{f}}}{m} \quad (5.9)$$

$$x_{\text{air}} + x_{\text{cg}} + x_{\text{f}} = 1 \quad (5.10)$$

To solve the mass balance in equations 5.4 to 5.6, the model needs the trapped in-cylinder mass, trapped air fraction and the trapped residual gas fraction. Trapped mass is estimated by using the ideal gas law given in equation 6.11.

$$m_{\text{t}} = \frac{p_{\text{t}} \cdot V_{\text{t}}}{R_{\text{t}} \cdot T_{\text{t}}} \quad (5.11)$$

In equation 6.11, the trapped pressure (p_{t}) is obtained from engine measurements and trapped volume (V_{t}) is equal to the cylinder volume at inlet valve closing, which is calculated from the crank angle [47]. The remaining two variables, i.e., the trapped mixture gas constant (R_{t}) and trapped temperature (T_{t}) are derived as follows. To calculate the gas constant at trapped condition by using equation 5.2, mass fractions of each mixture component are computed. The trapped residual gas fraction is strongly dictated by the valve overlap. The current test engine has no valve overlap since the exhaust valve closes before the opening of the inlet valve as seen from Table 4.1. This zero valve overlap restricts methane slip and scavenging, thus, trapping a good amount of residual combustion gas from the previous cycle at the point of inlet valve closing [15]. The trapped residual gas plays a crucial role in the combustion process to control the in-cylinder temperatures and also the NOx emissions. The amount of trapped residual gas in a zero valve overlap gas engine needs to be taken into account as the mass fraction was found to be higher than 15%. Therefore, the trapped air mass fraction is calculated as a function of the residual gas mass fraction, air-excess ratio (λ) and the stoichiometric air-to-fuel ratio presented in equation 5.12 [48]. Derivation for equation 5.12 is provided in Appendix C.3. After calculating the trapped air fraction, the trapped fuel fraction is obtained from equation 5.10.

$$x_{\text{air,t}} = \frac{m_{\text{air,t}}}{m_{\text{t}}} = \frac{(1 - x_{\text{rg,t}}) \cdot \sigma \cdot \lambda}{\sigma \cdot \lambda + 1} \quad (5.12)$$

The high amount of trapped residual gas, which is left behind after the exhaust blow-down, increases the temperature of the trapped mixture [15]. During the induction stroke, the induction temperature (T_{ind}) of the entering air-fuel mixture will be higher than the measured manifold temperature due to a heat pick-up from the inlet duct walls. Therefore, the final trapped temperature is higher due to the combined effect of the increased induction temperature and mixing with the hot residual combustion gases trapped from the previous cycle. Equation 5.13 accounts for the combined effect on the

trapped temperature. A derivation of the trapped temperature formulation along with the derivation of variables T_{ind} , p_{bld} and T_{bld} is presented in Appendix C.4.

$$\frac{1}{T_t} = \frac{(V_{IC} - V_{IO})}{V_{IC} \cdot T_{ind}} + \frac{V_{EC} \cdot p_{bld}}{V_{IC} \cdot p_t \cdot T_{bld}} \quad (5.13)$$

where, ' V_{IC} ', ' V_{IO} ' and ' V_{EC} ' are cylinder volumes at inlet valve closing, inlet valve opening and exhaust valve closing, respectively. ' p_{bld} ' and ' T_{bld} ' are pressure and temperature after blowdown when the exhaust valve opens.

In this manner, the trapped mass can be calculated and a correct estimation of the trapped residual gas fraction leads to an accurate estimation of the trapped fuel mass, trapped air mass, mass balance and composition balance that matches with the engine measurements.

5.4. HRR MODEL TO COMBUSTION CHARACTERIZATION

Using the above-described HRR model, the heat release process is studied for varying percentages of hydrogen-natural gas and carbon dioxide-natural gas fuel mixtures and engine loads. For each hydrogen-natural gas blend and at each engine load, the HRR model also simulates the in-cylinder process for engine leaning between 500 mgNm^{-3} of NOx and misfire to study the engine performance during leaning. The model uses in-cylinder pressure and crank-angle measurements to compute the mass-burn fraction/normalized reaction co-ordinate, net combustion heat, work output and temperature inside the cylinder at every crank angle. Figure 5.3 shows the average in-cylinder temperature and the RCO_{norm} simulated by the HRR model for 10H_2 -NG fuel blend at 375 kWe and 500 mgNm^{-3} of NOx. As seen in the figure below, the average in-cylinder temperature rises with combustion and reaches its maximum value after TDC. The normalized RCO represents the mass-burn fraction of the H_2 -NG fuel as the fuel begins to combust just after the spark is provided at 24° CA bTDC . After approximately 80% of the mass-burn fraction, the combustion process slows down as the normalized RCO reaches a value of 1 indicating the end of combustion.

The expected trend of normalized RCO indicating the start of combustion just after spark-timing and increasing to 1 is affected by the TDC shift. As explained by Ding in [46], TDC shift affects the HRR calculation. Ding applied a constant TDC shift to determine the corrected RCO_{norm} for diesel combustion. Similarly, in this research, a constant TDC shift of -0.9°CA is applied to all measurements, which was crucial in obtaining the correct normalized reaction co-ordinate shown in Figure 5.3(b). A value of normalized RCO beyond unity would indicate combustion of higher amount fuel than the amount injected into the cylinder. Figure C.1 in Appendix C.1 shows the comparison between the RCO_{norm} for only natural gas performance at 75% loading and 24°CA bTDC spark-timing with no TDC shift and with -0.9°CA TDC shift. The RCO_{norm} for zero TDC shift leads to a very late start of combustion and values much higher than 1, thus, indicating a higher heat release than possible. Therefore, simulating the correct RCO_{norm} is critical in capturing the heat release process

Since the measured crank-angle curve with the TDC shift and measured in-cylinder pressure curve are used as the HRR model inputs for all the measurements, HRR model outputs of work, heat, reaction co-ordinate, pressures and temperatures are used as the

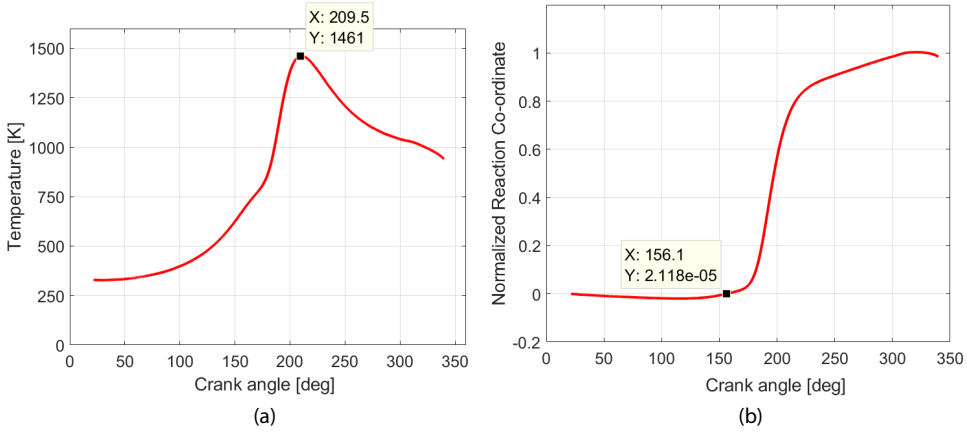


Figure 5.3: HRR model simulation of average in-cylinder temperature (a) and normalized reaction co-ordinate (b) for 10H₂-NG fuel blend at 375 kW load and 500 mgN m⁻³ NO_x

benchmark measured performance parameters for fitting and comparison in the combustion characterization process. This characterization of H₂-NG combustion using Seiliger and Wiebe modelling has been discussed in the next subsection.

5.4.1. HRR TO SEILIGER-BASED COMBUSTION CHARACTERIZATION MODEL

The Seiliger process uses five stages to thermodynamically describe the in-cylinder process out of which three stages describe the combustion process [31]. The three combustion stages are constant volume or isochoric combustion (2-3), constant pressure or isobaric combustion (3-4) and constant temperature or isothermal combustion (4-5) as shown in Figure 5.4(a). These three stages combined with the polytropic compression (1-2) and expansion (5-6) processes can be used to compute the temperature, pressure, net combustion heat and work during each stage within the in-cylinder process. Figure 5.4(a) shows the five stages of the Seiliger cycle represented in a pressure-volume diagram. In the Seiliger process, the thermodynamic relationships between each stage can be derived analytically to calculate the pressures (p), volumes (V) and temperatures (T) at the beginning and end of each stage. These analytical correlations are mainly based on three Seiliger combustion parameters, namely, Seiliger parameter 'a', Seiliger parameter 'b' and Seiliger parameter 'c'. The definitions of these Seiliger parameters have been presented in Figure 5.4(a), while the analytical thermodynamic correlations can be found in [31] by Stapersma.

To characterize the combustion process using the Seiliger cycle, the Seiliger parameters need to be determined. In this study, the Seiliger parameters are determined from the HRR model. Figure 5.4(b) shows the outline of the combustion characterization procedure using the Seiliger cycle. At first, the HRR model is used to capture the heat release process from the in-cylinder pressure measurements for a fixed operating point of load, hydrogen or carbon dioxide percentage and NO_x emission as explained in subsection 5.3. Next, the measured maximum pressure (p_{\max}) along with the HRR model outputs of maximum temperature (T_{\max}) and the net combustion heat (Q_{net}) are used

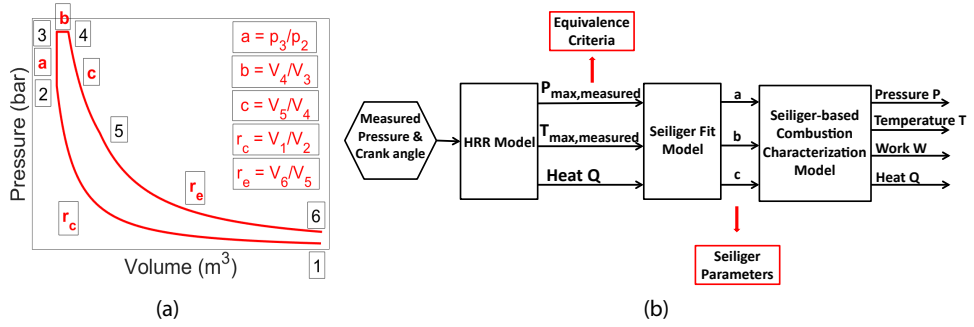


Figure 5.4: Definition of five-stage Seiliger process with in-cylinder pressure-volume diagram (a) and outline of combustion characterization procedure using the Seiliger process (b)

5

as equivalence criteria to numerically determine the Seiliger parameters ‘a’, ‘b’ and ‘c’ that fit the in-cylinder process in a Seiliger cycle. Then, these derived Seiliger parameters are used to compute the temperatures, pressures, work and heat quantities during each stage in the 0-D Seiliger-based characterization model by using the equations given in Table3-a and Table3-b of [31]. In Seiliger modelling, the work and heat quantities are made specific by dividing by trapped mass. The summation of work quantities during each stage gives the closed-cycle work produced by the engine per cylinder. The closed-cycle work, as the name suggests, corresponds to the work during the closed-cycle or power loop and does not include the gas-exchange work during the open-cycle. Similar to closed-cycle work, the summation of heat during the three stages of combustion provides the net combustion heat per cylinder, and the negative heat during the compression and expansion stage indicates the heat loss. The subsequent paragraph explains the Seiliger cycle fitting procedure in more detail.

In order to accurately fit the Seiliger cycle to the real H₂-NG or CO₂-NG in-cylinder and combustion process, a set of three equations is solved numerically to determine the ‘a’, ‘b’ and ‘c’ Seiliger parameters. Equations 5.14 to 5.16 depict this set of three equations for maximum pressure ($p_{\max, \text{Seiliger}}$), maximum temperature ($T_{\max, \text{Seiliger}}$) and net combustion heat ($q_{\text{net, Seiliger}}$) as a function of the Seiliger parameters [31].

$$p_{\max} = p_1 \cdot r_c^{n_c} \cdot a \quad (5.14)$$

$$T_{\max} = T_1 \cdot r_c^{n_c - 1} \cdot a \cdot b \quad (5.15)$$

$$q_{\text{net, Seiliger}} = q_{23} + q_{34} + q_{45} = c_v \cdot T_1 \cdot r_c^{n_c - 1} \cdot (a - 1) + c_v \cdot T_1 \cdot \gamma \cdot r_c^{n_c - 1} \cdot a \cdot (b - 1) + c_v \cdot T_1 \cdot (\gamma - 1) \cdot r_c^{n_c - 1} \cdot a \cdot b \cdot \log c \quad (5.16)$$

A Newton-Raphson multi-variable root finding method is applied to determine the three Seiliger parameters [33]. This iterative numerical method finds the Seiliger parameters once the following conditions are met.

$$P_{\max, \text{measured}} - P_{\max, \text{Seiliger}} < 1 \quad (5.17)$$

$$T_{\text{net, measured}} - T_{\max, \text{Seiliger}} < 1 \quad (5.18)$$

$$Q_{\text{net, measured}} - Q_{\text{net, Seiliger}} < 10 \quad (5.19)$$

where, ' $P_{\max, \text{measured}}$ ' is the maximum pressure in bar from the HRR model, ' $T_{\max, \text{measured}}$ ' is the maximum temperature in K from the HRR model and ' $Q_{\text{net, measured}}$ ' is the net combustion heat in kJ from the HRR model.

The Seiliger-based characterization model also requires the polytropic exponents for compression and expansion. The value of polytropic exponent for compression (n_c) is determined from the definition of the polytropic process given by equation 5.20. This value of n_c represents heat loss during the compression process when the polytropic factor for compression ($\eta_{\text{poly},c}$) in equation 5.21 is greater than one as derived in [31]. Similarly, the value of polytropic exponent for expansion (n_e) is set such that the polytropic factor for expansion ($\eta_{\text{poly},e}$) in equation 5.22 is less than one and thus, represents heat loss during the expansion process [31].

$$n_c = \log \frac{p_1/p_2}{V_2/V_1} \quad (5.20)$$

$$\eta_{\text{poly},c} = \frac{\gamma - 1}{n_c - 1} \quad (5.21)$$

$$\eta_{\text{poly},e} = \frac{n_e - 1}{\gamma - 1} \quad (5.22)$$

Following the above-described procedure, a 0-D Seiliger-based combustion characterization model is developed from engine measurements to capture the in-cylinder and combustion process for load, blend percentage and NOx emission variations.

5.4.2. HRR TO WIEBE-BASED COMBUSTION CHARACTERIZATION MODEL

Wiebe modelling uses semi-empirical functions to estimate the combustion process at every crank-angle, while Seiliger modelling is a first-principle, thermodynamic approach for a discretized three-stage representation of the combustion process. Wiebe functions have been used for alternative fuels, advanced combustion and system integration studies of sequential turbocharging and variable geometry turbines with engines [49–52]. A single Wiebe function is mathematically defined by three Wiebe coefficients, i.e., a combustion efficiency factor, a shape factor and the combustion duration [22, 23]. The shape factor dictates the shape of combustion or mass-burn fraction. A typical value of the combustion efficiency factor and the shape factor for SI gasoline engines is 5 and 2, respectively [53]. Diaz et. al. [26] used values of 2.8 and 2.4 for the combustion efficiency and shape factor in a single Wiebe function to study the influence of hydrogen-methane blends on the knock occurrence crank angle (KOCA) in a 2kW Cooperative Fuel Research (CRF) Engine. Shivapuji and Dasappa [54] used a single Wiebe function to model the

combustion of producer gas containing 18 % H₂ and 12 % CO₂ by volume in a 28 kW SI engine and showed that the Wiebe coefficients need to be adapted to capture the in-cylinder pressure variations.

Carrera et. al. performed CFD calculations to determine single Wiebe function coefficients as a function of compression ratio, engine speed, air-excess, spark-timing and carbon dioxide content (40 % by volume) to study biogas combustion [27]. Similarly, Rousseau et.al. used air-excess ratio, spark-timing and engine load to compute the single Wiebe function coefficients for combustion characterization of natural gas in a lean-burn SI engine [28]. However, they concluded that the single Wiebe approach failed in accurately reproducing the experimental mass-burn fraction and recommended further studies to test mathematical functions besides Wiebe. In Wiebe-based combustion modelling, the different combustion rates present during different combustion stages are difficult to capture with a single Wiebe function. Therefore, double Wiebe functions are preferred over single Wiebe functions to capture the premixed and the diffusion combustion stages of diesel. Similarly, the different combustion phases in a SI H₂-NG (or CO₂-NG) engine could be captured using a double-Wiebe function. Therefore, in this subsection, a double Wiebe function is employed in a zero-dimensional, single zone model to characterize the H₂-NG combustion process for different loads, hydrogen percentages and engine leaning.

The 0-D Wiebe-based combustion characterization model is an anti-causal model of the HRR model, which uses a double-Wiebe function to fit the normalized RCO obtained from the HRR model. The Wiebe-based characterization model solves the same mass, composition and energy balance as that presented in subsection 5.3 for the HRR model. The model computes the in-cylinder temperature by solving equation 5.1, in which the CRR is obtained by differentiating the Wiebe fitted RCO_{norm}. The in-cylinder pressure is estimated by using the ideal gas law. Similar to the HRR model, the heat loss is determined using the Woschni correlation [46], while all the mixture properties are calculated from compositions and temperatures. The outputs of the 0-D Wiebe-based combustion characterization model are work done and heat released along with average in-cylinder pressures and temperatures at every crank angle.

$$RCO_{norm} = b_1 \cdot (1 - \exp^{-a_1 \cdot \tau_1^{m_1+1}}) + b_2 \cdot (1 - \exp^{-a_2 \cdot \tau_2^{m_2+1}}) \quad (5.23)$$

where, $\tau_1 = \frac{\theta - SOC}{CD_1}$, $\tau_2 = \frac{\theta - SOC}{CD_2}$ and 'θ' is the Instantaneous crank-angle in degrees

$$a_1 = a_2 = \log(1 - \eta_{comb}) \quad (5.24)$$

For the Wiebe-based combustion characterization process, the normalized reaction co-ordinate (RCO_{norm}) or mass-burn rate obtained from HRR model is mathematically replicated using a double-Wiebe function. Figure 5.5 shows the outline of the combustion characterization procedure using Wiebe modelling. Equation 5.23 gives the double Wiebe function used to capture the H₂-NG combustion process. This double-Wiebe function in its generalized form uses eight parameters (a₁, a₂, b₁, b₂, m₁, m₂, CD₁ and CD₂) to characterize the combustion process. However, this function can be further simplified to reduce the number of independent parameters. In this double-Wiebe function, b₁ and b₂ are weighing factors defining the fraction of combustion process determined

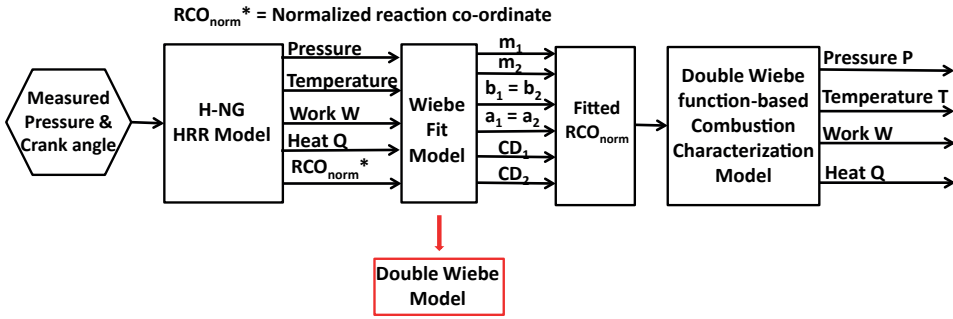


Figure 5.5: Outline of the combustion characterization procedure using Wiebe modelling

by each Wiebe function. These values are fixed at b_1 equal to 0.8 and b_2 equal to $1 - b_1$ or 0.2, as the first Wiebe function is able to capture the combustion process till about 80 % of mass-burn fraction, while the remaining 20 % is estimated by the second Wiebe function. The parameters a_1 and a_2 are equal and a function of combustion efficiency as given in equation 5.24. The combustion efficiency (η_{comb}) is determined by applying equation 4.2 from the previous chapter, which estimates the conversion rate of the carbon from the fuel to carbon dioxide. Thus, the combustion efficiency is estimated by dividing the carbon atoms in the exhaust carbon dioxide to the number of carbon atoms that are present in the incoming fuel. In this manner, four out of eight parameters in equation 5.23 are fixed and can be easily determined.

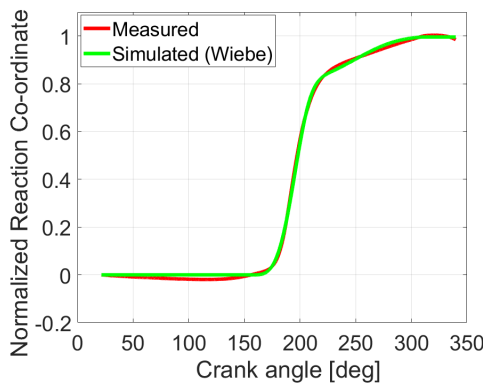


Figure 5.6: Comparison between measured and simulated (Wiebe) normalized reaction co-ordinate for 10H₂-NG fuel blend at 75 % engine load and 500 mgN m⁻³ of NOx

Out of the remaining four combustion parameters, CD_2 is the combustion duration from the start of combustion (SOC) to end of combustion (EOC), i.e., when the normalized RCO from the HRR model reaches unity. CD_1 is the combustion duration from the start of combustion to 80 % of mass-burn fraction while the parameters m_1 and m_2 are commonly referred to as the combustion shape or form factor [22, 55]. The second Wiebe function in equation 5.23 is used to capture the late burn phenomenon observed

in the final stage of combustion as shown in Figure 5.3(b) and Figure 5.6. This phenomenon of late combustion was also reported by Rousseau et al. [28], and confirmed by Ishii et al. [56] as they continuously detected light emissions by a sensor located in the cylinder head. A least-square fit method is used for the determination of the Wiebe combustion parameters m_1 , m_2 and CD_1 to fit the double-Wiebe function to the measured normalized RCO from the HRR model. In this study, the primary combustion phase is a combination of the flame-development phase (spark-discharge to 10 % mass-burn fraction) and the flame-propagation phase (rapid-burning phase) found in SI engines [24]. The flame-termination or the after-burning phase is analogous to the late combustion discussed in this research.

Figure 5.6 shows the comparison between the measured normalized RCO from the HRR model and the mass-burn fraction estimated by the double-Wiebe function at 75 % load for 10H₂-NG fuel blend at 500 mgN m⁻³ of NO_x (at 5 % reference oxygen). As shown in Figure 5.6, the simulated RCO by the double-Wiebe function satisfactorily captures the fuel combustion rate inside the cylinder from SOC to 80 % mass-burn fraction and then from 80 % mass-burn fraction to EOC as the combustion process slows down.

Both the double Wiebe function and Seiliger-based combustion characterization models are based on the HRR model, which uses the in-cylinder pressure measurements as a starting point to model the heat release process for varying hydrogen-natural gas blends, carbon dioxide-natural gas blends, loads and engine leaning. Therefore, the accuracy of the recorded pressure dictates the accuracy of the combustion process simulated by the models. For this purpose, Appendix B.2 discusses the impact of maximum deviation in pressure measurement on the accuracy of the combustion characterization models for 10H₂-NG fuel blend and 500 mgN m⁻³ of NO_x at 75 % load.

Following the above-described procedure, a 0-D Wiebe-based H₂-NG combustion characterization model is developed from engine measurements to capture the H₂-NG in-cylinder and combustion process for all load, hydrogen percentage and engine leaning (air-excess ratio/NO_x emission) variations. The double Wiebe function-based modelling approach could be also applied for CO₂-NG combustion characterization.

5.5. H₂-NG COMBUSTION CHARACTERIZATION MODELLING RESULTS

In this section, simulation results from the 0-D Seiliger and double Wiebe function-based combustion characterization models are compared against engine measurements for a single test condition. Additionally, values of Seiliger and Wiebe combustion parameters derived from the characterization process for different H₂-NG fuel blends and engine leaning or lean-burn combustion have been presented. A detailed discussion on the capabilities of both the models to capture the H₂-NG combustion process using these combustion parameters has been provided in section 5.6.

5.5.1. CHARACTERIZATION OF H₂-NG COMBUSTION USING SEILIGER MODELLING

After determining the Seiliger parameters and polytropic exponents, the Seiliger cycle can be used to capture the H₂-NG in-cylinder process using the equations in Table3-a

and Table 3-b of [31]. These equations combined form the Seiliger-based combustion characterization model present in Figure 5.4(b). Table 5.1 provides derived values of the Seiliger parameters and polytropic exponents for 10H₂-NG fuel blend at 75 % engine load and 500 mgN m⁻³ of NO_x. Figure 5.7 shows the comparison between the measured and simulated in-cylinder pressures and temperatures using the Seiliger-based combustion characterization model for the tested condition. Furthermore, the error percentages between the Seiliger model simulation values and the measured values for these performance parameters are very small as shown in Table 5.2. As seen in Figure 5.7 and Table 5.2, the Seiliger process is able to perfectly capture the H₂-NG in-cylinder process with an accurate estimation of pressures, temperatures, net combustion heat and effective work output.

Table 5.1: Seiliger parameters and polytropic exponents for 10H₂-NG fuel blend at 75 % engine load and 500 mgN m⁻³ NO_x

a	b	c	n _c	n _e
1.416	1.387	1.765	1.332	1.297

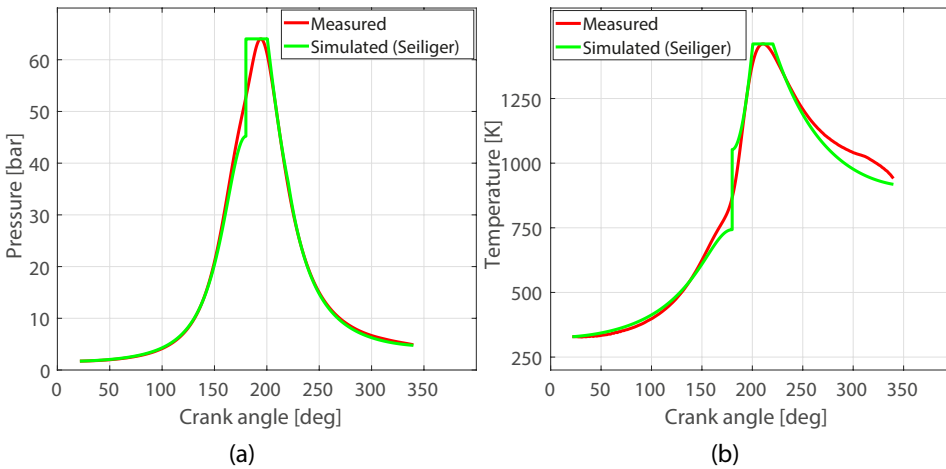


Figure 5.7: Comparison between measured and simulated (Seiliger) in-cylinder pressure (a) and in-cylinder temperature (b) for 10H₂-NG fuel blend at 75 % engine load and 500 mgN m⁻³ of NO_x

The above-demonstrated capability of the Seiliger-based modelling to accurately estimate the performance parameters is crucial in order to capture the effects of H₂-NG combustion since hydrogen addition and engine leaning have a direct effect on the peak pressures and temperatures. It is also important to accurately compute the work done and net combustion heat as these parameters are direct indicators of engine performance.

To study and capture the variations in H₂-NG combustion and in-cylinder process, the Seiliger-based characterization process is used to simulate the combustion process for 0H₂-NG (ONG) and 10H₂-NG fuel blends corresponding to 500 mgN m⁻³ and 250 mgN m⁻³

Table 5.2: Error between the Seiliger combustion characterization simulation and measured values of performance parameters for 10H₂-NG fuel blend at 75 % engine load and 500 mgN m⁻³ NOx

Parameters	p _{max}	T _{max}	Work	Q _{net}	p ₆	T ₆
Error [%]	0	2.8e-05	0.525	1.59e-04	-2.46	-2.436

Table 5.3: Combustion heat ratios for different H-NG fuel blends (0H₂-NG, 10H₂-NG) and NOx values (500 mgN m⁻³, 250 mgN m⁻³ of NOx) at 75 % engine load

	Q _{23,ratio}	Q _{34,ratio}	Q _{45,ratio}
ONG _{500NOx}	0.2279	0.5427	0.2294
10H ₂ – NG _{500NOx}	0.2703	0.5008	0.2289
ONG _{250NOx}	0.1298	0.5768	0.2934
10H ₂ – NG _{250NOx}	0.1447	0.5717	0.2836

Table 5.4: Seiliger parameters for different H₂-NG fuel blends (0H₂-NG, 10H₂-NG) and NOx values (500 mgN m⁻³, 250 mgN m⁻³ of NOx) at 75 % engine load

	a	b	c
NG _{500NOx}	1.3639	1.4522	1.7917
10H ₂ – NG _{500NOx}	1.4162	1.3870	1.7651
ONG _{250NOx}	1.2045	1.5374	2.1647
10H ₂ – NG _{250NOx}	1.2195	1.5057	2.0655

of NOx at 75 % load. The effects of hydrogen addition and engine leaning on the combustion process are understood by analysing the corresponding heat ratios and the ‘a’, ‘b’ and ‘c’ Seiliger parameters provided in Table 5.3 and Table 5.4 respectively. These simulated heat ratios are an indicator of the amount of heat released during each Seiliger combustion stage and are computed by dividing the combustion heat during a stage by the net combustion heat. The capability of Seiliger-based modelling to capture the shape and stability of the combustion process due to hydrogen addition and engine leaning has been discussed in section 5.6 by studying the variations in the combustion parameters and heat ratios listed in Table 5.3.

5.5.2. CHARACTERIZATION OF H₂-NG COMBUSTION USING WIEBE MODELLING

The ability of the 0-D Wiebe-based combustion characterization model to simulate the in-cylinder pressures and temperatures is demonstrated in Figure 5.8. It compares the measured in-cylinder pressures and temperatures from the H₂-NG HRR model to the ones computed by the Wiebe-based combustion characterization model for 10H₂-NG blend at 75 % engine load. Furthermore, Table 5.5 provides the derived values of the Wiebe parameters for the same operating conditions, while Table 5.6 shows the error percentages between the measured and the simulated values for various performance parameters using the Wiebe-based H₂-NG combustion characterization model.

As seen in Table 5.6, the errors between measured and simulated H₂-NG in-cylinder

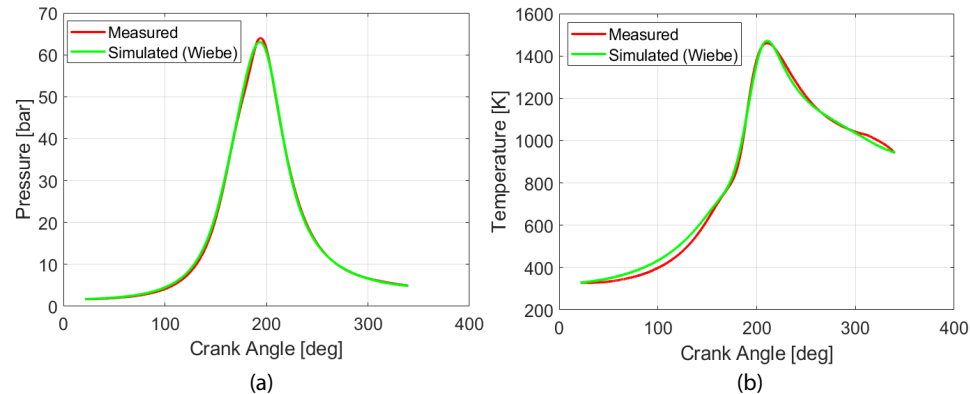
Table 5.5: Derived Wiebe parameters for 10H₂-NG fuel blend at 75 % engine load and 500 mgNm⁻³ NOx

m_1	m_2	CD_1	CD_2	η_{comb}
2.78	2.41	60.68	153	0.9777

Table 5.6: Error between the simulated (Wiebe) and measured values of performance parameters for 10H₂-NG fuel blend at 75 % engine load and 500 mgNm⁻³ NOx

Parameters	p_{max}	T_{max}	Work	Q_{net}	p_6	T_6
Error [%]	-1.5	0.68	-5.08	-2.4	-1.84	0.26

pressures and temperatures using the double Wiebe function are small and similar to those obtained from the Seiliger characterization process. However, unlike Seiliger, the error between simulated and measured work output is high. This is because work is calculated from the simulated in-cylinder pressure shown in Figure 5.8(a), which is dependent on the accuracy of determining the normalized RCO using the double Wiebe function. A small deviation between the measured RCO_{noem} from the H₂-NG HRR model and the fitted RCO_{norm} can produce errors in simulated work and heat. The accuracy of fitted RCO_{norm} depends on the estimation of Wiebe combustion parameters. Section 5.6 discusses the deviations and challenges in the estimation of Wiebe combustion parameters for different H₂-NG fuel blends, engine leaning and loads. Besides Wiebe combustion parameters, deviations in heat loss estimation also contribute to the error in the prediction of work output and also combustion heat. Although the error in prediction of net combustion heat using the Wiebe modelling approach is higher compared to the Seiliger process approach, it is a small deviation. Accurate estimation of work and combustion heat is of high significance since work and heat are main indicators of engine performance and hence, the engine efficiency [46].

Figure 5.8: Comparison between measured and simulated (Wiebe) in-cylinder pressure (a) and in-cylinder temperature (b) for 10H₂-NG fuel blend at 75 % engine load and 500 mgN m⁻³ of NOx

Similar to the Seiliger-based modelling, the Wiebe-based combustion characterization process is used to study the variations in the H₂-NG in-cylinder combustion pro-

Table 5.7: Wiebe parameters for different H₂-NG fuel blends (0H₂-NG, 10H₂-NG) and NO_x values (500 mgN m⁻³, 250 mgN m⁻³ of NO_x) at 75 % engine load

	m ₁	m ₂	CD ₁	CD ₂
NG _{500mgNm⁻³NO_x}	2.91	2.68	62.27	149.8
10H ₂ – NG _{500mgNm⁻³NO_x}	2.78	2.41	60.68	153
NG _{250mgNm⁻³NO_x}	2.71	4.4	69.4	139
10H ₂ – NG _{250mgNm⁻³NO_x}	2.75	2.86	67.17	150

cess. Simulations are performed for the same 0H₂-NG and 10H₂-NG fuel blends with engine leaning as described in subsection 5.5.1. Table 5.7 presents the values of Wiebe combustion parameters for each test case. The effects of hydrogen addition and engine leaning are understood by studying the variations in combustion duration and shape parameters, which have been discussed in section 5.6.

5

5.6. COMPARISON OF SEILIGER AND DOUBLE WIEBE FUNCTION-BASED MODELLING FOR H₂-NG COMBUSTION CHARACTERIZATION

The previous section compared the simulation results of Seiliger and Wiebe modelling approaches against engine measurements for 10H₂-NG fuel blend at 75 % engine load and 500 mgN m⁻³ of NO_x. In this section, the Seiliger and double Wiebe function-based combustion characterisation models are first compared and studied in terms of their ability to capture the variations in H₂-NG combustion process for different H₂-NG fuel blends and engine leaning or lean-burn operation. Then, the models are compared to capture the effects of H₂-NG combustion at different loads. Based on the comparison a suitable modelling approach will be selected and further adopted to capture CO₂-NG combustion.

5.6.1. EFFECTS OF DIFFERENT H₂-NG FUEL BLENDS AND LEAN-BURN OPERATION

In section 5.5, values of Seiliger and Wiebe combustion parameters derived for different H₂-NG fuel blends (0H₂-NG, 10H₂-NG) and engine leaning (500 mgN m⁻³, 250 mgN m⁻³ of NO_x) at 75 % engine load were presented. In this subsection, the derived combustion parameters are used in the combustion characterization models to simulate the H₂-NG combustion and in-cylinder process. The simulation results from the two modelling approaches are compared against measurements. Moreover, the capabilities of these to modelling approaches to capture the effects of different hydrogen blend percentages and engine leaning are also compared.

SEILIGER-BASED H₂-NG COMBUSTION MODELLING APPROACH

Figure 5.9(a) shows the in-cylinder pressure variations captured by Seiliger process due to increasing hydrogen percentage and decreasing NO_x emissions indicating engine leaning. By zooming around the maximum pressure values, the ability of the Seiliger process

to capture the minor but important in-cylinder pressure variations relative to the crank angle can be seen in Figure 5.9(b). Similarly, Figure 5.10(a) depicts the in-cylinder temperature variations at 75 % load for 0H₂-NG and 10H₂-NG fuel blends at 500 mgNm⁻³ and 250 mgNm⁻³ of NOx while Figure 5.10(b) zooms into the in-cylinder variations around the maximum temperatures. The variations in the H₂-NG combustion process are studied by analysing the Seiliger heat ratios and Seiliger combustion parameters provided in Table 5.3 and Table 5.4 respectively. Division of net combustion heat in three Seiliger stages can help capture the shape and stability of the combustion process due to hydrogen addition and engine leaning.

The eight times higher flame speed of hydrogen compared to natural gas, increases the combustion rate and decreases combustion duration [57, 58]. This increase in combustion rate is captured by the increase in Seiliger heat ratio at constant volume ($Q_{23,ratio}$). It increases with an increase in hydrogen percentage as shown in Table 5.3 and signifies faster combustion at constant volume for H₂-NG combustion. Increment in $Q_{23,ratio}$ leads to a higher value of Seiliger parameter ‘a’ and also maximum pressure as depicted in Table 5.4 and Figure 5.9. This increase in combustion heat at constant volume due to hydrogen addition is analogous to the combustion of gasoline that burns instantaneously to release heat at constant volume and is commonly referred to as the Otto-cycle [59]. On the other hand, the $Q_{23,ratio}$ drops along with the Seiliger parameter ‘a’ as the engine is leaned out to a lower NOx value of 250 mgNm⁻³. The resulting decrease in the maximum pressure and temperature values is evident from Table 5.3, Table 5.4 Figure 5.9 and Figure 5.10. The depreciation in the value of $Q_{23,ratio}$ due to engine leaning corresponds to the depreciation in combustion rate due to the dilution of incoming charge at higher air-excess ratios. This dilution of fuel charge indicates an increase in combustion instability and cycle-to-cycle variations as explained in [60, 61]. The combustion instability due to engine leaning is manifested in the Seiliger process by a higher value of Seiliger parameter ‘b’ and a higher combustion heat release at constant pressure ($Q_{34,ratio}$). Table 5.4 and Figure 5.9(b) clearly show that the value of ‘b’ and $Q_{34,ratio}$ increase as the engine is leaned to decrease the NOx values.

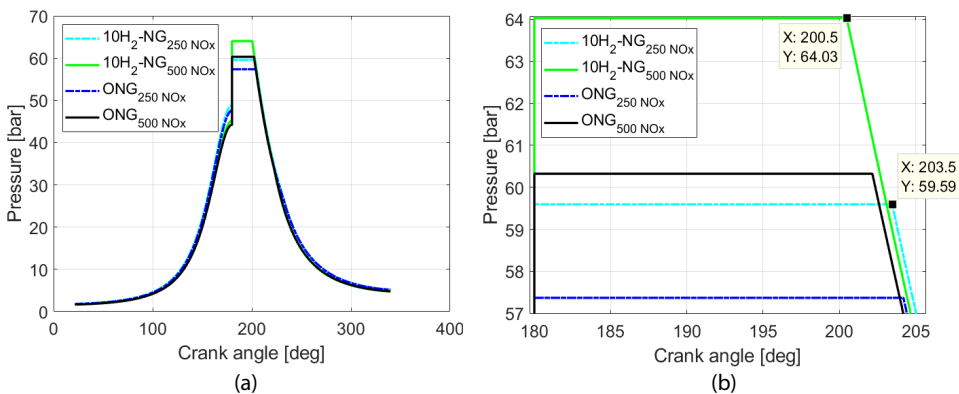


Figure 5.9: Normal (a) and zoomed-in (b) in-cylinder pressure variations using the Seiliger-based characterization for different H-NG fuel blends (0H₂-NG, 10H₂-NG) and NOx values (500 mgNm⁻³, 250 mgNm⁻³ of NOx) at 75 %

Contrary to engine leaning, hydrogen addition decreases the Seiliger parameter 'b' and also the $Q_{34, \text{ratio}}$, thus, representing the increase in combustion stability due to improved combustion rate. Besides 'b', Seiliger parameter 'c' can also help understand combustion stability. An increased value of 'c' in H_2 -NG combustion symbolises reduction in combustion rate and increased late combustion due to engine leaning (lean-burn operation) as more combustion heat is released into the expansion stroke at a constant temperature (higher $Q_{45, \text{ratio}}$). The decrease in combustion rate causes the combustion duration to increase, which pushes the point of peak temperature further into the expansion stroke. Thus, engine leaning to 250 mgN m^{-3} of NO_x not only decreases the peak temperature but also shifts it by about 10 CA degrees into the expansion stroke as seen in Figure 5.10(b). An even lower value of 'a' along with higher values of 'b' and 'c' would be indicative of engine misfire during steady-state operation, which causes the cyclic variations to increase drastically as explained in [62, 63]. Thus, Seiliger parameters 'a', 'b' and 'c' represent different physical phenomenon in the H_2 -NG combustion process.

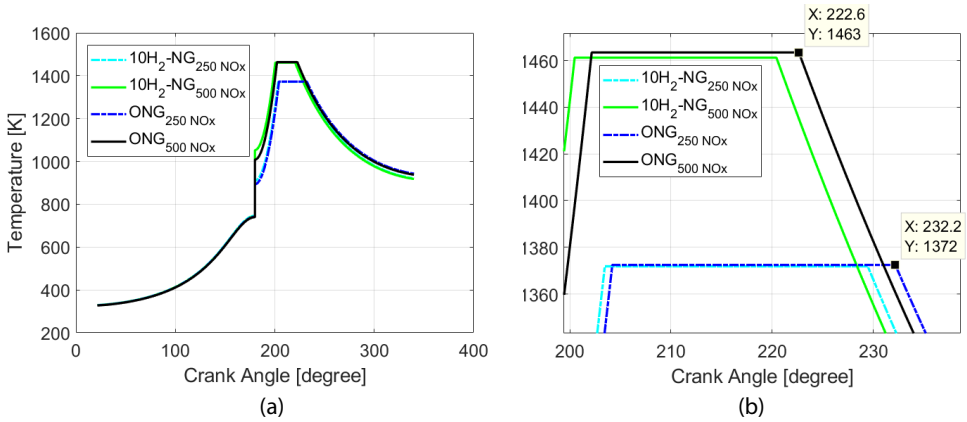


Figure 5.10: Normal (a) and zoomed-in (b) in-cylinder temperature variations using the Seiliger process characterization for different H_2 -NG fuel blends ($0H_2$ -NG, $10H_2$ -NG) and NO_x values (500 mgN m^{-3} , 250 mgN m^{-3} of NO_x) at 75 %

Table 5.8: Error percentages between the Seiliger combustion simulation and measured values of performance parameters for different H_2 -NG fuel blends ($0H_2$ -NG, $10H_2$ -NG) and NO_x values (500 mgN m^{-3} , 250 mgN m^{-3} of NO_x) at 75 % engine load

	p_{max} [%]	T_{max} [%]	Work [%]	Q_{net} [%]	p_6	T_6 [%]
ONG_{500NOx}	0	$2.2e-05$	-0.584	$2.38e-04$	-2.28	-2.27
$10H_2 - NG_{500NOx}$	0	$-2.8e-05$	-0.525	$1.59e-04$	-2.45	-2.44
ONG_{250NOx}	0	$1.92e-06$	0.139	$3.27e-05$	-2.55	-2.54
$10H_2 - NG_{250NOx}$	0	$-7.6e-05$	-0.012	$5.06e-05$	-2.66	-2.64

During this study of H_2 -NG combustion process, it was also found that the maximum temperatures do not show an excessive increase with hydrogen addition as shown in Figure 5.10. This finding is contrary to the common understanding of hydrogen directly

increasing in-cylinder temperatures [64] and can be explained in the following manner. NO_x emissions depend on three factors, namely, engine speed (residence time), air intake and in-cylinder temperatures [65–67]. Since the engine speed is kept constant during these experiments, NO_x emissions at a load point are dependent on the air intake and in-cylinder temperatures. During experiments, the air-intake is continuously controlled to measure engine performance at the same NO_x for all H₂-NG fuel blends, thus, directly linking NO_x emission values to in-cylinder temperatures. Therefore, as the air-intake is controlled and increased with hydrogen addition, the engine produces almost similar values of maximum in-cylinder temperatures to produce the same amount of NO_x emissions. This is evident from Figure 5.10, which shows that even for a decreased NO_x value of 250 mgN m⁻³, the maximum in-cylinder temperatures decreased to similar values for 0H₂-NG and 10H₂-NG fuel blends. Therefore, the leaning of air-fuel mixture has a strong counter effect on the in-cylinder temperatures as the hydrogen percentage in the fuel blend increases. Due to the air-intake control, the maximum increase in the peak in-cylinder temperature due to hydrogen addition at 500 mgN m⁻³ of NO_x was less than 3 % of only natural gas performance (ONG) at all loads. Therefore, combustion due to hydrogen addition can be controlled by governing the air-intake to control the maximum in-cylinder temperatures for NO_x production below the IMO TIER-III NO_x emission limits.

Although the in-cylinder temperatures due to hydrogen addition and NO_x control are quite similar, hydrogen addition results in slightly lower temperatures at the point of exhaust valve opening. This trend of slightly lower temperatures with hydrogen addition during exhaust valve opening was found for all engine measurements. As seen in Figure 5.10(b) and Table 5.4, the Seiliger parameters ‘b’ and ‘c’ decrease with increasing hydrogen percentage. Thus, shifting the point of maximum temperature more towards TDC compared to ONG. As the temperatures recede after reaching the maximum temperature at an advanced point, they cool down to a lower temperature at the point of exhaust valve opening.

In this manner, the Seiliger parameters ‘a’, ‘b’ and ‘c’ can be used to accurately characterize the H₂-NG combustion process and capture the effects of hydrogen addition and engine leaning or lean-burn combustion. Table 5.8 shows the error percentages between the simulation values and the measured values for various performance parameters. As seen from Table 5.8, Seiliger-based approach simulates the combustion process with minor deviations from measured values.

DOUBLE WIEBE FUNCTION-BASED H₂-NG COMBUSTION MODELLING APPROACH

To understand the variations in the H₂-NG in-cylinder combustion process, simulation results from the Wiebe-based combustion characterization model have been presented for the same 0H₂-NG and 10H₂-NG fuel blends with engine leaning as described in subsection 5.6.1 for Seiliger-based characterization. The effects of hydrogen addition and engine leaning can be well understood by studying the variations in combustion duration and shape parameters provided in Table 5.7 for each test case, while the normalized RCOs are shown in Figure 5.11.

With an increasing percentage of hydrogen in fuel blend, the flame speed of air-fuel mixture increases. This increased flame speed increases the combustion rate. The

increase in combustion rate is evident from the increasing steepness of the RCO_{norm} for 10H₂-NG fuel blends compared to 0H₂-NG blends in Figure 5.11. This increase in RCO_{norm} with increasing hydrogen percentage is distinctly visible after zooming-in around 80 % RCO_{norm} as shown in Figure 5.11(b). Contrary to hydrogen addition, engine leaning decreased the slope of RCO_{norm} , thus, depicting the deceleration in combustion rate due to charge dilution. The effects of hydrogen addition are also clear from the decreasing value of CD_1 shown in Table 5.7 for increasing hydrogen percentage. As expected, CD_1 increases with decreasing NO_x depicting engine leaning.

However, CD_2 representing the end phase of the combustion process does not seem to follow the expected and same trend as CD_1 . This can be explained by the difficulty in accurately determining and understanding the shape of end of combustion and the exact end of combustion as discussed by Heywood [24]. This could be due to deviations in accurate measurements of in-cylinder pressure-time signals plus the difficulty in accurate estimation of the time-varying heat loss to the cylinder walls, cylinder head and piston crown [24, 28]. Therefore, although the double Wiebe function is able to capture the variations in pressures, temperatures and reaction co-ordinate during the H₂-NG combustion process, it reached its limitations in precisely defining the H₂-NG combustion process due to unexpected variations in the combustion duration of the second Wiebe function representing the late burn stage (CD_2). The unexpected variations of CD_2 are also found for other H₂-NG fuel blends and are further discussed in subsection 5.6.2. In addition to combustion duration, m_1 and m_2 are combustion shape parameters, which respectively define the primary combustion phase till 80 % mass-burn fraction and the late burn phase represented by the remaining 20 %. The primary and late burn stages of the combustion process can be seen for varying H₂-NG fuel blends and NO_x values in Figure 5.12, which depicts the variations in non-dimensional combustion rate or non-dimensional heat release rate.

Table 5.7 and Figure 5.12 show that although the variations in the primary combustion phase with hydrogen addition and engine leaning are small, m_2 clearly decreases with increasing hydrogen percentage and increases with engine leaning. An increasing value of m_2 with engine leaning or increased lean-burn combustion signifies a deterioration of the combustion process as an increasing amount of heat is released during late combustion. Thus, charge dilution is accompanied by a small increase in heat release late into the expansion stroke. This late burn phase present in lean-burn combustion increases with increasing engine leaning as seen in Figure 5.12(a). Additional discussion on m_2 representing an increase in heat release during the late burn combustion phase has been presented in Appendix C.5. Conversely, hydrogen decreases the late burn phenomenon with a decreasing m_2 .

A combination of these Wiebe shape parameters and combustion duration dictates the final variations in in-cylinder pressures and temperatures as shown in Figure 5.13(a) and Figure 5.13(b) respectively. The increase in maximum pressure due to hydrogen addition can be attributed mainly to the decrease in combustion duration for the primary combustion phase (CD_1) and the relatively faster heat release depicted in Figure 5.12(b). Even though the maximum values of the non-dimensional combustion rate or non-dimensional heat release rate shown in Figure 5.12 are approximately the same. Similarly, the maximum pressure decreases with engine leaning as CD_1 increases and the

heat release slows down reaching a lower maximum value. This maximum value of heat release is further shifted into the expansion stroke as depicted in Figure 5.12(b).

Furthermore, as explained earlier in subsection 5.6.1, the maximum in-cylinder temperatures are controlled to produce the same NO_x value by controlling the air-intake with hydrogen addition. The temperatures distinctly decrease and retard into the expansion stroke with increased lean-burn operation. These effects on in-cylinder pressure and temperature variations match well to those found using the Seiliger process characterization. However, Wiebe-based characterization showed higher errors between the simulated and measured values of performance parameters as seen from Table 5.9. The maximum error was found to be around 5 % for computed work, while combustion heat deviated from measured value by 2.4 % at maximum. These higher errors found for Wiebe-based characterization are further discussed in subsection 5.6.2. In this manner, the Wiebe modelling approach is used to characterize the H₂-NG combustion process by using two combustion shape parameters and combustion durations of a double Wiebe function to define the primary combustion and the late burn combustion stage. The double Wiebe function is also able to capture the changes in late burn phase found in lean-burn NG and H₂-NG combustion.

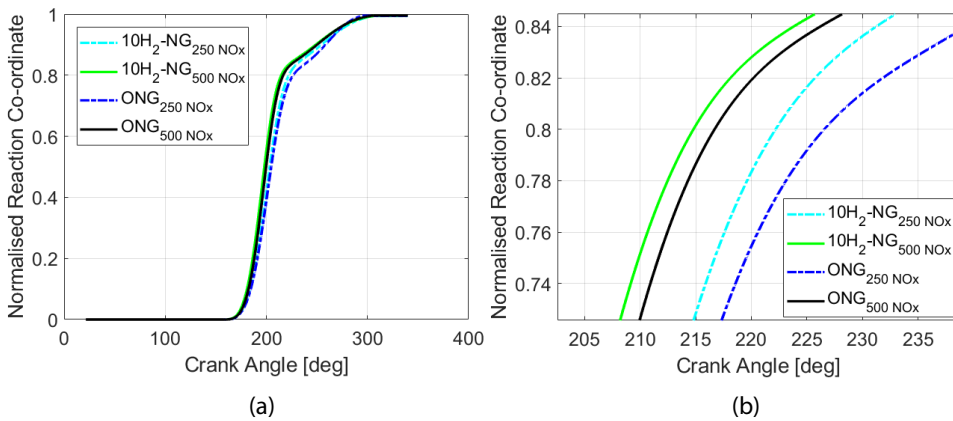


Figure 5.11: Normal (a) and zoomed-in (b) normalized reaction co-ordinate variations using the Wiebe modelling characterization for different H₂-NG fuel blends (0H₂-NG, 10H₂-NG) and NO_x values (500 mgN m⁻³, 250 mgN m⁻³ of NO_x) at 75 %

Table 5.9: Error percentages between the Wiebe-based combustion characterization simulation and measured values of performance parameters for different H₂-NG fuel blends (0H₂-NG, 10H₂-NG) and NO_x values (500 mgN m⁻³, 250 mgN m⁻³ of NO_x) at 75 % engine load

	p _{max} [%]	T _{max} [%]	Work [%]	Q _{net} [%]	p ₆ [%]	T ₆ [%]
ONG _{500NOx}	-1.17	0.67	-4.72	-1.98	0.5	0.5
10H ₂ - NG _{500NOx}	-1.5	0.68	-5.08	-2.4	0.24	0.25
ONG _{250NOx}	0.85	0.69	-4.16	-0.85	1.34	1.35
10H ₂ - NG _{250NOx}	0.54	0.81	-4.72	-1.89	0.51	0.52

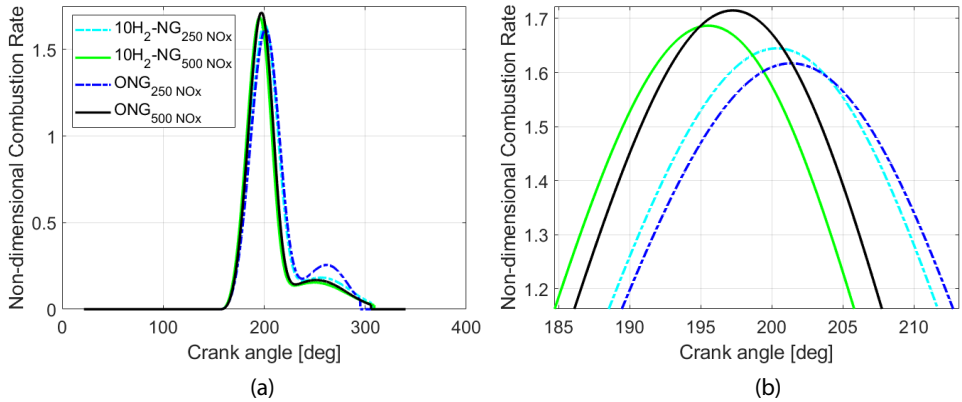


Figure 5.12: Normal (a) and zoomed-in (b) non-dimensional combustion rate variations using the Wiebe modelling characterization for different H₂-NG fuel blends (0H₂-NG, 10H₂-NG) and NO_x values (500 mgNm⁻³, 250 mgNm⁻³ of NO_x) at 75 %

5

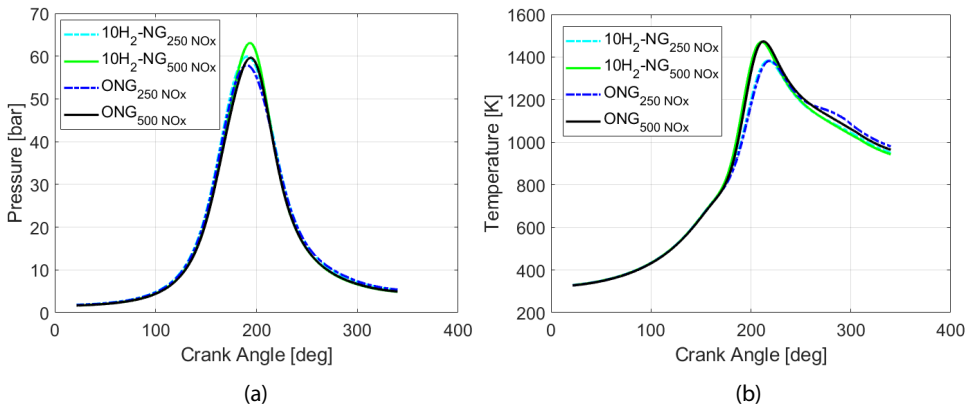


Figure 5.13: In-cylinder pressure (a) and temperature (b) variations using Wiebe characterization process for different H₂-NG fuel blends (0H₂-NG, 10H₂-NG) and NO_x values (500 mgN m⁻³, 250 mgN m⁻³ of NO_x) at 75 %

In this subsection, Seiliger and Wiebe modelling approaches were compared in terms of their ability to characterize and capture the H₂-NG combustion process for different hydrogen percentages and engine leaning. The Seiliger characterization process was able to accurately capture the variations in H₂-NG in-cylinder process over five discretized stages. Similarly, the Wiebe-based characterization was also able to effectively capture the variations in in-cylinder pressures and temperatures at every crank angle. However, it reached its limitations in precisely capturing the H₂-NG combustion process due to unexpected variations in the combustion duration of the second Wiebe function defining the late burn stage. Additionally, Wiebe-based characterization also produced larger errors in the estimation of work output. Both Wiebe and Seiliger modelling approaches showed that the addition of hydrogen strengthens combustion stability. The

increase in combustion stability was depicted in Wiebe modelling by the increased combustion rate or the decreased combustion duration (CD_1) and late combustion. The enhanced stability was also depicted via the Seiliger modelling approach by the increase in Seiliger parameter 'a' and the decrease in Seiliger parameters 'b' and 'c'. This enhanced combustion stability due to hydrogen addition allows engine leaning to higher air-excess ratios, which expands the operating window between the IMO TIER-III NOx limit (500 mgN m^{-3} at 5% reference O₂) and misfire in comparison to only natural gas marine engines.

In this study, p_{\max} , T_{\max} , work, net combustion heat, p_6 and T_6 modelling parameters are presented for the purpose of comparison between the two modelling approaches as these variables are vital for investigating system integration, controls and load variations. Additionally, these performance variables are the common parameters that can be obtained directly from both the modelling approaches as shown in Table C.1 of Appendix C.2. Therefore, these parameters can be studied to compare the capabilities of the Seiliger and Wiebe modelling approach in capturing the H₂-NG in-cylinder and combustion process. Other crank-resolved parameters such as CA₁₀, CA₅₀, CA₉₀, corresponding pressures, and temperatures along with the maximum rate of pressure rise can also be important parameters for combustion analysis. Appendix C.2 provides a discussion about the estimation of these parameters for 20H₂-NG fuel blend at 75% engine load and 500 mgN m^{-3} of NOx using the Seiliger and Wiebe modelling approaches.

5.6.2. EFFECTS OF DIFFERENT H₂-NG FUEL BLENDS AND ENGINE LOADS

To study the effects of hydrogen addition at a fixed engine load, first, the engine was controlled to operate at a fixed NOx with only natural gas fuel. Next, hydrogen was added to replace a fixed volumetric percentage of natural gas flow while controlling the air-intake to produce the same NOx value and the same engine load. This led to a decrease in the incoming natural gas flow with an increase in air-excess ratio compared to the initial or benchmark case of only natural gas operation. Therefore, at a fixed engine load and NOx value, all the effects of hydrogen addition on engine performance could be understood as deviations from the benchmark performance of the engine operating on only natural gas. In this section, the H₂-NG combustion process is studied in terms of deviations in Seiliger and Wiebe combustion parameters for different hydrogen blend percentages and engine loads at a fixed NOx of 500 mgN m^{-3} (at 5% reference O₂). The trends of combustion parameters for both the modelling approaches are discussed to understand their capabilities and limitations in capturing the combustion process over the engine load range. The values of performance parameters simulated for different engine loads by the two combustion characterization modelling approaches are compared with measured values.

To understand the deviations in combustion parameters, first, the combustion parameters are computed for all H₂-NG fuel blends (05H₂-NG, 10H₂-NG and 20H₂-NG) and engine loads by applying the combustion characterization approaches for Seiliger and Wiebe described in subsections 5.4.1 and 5.4.2. Next, the difference between the combustion parameters for hydrogen blends and only natural gas is computed for each H₂-NG blend at every load. This difference or delta in combustion parameters from the benchmark values of only natural gas performance at a fixed load is used to account

for the changes in the in-cylinder combustion process due to hydrogen addition at that engine load.

In this study, the 75 % load point is considered to be the nominal point for H₂-NG and CO₂-NG combustion as explained in the methodology subsection. Table 5.10 shows the 9 test points of different hydrogen blend percentages and engine loads used to understand the deviations in combustion parameters. The variations in load are represented by variations in normalized natural gas flow due to their linear relationship. For this purpose, the natural gas fuel mass injected per cylinder per cycle is normalized with respect to the nominal natural gas fuel mass measured at 75 % engine load for 0H₂-NG fuel blend and 500 mgN m⁻³ of NOx. The delta in Seiliger and Wiebe combustion parameters are presented as a function of the normalized natural gas fuel (m_{NG}^{norm}) and volumetric hydrogen blend percentage (H_{2v}) to study their trends and impact on the H₂-NG in-cylinder process over the engine load range.

Table 5.10: Tested hydrogen blend percentages and engine loads

Load [%]	H ₂ -NG blends	NOx [mgN m ⁻³]
25	05H ₂ -NG, 10H ₂ -NG, 20H ₂ -NG	500
50	05H ₂ -NG, 10H ₂ -NG, 20H ₂ -NG	500
75	05H ₂ -NG, 10H ₂ -NG, 20H ₂ -NG	500

SEILIGER-BASED H₂-NG COMBUSTION MODELLING APPROACH

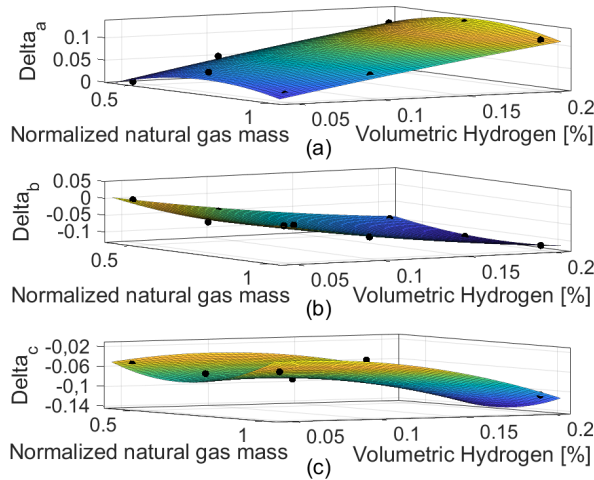


Figure 5.14: Three-dimensional surface representation of the delta in Seiliger parameters ‘a’, ‘b’ and ‘c’ as a function of the normalized natural gas fuel mass and the volumetric hydrogen percentage

Figure 5.14 shows the three-dimensional surface relationship for the deviations in Seiliger parameters ‘a’, ‘b’ and ‘c’ as a function of the (m_{NG}^{norm}) and (H_{2v}). It is evident from Figure 5.14 that the delta in Seiliger parameter ‘a’ increases at low normalized NG fuel

mass or load, reaches a maximum value and then decreases at higher loads. The delta in Seiliger parameter ‘a’ goes on increasing with increasing hydrogen percentage at all loads. As explained in subsection 5.6.1, this increase in the value of ‘a’ with increasing hydrogen percentage can be attributed to the increase in combustion heat release during stage 2-3 (at constant volume) due to the high combustion rate of hydrogen. Contrary to the deviation in ‘a’, delta in Seiliger parameter ‘b’ becomes negative with increasing hydrogen percentage. The delta in Seiliger parameter ‘c’ becomes increasingly negative with increasing hydrogen percentage at all engine loads as seen from Figure 5.14, thus, reducing late combustion and combustion instability. In this manner, the deviations in Seiliger combustion parameters follow expected trends and can be easily understood for varying engine loads and hydrogen percentages.

Table 5.11: Error percentages between the Seiliger combustion characterization simulation and measured values of performance parameters for different 20H₂-NG fuel blends and 500 mgN m⁻³ NO_x at 75 %, 50 % and 25 % engine load

Load [%]	p _{max} [%]	T _{max} [%]	Work	Q _{net} [%]	p ₆ [%]	T ₆ [%]
75	0	-1.36e-04	-0.68	9.92e-05	-2.67	-2.27
50	0	-1.65e-04	-1.72	-1.72 1.17e-04	-2.11	-2.1
25	0	-1.5e-05	-1.92	1.13e-04	-1.68	-1.65

The final value of a Seiliger parameter for a H₂-NG fuel blend and engine load is equal to the delta value added over the benchmark value of the parameter for only natural gas fuel. Using the computed values of Seiliger parameters, H₂-NG in-cylinder process is simulated for different engine loads and fixed 20H₂-NG fuel blend. Table 5.11 lists the error percentages between simulated and measured values of performance parameters for varying engine loads. As seen from Table 5.11, Seiliger-based combustion characterization model is able to capture the H₂-NG combustion process over the engine load range with about 2 % or lower deviations in estimations of work, exhaust pressure and temperature. Maximum in-cylinder pressure, temperature and combustion heat values are accurately simulated.

DOUBLE WIEBE FUNCTION-BASED H₂-NG COMBUSTION MODELLING APPROACH

Following the same above-described procedure, deviations in Wiebe combustion parameters are also found as a function of m_{NG}^{norm} and H_{2v}. Figure 5.15 shows the three-dimensional surface relationships for the deviations in Wiebe parameters due to hydrogen addition and engine loading.

The Wiebe shape factor m₁ decreased with increasing load percentage. For a fixed engine load, the variations in primary combustion phase are small for different H₂-NG fuel blends as shown in subsection 5.6.1. Appendix C.5 presents an additional discussion on the variations in m₁ and m₂ with load, hydrogen blend percentage and engine leaning. The delta of parameter m₁ should become increasingly positive with increasing hydrogen percentage as the heat release increases by a small margin. However, this trend is not followed for all hydrogen percentages and engine loads. This difficulty in identifying a clear trend and estimation of Wiebe shape factor was also reported by Rousseau et al. [28]. The delta in parameter m₂ increases in negative value with increasing hydro-

gen percentage at 75 % engine load. Thus, the decrease in the overall value of m_2 with increasing hydrogen would represent a decrease in late combustion [46]. However, at some operating points of lower engine loads, the value of m_2 increased with increasing hydrogen percentage relative to the benchmark values of only natural gas performance. Based on the explanation given in subsection 5.6.1, this behaviour of m_2 is contrary to the expected trend of hydrogen addition decreasing m_2 and reducing late combustion. Thus, both Wiebe shape factors showcase difficulty in establishing clear tendencies at all loads and hydrogen percentages.

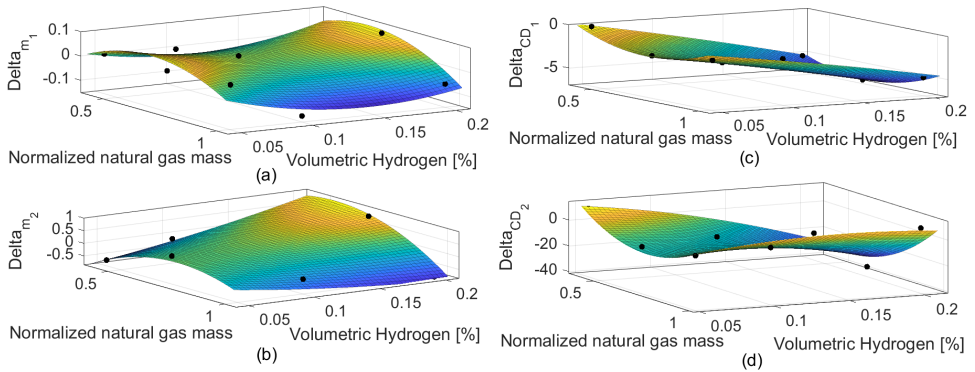


Figure 5.15: Three-dimensional surface representation of the delta in Wiebe combustion shape parameters ' m_1 ' (a), ' m_2 ' (b), CD_1 (c) and CD_2 (d) as a function of the normalized natural gas fuel mass and the volumetric hydrogen percentage

Contrary to the shape factors, the delta in combustion duration CD_1 shows a clear decreasing trend for increasing hydrogen percentage at all engine loads as shown in Figure 5.15(c). This decreasing trend can be explained by the increasing combustion rate of the air-fuel mixture as the hydrogen percentage increases. Similar to CD_1 , CD_2 also shows a general trend of decreasing total combustion duration with increasing hydrogen percentage. However, this expected trend was not found for all H_2 -NG fuel blends at 75 % engine load as seen from Figure 5.15(d) and also in subsection 5.6.1. This is due to the difficulty in accurately determining the exact end of combustion and the shape of end of combustion. Thus, the double Wiebe function-based combustion characterization process finds its limitation in identifying clear trends of shape parameters and CD_2 for all fuel blends and engine loads.

Using the derived values of Wiebe combustion parameters, H_2 -NG in-cylinder process is simulated for different engine loads and 20 H_2 -NG fuel blend. Table 5.12 lists the error percentages between simulated and measured values of performance parameters for varying engine loads using the Wiebe modelling approach. As seen from Table 5.12, double Wiebe function-based characterization model is able to capture the maximum pressure and temperature values within 2 % deviation while the exhaust pressure and temperature values deviate by a maximum of less than 3 %. However, the errors in the estimation of work and net combustion heat are higher than those found for Seiliger in the previous subsection, with a maximum error of about 5.2 %. As explained in subsection 5.5.2, the estimation of work and combustion heat is dependent on the fitted

RCO_{norm}. The accuracy of this simulated RCO_{norm} depends on the accurate estimation of Wiebe combustion parameters, which do not showcase clear tendencies with respect to load, hydrogen percentage and engine leaning. A small deviation in fitted RCO_{norm} can produce errors in simulated work and heat.

Table 5.12: Error percentages between the Seiliger combustion characterization simulation and measured values of performance parameters for different 20H₂-NG fuel blends and 500 mgNm⁻³ NO_x at 75 %, 50 % and 25 % engine load

Load [%]	p _{max} [%]	T _{max} [%]	Work [%]	Q _{net} [%]	p ₆ [%]	T ₆ [%]
75	-1.64	1.02	-5.20	-3.1	-0.47	-0.45
50	-1.66	0.51	-5.22	-5.25	-2.94	-2.93
25	-1.30	0.64	-4.26	-2.33	-0.05	-0.03

Although the results presented in this chapter for combustion modelling are at a fixed spark-timing of 24°CA bTDC, Appendix C.6 discusses the ability of Seiliger and Wiebe-based combustion modelling at three different spark-timings. Based on the above-described characterization of H₂-NG combustion, Seiliger combustion parameters showcase clear trends and good ability in capturing the H₂-NG combustion process variations for different H₂-NG fuel blends, loads and engine leaning. Therefore, Seiliger-based modelling approach is further adopted in the next section to capture the CO₂-NG combustion and in-cylinder process. By identifying clear trends in variations of combustion parameters, parametric equations can be derived as a function of normalized natural gas fuel mass (load), volumetric blend percentage, air-excess ratio and spark-timing to capture the combustion process and engine performance under varying test conditions that could not be tested experimentally. Furthermore, the derived parametric equations for Seiliger combustion models can be combined with mean value engine models to perform system integration, load variations and engine control studies, thus, extending the application of the modelling approaches and research presented. This approach of combustion parameterization and integration with an MVEM to simulate different test conditions of SOFC anode-off gas fuel blends is further discussed in the next chapter.

5.7. HRR MODEL RESULTS FOR CO₂-NG FUEL BLENDS

In the previous sections, the effects of combusting hydrogen from anode-off gas in a marine NG engine were understood. Hydrogen showed increased rate of combustion, better combustion stability and reduced late combustion, thus, improving the in-cylinder combustion process. However, the positive impacts of hydrogen could be countered by the presence of higher percentages of CO₂ in the anode-off gas as explained in section 5.1. The presence of carbon dioxide in anode-off gas relative to the amount of hydrogen also increases with SOFC fuel utilization as seen in Table 3.2. Additionally, experimental results for CO₂-NG fuel blends showed small improvements in combustion stability, UHC emissions and combustion efficiency as explained in subsection 4.3.2 of Chapter 4. Therefore, it is vital to understand and capture the effects of CO₂ addition on the performance of the natural gas engine.

As explained in the previous subsection, the Seiliger modelling approach was able to capture the in-cylinder combustion process with high accuracy. However, the Wiebe

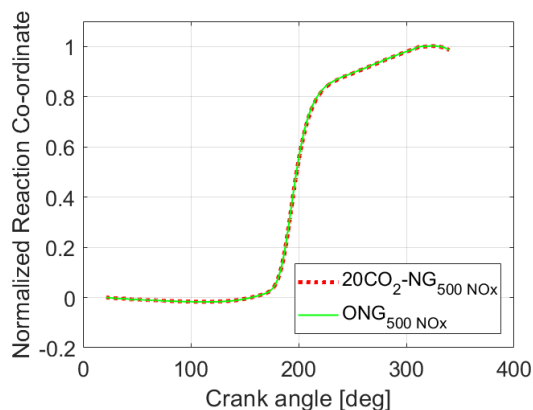


Figure 5.16: HRR model simulation of normalized reaction co-ordinate for 20CO₂-NG fuel blend and ONG at 375 kW load and 500 mgN m⁻³ NO_x

5

modelling approach produced higher deviations in the estimation of work output and combustion heat for different H₂-NG fuel blends, engine leaning and loads. Therefore, the Seiliger combustion characterization process explained in section 5.4.1 and depicted in Figure 5.4(b) is adopted to study the effects of CO₂ blending. Using the HRR model described in section 5.3, the heat release process is simulated for different CO₂-NG fuel blends based on engine measurements. In this section, the results of HRR model are discussed for CO₂-NG combustion relative to only natural gas combustion.

Figure 5.16 shows the RCO_{norm} for 20CO₂-NG fuel blend at 50 % load and 500 mgN m⁻³ of NO_x. The normalized reaction co-ordinate for 20CO₂-NG fuel blend is obtained from the HRR model and is compared against the RCO_{norm} simulated for the corresponding ONG performance at 50 % load and 500 mgN m⁻³ of NO_x. It is evident from Figure 5.16 that the 20CO₂-NG fuel blend has the same combustion rate as only natural gas performance for the same NO_x. This finding of same rate of combustion with carbon-dioxide addition can be explained in the following manner. Researchers have shown that CO₂ dilution can lead to reduced flame speeds causing the rate of combustion to decrease and increase in combustion duration, which increases combustion instability and possible engine derating as explained in subsection 2.4.1 and section 5.1. An additional effect of CO₂ is the impact on intake air for constant NO_x operation. To produce the same NO_x emission, the quantum of incoming air relative to that of fuel needed by the engine decreases with increasing carbon dioxide percentage. In such a case, the engine intake of natural gas increases to produce the required engine load and constant NO_x emission, thus, operating at a rich air-excess ratio compared to only natural gas performance. This richening of air-excess ratio increases the combustion rate, thus, countering the slowing-down effect due to CO₂ dilution. Therefore, richening of air-to-fuel ratio helps in countering the decrease in combustion stability due to CO₂ addition.

Similar to the finding in this research, Bauer et al. found that for 30 and 50CO₂-NG fuel blends engine operation at same NO_x emissions showcased a higher heat release compared to only NG performance. This similar or even high heat release would lead to

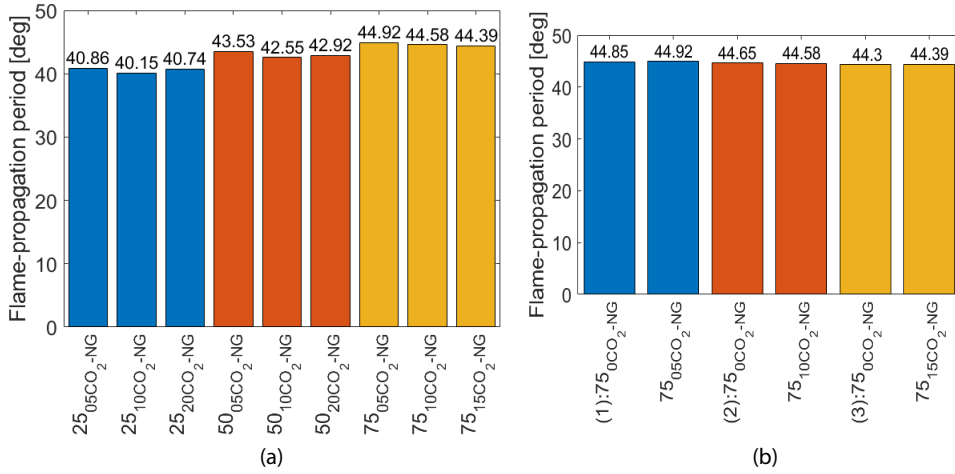


Figure 5.17: Flame-propagation period at 75 %, 50 % and 25 % engine loading for CO₂-NG fuel blends and 500 mgN m⁻³ of NO_x (a). Flame-propagation period at 75 % engine loading for CO₂-NG blends and their corresponding ONG performance measurements (b)

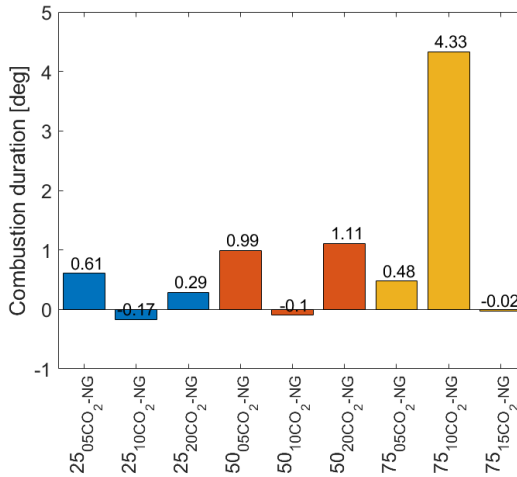


Figure 5.18: Delta in combustion duration for primary combustion at 75 %, 50 % and 25 % engine loading for CO₂-NG fuel blends and 500 mgN m⁻³ of NO_x relative to their corresponding ONG performance simulations using the HRR model

no depreciation of combustion stability and could explain the reduction in unburnt hydrocarbons and also COV_{IMEP} due to CO₂ blending found in Chapter 4. In addition to the normalised reaction co-ordinate, the countering impact of richening air-excess ratio due to CO₂ addition is also evident from the values of combustion durations obtained from the Ki-Box during engine measurements and the HRR model. The combustion duration directly obtained from the Ki-Box corresponding to the 10 to 90 % mass-burn fraction or

the flame-propagation period is shown in Figure 5.17(a) for increasing CO₂ percentage in the fuel blends at different engine loads. As seen from Figure 5.17 the values of flame-propagation period marginally change with CO₂ blending. The values showed, both, a minor increase and decrease for some CO₂ fuel blends compared to each other and their corresponding fuel blends. These small variations could be attributed to the complex interplay and the fine balance between the reduction of air causing a decrease in combustion duration and the addition of CO₂ leading to an increase in combustion duration in addition to the role played by the trapped residual gases. It is vital to note that, for the same amount of substitution, the changes in the flame-propagation period due to CO₂ addition are much smaller compared to the changes found due to hydrogen addition as observed in Figure 4.5(b) of the previous chapter. This trend of smaller fluctuations in parameters due to CO₂ addition relative to hydrogen was found for all performance and combustion parameters and is discussed further in the following sections.

As explained in section 4.2.2, the Ki-Box does not account for several in-cylinder phenomenon, therefore, the values of combustion performance parameters such as combustion duration provided by the Ki-Box are useful in obtaining a general indication of the variations in the parameters. However, for accurate combustion characterization, the heat release rate model is used. The HRR model estimates the combustion duration corresponding to the 0 to 80% mass-burn fraction, which is defined as primary combustion as explained earlier in subsection 5.4.2. The values of combustion duration for primary combustion obtained using the HRR model for CO₂ addition also (mostly) showed smaller variations as compared to the values computed for hydrogen addition, which is evident by comparing the values in Figure 5.18 and Figure 5.15(c). Furthermore, unlike hydrogen, CO₂ addition does not show a clear trend in one direction for the deviations in combustion duration relative to the corresponding only natural gas performance simulations due to strong competing effects. In the next section, the outputs of the HRR model are further used in the Seiliger-based combustion characterization process to simulate the combustion of CO₂-NG fuel blends in the engine.

5.8. CO₂-NG COMBUSTION CHARACTERIZATION MODELLING RESULTS

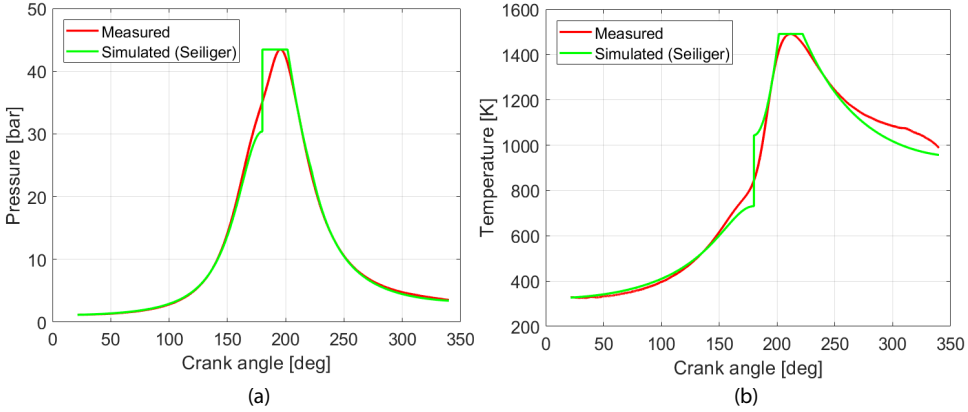
In this section, simulation results from the 0-D Seiliger-based combustion characterization models are compared against engine measurements for a single test condition. Furthermore, the variations in the combustion process are studied using the Seiliger modelling approach for different CO₂-NG fuel blends, engine leaning (lean-burn combustion) and loads.

5.8.1. CHARACTERIZATION OF CO₂-NG COMBUSTION USING SEILIGER MODELLING

Using the Seiliger-based combustion characterization process described in section 5.4.1, the Seiliger parameters and the polytropic exponents are derived for different CO₂-NG fuel blends, engine leaning and loads. The derived parameters are then used in the Seiliger-based combustion characterization model to capture the CO₂-NG in-cylinder process. Table 5.13 shows the Seiliger combustion parameters and the polytropic expo-

Table 5.13: Seiliger parameters and polytropic exponents for 20CO₂-NG fuel blend at 50 % engine load and 500 mgN m⁻³ NO_x

a	b	c	n _c	n _e
1.429	1.4296	1.792	1.327	1.292

Figure 5.19: Comparison between measured and simulated (Seiliger) in-cylinder pressure (a) and in-cylinder temperature (b) for 20CO₂-NG fuel blend at 50 % engine load and 500 mgN m⁻³ of NO_x

nents for 20CO₂-NG fuel blend at 50 percent engine load and 500 mgN m⁻³ of NO_x.

Table 5.14: Error between the Seiliger combustion characterization simulation and measured values of performance parameters for 20CO₂-NG fuel blend at 50 % engine load and 500 mgN m⁻³ NO_x

Parameters	p _{max}	T _{max}	Work	Q _{net}	p ₆	T ₆
Error [%]	0	3.47e-05	0.1293	3.16e-04	-3.203	-3.188

The derived parameters are used in the Seiliger cycles to simulate the in-cylinder process for the tested condition. As seen in Figure 5.19, the Seiliger modelling approach is able to satisfactorily capture the CO₂-NG in-cylinder and combustion process. Table 5.14 provides the error percentages between the Seiliger model simulation values and the measured values of performance parameters obtained from the HRR model. Table 5.14 showcases the capabilities of the Seiliger modelling approach in accurate estimation of pressures, temperatures, combustion heat and work output for CO₂-NG in-cylinder process. In the next subsection, the Seiliger modelling approach is employed to capture and understand the variations in the in-cylinder process due to engine leaning with CO₂-NG combustion.

5.8.2. EFFECTS OF CO₂-NG FUEL BLENDS WITH ENGINE LEANING

Like hydrogen, effects of carbon dioxide addition are understood as deviations from the corresponding and benchmark performance of only natural gas at same load and NO_x emission. Table 5.15 shows the deltas in Seiliger parameteres 20CO₂-NG fuel blend rel-

ative to the corresponding ONG performance. Additionally, Figure 5.20 compares the variations in in-cylinder pressure and temperature for the same operating conditions with 20CO₂-NG fuel blend and ONG performance.

Table 5.15: Delta in Seiliger parameters for 20CO₂-NG fuel blend relative to the corresponding ONG operating condition at 50 % engine load and 500 mgNm⁻³ NOx

Δa	Δb	Δc
0.0115	0.0078	0.0159

Seiliger parameter 'a' seems to increase with increasing CO₂ percentage. The increase in Seiliger parameter 'a' is caused by a larger decrease in trapped pressure and a minor decrease in maximum pressure as seen from Figure 5.20. The maximum pressure decrease due to the addition of carbon dioxide is very small as the decrease in the rate of pressure rise due to CO₂ is countered by the decrease in air-to-fuel ratio, which also reduces the trapped pressure. Like 'a', Seiliger parameter 'b' also increased with CO₂ addition, however, the delta is small, further indicating the controlled combustion rate due to air. A higher value of 'b' would indicate a much slower rate of combustion due to CO₂ addition without a counter effect from air, and, thus increase combustion instability. The value of Seiliger parameter 'c' also increases minutely compared to benchmark value of only natural gas performance, showcasing the controlled and marginal contribution of CO₂ addition to slow and late combustion for constant NOx operation.

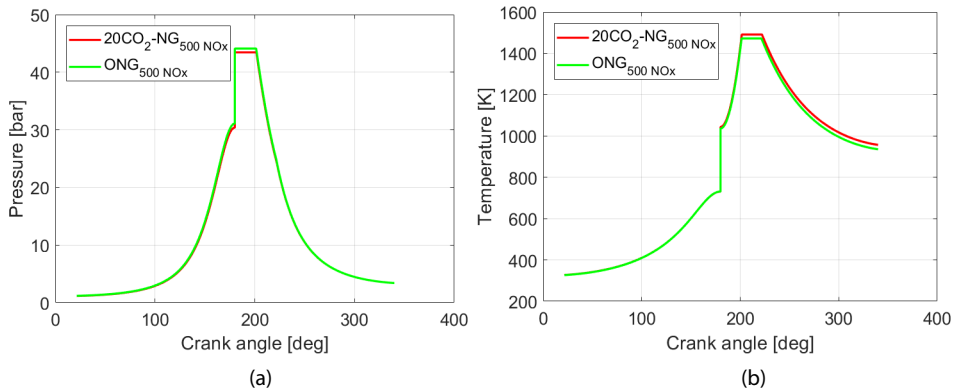


Figure 5.20: In-cylinder pressure (a) and in-cylinder temperature (b) variations for 20CO₂-NG and 0CO₂-NG fuel blend at 50 % engine load and 500 mgNm⁻³ of NOx

Addition of carbon dioxide has an impact on the in-cylinder temperature as seen from Figure 5.20(b). Once again, the NOx control leads to a direct link between the in-cylinder temperature development and NOx emissions. Since the air-intake is controlled to produce the same NOx emission of 500 mgNm⁻³, the richening of air-fuel mixture leads to similar values of maximum temperatures with increased CO₂ percentages in the fuel blend. In general, addition of CO₂ should result in lower in-cylinder temperatures due to the higher specific heat capacity. However, as seen from Figure 5.20(b), the richening of air-fuel mixture due to NOx control has a significant counter impact on the

in-cylinder process. This strong impact of air-intake due to NO_x control was also found for hydrogen addition, as explained in subsection 5.6.1.

Furthermore, addition of CO₂ shows a retarded point of maximum temperature in Figure 5.21 due to higher values of Seiliger parameters 'b' and 'c' compared to ONG, which is evident from Table 5.15. These retarded combustion temperatures due to CO₂ addition lead to higher values of exhaust temperatures at the point of exhaust valve opening. This increase in exhaust gas temperatures with CO₂ injection was also found during measurements. This trend of higher exhaust gas temperatures is opposite to that found for hydrogen addition, as explained in subsection 5.6.1.

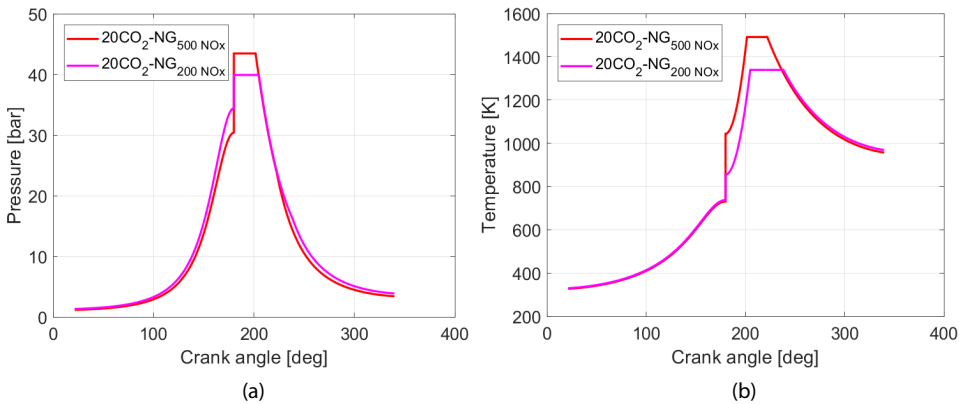


Figure 5.21: In-cylinder pressure (a) and in-cylinder temperature (b) variations for 20CO₂-NG fuel blend at 50% engine load and different NO_x values (500 mgN m⁻³, 200 mgNm⁻³) of NO_x

Table 5.16: Error percentages between the Seiliger-based combustion characterization simulation and measured values of performance parameters for 0CO₂-NG fuel blends at NO_x value of 500 mgN m⁻³ and 20CO₂-NG fuel blend at NO_x value of (200 mgN m⁻³ at 50% engine load

	p_{\max} [%]	T_{\max} [%]	Work [%]	Q_{net} [%]	p_6 [%]	T_6
ONG _{500NOx}	0	2.58e-05	0.109	2.81e-04	-3.22	-3.19
20CO ₂ - NG _{200NOx}	-1.17e-14	-1.81e-06	1.23	-8.29e-06	-2.58	-2.573

Next to CO₂ addition effects, Figure 5.21 shows the impact of engine leaning with CO₂ on the in-cylinder pressures and temperatures. As expected engine leaning to 200 mgN m⁻³ of NO_x causes a significant decrease in the in-cylinder pressures and temperatures. Thus, reducing the value of Seiliger parameter 'a' while increasing the values of Seiliger parameters 'b' and 'c' with engine leaning. Furthermore, the points of maximum pressure and temperature are shifted into expansion stroke due to a slower rate of combustion and higher late combustion. Table 5.21 showcases the high accuracy of the Seiliger modelling approach in capturing the performance parameters for engine leaning with CO₂ addition.

5.8.3. EFFECTS OF DIFFERENT CO₂-NG FUEL BLENDS AND ENGINE LOADS

To study the effects of CO₂ blending at a fixed engine load, the engine was first controlled at the same NO_x with only natural gas. Next, carbon dioxide was added to the natural gas flow based on the required CO₂-NG fuel blend volumetric percentage while controlling the air-intake to produce the same NO_x. As explained earlier in subsection 4.3.2 of previous chapter, the ONG performance measurements were performed for every CO₂-NG fuel blend. Therefore, the effects of CO₂ addition are understood and modelled as deviations from their corresponding ONG performance for the same operating conditions of load and NO_x emissions.

Table 5.17 shows the 9 test points of different carbon dioxide blend percentages and engine loads used to understand the deviations in combustion parameters relative to their corresponding ONG performance simulations. Similar to hydrogen, the natural gas fuel mass injected per cylinder per cycle is normalized with respect to the nominal natural gas fuel mass measured at 75 % engine load for 0CO₂-NG fuel blend and 500 mgN m⁻³ of NO_x. The delta in Seiliger combustion parameters relative to their corresponding ONG performances are presented as a function of the normalized natural gas fuel (m_{NG}^{norm}) or load and volumetric carbon dioxide blend percentage (CO_{2v}) to study their trends and impact on the CO₂-NG in-cylinder process over the engine load range.

Table 5.17: Tested carbon dioxide blend percentages and engine loads

Load [%]	CO ₂ -NG blends	NO _x [mgN m ⁻³]
25	05CO ₂ -NG, 10CO ₂ -NG, 20CO ₂ -NG	500
50	05CO ₂ -NG, 10CO ₂ -NG, 20CO ₂ -NG	500
75	05CO ₂ -NG, 10CO ₂ -NG, 15CO ₂ -NG	500

Figure 5.22 shows the three-dimensional surface relationship for the deviations in Seiliger parameters ‘a’, ‘b’ and ‘c’ as a function of m_{NG}^{norm} and CO_{2v}. Similar to hydrogen, the value of delta ‘a’ shows the trend of increasing to a maximum value and decreasing again at higher loads. Based on the discussion in subsection 5.8.2, the value of Seiliger parameter ‘a’ increased with CO₂ addition. However, this was not found for all CO₂-NG fuel blends at all loads. As seen in Figure 5.22(a), the delta in Seiliger parameter ‘a’ was found to be negative for some fuel blends. Similarly, the delta in Seiliger parameter ‘b’ also became negative relative to the corresponding ONG performance values. A negative value of delta in ‘b’ could be attributed to the counter-effect of richening air-to-fuel ratio due to CO₂ addition, which would indicate better combustion stability. However, the value of delta in Seiliger parameter ‘b’ was found to be positive at high CO₂ blending percentages. Next to ‘a’ and ‘b’, the delta in Seiliger parameter ‘c’ also showed positive and negative values. A negative value of delta in ‘c’ indicates reduced late combustion with CO₂ addition and NO_x control.

By comparing the values of deltas in Seiliger parameters for hydrogen and carbon dioxide given in Figure 5.14 and Figure 5.22, it is evident that the effects of hydrogen and carbon dioxide are not similar. The delta in Seiliger parameters due to CO₂ addition are much smaller than the delta in Seiliger parameters due to hydrogen addition. Therefore, The positive effects of hydrogen are more prominent than the negative effects of carbon dioxide for the same blending percentage. Furthermore, hydrogen addition in-

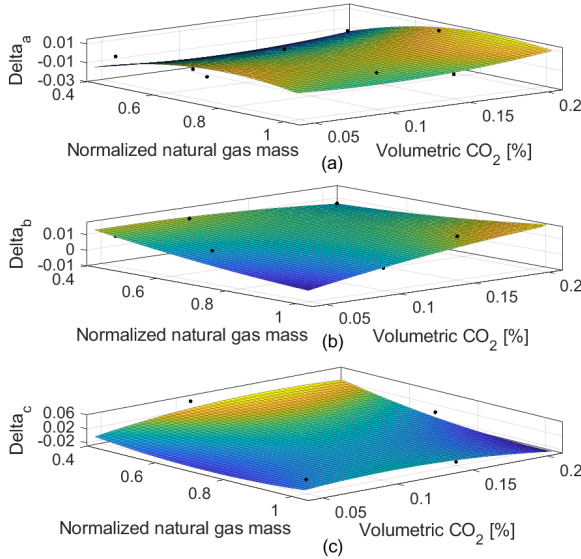


Figure 5.22: Three-dimensional surface representation of the delta in Seiliger parameters ‘a’, ‘b’ and ‘c’ as a function of the normalized natural gas fuel mass and the volumetric carbon dioxide percentage

diciates a clear trend of variations in Seiliger parameters for varying hydrogen blends and engine loads. However, unlike hydrogen, CO₂ addition did not indicate a single directional and clear trend of variations in Seiliger parameters for varying CO₂-NG fuel blends at all loads. This difficulty in finding single directional trends for CO₂ blending could be explained by two reasons. First, the counter effect of enriched air-fuel mixture during CO₂ addition could sometimes have a stronger impact on the in-cylinder and combustion process compared to the effects of increased CO₂ content. In other words, the high flame speed of hydrogen is always able to counter the reduction in combustion rate caused by more air-intake with hydrogen, thus, showcasing clear trends of variations in Seiliger parameters. On the other hand, the reduced combustion rate due to CO₂ could be countered by the enriched air-fuel mixture for constant NO_x operation without engine derating, which leads to the negative and positive delta values of Seiliger parameters due to CO₂ addition. The second reason could be the minor fluctuations in engine performance during CO₂-NG experiments explained in the previous chapter.

Table 5.18: Error percentages between the Seiliger-based combustion characterization simulation and measured values of performance parameters for 10CO₂-NG fuel blend at NO_x value of 500 mgN m⁻³ and different engine loads

Load [%]	p _{max} [%]	T _{max} [%]	Work [%]	Q _{net} [%]	p ₆ [%]	T ₆ [%]
75	0	1.264e-05	0.372	2.1e-04	-3.13	-3.116
50	0	1.906e-05	0.213	2.91e-04	-3.33	-3.32
25	0	1.89e-05	-0.283	2.93e-04	-3.48	-3.47

The final value of a Seiliger parameter for a CO₂-NG fuel blend and engine loads is

equal to the delta value added to the benchmark value of the parameters for the ONG performance. Using the computed values of Seiliger parameters, CO₂-NG in-cylinder process is simulated for different engine loads and fixed 20CO₂-NG fuel blend. Table 5.18 lists the error percentages between simulated and measured values of performance parameters for varying engine loads. As seen from Table 5.18, Seiliger-based combustion characterization model is able to capture the CO₂-NG combustion process over the engine load range with a maximum deviation of 3.48 % in estimations of exhaust pressure and temperature. Maximum in-cylinder pressure, temperature, work and combustion heat values are accurately simulated.

In this manner, the variations in the combustion and in-cylinder process are captured for different blend percentages of anode-off gas constituents (H₂ and CO₂) using the Seiliger modelling approach.

5.9. CONCLUSIONS

In this chapter, the effects of combusting blends of hydrogen-natural gas and carbon dioxide-natural gas in a marine lean-burn SI engine have been studied through combustion characterization modelling. Furthermore, a comparison has been presented between the capabilities of Seiliger and Wiebe-based modelling approach to characterize and capture the H₂-NG combustion process. The study presented a detailed methodology to develop 0-D Seiliger and double Wiebe function-based combustion characterization models based on engine measurements to study and capture the combustion process for different fuel blends, engine loads and engine leaning. The development of combustion characterization model for constituents of anode-off gas forms a crucial step in the development of a holistic simulation model capable of simulating the complete performance of the AOG-NG engine operating on different blends of anode-off gas and natural gas for SOFC-ICE integration. The research results presented in this chapter help in answering Research Question 3 and 4. Furthermore, the model simulations presented in this chapter help in gaining a detailed understanding of the impacts of ISVs such as engine fuel composition (varying blends of anode-off gas constituents and natural gas), air-excess ratio (engine leaning), engine loading and spark-timings on the in-cylinder process of the marine lean-burn NG engine, thus, providing insights to answer Research Question 5. The following concluding remarks are noted from the discussions presented in this chapter pertaining to H₂ – NG and CO₂ – NG combustion modelling:

- For the combustion characterization process and to simulate the heat release process of H₂-NG and CO₂-NG fuel blends based on engine measurements, a single-zone, 0-D, thermodynamic heat release rate (HRR) model was developed. The developed HRR model accounted for the impact of high amount of trapped residual gas found in the zero valve overlap test engine. The model also accounted for the increase in trapped mixture temperature due to the mixing of inducted mass with the hot residual combustion gases trapped from the previous cycle. The HRR model formed the first step towards the characterization of combustion using the Seiliger and double Wiebe function-based modelling approaches.

H₂-NG COMBUSTION MODELLING

- Next, the study found that Seiliger parameters 'a', 'b' and 'c' represent different physical phenomenon in the H₂-NG combustion process. Seiliger parameter 'a' can be directly related to the increase in combustion rate with increasing hydrogen addition. Seiliger parameter 'b' signified a measure of combustion stability while Seiliger parameter 'c' represented late combustion present in lean-burn combustion. Similar to Seiliger, a double-Wiebe function with combustion parameters 'm₁', 'm₂', "CD₁" and "CD₂" was presented to characterize the H₂-NG combustion process. In the Wiebe characterization process, the second Wiebe function helped capture the changes in late burn phase found in lean-burn NG and H-NG combustion.
- The investigation performed in this chapter also showed that the characterization of H₂-NG combustion using the Seiliger modelling approach can be used to capture the H₂-NG in-cylinder combustion process with high accuracy. Similarly, H₂-NG combustion can be simulated by using the Wiebe modelling approach with accurate estimation of the in-cylinder pressures and temperatures, however, it produced higher deviations in the estimation of work output and combustion heat for different H₂-NG fuel blends, engine leaning and loads. The Wiebe-based approach produced a maximum error of about 5.2% for both work output and combustion heat, while Seiliger error was less than 2% for both these variables. The better ability of Seiliger than Wiebe to capture the variations in H₂-NG combustion process for different fuel blends, engine leaning and loads could be attributed to the following factors:
 - Limitation of double Wiebe function in identifying clear trends of the Wiebe shape parameters and the combustion duration of the second Wiebe function (CD₂) for all fuel blends, engine leaning and loads.
 - Difficulty in the accurate fitting of normalized RCO.
- The H₂-NG combustion characterization process showed that maximum in-cylinder pressures and temperatures decreased with engine leaning, while hydrogen addition at the same NO_x emission increased the maximum in-cylinder pressure values. The characterization process also showed that as the air-intake is controlled, the engine produces almost similar values of maximum in-cylinder temperatures to produce the same amount of NO_x emissions. Therefore, the combustion due to hydrogen addition could be controlled by governing the air-intake to control the maximum in-cylinder temperatures to produce NO_x emissions within IMO TIER-III NO_x emission limits. Although the in-cylinder temperatures due to hydrogen addition and NO_x control are quite similar, hydrogen addition results in slightly lower temperatures at the point of exhaust valve opening.
- The investigation also found that Seiliger combustion parameters showcase clear trends and good ability in capturing the H₂-NG combustion process variations for different H₂-NG fuel blends, loads and engine leaning. Therefore, Seiliger-based modelling approach was further adopted to capture the CO₂-NG combustion and in-cylinder process.

CO₂-NG COMBUSTION MODELLING

- The heat release analysis for CO₂-NG combustion showed that the richening of air-excess ratio increases the combustion rate, which counters the slowing-down effect due to CO₂ dilution. The similar or even high heat release would lead to no depreciation of combustion stability and explain the reduction in unburnt hydrocarbons and also COV_{IMEP} due to CO₂ blending found in Chapter 4.
- Furthermore, the richening of air-fuel mixture leads to similar values of maximum temperatures with increased CO₂ percentages in the fuel blend. In general, addition of CO₂ should result in lower in-cylinder temperatures due to the higher specific heat capacity. However, the richening of air-fuel mixture due to NO_x control has a significant counter impact on the in-cylinder process. This strong impact of air-intake due to NO_x control was also found for hydrogen addition, as explained in subsection 5.6.1. CO₂ addition also showed higher values of exhaust temperatures at the point of exhaust valve opening.
- Similar to hydrogen, the Seiliger modelling approach demonstrated significant capabilities in accurate estimation of pressures, temperatures, combustion heat and work output for CO₂-NG combustion. With CO₂ addition, Seiliger parameter 'a' increased due to lower trapped pressure. Seiliger parameter 'b' also increased by a small margin indicating the controlled combustion rate due to richening of air-fuel ratio. Additionally, the value of Seiliger parameter 'c' also increased minutely compared to benchmark value of only natural gas performance, showcasing the controlled and marginal contribution of CO₂ addition to slow and late combustion for constant NO_x operation. The modelling research presented in this chapter showed that at a fixed engine load and NO_x value, the effects of hydrogen and carbon dioxide addition on the in-cylinder process could be understood as deviations from the benchmark performance of the engine operating on only natural gas.
- The modelling results also showed that the positive effects of hydrogen on the in-cylinder process are more prominent than the negative effects of carbon dioxide for the same blending percentage. Furthermore, unlike hydrogen, CO₂ addition did not indicate a single directional and clear trend of variations in Seiliger parameters for varying CO₂-NG fuel blends at all loads. The modelling results also indicated that the high flame speed of hydrogen is always able to counter the reduction in combustion rate caused by more air-intake with hydrogen, thus, showcasing clear trends of variations in Seiliger parameters. On the other hand, the reduced combustion rate due to CO₂ could be countered by the enriched air-fuel mixture for constant NO_x operation, which leads to the negative and positive delta values of Seiliger parameters due to CO₂ addition.

Based on the combustion modelling capabilities demonstrated in this chapter, the presented methodology and modelling approaches could be applied to other alternative fuels and automotive engines. In this chapter, the developed Seiliger and Wiebe-based simulation models helped in understanding the impact of AOG constituents on the in-cylinder process, thus, providing an answer to Research Question 3. Next, the research

presented in this chapter found that the Seiliger modelling approach can be used to accurately quantify the combustion and in-cylinder pressure variations due to anode-off gas constituents, which helps in partially answering Research Question 4.

The modelling results presented in this chapter indicate that by identifying trends in variations of combustion parameters, parametric equations could be derived as a function of normalized natural gas fuel mass (load), volumetric blend percentage, air-excess ratio and spark-timing to capture the combustion process and engine performance under varying test conditions that could not be tested experimentally. These derived parametric equations for Seiliger combustion models can be combined with mean value engine models to perform system integration, load variations and engine control studies, thus, extending the application of the modelling approaches and research presented. This approach of combustion parameterization and integration with an MVEM to simulate different test conditions of SOFC anode-off gas fuel blends is further discussed in the next chapter.

REFERENCES

- [1] H.D. Sapra et al. Hydrogen-Natural Gas Combustion in a Marine Lean-Burn SI Engine: A Comparative Analysis of Seiliger and Double Wiebe Function-Based Zero-Dimensional Modelling. *Energy Conversion and Management*, 2020.
- [2] H.D. Sapra et al. Integration of Solid Oxide Fuel Cell and Internal Combustion Engine for Maritime Applications. *Applied Energy*, 2020.
- [3] R.D. Reitz and G. Duraisamy. Review of High Efficiency and Clean Reactivity Controlled Compression Ignition (RCCI) Combustion in Internal Combustion Engines. *Progress in Energy and Combustion Science*, 2015.
- [4] E. Hendricks. Engine Modelling for Control Applications: A Critical Survey. *Meccanica*, 1997.
- [5] S.I. Raptotasio, N.F. Sakellariadis, R.G. Papagiannakis, and D.T. Hountalas. Application of a Multi-Zone Combustion Model to Investigate the NO_x Reduction Potential of Two-Stroke Marine Diesel Engines Using EGR. *Applied Energy*, 2015.
- [6] G. Benvenuto and U. Campora. Dynamic Simulation of a High-Performance Sequentially Turbocharged Marine Diesel Engine. *Journal of Engineering for the Maritime Environment*, 2011.
- [7] R. Schulz, Y.M. Wright, and K. Boulouchos. Progress in Computational Fluid Dynamics (CFD) Applications for Large Diesel Engine Development. In *CIMAC*, 2004.
- [8] M. Baratta, D. Misul, L. Viglione, and J. Xu. Combustion Chamber Design for a High-Performance Natural Gas Engine: CFD Modeling and Experimental Investigation. *Energy Conversion and Management*, 2019.
- [9] R.D. Geertsma et al. Pitch Control for Ships with Diesel Mechanical and Hybrid Propulsion: Modelling, Validation and Performance Quantification. *Applied Energy*, 2017.
- [10] M.S. Cellek and A. Pınarbaşı. Investigations on Performance and Emission Characteristics of an Industrial Low Swirl Burner while Burning Natural Gas, Methane,

- Hydrogen-Enriched Natural Gas and Hydrogen as Fuels. *International Journal of Hydrogen Energy*, 2018.
- [11] A. Hadeif, A. Mameri, F. Tabet, and Z. Aouachria. Numerical Study of the Impact of CO₂ Dilution on Emissions in Turbulent Diffusion Flame. *Energy Procedia*, 2017.
- [12] X. Ling, F. Wu, and D. Yao. A Reduced Combustion Kinetic Model for the Methanol-Gasoline Blended Fuels on SI Engines. *Science China Technological Sciences*, 2016.
- [13] A. Kakoei and A. Gharehghani. Comparative Study of Hydrogen Addition Effects on the Natural-Gas/Diesel and Natural-Gas/Dimethyl-Ether Reactivity Controlled Compression Ignition Mode of Operation. *Energy Conversion and Management*, 2019.
- [14] İ. Altın and A. Bilgin. Quasi-Dimensional Modeling of a Fast-Burn Combustion Dual-Plug Spark-Ignition Engine with Complex Combustion Chamber Geometries. *Applied Thermal Engineering*, 2015.
- [15] X. Duan et al. Experimental and Numerical Investigation of the Effects of Low-Pressure, High-Pressure and Internal EGR Configurations on the Performance, Combustion and Emission Characteristics in a Hydrogen-Enriched Heavy-Duty Lean-Burn Natural Gas SI Engine. *Energy Conversion and Management*, 2019.
- [16] R. Slefarski. Study on the Combustion Process of Premixed Methane Flames with CO₂ Dilution at Elevated Pressures. *Energies*, 2019.
- [17] C.D. Rakopoulos, M.A. Scott, D.C. Kyritsis, and E.G. Giakoumis. Availability Analysis of Hydrogen/Natural Gas Blends Combustion in Internal Combustion Engines. *Energy*, 2008.
- [18] L. Xiang, G. Theotokatos, and Y. Ding. Investigation on Gaseous Fuels Interchangeability with an Extended Zero-Dimensional Engine Model. *Energy Conversion and Management*, 2019.
- [19] C.D. Rakopoulos and C.N. Michos. Development and Validation of a Multi-Zone Combustion Model for Performance and Nitric Oxide Formation in Syngas Fueled Spark Ignition Engine. *Energy Conversion and Management*, 2008.
- [20] M. Yıldız and B. Albayrak Çeper. Zero-Dimensional Single Zone Engine Modeling of an SI Engine Fuelled with Methane and Methane-Hydrogen Blend Using Single and Double Wiebe Function: A Comparative Study. *International Journal of Hydrogen Energy*, 2017.
- [21] Y. Tang et al. Development of a Real-Time Two-Stroke Marine Diesel Engine Model with In-Cylinder Pressure Prediction Capability. *Applied Energy*, 2017.
- [22] J.I. Ghojel. Review of the Development and Applications of the Wiebe Function: A Tribute to the Contribution of Ivan Wiebe to Engine Research. *International Journal of Engine Research*, 2010.
- [23] G. Abbaszadehmosayebi and L. Ganippa. Determination of Specific Heat Ratio and Error Analysis for Engine Heat Release Calculations. *Applied Energy*, 2014.
- [24] J.B. Heywood. *Internal Combustion Engine Fundamentals*. McGraw-Hill Series in Mechanical Engineering, 1988.

- [25] J. Liu and C.E. Dumitrescu. Single and Double Wiebe Function Combustion Model for a Heavy-Duty Diesel Engine Retrofitted to Natural-Gas Spark-Ignition. *Applied Energy*, 2019.
- [26] G.J. Amador Diaz et al. Influence of Engine Operating Conditions on Combustion Parameters in a Spark Ignited Internal Combustion Engine Fueled with Blends of Methane and Hydrogen. *Energy Conversion and Management*, 2019.
- [27] J.L.E. Carrera et al. Numerical Study on the Combustion Process of a Biogas Spark Ignition Engine, 2013.
- [28] S. Rousseau, B. Lemoult, and M. Tazerout. Combustion Characterization of Natural Gas in a Lean Burn Spark-Ignition Engine. *Proceedings of the Institution of Mechanical Engineers, Part D: Journal of Automobile Engineering*, 1999.
- [29] K. Packham. Lean-Burn Engine Technology Increases Efficiency, Reduces NOx Emissions (White paper). 2007.
- [30] S. Hou. Heat Transfer Effects on the Performance of an Air Standard Dual cycle. *Energy Conversion and Management*, 2004.
- [31] D. Stapersma. *Diesel Engines: A Fundamental Approach to Performance Analysis, Turbocharging, Combustion, Emissions and Heat Transfer Including Thermodynamical Principles. Vol. 1: Performance Analysis*. Delft University of Technology, 2010.
- [32] P. Schulten. *The Interaction Between Diesel Engines, Ship And Propellers During Manoeuvring*. PhD thesis, 2005.
- [33] Y. Ding, C. Sui, and J. Li. An Experimental Investigation into Combustion Fitting in a Direct Injection Marine Diesel Engine. *Applied Sciences*, 2018.
- [34] C. Sui, E. Song, D. Stapersma, and Y. Ding. Mean Value Modelling of Diesel Engine Combustion Based on Parameterized Finite Stage Cylinder Process. *Ocean Engineering*, 2017.
- [35] I. Georgescu, D. Stapersma, and B. Mestemaker. Dynamic Behaviour of Gas and Dual-Fuel Engines: Using Models and Simulations to Aid System Integration. In *CIMAC*, 2016.
- [36] H.D. Sapra et al. Experimental and Simulation-Based Investigations of Marine Diesel Engine Performance Against Static Back Pressure. *Applied Energy*, 2017.
- [37] P. Skogtjarn. Modelling of the Exhaust Gas Temperature for Diesel Engines, 2002.
- [38] H. Guo and G.J. Smallwood. A Numerical Study on the Influence of CO₂ Addition on Soot Formation in an Ethylene/Air Diffusion Flame. *Combustion Science and Technology*, 2008.
- [39] G. Bagheri et al. Comprehensive Kinetic Study of Combustion Technologies for Low Environmental Impact: MILD and OXY-Fuel Combustion of Methane. *Combustion and Flame*, 2020.
- [40] A. Mazas, D. Lacoste, and T. Schuller. Experimental and Numerical Investigation on the Laminar Flame Speed of CH₄/O₂ Mixtures Diluted with CO₂ and H₂O. In *ASME Turbo Expo*, 2010.

- [41] E. Doosje. *Limits of Mixture Dilution in Gas Engines*. PhD thesis, Eindhoven University of Technology, 2010.
- [42] J.M. Hansen et al. Modelling for Control of Exhaust Gas Recirculation on Large Diesel Engines. In *IFAC Proceedings Volumes*, 2013.
- [43] D.I. Swain and S.O.B. Shrestha. CFD Performance Analysis of a Spark Ignition Engine Fueled by Landfill Gas. *The Open Fuels & Energy Science Journal*, 2014.
- [44] S. Schlesinger et al. Terminology for Model Credibility. Technical report, SCS Technical Committees.
- [45] A. Vrijdag, D. Stapersma, and T. van Terwisga. Systematic Modelling, Verification, Calibration and Validation of a Ship Propulsion Simulation Model. *Journal of Marine Engineering & Technology*, 2014.
- [46] Y. Ding. *Characterising Combustion in Diesel Engines*. PhD thesis, Delft University of Technology, 2011.
- [47] D. Stapersma. *Diesel Engines: A Fundamental Approach to Performance Analysis, Turbocharging, Combustion, Emissions and Heat Transfer Including Thermodynamical Principles. Vol. 3: Combustion*. Delft University of Technology, Delft, 2009.
- [48] S.M. Krol. Modelling and Performance Investigation of Anode-Off Gas Combustion in an IC Engine for Power Generation, 2018.
- [49] Y. Sun, H. Wang, C. Yang, and Y. Wang. Development and Validation of a Marine Sequential Turbocharging Diesel Engine Combustion Model Based on Double Wiebe Function and Partial Least Squares Method. *Energy Conversion and Management*, 2017.
- [50] F. Maroteaux, C. Saad, and F. Aubertin. Development and Validation of Double and Single Wiebe Function for Multi-Injection Mode Diesel Engine Combustion Modelling for Hardware-In-The-Loop Applications. *Energy Conversion and Management*, 2015.
- [51] H. Yasar et al. Double-Wiebe Function: An Approach for Single-Zone HCCI Engine Modeling. *Applied Thermal Engineering*, 2008.
- [52] F. Baldi, G. Theotokatos, and K. Andersson. Development of a Combined Mean Value-Zero Dimensional Model and Application for a Large Marine Four-Stroke Diesel Engine Simulation. *Applied Energy*, 2015.
- [53] Y. Yeliana et al. Estimation of Double-Wiebe Function Parameters Using Least Square Method for Burn Durations of Ethanol-Gasoline Blends in Spark Ignition Engine Over Variable Compression Ratios and EGR Levels. *Applied Thermal Engineering*, 2011.
- [54] A.M. Shivapuji and S. Dasappa. Experiments and Zero D Modeling Studies Using Specific Wiebe Coefficients for Producer Gas as Fuel in Spark-Ignited Engines. 2012.
- [55] H. Cho, S.R. Krishnan, R. Luck, and K.K. Srinivasan. Comprehensive Uncertainty Analysis of a Wiebe Function-Based Combustion Model for Pilot-Ignited Natural Gas Engines. 2008.

- [56] K. Ishii et al. Investigation of Cyclic Variation of IMEP Under Lean Burn Operation in Spark-Ignition Engine, 1997.
- [57] F. Ma and Y. Wang. Study on the Extension of Lean Operation Limit Through Hydrogen Enrichment in a Natural Gas Spark-Ignition Engine. *International Journal of Hydrogen Energy*, 2008.
- [58] G.A. Karim, I. Wierzba, and Y. Al-Alousi. Methane-Hydrogen Mixtures as Fuels. *International Journal of Hydrogen Energy*, 1996.
- [59] I. Georgescu, D. Stapersma, L.M. Nerheim, and B. Mestemaker. Characterisation of Large Gas and Dual-Fuel Engines. *MTZ Industrial*, 2016.
- [60] F. Ma et al. Effects of Hydrogen Addition on Cycle-By-Cycle Variations in a Lean Burn Natural Gas Spark-Ignition Engine. *International Journal of Hydrogen Energy*, 2008.
- [61] J. Wang, H. Chen, B. Liu, and Z. Huang. Study of Cycle-By-Cycle Variations of a Spark Ignition Engine Fueled with Natural Gas-Hydrogen Blends. *International Journal of Hydrogen Energy*, 2008.
- [62] F. Ma et al. Study on Combustion Behaviors and Cycle-By-Cycle Variations in a Turbocharged Lean Burn Natural Gas S.I. Engine with Hydrogen Enrichment. *International Journal of Hydrogen Energy*, 2008.
- [63] Z.H. Huang et al. Study on Cycle-By-Cycle Variations of Combustion in a Natural-Gas Direct-Injection Engine. *Proceedings of the Institution of Mechanical Engineers, Part D: Journal of Automobile Engineering*.
- [64] B. Huang et al. Cycle-By-Cycle Variations in a Spark Ignition Engine Fueled with Natural Gas-Hydrogen Blends Combined with EGR. *International Journal of Hydrogen Energy*, 2009.
- [65] H. Spliethoff, U. Greul, H. Maier, and K.R.G. Hein. Low-NO_x Combustion for Pulverized Coal - A Comparison of Air Staging and Reburning. In *The Institute of Energy's Second International Conference on Combustion & Emissions Control*, 1995.
- [66] G.J. Nebel and M.W. Jackson. Some Factors Affecting the Concentration of Oxides of Nitrogen in Exhaust Gases from Spark Ignition Engines. *Journal of the Air Pollution Control Association*, 1958.
- [67] D. Stapersma. *Diesel Engines: A Fundamental Approach to Performance Analysis, Turbocharging, Combustion, Emissions and Heat Transfer including Thermodynamical Principles: Vol. 4: Emissions and Heat Transfer*. Delft University of Technology, 2010.

6

MEAN VALUE ENGINE MODEL FOR SOFC-ICE INTEGRATION

By employing the combustion characterization process described in the previous chapter, Seiliger parameters were derived for H₂-NG and CO₂-NG combustion. The combustion characterization and parameterization approach applied for CO₂-NG combustion is directly based on the methodology developed for H₂-NG combustion. In this chapter, parametric equations are first derived to compute the Seiliger parameters based on load, normalized natural gas fuel mass and blend percentage of hydrogen and carbon dioxide. The estimated Seiliger parameters are further used to simulate the in-cylinder process for varying anode-off gas and natural gas fuel blends in this chapter. Next, the Seiliger in-cylinder model with the parametric equations is combined with a mean value engine model (MVEM) to capture the complete engine performance for different blends of anode-off gas and natural gas. The developed in-cylinder modelling approach and the MVEM are validated against engine measurements and tested to simulate conditions that could not be investigated experimentally. Furthermore, the impact of fuel compositions (ISV) on turbocharging and engine performance are discussed, thus, providing additional insights to answer Research Question 5.

Based on the validation and confidence in simulating the experimentally untested conditions, the AOG-NG MVEM in combination with the Seiliger modelling approach is further employed in the next chapter to study SOFC-ICE integration, thus, answering Research Question 4.

6.1. AOG-NG COMBUSTION MODELLING

In the previous research chapter, it was concluded that at a fixed engine load and NO_x value, all the effects of hydrogen and carbon dioxide addition on the in-cylinder process could be understood as deviations from the benchmark performance of the engine operating on only natural gas. To understand the deviations in combustion parameters, first,

Parts of this chapter have been published in Applied Energy [1].

the combustion parameters were computed for all the H₂-NG and CO₂-NG fuel blends and engine loads given in Table 5.10 and Table 5.17 by applying the Seiliger-based combustion characterization approach. Next, the differences between the combustion parameters for blends and only natural gas were computed for each H₂-NG and CO₂-NG blend at every load and fixed NO_x value as described in the previous chapter. In the current and the next chapter, all simulations and analysis are performed and presented at a fixed engine NO_x of 500 mgN m⁻³.

In this section, the difference or delta in combustion parameters, obtained from combustion characterization explained in the previous chapter, is parametrized through regression. This combustion parametrization process helps derive parametric equations to compute the Seiliger parameters as a function of the load and blend percentage of the individual constituents of anode-off gas (hydrogen and carbon dioxide). Further on, the parametrization for the individual components of AOG is further adopted to compute the Seiliger parameters for SOFC anode-off gas and natural gas fuel blends. The Seiliger parameters computed from the parametric equations are further used to simulate the in-cylinder process and engine performance with varying AOG-NG fuel blends, which is crucial for development of SOFC-ICE integration.

6.1.1. PARAMETRIZATION OF HYDROGEN-NATURAL GAS COMBUSTION

In the combustion parameterization process, parametric equations are derived for the Seiliger combustion parameters based on three input variables, namely, normalized engine load, normalized natural gas fuel mass and hydrogen, carbon dioxide percentage. In this study, parametric equations of Seiliger parameters are first derived for ONG combustion. Then, the estimated values of these combustion parameters are used as benchmark values to compute the parameters for H₂-NG or CO₂-NG or AOG-NG combustion. To derive the parametric equations for ONG combustion, fuel mass of natural gas injected into the cylinder per cycle has been normalized with respect to the nominal natural gas fuel mass measurement at 75 % engine load for ONG fuel blend. After normalizing, a linear relation given by equation 6.1 is derived via regression fitting between the engine load setting (L) and the normalized natural gas fuel mass ($m_{\text{NH,ONG}}^{\text{norm}}$). 'L' is the ratio of load setpoint (required load) to the maximum engine power out of 500 kW.

$$m_{\text{NG,ONG}}^{\text{norm}} = 1.117.L + 0.1621 \quad (6.1)$$

Using this linear relationship, the normalized natural gas fuel mass is derived based on engine load input. The estimated value of normalized natural gas fuel mass is further used to derive the values of the Seiliger combustion parameters for ONG and H₂-NG combustion as discussed further. Following the combustion characterization approach described in the previous chapter, Seiliger parameters were estimated at different loads and H₂-NG fuel blends. Using the computed values of Seiliger parameters for ONG fuel blend at 25 %, 50 % and 75 % engine load, parametric equations are derived using multivariable regression. The general form of these empirical relations between the Seiliger parameters and the normalized natural gas fuel mass is given by equation 6.2. The regression fit coefficients k_i^{par} in equation 6.2 for the three Seiliger parameters, natural gas fuel mass, air-excess ratio and unburnt hydrocarbons (UHC) have been provided in Table 6.1. Regression data for natural gas fuel mass, UHC and air-excess ratio is based on

engine measurements. These performance variables are used in the MVEM to simulate the complete engine performance as will be explained in section 6.2. In engine simulations, the Seiliger parameters, natural gas fuel mass and UHC (in ppmv) obtained from the parametric equations are used as final values to estimate the engine performance in the MVEM while the air-excess ratio obtained from the parametric equations is used as an initial value for the MVEM pre-simulation as will be explained in section 6.2.

$$\text{par}_{\text{ONG}} = k_0^{\text{par}} \cdot m_{\text{NG,ONG}}^{\text{norm}} k_1^{\text{par}} + k_2^{\text{par}} \quad (6.2)$$

Using the above equations for ONG fuel blend, the Seiliger process can be used to sim-

Table 6.1: Parametric regression equation coefficients for only natural gas fuel

Parameter	k_0^{par}	k_1^{par}	k_2^{par}
$a_{\text{Seil,ONG}}$	-0.0837	-2.318	1.448
$b_{\text{Seil,ONG}}$	0.317	0.2943	1.135
$c_{\text{Seil,ONG}}$	0.2688	1.566	1.523
$\lambda_{\text{initial,ONG}}$	-0.04435	-1.382	1.671
UHC_{ONG}	-768.6	0.1512	1741

ulate the ONG combustion and in-cylinder process at different loads.

All the effects of hydrogen addition on in-cylinder process could be understood as deviations from the benchmark performance of the engine operating on only natural gas. Following this idea, the Seiliger combustion parameters for hydrogen addition are estimated by first calculating them at the benchmark performance with only natural gas and then adding the deviation in those parameters due to hydrogen addition. As discussed in subsection 5.6.2 of the previous chapter, the deviations in combustion parameters are calculated for all H₂-NG fuel blends (05H₂-NG, 10H₂-NG and 20H₂-NG) and all engine loads at constant NO_x of 500 mgN m⁻³ by using the characterization process. To simulate the effects of H₂-NG combustion, parametric equations are derived via multivariable regression, which relates this delta or deviation in each combustion parameter due to hydrogen addition as a function of the normalized natural gas fuel mass ($m_{\text{NH,ONG}}^{\text{norm}}$) and the volumetric percentage of hydrogen (H_{2v}) in the blend. The parametric equations are a mathematical representation of the three-dimensional surface for the deviations in Seiliger parameters 'a', 'b' and 'c' as a function of the $m_{\text{NG,ONG}}^{\text{norm}}$ and H_{2v} shown in Figure 5.14 of Chapter 5. Equation 6.3 shows the generic form of the parametric relation for computing the delta in each parameter (par) as a function of $m_{\text{NG,ONG}}^{\text{norm}}$ and H_{2v}.

$$\Delta \text{par}_{\text{H}_2\text{-NG}} = s_0^{\text{par}} + m_{\text{NG,ONG}}^{\text{norm}} \cdot s_1^{\text{par}} + \text{H}_{2v} \cdot s_2^{\text{par}} + m_{\text{NG,ONG}}^{\text{norm}^2} \cdot s_3^{\text{par}} + m_{\text{NG,ONG}}^{\text{norm}} \cdot \text{H}_{2v} \cdot s_4^{\text{par}} + \text{H}_{2v}^2 \cdot s_5^{\text{par}} \quad (6.3)$$

$$\text{par}_{\text{H}_2\text{-NG}} = \Delta \text{par}_{\text{H}_2\text{-NG}} + \text{par}_{\text{NG,ONG}} \quad (6.4)$$

In addition to the Seiliger parameters, the delta in natural gas fuel mass and unburnt hydrocarbons (in ppmv) due to hydrogen addition is also derived by using the same general form of multivariable regression given by equation 6.3. The polynomial regression

coefficients s_i^{par} in equation 6.3 have been provided in Table 6.2 and Table 6.3 for each parameter. After calculating the delta for each parameter due to hydrogen addition, the absolute value of the parameters for the corresponding H₂-NG fuel blend is calculated by using equation 6.4.

Table 6.2: Part I: Parametric regression equation coefficients for H₂-NG fuel blends

Parameter	s_0^{par}	s_1^{par}	s_2^{par}	s_3^{par}
$\Delta a_{\text{Seil},\text{H}_2-\text{NG}}$	-0.169	0.4481	0.815	-0.2938
$\Delta b_{\text{Seil},\text{H}_2-\text{NG}}$	0.1339	-0.29951	-0.9673	0.1882
$\Delta c_{\text{Seil},\text{H}_2-\text{NG}}$	0.08155	-0.5649	1.029	0.4371
$\Delta m_{\text{NG},\text{H}_2-\text{NG}}$	4.493e-6	-1.01e-5	-1.08e-5	5.834e-6
$\Delta \lambda_{\text{initial},\text{H}_2-\text{NG}}$	0.0679	-0.2753	0.6972	0.1896
$\Delta \text{UHC}_{\text{H}_2-\text{NG}}$	-768.6	0.1512	1741	248.1

Table 6.3: Part II: Parametric regression equation coefficients for H₂-NG fuel blends

Parameter	s_4^{par}	s_5^{par}
$\Delta a_{\text{Seil},\text{H}_2-\text{NG}}$	-0.092	-0.4845
$\Delta b_{\text{Seil},\text{H}_2-\text{NG}}$	-0.0354	1.583
$\Delta c_{\text{Seil},\text{H}_2-\text{NG}}$	-0.5361	-4.066
$\Delta m_{\text{NG},\text{H}_2-\text{NG}}$	-0.0001505	6.273e-5
$\Delta \lambda_{\text{initial},\text{H}_2-\text{NG}}$	0.2081	-1.427
$\Delta \text{UHC}_{\text{H}_2-\text{NG}}$	783.4	129.2

Table 6.4: Derived Seiliger parameters based on combustion parameterization for 20H₂-NG fuel blend and 500 mgN m⁻³ NOx at 75 % load

Seiliger Parameter	a	b	c
Value	1.4749	1.3373	1.6814

Table 6.5: Error percentages between the predicted and measured values of performance parameters 20H₂-NG fuel blend and 500 mgN m⁻³ NOx at 75 % load

Parameter	p_{max}	T_{max}	Work	Q_{net}	p_6	T_6	$m_{\text{NG},\text{H}_2-\text{NG}}$	UHC
Error [%]	-0.13	-0.48	-0.94	-0.57	-2.74	-3.18	0.032	1.71

Following the above-described methodology of parametrization of H₂-NG combustion, Seiliger parameters, natural gas fuel mass, initial estimate of the air-excess ratio and UHC are derived for different percentages of hydrogen from the anode-off gas. Table 6.4 shows the Seiliger parameters 'a', 'b' and 'c' computed using the above parametric equations for 20H₂-NG fuel blend at 75 % load.

The H_2 -NG combustion and in-cylinder process for 20 H_2 -NG fuel blend at 75 % engine load is simulated by using the above-derived combustion parameters in the Seiliger process model described in previous chapter. Furthermore, the final values of natural gas fuel mass and UHC are also computed for the same operating condition using the parametric equations. Table 6.5 provides the error between simulated and measured performance variables for 20 H_2 -NG fuel blend at 75 %. Figure 6.1 shows the comparison between the predicted and the measured values of in-cylinder pressure and temperature using the Seiliger modelling approach. The in-cylinder temperature values are obtained from the HRR model described in Chapter 5.

As seen from Table 6.5 and Figure 6.1, the Seiliger-based modelling combined with the multivariable regression equations is able to accurately estimate the performance parameters, which is crucial in order to capture the effects of hydrogen addition from anode-off gas. It is also important to accurately compute the work done and net combustion heat as these parameters are direct indicators of engine performance. Furthermore, estimation of these performance variables along with exhaust pressure and temperature at the end of expansion stroke is essential as they dictate the turbocharger performance and also turbine outlet temperature, which can be critical for system integration with the SOFC.

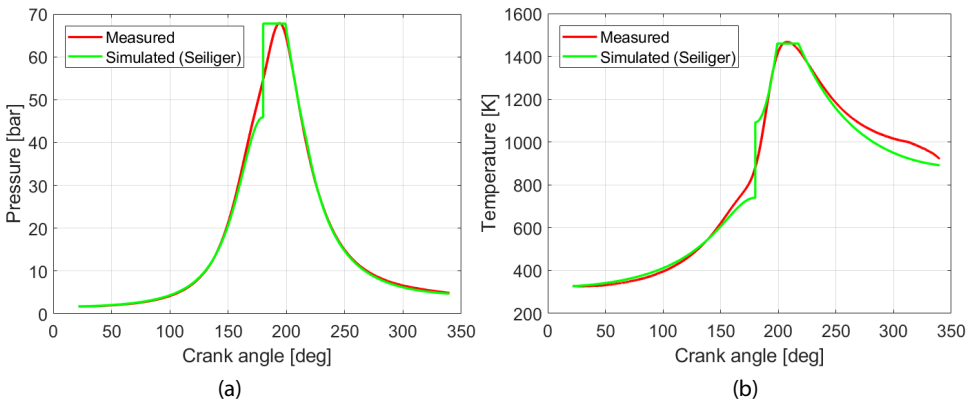


Figure 6.1: Comparison between measured and simulated in-cylinder pressure (a) and temperature (b) using the Seiliger process modelling approach for 20 H_2 -NG fuel blend at 75 %

In this manner, the effects of different percentages of hydrogen in the SOFC anode-off gas on the in-cylinder process and engine performance can be captured and simulated by employing the Seiliger modelling approach in combination with the multivariable parametric equations.

6.1.2. PARAMETRIZATION OF CARBON DIOXIDE-NATURAL GAS COMBUSTION

In the previous subsection, effects of hydrogen from anode-off gas on the in-cylinder process were simulated. Similar to the methodology followed for hydrogen, engine experiments, HRR model, the Seiliger-based combustion characterization modelling approach and combustion parameterization were combined to capture the effects of car-

bon dioxide and natural gas fuel blends on the combustion process and in-cylinder process.

Like hydrogen, effects of CO₂ addition can be also studied as deviations in Seiliger and engine performance parameters relative to only natural gas performance. Using the Seiliger-based characterization process, deltas are computed for different percentages of CO₂ and load at 500 mgNm⁻³ of NOx. Figure 5.22 in Chapter 5 provides the three-dimensional surface representation of the variations in deltas of Seiliger parameters as a function of the normalized natural gas fuel mass and volumetric CO₂ percentage. To simulate the effects of CO₂-NG combustion, parametric equations are derived via multi-variable regression, which mathematically relates the delta or deviation in each combustion parameter due to carbon dioxide addition as a function of the normalized natural gas fuel mass ($m_{\text{NH,ONG}}^{\text{norm}}$) and the volumetric percentage of carbon dioxide (CO_{2v}) in the blend. The parametric equations for CO₂ substitution have the same generic form as that presented in equation 6.3. The polynomial regression coefficients r_i^{par} of parametric equation for CO₂ have been provided in Table 6.6 and Table 6.7 for the three Seiliger parameters, natural gas fuel mass, initial air-excess ratio and UHC. After calculating the delta for each parameter due to carbon dioxide addition, the absolute value of the parameters based on regression for the corresponding CO₂-NG fuel blend is calculated by using equation 6.4 adopted for CO₂.

Table 6.6: Part I: Parametric regression equation coefficients for CO₂-NG fuel blends

Parameter	r_0^{par}	r_1^{par}	r_2^{par}	r_3^{par}
$\Delta a_{\text{Seil,CO}_2\text{-NG}}$	-0.07639	0.2275	-0.2426	-0.1414
$\Delta b_{\text{Seil,CO}_2\text{-NG}}$	0.03385	-0.05966	-0.06964	0.01828
$\Delta c_{\text{Seil,CO}_2\text{-NG}}$	0.03342	-0.2332	1.098	0.171
$\Delta m_{\text{NG,CO}_2\text{-NG}}$	1.888e-06	-2.812e-06	8.688e-06	8.605e-07
$\Delta \lambda_{\text{initial,CO}_2\text{-NG}}$	0.01205	-0.156	1.182	0.0675
$\Delta \text{UHC}_{\text{CO}_2\text{-NG}}$	-0.01053	-136.4	-2082	102.5

Table 6.7: Part II: Parametric regression equation coefficients for CO₂-NG fuel blends

Parameter	r_4^{par}	r_5^{par}
$\Delta a_{\text{Seil,CO}_2\text{-NG}}$	0.06626	0.894
$\Delta b_{\text{Seil,CO}_2\text{-NG}}$	0.25	-0.258
$\Delta c_{\text{Seil,CO}_2\text{-NG}}$	-0.5117	-2.81
$\Delta m_{\text{NG,CO}_2\text{-NG}}$	8.285e-06	-3.919e-05
$\Delta \lambda_{\text{initial,CO}_2\text{-NG}}$	-0.0163	-7.177
$\Delta \text{UHC}_{\text{CO}_2\text{-NG}}$	985.6	6055

Using the above-discussed methodology of parametrization of CO₂-NG combustion, the final values of Seiliger parameters, natural gas fuel mass and UHC are derived for different percentages of CO₂. Table 6.8 shows the simulated values of Seiliger parameters for 20CO₂-NG fuel blend at 50 % engine load. Figure 6.2 shows the in-cylinder process

simulated for the above operating condition by using the computed Seiliger parameters in the Seiliger process model. Furthermore, Table 6.9 presents the error percentages for UHC and the mass of natural gas computed using the parametric regression equations along with errors for other in-cylinder performance parameters.

Table 6.8: Derived Seiliger parameters based on combustion parametrization for 20CO₂-NG fuel blend and 500 mgN m⁻³ NO_x at 50 % load

Seiliger Parameter	a	b	c
Value	1.4198	1.435	1.6715

Table 6.9: Error percentages between the predicted and measured values of performance parameters 20CO₂-NG fuel blend and 500 mgN m⁻³ NO_x at 50 % load

Parameter	p _{max}	T _{max}	Work	Q _{net}	p ₆	T ₆	m _{NG,CO₂-NG}	UHC
Error [%]	-0.64	-0.14	-2.55	-2.46	-5.93	-5.77	0.14	5.71

As seen from Figure 6.2, the combination of Seiliger modelling and multivariable regression is able to capture the in-cylinder process for CO₂ blending. The performance parameters are satisfactorily estimated with a maximum error percentage of about 6 % for exhaust temperatures at the point of exhaust valve opening. On comparison with error percentages found during H₂-NG combustion parametrization, CO₂-NG combustion parameterization showed slightly higher errors. This could be attributed to the Chapter 5 finding of delta in parameters not showing a single directional trend due to CO₂ addition. As explained earlier, the strong countering effects of the air-to-fuel ratio and CO₂ addition on the in-cylinder process resulted in positive and negative delta values for the parameters. Thus, the regression fit for CO₂-NG combustion parameterization is adversely impacted, however, the variations due to CO₂ addition are small and can be captured with satisfactory accuracy as seen from Table 6.9 and Figure 6.2.

In this manner, the individual effects of hydrogen and carbon dioxide percentages from SOFC anode-off gas on the in-cylinder process are simulated. These individual effects of both the anode-off gas constituents are combined to capture the in-cylinder process of the engine operating on different blends of hydrogen and carbon dioxide from anode-off gas. As mentioned earlier, the effects of carbon monoxide from the anode-off gas were not taken into consideration in this phase of the research.

6.1.3. ANODE-OFF GAS AND NATURAL GAS BLEND COMBUSTION

For SOFC-ICE integration, effects of blending and combusting anode-off gas with natural gas need to be captured. Based on the compositions provided in Table 3.2 of Chapter 3, combined effects of combusting hydrogen and carbon dioxide together with natural gas are simulated and compared with experiments in this section. For this reason, engine experiments were also performed for three different blends of hydrogen, carbon dioxide and natural gas given in Table 6.10 at 75 % load and 500 mgN m⁻³ of NO_x. Composition 1 and 2 replicate the anode-off gas composition available at fuel utilization of 75 % while composition number 3 corresponds to a much higher fuel utilization with a

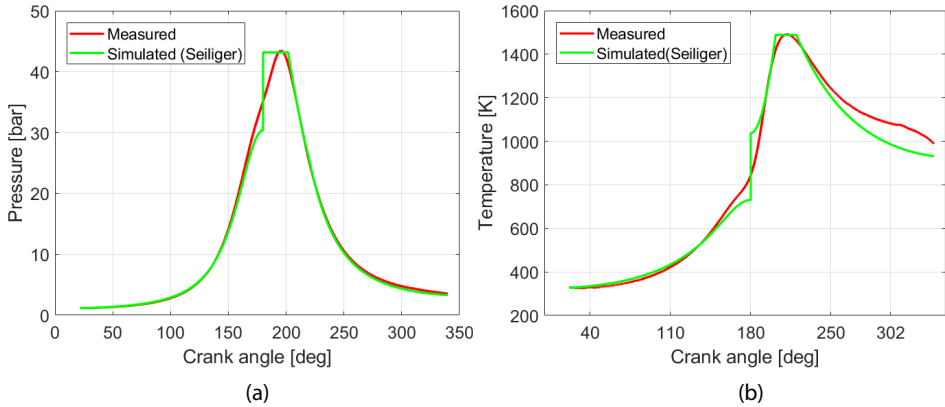


Figure 6.2: Comparison between measured and simulated in-cylinder pressure (a) and temperature (b) using the Seiliger process modelling approach for 20CO₂-NG fuel blend at 50% load

CO₂ to H₂ ratio of 1.9. Thus, these experimentally tested fuel blends of hydrogen, carbon dioxide and natural gas emulate the SOFC anode-off gas and natural gas fuel blends entering the engine.

6

Table 6.10: Tested AOG-NG fuel blends for 500 mgN m⁻³ of NO_x at 75% load

Composition No	H ₂ [Vol. %]	CO ₂ [Vol. %]	NG [Vol. %]
1	15	15	70
2	12.65	12.65	74.7
3	9.2	17.5	73.3

The discussions in the previous sections show that the effects of hydrogen and carbon dioxide on the in-cylinder process can be captured as deviations from the only natural gas performance. Following this approach, the effects of combusting a blend of hydrogen, carbon dioxide and natural gas can be simulated as a combined effect of deviations due to hydrogen and carbon dioxide relative to only natural gas combustion. Therefore, the parametric equations presented in the preceding subsections are used to estimate the deviations due to hydrogen and carbon dioxide for the combined effects of blending hydrogen and carbon dioxide together with natural gas. As explained earlier, the combined blend of hydrogen and carbon dioxide forms the anode-off gas, which replaces natural gas going into the engine. The value of Seiliger and performance parameters for anode-off gas - natural gas blends depicted in Table 6.10 are computed by using equation 6.5.

$$\text{par}_{\text{AOG-NG}} = \Delta \text{par}_{\text{H}_2\text{-NG}} + \Delta \text{par}_{\text{CO}_2\text{-NG}} + \text{par}_{\text{ONG}} \quad (6.5)$$

To simulate the in-cylinder process of the engine operating on anode-off gas-natural gas blends, the delta in parameters for hydrogen and carbon dioxide percentages in equation 6.5 are calculated by using the parametric equations derived in section 6.1.1 and section 6.1.2. The derived parametric equations are for individual hydrogen and car-

bon dioxide percentages relative to 100 % natural gas. Therefore, for a combined blend of hydrogen, carbon dioxide and natural gas, the percentage of hydrogen and carbon dioxide are recalculated relative (rel) to 100 % natural gas and substituted in equation 6.5 to estimate the delta in parameters. Equation 6.6 and equation 6.7 give the recalculated blend percentages relative to 100 % natural gas.

$$H_{2v,rel} = \frac{H_{2v}}{100 - (H_{2v} + CO_{2v})} \quad (6.6)$$

$$CO_{2v,rel} = \frac{CO_{2v}}{100 - (H_{2v} + CO_{2v})} \quad (6.7)$$

where, ' H_{2v} ', and ' CO_{2v} ', correspond to the volumetric percentages of hydrogen and carbon dioxide provided in Table 6.10.

In this manner, the delta in Seiliger and performance parameters for AOG-NG blends provided in Table 6.10 are calculated by using the relative values of hydrogen and carbon dioxide percentages in the derived parametric equations. The final values of the parameters for these blends are computed by using equation 6.5. Table 6.11 shows the values of the estimated Seiliger parameters and natural gas fuel mass for the three compositions relative to only natural gas performance at 75 % engine load. Table 6.11 also shows the measured natural gas fuel mass for the purpose of comparison.

Table 6.11: Derived Seiliger parameters and natural gas fuel mass based on combustion parameterization for ONG fuel and the three anode-off gas and natural gas fuel compositions provided in Table 6.10 at 500 mgNm⁻³ NOx and 75 % load

Composition	a	b	c	m_{NG}^{sim} [kg]	m_{NG}^{meas} [kg]
ONG	1.3643	1.452	1.7917	2.9025e-4	2.9029e-4
1	1.4953	1.3517	1.6322	2.6058e-4	2.6465e-4
2	1.4637	1.3658	1.7022	2.6666e-4	2.6818e-4
3	1.4513	1.3945	1.6943	2.7298e-4	2.7877e-4

As seen from Table 6.11, the measured and estimated natural gas fuel mass match well. The natural gas fuel mass is the least for composition 1, due to the maximum amount of hydrogen percentage. The values of natural gas fuel mass for the three tested compositions are lower than the value for ONG performance, which indicates improved engine efficiency. The estimation of engine efficiency for varying fuel compositions has been presented in section 6.3. Furthermore, the Seiliger parameters follow expected trends as the tested fuel blends exhibit a higher value of 'a' compared to ONG performance. Seiliger parameter 'b' decreases signifying improved combustion stability and combustion rate because of hydrogen. In addition to hydrogen, carbon dioxide can also play a positive role due to the counter effect provided by richening of air-fuel mixture increasing the combustion rate and combustion stability as explained in the previous chapter. Lastly, the Seiliger parameter 'c' evidently is lower for the hydrogen, carbon dioxide and natural gas fuel blends compared to only natural gas, thus, depicting less late combustion at constant NOx operation. Seiliger parameters 'b' and 'c' are a result of the complex interaction during the combustion process between hydrogen, carbon dioxide, natural gas and air present in the incoming air-fuel charge.

Table 6.12: Error percentages between the predicted and measured values of performance parameters for the three anode-off gas and natural gas fuel compositions provided in Table 6.10 at 500 mgNm^{-3} NOx and 75 % load

Composition	p_{max} [%]	T_{max} [%]	Work [%]	Q_{net} [%]	p_6 [%]	T_6 [%]
1	1.06	1.61	0.94	-0.28	-4.07	-4.42
2	-0.20	0.77	0.54	-0.06	-3.94	-4.2
3	-0.29	1.77	1.48	0.96	-2.6	-2.76

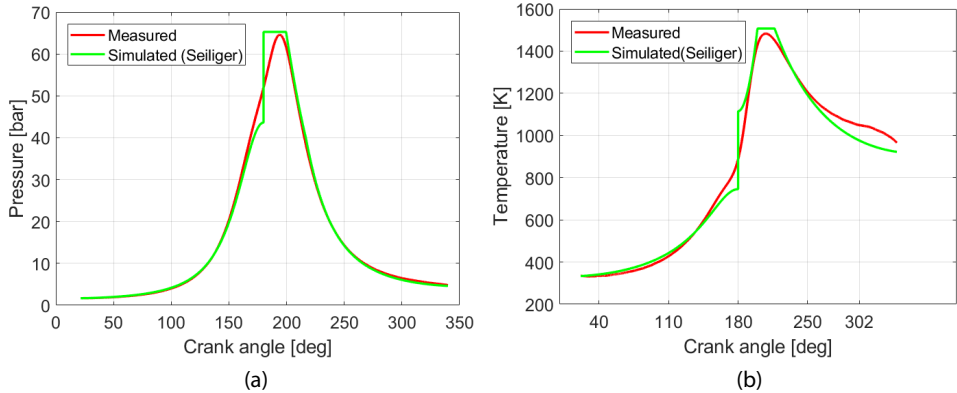


Figure 6.3: Comparison between measured and simulated in-cylinder pressure (a) and temperature (b) using the Seiliger process modelling approach for 15% H_2 -15% CO_2 -70% NG fuel blend at 75 % load

In order to capture the in-cylinder process for the anode-off gas and natural gas fuel blends, the above derived Seiliger parameters are used in the Seiliger process model. The simulated in-cylinder pressures and temperatures are compared against engine measurements for the validation of methodology and the parametric equations. Engine performance variables obtained from the Seiliger process model are compared against values obtained from measurements and presented in Table 6.12 for further validation. Figure 6.3 shows the comparison between the measured and simulated in-cylinder process for composition 1 of the anode-off gas and natural gas fuel blend from Table 6.10. The comparison against measurements for composition 2 and 3 has been provided in Appendix D.

It is evident from Figure 6.3 and Table 6.12 that the simulated engine performance for the tested AOG-NG fuel blends matches well with the measurements. Therefore, the combination of first-principle Seiliger modelling approach and parametric equations for each anode-off gas constituent is used to model the in-cylinder process for anode-off gas and natural gas fuel blends. By combining the Seiliger closed-cycle in-cylinder model with an open-cycle mean value model, a wholistic engine performance model for AOG-NG fuel blends is developed to study SOFC-ICE integration.

6.2. AOG-NG MVEM

To integrate the SOFC with the engine in the proposed system, heat from the engine exhaust is required to manage the heat balance within the system. The impact of AOG-NG fuel blends on turbocharging needs to be understood as turbocharger matching impacts engine performance, dynamic capabilities and the heat available in the engine exhaust. The engine model also simulates engine control that helps in meeting the required engine load, which is crucial for capturing the engine performance at different loads and also for efficiency calculations. Furthermore, engine emissions need to be estimated to fully investigate the potential of such a system for maritime applications. Therefore, an open-cycle mean value engine model (MVEM) in combination with the Seiliger closed in-cylinder process model is developed to capture the complete performance of an AOG-NG engine. The AOG-NG engine is capable of operating on only natural gas, natural gas blended with hydrogen, natural gas blended with carbon dioxide and natural gas blended with hydrogen and carbon dioxide or the AOG-NG fuel blends. The current section describes the mean value engine model for simulating the complete engine performance with AOG-NG fuel blends, which is crucial for SOFC-ICE integration. In the following subsections, first, an overview of the MVEM has been presented followed by the equations used in the MVEM.

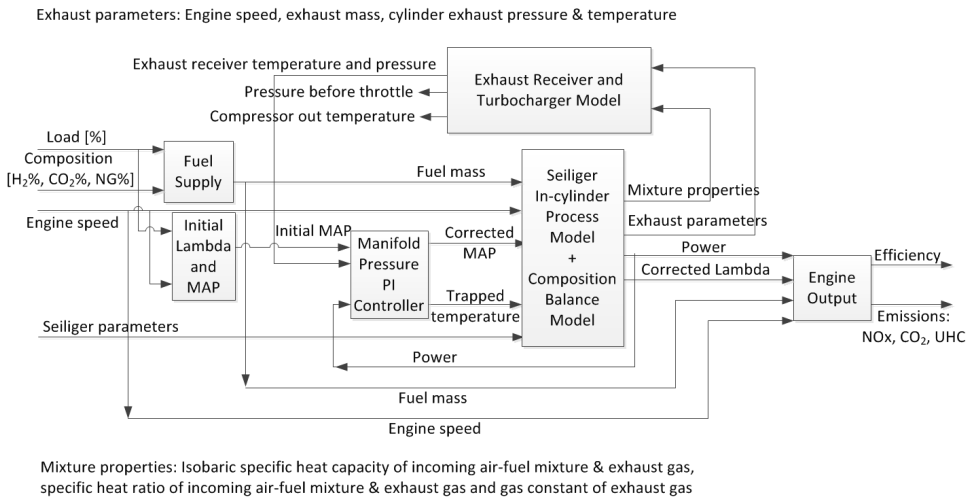


Figure 6.4: Schematic representation of AOG-NG mean value engine model

Figure 6.4 shows the schematic representation of the MVEM. The model inputs for the MVEM are load percentage, fuel composition and engine speed. Based on the fuel composition and load setpoint, the model calculates the incoming fuel mass by employing the parametric equations derived in the previous sections. Similarly, the model estimates the Seiliger parameters, which are used in the Seiliger process model to simulate the in-cylinder process. The in-cylinder process model computes the closed-cycle work ($w_{\text{cycle,seil}}$) done per cylinder per unit trapped mass (m_1) by using the Seiliger process. To account for the gas exchange, a defined percentage of the closed-cycle work is

assumed to be lost as pumping work loss ($w_{\text{cycle,pump}}$). The defined gas exchange percentage is estimated from in-cylinder pressure measurements and derived as a function of engine loading. Closed-cycle work minus the gas exchange gives the indicated work, which on multiplying by firing frequency (f), trapped mass, generator efficiency (η_{gen}) and mechanical efficiency (η_{mech}) gives the simulated brake power (P_{ICE}). The brake power produced by the engine is estimated from equation 6.8.

$$P_{\text{ICE}} = m_1 \cdot (w_{\text{cycle,seil}} - w_{\text{cycle,pump}}) \cdot f \cdot \eta_{\text{mech}} \cdot \eta_{\text{gen}} \quad (6.8)$$

The closed-cycle work is a summation of the work during each stage of the Seiliger cycle as explained in the previous chapter. The trapped pressure estimation is required to compute the trapped mass, in-cylinder pressures and temperatures, which are used to estimate the closed-cycle work, net combustion heat and brake power. In this research, trapped pressure is assumed to be equal to the manifold pressure after the throttle. The initial value of manifold pressure is derived from fuel flow rate and an initial estimation of air-excess ratio. Subsection 6.2.1 presents the derivation of initial manifold pressure. As explained earlier, the fuel flow rate is accurately calculated from the parametric equations derived in the previous section. The parametric equations are also used to calculate the initial value of air-excess ratio for a fixed load percentage and fuel composition as described in the previous section.

Besides work and heat, the Seiliger in-cylinder process model also simulates the exhaust parameters such as temperature, pressure and in-cylinder mass at the point of exhaust valve opening. Since the modelled test engine has a zero valve overlap, the sum of fuel and air mass at trapped condition amount to the total mass exiting the cylinder, however, the composition inside the cylinder changes due to combustion. The change in mass and composition during each Seiliger stage is computed by the mass and composition balance model, which has been described in subsection 6.2.2. Mixture properties such as gas constants and specific heat capacities are calculated as a function of composition and temperature [2]. The exhaust parameters and mixture properties listed in Figure 6.4 are used as inputs for the turbocharger and exhaust receiver model. A description of these models has been presented in subsection 6.2.4. In the AOG-NG MVEM, the effect of two parallel turbochargers, one for each cylinder bank, shown in Figure 4.1 of Chapter 4 is simulated by one large turbocharger for the entire engine. The turbocharger and exhaust receiver model solve for the exhaust temperatures, pressures, charge pressure after the compressor or before the throttle and compressor outlet temperature using the zinner blowdown, Büchi balance and elliptical law. The computed pressure and temperature in the exhaust receiver are used to estimate the trapped temperature, which is given by equation 6.28 presented in subsection 6.2.3.

Based on the above description and model equations described in next subsections, the MVEM runs a pre-simulation for an initial estimate of the complete engine performance. The pre-simulation, along with other engine performance variables, gives an estimate of the initial brake-power, which is compared against the input load set-point. The pre-simulation under or overestimates the brake power due to deviations in estimation of work and initial trapped mass. If the MVEM engine estimates a lower value of brake power then, the manifold pressure (MAP) controller shown in Figure 6.4 opens the throttle valve to allow an increased intake of air-fuel charge. The increased air-fuel

charge raises the trapped pressure and trapped mass, which also increases the brake power. The proportional and integral (PI) manifold pressure controller keeps opening the throttle valve till the estimated brake power matches the required load set-point. In case of a higher initial estimation of the brake power, the PI controller closes the throttle valve till the brake power delivered by the engine reduces and matches the set load point. This modelling approach of engine operation is similar to the engine control on the real engine, which operates the throttle valve based on mapped values of air-excess ratio, MAP and gas flow obtained from extensive trial runs. In this model, the mapped values are replaced by parametric equations obtained from regression using 21 operating points for three engine loads and different blends of hydrogen and carbon dioxide with natural gas.

For every changing value of MAP until the brake power matches, the MVEM iteratively resimulates the outputs of the submodels shown in Figure 6.4 and, hence, engine performance. These iterative simulations of the MVEM can be understood in the following manner. For every change in value of manifold pressure, a new value of air-excess ratio is computed considering the fuel mass estimation to be accurate and fixed based on the parametric equation. At each step, the changing MAP changes the trapped mass, trapped temperature, air-excess ratio, mass balance, composition balance, in-cylinder pressures, temperatures, turbocharger performance and emissions. The final and corrected value of manifold pressure and air-excess ratio correspond to the iteration for which simulated brake-power is equal to the required load. The MVEM resimulates the engine performance for this final iteration based on the final value of MAP and air-excess ratio, by solving the equations for the Seiliger in-cylinder process model, mass and composition balance model and the turbocharger plus exhaust receiver model. Furthermore, the new and final air-excess ratio value is also used to calculate the final values of engine exhaust emissions. The equations for calculating the engine exhaust emissions have been covered in subsection 6.2.5. In addition to the engine emissions, engine efficiency is also calculated as model output by using equation 6.9.

$$\eta_{ICE} = \frac{P_{ICE}}{\dot{m}_{fuel} \cdot LHV_{fuel}} \quad (6.9)$$

where, 'P_{ICE}' is the brake engine power in kW. 'm_{fuel}' is the total fuel flow rate in kg s⁻¹ and 'LHV' is the lower heating value of the fuel calculated in kJ kg⁻¹. Fuel properties such as stoichiometric air-fuel ratio, density and lower heating value for the engine model are based on fuel composition and vary with changing percentages of hydrogen, carbon dioxide and natural gas in the fuel. This concludes the MVEM overview while the MVEM submodels and equations are described in more detail in the next subsections.

6.2.1. INITIAL ESTIMATION OF MANIFOLD PRESSURE

Manifold pressure is the pressure after the throttle valve in the manifold. It is assumed to be equal to the trapped pressure and plays an important role in accurate estimation of the closed-cycle work, trapped mass and engine brake power. The pre-simulation run estimates the initial value of MAP as a function of initial air-excess ratio and gas flow. The derivation of initial MAP is as follows:

For the condition after the throttle valve, initial value of MAP can be computed by

applying the ideal gas law given in equation 6.10

$$\text{MAP}_{\text{initial}} = \frac{m_{\text{mix}} \cdot R_{\text{mix}} \cdot \text{MAT}_{\text{initial}}}{V_{\text{MAN}}} \quad (6.10)$$

where, ' m_{mix} ' is the mass of air-fuel mixture after the throttle measured in kg. 'R' is the gas constant of the trapped mixture in $\text{kJ kg}^{-1} \text{K}^{-1}$, ' $\text{MAT}_{\text{initial}}$ ' is the initial manifold temperature measured in K and ' V_{MAN} ' is manifold volume in m^3 . In equation 6.10, the gas constant and manifold temperature are kept constant at a value corresponding to ONG performance at 75% load while the manifold volume is calculated from the manifold length and diameter. Manifold length and diameter are expressed as a function of the cylinder diameter.

To derive the value of initial MAP, manifold mixture mass is estimated in the following manner. The air-fuel mixture mass can be written as a product of the mixture density (ρ_{mix}) in kg m^{-3} and the total air-fuel mixture flow (F_{mix}) measured in m^3 . The total air-fuel flow is a sum of the fuel flow (F_{fuel}) and air flow (F_{air}) after the throttle as shown in equation 6.12.

$$m_{\text{mix}} = \rho_{\text{mix}} \cdot F_{\text{mix}} \quad (6.11)$$

$$F_{\text{mix}} = F_{\text{air}} + F_{\text{fuel}} \quad (6.12)$$

In equation 6.12, the total air flow is estimated by multiplying the volumetric fuel flow with the air-fuel ratio based on volume. The volume-based air-fuel ratio can be written as a function of the air-excess ratio (λ) and the volume-based stoichiometric air-fuel ratio (σ_{vol}). Thus, the air flow is estimated by applying the following equation.

$$F_{\text{air}} = F_{\text{fuel}} \cdot \sigma_{\text{vol}} \cdot \lambda_{\text{initial}} \quad (6.13)$$

The initial estimation of air-excess ratio used in equation 6.13 is obtained from the parametric equations derived for air-excess ratio as discussed earlier. Equation 6.13 is substituted in equation 6.12 to estimate the total mixture flow, which is further used to calculate the total mixture mass given by the adapted equation 6.15.

$$F_{\text{mix}} = F_{\text{fuel}} \cdot (1 + \sigma_{\text{vol}} \cdot \lambda_{\text{initial}}) \quad (6.14)$$

$$m_{\text{mix}} = \rho_{\text{mix}} \cdot F_{\text{fuel}} \cdot (1 + \sigma_{\text{vol}} \cdot \lambda_{\text{initial}}) \quad (6.15)$$

In order to calculate the mixture mass, density of the mixture is estimated as a sum of the products of density and volume fraction for fuel and air. The volume fractions are further written as a function of the fuel, air and total flow present in the manifold as given in equation 6.16

$$\rho_{\text{mix}} = \rho_{\text{fuel}} \cdot \frac{F_{\text{fuel}}}{F_{\text{mix}}} + \rho_{\text{air}} \cdot \frac{F_{\text{air}}}{F_{\text{mix}}} \quad (6.16)$$

Equation 6.16 is rewritten as a function of the volume-based stoichiometric air-fuel ratio and air-excess ratio by substituting the fuel and air flow fractions from equation 6.15.

$$\rho_{\text{mix}} = \rho_{\text{fuel}} \cdot \frac{1}{(1 + \sigma_{\text{vol}} \cdot \lambda_{\text{initial}})} + \rho_{\text{air}} \cdot \frac{1}{\left(\frac{1}{\sigma_{\text{vol}} \cdot \lambda_{\text{initial}}} + 1\right)} \quad (6.17)$$

By using equation 6.17 for density calculation in equation 6.15, the total mixture mass can be estimated. In equation 6.15, the fuel flow is estimated from fuel density and fuel mass. The fuel mass is computed by using the derived parametric equations in section 6.1.1, section 6.1.2 and section 6.1.3 for the given load point, hydrogen and carbon dioxide percentage in the fuel.

By substituting equation 6.15 in equation 6.10, the initial MAP value for the pre-simulation is estimated from the initial air-excess ratio and fuel flow as given by equation 6.18.

$$\text{MAP}_{\text{initial}} = \frac{\rho_{\text{mix}} \cdot F_{\text{fuel}} \cdot (1 + \sigma_{\text{vol}} \cdot \lambda_{\text{initial}}) \cdot R_{\text{mix}} \cdot \text{MAT}_{\text{initial}}}{V_{\text{MAN}}} \quad (6.18)$$

The derived initial value of MAP is further used for initial estimation of the trapped mass in the pre-simulation by applying the ideal gas law for the condition of inlet valve opening.

6.2.2. SEILIGER PROCESS, MASS AND COMPOSITION BALANCE MODEL

To simulate the in-cylinder process, thermodynamic relations for each stage of Seiliger cycle based on MAP or trapped pressure and the Seiliger parameters are used to calculate the volume, pressure and temperature at the beginning and end of each stage. The Seiliger cycle and the computation of work and heat quantities during each stage have been covered in the previous chapter. The Seiliger parameters are estimated based on the load percentage and fuel composition by employing the parametric equations derived earlier. In the Seiliger process model, work and heat quantities are made specific by dividing by trapped mass. The summation of specific work during each stage gives the closed-cycle work while the summation of heat during the three stages of combustion gives the net combustion heat released. As described in the previous chapter, heat ratios for each combustion stage are estimated by dividing the released heat during each stage by the net combustion heat. The heat ratio of each stage signifies the percentage of heat released during that stage of combustion. A detailed description of the Seiliger process model and its equations can be found in previous chapter.

For the pre-simulation, the model estimates all the initial properties of the in-cylinder process based on the initial value of MAP and Seiliger parameters. During the pre-run, the model calculates the effective work and the initial estimation of the brake power. The MAP controller compares this initial estimation of brake power against the required load to activate the throttle valve and run the main simulation as explained in beginning of section 6.2. In order to calculate the work and heat release during each Seiliger stage along with the total closed-cycle work, the pre-simulation estimates the mass and composition balance at the trapped condition. The initial value of trapped mass is calculated from the preliminary MAP estimation explained in the previous subsection. To estimate the initial trapped mass by ideal gas equation, trapped temperature is fixed at value corresponding to ONG performance at 75 % load. The pre-run solves the following mass balance at trapped condition.

$$m_{\text{rg,t}} = m_{1,\text{initial}} - (m_{\text{air,t,initial}} + m_{\text{fuel}}) \quad (6.19)$$

where, 'm_{rg,t}' is the mass of residual gas per cycle per cylinder in kg. Residual gas is combustion gas trapped from previous cycle. 'm_{fuel}' is the mass of fuel per cylinder per

cycle in kg and is computed from the parametric equations described earlier. ' $m_{\text{air,t,initial}}$ ' is the initial mass of air, also in kg, and is derived by applying equation 6.20.

$$m_{\text{air,t,initial}} = m_{\text{fuel}} \cdot \sigma \cdot \lambda_{\text{initial}} \quad (6.20)$$

where, ' σ ' is the mass-based stoichiometric air-fuel ratio. Using the initial estimations of the total mass and air mass along with fuel and residual gas mass at trapped condition, mass fractions for fuel, air and residual gas are computed by using the following equations.

$$x_{\text{air,t,initial}} = \frac{m_{\text{air,t,initial}}}{m_{1,\text{initial}}} \quad (6.21)$$

$$x_{\text{fuel,initial}} = \frac{m_{\text{fuel}}}{m_{1,\text{initial}}} \quad (6.22)$$

$$x_{\text{rg,t,initial}} = \frac{m_{\text{rg,t}}}{m_{1,\text{initial}}} \quad (6.23)$$

The modelled test engine has a zero valve overlap, therefore, the amount of trapped residual gas is high. Based on measurements, the mass fraction of residual gas was found to be higher than 15%. High amount of trapped residual gas can impact the heat release and the in-cylinder temperatures along with NOx emissions. Therefore, the high percentage of residual combustion gas needs to be taken into account for modelling the in-cylinder process. Based on the above-computed compositions at trapped condition, the model calculates the mixture properties during the in-cylinder process. Gas constant and isobaric specific heat capacity are calculated as a summation of the products of trapped species compositions and their corresponding gas constants and specific heat capacities at constant pressure. Specific heat capacity at constant volume is the difference between gas constant and isobaric specific heat capacity while the ratio of the two heat capacities gives the specific heat capacity ratio (γ). These mixture properties along with the initial MAP and Seiliger parameters are used in the pre-simulation to solve the Seiliger process model. The initial solution of the Seiliger process model gives the initial estimate of the brake power along with heat ratios for each stage, which are needed for the main simulation.

The specific heat ratios ($q_{\text{lm,ratio}}$) are an indicator of the heat released during each stage of combustion, where 'l' and 'm' signify the stage boundary. For instance, $q_{23,\text{ratio}}$ corresponds to the specific heat ratio for the isochoric combustion stage of the Seiliger cycle depicted in Figure 5.4(a) of the previous chapter. The combustion heat released during each stage is proportional to the fuel mass burnt during each stage. Therefore, heat ratio is equivalent to the mass fraction of fuel combusted during each stage. In the main simulation, the heat ratios computed during the pre-simulation are used to compute the fuel mass combusted during each combustion stage as given by equation 6.24.

$$m_{\text{fuel,lm}} = q_{\text{lm,ratio}} \cdot m_{\text{fuel}} \quad (6.24)$$

where, ' $m_{\text{fuel,lm}}$ ' is the fuel mass in kg combusted during the corresponding combustion stage 'l-m'. Using the estimated fuel mass combusted during each combustion stage, the

following mass balance is solved for the combustion stages to compute the changes in air, fuel and combustion gas during combustion.

$$m_{\text{air,lm}} = m_{\text{air,t}} - m_{\text{fuel,lm}} \cdot \sigma \quad (6.25)$$

$$m_{\text{cg,lm}} = m_{\text{rg,t}} + m_{\text{fuel,lm}} \cdot (\sigma + 1) \quad (6.26)$$

$$m = m_{\text{air,lm}} + m_{\text{fuel,lm}} + m_{\text{cg,lm}} = m_1 \quad (6.27)$$

Equation 6.27 sets the condition that the total mass in each stage and in the cylinder always remains constant and equal to trapped mass assuming there are zero blow-by and crevice losses. In the main simulation, the trapped amount of fuel, air and residual gas change with each iteration as the changing MAP also changes the trapped mass. This change in MAP, trapped temperature and air-excess ratio is further discussed in section 6.2.3 Using the total mass and the mass of each species during each stage, mass fractions of air, fuel and gas are recalculated for each stage using equations 6.21 to 6.23. Species compositions during the compression stage are equal to compositions during trapped condition while during the expansion stage compositions are equal to the values computed during the isothermal combustion stage. Based on these changing mass fractions, mixture properties are calculated in the mass and composition balance model for each iteration, which are used to resimulate the Seiliger-based in-cylinder process with the changing trapped pressure and mass. The mixture properties and the exhaust parameters computed during each iteration of the main simulation are directed as inputs to the turbocharger model as shown in Figure 6.4.

6.2.3. CHANGING MAP, TRAPPED TEMPERATURE, MASS AND AIR-EXCESS RATIO

In the main simulation, the opening or closing of the throttle valve changes the value of MAP for each iteration. With changing MAP, the model recalculates the trapped temperature, trapped mass, air-excess ratio and trapped species compositions. For every new value of MAP, a new value of trapped temperature is calculated for the zero valve overlap engine by using equation 6.28. Equation 6.28 is the same as equation 5.13.

$$\frac{1}{T_1} = \frac{V_{\text{IC}} - V_{\text{IO}}}{V_{\text{IC}} \cdot T_{\text{ind}}} + \frac{V_{\text{EC}} \cdot P_d}{V_{\text{IC}} \cdot \text{MAP} \cdot T_d} \quad (6.28)$$

where, ' V_{IC} ', ' V_{IO} ' and ' V_{EC} ' are the cylinder volumes in m^3 at inlet valve closing, inlet valve opening and exhaust valve opening, respectively. ' P_d ' and ' T_d ' are the turbine inlet pressure in Pa and exhaust receiver temperature in K obtained from the turbocharger model. ' T_{ind} ' is the induction temperature, which accounts for the heat pick-up in the inlet duct as explained in the subsequent paragraph.

Trapped temperature inside a cylinder differs from the manifold temperature. MAT is the temperature in K of the mixture in the inlet manifold after the inter-cooler, however, the temperature of the incoming air-fuel charge rises as it travels through the manifold and is inducted into the cylinder during the inlet stroke. The final trapped temperature is a result of the increase in temperature due to heat pick-up from the inlet duct walls and also mixing with the hot residual combustion gases trapped from the previous cycle. As

explained earlier, and in the previous chapter, the modelled zero valve overlap engine has high amounts of trapped residual gases, which affect the trapped mixture temperature. Using the new value of trapped temperature computed from equation 6.28 and the new value of trapped pressure or MAP, corresponding value of trapped mass can be calculated from the ideal gas.

With the new value of trapped mass and pressure, the AOG-NG MVEM resimulates the in-cylinder process model and the turbocharger model explained in the next subsection. At the same time, the MVEM also estimates a renewed value of air-excess ratio during the iteration. After calculating the new trapped mass, the fuel mass calculated from the parametric equations and the residual gas mass calculated from equation 6.19 are assumed to remain the same. Therefore, the increase in trapped mass would be due to the increase in the mass of air caused by the opening of throttle valve. This assumption is supported by the fact that the amount of air required for combustion in the cylinder is significantly higher than the fuel and residual gas mass. With a fixed value of fuel and residual gas, the new value of trapped air mass ($m_{\text{air,t,new}}$) is calculated from equation 6.29

$$m_{\text{air,t,new}} = m_{1,\text{new}} - m_{\text{fuel}} + m_{\text{rg,t}} \quad (6.29)$$

where, ' $m_{1,\text{t,new}}$ ' is the new value of trapped mass in kg estimated in the main simulation. Based on the new value of trapped air mass, revised value of air-excess ratio is calculated by dividing the air mass with the product of fuel mass and stoichiometric air-fuel ratio. The new values of trapped air mass and total mass also change the trapped air, fuel and residual gas mass fractions by a small margin as the fractions are calculated by applying equations 6.21 to 6.23. As part of the butterfly effect, the mixture properties also change since they are based on the species composition.

In this manner, MAP, trapped conditions, air-excess ratio, in-cylinder process, mass and composition balance along with the turbocharger model outputs change until equilibrium is reached between the required and simulated power, which provides the final steady-state engine performance.

6.2.4. TURBOCHARGER AND EXHAUST RECEIVER MODEL

After the simulating in-cylinder process along with the mass and composition balance, the exhaust gas parameters such as cylinder mass per cylinder per cycle (m_1), speed (n) in rps, cylinder exhaust pressure (p_6) and cylinder exhaust temperature (T_6). Additionally, the in-cylinder submodel computes mixture properties such as isobaric specific heat capacity of incoming air-fuel mixture ($c_{p,\text{af}}$) and exhaust gas ($c_{p,\text{g}}$), specific heat capacity ratio of incoming air-fuel mixture (γ_{af}) and gas (γ_{g}) and gas constant of exhaust flow (R_{g}), which are used as inputs for the turbocharger and exhaust receiver model.

ZINNER BLOWDOWN

The Seiliger model simulates the closed in-cylinder process till the point of exhaust valve opening. After the exhaust valve opens, the in-cylinder mass (m_6) is assumed to instantly blowdown into the exhaust receiver based on the Zinner blowdown theory [3]. After the exhaust stroke or blowdown process, the pressure and the temperature of the mass still remaining inside the cylinder is equal to the blowdown pressure and blowdown temperature [3]. The blowdown temperature and pressure can be assumed to be equal to the

temperature and pressure in the exhaust receiver as there is no slip and scavenging due to zero valve overlap. Thus, temperature (T_d) and pressure (p_d) in the exhaust receiver are directly linked through the blowdown process and can be written as a function of the pressure and temperature at the point of exhaust valve opening. Equation 6.30 gives the mathematical representation of the zinner blowdown process to compute the blowdown temperature [3].

$$T_d = T_6 \cdot \left(\frac{1}{n_{\text{bld}}} + \frac{n_{\text{bld}} - 1}{n_{\text{bld}}} \cdot \frac{p_d}{p_6} \right) \quad (6.30)$$

where, ' n_{bld} ' is the polytropic expansion coefficient representing heat transfer to the cylinder, exhaust valve and manifold. The blowdown polytropic exponent is assumed to be equal to the polytropic expansion coefficient used in the Seiliger process model for the expansion stage (5-6) [4].

TURBINE FLOW AND PRESSURE CHARACTERISTIC

The exhaust gas pressure and mass flow at the turbine inlet dictate the turbine characteristics. In the modelled test engine, air and fuel enter the cylinders together through the manifold during the induction stroke. The trapped mass consists of air, fuel and residual gas from the previous cycles that takes part in the closed cycle. The mass exiting the cylinders can be assumed to be equal to the mass entering the cylinder since there is no slip in addition to the assumption of no blow-by and crevice losses. Therefore, the trapped mass flow times the number of cylinders can be assumed to be the flow through the turbine. The mass flow rate through the turbine is derived from equation 6.31 based on the ellipse law [3, 5].

$$\dot{m}_1 = \alpha \cdot A_{\text{eff}} \cdot \frac{p_d}{\sqrt{R_g \cdot T_d}} \cdot \sqrt{1 - \left(\frac{p_e}{p_d} \right)^2} \quad (6.31)$$

After squaring both the sides and rearranging the above equation 6.31, exhaust pressure can be written as follows [5]:

$$p_d = \sqrt{\frac{\dot{m}_1^2 \cdot R_g \cdot T_d}{\alpha^2 \cdot A_{\text{eff}}^2} + p_e^2} \quad (6.32)$$

where, ' α ' is the zinner turbine area factor, which is equal to 1 for a constant pressure turbocharging system [5]. ' A_{eff} ' is the effective turbine area in m and ' p_e ' is the pressure in Pa at the turbine outlet, which is equal to atmospheric pressure. To compute the turbine pressure and flow characteristics, equation 6.30 and equation 6.32 are combined and solved as a quadratic function given by equation 6.33 [5].

$$p_d^2 - \left[\frac{\dot{m}_1^2 \cdot R_g \cdot T_6 \cdot \left(\frac{n_{\text{bld}} - 1}{n_{\text{bld}}} \right)}{\alpha^2 \cdot A_{\text{eff}}^2 \cdot p_6} \right] \cdot p_d - \left[\frac{\dot{m}_1^2 \cdot R_g \cdot T_6 \cdot \frac{1}{n_{\text{bld}}}}{\alpha^2 \cdot A_{\text{eff}}^2} + p_e^2 \right] = 0 \quad (6.33)$$

BÜCHI BALANCE

In the developed AOG-NG MVEM, Büchi balance is used to solve the power balance between the compressor and the turbine. After determining the exhaust receiver pressures and temperatures, equation 6.34 is solved to determine the compressor outlet pressure

or charge pressure before the throttle (P_{bt}). Equation 6.34 is derived by equating the power delivered by the turbine to the power required by the compressor [3].

$$P_{bt} = \left[1 + \frac{c_{p,g}}{c_{p,af}} \cdot \delta \cdot \eta_{TC} \cdot \frac{T_d}{T_{amb}} \cdot \left(1 - \frac{1}{\frac{P_d}{P_e} \frac{\gamma_g^{-1}}{\gamma_{af}^{-1}}} \right) \right]^{\frac{\gamma_{af}^{-1}}{\gamma_{af}}} \cdot P_{amb} \quad (6.34)$$

where, the specific heat capacities and heat capacity ratios are computed in the mass and composition balance model. ' η_{TC} ' is the turbocharger efficiency, which is simulated as a quadratic function of the compressor outlet pressure in the model [6]. ' P_{amb} ' and ' T_{amb} ' are the atmospheric pressure in Pa and atmospheric temperature in K at the compressor inlet.

In equation 6.34, ' δ ' is the ratio of mass flow through the turbine to the mass flow through the compressor. The total mass at compressor outlet is calculated in the following manner. Equation 6.35 is used to compute the isentropic compressor outlet temperature ($T_{com,is}$) from compressor inlet conditions and compressor outlet pressure. Next, the MVEM computes the compressor outlet temperature (T_{com}) based on isentropic compressor efficiency ($\eta_{com,is}$). The isentropic compressor and turbine efficiencies are assumed as constant.

$$T_{com,is} = \frac{P_{bt}}{P_{amb}}^{\frac{\gamma_{af}^{-1}}{\gamma_{af}}} \cdot T_{amb} \quad (6.35)$$

$$T_{com} = \frac{T_{com,is} - T_{atm}}{\eta_{com,is}} + T_{amb} \quad (6.36)$$

$$m_{com} = \frac{P_{bt} \cdot V_{com,out}}{T_{com} \cdot R_{af}} \quad (6.37)$$

where, ' $V_{com,out}$ ' is the volume of the receiver in m^3 after the compressor outlet with the receiver length and diameter expressed as a function of the cylinder diameter. ' R_{af} ' is the gas constant of the incoming air-fuel mixture in $\text{kJ kg}^{-1} \text{K}^{-1}$.

EXHAUST GAS TEMPERATURE ESTIMATION

After solving the Büchi balance, the exhaust stack or turbine outlet temperature is determined by using the formulation given in equation 6.38 [5].

$$T_e = T_{e,id} - \frac{q_{hl,exh}}{c_{p,g}} \quad (6.38)$$

where, ' $T_{e,id}$ ' is the ideal turbine outlet temperature including turbine losses. The ideal turbine outlet temperature without heat loss is determined from the isentropic turbine efficiency ($\eta_{tur,is}$), turbine work and compressor work. The equation for estimating ' $T_{e,id}$ ' is as follows.

$$T_{e,id} = T_d - \frac{\eta_{tur,is}}{c_{p,g} \cdot \eta_{TC}} \cdot c_{p,af} \cdot \left(\frac{P_{bt}}{P_{amb}}^{\frac{\gamma_{af}^{-1}}{\gamma_{af}}} - 1 \right) \cdot T_{amb} \quad (6.39)$$

The nominal heat loss ($q_{hl,exh,nom}$) in turbine outlet duct is estimated as a product of the specific heat capacity of exhaust gas and the difference between the ideal turbine temperature and measured turbine temperature, which is fixed at 650 K. In equation 6.39,

($q_{hl,exh}$) is calculated from equation 6.40.

$$q_{hl,exh} = q_{hl,exh,nom} \cdot \frac{T_d - T_{amb}}{T_{d,nom} - T_{amb}} \cdot \frac{\dot{m}_{1,nom}}{\dot{m}_1} \quad (6.40)$$

where, ' $T_{d,nom}$ ' and ' $\dot{m}_{1,nom}$ ' is calculated during pre-simulation by using equation 6.30 for the nominal reference condition of ONG engine performance at 75 % load.

6.2.5. EMISSIONS

In the developed MVEM, the unburnt hydrocarbon emissions are computed from the parametric equations based on load, normalized natural gas fuel mass (load) and hydrogen, and carbon dioxide volumetric percentages. Determination of UHC is vital for natural gas engines, as methane is exhausted as UHC emissions. The global warming potential of methane is 23 times more than that of CO_2 . The other two serious emissions of natural gas engines are NO_x and carbon dioxide. As mentioned earlier, engine performance modelled in the current and next chapter is for 500 mgN m^{-3} at 5 % reference oxygen in the exhaust. Although the pollution emission mass concentration (pemc) of NO_x in mgN m^{-3} remains constant, it changes with respect to load, hydrogen percentage and carbon dioxide percentage when measured as specific emission (spe) in $\text{gkW}^{-1} \text{ h}^{-1}$. To compute the ' spe_{NO_x} ' value, ' $pemc_{NO_x}$ ' value at reference O_2 is converted to parts per million in volume (ppmv) by using equation 6.41 [7].

$$ppmv_{NO_x,5\%O_2} = \frac{pemc_{NO_x,5\%O_2}}{\rho_{NO_2}} \quad (6.41)$$

where, ' ρ_{NO_2} ' is the density of NO_2 and is equal to 2.05 kgm^{-3} . The ' $ppmv_{NO_x,5\%O_2}$ ' value of NO_x is converted to NO_x value in ppmv for the O_2 % in the exhaust corresponding to the simulated operating condition. Equation 6.42 gives the corrected value of NO_x in ppmv for the actual amount of O_2 or air present in the exhaust [7].

$$ppmv_{NO_x} = ppmv_{NO_x,5\%O_2} \cdot \frac{y_{O_2}^{a-in} - y_{O_2}^{g-out}}{y_{O_2}^{a-in} - y_{O_2}^{g-ref}} \quad (6.42)$$

where, ' $y_{O_2}^{a-in}$ ' is the volumetric percentage of oxygen in the incoming air and is equal to 20.95%. ' $y_{O_2}^{g-ref}$ ' is the 5 % reference oxygen. ' $y_{O_2}^{g-out}$ ' is the actual oxygen percentage in the exhaust and is calculated from the final value of air-excess ratio estimated in the Seiliger process, mass and composition balance model. ' $y_{O_2}^{g-out}$ ' is calculated from equation 6.43 [7].

$$y_{O_2}^{g-out} = \frac{y_{O_2}^{a-in} \cdot (1 - \lambda)}{\frac{1}{4} \cdot \frac{x_H^{fuel}}{M_H} \cdot \frac{M_{air}}{\sigma} - \lambda} \quad (6.43)$$

where, ' x_H^{fuel} ' is the mass fraction of hydrogen in the fuel and ' M_H ' is the molecular weight of hydrogen. Similarly, ' M_{air} ' is the molecular weight of air. Using the ' $ppmv_{NO_x}$ ' value, ' spe_{NO_x} ' is calculated by applying equation 6.44 [7].

$$spe_{NO_x} = \frac{ppmv_{NO_x}}{10^6} \cdot \frac{\rho_{NO_2}}{\rho_{gas}} \cdot (\lambda \cdot \sigma + 1 - 0.5 \cdot \frac{M_{H_2O}}{M_H} \cdot x_H^{fuel}) \cdot sfc \quad (6.44)$$

where, ' ρ_{gas} ' is the density of exhaust gas, which is equal to 1.362 kgm^{-3} [7]. ' $M_{\text{H}_2\text{O}}$ ' is molecular weight of water vapour in the exhaust. 'sfc' is the specific fuel consumption in $\text{gkW}^{-1} \text{h}^{-1}$.

In a similar manner, 'spe $_{\text{CO}_2}$ ' emission in $\text{gkW}^{-1} \text{h}^{-1}$ is also calculated using equation 6.44 adapted for carbon dioxide. For this purpose, density of CO_2 equal to 1.96 kgm^{-3} is used and 'ppmv $_{\text{CO}_2}$ ' is calculated from air-excess ratio using equation 6.45 [7].

$$\text{ppmv}_{\text{CO}_2} = \frac{x_{\text{C}}^{\text{fuel}}}{M_{\text{C}}} \cdot \left(\frac{1}{\frac{\sigma \cdot \lambda}{M_{\text{air}}} - 0.25 \cdot \frac{x_{\text{H}}^{\text{fuel}}}{M_{\text{H}}}} \right) \cdot 10^4 \quad (6.45)$$

where, ' $x_{\text{C}}^{\text{fuel}}$ ' is the mass fraction of carbon in fuel and ' M_{C} ' is the molecular weight of carbon.

This concludes the description of the AOG-NG mean value engine model. In the next section, the MVEM is validated against engine measurements and tested for varying test conditions that could not be studied experimentally.

6.3. AOG-NG MVEM VALIDATION AND POTENTIAL

To validate the above-described AOG-NG MVEM, engine performance is simulated for the three compositions listed in Table 6.10. Engine performance parameters such as air-excess ratio, charge pressure before throttle, manifold pressure, exhaust receiver pressure, exhaust receiver temperature and turbine outlet temperature are compared against measurements. Table 6.13 shows the error percentages between the measured and MVEM simulated performance parameters for different fuel blends. The MVEM is able to capture the engine performance with sufficient accuracy for the three AOG-NG fuel compositions at 75 % engine load. The maximum deviation was found to be 7 % for exhaust receiver. Other engine parameters were simulated with error percentages equal to or lower than 5 %.

Table 6.13: Simulated engine efficiency and error percentages between the simulated and measured values of performance parameters for the three anode-off gas and natural gas fuel compositions provided in Table 6.10 at 500 mgN m^{-3} NOx and 75 % load

Composition	η_{ICE} [%]	λ [%]	p_{bt} [%]	MAP [%]	p_{d} [%]	T_{d} [%]	T_{e} [%]
1	34.47	1.54	3.16	2.82	7.07	-0.2289	-3.28
2	34.17	0.81	3.38	3.75	6.46	-1.78	-5.17
3	33.80	0.58	2.57	2.21	7.29	1.51	-2.07

Table 6.13 also shows the simulated engine efficiencies for the three fuel compositions. The simulated and measured engine efficiency for ONG performance at 75 % load is 33.68 %. Composition 1 with 15 % hydrogen and 15 % carbon dioxide blend showcases the highest efficiency. The efficiency decreases with an increasing percentage of carbon dioxide with no significant penalty due to high CO_2 percentages at high fuel utilizations of 85 %. Therefore, the simulations show that the AOG-NG engine is able to sustain the performance without engine derating and with possible efficiency improvements for different AOG-NG compositions based on SOFC fuel utilizations.

In addition to comparing simulation results against engine measurements, simulations were performed for test cases that could not be tested experimentally. These additional test cases are used to further verify the simulation capabilities and potential of the MVEM in addition to understanding the impact of different fuel compositions (ISV) on engine performance and turbocharging. Figure 6.5 shows the variations in exhaust receiver temperature, pressure before the throttle, manifold pressure and the air-excess ratio for the two experimentally untested cases at 500 kW_e load (100 %) and 20H₂-NG and 20CO₂-NG fuel blends. Additionally, simulation results for 375 kW_e load (75 %) and 20H₂-NG and 20CO₂-NG fuel blends are also presented for comparison.

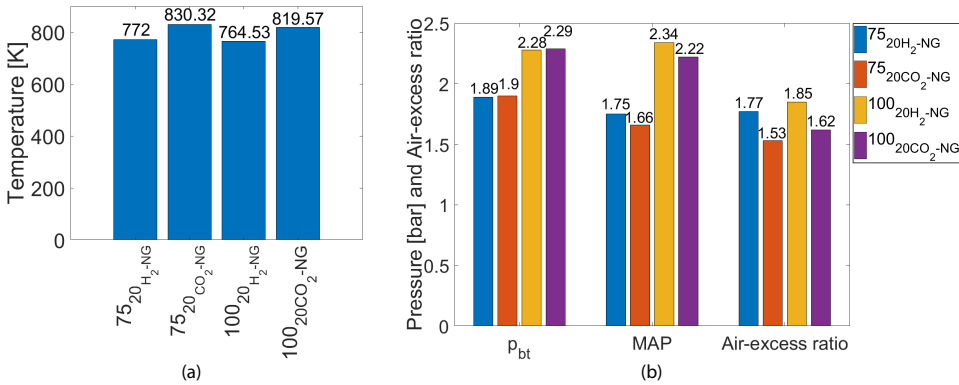


Figure 6.5: Exhaust receiver temperature (a) and pressure before the throttle, manifold pressure and the air-excess ratio (b) for only natural gas, 20H₂-NG and 20CO₂-NG fuel blend at 100 % engine loading and 500 mgNm⁻³

As seen in Figure 6.5(a), the exhaust receiver temperature decreases for 20H₂-NG fuel blend and increases for 20CO₂-NG fuel blend at 75 % and 100 % engine loading. The decrease in exhaust temperature due to hydrogen addition is caused by an advanced point of peak temperature while the increase in exhaust temperature due to CO₂ addition is related to the retardation of maximum temperature, as explained in the previous chapter. The higher temperature due to CO₂ blending corresponds to the higher exhaust energy entering the turbine, which leads to more power being delivered to the compressor and, thus, a higher compressor outlet pressure or pressure before throttle. The MVEM shows a marginal increase in charge pressure due to CO₂ addition, thus, underpredicting the increment. Based on engine measurements, the value for pressure before throttle for 75 % load and 15 % carbon dioxide addition should be about 1.96 compared to the value of 1.86 found for 20 % hydrogen addition at 75 % engine loading.

Contrary to increasing the charge pressure, CO₂ addition requires less amount of air to produce the same NO_x, which leads to a lower manifold pressure for the 20CO₂-NG fuel blend at 375 kW_e and 500 kW_e load as seen in Figure 6.5(b). This leads to a positive delta between the pressure before throttle and after throttle (manifold pressure). In addition to the pressures, Figure 6.5(b) also simulates a decrease in air-excess due to CO₂ blending, which further indicates the lower amount of air required for CO₂-NG fuel blends relative to H₂-NG fuel blends.

In contrast to CO₂-NG fuel blend, hydrogen blending leads to a lower value of pressure before throttle because of lower exhaust temperatures at turbine inlet and, thus, lower exhaust energy entering the turbine. Unlike carbon dioxide, hydrogen addition requires more air to produce the same amount of NO_x, which cause the MAP and air-excess ratio to increase. Interestingly, the MVEM shows that there is a mismatch between the p_{bt} and MAP for 20H₂-NG fuel blend at 500 kWe as seen in Figure 6.5(b). The simulation shows that a higher value of MAP is required in comparison to the pressure before throttle for hydrogen addition at 100 % load. Thus, the turbocharging capacity of the engine needs to be increased to run with hydrogen at 500 kWe. During engine measurements, it would not be possible to study this test case since the engine would reach its current turbocharging capacity. Thus, the MVEM is able to provide insights into test cases that could not be tested experimentally and help understand the engine performance.

6.4. CONCLUSION

In this research, the Seiliger-based modelling approach in combination with mean value engine modelling was able to accurately simulate the complete AOG-NG engine performance for different SOFC anode-off gas and natural gas fuel blends. The current chapter covers a detailed description of the developed AOG-NG MVEM for SOFC-ICE integration. To investigate the simulation capabilities of the MVEM, simulation and engine measurements were compared in addition to simulating engine performance for test conditions that could not be investigated through experimentation. The following concluding remarks are noted from the discussions presented in this chapter:

- The Seiliger-based combustion characterization and parameterization methodology was able to satisfactorily capture the combustion effects and in-cylinder process variations for individual blends of hydrogen and carbon dioxide with natural gas. In the case of hydrogen-natural gas fuel and carbon dioxide-natural gas fuel blends, the maximum deviation simulated by the Seiliger-based in-cylinder model was about 3 % and 6 %, respectively, for temperature at exhaust valve opening.
- The simulation results showed that the variations in in-cylinder process for an anode-off gas-natural gas fuel blend can be understood and captured as deviations in Seiliger parameters for each individual anode-off gas constituent (H₂ and CO₂).
- The derived parametric equations of Seiliger parameters for individual anode-off gas constituents were able to substantially simulate the combustion and in-cylinder process for different blends of anode-off gas and natural gas fuel blends. The maximum error in simulation of in-cylinder performance parameters obtained by Seiliger-based modelling was about 4 % for the three tested anode-off gas-natural gas fuel blends.
- During MVEM validation, the maximum deviation was about 7 % for exhaust receiver pressure. Other engine parameters were simulated with error percentages equal to or lower than 5 %.
- The MVEM showed that there was a mismatch between the pressure before throttle and manifold pressure for 20H₂-NG fuel blend at 500 kWe. The simulation showed that

a higher value of manifold pressure would be required in comparison to the pressure before throttle for hydrogen addition at 100 % load. The mismatch is caused by the lower exhaust temperatures due to hydrogen addition leading to a reduced pressure before throttle in contrast to the increased manifold pressure caused by additional requirements for same NO_x operation with hydrogen.

- Contrary to hydrogen, CO₂ addition required less amount of air to produce the same NO_x, thus, showing a positive delta between the pressure before throttle and manifold pressure at 500 kWe. Thus, the test engine could run on a 20CO₂-NG fuel blend at 100 % load, however, it would reach its current turbocharging capacity on a 20H₂-NG fuel blend during engine measurements. Therefore, the turbocharging capacity of the engine would have to be increased to run with hydrogen at 500 kWe load. In this manner, the MVEM is able to provide insights into test cases that could not be tested experimentally and help understand the impact of different fuel compositions (ISV) on engine performance and turbocharging, thus, presenting additional insights to answer Research Question 5.

Based on the validation and confidence in simulating the experimentally untested conditions, the AOG-NG MVEM and the Seiliger modelling approach in combination with the 0-D SOFC model are further employed in the next chapter to study SOFC-ICE integration, thus, answering Research Question 4.

REFERENCES

- [1] H.D. Sapra et al. Integration of Solid Oxide Fuel Cell and Internal Combustion Engine for Maritime Applications. *Applied Energy*, 2020.
- [2] D. Stapersma. *Diesel Engines: A Fundamental Approach to Performance Analysis, Turbocharging, Combustion, Emissions and Heat Transfer Including Thermodynamical Principles. Vol. 6: Thermodynamical Principles II*. Delft University of Technology, 2010.
- [3] D. Stapersma. *Diesel Engines: A Fundamental Approach to Performance Analysis, Turbocharging, Combustion, Emissions and Heat Transfer Including Thermodynamical Principles. Vol. 2: Turbocharging*. Delft University of Technology, 2010.
- [4] D. Stapersma. *Diesel Engines: A Fundamental Approach to Performance Analysis, Turbocharging, Combustion, Emissions and Heat Transfer Including Thermodynamical Principles. Vol. 1: Performance Analysis*. Delft University of Technology, 2010.
- [5] R.D. Geertsma et al. Pitch Control for Ships with Diesel Mechanical and Hybrid Propulsion: Modelling, Validation and Performance Quantification. *Applied Energy*, 2017.
- [6] R.D. Geertsma. *Autonomous Control for Adaptive Ships with Hybrid Propulsion and Power Generation*. PhD thesis, Delft University of Technology, 2019.
- [7] D. Stapersma. *Diesel Engines: A Fundamental Approach to Performance Analysis, Turbocharging, Combustion, Emissions and Heat Transfer Including Thermodynamical Principles: Vol. 4: Emissions and Heat Transfer*. Delft University of Technology, 2010.

7

SOFC-ICE INTEGRATION

In this chapter, the 0-D SOFC model and the AOG-NG MVEM are used to simulate an integrated SOFC-ICE system producing a total power output of 750 kW_e. As mentioned in section 1.6 of Chapter 1, a combined system and component level investigation is required to study SOFC-ICE integration due to complex interactions between the integrated system variables (ISVs). Therefore, the impacts of ISVs such as current density, pre-reforming ratio, fuel utilization, heat integration and power split on SOFC-ICE integration are discussed in this chapter to answer Research Question 5. Next, this chapter presents a discussion on the optimal AOG composition for SOFC-ICE integration, which is crucial for answering Research Question 6. Additionally, a comparison between the SOFC-ICE power pack and a conventional marine engine in terms of efficiency, emissions and power density has been covered in this chapter, which provides insights to answer Research Question 7.

For successful development of the SOFC-ICE power plant, a balance between the outgoing and incoming heat flows needs to be achieved to sustain high-efficiency SOFC operation. Therefore, this chapter covers the heat integration between the SOFC and the engine. Furthermore, SOFC-ICE integration performance is investigated for different power splits between the SOFC and the engine showcasing the potential of SOFC-ICE integration for maritime applications. Next, the chapter provides a comparison between the load response of the SOFC and the ICE. The chapter also presents a discussion on the impact of anode-off gas constituents on the load response of the marine NG engine to completely answer Research Question 3, which is related to effects of AOG constituents on engine performance. The chapter concludes with a discussion on the untapped potential of SOFC-ICE integration for maritime applications by presenting ideas for future research.

Parts of this chapter have been published in Applied Energy [1] and The International Naval Engineering Conference 2020 [2].

7.1. SOFC-ICE INTEGRATION RESULTS

Interactions between the ISVs directly impact the efficiencies of individual energy conversion device, system efficiency, overall emissions and system power density. To understand and quantify these complex interactions and their impact, first, a sensitivity study is performed. In this study, the impact of SOFC control parameters such as current density, pre-reforming ratio and fuel utilization on the efficiency of the SOFC-ICE integrated power plant is analysed. For this study, the following control and input parameters are kept constant for the models, unless mentioned otherwise. As explained in Chapter 3, the fuel and air inlet temperatures are kept constant at 1073 K with ambient operating pressure. The current density is maintained at 5000 A m^{-2} , fuel utilization at 80 % and the steam-to-carbon ratio (S/C) ratio at 2. The air-excess ratio is controlled by the PI controller to maintain the difference between the inlet and outlet temperatures of the cell within 100 K. The pre-reforming ratio (PRR) is fixed at 0.3 and the pre-reforming reaction heat is obtained from the SOFC. The number of cells in the stack is equal to 11000, which corresponds to a total cell area of 110 m^2 . Additionally, all simulations are performed for a SOFC-ICE combined power output of 750 kWe. The blend percentages of hydrogen and carbon dioxide directed into the engine are based on the ratio of hydrogen and carbon dioxide present in the incoming SOFC anode-off gas. Since the AOG-NG MVEM has been validated for a maximum blend percentage of 30 % AOG and 70 % NG, the maximum blend percentage of anode-off gas in all the proceeding analysis is kept at 30 %.

Figure 7.1(a) shows the simulated efficiencies of the standalone AOG-NG engine, integrated AOG-NG engine, SOFC only and the integrated SOFC-ICE system at different current densities. The difference between the standalone AOG-NG engine and the integrated AOG-NG engine lies in the method of efficiency calculation. The efficiency of the standalone AOG-NG engine (η_{ICE}) is computed from equation 6.9, which includes the energy contribution of hydrogen from the anode-off gas. On the other hand, the efficiency of the integrated AOG-NG engine ($\eta_{\text{I-ICE}}$) is calculated from equation 7.1, which excludes the incoming energy contribution of hydrogen since it is accounted for in the SOFC efficiency calculation, thus, providing a "free" energy input to the ICE. Therefore, the efficiency of the integrated AOG-NG engine is higher than the standalone AOG-NG engine efficiency. For the integrated SOFC-ICE system, the efficiency is calculated by applying equation 7.2.

$$\eta_{\text{I-ICE}} = \frac{P_{\text{ICE}}}{\dot{m}_{\text{fuel}} \cdot \text{LHV}_{\text{fuel}} - \dot{m}_{\text{H}_2} \cdot \text{LHV}_{\text{H}_2}} \quad (7.1)$$

$$\eta_{\text{SOFC-ICE}} = \frac{P_{\text{SOFC-ICE}}}{\text{EC}_{\text{SOFC}} + \text{EC}_{\text{I-ICE}}} \approx \frac{P_{\text{SOFC-ICE}}}{\dot{N}_{\text{CH}_4} \cdot \text{LHV}_{\text{CH}_4} + \dot{m}_{\text{NG}} \cdot \text{LHV}_{\text{NG}}} \quad (7.2)$$

where, ' $P_{\text{SOFC-ICE}}$ ' is the total power output of the SOFC-ICE integrated system in kWe. ' EC_{SOFC} ' represents the incoming energy contribution of the SOFC while ' $\text{EC}_{\text{I-ICE}}$ ' represents the incoming energy contribution of the integrated engine. ' $\dot{N}_{\text{CH}_4}^{\text{in}}$ ' is the molar flow rate of methane entering the SOFC in mols^{-1} , ' \dot{m}_{NG} ' is the fuel flow rate of natural gas entering the integrated ICE in kgs^{-1} , ' LHV_{CH_4} ' is the lower heating value of the methane in kJ mol^{-1} and ' LHV_{NG} ' is the lower heating value of natural gas in kJ kg^{-1} .

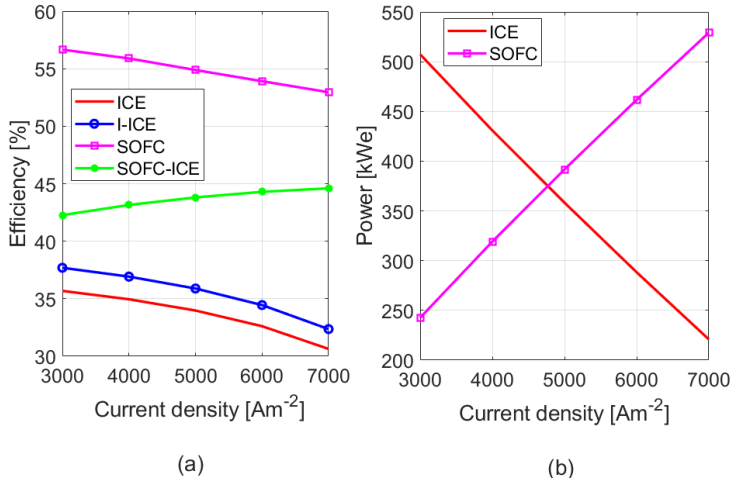


Figure 7.1: Simulated efficiencies (a) and power outputs (b) for SOFC-ICE integration at different current densities with total system power output of 750 kW_e

Increasing current density at constant fuel utilization adversely impacts cell voltage but leads to an increase in the power produced by the SOFC. The increase in power comes at the cost of higher fuel intake, which results in reduced SOFC electrical efficiency with increasing current density as seen from Figure 7.1(a). Furthermore, the increase in power produced by the SOFC leads to a reduced load on the engine since the combined SOFC-ICE power output is maintained at 750 kW_e as seen from Figure 7.1(b). Operation of the integrated AOG-NG engine at lower loads causes the engine efficiency to decrease at higher current densities. Although the efficiencies of the SOFC and the ICE decrease with increasing current density, the efficiency of the integrated SOFC-ICE power plant increases with increments in current density for a fixed total power output as seen from Figure 7.1(a). The efficiency of the SOFC-ICE system increases because the power split favours the SOFC at higher current densities, which is more efficient than the engine. Although the efficiency of the integrated SOFC-ICE power plant improves at higher current densities for a fixed total power output, operation at high current densities can reduce fuel cell lifetime. Khan et al. found that during long-term testing voltage loss over time greatly increases with higher current density leading to performance degradation [3]. Consequently, Aguiar et al. chose 5000 Am^{-2} as a suitable current density for their analysis as it provides a good balance between capital cost, efficiency, stable and realistic operation and power density [4]. Therefore, performance analysis in this research is performed at or close to 5000 Am^{-2} .

Contrary to current density, increments in methane pre-reforming ratio at constant fuel utilization and current density led to improvements in SOFC efficiency as depicted in Figure 7.2(a). As explained in section 3.6 of Chapter 3, increase in pre-reforming increases the operating cell voltage, which causes the SOFC power output to increase as seen in Figure 7.2(b). The increment in SOFC power is obtained while maintaining a constant fuel intake, thus, improving fuel cell efficiency. Since the fuel utilization is fixed

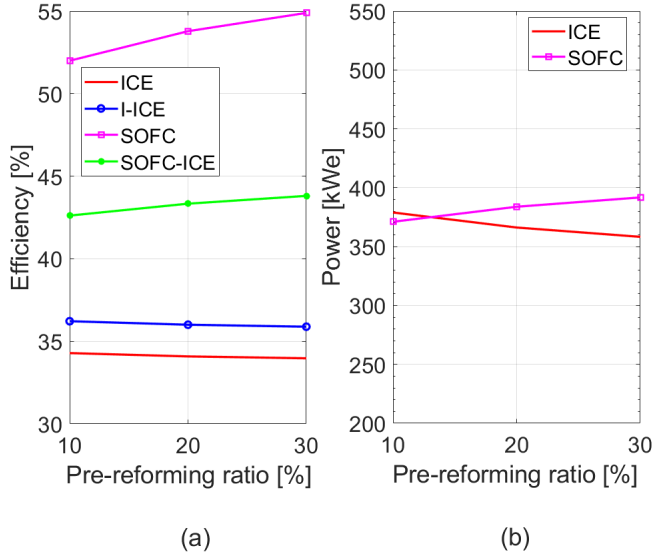


Figure 7.2: Simulated efficiencies (a) and power outputs (b) for SOFC-ICE integration at different pre-reforming ratios with total system power output of 750 kW

at 80 %, the ratio of hydrogen to carbon dioxide entering the engine is fixed at about 0.75. Increments in SOFC power output once again lead to lower loads share of the engine as seen in Figure 7.2(b), however, the variations in power split with changing pre-reforming ratio are small. Therefore, the efficiency of the integrated AOG-NG engine marginally reduces with increase in pre-reforming. Increase in SOFC load share and efficiency with increasing pre-reforming ratio leads to an increase in the overall system efficiency of the SOFC-ICE power plant as seen in Figure 7.2(a). It is vital to note that increments in pre-reforming will increase the size of the pre-reformer, thus, reducing the power density of the system. Furthermore, increased pre-reforming will increase heat and steam requirements from the SOFC, which could complicate and strain the Balance-of-Plant (BoP) and fuel cell operations [5]. Therefore, in this research, a maximum pre-reforming ratio of 0.3 is maintained for all proceeding simulations.

To study the effects of varying fuel utilization, current density was kept constant at 4750 Am^{-2} while the remaining control and input parameters were fixed at default values provided at the beginning of this section. SOFC operation at different fuel utilizations is achieved by controlling the incoming methane fuel flow-rate. Fixing the current density at 4750 Am^{-2} helps in operating the SOFC close to 375 kW, which helps in attaining a SOFC-ICE power split close to 50-50. As shown in section 3.6, the cell voltage simulated by the 0-D SOFC model reduces by a small margin with increasing fuel utilization while the current density and number of cells are kept constant. Therefore, the SOFC power simulated by the 0-D model varied from 376 kW to 371 kW for fuel utilizations varying from 70 % to 85 %. This small deviation from 375 kW in SOFC power output keeps the power split between the SOFC and the engine close to 50-50 for different fuel utilizations. However, it is vital to note that as explained earlier in section 3.6 of

Chapter 3, the decrease in cell voltage and, hence, power output simulated by the 0-D SOFC model at high fuel utilizations may be somewhat underestimated [6, 7], which can also impact cell efficiency improvements at high fuel utilizations.

Table 7.1 shows the flow rates of hydrogen and carbon dioxide present in the SOFC anode-off gas after the removal of water vapour for different fuel utilizations. The blend percentages of hydrogen and carbon dioxide directed into the engine are shown in Table 7.2. The blend percentages are based on the ratio of hydrogen and carbon dioxide present in the incoming SOFC anode-off gas. Figure 7.3 shows the simulated efficiencies of the standalone AOG-NG engine, integrated AOG-NG engine, SOFC only and the integrated SOFC-ICE power plant for the different fuel utilizations.

Table 7.1: Flow-rates of hydrogen and carbon dioxide present in SOFC anode-off gas for different fuel utilizations

U_f %	$H_{2,SOFC} [m^3 h^{-1}]$	$CO_{2,SOFC} [m^3 h^{-1}]$
70	80.62	63.30
75	62.43	62.43
80	46.33	62.17
85	32.87	61.94

Table 7.2: Blend percentages and flow-rates of hydrogen and carbon dioxide (from SOFC anode-off gas) directed into the engine for different fuel utilizations

U_f [%]	$H_{2,ENG} Vol. [%]$	$CO_{2,ENG} Vol. [%]$	$H_{2,ENG} [m^3 h^{-1}]$	$CO_{2,ENG} [m^3 h^{-1}]$
70	16.81	13.19	26.17	20.54
75	15	15	23.67	23.67
80	12.81	17.19	20.65	27.51
85	10.40	19.59	17.14	32.29

The electrical efficiency (LHV) of the integrated system increases with increasing fuel utilization as shown in Figure 7.3. The efficiency of the integrated AOG-NG engine is higher than the standalone AOG-NG engine efficiency by a maximum of 2.55 % at 70 % fuel utilization. This improvement increases to 3.55 % when compared to ONG performance of the standalone engine producing the same power output. The efficiency improvement is attained through a combination of improved combustion and replacement of natural gas fuel by hydrogen. As fuel utilization increases, the efficiency of the integrated AOG-NG engine decreases marginally due to the presence of significantly higher percentages of carbon dioxide than hydrogen in the AOG-NG fuel blend. The decrease in engine efficiency is more than compensated by the increase in SOFC efficiency at higher fuel utilizations as seen in Figure 7.3 and explained earlier in section 3.6. The integration between the SOFC and the integrated AOG-NG engine provides a maximum efficiency improvement of 7.2 % at 85 % fuel utilization in comparison to the simulated efficiency of the standalone marine engine operating on only natural gas at 750 kW. Table 7.3 shows the efficiency improvement attained at different fuel utilizations from the SOFC-ICE integration compared to the standalone ONG marine engine efficiency at 750 kW.

The efficiency of ONG performance for the standalone marine engine simulated by the MVEM is 36.80 %. This simulated efficiency is close to the expected efficiency provided by [8] for the modelled test engine with 16 cylinders to operate at higher power outputs.

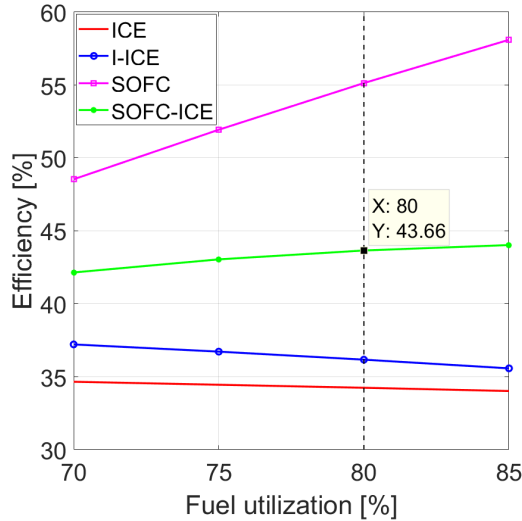


Figure 7.3: Simulated efficiencies of SOFC-ICE integration for different fuel utilizations at system power output of 750 kW. Appendix E provides an example of efficiency calculation of the SOFC-ICE integration for the test condition depicted with a dashed vertical line in the above figure corresponding to 80 % fuel utilization

7

Table 7.3: Efficiency improvement for different fuel utilizations obtained from the SOFC-ICE integration compared to the standalone ONG marine engine performance at 750 kW

U_f [%]	$\eta_{\text{improvement}}$ [%]
70	5.34
75	6.24
80	6.85
85	7.21

The efficiency improvement obtained by integrating the SOFC and the AOG-NG engine for maritime applications is clearly visible from Table 7.3. SOFC operation at fuel utilizations from 70 to 85 % can provide efficiency improvements of 5.3 % to 7.2 %. The SOFC operation is favourable for the range of 75 % to 80 % fuel utilization as it ensures safe fuel cell operation, high SOFC efficiency and a good ratio of hydrogen and carbon dioxide in AOG-NG blend for improved engine operation. For this reason, the potential of SOFC-ICE integration is further investigated by fixing the SOFC fuel utilization at 80 %.

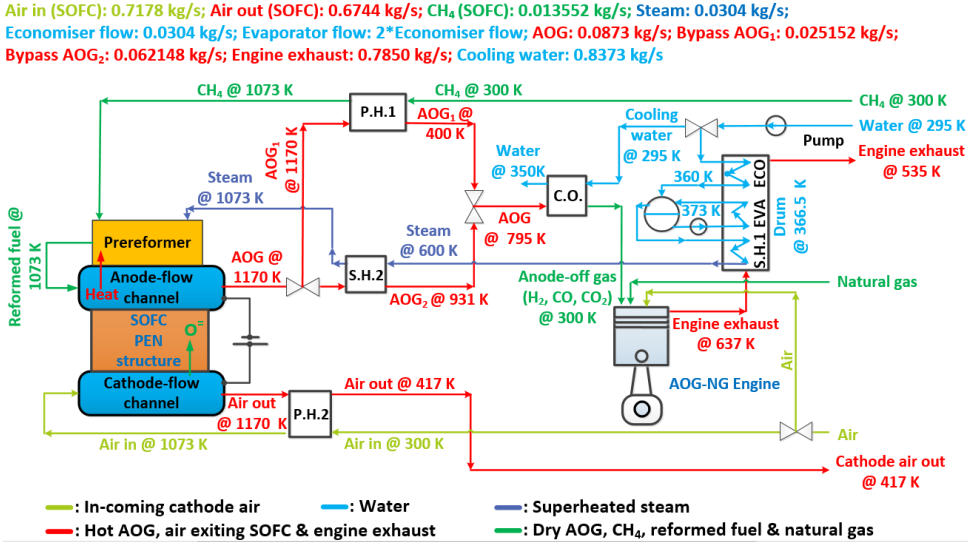


Figure 7.4: Heat management for SOFC-ICE integration with 50-50 power split at 80% fuel utilization and total power output of 750 kWe. P.H.: Preheater, S.H. Superheater, C.O.: Condenser, EVA: Evaporator, ECO: Economiser

7.2. HEAT INTEGRATION

For high-efficiency SOFC operation, the heat balance of the SOFC needs to be maintained ideally without external heat supply. Therefore, heat management is vital for SOFC-ICE integration. Figure 7.4 shows the heat balance of the integrated SOFC-ICE system for a 50-50 power split and 80% fuel utilization. Heat from the engine exhaust is utilized to superheat the steam to 600 K while the heat required to further superheat the steam to input temperature of 1073 K is attained from the AOG₂ flow. The outgoing anode-off gas is split into two flows to heat up the incoming fuel and to superheat the steam. The incoming air is heated up to the inlet temperature by the outgoing depleted cathode air. The water vapour in the anode-off gas is condensed out in the cooler (C.O.). For SOFC-ICE integration, the moisture free AOG flow is supplied to the marine SI engine for blending and combustion with natural gas. Figure 7.4 also shows the corresponding flow-rates needed for heat balance in the presented SOFC-ICE integration system layout. The presented heat balance proves that sufficient heat is available for successful integration of the SOFC and the engine. The equations used to solve the heat balance of each heat exchanging element for the test case presented in Figure 7.4 have been discussed in the following paragraphs.

As explained earlier, the incoming heat from the engine exhaust ($T_{\text{exh,in}}$) at 637 K is used to superheat the steam required by the SOFC to 600 K. The exhaust gas boiler consists of an economiser (ECO), evaporator (EVA) and a superheater (S.H.1). In the gas boiler, water equivalent to the required steam production is first heated to 360 K in the economiser. Next, the water flow entering the evaporator is maintained at twice the steam production rate. The final mixture leaving the evaporator consists of saturated

steam and water in 1:1 ratio [9]. The saturated steam is then supplied to the superheater within the gas boiler, which results in superheated steam exiting the boiler at 600 K. At the same time, the engine exhaust gas exits the boiler ($T_{\text{exh,out}}$) as seen in Figure 7.4. Equation 7.3 gives the heat balance inside the steam drum to calculate the drum water temperature ($T_{\text{w,drum}}$), which is estimated to be 366.5 K.

$$\dot{m}_{\text{w,ECO}} \cdot h_{\text{w,ECO,out}} + \dot{m}_{\text{w,EVA}} \cdot h_{\text{w,EVA,out}} + \dot{m}_{\text{st,EVA}} \cdot h_{\text{st,EVA,out}} = \dot{m}_{\text{w,drum}} \cdot h_{\text{w,drum}} + \dot{m}_{\text{st}} \cdot h_{\text{st,sat}} \quad (7.3)$$

where, ' $\dot{m}_{\text{w,ECO}}$ ' is the mass flow rate in kg s^{-1} of water flowing through the economiser, ' $h_{\text{w,ECO,out}}$ ' is the specific enthalpy of liquid water exiting the economiser at 360 K equal to $364.35 \text{ kJ kg}^{-1}$, ' $\dot{m}_{\text{w,EVA}}$ ' is the mass flow rate in kg s^{-1} of water exiting the evaporator, ' $h_{\text{w,EVA,out}}$ ' is the specific enthalpy of water exiting the evaporator at 373 K equal to $418.94 \text{ kJ kg}^{-1}$, ' $\dot{m}_{\text{st,EVA}}$ ' is the mass flow rate in kg s^{-1} of saturated steam at 373 K entering the drum from the evaporator, ' $h_{\text{st,EVA,out}}$ ' is the specific enthalpy of the saturated steam equal to $2676.1 \text{ kJ kg}^{-1}$, ' $\dot{m}_{\text{w,drum}}$ ' is the total mass flow rate in kg s^{-1} of water entering the evaporator from the drum, which is twice of the required steam production, ' $h_{\text{w,drum}}$ ' is the specific enthalpy of the water from the steam drum in kJ kg^{-1} , ' \dot{m}_{st} ' is the mass flow rate in kg s^{-1} of the saturated steam leaving the drum and entering the superheater in the gas boiler and ' $h_{\text{st,sat}}$ ' is the specific enthalpy of the saturated steam equal to $2676.1 \text{ kJ kg}^{-1}$.

After calculating the steam drum temperature, the heat balance inside the exhaust gas boiler is solved by using equation 7.4 to compute the temperature of the engine exhaust gas leaving the boiler. The computed value of engine exhaust leaving the boiler is 535 K as shown in Figure 7.4.

$$\begin{aligned} \dot{m}_{\text{exh}} \cdot c_{\text{p,exh,in}} \cdot T_{\text{exh,in}} + \dot{m}_{\text{w,ECO}} \cdot h_{\text{w,ECO,in}} + \dot{m}_{\text{w,drum}} \cdot h_{\text{w,drum}} + \dot{m}_{\text{st}} \cdot h_{\text{st,sat}} = \\ \dot{m}_{\text{exh}} \cdot c_{\text{p,exh,out}} \cdot T_{\text{exh,out}} + \dot{m}_{\text{w,ECO}} \cdot h_{\text{w,ECO,out}} \quad (7.4) \\ + \dot{m}_{\text{w,EVA}} \cdot h_{\text{w,EVA,out}} + \dot{m}_{\text{st,EVA}} \cdot h_{\text{st,EVA,out}} + \dot{m}_{\text{st,S.H.1}} \cdot h_{\text{st,S.H.1,out}} \end{aligned}$$

where, ' \dot{m}_{exh} ' is the mass flow rate in kg s^{-1} of the engine exhaust entering the boiler, ' $c_{\text{p,exh,in}}$ ' is the isobaric specific heat capacity of the exhaust gas equal to $1.158 \text{ kJ kg}^{-1} \text{ K}^{-1}$ at entry temperature ($T_{\text{exh,in}}$) of 637 K, ' $h_{\text{w,ECO,in}}$ ' is the specific enthalpy of the water entering the economiser at 295 K equal to 92.20 kJ kg^{-1} , ' $c_{\text{p,exh,out}}$ ' is the isobaric specific heat capacity of the exhaust gas also taken to be equal to $1.158 \text{ kJ kg}^{-1} \text{ K}^{-1}$ at boiler exit, ' $\dot{m}_{\text{st,S.H.1}}$ ' is the mass flow rate of the steam required by the SOFC exiting the superheater and ' $h_{\text{st,S.H.1,out}}$ ' is the corresponding specific enthalpy of the superheated steam at 600 K equal to $3128.75 \text{ kJ kg}^{-1}$.

In the proposed heat integration approach, the outcoming SOFC anode-off gas is split into two flows to heat up the incoming fuel and to further superheat the steam. As shown in Figure 7.4, the bypassed 'AOG₁' flow at 1170 K is used in preheater 1 (P.H.1) to preheat the incoming methane flow to 1073 K. The heat balance for P.H.1 is solved in equation 7.5. This heat balance is solved along with equation 7.6 to determine the mass flow rate of AOG₁ while the anode-off gas is cooled down to 400 K as seen in Figure 7.4. The estimated mass flow rate of AOG₁ and the corresponding temperatures have been

depicted in Figure 7.4.

$$\begin{aligned} \dot{m}_{\text{AOG,tot}} \cdot X_{\text{Bypass}} \cdot \sum \frac{c_{p,\text{AOG,P.H.1}}(T_i) + c_{p,\text{AOG,P.H.1}}(T_{i-100})}{2} \cdot \Delta T_{\text{AOG}_1,\text{P.H.1}} \\ = \dot{m}_{\text{CH}_4} \cdot \sum \frac{c_{p,\text{CH}_4,\text{P.H.1}}(T_j) + c_{p,\text{CH}_4,\text{P.H.1}}(T_{j+100})}{2} \cdot \Delta T_{\text{CH}_4,\text{P.H.1}} \end{aligned} \quad (7.5)$$

$$X_{\text{Bypass}} = \frac{\dot{m}_{\text{AOG}_1}}{\dot{m}_{\text{AOG,tot}}} \quad (7.6)$$

where, ' $\dot{m}_{\text{AOG,tot}}$ ' is the total mass flow rate of AOG coming from the SOFC in kg s^{-1} , ' \dot{m}_{AOG_1} ' is the mass flow rate of AOG₁ bypassed to P.H.1, ' $c_{p,\text{AOG,P.H.1}}$ ' is the isobaric specific heat capacity of the AOG at temperatures ' T_i ' and ' T_{i-100} '. Average specific heat capacities are calculated for every 100 K of temperature gradient till the final flow temperature is reached as seen from equation 7.5. The specific heat capacities of AOG are calculated in $\text{kJ kg}^{-1} \text{K}^{-1}$ as a function of the AOG composition and polynomial fit of temperature [10]. The entry temperature of AOG₁ in P.H.1 is 1170 K as it cools down to an exit temperature of 400 K while preheating the incoming methane fuel. Similar to AOG, ' $c_{p,\text{CH}_4,\text{P.H.1}}$ ' is the isobaric specific heat capacity of the CH₄ at temperatures ' T_j ' and ' T_{j+100} '. The entry temperature of methane at the entrance of P.H.1 is 300 K, which increased to 1073 K at P.H.1 exit.

After computing the value of ' \dot{m}_{AOG_1} ', the mass flow rate ' \dot{m}_{AOG_2} ' can be computed by subtracting ' \dot{m}_{AOG_1} ' from ' $\dot{m}_{\text{AOG,tot}}$ '. The flow AOG₂ is directed into the superheater (S.H.2) with entry temperature ($T_{\text{AOG}_2,\text{S.H.2, in}}$) of 1170 K to superheat the steam from 600 K to 1073 K. The heat balance of the superheater is solved by equation 7.7 to estimate the temperature ($T_{\text{AOG}_2,\text{S.H.2, out}}$) at the exit of the superheater. The temperature of bypassed anode-off gas at S.H.2 exit is equal to 931 K.

$$\begin{aligned} \dot{m}_{\text{AOG}_2} \cdot (c_{p,\text{AOG,S.H.2, in}} \cdot T_{\text{AOG}_2,\text{S.H.2, in}} - c_{p,\text{AOG,S.H.2, out}} \cdot T_{\text{AOG}_2,\text{S.H.2, out}}) = \\ \dot{m}_{\text{st,S.H.2}} \cdot (h_{\text{st,S.H.2, out}} - h_{\text{st,S.H.2, in}}) \end{aligned} \quad (7.7)$$

where, ' $c_{p,\text{AOG,S.H.2, in}}$ ' is the isobaric specific heat capacity of the AOG₂ flow entering the superheater at 1170 K equal to $2.108 \text{ kJ kg}^{-1} \text{K}^{-1}$, ' $c_{p,\text{AOG,S.H.2, out}}$ ' is the isobaric specific heat capacity of the AOG₂ flow exiting the superheater at 931 K equal to $2.018 \text{ kJ kg}^{-1} \text{K}^{-1}$, ' $\dot{m}_{\text{st,S.H.2}}$ ' is the mass flow rate of superheated steam required by the SOFC. ' $h_{\text{st,S.H.2, out}}$ ' is the specific enthalpy of the superheated steam exiting the superheater at 1073 K equal to $4159.88 \text{ kJ kg}^{-1}$ and ' $h_{\text{st,S.H.2, in}}$ ' is the specific enthalpy of the superheated steam entering the superheater at 600 K equal to $3128.75 \text{ kJ kg}^{-1}$.

The AOG₂ flow exiting S.H.2 and the AOG₁ flow are combined before entering the cooler (C.O.) as seen in Figure 7.4. Inside the cooler, the total anode-off gas flow is cooled down from a mixture temperature of 795 K ($T_{\text{AOG}_2,\text{C.O., in}}$) to 300 K ($T_{\text{AOG}_2,\text{C.O., out}}$). The water vapour from the anode-off gas is condensed out as it exchanges heat with the cooling water. The heat balance for the cooler is solved in equation 7.8 to compute the amount of cooling water required in the cooler. The total amount of cooling water

required ($\dot{m}_{\text{H}_2\text{O, cool}}$) is equal to 0.8373 kgs^{-1} as shown in Figure 7.4.

$$\begin{aligned} \dot{m}_{\text{AOG}_{\text{tot}}} \cdot \sum \frac{c_{p,\text{AOG,C.O.}}(T_{\text{AOG,C.O.in}}) + c_{p,\text{AOG,C.O.}}(T = 373\text{K})}{2} \cdot (T_{\text{AOG,C.O.in}} - 373) \\ + \dot{m}_{\text{H}_2\text{O,cond}} \cdot h_{\text{cond}} + \\ \dot{m}_{\text{AOG}_{\text{tot}}} \cdot \sum \frac{c_{p,\text{AOG,C.O.}}(T = 373\text{K}) + c_{p,\text{AOG,C.O.}}(T_{\text{AOG,C.O.,out}})}{2} \cdot (373 - T_{\text{AOG,C.O.,out}}) \\ = \dot{m}_{\text{H}_2\text{O,cool}} \cdot (h_{\text{H}_2\text{O,C.O.,out}} - h_{\text{H}_2\text{O,C.O.,in}}) \end{aligned} \quad (7.8)$$

where, ' $c_{p,\text{AOG,C.O.}}$ ' is the isobaric specific heat capacity of AOG flow in C.O. at temperatures corresponding to ' $T_{\text{AOG,C.O.in}} = 795 \text{ K}$, 373 K and ' $T_{\text{AOG,C.O.out}} = 300 \text{ K}$ ' ' $\dot{m}_{\text{H}_2\text{O,cond}}$ ' is the total mass flow rate in kgs^{-1} of water present in the AOG and condensed out. It is calculated by multiplying the total volume flow rate of water in AOG by its density at 1170 K . ' h_{cond} ' is the heat of condensation of water at 373 K equal to 2257 kJkg^{-1} . ' $h_{\text{H}_2\text{O,C.O.,in}}$ ' and ' $h_{\text{H}_2\text{O,C.O.,out}}$ ' are the specific enthalpies of water at temperatures of 295 K and 350 K corresponding to 92.20 kJkg^{-1} and 322.34 kJkg^{-1} , respectively. The condensed water can be reused in the system for steam production or for onboard water requirements.

Next, the incoming cathode air is directed to a heat exchanger (P.H.2) to raise its temperature at P.H.2 exit ($T_{\text{air-in,H.E.2,out}}$) to 1073 K . This incoming air is heated by using the outgoing cathode air exiting the SOFC. The outgoing cathode air enters the heat exchanger at a temperature ($T_{\text{air-out,H.E.2,in}}$) of 1170 K . The heat balance for P.H.2 is solved by using equation 7.9 to compute the outgoing cathode air temperature ($T_{\text{air-out,H.E.2,out}}$) at P.H.2 exit. The computed value of the outgoing cathode air at P.H.2 exit is equal to 417 K .

$$\begin{aligned} \dot{m}_{\text{air-out}} \cdot \sum \frac{c_{p,\text{air-out,P.H.2}}(T_r) + c_{p,\text{air-out,P.H.2}}(T_{r-100})}{2} \cdot \Delta T_{\text{air-out,P.H.2}} = \\ \dot{m}_{\text{air-in}} \cdot \sum \frac{c_{p,\text{air-in,P.H.2}}(T_s) + c_{p,\text{air-in,P.H.2}}(T_{s+100})}{2} \cdot \Delta T_{\text{air-in,P.H.2}} \end{aligned} \quad (7.9)$$

where, ' $\dot{m}_{\text{air-out}}$ ' is the mass flow rate of outgoing cathode air in kgs^{-1} . ' $c_{p,\text{air-out,P.H.2}}$ ' is the isobaric specific heat capacity of the outgoing cathode air at temperatures ' T_r ' and ' T_{r-100} '. Similarly, ' $c_{p,\text{air-in,P.H.2}}$ ' is the isobaric specific heat capacity of the incoming cathode air at temperatures ' T_s ' and ' T_{s+100} '. Average specific heat capacities are calculated for every 100 K of temperature gradient till the final flow temperature is reached.

Based on the above calculations of the heat exchanging elements, the heat exchanger areas are calculated for each element except the boiler. The areas are calculated by estimating a log mean temperature difference (LMTD) and assuming overall heat transfer coefficient values of $30 \text{ W m}^{-2} \text{ K}^{-1}$ for gas-to-gas heat exchange and $1250 \text{ W m}^{-2} \text{ K}^{-1}$ for steam (water vapour)-to-liquid (water) heat exchange (in the cooler), respectively [11]. Table 7.4 shows the computed areas for the different heat exchanging elements. As seen in Table 7.4, the maximum area is required for the P.H.2 preheater, which uses the outgoing cathode air to preheat the incoming cathode air to 1073 K . The large size is due to the high amount of air flows entering and exiting P.H.2 as seen in Figure 7.4.

The above calculation provides evidence for sufficient heat availability within the system to allow for optimized heat integration with high-efficiency SOFC and system operation. The Balance-of-Plant can be further optimised with numerous configurations. For

Table 7.4: Areas of different heat exchanging elements for SOFC-ICE integration with 50-50 power split at 80 % fuel utilization and total power output of 750 kW_e

Elements	H.E. area [m ²]
P.H.1	12.4
P.H.2	186
C.O.	1.6
S.H.2	5.5

instance, anode-off gas recirculation with or without a combustor can be adopted to directly supply the required heat and steam for pre-reforming and preheating of incoming flows, thus, optimising the BoP [12]. By implementing a bypass for the anode-off gas, the percentage of anode-off gas recirculated and the amount supplied to the engine can be controlled for further optimization. The potential of anode-off gas recirculation for SOFC-ICE integration should be investigated in future.

7.3. LOAD SHARING, ENGINE LOAD RESPONSE AND UNEXPLORED POTENTIAL OF SOFC-ICE INTEGRATION

In this section, a discussion on the potential of SOFC-ICE integration for maritime applications has been presented. The section covers an analysis of different power splits between the SOFC and the engine and their impact on system efficiency, power density and emissions. Furthermore, a qualitative and quantitative investigation has been presented to understand the impact of AOG constituents on the load-taking capabilities of the engine. Lastly, the chapter provides a discussion on the unexplored potential of SOFC-ICE integration for future research.

7.3.1. LOAD SHARING

The SOFC-ICE combined cycles analysed in existing literature present a 13 to 15 % load share of the engine [12–14], which corresponds to the engine output attained by directly combusting SOFC anode-off gas. Additionally, the power split favours the SOFC to attain high system efficiency. However, other operational requirements such as good transient capabilities, space and weight considerations and economics are critical for power generation onboard ships. As explained earlier, a small load share of the engine could restrict the transient capabilities of the engine as the system load pick-up capabilities would be dictated by the SOFC, which are limited. Additionally, marine power generation with a large SOFC load share would require high capital expenditure in addition to high space and weight considerations. Therefore, power split favouring the SOFC load share may not be ideal for maritime applications.

Variations in power splits can help optimize SOFC-ICE integration for different ship types. Different ships have numerous operational profiles, which include various ship operations such as manoeuvring, range, cruising, acceleration, high speed, bollard-pull, etc. Therefore, power and transient operation requirements of ships can be significantly different. For these reasons, the potential of SOFC-ICE integration proposed in this re-

search is investigated for different load sharing strategies in this section.

To investigate SOFC-ICE integration with different power splits, the rated power of the SOFC and engine is varied. The number of cells in the SOFC are varied for different power outputs while the current density and fuel utilization are fixed at 5000 A cm^{-2} and 80 % respectively. Table 7.5 shows the three different power splits investigated with total system power kept constant at 750 kWe. Furthermore, besides the number of cells, Table 7.5 also shows the flow rates of hydrogen and carbon dioxide present in the SOFC anode-off gas after the removal of water vapour for the three load sharing strategies. After water vapour removal, anode-off gas is directed into the engine for blending with natural gas and remaining power generation. The AOG-NG blend ratios are fixed at 30-70 based on volumetric blend percentages. Table 7.6 shows the anode-off gas flow composition and flow rates of hydrogen and carbon dioxide utilised in the engine.

Table 7.5: Tested power splits (SOFC-ICE) with corresponding anode-off gas flow-rates in $\text{m}^3 \text{ h}^{-1}$

Case	Cells	Power split [%]	Power split [kW]	$\text{H}_{2,\text{SOFC}}$	$\text{CO}_{2,\text{SOFC}}$
1	7000	33-67	250-500	31.03	41.67
2	10550	50-50	375-375	46.79	63.73
3	14000	67-33	500-250	62.06	83.26

Table 7.6: Anode-off gas flow compositions and flow-rates corresponding to the AOG-NG engine for the three test cases with varying power splits

Case	$\text{H}_{2,\text{ENG}} \text{Vol.}[\%]$	$\text{CO}_{2,\text{ENG}} \text{Vol.}[\%]$	$\text{H}_{2,\text{ENG}} [\text{m}^3 \text{ h}^{-1}]$	$\text{CO}_{2,\text{ENG}} [\text{m}^3 \text{ h}^{-1}]$
1	12.81	17.19	26.40	35.43
2	12.81	17.19	20.59	27.64
3	12.81	17.19	14.87	19.96

As seen in Table 7.5 and Table 7.6, the percentage of hydrogen and carbon dioxide in AOG remains constant due to same fuel utilization, thus, fixing the blend ratio of carbon dioxide to hydrogen at 1.34. Figure 7.5 shows the simulated efficiencies of the standalone AOG-NG engine, integrated AOG-NG engine, SOFC only and the integrated SOFC-ICE system for different power splits. Table 7.7 presents the efficiency improvements obtained for different power splits compared to a standalone marine natural gas engine with the same power output. Additionally, Table 7.7 also shows the possible reductions in efficiency for the proposed SOFC-ICE integration approach compared to a standalone SOFC with the same power output of 750 kWe.

The efficiency of the SOFC remained constant for different power splits because the cell performance remains constant due to fixed fuel utilization and current density. The increased power output is achieved by increasing the number of cells as shown in Table 7.5. Therefore, the number of cells were increased to 21000 to obtain the power output of 750 kWe from the standalone SOFC. Contrary to the SOFC, the efficiency of the integrated engine reduces with decreasing load share. The overall system efficiency increases with increasing load share of the SOFC. An efficiency improvement of 5.23 % was found compared to a standalone ONG marine engine even for a 33-67 SOFC-ICE

power split with a maximum improvement of more than 8 % with a 67-33 load share. At the same time, it is clear from Table 7.7 that the efficiency of the proposed SOFC-ICE system is lower than that of a standalone SOFC producing the same power. However, as explained in subsection 2.2, dynamic capabilities and space and weight requirements are of equal or more importance compared to efficiency for maritime applications. For instance, a standalone SOFC would account for about 3.3 times the space and weight requirements. Additionally, SOFCs have limited dynamic capabilities, which would restrict their load-taking capabilities and application during sudden and large load changes of ships. Therefore, in this research, the performance of the integrated SOFC-ICE system is compared to a marine natural gas engine. The impact of SOFC-ICE power splits on the space and weight requirements of the system are discussed further in this subsection while the impact of SOFC and ICE transients on the design power split of the system has been discussed from a maritime perspective in the next subsection.

It is evident from Figure 7.5 and Table 7.7 that a significant efficiency improvement is attainable by integrating a small SOFC with a larger engine. The smaller load share of SOFC can help meet all the base load requirements with continuous SOFC operation. At the same time, higher loads and load transients can be accommodated by the integrated AOG-NG engine leading to improved propulsion efficiency. Furthermore, there is a potential to further improve the efficiency for SOFC-ICE integration since higher amounts of hydrogen is available for consumption inside the engine than the amount tested in this research. The higher availability of hydrogen for blending and combustion in the engine is evident from Table 7.5 and Table 7.6.

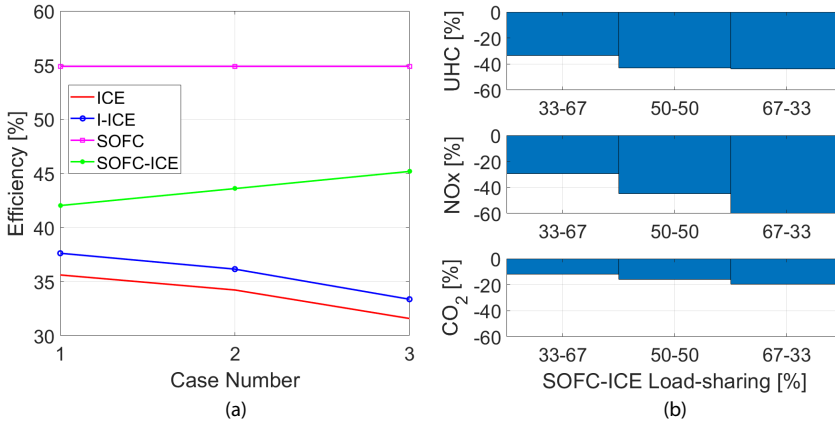


Figure 7.5: Simulated efficiencies (a) and emission reductions [%] of SOFC-ICE integration at different power splits with a total system power output of 750 kW. All emissions are calculated in $\text{gkW}^{-1} \text{h}^{-1}$

To implement the SOFC-ICE combined cycle for maritime applications, other factors such as environmental impact, system size and weight also need to be considered. For this reason, Figure 7.5(b) shows the improvement in mitigating harmful ship emissions, namely, unburnt hydrocarbons, CO₂ and NOx. The UHC and NOx emissions are engine-out emissions while CO₂ emissions from both the SOFC and the engine are taken into consideration. For a 50-50 power split, UHC and NOx reductions of about 40 % are

Table 7.7: Integrated SOFC-ICE system efficiency improvement and reduction for the three test cases of varying power splits compared to the standalone ONG marine engine performance and standalone SOFC at 750 kWe power output

Test case	$\eta_{(+)}$ v/s ICE [%]	$\eta_{(-)}$ v/s SOFC [%]
1	5.23	-12.85
2	6.79	-11.29
3	8.37	-9.70

achievable in comparison to a conventional marine NG engine of same power output, which is already capable of meeting IMO Tier-III regulations. The engine emissions are reduced due to controlled combustion of hydrogen and carbon dioxide from anode-off gas as explained in section 6.1.1 and section 6.1.2. Although there are no global emission regulations for methane, methane slip from natural gas-fuelled marine engines is identified as a serious concern for maritime applications due to its significantly higher global warming potential compared to CO₂. Therefore, the reductions in UHC (methane) emissions found in this research for SOFC-ICE integration are of high significance for maritime applications as increasing number of natural gas-fuelled ships are being built and operated, which can employ the proposed system. Furthermore, carbon dioxide reductions range from 12 to about 20%. Significant emission reductions in UHC and NO_x can be achieved from SOFC-ICE integration even when the power split favours the engine. Table 7.8 shows the gravimetric and volumetric densities of the systems for the three power splits in comparison to an engine with the same total power output. The computed gravimetric and volumetric density of the SOFC are 2.93 Wkg⁻¹ and 10.11 WL⁻¹ and are based on the data found for a commercially existing standalone SOFC of 300 kWe rated power [15]. For the engine, system size and weight densities are based on the data found for a commercially available NG SI engine of 400 kWe power output [16].

Table 7.8: Gravimetric and volumetric densities of a standalone engine and SOFC-ICE integration for four power splits including the three power splits presented in Table 7.5 with the same rated power outputs of 750 kWe. PS = SOFC-ICE power split

	ICE	PS: 33-67	PS: 50-50	67-33	PS: 85-15
Gravimetric density [Wkg ⁻¹]	69.93	39.28	32.22	27.31	23.39
Volumetric density [WL ⁻¹]	33.72	18.96	15.55	13.19	11.30

An increasing percentage of SOFC load share leads to significant increments in system size and weight. Although a 33-67 SOFC-ICE power split requires about 1.7 times the space and weight considerations, a 67-33 split is almost 2.5 times larger and heavier in comparison to the engine. Additionally, Table 7.8 also shows that an 85-15% SOFC-ICE power split, which matches with the SOFC-ICE combined cycles analysed in existing literature would be about 3 times larger and heavier than the engine. Therefore, by employing the SOFC-ICE integration proposed in this research for maritime applications, promising improvements in efficiency and emission reductions can be achieved with comparatively smaller increments in size and weight for a 33-67 power split. Furthermore, the efficiency improvements and emissions reductions are attained with a com-

mercially existing engine and without any structural modifications.

7.3.2. LOAD RESPONSE OF SOFC AND ICE

The dynamic load response of the integrated SOFC-ICE system can impact system design, control and optimization. An investigation into the dynamic capabilities of the individual power components is crucial for the development of the integrated system. In this subsection, the dynamic capabilities of the SOFC and ICE are compared for the same load pick-up. Additionally, the impact of AOG constituents on the dynamic response of the ICE is also discussed. In this research, the SOFC load response is studied with the aid of the developed 0-D SOFC model and the transient response of the ICE is based on engine experiments.

LOAD RESPONSE OF SOFC VERSUS ICE

To investigate the dynamic response of the SOFC, the capabilities of the 0-D SOFC model were first verified by comparing against the dynamic results provided by Salogni et al. for same test conditions [17, 18]. Salogni et al. simulated the dynamic response with a 1-D model verified with the same fuel cell data available from Aguiar et al. for a planar IT-SOFC [4].

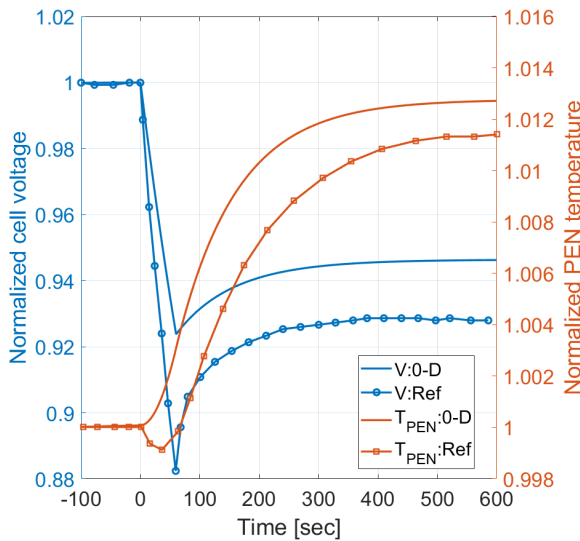


Figure 7.6: 0-D SOFC model verification in simulating dynamic response. Normalized SOFC voltage and PEN temperature response for change in current density from 5000 to 7000 Am^{-2} . The simulation output of the 0-D SOFC model is compared against results reported in [17]

The 0-D model input parameters for the dynamic load response simulations are as follows [17, 18]. Fuel and air inlet temperatures are kept at 1023 K . The operating pressure is ambient (100 kPa); initial current density in the 0-D model is maintained at 5000 Am^{-2} ; fuel utilization is constant at 75% and air-excess ratio is constant at 8.5 . The incoming composition for the anode-flow channel is obtained as a result of 10% pre-reforming

with S/C ratio of 2. To verify the dynamic simulation capabilities of the 0-D SOFC model, the 0-D model is tested for a $+2000 \text{ Am}^{-2}$ current density ramp in 60 seconds [17, 18]. In this simulation study, the ramp is introduced after the model reaches steady state conditions for 5000 Am^{-2} current density. After reaching steady state, the model simulates the load response for change in current density from 5000 Am^{-2} to 7000 Am^{-2} .

Figure 7.6 depicts the verification of the dynamic capabilities of the 0-D model by comparing the normalized cell voltage and PEN temperature against the results reported by the reference publication of Salogni et al. [17] for the same test conditions. As seen from the figure, the qualitative trends of voltage and temperature simulated by the 0-D model match well with that of the reference. The absolute values of PEN temperature simulated by the 0-D model are quite close to the values obtained from the reference 1-D model. Both the models show a drop (undershoot) in cell voltage followed by a settling period due to the ramp in current density while the PEN temperature increases. As the current density is increased, the ohmic and activation losses increase causing the cell voltage to drop. At the same time, the fuel flow increases to maintain the same fuel utilization, thus, resulting in higher PEN temperatures due to the increased heat release during the hydrogen oxidation of more incoming hydrogen at higher current densities. However, there is a lag in temperature response compared to the chemical kinetics, which leads to larger voltage losses and an undershoot in cell voltage due to lower temperatures. As the PEN temperature increases and settles, the cell voltage also progresses through a settling period and reaches steady state. Both the models depict very similar settling periods and the time scales for reaching steady state.

Although the overall dynamic response simulated by the 0-D model qualitatively matches well with the reference, a few differences can be noted in simulation results. The 1-D reference model depicts a larger voltage drop. Furthermore, the 1-D model from the reference shows an initial drop in PEN temperature, which significantly contributes to the lag and, hence, the large voltage drop as seen in Figure 7.6. This initial drop in PEN temperature was simulated by the 1-D model at the exhaust discharge section [17] and could be attributed to the sudden increase in air-intake to maintain the same air-excess ratio of 8.5. This drop in PEN temperature at the exhaust discharge section is not simulated by the 0-D SOFC model. A 1-D model is recommended to more accurately capture the temperature and voltage response while accounting for thermal gradients and stresses in SOFC load response.

It is clear from the previous discussion that although the 0-D model found some limitations in accurately simulating the quantitative voltage and temperature dynamics, it was successful in capturing the time scales for a SOFC load response. Based on this confidence, the 0-D SOFC model was used to simulate the change in load demand from 250 kWe to 375 kWe. The total number of cells was fixed at 11000. For this simulation study, all model input parameters remained the same except for current density. The initial current density was changed to 3450 Am^{-2} corresponding to the power output of 250 kWe. In this subsection, the SOFC dynamic load response is discussed by focussing on stabilization time and ramp rate limitations. Therefore, to simulate the load change to 375 kWe, first, an optimistic current density ramp of $+2000 \text{ Am}^{-2} \text{ min}^{-1}$ was simulated to discuss the stabilization time parameter. Second, the same load change was performed with a current density ramp rate of $+200 \text{ Am}^{-2} \text{ min}^{-1}$ (10 times slower). In

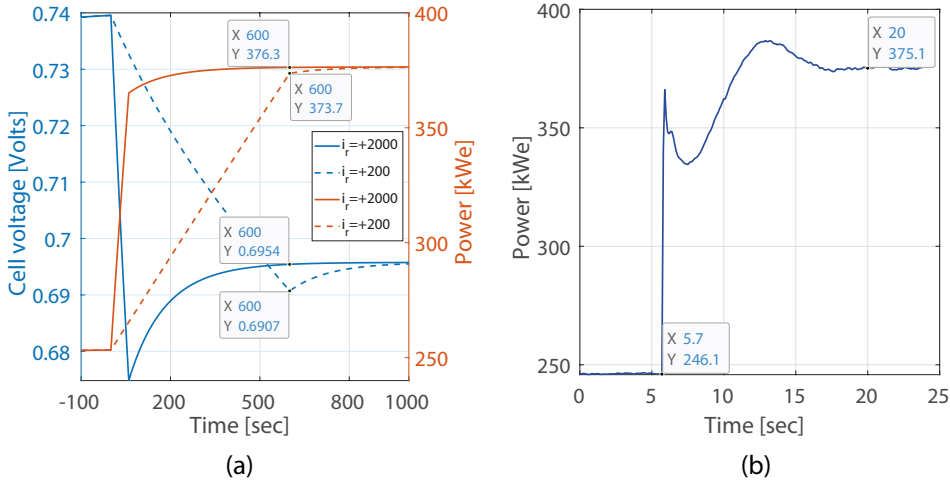


Figure 7.7: Comparison between the dynamic response of SOFC (a) and ICE (b) for load change from 250 to 375 kWe. In (a) response of fuel cell voltage and AC power output have been plotted. ' i_r ' is the current density ramp rate measured in $\text{Am}^{-2} \text{min}^{-1}$

practical SOFC systems, ramp rates prescribed by the manufacturer are limited to values such as $+200 \text{ Am}^{-2} \text{ min}^{-1}$ to allow the BoP components to respond accordingly and maintain, among others, fuel supply, air supply, the peak temperatures and temperature gradient within the operational limits of the stack [19]. Fast ramp-up rates can lead to high thermal gradients, which can damage the stack. One of the expected consequences of large thermal gradients can be cracking of the glass-ceramic sealing that joins the fuel cell to the interconnect and makes the anode and cathode volume channels gas tight [20].

Figure 7.7(a) shows the dynamic load response of the SOFC in terms of the power output and cell voltage. The cell voltage response corresponding to the $+2000 \text{ Am}^{-2} \text{ min}^{-1}$ ramp rate is similar to the response discussed earlier. In response to this current ramp, the electrochemistry and, thus, the voltage respond instantly increasing the power output to 365 kWe in about 60 seconds, however, the SOFC takes almost 500 to 600 seconds to reach steady state and the required load demand of 375 kWe due to the thermodynamic response lag [17, 21]. The thermodynamic response lag has been discussed earlier in this subsection while the high stabilization time corresponding to the optimistic ramp rate of $+2000 \text{ Am}^{-2} \text{ min}^{-1}$ can be seen in Figure 7.7(a). This long stabilization time can pose a challenge in a dynamic loading environment like maritime since long stabilization times can make the SOFC vulnerable to thermal overloading and stressing of cells in case of frequent load changes [22].

Contrary to the ramp rate of $+2000 \text{ Am}^{-2} \text{ min}^{-1}$, the SOFC has a much smaller voltage undershoot and a much shorter stabilization time for the $+200 \text{ Am}^{-2} \text{ min}^{-1}$ ramp rate, as seen in Figure 7.7(a). However, for the practical $+200 \text{ Am}^{-2} \text{ min}^{-1}$ ramp rate, the SOFC takes about 600 seconds to reach a value close to the required load of 375 kWe before the settling period starts, thus, showcasing the slow transient response of the SOFC. In

addition to this, Biert et al. found that a PID air flowrate controller was unable to keep the maximum PEN temperature gradient below the advised value of $10^{\circ}\text{Ccm}^{-1}$ for the manufacturer prescribed ramp rate of $+200\text{Am}^{-2}\text{min}^{-1}$ [23]. Furthermore, Andrea et al. found that a maximum current ramp rate of only $+0.3\text{Amin}^{-1}$ ($+30\text{Am}^{-2}\text{min}^{-1}$) was feasible without encroaching beyond the operating temperature limit given by the manufacturer [20]. This lower maximum ramp rate of $+0.3\text{Amin}^{-1}$ would correspond to an even larger timescale than 600 seconds to achieve the required load change. Therefore, it is clear from the above discussion that the ramp rate and the dynamic capabilities of the SOFC are currently limited.

In comparison to the several hundreds of seconds taken by the SOFC, the ICE operating on only natural gas took about 14 seconds for the same load change from 250 kWe to 375 kWe, based on experiments. Figure 7.7 shows the comparison between the time scales of the SOFC and the ICE for the same load change. The dynamic load response of the ICE was measured on the lean-burn, spark-ignited, natural gas test engine used in this research. The load response was measured at 1500 rpm and fixed initial NO_x of 500mgNm^{-3} . The spark-timing for these engine experiments was fixed at 24°CA bTDC .

Based on the comparison presented in Figure 7.7, it is evident that large and fast load changes could be challenging to meet with a SOFC. Depending on the application, operating conditions and ship operations, load demand in maritime can be close to fixed for hotelling and propulsion, however, changes in load demand can also be sudden requiring large load changes in tens of seconds. For instance, Taskar et al. showed that for a ship in head waves during harsh weather conditions, power fluctuations of 40 % of rated power can be encountered in about 10 seconds [22, 24]. Similarly, Theotokatos simulated the transient behaviour of a merchant ship (bulk carrier) under both acceleration and deceleration operating conditions [25]. The author showed that the effective power of the power generation unit (diesel engine) during acceleration increased from about 3000 kW (26 % of rated power) to 7000 kW (about 61 % of rated power) in about 120 seconds. Comparatively, the SOFC took about 600 seconds to change the load from 250 kWe to 375 kWe, as seen from Figure 7.7(a). At the same time, the NG-fuelled test ICE took about 14 seconds for the same load change of 25 % rated power (500 kWe), as explained earlier. Therefore, it is clear from the above discussion that the NG-fuelled ICE has better dynamic load response capabilities than that of a SOFC for maritime applications.

Thus, in the SOFC-ICE system proposed for maritime applications, a power split that favours the ICE would significantly improve the dynamic capabilities of the combined system and the possible sudden and large load changes can be met by the ICE.

IMPACT OF AOG CONSTITUENTS ON THE LOAD RESPONSE OF ICE

In the above subsection, the relatively faster dynamic capabilities of the ICE compared to the SOFC were discussed. As explained earlier, a marine propulsion system can be exposed to sudden and large load changes depending on the application. Therefore, the transient capabilities of the ICE are of significant interest in an integrated system. When integrating with the SOFC, the dynamic capabilities of the NG-fuelled ICE can be impacted by the constituents of AOG. Blending hydrogen and carbon dioxide with natural gas can impact the engine transients, which is a crucial part of the broad definition of engine performance. Thus, in this subsection, the impact of AOG constituents (hydrogen

and carbon dioxide) on engine dynamics is quantitatively and qualitatively investigated to completely answer Research Question 3, which raises the question pertaining to the effects of combusting anode-off gas (constituents) on the performance of the marine NG engine.

In this research, the effects of hydrogen addition on NG engine dynamics are quantitatively discussed based on engine experiments. For this experimental study, tests were performed on the lean-burn SI, NG test engine with only natural gas and 10H₂-NG fuel blend for a load change from 250 kW_e to 375 kW_e. During both these dynamic engine tests, the initial NO_x value at 250 kW_e load was kept close to 500 mgN m⁻³, after which the demand for load pick-up was applied. The spark-timing for all engine experiments discussed in this subsection is 24° CA bTDC. Figure 7.8(a) shows the NO_x and the exhaust O₂ response when the load change was applied. Figure 7.8(b) depicts the engine load and speed response for the two test cases. The ICE load transients plotted in Figure 7.7(b) and Figure 7.8(b) are the same. Figure 7.7(b) in the previous subsection shows the data marker of 20 seconds corresponding to the steady state point of 375 kW_e for ICE transients with ONG. As seen in Figure 7.8(b), the ICE with 10H₂-NG fuel blend has a slower load and speed response and takes about 3.5 seconds more to reach steady state and the 375 kW_e output compared to only natural gas. Therefore, it is evident from Figure 7.8(b) that hydrogen addition slows down the ICE dynamic load response capabilities. The reasoning behind this phenomenon is discussed further in the upcoming paragraphs.

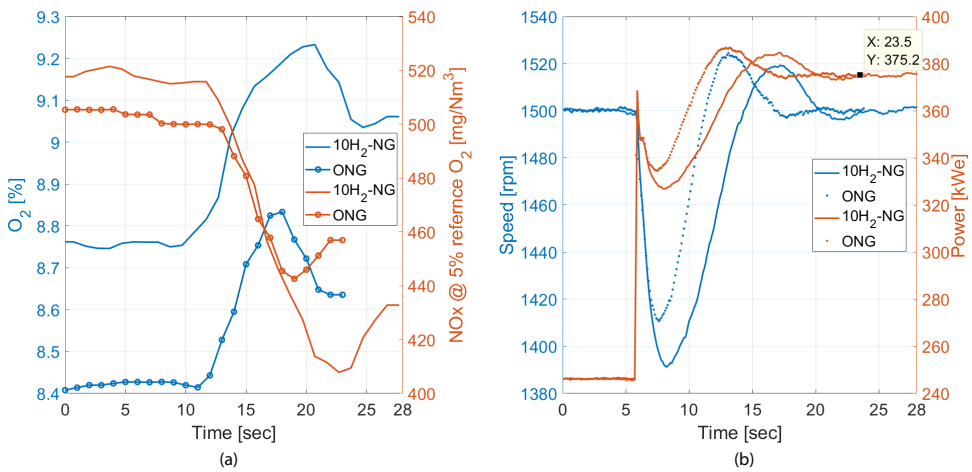


Figure 7.8: Comparison between the dynamic response of ICE operating on only natural gas and 10H₂-NG blend for a load change from 250 to 375 kW_e. O₂ % in exhaust and NO_x in mgN m⁻³ at 5% O₂ reference (a). Corresponding engine speed and power response (b)

On applying the load change at 5.7 seconds as seen in Figure 7.8(b), the first response of the ICE is to fully open the throttle valve to allow for a quick increase in air-fuel mass that is present before the throttle under steady-state conditions. Introduction of this additional mass allows for the instant increase in engine power output to about 360 kW_e at 6 seconds. At this point, the sudden opening of the throttle valve causes the pres-

sure before throttle to decrease to the lowest value as seen in Figure 7.9. After about 6 seconds, the supply of additional mass into the ICE is dictated by the turbocharger response. The lag in turbocharger ramp causes the engine load and speed to drop. As the turbocharger starts spooling and providing more air, the mixture inside the cylinder becomes increasingly leaner, which is indicated by the increase in O_2 % in the exhaust gas, which is evident from Figure 7.8(a).

As the engine speed and load drop, and the manifold pressure increases indicating leaner in-cylinder mixtures, the engine fuel controller starts increasing the amount of fuel. In addition to the response from the fuel controller, the generator voltage controller reduces the load demand as the speed drops below 1490 rpm to keep the engine alive. This drop in power demand due to generator voltage controller is visualized by the small fluctuation in ICE power, noticeable at about 6.3 seconds, followed by a controlled drop in power till about 7.5 to 8 seconds for the ONG and H_2 -NG fuel blend as seen in Figure 7.8(b).

The increasing fuel flow helps in spooling up the turbocharger, which increases the pressure before throttle allowing the engine speed and power output to start increasing again after reaching the minimum value at about 7.5 to 8 seconds. Once the engine speed overshoots beyond its rated speed of 1500 rpm, the throttle valve starts closing restricting the air-fuel mass entering the cylinders while the fuel controller reduces the amount of fuel to reach steady state and the required load of 375 kW.

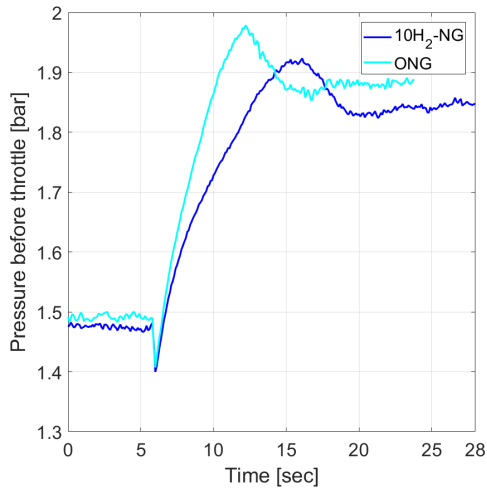


Figure 7.9: Comparison between pressure before throttle response of ICE operating on only natural gas and $10H_2$ -NG blend for a load change from 250 to 375 kW

As seen from Figure 7.8(a), the NO_x values for both ONG and $10H_2$ -NG fuel blend are similar during the load change with initial values corresponding to about 500 mgNm^{-3} of NO_x . As explained earlier in section 6.3 of Chapter 6, more air is needed with hydrogen addition to maintain the similar values of NO_x , thus, resulting in higher values of manifold pressure. At the same time, the gas temperature and energy entering the turbocharger reduce with increasing hydrogen blending, which slows down the response of

the turbocharger. This reduces the rate at which the pressure before throttle builds up, thus, creating a mismatch between the supply and demand of air. The slower increase in pressure before throttle for the 10H₂-NG blend compared to ONG can be seen in Figure 7.9. This turbocharger lag with hydrogen addition at same NO_x contributes to the slower dynamic response of the ICE found for the H₂-NG fuel blend. Extrapolating from this explanation, it can be understood that increasing the percentage of hydrogen blend in natural gas will lead to even slower engine load response for load changes at similar NO_x values.

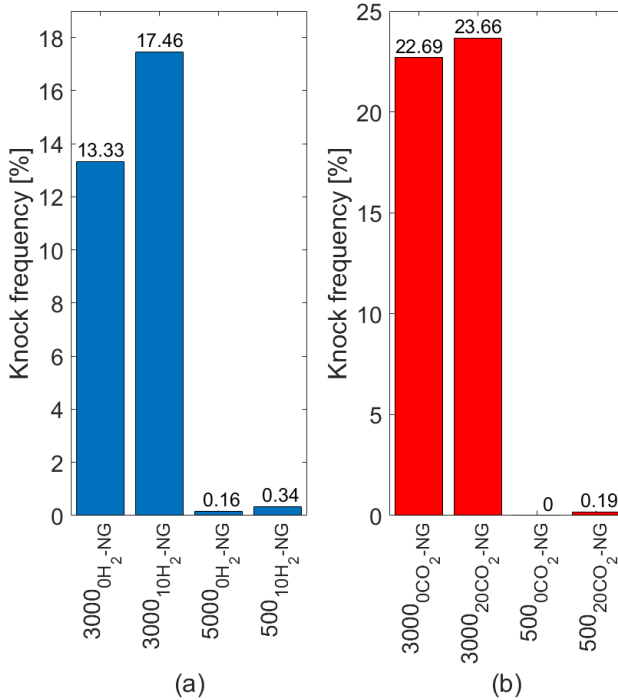


Figure 7.10: Comparison between the knocking frequencies recorded for only natural gas and 10H₂-NG fuel blends (a); and only natural gas and 20CO₂-NG blends at 250 kW load and 500 and 3000 mgN m⁻³ of NO_x

In contrast to applying the load change with same initial NO_x values, an idea could be to initiate transients with H₂ addition at a higher NO_x value compared to ONG. This could help counter the slower dynamic load response due to hydrogen addition as the in-cylinder and exhaust temperatures are increased at higher NO_x, allowing the turbocharger to spool up faster. However, operation with hydrogen addition at higher NO_x is limited by the higher knocking tendency of H₂ [26]. Based on the steady state experiments performed in this research, the addition of H₂ showed higher knocking tendency at the same NO_x and load operation.

In this research, the knock tendency of a fuel blend during steady state measurements is analysed by studying the knock frequency recorded for the different fuel blends. Knock frequency is defined as the percentage of total (145) number of cycles in which knocking

is detected during static measurements. A cycle is considered to be knocking if knock ratio is detected to be higher than a knock factor of 1.5 [27]. The knock detection method applied in this research, using the Ki-Box, is based on the Siemens-VDO method described by Trijselaar [27]. A higher knock frequency measurement is considered to be an indicator of a higher knock tendency.

As seen in Figure 7.10(a), addition of 10% H₂ at 250 kWe load and 500 mgN m⁻³ of NO_x showed a marginal increase in knock frequency compared to ONG performance at same operating conditions. However, operating at higher values of 3000 mgN m⁻³ of NO_x drastically increased the knock frequency for the 10H₂-NG fuel blend compared to ONG at 250 kWe load. Thus, indicating that for hydrogen addition and higher NO_x values knocking tendency increases. This indicates that load change at higher NO_x values with hydrogen addition compared to ONG performance would be highly restricted by the knock. Therefore, compared to ONG operation, an ICE load change will have to be performed at same or lower NO_x values with increasing hydrogen addition percentages, which would lead to higher timescales for a load change, thus, reducing the dynamic capabilities of the ICE. In other words, it can be concluded that marine gas engines operating on high hydrogen blend percentages or 100% hydrogen would have reduced dynamic capabilities compared to 100% natural gas engines.

In addition to H₂, SOFC anode-off gas contains high percentages of CO₂. As explained earlier in section 6.3 of Chapter 6, contrary to hydrogen, CO₂-NG fuel blends require less air and produce higher values of pressure before throttle at same NO_x values. The higher values of pressure before throttle are available from the turbocharger due to higher exhaust gas temperatures, thus, leading to the positive delta between the demand and supply of air. Therefore, by adding high percentages of CO₂ to natural gas, the turbocharger could spool up faster leading to faster dynamics at the same NO_x. This potential of improved ICE transients with CO₂ addition could be of interest when integrating with the SOFC. By increasing the fuel utilization of the SOFC to high values of 80 to 85%, the percentage of CO₂ in anode-off gas and, thus, in the fuel blend entering the cylinder could be increased during a load change. Allowing the ICE to operate with higher CO₂ blend percentages may help in reducing the timescale for a load change, which may allow for larger load steps of gas engines, thus, improving the dynamic capabilities.

To further understand the engine dynamics with CO₂ addition, the impact of CO₂-NG fuel blends on knock frequency was investigated. Figure 7.10(b) compares the knock frequencies for 20CO₂-NG fuel blends and the corresponding only natural gas operations at 250 kWe load and same values of 500 and 3000 mgN m⁻³ of NO_x. As explained in subsection 4.3.2 of Chapter 4, engine performance showed minor but important fluctuations during the CO₂-NG experiments compared to the H₂-NG experiments, which were performed separately. Therefore, the engine performance due to CO₂ addition cannot be directly compared with the H₂-NG results. However, the impact of CO₂ addition can be compared against the corresponding ONG or 0CO₂-NG fuel blends as shown in Figure 7.10(b).

Looking at Figure 7.10(b), it is evident that CO₂-NG fuel blends showed similar knock tendencies compared to ONG for same NO_x and load operation. This indicates that it may be possible to gain some improvements in the load response of the ICE compared to ONG operation by adding higher CO₂ percentages with the same NO_x values during

load pick-up. However, like hydrogen, load change at high NO_x values with CO₂ addition and ONG may be restricted due to the significantly high knock frequencies recorded at NO_x values of 3000 mgNm⁻³. Therefore, for a better understanding of the transient capabilities of the integrated engine, it may be worthwhile to further study the dynamic response of the ICE with AOG-NG blends containing higher percentages of CO₂ corresponding to SOFC operation at high fuel utilizations. This investigation is recommended for future research. However, it is vital to note that the presence of relatively smaller hydrogen percentages in the AOG at high fuel utilizations may counter the improvements in engine dynamic response obtained by CO₂ addition. In such a case, it may be interesting and simpler to operate the ICE on only NG during load transients while the anode-off gas is recirculated back to the SOFC.

For a comprehensive understanding of the dynamic capabilities of the integrated SOFC-ICE system for marine power generation, a detailed and experimentally validated modelling study is recommended that captures the complex interactions between the SOFC, ICE and balance-of-plant components such as heat exchangers, blowers, pumps, etc.

7.3.3. UNEXPLORED POTENTIAL OF SOFC-ICE INTEGRATION

It is evident from the earlier discussions in this chapter that the proposed SOFC-ICE integration can improve power generation efficiency and reduce ship emissions. The concept of SOFC-ICE integration has additional unexplored potential that can initiate a paradigm shift in ship performance and operations. Further research is required to completely realise the potential of SOFC-ICE integration. This subsection covers future research ideas that need further investigation to unlock the untapped potential of SOFC-ICE integration, which are as follows:

- The analysis performed in the earlier sections showcasing the efficiency improvements with SOFC-ICE integration is performed for a rated power output. However, a power generation unit onboard a ship frequently operates at part load conditions. Engines have poor part load efficiencies [28]. Contrary to which, a SOFC-ICE power plant could provide high-efficiency operation at part loads. The following paragraphs shed light upon this unexplored potential.

In this dissertation, until now, the integrated SOFC-ICE system was operated with a constant 30-70 AOG-NG blend inside the engine, which improved engine and system performance based on experimental and simulation studies. In the current analysis, an extension of this SOFC-ICE integration approach is proposed, which showcases the untapped potential of SOFC-ICE integration. This extended method or approach is called as the flexible fuel blend (FFb) method, in which, the SOFC is integrated with a flexible fuel blend (FFb) engine capable of operating on any blend of anode-off gas and natural gas ranging from 100 % AOG to 30-70 AOG-NG to 100 % NG. In this method, upto a certain load, the FFb engine would operate on only AOG to meet the small part load requirements. Beyond that load percentage, the amount of NG blended with AOG would be increased to generate additional power at higher load percentages. Operation on only AOG could lead to system operation efficiency of 60 % and higher. The efficiency improvement can be attributed to additional power generation by the en-

gine operating on only SOFC AOG. Operation at higher loads would require blending of NG with the AOG to produce the higher power outputs, thus, decreasing the system efficiency below 60 %. However, the efficiencies could still be much higher than a conventional marine NG engine at the same load due to large percentages of anode-off gas in the AOG-NG fuel blend.

To demonstrate this unexplored potential of SOFC-ICE integration for marine power generation, a notional vessel is considered to be powered by the GasDrive system or the integrated SOFC-ICE system. Based on the results from subsection 7.3.1, the installed SOFC-ICE system is assumed to have a power split of 33-67. The SOFC is matched to provide the constant load demand of hotel load during ship operation, thus, providing constant and high-efficiency power generation. The propulsion power needed for 0 to 15 knots of ship speed is delivered by the integrated ICE. As the ship speed increases, the real-time SOFC-ICE PS changes with increasing load demand, as seen in Figure 7.11(a). For instance, at 1 knots, the SOFC load share is about 92 %, which decreases to about 33 % at 15 knots because the SOFC power remains constant (hotel load) while the load share of the integrated engine increases. In this analysis, the SOFCs are considered to provide the constant hotel load demands due to their limited dynamic capabilities, as explained in subsection 7.3.2.

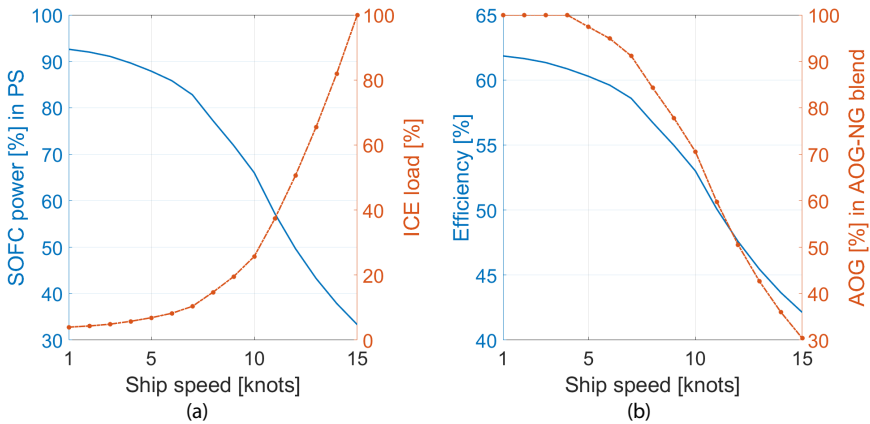


Figure 7.11: Load sharing between the components for SOFC-ICE integration (a) Projected efficiency based on the FFb method (b) at different ships speeds

In this notional vessel analysis with the FFb method, the unexplored potential of SOFC-ICE integration is investigated based on certain assumptions, which are as follows. In the FFb method, the integrated FFb engine is assumed to be able to produce 10 % of SOFC-ICE system load operating on only SOFC AOG. Chuahy et al. and Kim et al. showed that a SOFC-ICE system with about 85-15 PS could yield greater than 60 % efficiency while the engine operated on only AOG using advanced combustion technology [14, 29]. Beyond the 10 % load share, the efficiency is assumed to linearly decrease as the engine load and the amount of NG blended with AOG increases. For this analysis, the efficiency of the SOFC is assumed to be about 55 % based on the 0-D SOFC model simulations from subsection 7.3.1. To estimate the SOFC-ICE efficiency

and the percentage of NG in the AOG-NG fuel blend, linear relations are fitted with the FFb engine load share from the SOFC-ICE PS as the input.

Based on this approach, the SOFC-ICE efficiency for the FFb method would decrease from about 60 % at about 10 % load share and only AOG to about 42 % at 67 % engine load share and 30-70 AOG-NG blend, corresponding to 100 % propulsion power at 15 knots as seen from Figure 7.11. At speeds of about 10 knots corresponding to part load system performance, system efficiencies of greater than 50 % could be achieved, which is very high compared to conventional marine engines as the efficiency of marine engines significantly reduces at part loads. The very high projected efficiencies found for the FFb method at low speeds are due to the higher load share of SOFC in addition to the much higher efficiencies of the FFb ICE operating on flexible blends with much higher percentages of AOG than NG.

If a flexible fuel blend AOG-NG engine capable of operating on any blend of anode-off gas and natural gas can be developed, unprecedented efficiency improvements could be gained at part load operation. Therefore, further research should be performed to investigate the operation of the marine SI engine at different loads on only anode-off gas and AOG-NG blends with the percentage of anode-off gas greater than 30 %. For the development of the flexible fuel blend AOG-NG engine, advanced combustion technologies such as spark-assisted (SAI) combustion could be interesting and should be considered for future research.

The reader is directed to a recent paper by the author [2], in which, the potential of SOFC-ICE integration was studied for three case studies of naval vessels, namely, an oceangoing patrol vessel, a landing platform dock and a high-speed surface combatant based on early design phase calculations. Using the operational profiles of the vessels, optimal load sharing strategies between the two energy conversion devices were investigated for the three cases studies. Based on the optimal power split, this unexplored potential of SOFC-ICE integration was discussed for part load operations and compared against the conventional and existing power plants onboard comparable ships.

- In this research, the engine performance analysis for SOFC-ICE integration is based on a NG engine with an efficiency of about 33.6 % at power output of 375 kWe. However, new state-of-the-art NG engines can operate with a maximum efficiency of about 43 % at power output of 400 kWe [16]. By integrating the SOFC with such a state-of-the-art NG engine, SOFC-ICE integration could allow operation at even higher efficiencies than those found in this research. Therefore, SOFC integration with such a state-of-the-art NG engine should be researched in future.
- In the current research, natural gas is used as a primary fuel for the SOFC-ICE power plant. In addition to natural gas, methanol and ammonia are also gathering increasing interest in the maritime industry due to their promise of renewable production and substantially low emissions [30–32]. While ammonia can be cracked in a SOFC, methanol can be reformed like natural gas for power generation in a SOFC [33, 34]. Additionally, both methanol and ammonia can be combusted in an ICE for power generation [35, 36]. Methanol and ammonia powered SOFC-ICE power plants could be an

interesting alternative to the traditional marine engines due to their promise of very low emissions and high-efficiency operation. Therefore, methanol and ammonia powered SOFC-ICE power plants should be researched in future.

7.4. CONCLUSIONS

In this chapter, the 0-D SOFC model and the AOG-NG MVEM were used to simulate the performance of the SOFC-ICE power plant. The impact of ISVs such as current density, pre-reforming ratio, fuel utilization, heat integration and power splits on the integrated SOFC-ICE system were studied. Table 7.9 summarizes the impact of SOFC control parameters on the efficiency of the SOFC, integrated AOG-NG engine and the SOFC-ICE power plant, thus, shedding light on the interactions between the SOFC performance, AOG composition and the integrated AOG-NG engine performance. The summary provided in Table 7.9 and the discussion on the impact of heat integration and power splits help answer Research Question 5. The following concluding remarks are noted from the discussions presented in this chapter:

Table 7.9: Summary of effects of SOFC control parameters on the efficiency of the SOFC, integrated AOG-NG engine and the SOFC-ICE power plant

Parameter	η_{SOFC}	$\eta_{\text{I-ICE}}$	$\eta_{\text{SOFC-ICE}}$
Current density	-	-	+
Pre-reforming ratio	+	-	+
Fuel utilization	+	-	+

SOFC-ICE INTEGRATION

- As seen from Table 7.9, increase in current density reduced SOFC and engine efficiency, however, the efficiency of the integrated power plant increased due to a larger load-share of the SOFC when producing a fixed system power output. For other steady state simulations, current density was fixed at or close to 5000 Am^{-2} because it provides a good balance between capital cost, efficiency, stable and realistic operation and power density.
- Next, with increasing pre-reforming ratio, the SOFC efficiency improved due to a small increase in its power output. However, the efficiency of the integrated AOG-NG engine reduced with increasing pre-reforming ratio due to operation at reduced loads. Pre-reforming ratio was kept constant at 30 % as increased pre-reforming can increase the size of the pre-reformer, thus, reducing power density of the system. Furthermore, increased pre-reforming leads to an increase in heat and steam requirements from the SOFC, which could complicate and strain the Balance-of-Plant (BoP) and fuel cell operations. Increments in both current density and pre-reforming ratio showed increments in SOFC-ICE power plant efficiency due to a larger load share of the SOFC in the power split.
- Operation at high fuel utilizations showed improvements in SOFC efficiency, however, the engine efficiency dropped due to larger percentages of carbon dioxide in the

anode-off gas. Although increasing fuel utilization led to efficiency improvements, operation at high fuel utilization adversely affects the cell lifetime due to fuel starvation. The efficiency of the integrated AOG-NG engine was higher than the standalone AOG-NG engine efficiency by a maximum of 2.55 % at 70 % fuel utilization. This improvement increased to 3.55 % when compared to ONG performance of the standalone engine producing the same power output. The integration between the SOFC and the integrated AOG-NG engine provided a maximum efficiency improvement of 7.2 % at 85 % fuel utilization in comparison to the simulated efficiency of the standalone marine engine operating on only natural gas at 750 kWe.

- In this research, operation was found to be favourable at 75 % to 80 % fuel utilization as it ensures safe fuel cell operation, high SOFC efficiency and a good ratio of hydrogen and carbon dioxide in AOG-NG blend for improved engine operation. Thus, an optimal anode-off composition would correspond to fuel utilizations in the range of 75 % to 80 %, thus, answering Research Question 6.
- In addition to SOFC control parameters, the performance of the SOFC-ICE power plant was also investigated for different power splits. The SOFC-ICE power split of 67-33 showed the highest efficiency improvement of about 8 %, while UHC and NO_x emissions reduced by about 43 % and 60 % in comparison to a conventional marine natural gas engine. Furthermore, carbon dioxide (CO₂) emissions reduced by 20.74 %. However, the 67-33 power split also accounted for space and weight increments of approximately two and a half times.
- For maritime applications, promising improvements in efficiency of 5.2 %, UHC and NO_x reductions of about 30 % and CO₂ reductions of about 12 % can be achieved from a 33-67 SOFC-ICE power split with comparatively much smaller increments in size and weight of 1.7 times compared to a conventional marine natural gas engine. This research shows that significant enhancements in efficiency and reductions in emissions can be attained by integrating the SOFC with a commercially existing engine technology. In this manner, Research Question 7 is addressed in this dissertation.
- Next, the analysis in the chapter also shows that there is sufficient heat available within the system to allow for optimized heat integration with high-efficiency SOFC and system operation.

LOAD RESPONSE

- The 0-D SOFC model simulations showed that the SOFC took about 500 to 600 seconds to reach steady state (for a +2000 Am⁻² min⁻¹ ramp rate) and 600 seconds to reach the required load (for a +200 Am⁻² min⁻¹ ramp rate) during a load change from 250 to 375 kWe. Comparatively, the ICE achieved the same load change in about 14 seconds based on dynamic engine experiments. The study concluded that in the SOFC-ICE system proposed for maritime applications, a power split that favours the ICE would significantly improve the dynamic capabilities of the combined system and the possible sudden and large load changes can be met by the ICE.
- In this research, dynamic engine experiments were performed to study the impact of AOG constituents on the load response of a marine NG engine to completely answer

Research Question 3. The experimental results indicated that marine gas engine operating on hydrogen-natural gas blends or 100 % hydrogen would have reduced transient capabilities compared to ONG marine engines due to the increased turbocharger lag and higher knocking tendency of hydrogen at same NO_x and engine loading.

- The experimental analysis also indicated that allowing the ICE to operate with higher CO₂ blend percentages may help in reducing the timescale of for a load change due to the better turbocharger response with CO₂ addition at same NO_x and loading. Therefore, for a better understanding of the transient capabilities of the integrated engine, it may be worthwhile to further study the dynamic response of the ICE with AOG-NG blends containing higher percentages of CO₂ corresponding to SOFC operation at high fuel utilizations. However, it is vital to note that the presence of relatively smaller hydrogen percentages in the AOG at high fuel utilizations may counter the improvements in engine dynamic response obtained by CO₂ addition. In such a case, it may be interesting and simpler to operate the ICE on only NG during load transients while the anode-off gas is recirculated back to the SOFC.
- Like hydrogen, load change at high NO_x values with CO₂ addition and ONG may be restricted due to the significantly high knock frequencies recorded at NO_x values of 3000 mgN m⁻³.

UNEXPLORED POTENTIAL

- In addition to system performance analysis and load response, the chapter also highlighted the untapped potential of SOFC-ICE integration for future research. Further research into a flexible fuel blend AOG-NG engine capable of operating on any blend of anode-off gas and natural gas is recommended as it could lead to unprecedented efficiency improvements at part and full load operation.
- Lastly, methanol and ammonia powered SOFC-ICE power plants should be researched in future due to their promise of very low emissions and high-efficiency operation. In totality, the concept of SOFC-ICE integration has unexplored potential that can initiate a paradigm shift in ship performance and operations.

REFERENCES

- [1] H.D. Sapra et al. Integration of Solid Oxide Fuel Cell and Internal Combustion Engine for Maritime Applications. *Applied Energy*, 2020.
- [2] H.D. Sapra et al. Potential of COmbined drive of Fuel cell And Internal Combustion Engine (COFAICE) for naval ships. *International Naval Engineering Conference*, 2020.
- [3] M.Z. Khan et al. Effect of Applied Current Density on the Degradation Behavior of Anode-Supported Flat-Tubular Solid Oxide Fuel Cells. *Journal of the European Ceramic Society*, 2020.
- [4] P. Aguiar, C. S. Adjiman, and N. P. Brandon. Anode-Supported Intermediate Temperature Direct Internal Reforming Solid Oxide Fuel Cell. I: Model-Based Steady-State Performance. *Journal of Power Sources*, 2004.

- [5] M. Halinen. *Improving the Performance of Solid Oxide Fuel Cell Systems*. PhD thesis, Aalto University School of Science, 2015.
- [6] J.S. Szmyd et al. The Effect of Applied Control Strategy on the Current-Voltage Correlation of a Solid Oxide Fuel Cell Stack during Dynamic Operation. *Archives of Thermodynamics*, 2014.
- [7] J.H. Hirschenhofer, D.B. Stauffer, R.R. Engleman, and M.G. Klett. *Fuel Cell Handbook, Fourth Edition*. 1998.
- [8] CAT G3516A Gas Generator. https://www.cat.com/en_US/products/new/power-systems/electric-power/gas-generator-sets/18486985.html.
- [9] H.K. Woud and D. Stapersma. *Selected Chapters from "Design of Auxiliary Systems, Shafting and Flexible Mounting Systems"*. Delft University of Technology, 2016.
- [10] D. Stapersma. *Diesel Engines: A Fundamental Approach to Performance Analysis, Turbocharging, Combustion, Emissions and Heat Transfer Including Thermodynamical Principles. Vol. 6: Thermodynamical Principles II*. Delft University of Technology, 2010.
- [11] A.C. Dimian and C.S. Bildea. *Chemical Process Design*. Wiley-VCH, 2008.
- [12] L. van Biert et al. A Thermodynamic Comparison of Solid Oxide Fuel Cell-Combined Cycles. *Journal of Power Sources*, 2018.
- [13] S.H. Park, Y.D. Lee, and K.Y. Ahn. Performance Analysis of an SOFC/HCCI Engine Hybrid System: System Simulation and Thermo-Economic Comparison. *International Journal of Hydrogen Energy*, 2014.
- [14] F.D.F. Chuahy and S.L. Kokjohn. Solid oxide fuel cell and advanced combustion engine combined cycle: A pathway to 70% electrical efficiency. *Applied Energy*, 235:391–408, feb 2019.
- [15] Energy Server ES5-300 kW Data Sheet. <https://www.bloomenergy.com/datasheets/energy-server-es5-300kw>.
- [16] CAT CG132B-8 Gas Generator. https://www.cat.com/en_US/products/new/power-systems/electric-power/gas-generator-sets/2841734473578834.html.
- [17] A. Salogni and P. Colonna. Modeling of Solid Oxide Fuel Cells for Dynamic Simulations of Integrated Systems. *Applied Thermal Engineering*, 2010.
- [18] P. Iora, P. Aguiar, C.S. Adjiman, and N.P. Brandon. Comparison of Two IT DIR-SOFC Models: Impact of Variable Thermodynamic, Physical, and Flow Properties. Steady-State and Dynamic Analysis. *Chemical Engineering Science*, 2005.
- [19] Technical Documentation, Integrated Stack Module (ISM). Technical report, Staxera, 2010.
- [20] G.D. Andrea, M. Gandiglio, A. Lanzini, and M. Santarelli. Dynamic Model with Experimental Validation of a Biogas-Fed SOFC Plant. *Energy Conversion and Management*, 2017.
- [21] S. Kang and K.Y. Ahn. Dynamic Modeling of Solid Oxide Fuel Cell and Engine Hybrid System for Distributed Power Generation. *Applied Energy*, 2017.

- [22] B. Taskar, K.K. Yum, S. Steen, and E. Pedersen. The Effect of Waves on Engine-Propeller Dynamics and Propulsion Performance of Dhps. *Ocean Engineering*, 2016.
- [23] L. van Biert, M. Godjevac, K. Visser, and P.V. Aravind. Dynamic Modelling of a Direct Internal Reforming Solid Oxide Fuel Cell Stack Based on Single Cell Experiments. *Applied Energy*, 2019.
- [24] CIMAC WG17 'Gas Engines'. Transient Response Behaviour of Gas Engines. 2011.
- [25] G.P. Theotokatos. A Modelling Approach for the Overall Ship Propulsion Plant Simulation. In *8th WSEAS Conference on System Science and Simulation in Engineering*, 2007.
- [26] S.M.V. Sagar and A.K. Agarwal. Knocking Behavior and Emission Characteristics of a Port Fuel Injected Hydrogen Enriched Compressed Natural Gas Fueled Spark Ignition Engine. *Applied Thermal Engineering*, 2018.
- [27] A. Trijselaar. Knock Prediction in Gas-Fired Reciprocating Engines. Master's thesis, University of Twente, 2012.
- [28] M.C. Ekwonu, S. Perry, and E.A. Oyedoh. Modelling and Simulation of Gas Engines Using Aspen HYSYS. *Journal of Engineering Science and Technology Review*, 2013.
- [29] J. Kim et al. Analysis on the Operating Performance of 5-kW Class Solid Oxide Fuel Cell-Internal Combustion Engine Hybrid System Using Spark-Assisted Ignition. *Applied Energy*, 2020.
- [30] Green Maritime Methanol Takes off With a Short List of Nine Ships. <https://www.marin.nl/green-maritime-methanol-takes-off-with-a-short-list-of-nine-ships>.
- [31] Methanol as a Marine Fuel. <https://www.methanex.com/about-methanol/methanol-marine-fuel>.
- [32] NH3 Fuel Association, Cardiff University, Yara, MAN, and C-JOB. Ammonia as Marine Fuel. In *NH3 Fuel Conference*, 2018.
- [33] D. Cheddie. Ammonia as a Hydrogen Source for Fuel Cells: A Review. In *Hydrogen Energy - Challenges and Perspectives*. InTech, 2012.
- [34] M. Liu et al. Direct Liquid Methanol-Fueled Solid Oxide Fuel Cell. *Journal of Power Sources*, 2008.
- [35] S. Verhelst, J.W.G. Turner, L. Sileghem, and J. Vancoillie. Methanol as a Fuel for Internal Combustion Engines. *Progress in Energy and Combustion Science*, 2019.
- [36] A. Valera-Medina et al. Ammonia for Power. *Progress in Energy and Combustion Science*, 2018.

8

UNDERWATER EXHAUST SYSTEM AND MARINE ENGINE PERFORMANCE

Currently, in automobiles and ships, exhaust systems are equipped with end-of-pipe-technologies to reduce harmful emissions. For instance, ship emissions have been subjected to strict restrictions by IMO TIER III regulations, which are applicable from 1 January 2016 [1]. According to engine manufacturers, TIER III emission regulations can be met by retrofitting marine engines with exhaust gas after-treatment technologies such as scrubbers and/or selective catalytic reactors (SCR) [2, 3]. However, aftertreatment technologies cause a pressure loss in the exhaust piping [4]. Another trend in the maritime industry is to employ underwater exhaust systems, as they provide zero direct emissions to the atmosphere (emissions still exist), space saving, and reduction in noise and pollution on working decks. Other advantages of expelling underwater are decreased risk of hotspot detection for naval ships, and improved aesthetics of luxury ships due to the elimination of bulky and un-appealing vertical exhaust funnels that pass through decks. Capitalizing on these advantages and more, the GasDrive ship propulsion concept employs underwater exhaust systems. As explained in Chapter 1, the GasDrive project uses the underwater exhaust system in combination with nano-hull coatings. The exhaust gases are expelled below the waterline by the underwater exhaust while they are captured by the nano-hull coatings to allow for drag reduction by gas lubrication. The drag reduction could lead to further reduction in fuel consumption, carbon dioxide emissions and space and weight requirements of the integrated SOFC-ICE system as the required installed power will be lowered. Therefore, in addition to SOFC-ICE integration, this dissertation also investigates the performance of a marine engine operating with underwater exhaust systems.

Underwater expulsion of exhaust gases has many advantages, however, the exiting

Parts of this chapter have been published in Applied Energy [5] and the ASME ICEF-2019 Conference [6].

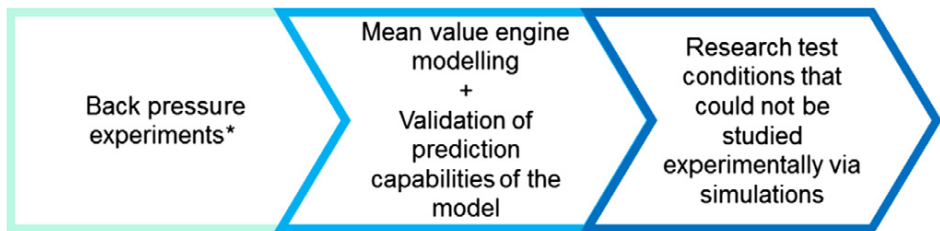
gases experience a flow resistance due to the pressure applied by the water at the outlet of underwater exhaust systems. The water or the sea waves at the outlet of the submerged exhaust impose a high and fluctuating resistance to the exhaust gas flow of the engine. The cumulative value of pressure loss or flow resistance in the exhaust system measured at the turbine outlet of a turbocharged engine or the outlet of the exhaust manifold of a naturally aspirated engine is the back pressure felt by the engine. The flow resistance in case of underwater exhaust systems is similar to the fluctuating flow resistance experienced by a submarine engine at snorkelling depth. At this depth, the pressure loss in the exhaust piping plus the static pressure due to the water head above the snorkel and the dynamic back pressure due to sea waves at the water surface accumulate to form a high and fluctuating pressure loss or back pressure, which is felt at the turbine outlet of the turbocharged engine. Although the underwater exhaust system for a ship is designed and positioned to reduce the static pressure head above the exhaust outlet [7], the sea waves at the exhaust outlet can cause the back pressure to fluctuate in amplitude and time period as a ship operates in varying sea-states depending on the geographical location of the ship and weather conditions. High and fluctuating back pressure due to underwater exhaust systems can adversely impact marine engine performance. Therefore, the research presented in this chapter focusses on understanding the effects of static and dynamic back pressure (ISV) on marine engine performance due to an underwater exhaust system, thus, answering Research Questions 8 and 9.

8.1. INVESTIGATIONS OF MARINE DIESEL ENGINE PERFORMANCE AGAINST STATIC BACK PRESSURE

The study of the effects of static back pressure on engine performance was carried out via experiments and simulations. The research methodology applied and the experimental test setup is described in this section, followed by a description of the diesel engine simulation model used for this investigation. The section concludes with the calibration of the engine model and its validation to further study the effects of static back pressure on engine performance.

8.1.1. METHODOLOGY AND TEST SETUP FOR STATIC BACK PRESSURE

METHODOLOGY



*on a pulse turbocharged, medium speed, 4-stroke diesel engine

Figure 8.1: Research methodology to study the effects of static back pressure

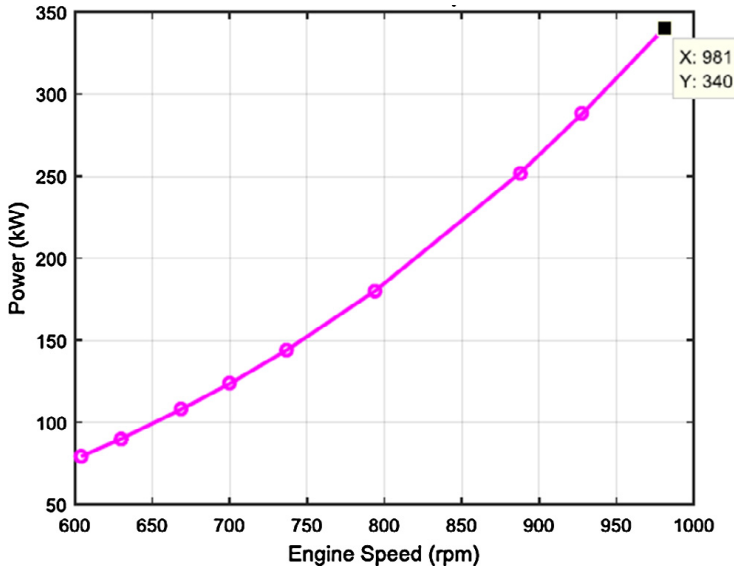


Figure 8.2: Measurement setpoints along the propeller curve

In this research, engine model simulations along with experiments on a pulse turbocharged, medium speed, and 4-stroke diesel engine are used as tools to study effects of static back pressure on engine performance. Figure 8.1 shows the basic approach followed for this research. An extended mean value engine model (Ex-MVEM) is adopted to simulate engine performance against externally applied high static back pressure, which could not be studied experimentally.

Table 8.1: Engine specifications

Parameter	
Engine model	MAN4L2027
Number of cylinders	4
Bore	0.20 m
Stroke	0.27 m
Rated speed	1000 rpm
Rated power	360 kW
Compression ratio	13.4
Fuel injection system	Plunger pump, direct injection
Turbocharger system	Pulse
Maximum back pressure	25 mbar (0.25 mWC)

During the experiments, engine parameters were first measured at 9 different setpoints of load and engine speed, against three cases of back pressure. Figure 8.2 depicts the 9 setpoints measured. In the first case, engine performance with no externally applied back pressure was measured. The second and the third cases were for 0.25 mWC

and 0.5 mWC of externally applied back pressure respectively. For each case of back pressure, and at each setpoint, engine parameters such as temperature, pressure, air flow-rate and fuel consumption were measured. The engine was allowed to settle for 15 min between each setpoint and each case of externally applied back pressure, to make sure that all the engine parameters were stabilized before measuring.

The second step was to use engine measurements against no external back pressure, to calibrate and match the Ex-MVEM to simulate the performance of the test engine. Once calibrated and matched, the model was used to simulate the engine performance against the remaining two cases of back pressure. The simulations were then compared against test engine measurements to validate the model.

Furthermore, engine measurements were restricted to the maximum setpoint of 340 kW at 981 rpm, while the actual rated power of this engine was 360 kW at 1000 rpm. However, Ex-MVEM was used to predict engine performance against static back pressure at 360 kW and 1000 rpm. Thus, for all the proceeding results shown for static back pressure, 100 percent load point corresponds to 340 kW while the 105.9 % load point corresponds to 360 kW, and 100 % rpm percentage point (especially for the results in section 8.1.3) corresponds to 1000 rpm of engine speed.

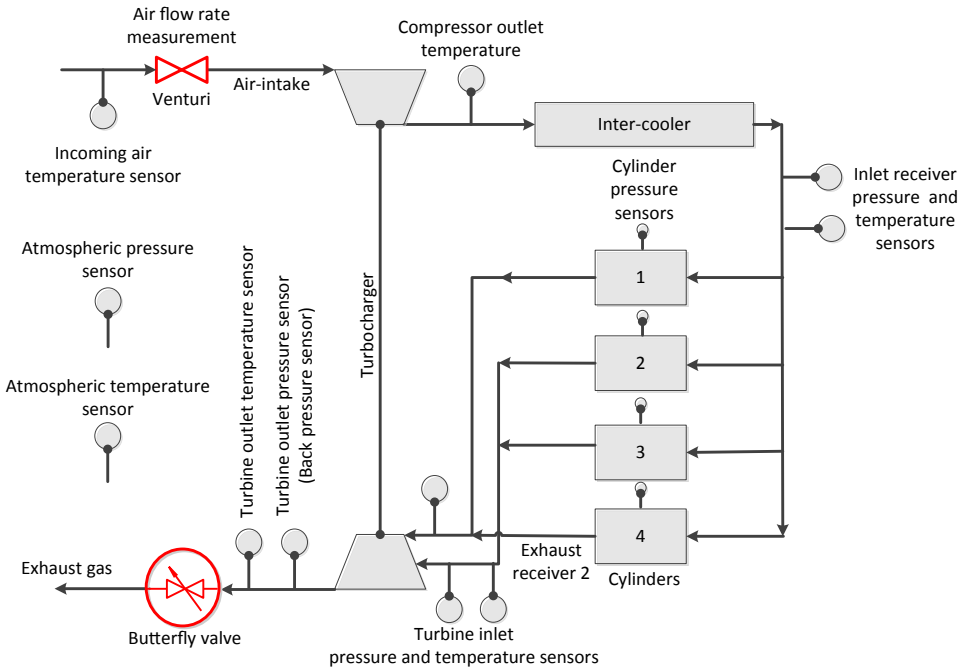


Figure 8.3: Outline of test setup along with the butterfly valve and sensor placement

Combination of experiments and simulation not only helped validate the prediction capabilities of the Ex-MVEM against static back pressure but also to study related engine performance. The validated model was used to understand and apply the concepts of smoke limit and thermal overloading to define back pressure limits. Lastly, the effect

of different engine valve overlaps on engine performance against high back pressure, and capabilities of a pulse turbocharged and a constant pressure turbocharged engine at handling back pressure of 1 mWC, which could not be studied experimentally, was also investigated via model simulations.

TEST SETUP

Back pressure experiments are performed on a 4-stroke, pulse turbocharged and marine diesel engine. Table 8.1 lists the specifications of this test engine. The test engine is connected to a water-brake to apply the required load. In this manner, the engine is made to run at any setpoint of speed and load. The engine governor keeps the engine at this specific engine speed point by controlling the fuel input in case of any back pressure fluctuations.

A manually operated butterfly valve, installed downstream of the turbine, is used to apply back pressure. Figure 8.3 gives a schematic representation of the engine test setup, along with the locations at which different measurements of pressure, temperature and air flow are taken. The same test engine is used to study the effects of dynamic back pressure on marine diesel engine performance. The research methodology for dynamic back pressure is addressed separately in section 8.2.1.

8.1.2. EXTENDED MEAN VALUE ENGINE MODEL DESCRIPTION

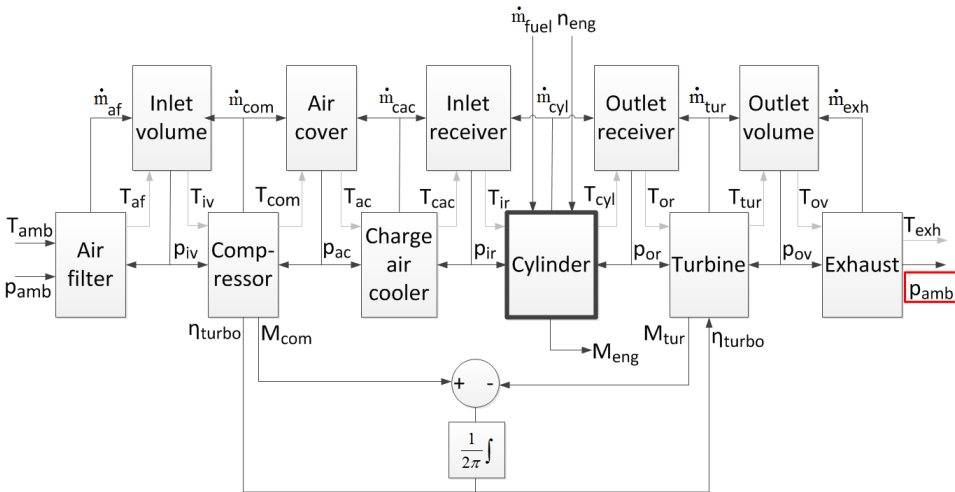


Figure 8.4: Extended mean value engine model [8, 9]

For the purpose of this research, the objective is to understand the effects of back pressure on overall engine parameters such as exhaust gas (exhaust receiver) temperatures, mass flow rates, manifold pressures, fuel consumption, etc. Thus, a mean value engine modelling approach was chosen, which included the gas exchange model along with a compressor-turbine model that proved vital when researching the effects of different engine valve overlaps and turbocharger configurations against back pressure. The

adopted model shown in Figure 8.4 has been developed at the Netherlands Defence Academy (NLDA) and Delft University of Technology (TU Delft). Different engine components such as the inlet volume, air-cover, inlet receiver, outlet receiver, cylinder and silencer/outlet volumes are modelled as a series of control volumes or 'volume elements'. These control volumes are connected to each other via resistances or 'resistance elements', as shown in Figure 8.4. The control volumes calculate the instantaneous mass by integrating the net mass flow (conservation of mass), and the instantaneous temperature by integrating the net energy flow associated with the mass flows (conservation of energy). The instantaneous pressure of the element is calculated using the ideal gas law.

On the other hand, resistance elements estimate the mass flow as a function of pressure difference using the momentum equation. The cylinder sub-model solves the Seiliger in-cylinder process along with the gas exchange to account for the induction, scavenging, blowdown and outgoing flows [8, 10]. At the same time, generic turbine and compressor maps are used to calculate turbine and compressor characteristics [11, 12]. The primary output is engine torque; however, temperatures, pressures and mass flows can be obtained for different engine components. Furthermore, friction losses are calculated using an adaptation of the empirical formula given by Chen and Flynn [13], with adaptable coefficients, which are estimated to get the correct specific-fuel consumption. A detailed description of the model including the in-cylinder Seiliger model for diesel combustion, gas exchange, model equations etc. can be found in [10, 11, 14–16]. The value of ambient pressure at exhaust outlet (p_{amb}), highlighted by a red box in Figure 8.4, was converted into an input for the model to apply external back pressure ($p_{BP_{Applied}}$). In this manner, the model was used to study engine performance against externally applied back pressure.

In this dissertation, the engine model shown in Figure 8.4 is referred to as the Ex-MVEM to distinguish it from the MVEM shown in Figure 6.4 of Chapter 6. The Ex-MVEM can be understood as an extension of the AOG-NG MVEM as it simulates different engine components as a combination of volume and resistance elements. The extended MVEM also models the gas exchange, which is crucial to capture the effects of back pressure on scavenging during different valve overlaps. Furthermore, the impact of back pressure on turbine characteristics is also captured in the Ex-MVEM, which in turn dictates the compressor characteristics and incoming mass flow entering the cylinder.

EX-MVEM WITH PULSE TURBOCHARGING

The test engine used for this research was equipped with a pulse turbocharger. Thus, a pulse turbocharger model was implemented in the Ex-MVEM. However, a pulse turbocharger system is not a mean value system. This is evident from Figure 8.5, which shows a typical pressure pulse measured at the turbine inlet. The Ex-MVEM used in this analysis has a pulse turbocharging model, which was originally developed by Baan [18]. The pulse model is based on the concept of pulse turbocharging given by Zinner [19] and is described in the following paragraphs.

In a pulse turbocharging system, the flow through the turbine reduces compared to that in case of a constant pressure system. Moreover, a pulse system turbine delivers more work than a constant pressure system [10]. This pulse effect of reduced mass flow

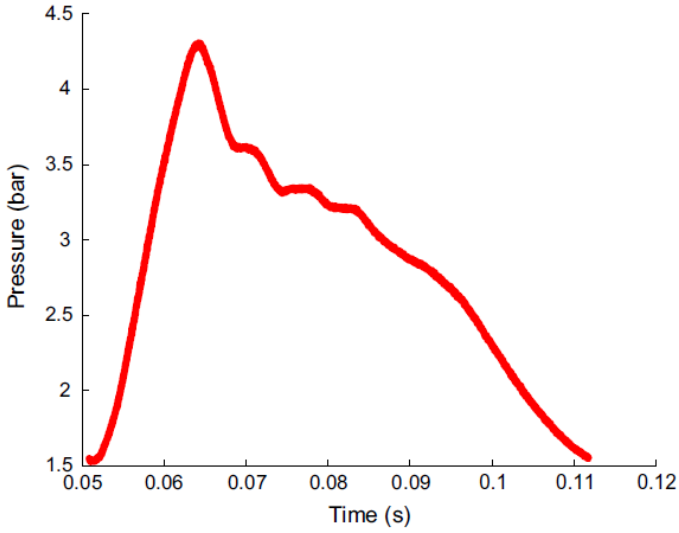


Figure 8.5: Measured turbine inlet pressure pulse

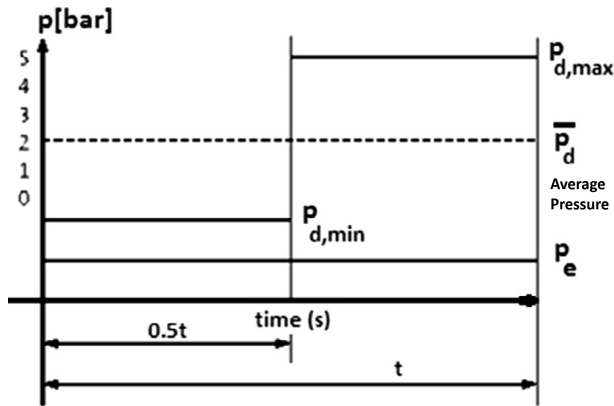


Figure 8.6: Simplified (Step function) turbine inlet pressure pulse [17]

and extra work is given by correction factors α and β , given by equation 8.1 and 8.2.

$$\alpha = \frac{\dot{m}_{\text{tur,pulse}}}{\dot{m}_{\text{tur,const}}} \tag{8.1}$$

$$\beta = \frac{\dot{W}_{\text{tur,pulse}}}{\dot{W}_{\text{tur,const}}} \tag{8.2}$$

where, ' $\dot{W}_{\text{tur,const}}$ ' is the work rate for a constant pressure system in kJ s^{-1} and ' $\dot{m}_{\text{tur,const}}$ ' is the turbine mass flow rate in kg s^{-1} for a constant pressure system.

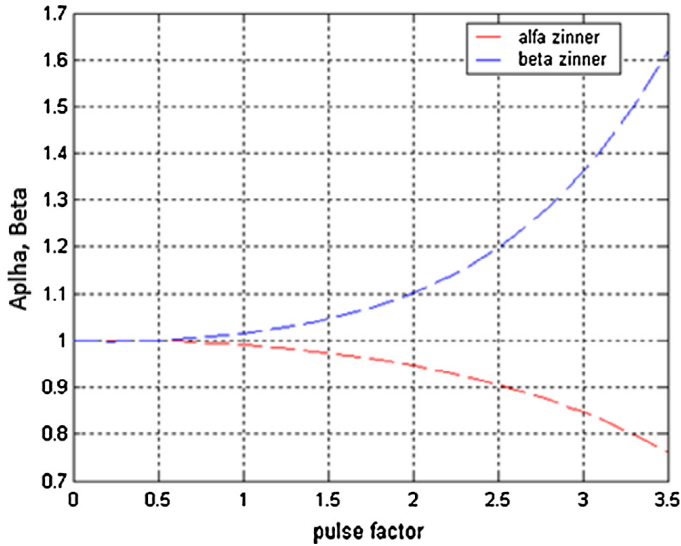


Figure 8.7: Correction factors α and β as a function of the pulse factor suggested by Zinner, according to Stapersma [10, 17]

The values of α and β can be derived by analysing the turbine inlet pressure pulse. The simplest way of representing the pulse is by means of a block or a step function. The block pulse, shown in Figure 8.6, is half the time at minimum discharge pressure and remaining at maximum discharge pressure. Zinner [19] showed with measurements that the correction factors α and β can be approximated as functions of a pulse factor. A pulse factor is defined as the ratio of the difference between the maximum ($p_{d,max}$) and minimum pressure ($p_{d,min}$) of the pulse and the difference of the mean outlet receiver pressure (\bar{p}_d) and the turbine outlet pressure (p_e) shown in Figure 8.6. The dependency of the correction factors on the pulse factor as suggested by Zinner is shown in Figure 8.7, and mathematically represented by equation 8.3 and 8.4.

$$\alpha = f_1\left(\frac{p_{d,max} - p_{d,min}}{\bar{p}_d - p_e}\right) \quad (8.3)$$

$$\beta = f_2\left(\frac{p_{d,max} - p_{d,min}}{\bar{p}_d - p_e}\right) \quad (8.4)$$

Ligtvoet, following Zinner, realized that using a step-function to describe a pressure pulse is a very crude approximation [17]. Therefore, in this research, measured pulses were used to understand the effect of pulse in terms of α and β correction factors. The underlying equations for this analysis, which will be covered in the next paragraphs, can be found in [10, 17]. For this analysis, the measured turbine inlet pressure pulse was discretized into multiple outlet receiver pressures, as shown in Figure 8.8.

For the pulse defined in Figure 8.8, the correction factor α was calculated by comparing the mass flow through the turbine in case of constant receiver pressure (with mean

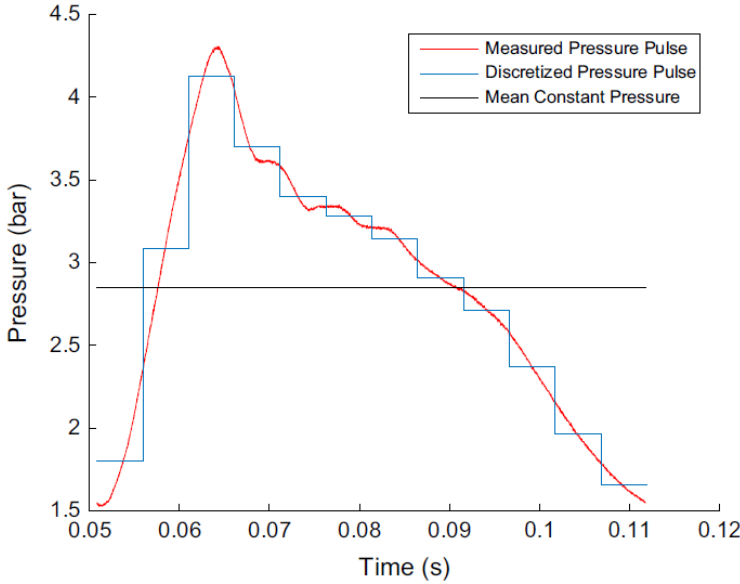


Figure 8.8: Discretization of measured turbine inlet pressure pulse at 340 kW and 981 rpm

constant pressure equal to mean of the pulse) to the sum of mass flows for different discrete pressures of the discrete pressure pulse.

$$\dot{m}_{tur,const} \approx \sqrt{\bar{p}_d - p_e} \tag{8.5}$$

$$\dot{m}_{tur,pulse} \approx \sum_{i=1}^x \sqrt{p_{d,i} - p_e} \tag{8.6}$$

where, 'i' = 1: number of discretized parts. The dependency of mass flow rate (\dot{m}_{tur}) through the turbine on square root of pressure difference between outlet receiver pressure and turbine outlet pressure is given by Stapersma in [10] and has been shown in equation 8.7

$$\dot{m}_{tur} \approx \sqrt{p_d - p_e} \tag{8.7}$$

Then, the correction factor (α) was calculated using equation 8.8.

$$\alpha = \frac{\dot{m}_{tur,pulse}}{\dot{m}_{tur,const}} = \frac{\sum_{i=1}^x \sqrt{p_{d,i} - p_e}}{\sqrt{\bar{p}_d - p_e}} \tag{8.8}$$

In a similar manner, β was calculated by applying equation 8.9.

$$\beta = \frac{\dot{W}_{tur,pulse}}{\dot{W}_{tur,const}} = \frac{\sum_{i=1}^x \dot{m}_{tur,pulse} \cdot (p_{d,i} - p_e)}{\dot{m}_{tur,const} \cdot (\bar{p}_d - p_e)} \tag{8.9}$$

Following this method, each turbine inlet pressure pulse, measured at the 9 setpoints is discretised into 12 parts and used to calculate the values of α and β . The results are provided in Table 8.2.

Table 8.2: Values of α and β calculated from the discretization pulse

RPM [%]	Load [%]	α	β
98.12	100	0.9763	1.06
92.83	84.7	0.9769	1.0629
88.79	74.11	0.9694	1.08455
79.37	52.94	0.9642	1.0867
73.68	42.35	0.9602	1.09529
70	36.32	0.9629	1.10425
66.9	31.76	0.9724	1.08267
62.99	26.47	0.9633	1.1046
60.37	23.23	0.9633	1.1527

Table 8.2 shows the values of α and β for the pulse system on the test bench engine. As expected, the values of α were found to be less than 1, while that of β were greater than 1. Thus, showing that for a pulse system the effective flow is lower and the effective turbine work is higher than that of a constant pressure system with the same mean pressure (as that of pulse) at the turbine inlet. In this way, the measured pressure pulses were used to derive the values of α and β correction factors given by Zinner. These values were then compared with simulated values of α and β , which were calculated in the model as a function of pulse factor using Figure 8.7, and equation 8.3 and 8.4, given by Zinner. However, in order to calculate the pulse factor from the parameters obtained from the Ex-MVEM, a modified pulse factor was adopted [20];

$$\text{Pulsefactor}_{\text{modified}} = C_{\text{pulse}} \left(\frac{p_6 - p_{sv}}{p_d - p_{sv}} \right) \quad (8.10)$$

where, (the maximum pressure) ' p_6 ' is the pressure obtained from the Seiliger process in Pa, ' p_{sv} ' is the pressure at turbine outlet (silencer volume) in Pa, ' p_d ' is the mean pressure in the outlet receiver in Pa obtained from the Ex-MVEM. The calculated modified pulse factor is much higher than the pulse factor proposed by Zinner. Therefore, a pulse correction factor (C_{pulse}) is introduced. This C_{pulse} factor is used as a tuning factor to get the correct charge pressure while closely comparing the α and β values obtained from the measured pulse and simulations.

CALIBRATION OF EX-MVEM

In order to apply the Ex-MVEM to simulate conditions that could not be studied experimentally, the model first needs to be calibrated and matched to simulate the performance of the test engine. Therefore, this section briefly discusses the setup of the Ex-MVEM and its calibration.

The Ex-MVEM is implemented in a MATLAB/Simulink environment and a number of parameters in principle must be specified. These parameters are arranged in an orderly set of parameter files and each file corresponds to a different component. For example, the 'cylinder_data.m' file contains all the parameters required to model the process within the cylinder. A pre-simulation creates a file 'initial_condition.mat' where the initial

values of all engine model parameters, which are required for the main engine simulation to break the loops at the initial time step, are saved. These parameters can be better understood by dividing them in the following manner [21]:

- (a) The known parameters;
- (b) The (arbitrarily) set parameters;
- (c) The unknown parameters.

The first category is simply known data such as the number and size of cylinders, type of engine, compression ratio, etc. This data is usually available from the engine manufacturers (found in the engine specifications guide). The second category of parameters is estimated, for instance, by expressing them non-dimensionally as a function of a known parameter. Examples are engine dimensions that are difficult to obtain (valve diameter, inlet and exhaust manifold diameters, etc.). These parameters can be set to a certain percentage of bore diameters. Their values can also be obtained from the engine test setup, if available.

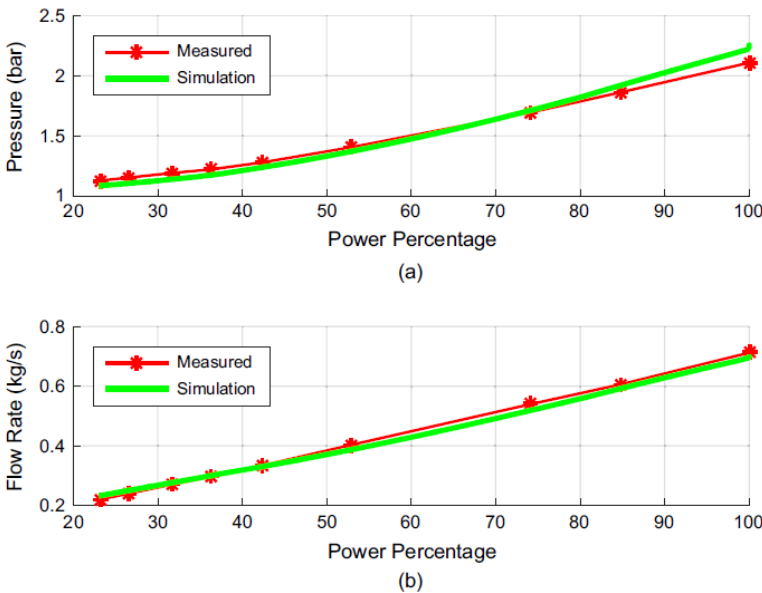


Figure 8.9: Comparison between measured and simulated inlet receiver pressure (a), and air mass flow rate (b)

The last category of parameters is mostly parameters that are intrinsic to the model and needed to simulate a certain phenomenon that is present in the real (full scale) system. For example, the ‘mu-phi’ parameter, a product of resistance/loss and contraction factor in the inlet and outlet valves; is used to determine the flow through the engine. The ‘mu-phi’ parameter is estimated to find the correct compressor size and thus, match the air-swallow characteristic of the compressor to that obtained from measurements. Furthermore, for an integrated system, several subsystems need to perform optimally. For

this purpose, some parameters (for instance, flow areas, piping lengths) need to be sized such that certain requirements are met. This is matching of the subsystems or briefly “system matching”, which is a key activity in system integration. Such a matching also needs to be performed for the Ex-MVEM. The analytical turbine and compressor models have some unknown parameters that need to be estimated to match the performance of the turbocharger and the diesel engine. This matching has been divided into the following three parts:

- (i) Matching the compressor flow to the engine inlet flow at the appropriate inlet receiver pressure and compressor and engine speed. This means matching the air-swallow characteristic of the compressor.
- (ii) Matching the turbine flow to the engine exhaust flow at the appropriate exhaust receiver pressure and temperature and turbine and engine speed. This means matching the turbine characteristic.
- (iii) Matching the turbine power to the compressor power. This ultimately boils down to the Büchi balance which links the inlet receiver pressure to the outlet receiver pressure as built up by the turbine and given the inlet temperature before the turbine in relation to the compressor inlet temperature.

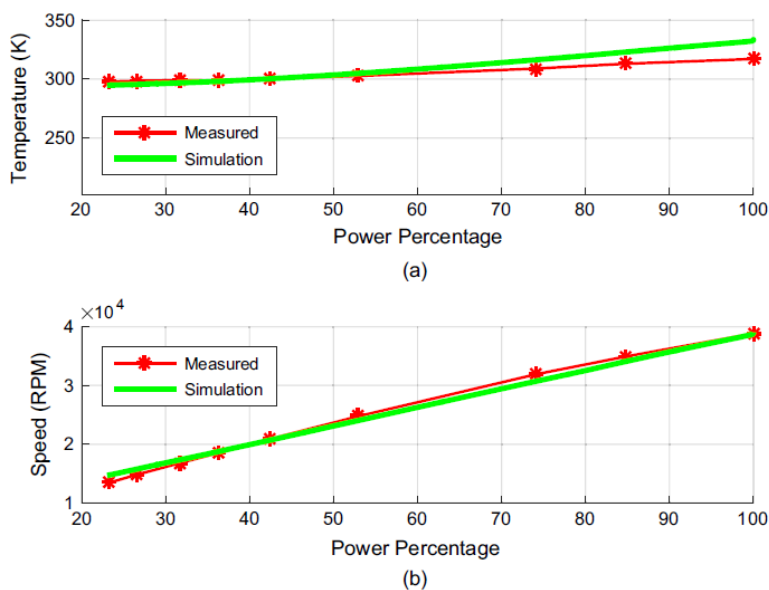


Figure 8.10: Comparison between measured and simulated inlet receiver temperature (a), and turbocharger speed (b)

Using the above-discussed parameters and method, the Ex-MVEM was calibrated and matched to simulate the performance of the test engine. A number of parameters were iteratively adjusted while comparing the simulation results with the test-bench

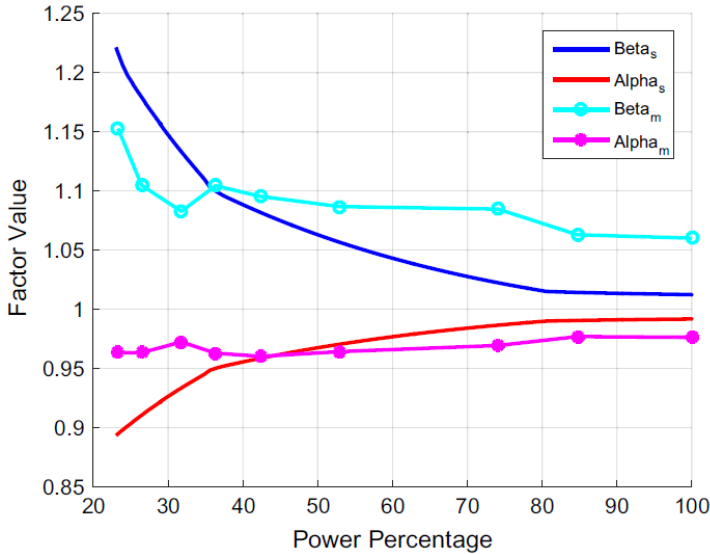


Figure 8.11: Comparison between α , β values obtained from simulation (s) and values calculated from measurements (m)

measurements. In the remainder of this section, simulated engine parameters have been compared with test-bench measurements to showcase the calibrated and matched Ex-MVEM simulating the performance of the test engine only for the case of no external back pressure. In the next section, the calibrated and matched model is validated against measurement with external back pressure.

The first proof of a good match between simulation and measurements is visible from Figure 8.9(a) and (b). These figures present the compressor performance of the engine, obtaining the correct air flow for the corresponding pressure. For a good matching, it is also essential to simulate the temperatures as accurately as possible. Figure 8.10(a) compares the simulated and measured inlet receiver temperature. The maximum error between the simulated and measured inlet receiver temperature is about 5 % at 100 % load. Furthermore, Figure 8.10(b) shows a good estimation of turbocharger speed.

The objective of a turbocharger model is to estimate the correct charge pressure and flow. However, it is also vital to estimate correct turbine pressures and temperatures. As explained earlier, the Ex-MVEM was applied to simulate the performance of a pulse turbocharged engine, which is not a mean value system and corrections had to be applied to the model. This gives deviations between simulated and measured turbine performance parameters. On the other hand, a constant pressure system (currently used turbocharger technology) would have a constant pressure in the outlet receiver, before the turbine, making it easier to simulate for a mean value model like the Ex-MVEM. Thus, the model would perform better with a constant pressure turbocharger system, like the AOG-NG MVEM.

Focussing back to the validation, Figure 8.11 shows the comparison between the values of α and β , simulated and the correction factors calculated for the measured turbine

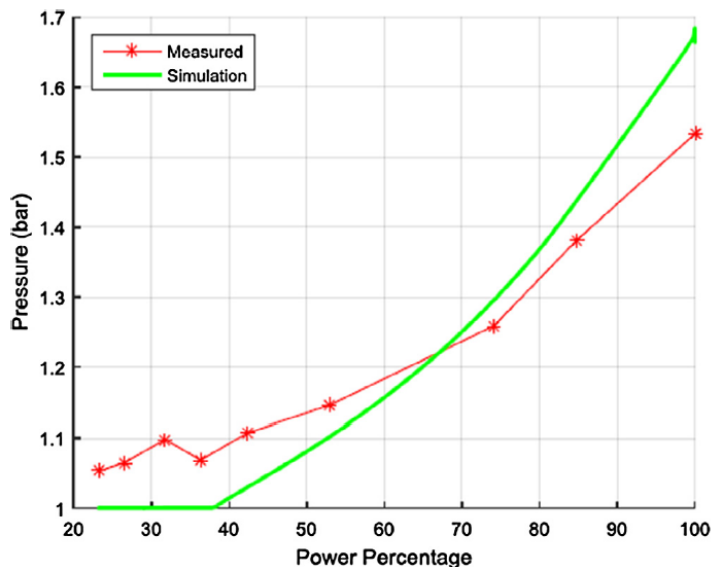


Figure 8.12: Comparison between measured and simulated values of lowest turbine inlet pressure

pulses, shown in Table 8.2. As seen in Figure 8.11, the β factor increases at part loads (or engine speeds along the propeller curve), implying an increase in work delivered by the turbine to the compressor. This is because at part loads the pulse factor increases, which increases the β value and decreases α . The increase in turbine work at part load is followed by an increase in the charge pressure and, hence, air flow rate, compared to the modern constant pressure systems. This difference in air flow rate delivered by a pulse and a constant pressure system can be very crucial against high back pressure and is discussed in detail in section 8.1.3. At the same time, the flow through the turbine drops, as the α factor drops with decreasing load. This is in alignment with the working principle of a pulse turbocharging system, which is known to improve part load performance of diesel engines by increasing the incoming flow-rate of air [22].

However, as the Ex-MVEM is a mean value model, the turbine inlet pressure can closely simulate any one single value on the pressure pulse. Thus, an iterative method was adopted, where the turbine inlet pressure was matched to either the maximum or the mean or the minimum pulse pressure, by changing a number of parameters in the turbocharger model. The criterion for this matching is to acquire the correct charge pressure and incoming air flow rate (Figure 8.9–8.11) as well as turbine temperature estimations, within 15% deviation from the measurements. Following this method, it was found that the model gave best results, for the above criterion, when turbine inlet pressure was made to simulate the lowest pulse pressure. This can be seen in Figure 8.12 and 8.13.

In Figure 8.12, the turbine inlet pressure shows a maximum deviation of about 10 percent, while the increasing trend of the measurements is well depicted by the model simulation as well. Besides this, the turbine inlet temperature gives a maximum per-

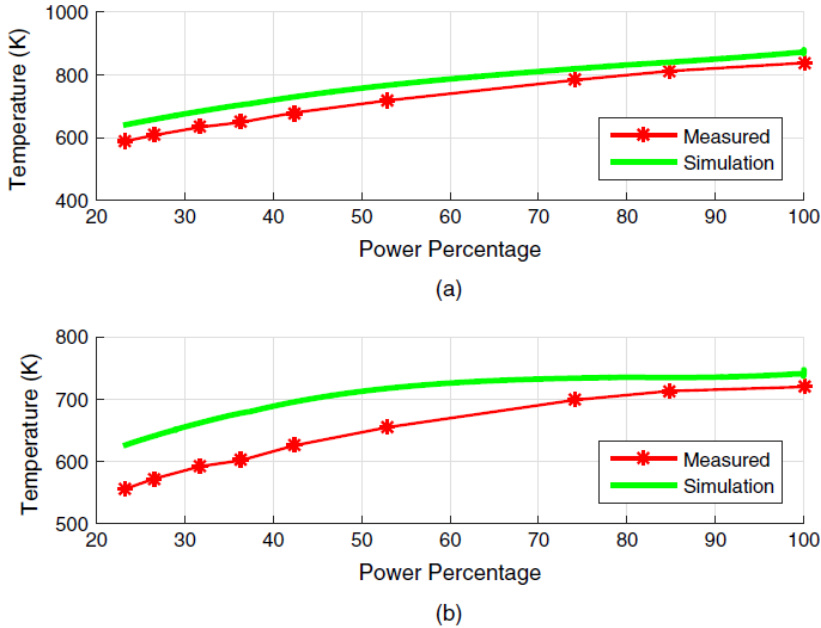


Figure 8.13: Comparison between measured and simulated turbine inlet (a), and outlet temperatures (b)

centage difference of about 9 percent, at lowest load, and a difference of about 12 percent for turbine outlet temperature, as seen in Figure 8.13(a) and (b). This concludes the calibration and matching of the Ex-MVEM to simulate the performance of the pulse turbocharged test engine. This section also highlighted the shortcomings of the model related to the difficulty in simulating the pressure pulse. However, in a separate study, this model successfully simulated the performance of an engine running with a constant pressure turbocharger system [7].

VALIDATION OF EX-MVEM

After calibrating and matching the Ex-MVEM to simulate the performance of the pulse turbocharged test engine with no external back pressure, the model was tested to predict the engine performance against back pressures of 0.25 mWC and 0.5 mWC. The model was further used to simulate the engine performance at rated setpoint (360 kW at 1000 rpm), which could not be studied experimentally. This section focuses on the effects of back pressure based on these simulation tests and also measurements for the same values of externally applied back pressure.

Back pressure is the pressure measured at the turbine outlet. Thus, an increase in back pressure means an increase in turbine outlet pressure, marking the turbocharger (turbine) as the first defence line. An increase in turbine outlet pressure results in a decrease in turbine pressure ratio [23], as this is defined as the pressure at turbine inlet over outlet. A drop in turbine pressure ratio reduces the power delivered by the turbine and slows down the turbocharger. This decrease in turbocharger speed at higher back pressures is seen in Figure 8.14, along with the turbo speed trend predicted by the model.

The measurements give a maximum decrease of about 4.4%, while the simulations calculated a decrease of about 5.5% for the same load point, at lowest load. Thus, the effect of steady state back pressure on turbocharger speed is small. The balance of power between the compressor and the turbine is used to calculate the charge pressure that can be delivered by the compressor. The charge pressure (obtained from compressor pressure ratio) is calculated as a function of turbine pressure ratio and other turbocharger variables as shown in equation 8.11, which is the Büchi balance from Chapter 6 [10].

$$\pi_{\text{com}} = [1 + \beta \cdot \psi \cdot \delta \cdot \eta_{\text{TC}} \cdot \tau_{\text{TC}} \cdot (1 - \frac{1}{\frac{p_d}{p_e} \frac{\gamma_g^{-1}}{\gamma_a}})]^{\frac{\gamma_a^{-1}}{\gamma_a}} \quad (8.11)$$

where, ' π_{com} ' = compressor pressure ratio, ' π_{tur} ' = turbine pressure ratio, ' β ' = pulse correction factor, ' δ ' = $1/(1 + \text{afr})$, ' afr ' = air-fuel ratio, ' ψ ' = ratio of specific heats for exhaust gas and compressor air, ' η_{TC} ' = turbocharger efficiency, ' τ_{TC} ' = turbocharger temperature ratio, and ' γ ' = ratio of specific heats.

The β factor takes into account the effect of extra power delivered by the pulse turbocharger, which is also called the 'Büchi turbocharger system' [24]. Equation 8.11 shows that a decrease in turbine pressure ratio causes the compressor pressure ratio to reduce. A drop in compressor pressure ratio leads to a decrease in the inlet receiver pressure and also the air flow through the engine as shown in Figure 8.15 and 8.16 respectively.

Once again, the simulations and measurements show a minor effect on the inlet receiver pressure and air flow rate. The trends of inlet receiver pressure and air flow rate simulated by the Ex-MVEM deviate from test bench measurements by a maximum of 6%. Even though the effects on the compressor side due to increasing back pressure

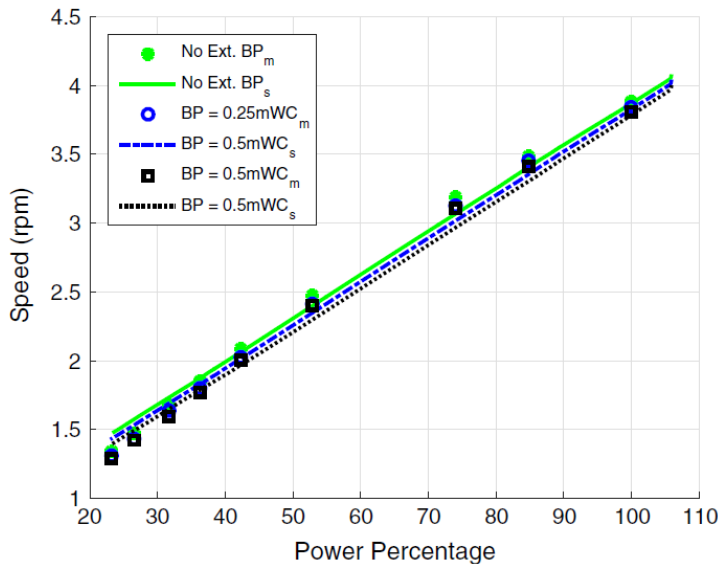


Figure 8.14: Back pressure effect on turbocharger speed based on measurements (m) and simulations (s)

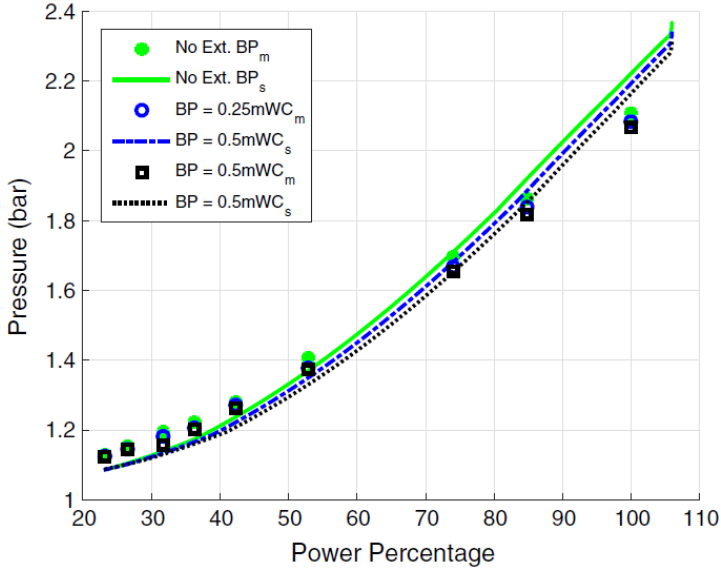


Figure 8.15: Back pressure effect inlet receiver pressure based on measurements (m) and simulations (s)

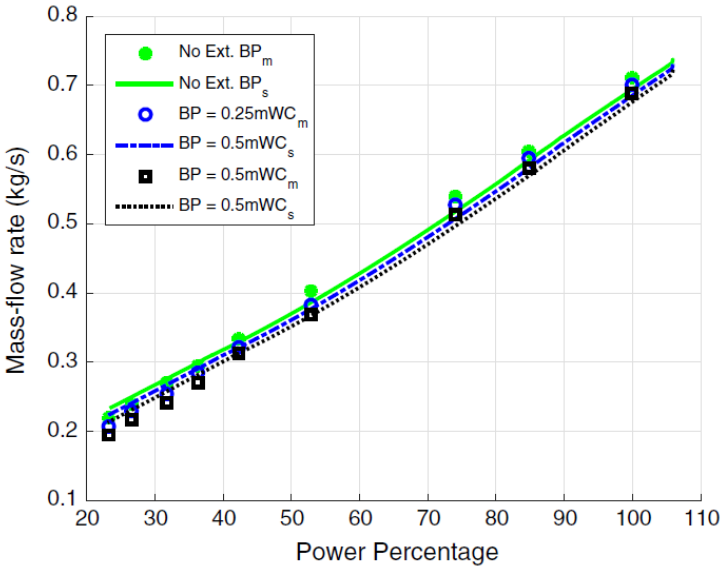


Figure 8.16: Back pressure effect on air mass-flow rate based on measurements (m) and simulations (s)

are small, the effects are more noticeable and critical on the turbine side, especially the effect on turbine temperatures.

Increased back pressure means the engine would need to do more work to pump out

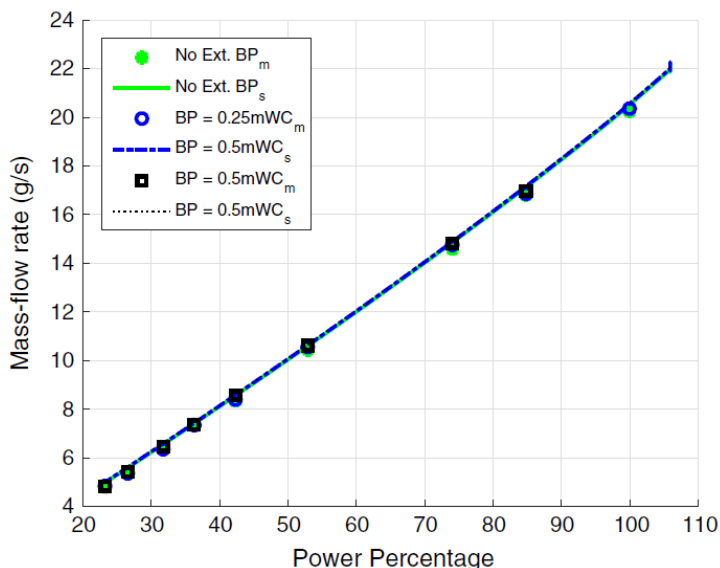


Figure 8.17: Back pressure effect on fuel consumption based on measurements (m) and simulations (s)

the exhaust gases. However, the load demand from the water-brake remains constant. This decelerates the diesel engine, activating the governor, which pushes in more fuel in order to offset the deceleration. Thus, an increase in back pressure would increase fuel consumption. Simulations and measurements exhibited a small increase in fuel consumption of about 3 % at 42 % load and 0.5 mWC of back pressure. Figure 8.17 shows the minor increase in fuel consumption due to increased back pressure.

Therefore, static back pressure causes an increase in fuel consumption (even though small) and drops air intake, leading to incomplete combustion and increase in in-cylinder and exhaust receiver temperatures, as seen in Figure 8.18. Measurements and simulations show that the rise in turbine inlet (exhaust receiver) temperature due to back pressure is more significant at lower loads than at higher loads. Based on measurements, turbine inlet temperature increased by a maximum of 6.7 % at the lowest load; and by 4.5 % based on simulations. Thus, the relative increase in temperatures predicted by simulations matched the measured. Excessive exhaust gas (exhaust receiver) temperatures can increase thermal stresses and cause serious damage to the turbocharger. Excessive exhaust temperatures can damage seals and grooves causing unintended oil and exhaust gas leakage [25]. High exhaust gas temperatures can also lead to a coked centre housing, which will affect turbocharger performance and life.

It is clear that the Ex-MVEM is satisfactorily able to predict the performance of the test engine, with and without externally applied back pressure. Based on this validation, the Ex-MVEM was made to simulate the performance of the test engine with different turbocharger configurations and valve overlaps to tackle high values of static back pressure. The next section discusses the results of these simulations while describing a methodology to define acceptable limits of static back pressure for any diesel engine.

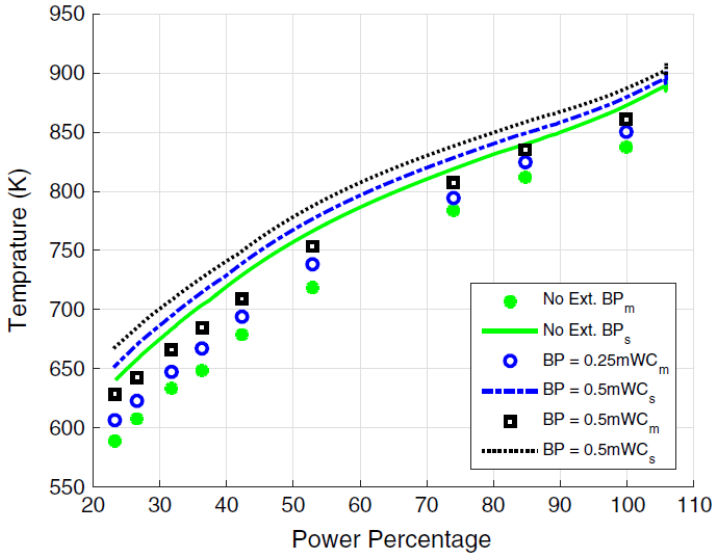


Figure 8.18: Back pressure effect on turbine inlet temperature based on measurements (m) and simulations (s)

8.1.3. DISCUSSION: DEFINING STATIC BACK PRESSURE LIMITS

The previous section showed that back pressure causes a drop in incoming air, increases fuel consumption and raises outlet receiver temperatures. Out of these, the effect on fuel consumption was found to be small; however, increased outlet receiver temperatures and decreased air intake could have alarming effects on turbocharger performance (damage to oil seals, coked housing) and the environment (smoke). Another parameter that is strongly affected by back pressure is the exhaust valve temperature. The increase in exhaust valve temperature and exhaust receiver (turbine inlet) temperature can be used as an indicator of thermal overloading of the engine [26, 27]. Furthermore, a diesel engine also needs a minimum amount of incoming air, i.e., low air-excess ratios can lead to high exhaust receiver temperatures (thermal overloading) and engine smoking [28, 29]. These boundaries of smoke and thermal overload can be further used to find limits of static back pressure that are acceptable for an engine, which will be covered in this section.

SMOKE AND THERMAL OVERLOAD LIMIT

Back pressure reduces the air-intake of the engine. This air-intake of a turbocharged, 4-stroke diesel engine can be divided into mainly two parts. Part one is the air that enters the cylinder during the induction process, the downward suction stroke of the piston. The second (smaller) part of the air mass in the cylinder can be considered to come from the scavenging process, during the overlap of inlet and exhaust valves. The total fresh air mass ending up in the cylinder is, therefore, a larger percentage of the induction mass flow and a smaller percentage of the trapped scavenging mass. The ratio of total fresh air mass in the cylinder to the minimum amount of air required for combustion is defined as the air-excess ratio [30].

The air-excess ratio can be used as an indicator to define the smoke limit of a diesel engine. In order to define such a limit, lines of constant air-excess ratio were drawn in a static engine map. In order to capture constant lines of engine performance parameters (air-excess ratio, charge pressure, exhaust valve temperature) in a static engine map; the model was run at different engine speeds and loads to cover the operating limits of the static engine map prescribed by the engine manufacturer. Figure 8.19 shows the grid of simulated engine speeds and load settings (blue markers) along with approximate engine operating limits (black line) given by the engine manufacturer, representing the static map of the engine.

In this manner, the model was made to simulate the performance of an engine (same rating, size and 100 degree valve overlap) with a constant pressure turbocharger, which is more widely accepted than the old pulse turbocharger system. Figure 8.20(a) shows the lines of constant air-excess ratio and Figure 8.20(b) captures lines of constant charge pressure calculated within the operating envelope of the engine.

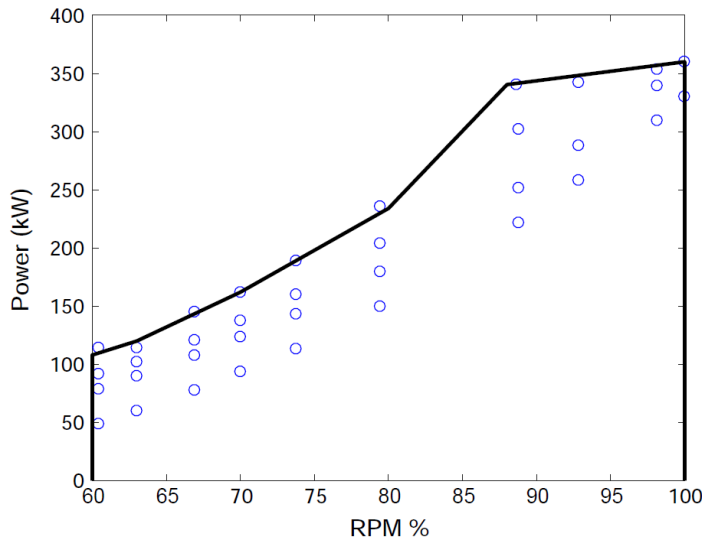


Figure 8.19: Simulated load and engine rpm points (blue points) along with engine envelope (black line)

Figure 8.20(a) shows that the lines of constant air-excess ratio within the engine map are more concave than a typical engine limit as given by the engine manufacturer, with a decreasing trend along constant engine rpm and increasing engine power. As mentioned earlier, an increase in back pressure reduces charge pressure and decreases air-excess ratio. For higher values of back pressure, the air-excess ratio can lie far beyond the values associated with the smoke limit. Although it is not possible to measure air-excess ratio directly, it can be related back to charge pressure, which can also be plotted in the static engine map as shown in Figure 8.20(b). Nowadays, in most engines, charge pressure is used as a measure of the fresh air mass.

In addition to using lines of constant air-excess ratio to define the smoke limit, the perhaps more important thermal overloading of the engine could be characterized by

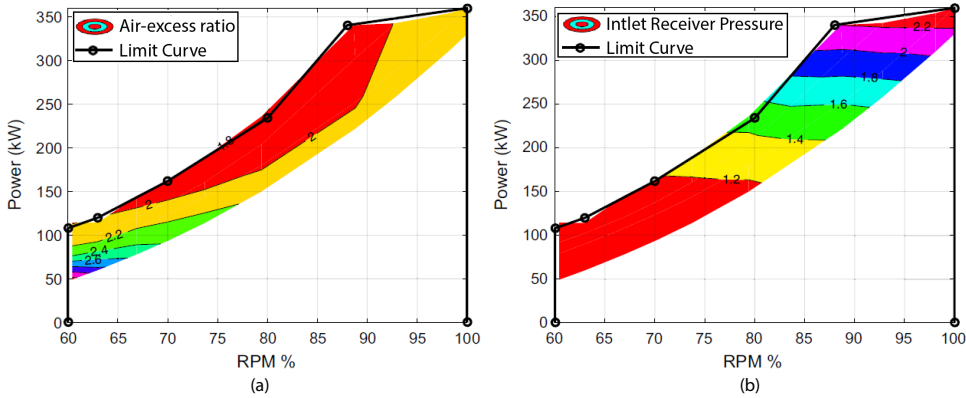


Figure 8.20: Static engine map with lines of constant air-excess ratio (a), and lines of constant charge pressure (b) for a 100 degree valve overlap constant pressure turbocharged engine

lines of constant exhaust valve temperature in a static engine map of power and engine speed. For this purpose, an exhaust valve temperature estimator ($T_{EV,est}$) was introduced into the Ex-MVEM, which is based on the formulation given in [26]. The total heating up of the exhaust valve is due to the heating during the blowdown process and the successive cooling during the scavenging period of the engine. The temperature of the exhaust valve is estimated as a combination of cylinder temperature just before the opening of the exhaust valve (T_6), representing heating during blowdown, and inlet receiver temperature (T_{IR}), which represents cooling temperature during scavenging. Therefore, the exhaust valve temperature is estimated by the following equation:

$$T_{EV,est} = \frac{T_6 + r \cdot T_{IR}}{1 + r} \tag{8.12}$$

$$r = s^{0.8} \cdot \left[\frac{T_{IR}}{T_6} \right]^{0.25} \cdot \left[\frac{EC - IO}{IO - EO} \right]^{0.2} \tag{8.13}$$

where, 'r' is a function of scavenge factor 's', T_6 , T_{IR} and ratio of the crank angle available for scavenging and blowdown. Scavenge factor (s) is defined as the ratio of the mean mass flow that goes through the engine during scavenging and the mean mass flow required for combustion.

The exhaust valve temperature estimator model introduced into the Ex-MVEM was used to simulate these temperatures for all the load and engine rpm points, shown in Figure 8.19. Figure 8.21 (a) shows the lines of constant exhaust valve temperature. Like air excess ratio, the exhaust valve temperature cannot be easily measured in an actual engine. However, as a next best quantity, the exhaust receiver temperature can be measured, and calculated contour curves are shown in Figure 8.21 (b).

As seen in these figures, the lines of constant exhaust valve and exhaust receiver temperature follow the characteristic of the limit curve, given by the engine manufacturer, much better than the contours of air-excess ratio presented in the previous figures. The hypothesis is that the exhaust valve temperature and, in its wake, the exhaust receiver

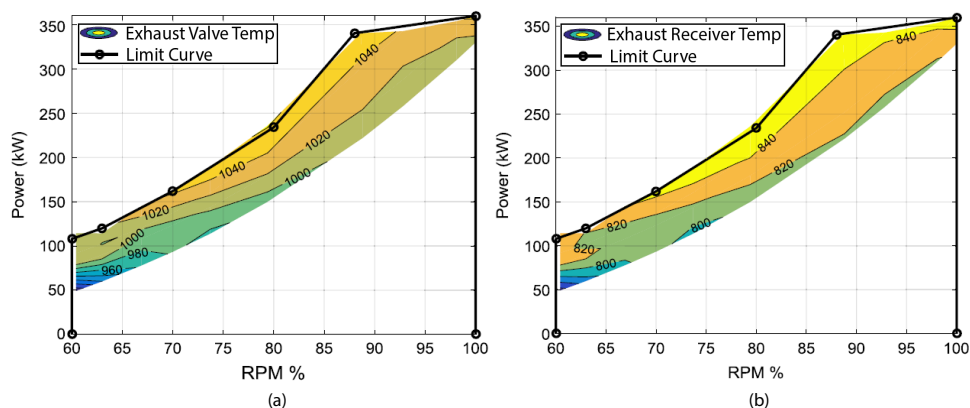


Figure 8.21: Static engine map with lines of constant exhaust valve temperature (a) and constant exhaust receiver temperature (b) for a 100 degree valve overlap constant pressure turbocharged engine

temperature really capture thermal loading of an engine. Thus, giving a value of maximum allowable temperature defines a limit in the power/speed envelope and is a way to safeguard the engine from thermal overloading. It is evident from Figure 8.21 that the lines of constant exhaust valve temperature and exhaust gas (exhaust receiver) temperature have the same trend, and hence both of them can be used to capture the effect of thermal overloading and define back pressure limits. In this research, exhaust valve temperature has been adopted as an indicator for thermal overloading since it is considered to be the more critical quantity, however, exhaust receiver temperature can be measured in practice.

APPLICATION OF SMOKE AND THERMAL OVERLOAD LIMIT: DEFINING ACCEPTABLE BACK PRESSURE

In order to better understand smoking and thermal overloading limits to define the ceiling for acceptable back pressure, the power on the y-axis and the quantities along contour lines in Figure 8.20 and 8.21 were flipped, as presented in Figure 8.22. These flipped graphs can be used to mark on their y-axis the values of maximum allowed air-excess ratio or exhaust valve temperature for each engine rpm and thus indicate the region where the engine could smoke or be thermally overloaded. The coloured area under the manufacturer's limit in Figure 8.20 and 8.21 is converted into a corresponding area in Figure 8.22. Besides this, Figure 8.22(a) and (b) also depict the decrease in air-excess ratio and the increase in exhaust valve temperature due to increased external back pressure at constant power and speed. All the cases of increased back pressure have been simulated along the same propeller curve shown in Figure 8.2.

Simulations show that for a back pressure of 0.35 mWC, the air-excess ratio could drop to alarmingly low values, and far into the region representing a relatively fuel-rich mixture for a diesel engine, which could lead to engine smoking. Black engine smoke primarily contains elemental carbon (soot), which is considered to be the second-largest human contributor to climate change [31, 32]. Additionally, black smoke can be a serious problem for a naval ship as it can increase the chances of detection. Figure 8.22(a)

illustrates that the air-excess ratio could drop drastically, thus indicating the possibility of engine smoke, especially at lower rpms [33]. The exhaust valve thermal overloading graph given in Figure 8.22(b) also shows that a back pressure of 0.35 mWC would be unacceptable for this engine and again the effect is most severe at low engine speed.

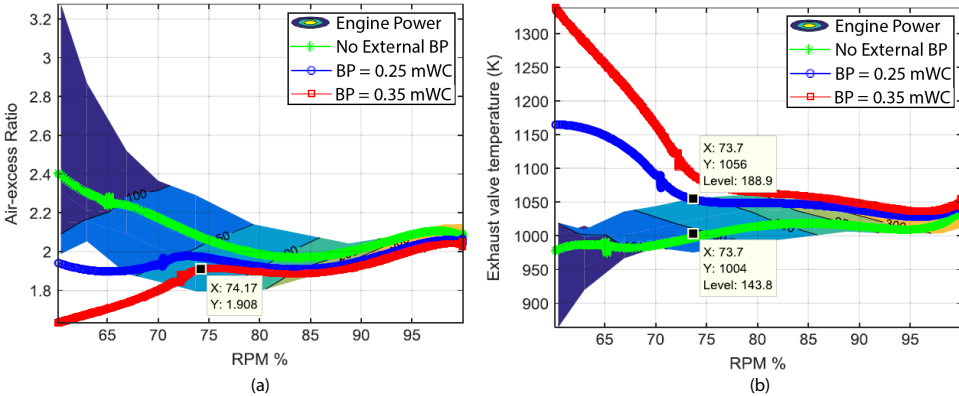


Figure 8.22: Back pressure effect on air-excess ratio (a) and exhaust valve temperature (b) of a constant pressure turbocharged engine with 100 degree valve overlap

As seen in Figure 8.22(b), the values of exhaust valve temperature for the case of no external back pressure lie within the limits of maximum allowable temperature at each engine rpm. However, the exhaust valve temperature, below 74 percent of engine speed, for back pressure of 0.25 mWC moves beyond the temperature limit obtained from the engine limit curve, thus, indicating thermal overloading and representing a back pressure limit. Besides defining limits of acceptable values of back pressure, the graph in Figure 8.22(b) also provides two ways to avoid thermal overloading. One solution would be to reduce back pressure by switching from underwater to above water exhaust system at the point of thermal overload for a particular engine speed. For instance, for this engine, it would be necessary to switch from underwater to above water exhaust at speeds below 75 %. Furthermore, Figure 8.22(b) shows that the effects of back pressure are more severe at lower RPM values of engine speed, thus asserting a higher need to switch to above water exhaust systems at lower rpms than at higher rpms. Another solution would be to reduce the engine power at constant engine speed. For example, decreasing engine power along 74 % engine speed can help reduce the temperature and avoid thermal overload. In this manner, the Ex-MVEM can be used to define back pressure limits at any engine speed by applying the concept of smoke limit and thermal overloading.

The drop and knuckle seen at 74 % engine speed (0.25 mWC) is because the pressure ratio across the engine at these points approaches 1. In other words, the pressure on the exhaust receiver side is almost equal to the pressure on the inlet receiver side. Flow direction of the engine fluctuates giving the knuckle. After this point, the engine experiences negative scavenging, and the flow reverses during the 100 degree valve overlap [34]. This causes a further loss of trapped fresh air mass, as the air inside the cylinder gets replaced by exhaust gas during scavenging. These trapped exhaust gases raise the temperature of trapped mass at the beginning of compression, thus raising the overall in-cylinder and

exhaust receiver temperatures. Additionally, negative scavenging creates a counter pressure at the compressor outlet, pushing the compressor towards compressor surge, which can damage the compressor [35].

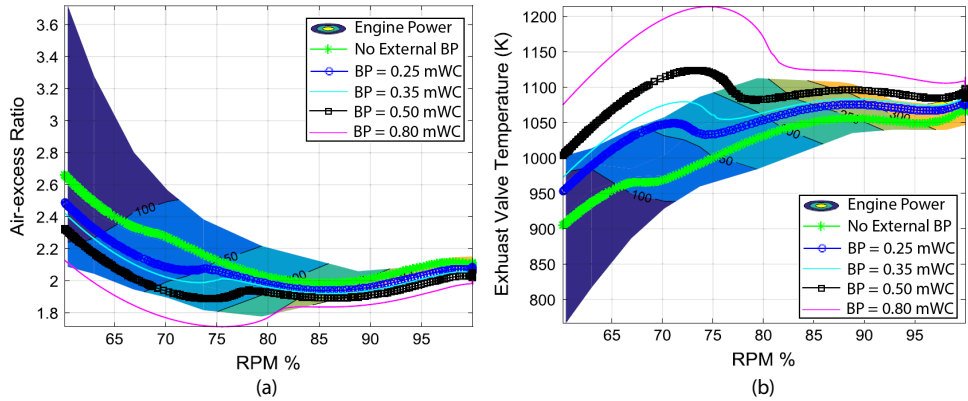


Figure 8.23: Back pressure effect on air-excess ratio (a), and exhaust valve temperature (b) of a constant pressure turbocharged engine with 30 degree valve overlap

An engine with a smaller valve overlap could reduce the negative scavenging and keep the air-excess ratio from dropping too low. Figure 8.23(a) shows the improvement in the air-excess ratio characteristic, predicted by the Ex-MVEM for the same engine with a 30 degree valve overlap and constant pressure turbocharger system. This proves that an engine with a smaller valve overlap will be able to handle higher values of back pressure. A 30 degree valve overlap increases the amount of total trapped air in the cylinder in two ways. First, it increases the amount of induction air as the exhaust valve closes earlier than in the case of 100 degree valve overlap (assuming that the inlet valve opens at the same moment for both the cases). Secondly, a small overlap means reduced negative scavenging and more trapped air compared to a larger valve overlap. However, the higher the back pressure, the lower the charge pressure (K), meaning the point of negative scavenging is reached at a much higher power percentage. This reduces the excess air and gives the peculiar characteristic of the lambda curve, shown in Figure 8.23(a). The improved air-excess ratio due to reduced valve overlap helps reduce exhaust valve temperatures and this is clearly evident in Figure 8.23(b). As seen in Figure 8.23(b), the engine can now easily handle higher back pressure of 0.25 mWC without any thermal overloading and also 0.35 mWC of back pressure at most engine speeds. The effect of back pressure is, once again, more pronounced at low engine rpms, and the speed where back flow is initiated creeps up. The need to switch to above water exhaust is evident at low engine speeds.

In order to improve the back pressure handling capabilities at low rpms, it is important to further increase the air-intake of the engine, which would require higher charge pressures. As explained in section 8.1.2, the pulse turbocharger system delivers extra work to the compressor. The extra work or β factor helps keep the charge pressure high (equation 8.11), and also the amount of total air in the cylinder. In pulse turbocharger systems, this extra work is most effective at part loads (or engine speeds along the pro-

PELLER CURVE), as shown in Figure 8.11, and hence keeps the air excess ratio from dropping at these loads. On the other hand, in a constant pressure system, the pressure pulses are collected in an exhaust receiver before entering the turbine, the turbine inlet pressure drops to a lower and a constant value in contrast to that of a pulse system. Since, the pressure at the turbine inlet is constant, in case of constant pressure turbochargers, there is an absence of extra work delivered due to the pulse, making the β equal to 1 [10]. Figure 8.24 shows the simulated increase in inlet receiver pressure and air mass flow rate for a 30 degree valve overlap engine with a pulse turbocharger compared to the constant pressure turbocharger engine when no external back pressure is applied.

Figure 8.24 shows that at rated speed the pulse turbocharger and constant pressure turbocharger have almost equal values of inlet receiver pressure and air flow rate. However, at lower rpms (or load along the propeller curve) the pulse system delivers much higher values of charger pressure and air intake compared to the constant pressure turbocharger. Simulations show that the air intake for a pulse turbocharger is more by 68 percent, at lowest speed, when compared to that delivered by a constant pressure system. This drastically improves the back pressure handling capabilities of the engine as depicted in Figure 8.25.

As evident in Figure 8.25, the 30 degree valve overlap engine with a pulse turbocharger can sustain 1 mWC of back pressure with signs of thermal overloading only above 90 percent engine speed. Furthermore, Figure 8.25 shows that the air-excess ratio of a pulse turbocharged engine hardly drops below 1.9 at a back pressure of 1 mWC, indicating no signs of engine smoke. The model shows that such a system would easily be able to counter the high values of back pressure due to the pulse effect, and also reduced back flow in case of any negative scavenging (smaller valve overlap). This would cancel the need to switch to an above water exhaust, at lower rpms.

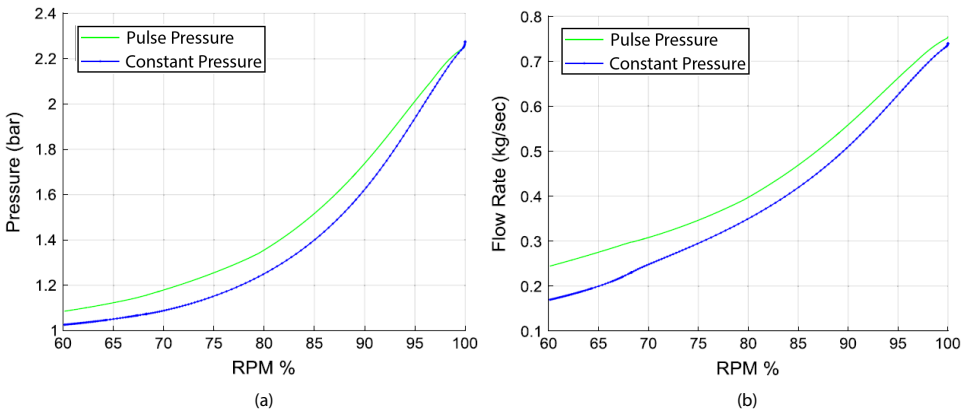


Figure 8.24: Comparison between inlet receiver pressure (a) and air mass-flow rate (b) delivered by a pulse turbocharger and constant pressure turbocharger with a 30 degree valve overlap engine

This section shows that both smoke and thermal overloading, simulated by the Ex-MVEM, can be used as an indicator to define limits of acceptable static back pressure at any engine speed. A thermally overloaded engine can be unloaded by either reducing

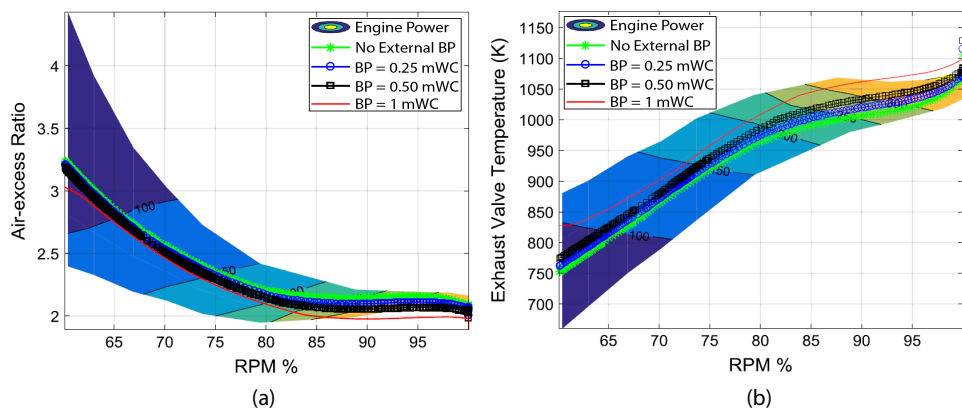


Figure 8.25: Back pressure effect on air-excess ratio (a) and exhaust valve temperature (b) of a pulse pressure turbocharged engine with 30 degree valve overlap

engine power or back pressure. This section also proves that a pulse turbocharged engine and a small overlap can drastically help improve back pressure handling capabilities of an engine compared to a constant pressure turbocharger system and large valve overlap. This completes the investigation of marine diesel engine performance against high static back pressure due to an underwater exhaust system. The next section discusses the impact of dynamic back pressure on marine engine performance.

8.2. EXPERIMENTAL INVESTIGATIONS OF MARINE DIESEL ENGINE PERFORMANCE AGAINST DYNAMIC BACK PRESSURE

In the previous section, the effects of static back pressure on the performance of a marine diesel engine were investigated. However, the back pressure felt by a marine engine due to an underwater exhaust system is highly fluctuating in amplitude and time period rather than static [23, 36]. Therefore, the objective of this section is an experimental investigation of marine diesel engine performance against dynamic back pressure of varying amplitudes and time periods due to an underwater exhaust system operating in different sea-states.

8.2.1. METHODOLOGY AND TEST SETUP FOR DYNAMIC BACK PRESSURE

The effects of dynamic back pressure on marine engine performance were studied using experiments. The experimental and research methodology along with the engine test setup are described in this section.

METHODOLOGY

A marine engine operating with an underwater exhaust system is exposed to continuous and fluctuating back pressures due to the sea waves at the exhaust outlet. These waves vary in amplitude or significant wave height (WVHT) and average time period (APD) based on the sea-state in which the ship is operating. Sea-state scales are defined by

the World Meteorological Organization (WMO). A sea-state 1 corresponds to calm rippled waters with a wave amplitude of 0.10m. Higher the wave amplitudes higher is the corresponding sea-state [37]. The waves recorded during real ship operations can be of varying sea-states with different wave amplitudes and wave periods based on the geographical location of the ship and also weather conditions. Table 8.3 shows wave data of varying wave amplitudes and wave periods (maximum and minimum) for two sea-states recorded near the east coast of The United States of America and obtained from the National Data Buoy Center (NDBC) [38]. These sea waves of varying wave amplitudes and wave periods create a dynamic back pressure at the outlet of the underwater system. During experiments, the dynamic back pressure was applied with the help of an electronically controlled butterfly valve. The applied back pressure waves were based on the wave data obtained from the NDBC. In this research, the maximum applied back pressure is kept below 0.5 mWC to avoid damage to the turbocharger due to thermal overloading. This value of 0.5 mWC back pressure corresponds to sea state 2 and is twice the back pressure limit prescribed by the engine manufacturer as seen in Table 8.1.

Table 8.3: Wave data of varying wave heights and wave periods obtained from NDBC [38]

WVHT [m]	APD _{min} [s]	APD _{max} [s]	sea-state
0.39	4.93	6.86	2
0.5	3.82	6.73	2
0.75	3.66	6.65	3
1	3.96	6.9	3

In addition to the incoming sea wave, the back pressure felt by the engine depends on the position of the exhaust outlet relative to the waterline [7]. For instance, the dynamic back pressure felt by a submarine engine is a sum of the static pressure due to the water head above the snorkel and the dynamic pressure due to the sea waves at the water surface. The position of the submarine exhaust outlet can be visualized in Figure 8.26(a) by position 3. An underwater exhaust system on a ship is designed and positioned to reduce the static water head above the exhaust outlet [7]. An ideal position of an underwater exhaust outlet relative to the sea wave, from the perspective of back pressure, could be represented by points 1 and 2 as shown in Figure 8.26(a). In this study, the exhaust outlet is considered to be positioned at point 2. The engine would experience a higher and more fluctuating back pressure with the underwater exhaust system positioned at point 2 in comparison to the back pressure experienced by the engine due to the position of exhaust outlet corresponding to point 1. Figure 8.26(b) shows the back pressure wave produced at the exhaust outlet when the underwater exhaust system is positioned at point 2. It is vital to note that for an underwater exhaust system, position 1 and position 3, with a small static water head, are also possible exhaust outlet positions and should be investigated in future.

In this research, the effects of dynamic back pressure were studied by measuring engine performance against single and multiple back pressure waves of varying amplitudes and wave periods. As explained earlier, the applied back pressure waves are based on real recorded wave data obtained from the NDBC. Table 8.4 shows the wave data for the experimentally simulated single and multiple back pressure waves used to understand

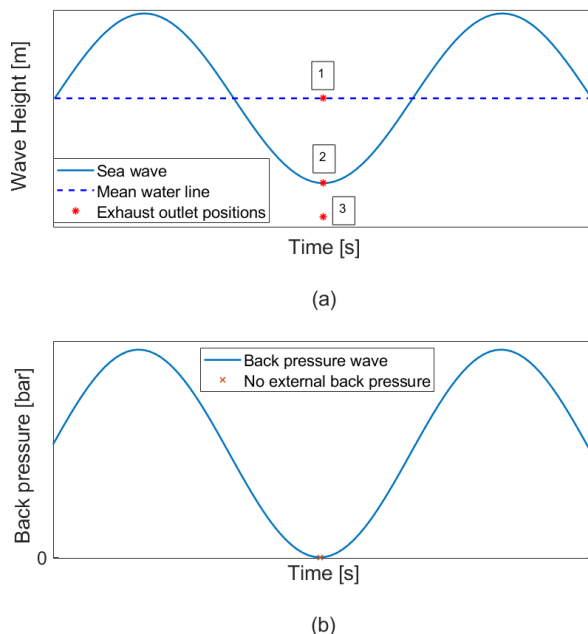


Figure 8.26: Possible exhaust outlet positions relative to a sea wave (a) and a representation of the external back pressure wave corresponding to underwater exhaust system at position 2 (b)

Table 8.4: Wave data for experimentally simulated single and multiple back pressure waves

Wave input	Parameter change	WVHT [m]	APD [s]
Single wave	Amplitude	0.25, 0.45	6
Single wave	Wave period	0.45	4, 8
Multiple waves	Amplitude	0.35, 0.45	6
Multiple waves	Waves	0.45	4, 8

the effects of dynamic back pressure in this research. As seen in Table 8.4, the effects of amplitude variations were studied for a back pressure wave of maximum 0.45 mWC amplitude while the maximum tested wave period was 8 seconds. These back pressure waves were applied at a fixed engine setpoint after 15 minutes of settling time between each setpoint and test case of static or dynamic back pressure to make sure that all engine parameters (especially temperatures) were stabilized before the next measurement and, thus, mismeasurement can be avoided.

Engine performance was measured while the butterfly valve completed the prescribed number of closing and opening cycles to apply the required dynamic back pressure. Additionally, engine performance was also measured against static back pressures of 0.45 mWC and 0.35 mWC at fixed engine setpoints to compare the effects on engine performance due to static and dynamic back pressures. It is vital to note that the experiments of dynamic back pressure were conducted separately from the experiments discussed in

section 8.1.1. In this manner, the effects of static and dynamic back pressure were measured along the propeller curve of a marine diesel engine. The next subsection covers the test setup and the engine setpoints along the propeller curve at which dynamic back pressure effects were studied.

TEST SETUP

Experiments were performed on the same 4-stroke, turbocharged marine diesel engine detailed in section 8.1.1. As explained earlier, in this experimental study, the engine measurements were restricted to the maximum set point of 340 kW at 981 rpm. Therefore, the 100 % load point presented in this research corresponds to 340 KW at 981 rpm. The test engine was connected to a water-brake to apply the required load, which allowed the engine to run at any setpoint of load speed. Engine performance against dynamic back pressure was studied at four setpoints along the propeller curve as designated in Figure 8.27.

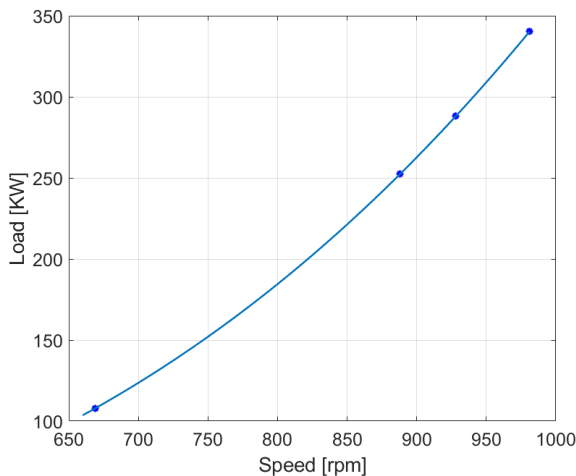


Figure 8.27: Measurement setpoints along the propeller curve

To apply the external dynamic back pressure, the manually operated butterfly valve mentioned in the subsection 8.1.1 was replaced by an electronically controlled butterfly valve installed downstream of the turbine in the exhaust line. Figure 8.3 gives the schematic representation of the engine test setup along with the location of the butterfly valve and the different pressure and temperature sensors. The electronic butterfly valve was employed to replicate the dynamic back pressure created by the sea waves at the exhaust outlet of the underwater exhaust system. During experiments, the resistance to the exhaust gas flow was increased and decreased by electronically controlling the input angle of the butterfly valve to apply a static or fluctuating external back pressure at a fixed engine setpoint.

Figure 8.28(a) shows the butterfly valve angle and time input in the form of a single sinusoidal waveform along with the corresponding back pressure wave experienced by the engine. The actual sea waves are trochoidal in nature with sharper peaks than

troughs and are difficult to mathematically manipulate as input to the butterfly valve [39]. Therefore, the applied wave input has a sinusoidal form, which can be easily simulated as shown in Figure 8.28(a).

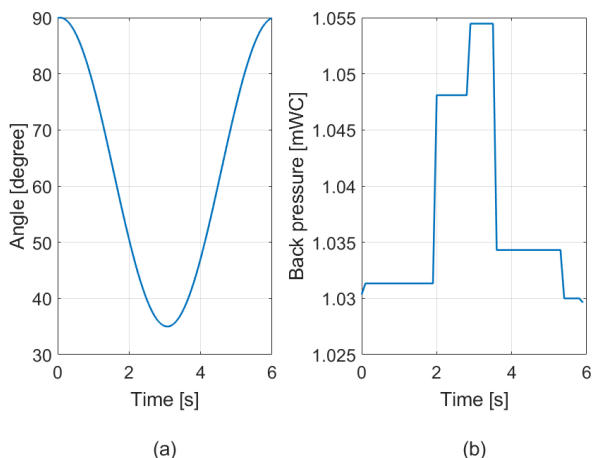


Figure 8.28: Angle and time input of a sinusoidal waveform for the butterfly valve (a) and the corresponding back pressure wave produced (b)

As depicted in Figure 8.28(a), the valve is fully open at the 90 degree valve position whereas the 0 degree position corresponds to the fully closed position of the valve. The time period on the x-axis represents the wave period of the back pressure wave that matches the average wave period of the sea wave at the exhaust outlet. As seen in Figure 8.28(b), the initial effect of the butterfly valve on the back pressure, as it starts closing in small steps, is small. However, as it closes further the back pressure increases non-linearly by a higher value. This is due to the inertia and the step-wise movement of the butterfly valve in addition to the non-linear effect of the valve movement on the back pressure. Therefore, the final applied back pressure wave at the turbine outlet has a square waveform with discrete steps rather than a sinusoidal waveform. In this manner, a back pressure wave of 0.45 mWC or 45 mbar (gauge) corresponding to a wave amplitude of 0.45 m and 6 seconds wave period was created at 100 % setpoint and engine performance against dynamic back pressure was measured. The non-linear motion of the inflowing and outflowing water as the sea waves pass by the exhaust outlet may also produce a similar and discretized waveform instead of a perfect sinusoidal waveform of dynamic back pressure at the turbine outlet during real sea operations. This shape of the dynamic waveform at the turbine outlet should be further investigated as it may depend on various parameters such as ship operations, exhaust system design and its position [7]. However, other than the waveform, a dynamic back pressure wave felt by the engine could be characterized by wave amplitude and wave period, which form the basis of this study.

During this study, although the effects of static back pressure on fuel consumption were measured, it was not possible to perform fuel consumption measurements against dynamic back pressure. The fuel consumption measurements were performed by record-

ing the time required to consume a fixed amount of fuel during steady state operation of the engine against static back pressure. This method helped calculate the fuel consumed by the engine in kilograms per second and worked well during steady state measurements, however, it was found to be a complex and inaccurate method for dynamic back pressure measurements due to much shorter measurement time periods in comparison to static back pressure measurements. Therefore, in this research the effects of dynamic back pressure on fuel consumption are discussed qualitatively and relative to the fuel consumption measured during static back pressure measurements.

8.2.2. RESULTS

To understand the qualitative and quantitative effects of dynamic back pressure on marine diesel engine operation, engine performance was first experimentally studied for single and multiple waves of back pressure with varying amplitudes and a fixed time period. Next, to capture the effects due to varying wave periods, back pressure wave amplitude was fixed while the time period was varied. The tested amplitudes and time periods were chosen based on waves recorded for different sea-states by the NDBC as detailed in the methodology section

SINGLE BACK PRESSURE WAVE WITH AMPLITUDE VARIATIONS

Back pressure is the pressure felt at the turbine outlet of the turbocharger. Therefore, when a single wave of back pressure is exerted, the turbine outlet pressure first increases to a maximum value and then decreases to its initial value as the wave passes by. Figure 8.29 shows the increasing and decreasing wave of back pressure measured at the turbine outlet when the butterfly valve was controlled to exert a single back pressure wave of 0.45 mWC or 45 mbar pressure amplitude (gauge) with a wave period of 6 seconds at 340 kW load. This pressure amplitude and wave period match the wave data for sea-state 2. As explained in the methodology section, a sinusoidal wave input to the butterfly valve created a square wave of back pressure due to the inertia and the step-wise movement of the valve in addition to the non-linear response of back pressure to the valve movement.

As explained earlier, an increase in back pressure causes the turbine pressure ratio to decrease and slows down the turbocharger. The decreased turbine pressure ratio corresponds to a decrease in the power delivered by the turbine to the compressor, which in turn reduces the inlet receiver pressure or the charge pressure at the compressor outlet. Figure 8.30 shows the drop and increase in the inlet receiver pressure due to the exerted back pressure wave. The decrease in inlet receiver pressure reduces the air-flow rate into the engine. As discussed in section 8.1.2, an increase in back pressure would increase the fuel flow while decreasing the air-intake. This leads to a relatively fuel-rich combustion or reduced air-excess ratio, which increases the temperatures in the exhaust receiver.

Figure 8.31 shows the increase in turbine inlet and outlet temperatures as the single wave of 0.45 mWC or 45 mbar back pressure and 6 second wave period is applied. The exhaust receiver temperature (pre-turbine temperature) follows an opposite trend to that of the air-excess ratio. As discussed earlier, a large drop in the air-excess ratio could lead to engine smoking and would correspond to a large increase in the exhaust receiver temperature, thus, causing thermal overloading. To avoid any damage to the turbocharger, engine experiments to study the effects of dynamic back pressure were restricted to back

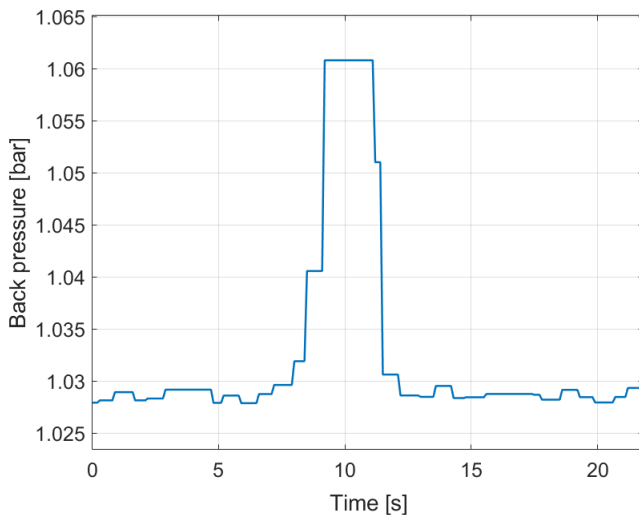


Figure 8.29: Applied single back pressure wave of 0.45 mWC pressure amplitude with a 6 seconds wave period at 340 kW load

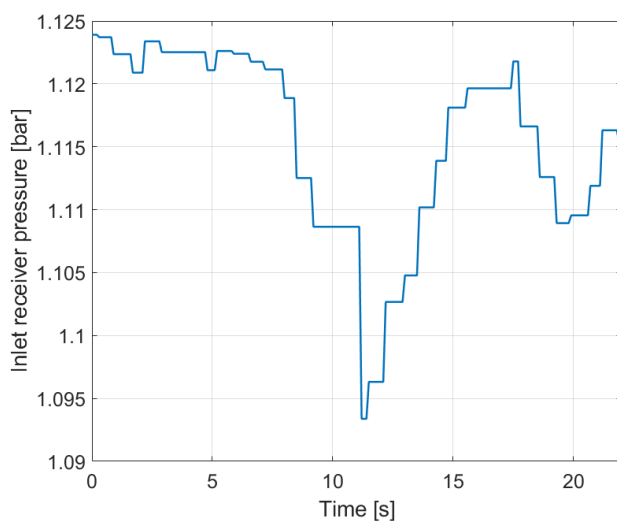


Figure 8.30: Measured effect on inlet receiver pressure due to the applied single back pressure wave of 0.45 mWC pressure amplitude with 6 seconds wave period at 340 kW load

pressures lower than 0.5 mWC or 50 mbar (gauge) and a maximum engine load of 340 kW.

As seen in Figure 8.31, the turbine temperatures increase to a maximum value, however, there is a lag in the response of exhaust temperatures. Therefore, although the decrease from maximum temperatures is visible the return of turbine temperatures to

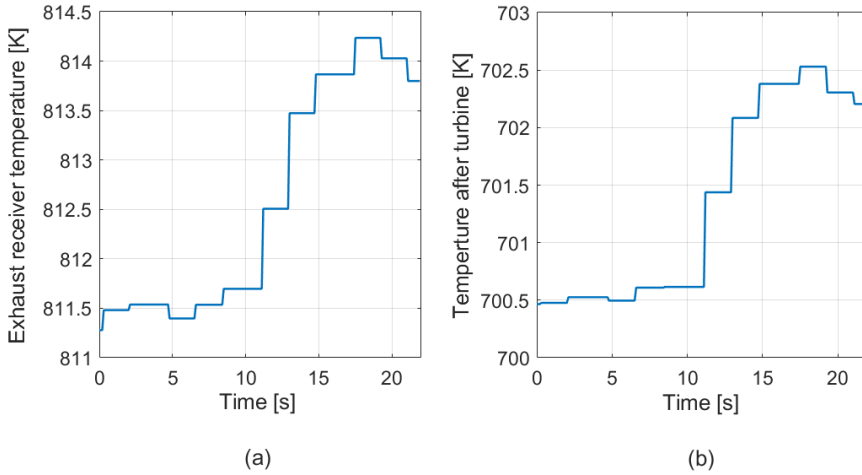


Figure 8.31: Measured effect on turbine inlet temperature (a) and outlet temperature (b) due to the applied single back pressure wave of 0.45 mWC pressure amplitude with 6 seconds wave period at 340 kW load

their initial values is not visible. This return of exhaust receiver temperature to its initial value will be discussed in the next subsection. Thus, the inlet receiver pressure and exhaust temperatures follow the applied back pressure wave with a noticeable lag in the response of exhaust temperatures.

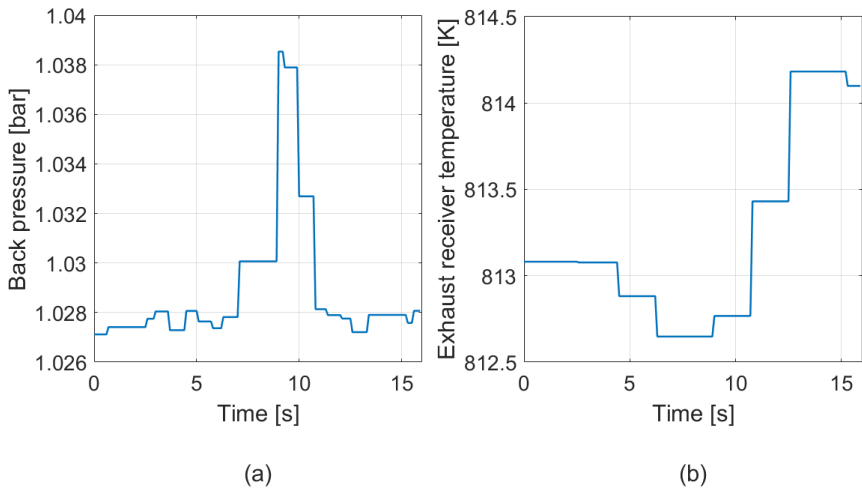


Figure 8.32: Applied single back pressure wave (a) of 0.25 mWC pressure amplitude with 6 seconds wave period at 340 kW load and its effect on exhaust receiver temperature (b)

In the earlier study of only static back pressure, the fuel penalty due to static back pressure was small while the exhaust receiver temperature and exhaust valve temperature were identified as critical parameters against static and high back pressure. Fur-

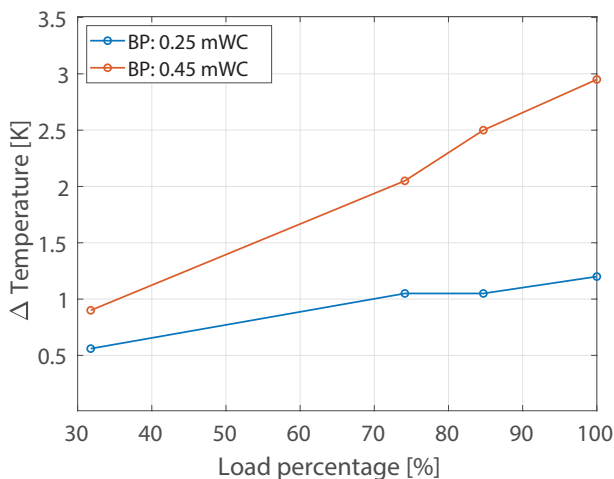


Figure 8.33: Measured maximum increase in exhaust receiver temperature due to a single back pressure wave of 0.25 mWC and 0.45 mWC pressure amplitude with 6 seconds wave period at varying engine loads along the propeller curve

thermore, the exhaust valve temperature, and in its wake, the exhaust receiver temperature were used to quantify thermal overloading, which formed the conceptual basis of a proposed methodology to find acceptable limits of static back pressure for an engine. Therefore, this current research first studies the variations in exhaust receiver temperature to quantify the effects of dynamic back pressure on marine engine performance. Then, the effects of dynamic back pressure on fuel penalty are studied qualitatively and relative to the fuel penalty measured against static back pressure. This discussion on fuel penalty has been presented in subsection 8.2.3.

The maximum increase in exhaust receiver temperature due to the single back pressure wave of 0.45 mWC amplitude is approximately 2.8°C as seen in Figure 8.31. However, this increment in turbine inlet temperature decreased to 1.5°C for a single back pressure wave of 0.25 mWC amplitude and 6 seconds wave period applied at 340 kW load as seen in Figure 8.32. Therefore, higher the wave amplitude or the significant wave height, higher is the increase in the exhaust receiver temperature. This trend of increase in exhaust receiver temperatures due to increasing wave amplitude is consistent at all loads as shown in Figure 8.33. Figure 8.33 also shows that the maximum increase is about 2.8°C for a single back pressure wave with an amplitude of 0.45 mWC, which corresponds to sea-state 2. This increase of 2.8°C for sea-state 2 is quite insignificant as discussed in subsection 8.2.3.

MULTIPLE BACK PRESSURE WAVE WITH AMPLITUDE VARIATIONS

An underwater exhaust system under real operating conditions is exposed to continuous and multiple waves of varying sea-states. Therefore, the engine is required to perform against multiple waves of back pressure. To emulate the performance of a marine engine with an underwater exhaust system under real operating conditions, engine performance was studied against multiple waves of varying back pressure. Figure 8.34

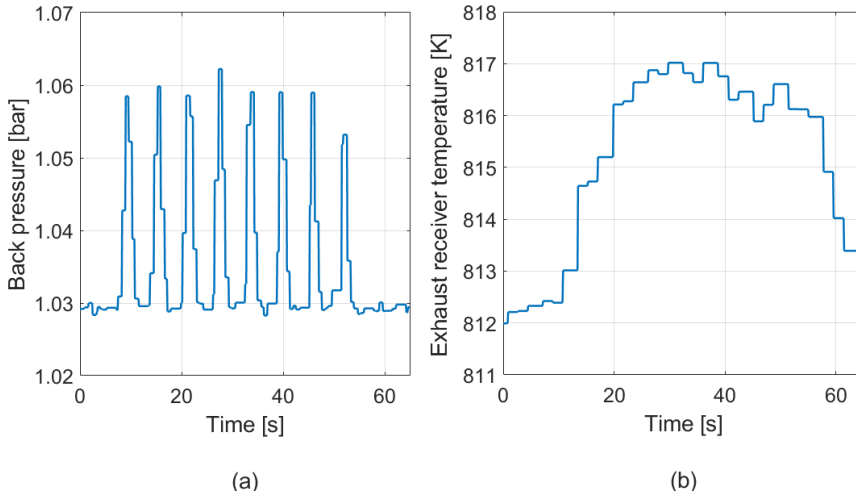


Figure 8.34: Applied multiple back pressure wave (a) of 0.45 mWC pressure amplitude with 6 seconds wave period at 340 kW and its effect on exhaust receiver temperature (b)

shows the fluctuations in exhaust receiver temperature due to the applied multiple back pressure waves of 0.45 mWC with a 6 seconds wave period at 340 kW load. Since the temperature sensor has a low sampling frequency, it records the fluctuations in exhaust receiver temperature close to the crests and is unable to capture the troughs. This can also be seen in Figure 8.35, which shows the measured fluctuations in exhaust receiver temperature due to multiple waves of 0.35 mWC pressure amplitude and 6 seconds wave period. Furthermore, the lag in the exhaust receiver temperature response is once again clearly visible in Figure 8.35. The decreasing trend of exhaust receiver temperature with decreasing back pressure can be seen in Figure 8.34(b).

The maximum increase in exhaust receiver temperature at 340 kW due to multiple waves of 0.45 mWC pressure amplitude is about 5.5 °C while that for waves of 0.35 mWC back pressure is 4.5 °C. Therefore, it can be concluded once again that the exhaust receiver temperature increases with increasing wave amplitude. Additionally, this increase is confirmed at all loads as shown in Figure 8.36. It is important to note that at a certain critical and higher value of wave or pressure amplitude, the exhaust receiver temperature can rise by much higher values causing thermal overloading and possible damage to the turbocharger, which should be avoided.

Interestingly, this maximum increase in exhaust receiver temperature is higher than that recorded for a single wave with the same wave amplitude. This increase due to multiple waves is about 5.5 °C while the increment for a single wave was 2.8 °C. As explained earlier, the increase in exhaust temperature arises from the increased fuel-intake and reduced air-intake due to increasing back pressure. Since the fuel flow is controlled by the governor, it responds to the pulsating waves of back pressure with an overshoot and undershoot in fuel flow due to a Proportional-Integral (PI) controller. A continuous trend of overshooting and undershooting fuel-intake could contribute to the higher increase in exhaust receiver temperatures caused by multiple back pressure waves. The gover-

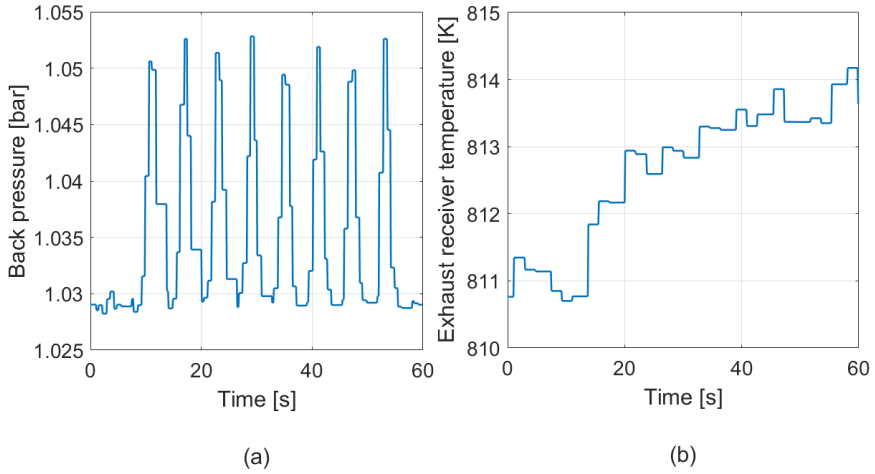


Figure 8.35: Applied multiple back pressure wave (a) of 0.35 mWC pressure amplitude with 6 seconds wave period at 340 kW and its effect on exhaust receiver temperature (b)

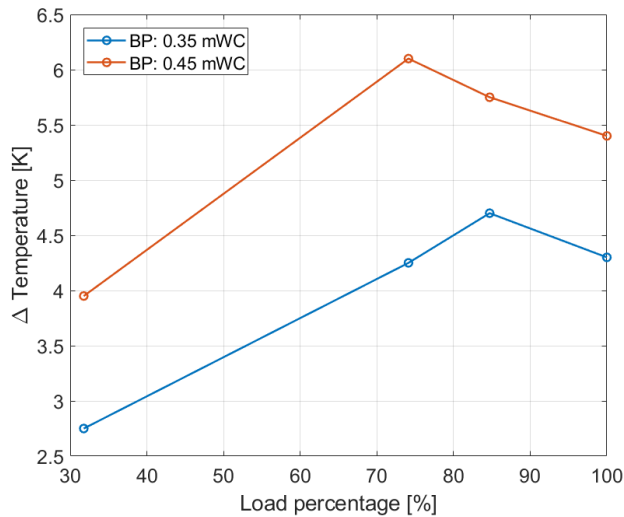


Figure 8.36: Measured maximum increase in exhaust receiver temperature due to multiple back pressure wave of 0.35 mWC and 0.45 mWC pressure amplitude with 6 seconds wave period at varying engine loads along the propeller curve

nor response and its effect on fuel flow and exhaust temperature are further discussed in subsection 8.2.3.

SINGLE BACK PRESSURE WAVE WITH WAVE PERIOD VARIATIONS

In addition to wave amplitude variations, marine engine performance was also studied against varying wave periods. In this and the next subsection, results have been pre-

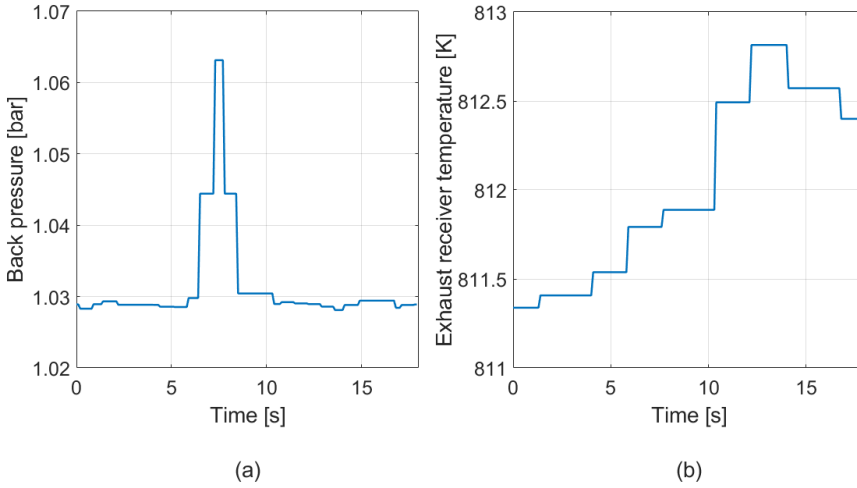


Figure 8.37: Applied single back pressure wave (a) of 0.45 mWC pressure amplitude with 4 seconds wave period at 340 kW and its effect on exhaust receiver temperature (b)

sented to showcase the effect of single and multiple waves with a fixed back pressure amplitude of 0.45 mWC and two wave periods of 4 seconds and 8 seconds.

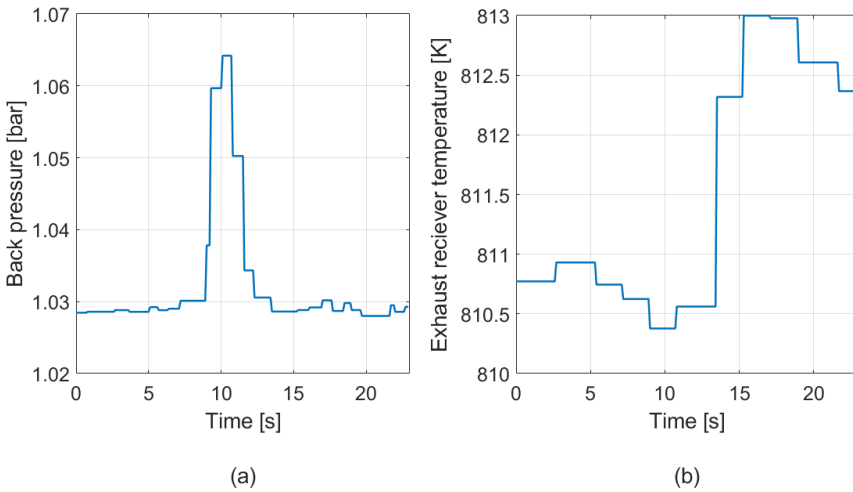


Figure 8.38: Applied single back pressure wave (a) of 0.45 mWC pressure amplitude with 8 seconds wave period at 340 kW and its effect on exhaust receiver temperature (b)

It is clear from the discussion in the previous subsection that higher the wave amplitude, higher is the increase in exhaust receiver temperature. This trend also holds true for wave periods. Figure 8.37 and Figure 8.38, show the increase in exhaust receiver temperature due to a single back pressure wave of 0.45 mWC amplitude with wave periods

of 4 seconds and 8 seconds respectively. The maximum temperature increase is about

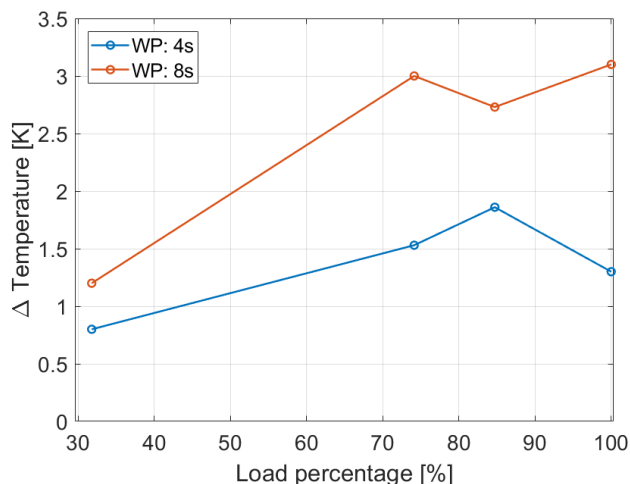


Figure 8.39: Measured maximum increase in exhaust receiver temperature due to a single back pressure wave of 0.45 mWC pressure amplitude with 4 and 8 seconds wave period at varying engine loads along the propeller curve

3°C for the 8 seconds wave period while it is about 1.25°C for the 4 seconds wave period. These values of increment in turbine inlet temperature are very close to the ones found for amplitude variations. As the wave period reduces to 4 seconds or below, the fluctuations and the rise in exhaust receiver temperature could go on reducing. This could be due to the finite response time of the governor to react to the fluctuations in back pressure. The increase in maximum exhaust receiver temperature at higher wave periods can be seen at all engine loads as seen in Figure 8.39.

8

MULTIPLE BACK PRESSURE WAVE WITH WAVE PERIOD VARIATIONS

On applying multiple waves of back pressure with 4 seconds and 8 seconds wave periods, the maximum increase in exhaust receiver temperature was higher for the higher wave period. This can be seen by comparing Figure 8.40 and Figure 8.41, which show the variations in exhaust receiver temperature for multiple back pressure waves of 0.45 mWC pressure amplitude with wave periods of 4 seconds and 8 seconds respectively. This trend of higher increment in exhaust receiver temperature with higher wave period was once again present at all loads and can be seen in Figure 8.42.

This finding of increasing exhaust receiver temperatures with increasing wave period can be compared to the findings of Tauzia et.al [40], as they concluded that the varying wave periods have little influence on the exhaust receiver temperature as the wave time periods were long compared to the engine response time based on engine model simulations. These effects of wave period on engine performance can be compared and further understood in the following manner. Increasing wave period means increasing time period during which the engine feels back pressure values close to maximum. Due to these increased time periods of back pressure close to the maximum value, the en-

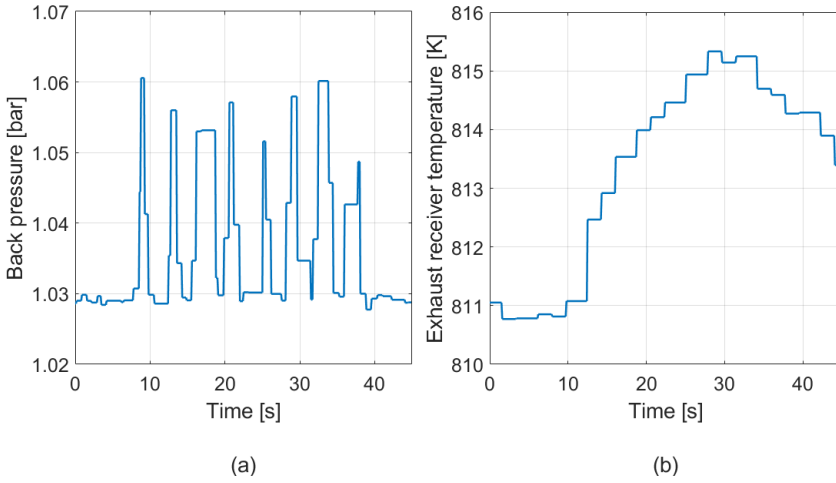


Figure 8.40: Applied multiple back pressure wave (a) of 0.45 mWC pressure amplitude with 4 seconds wave period at 340 kW and its effect on exhaust receiver temperature (b)

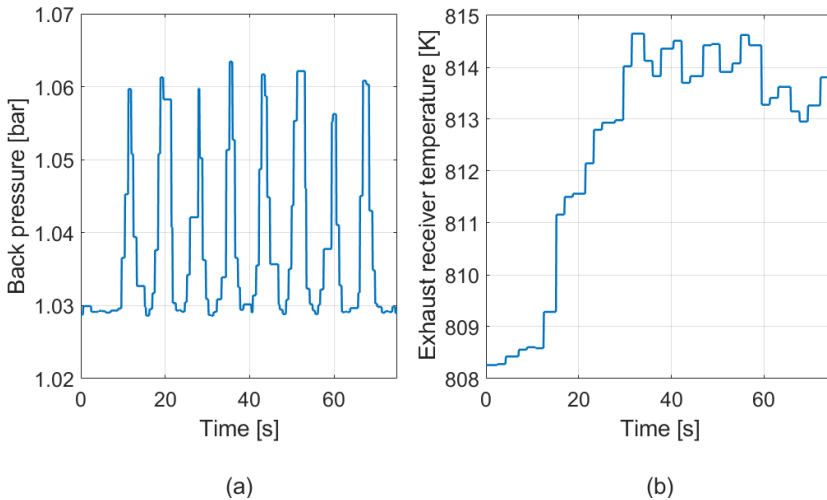


Figure 8.41: Applied multiple back pressure wave (a) of 0.45 mWC pressure amplitude with 8 seconds wave period at 340 kW and its effect on exhaust receiver temperature (b)

gine produces higher exhaust temperatures. Therefore, at some critical and high wave period, the engine may be exposed to maximum back pressures for a prolonged period of time replicating conditions closer to the application of static back pressure. Thus, the engine exhaust temperatures may increase by similar values as those found during static back pressure measurements. After reaching this critical wave period, the increment or amplitude of fluctuation in exhaust receiver temperature and fuel consumption may remain almost the same, thus, showing little or no influence on engine performance

parameters at even higher wave periods. This explanation matches well with the finding of Hield [23], as he found this critical wave period to be about 12 seconds based on engine model simulations. He showed that increasing the wave period after this critical wave period of 12 seconds has no further influence on the amplitude of fuel flow fluctuations. This critical value of wave period may depend on different engine parameters such as the PI-controller settings of the governor, turbocharger matching, valve timings, etc. Therefore, further investigations are needed to better understand this phenomenon of critical wave period.

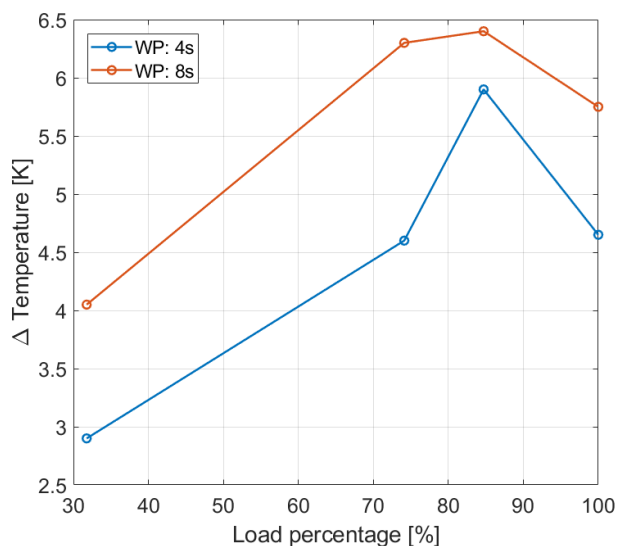


Figure 8.42: Measured maximum increase in exhaust receiver temperature due to multiple back pressure waves of 0.45 mWC pressure amplitude with 4 and 8 seconds wave period at varying engine loads along the propeller curve

Lastly, multiple back pressure waves produced higher maximum temperature increments compared to a single back pressure wave with the same wave amplitude and wave period. This was also seen in the case of back pressure waves with fixed wave periods and changing amplitudes. The increase in maximum temperature due to multiple back pressure waves of 4 seconds and 8 seconds wave period at 340 kW is approximately 5.75 °C and 4.5 °C respectively. This matches well with the increments found earlier for multiple waves with changing wave amplitudes.

8.2.3. DISCUSSION: FUEL PENALTY

The results presented in above subsections show that a marine engine operating with an underwater exhaust system is subjected to higher exhaust temperatures and thermal loading at higher wave amplitudes and wave periods. Based on this understanding of dynamic back pressure effects, ship operations in high sea-state codes such as sea-states 3, 4, 5 or higher, combined with high wave period regions could be of the highest significance when operating with underwater exhaust systems.

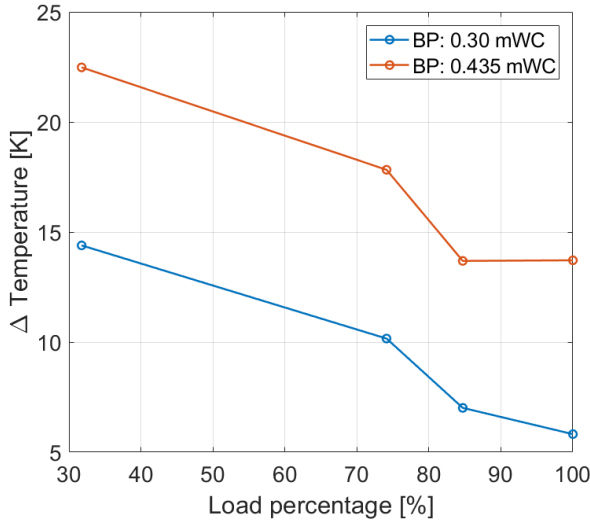


Figure 8.43: Measured maximum increase in exhaust receiver temperature due to static back pressure of 0.30 and 0.435 mWC pressure amplitude at varying engine loads along the propeller curve

In addition to exhaust receiver temperature and thermal loading, back pressure also increases fuel flow as the engine needs to produce extra work to push out the exhaust gases against the applied back pressure. The effects of dynamic back pressure on fuel penalty and its relationship with temperature dynamics, which could not be experimentally studied, can be understood in the following manner based on static back pressure measurements. As explained earlier, dynamic fluctuations in back pressure affect the turbocharger performance, thus, producing fluctuations in inlet receiver pressure and air-intake. Therefore, turbocharger matching and dynamics have a direct impact on controlling the air-intake against dynamic back pressure. The variations in air-intake along with fuel flow dictate the oscillations and the increment in exhaust receiver temperature. During static back pressure measurements, a fuel flow increase of 1.9% caused the 14 °C increment in exhaust receiver temperature against a static back pressure of 0.435 mWC amplitude at 340 kW load. Figure 8.43 shows the increment in exhaust receiver temperature against static back pressure while the corresponding fuel penalty is shown in Figure 8.44. However, it is important to note that the highest increase in temperatures for dynamic back pressure was about 5.75 °C against multiple back pressure waves of 0.45 mWC (gauge) pressure amplitude and a wave period of 8 seconds, which corresponds to sea-state 2. This increment in temperatures for a sea-state 2 is very small especially in comparison to the increment in exhaust receiver temperatures found during steady state or static back pressure measurements.

Since the fuel flow is controlled by the governor, governor control and response could play an important role against dynamic back pressure fluctuations. The quick and continuous response of the governor to control the fuel flow could help limit the maximum fuel flow against dynamic back pressure below the fuel flow value measured against the static back pressure of 0.435 mWC. A lower value of fuel flow reached during dynamic

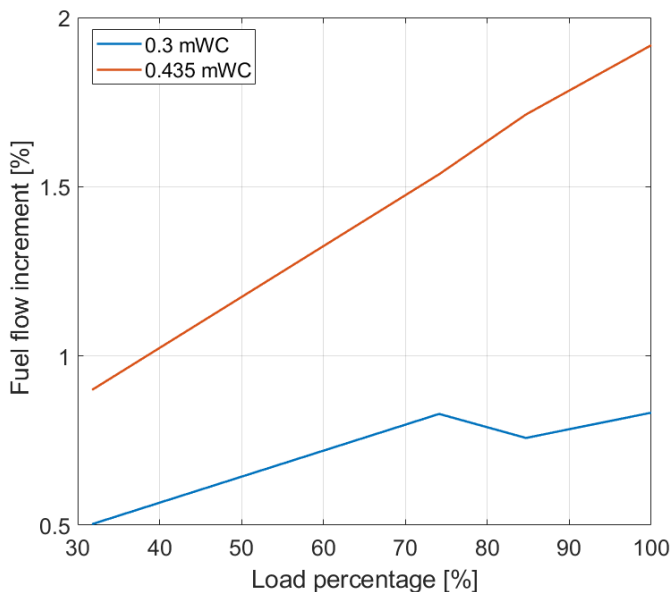


Figure 8.44: Measured percentage increment in fuel flow due to static back pressure of 0.30 and 0.435 mWC pressure amplitude at varying engine loads along the propeller curve

back pressure would indicate an even lower fuel penalty compared to that found during static back pressure. This fast control of fuel flow by the governor to limit the fuel increment and the turbocharger response to control the air-intake could also help explain the smaller increments in exhaust receiver temperatures found during dynamic back pressure. This explanation of lower maximum exhaust receiver temperatures during dynamic back pressure compared to static back pressure is contradictory to the results presented by Tazzia et al. [40], who showed that the exhaust receiver temperatures (turbine inlet temperatures) found using engine model simulations peaked to the same maximum values as those found during static back pressure. However, it is important to note that Tazzia et al. modelled dynamic back pressure effects for high wave periods of up to 16.4 seconds, which could be close to or higher than the critical wave period, explained in the previous subsection. This would explain the same values of maximum exhaust receiver temperatures found against dynamic and static back pressure by Tazzia et al [40]. Furthermore, a discussion specifically on the effects of governor control, its controller settings and critical wave period on engine performance against dynamic back pressure was not presented. Therefore, the effect of governor control on fuel penalty against dynamic back pressure needs further research. It should be investigated by using both experiments and engine model simulations as tools to gain a validated understanding of the process. The application of Ex-MVEM is recommended to investigate the effect of governor control on fuel penalty and also the phenomenon of critical wave period.

Although the discussion shows that the governor and turbocharger dynamics may be able to keep the fuel penalty and increments in exhaust receiver temperatures low

against dynamic back pressure, at a certain critical value of wave (pressure) amplitude and/or wave period the governor and turbocharger response may be unable to dampen the adverse effects of dynamic back pressure. Therefore, these critical values of wave amplitude and wave period should be investigated further. From the above discussion, it is clear that governor control and turbocharger dynamics could play an important role in keeping the adverse effects of dynamic back pressure lower than those found against static back pressure. Furthermore, it is clear from the results of this study that the effects found during dynamic back pressure fluctuations were not as severe as those found during static back pressure measurements for the same back pressure amplitude. Therefore, a marine engine may be able to handle much higher levels of dynamic back pressures when operating with underwater exhaust systems in higher sea-states.

8.3. CONCLUSION

This chapter provides a detailed understanding of static and dynamic back pressure (ISV) effects on marine engine performance when running against high back pressure due to an underwater exhaust system, thus, answering Research Question 8 and 9. The following concluding remarks are noted from the discussions presented in this chapter pertaining to the effects of static and dynamic back pressure:

EFFECTS OF STATIC BACK PRESSURE

- The study found that air-excess ratio, exhaust receiver and exhaust valve temperature are the most critical engine parameters against high back pressure. The effect of static back pressure on fuel consumption was found to be less significant.
- Static back pressure effects on air-excess ratio, exhaust receiver and valve temperatures were more pronounced at lower engine speeds (or loads along the propeller curve). Effects were inconsequential at high engine speeds, suggesting that engine performance at lower speeds needs more attention than that at higher speeds when exhausting underwater.
- Exhaust valve temperature and exhaust receiver temperature could be used to quantify thermal overloading of the exhaust valve and turbine blading, respectively. A method was presented that can be applied in practice by using a conceptual model of the smoke limit as well as thermal overloading to define acceptable limits of back pressure for an engine.
- Simulation results showed that an engine with a large valve overlap, and a constant pressure turbocharger, exhibits a drastically decreased air-excess ratio at low speeds even at relatively low levels of back pressure. Additionally, the engine was also found to be thermally overloaded again, at low speeds and same values of low back pressure.
- The study also found that an engine with a constant pressure turbocharging system and a small valve overlap is able to sustain higher static back pressures compared to an engine with a large valve overlap. Thermal overloading was found at low speeds, thus, showing a need to temporarily switch to an exhaust above the water, when using an underwater exhaust systems and constant pressure turbochargers.

- Interestingly, the research also found that a pulse turbocharged engine with a small valve overlap is better at handling high static back pressure than the modern, constant pressure turbocharged engines with the same valve overlap.
- This research also shows that a mean value engine model can provide vital engine performance information to yacht builders, shipyards, engine manufacturers and the exhaust system manufacturers, to optimize engine and ship performance.

EFFECTS OF DYNAMIC BACK PRESSURE

After investigating the effects of static back pressure, an experimental study was performed to study the performance of a marine diesel engine against dynamic back pressure in varying sea-states due to underwater exhaust systems. The study was performed on the same pulse turbocharged, marine diesel engine by applying single and multiple back pressure waves using an electronically controlled butterfly valve at the turbine outlet. To gain a qualitative and quantitative understanding of the engine performance against dynamic back pressure, engine performance was investigated against waves of varying amplitudes and wave periods based on real sea-state conditions. Conclusions related to dynamic back pressure effects are as follows:

- The experimental results showed that increasing wave amplitude of single and multiple back pressure waves increased exhaust receiver temperatures or thermal loading. Therefore, higher the sea-state higher will be the increment in exhaust receiver temperature.
- Increasing wave period of back pressure waves also increases the exhaust receiver temperatures. A smaller wave period is of less significance when operating with underwater exhaust systems possibly due to the finite response time of the governor against back pressure fluctuations. Therefore, ship operations in a high sea-state and high wave period region could be of the highest significance when operating with underwater exhaust systems.
- The increments in maximum exhaust receiver temperature were higher against multiple back pressure waves compared to those found against a single back pressure wave of same wave amplitude and wave period.
- Interestingly, this research found that the effects of dynamic back pressure fluctuations were not as severe as those found during static back pressure measurements. During dynamic and multiple back pressure waves the exhaust receiver temperature increased by a maximum value of only 5.7 °C in comparison to the increment of 14 °C found against the static back pressure of the same amplitude. Therefore, a marine engine may be able to handle much higher levels of dynamic back pressures when operating with underwater exhaust systems in higher sea-states.
- The quick and continuous control of fuel flow by the governor and the air-intake controlled by the turbocharger response could play an important role in keeping the fuel penalty and exhaust receiver temperatures against dynamic back pressure below the values reached for a static back pressure of similar pressure amplitude. However, at

a certain critical value of dynamic wave (pressure) amplitude and/or wave period the governor and turbocharger response may be unable to dampen the adverse effects of dynamic back pressure. These critical values of wave amplitude and wave period should be investigated further.

If the underwater exhaust gas expulsion and lubrication indeed lower the ship resistance, as intended from the GasDrive project, the required power to be installed onboard a ship can be lowered, which will help in further reducing the fuel consumption and the space and weight requirements of the integrated SOFC-ICE system. Expanding on the study presented in this chapter and for successful implementation of the GasDrive concept, it is crucial to investigate the performance of a natural gas engine against back pressure due to underwater exhaust systems in future. In this research, the effects of static and dynamic back pressure were studied on a marine diesel engine. The findings of this investigation lay the foundation for future research to capture marine natural gas engine performance against static and dynamic back pressure. In the case of marine natural gas engines, the impact of back pressure on knock and misfire limits may be critical and should be investigated in future research. Additionally, finding engine back pressure limits based on emissions in addition to exhaust temperatures could be a very promising methodology for defining an acceptable back pressure ceiling for any engine. Lastly, further adoption of the AOG-NG MVEM and the Ex-MVEM in combination with experiments can help in gaining a comprehensive understanding of the static and dynamic back pressure effects on a marine natural gas engine.

REFERENCES

- [1] International Maritime Organization. MARPOL ANNEX VI and NTC 2008 with Guidelines for Implementation - Supplement. 2015.
- [2] Emission Technology. <http://www.marquip.nl/exhaust-systems-expertise/emission-technology>.
- [3] M. Vejlggaard-Laursen and H.R. Olesen. Controlling Tier III Technologies. In *CIMAC*, 2016.
- [4] Marine Solutions Wärtsilä. Wärtsilä Environmental Product Guide. Technical report, 2015.
- [5] H.D. Sapra et al. Experimental and Simulation-Based Investigations of Marine Diesel Engine Performance Against Static Back Pressure. *Applied Energy*, 2017.
- [6] H.D. Sapra et al. Experimental Investigations of Marine Diesel Engine Performance Against Dynamic Back Pressure at Varying Sea-States Due to Underwater Exhaust Systems. In *ASME 2019 ICEF Technical Conference*, 2019.
- [7] H.D. Sapra. Study of Effects of on Performance of a Diesel Engine Due to Varying Back Pressure for an Underwater Exhaust System. Master's thesis, Delft University of Technology, 2015.
- [8] P.J.M. Schulten and D. Stapersma. Mean Value Modelling of the Gas Exchange of a 4-Stroke Diesel Engine for Use in Powertrain Applications. In *SAE World Congress & Exhibition*, 2003.

- [9] P.J.M. Schulten, S.I. Toxopeus, and D. Stapersma. Propeller - Diesel Engine Interaction in a Turn. In *International Naval Engineering Conference*, 2004.
- [10] D. Stapersma. *Diesel Engines: A Fundamental Approach to Performance Analysis, Turbocharging, Combustion, Emissions and Heat Transfer including Thermodynamical Principles. Vol. 2: Turbocharging*. Delft University of Technology, 2010.
- [11] P.J.M. Schulten. *The Interaction Between Diesel Engines, Ship and Propellers During Manoeuvring*. PhD thesis, 2005.
- [12] D. Stapersma. A General Model for Off-Design Performance of a Single Stage Turbomachine, Internal report. 2013.
- [13] S. Chen and P. Flynn. Development of a Single Cylinder Compression Ignition Research Engine. *SAE Technical Paper*, 1965.
- [14] Y. Ding. *Characterising Combustion in Diesel Engines*. PhD thesis, Delft University of Technology, 2011.
- [15] H.T. Grimmeliuss, E. Mesbahi, P.J.M. Schulten, and D. Stapersma. The Use of Diesel Engine Simulation Models in Ship Propulsion Plant Design and Operation. In *CIMAC*, 2007.
- [16] C. Dijkstra. Description of Simulink Mean Value Diesel Engine Model "DEII", DMS 04/10, Internal. Technical report, Delft University of Technology.
- [17] M.P.J. Ligtoet. The Matching and Validation of a Mean Value 4-Stroke Diesel Engine Model, 2004.
- [18] Baan. Doorontwikkeling Modulair Simulatiemodel van Een Dieselmotor. Technical report, 1998.
- [19] K.A. Zinner. *Aufladung von Verbrennungsmotoren*. Springer-Verlag Berlin Heidelberg, 2 edition, 1980.
- [20] Kom, M. Effect of Pressure Pulse in the Exhaust Receiver, Internal. Technical report, Delft University of Technology, 2006.
- [21] D. Stapersma. Calibrating and Matching the Mean Value First Principle Diesel Engine Model (KIM-PFS-2011-188, Issue A and Issue B). Technical report, Royal Netherlands Naval College, 2015.
- [22] E. Codan, I. Vlaskos, N. Kyrtatos, and N. Alexandrakis. Controlled Pulse Turbocharging of Medium Speed 5-Cylinder Diesel Engines. Technical report, 2005.
- [23] P. Hield. The Effect of Back Pressure on the Operation of a Diesel Engine. 2011.
- [24] A.J. Büchi. *Exhaust Turbocharging of Internal Combustion Engines: Its Origin, Evolution, Present State of Development, and Future Potentialities*. Journal of the Frankline Institute, 1953.
- [25] M. Idzior, W. Karpiuk, and M. Bieliński. Operating Problems of Turbocharging Systems in Compression-Ignition Engines. *Journal of Polish CIMAC*.
- [26] H.T. Grimmeliuss and D. Stapersma. Control Optimisation and Load Prediction for Marine Diesel Engines Using a Mean Value Simulation Model. In *ENSUS 2000, Conference Proceedings*, 2000.

- [27] H.T. Grimmelius and D. Stapersma. The Impact of Propulsion Plant Control on Diesel Engine Thermal Loading. In *CIMAC*, 2001.
- [28] S.K. Nanda, B. Jia, A. Smallbone, and A.P. Roskilly. Fundamental Analysis of Thermal Overload in Diesel Engines: Hypothesis and Validation. *Energies*, 2017.
- [29] S.K. Nanda, B. Jia, A. Smallbone, and A.P. Roskilly. Investigation on the Effect of the Gas Exchange Process on the Diesel Engine Thermal Overload with Experimental Results. *Energies*, 2017.
- [30] D. Stapersma. *Diesel Engines: A Fundamental Approach to Performance Analysis, Turbocharging, Combustion, Emissions and Heat Transfer Including Thermodynamical Principles. Vol. 3: Combustion*. Delft University of Technology, 2010.
- [31] J. Eilperin et al. Black Carbon Ranks as Second-Biggest Human Cause of Global Warming. 2013.
- [32] T.C. Bond et al. Bounding the Role of Black Carbon in the Climate System: A Scientific Assessment. *Journal of Geophysical Research: Atmospheres*, 2013.
- [33] N. Burnete, D. Moldovanu, D. Baldean, and L. Kocsis. Studies Regarding the Influence of Exhaust Backpressure on the Performances of a Compression Ignited Engine. In *Proceedings of the European Automotive Congress EAEC-ESFA 2015*. Springer International Publishing, 2015.
- [34] MAN B&W: Operating Manual for Diesel Engines. Technical report.
- [35] Ghanbariannaeni, A. and Ghazanfarihashemi, G. Protecting a Centrifugal Compressor from Surge. *Gas and Pipeline Journal*, 2012.
- [36] J. Singh. Experimental and Simulated Investigations of Marine Diesel Engine Performance Against Dynamic Back Pressure at Varying Sea-States Due to Underwater Exhaust Systems. Master's thesis, Delft University of Technology, 2019.
- [37] Upper Ocean Thermal DAC. WMO Code Tables, 2002.
- [38] U.S. Department of Commerce. National Data Buoy Center.
- [39] B. Kinsman. *Wind Waves, Their Generation and Propagation on the Ocean Surface*. General Publishing Company Ltd., 2002.
- [40] X. Tauzia, P. Chessé, and A. Maiboom. Simulation Study of a Ship's Engine Behaviour Running with a Periodically Immersed Exhaust. *Proceedings of the Institution of Mechanical Engineers, Part M: Journal of Engineering for the Maritime Environment*, 2008.

9

CONCLUSIONS AND FUTURE RESEARCH

In this chapter, concluding remarks about the contributions of this dissertation are presented. The research questions provided in Chapter 1 are revisited while presenting a discussion to answer each research question on the basis of the results provided within the thesis. Moreover, the chapter covers a list of future research directions to expand on the research presented in this dissertation.

9.1. CONCLUSIONS

The ultimate objective of the research performed in this dissertation has been to answer the main research question shown below. This research focusses on SOFC-ICE integration for maritime applications and the effects of high static and dynamic back pressure on marine engine performance due to underwater exhaust systems. In this dissertation, the main research question has been divided into multiple sub research questions, which are solved progressively to achieve the ultimate objective. In this section, the main research question and the sub research questions raised in Chapter 1 are individually answered.

Main research question: What is the impact of SOFC-ICE integration and UWE on marine engine performance and how to quantify the operation of the integrated SOFC-ICE system for maritime applications to demonstrate feasibility, energy efficiency improvement and emission reduction?

In this dissertation, the development of the integrated SOFC-ICE system for maritime applications is performed by combining literature study with experimental and numerical investigations. This approach has led to the identification of a novel SOFC-ICE integration approach for marine power generation, which integrates the SOFC with an engine capable of operating on different anode-off gas and natural gas (AOG-NG) fuel blends for additional power generation.

To investigate the potential of SOFC-ICE integration, a 0-D SOFC model was combined with a Seiliger-based in-cylinder model and an AOG-NG mean value engine model developed from engine measurements. In this manner, a comprehensive component level and combined system-level investigation was performed to study the complex interactions between the integrated system variables (listed in Chapter 1), which impact the efficiencies of the individual energy conversion devices, system efficiency, feasibility, overall emissions and system power density.

For the proposed SOFC-ICE integration approach, maximum efficiency improvements of about 8 % were found for a 67-33 power split between the SOFC and the ICE while producing a total power output of 750 kWe. At the same time, UHC and NO_x emissions reduced by about 43 % and 60 % in comparison to a conventional marine natural gas engine. Furthermore, carbon dioxide (CO₂) emissions reduced by 20.74 %. For maritime applications, promising improvements in efficiency of 5.2 %, UHC and NO_x reductions of about 30 % and CO₂ reductions of about 12 % can be achieved from a 33-67 SOFC-ICE power split with comparatively much smaller increments in size and weight of 1.7 times compared to a conventional marine natural gas engine. This research shows that significant enhancements in efficiency and reductions in emissions can be attained by integrating the SOFC with a commercially existing engine technology.

In addition, SOFC-ICE integration has further unexplored potential to achieve unprecedented efficiency improvements at part load operation. Numerous research directions such as the development of a flexible fuel blend AOG-NG engine with advanced combustion, integration with a state-of-the-art marine NG engine and development of methanol and ammonia powered SOFC-ICE power plants could help achieve further improvements in efficiency and near-zero emissions. For successful implementation of the SOFC-ICE power pack onboard ships, an operational test setup with an integrated SOFC and ICE should be developed. This will help in gaining an experimentally validated understanding of the system while providing insights into the challenges associated with building such a system.

Besides, SOFC-ICE integration, the research performed in this PhD also focussed on the effects of static and dynamic back pressure due to underwater exhaust systems on marine engine performance. In this work, a pulse turbocharged, medium speed, diesel engine was tested at different loads and engine speeds; against different values of static and dynamic back pressure. Additionally, mean value engine model simulations were validated and used to compare the performance of a pulse and constant pressure turbocharged engine against high back pressures of 1 meter water-column (mWC), and for two different values of valve overlap. The findings of this investigation lay the foundation for future research to capture marine natural gas engine performance against static and dynamic back pressure.

Using the validated simulation model, the conceptual basis for the engine smoke limit as well as for thermal overloading was investigated. Furthermore, a methodology applying the conceptual basis to define boundaries of acceptable back pressures has been presented. A combination of a pulse turbocharger system and small valve overlap showed to significantly improve the back pressure handling capabilities of engines. Interestingly, this research found that the effects of dynamic back pressure fluctuations were not as severe as those found during static back pressure measurements. Therefore,

a marine engine may be able to handle much higher levels of dynamic back pressures when operating with underwater exhaust systems in higher sea-states.

1. *Is the bottoming cycle approach presented in existing literature, which has been reviewed in Chapter 2, the right way to approach SOFC-ICE integration for ships?*

To address this research question, an overview of SOFC technology and SOFC combined cycles in current literature has been provided in Chapter 2. The literature study shows that existing studies on SOFC-ICE integration and combined cycles are mainly focussed towards land-based distributed power generation with advanced combustion engine technology and turbines employed as part of a SOFC bottoming cycle to produce a small load share. Furthermore, numerous challenges of implementing SOFC-ICE bottoming cycle for maritime applications have been debated in Chapter 2. By analysing the shortcomings of the existing SOFC-ICE integration approach in literature, with respect to the necessary considerations for power generation on-board ships, a novel SOFC and AOG-NG Engine integration approach for maritime applications has been proposed in this dissertation. This novel approach of SOFC-ICE integration allows for high-efficiency power generation while the SOFC anode-off gas is blended with natural gas and combusted in a conventional spark-ignited, lean-burn, marine engine for additional power generation. Governed by SOFC and system performance, variations in blend percentages of anode-off gas and natural gas fuel require the engine to operate on flexible anode-off gas-natural gas (AOG-NG) fuel blends for power generation rather than operating as a bottoming cycle working on only anode-off gas.

2. *What is the detailed composition of anode-off gas, how does it vary with SOFC performance and how to model the compositions of anode-off gas based on SOFC performance?*

In this dissertation, a 0-D SOFC single cell-to-stack performance model has been presented. The 0-D cell model simulates an anode-supported, intermediate temperature, planar cell with an integrated pre-reformer and co-flow configuration based on the data available from literature. The 0-D model consists of a pre-reformer model, an equilibrium model for anode-off gas composition and an electrochemical model in addition to a mass and energy balance solver to compute cell voltage, anode-off gas composition, anode-off gas flow rates, polarization or current-voltage (i-V) curve, cell power, efficiency and temperature curves. The SOFC stack performance is extrapolated from a single cell model.

Chapter 3 describes the 0-D SOFC model, which has been used to study the impact of SOFC control parameters such as current density, pre-reforming ratio and fuel utilization on SOFC performance and SOFC-ICE integration. The SOFC model is capable of computing the quality (composition) and quantity of anode-off gas for different SOFC fuel utilizations, which will dictate the engine performance for SOFC-ICE integration. In SOFC anode-off gas, the largest constituent was found to be water-vapour (64.88 %, by volume) while percentages of carbon monoxide (4.83 %, by volume) were estimated to be the smallest. The volumetric percentage of hydrogen and carbon dioxide (15.17 %, by volume) were found to be equal at 75 % fuel utilization. A lower

value of fuel utilization resulted in higher amount of hydrogen and a higher value of fuel utilization showed an increase in the percentage of carbon dioxide.

3. *What are the effects of combusting anode-off gas (constituents) on the performance, in-cylinder process, operating limits and emissions of a marine NG engine?*

The effects of combusting anode-off gas constituents on the performance, operating limits and emissions of a marine natural gas (NG) engine have been studied by experimenting on a spark-ignited (SI), zero valve overlap, lean-burn and turbocharged engine. For the SOFC-ICE integration approach presented in this dissertation, water vapour from the anode-off gas is removed by condensation before combusting the AOG in the marine natural gas engine for additional power generation. Furthermore, the effects of carbon monoxide from anode-off gas have not been considered in this research due to the small percentages of CO in anode-off gas. The main constituents of anode-off gas investigated in this research for combustion in a marine NG engine are hydrogen and carbon dioxide. The experimental results of H₂-NG and CO₂-NG combustion have been presented in Chapter 4.

The experimental results showed that increasing hydrogen percentage in fuel expands the operating window by improving the leaning capabilities of the engine. With hydrogen blending, marine hydrogen-natural gas engines could operate at high loads with a wider operating window and better leaning capabilities, thus, allowing stable and efficient operation at reduced NO_x emissions. Furthermore, addition of hydrogen improved engine efficiency while reducing carbon monoxide and unburnt hydrocarbon emissions. Blending hydrogen with natural gas also led to improvements in combustion efficiency at constant air-excess ratios. However, hydrogen addition at constant NO_x values did not show much improvements in combustion efficiency, thus, indicating that the reduction in UHC at constant NO_x emissions may be mainly due to replacement of natural gas by hydrogen. Furthermore, the experimental investigation concluded that advancing ignition timing can help increase the engine efficiency of lean-burn marine hydrogen-natural gas engines.

Contrary to hydrogen, carbon dioxide blending reduced engine efficiency, however, addition of CO₂ indicated no depreciation or even improvement in combustion stability for higher CO₂-NG fuel blends at constant NO_x emissions. Addition of CO₂ with constant NO_x operation also led to reduction of air-excess ratio, thus, indicating richening of air-fuel mixture. The richening of air-to-fuel ratio for engine operation at constant NO_x showed a profound effect in countering the decrease in combustion rate and combustion stability due to CO₂ addition. Interestingly, carbon dioxide addition provided small improvements in combustion efficiency at constant NO_x emissions, which also has a positive impact on unburnt hydrocarbons as small reductions in unburnt hydrocarbons with CO₂ blending were found in the present research at different engine loadings. A detailed discussion on the effects of AOG constituents on the in-cylinder and combustion process has been covered in Chapter 5 based on developed model simulations.

Next to steady-state operation, blending hydrogen and carbon dioxide with natural gas can impact the engine transients. The impact of engine dynamics has been quantitatively and qualitatively discussed in Chapter 7 based on engine experiments.

The experimental results indicated that marine gas engine operating on hydrogen-natural gas blends or 100 % hydrogen would have reduced transient capabilities compared to ONG marine engines due to the increased turbocharger lag and higher knocking tendency of hydrogen at same NO_x and engine loading. The experimental analysis also indicated that allowing the ICE to operate with higher CO₂ blend percentages may help in reducing the timescale of a load change due to the better turbocharger response with CO₂ addition at same NO_x and loading. Therefore, for a better understanding of the transient capabilities of the integrated engine, it may be worthwhile to further study the dynamic response of the ICE with AOG-NG blends containing higher percentages of CO₂ corresponding to SOFC operation at high fuel utilizations. However, it is vital to note that the presence of relatively smaller hydrogen percentages in the AOG at high fuel utilizations may counter the improvements in engine dynamic response obtained by CO₂ addition. In such a case, it may be interesting and simpler to operate the ICE on only NG during load transients while the anode-off gas is recirculated back to the SOFC.

4. *What simulation model can be used to quantify engine performance with anode-off gas effects and study system integration between the SOFC and the engine?*

In Chapter 5, a comprehensive literature study has been presented to explain the different type of engine modelling approaches. The choice of engine modelling approach can vary from detailed computational fluid dynamics (CFD) models to straight forward transfer function models depending on the required accuracy, amount of information and computational time required. The study discusses the application of different modelling approaches in current literature for capturing combustion and engine performance on varying H₂-NG and CO₂-NG fuel blends. In this research, to study the potential of SOFC-ICE integration, it is vital to capture the variations in the in-cylinder and combustion process due to addition of anode-off gas constituents. 0-D combustion models can provide sufficient details of the in-cylinder and combustion process while providing the opportunity to combine them with open-cycle mean value engine models (MVEMs) to simulate the entire performance of the engine for SOFC-ICE integration. Therefore, in this research, a 0-D modelling approach is chosen to capture the combustion of blending anode-off gas constituents (H₂ and CO₂) in an SI lean-burn marine natural gas engine.

In Chapter 5, a detailed methodology to develop 0-D Seiliger and double Wiebe function-based combustion characterization models based on engine measurements to study and capture the combustion process for different fuel blends, engine loads and engine leaning has been presented. The investigation performed showed that the characterization of combustion using the Seiliger modelling approach can be used to capture the H₂-NG in-cylinder combustion process with high accuracy. Similarly, H₂-NG combustion can be simulated by using the Wiebe modelling approach with accurate estimation of the in-cylinder pressures and temperatures, however, it produced higher deviations in the estimation of work output and combustion heat for different H₂-NG fuel blends, engine leaning and loads. The investigation also found that Seiliger combustion parameters showcase clear trends and good ability in capturing the H₂-NG combustion process variations for different H₂-NG fuel blends, loads

and engine leaning. On the contrary, the double Wiebe function found its limitations in identifying clear trends of the Wiebe shape parameters and the combustion duration of the second Wiebe function (CD_2) for all fuel blends, engine leaning and loads. Therefore, Seiliger-based modelling approach was further adopted to capture the CO_2 -NG combustion and in-cylinder process.

The research presented in Chapter 5 found that the Seiliger modelling approach can be used to quantify the combustion and in-cylinder pressure variations due to anode-off gas constituents. Moreover, by identifying trends in variations of combustion parameters, parametric equations have been derived as a function of normalized natural gas fuel mass (load) and volumetric blend percentages of H_2 and CO_2 . The parametric equations are used to capture the combustion process and engine performance for different blends of anode-off gas and natural gas under varying test conditions. Next, the derived parametric equations for Seiliger combustion models are combined with a mean value engine model to capture the complete engine performance for SOFC-ICE integration. This approach of combustion parameterization and integration with an MVEM to simulate different test conditions of SOFC anode-off gas fuel blends has been presented in Chapter 6. Chapter 5 provides an in-detail understanding of the effects of combusting blends of hydrogen-natural gas and carbon dioxide-natural gas in a marine lean-burn SI engine through combustion characterization modelling.

5. *What are the effects of ISVs on SOFC and engine operation, and how do they impact the performance of the integrated SOFC-ICE power plant?*

In this dissertation, the effects of ISVs such as current density, pre-reforming ratio and fuel utilization on SOFC performance have been covered in Chapter 3. Increasing current density at constant fuel utilization led to high PEN temperatures and reduced cell voltages. The SOFC voltage and efficiency increase at low current densities and low load operation, which is contradictory to engine operation. The cell voltage increased with increasing pre-reforming ratio. However, operation at high fuel utilizations reduced cell voltage while efficiency increased.

The experimental and model simulation study in Chapter 4 and Chapter 5 helped in understanding the effects of ISVs such as engine fuel composition (varying blends of anode-off gas constituents and natural gas), air-excess ratio (engine leaning), spark-timing and engine loading on the operating limits, engine emissions, efficiency and the in-cylinder process of the marine lean-burn NG engine. The H_2 -NG combustion characterization process detailed in Chapter 5 showed that maximum in-cylinder pressures and temperatures decreased with engine leaning, while hydrogen addition at the same NO_x emission increased the maximum in-cylinder pressure values. The characterization process also showed that as the air-intake is controlled, the engine produces almost similar values of maximum in-cylinder temperatures to produce the same amount of NO_x emissions. Therefore, the combustion due to hydrogen addition could be controlled by governing the air-intake to control the maximum in-cylinder temperatures to produce NO_x emissions within IMO TIER-III NO_x emission limits. Although the in-cylinder temperatures due to hydrogen addition and NO_x control are quite similar, hydrogen addition results in slightly lower temperatures at the point of

exhaust valve opening.

Next, the heat release analysis for CO₂-NG combustion showed that the richening of air-excess ratio increases the combustion rate, which counters the slowing-down effect due to CO₂ dilution. The similar or even high heat release found for CO₂-NG combustion compared to ONG indicates no depreciation of combustion stability and explained the reduction in unburnt hydrocarbons and also COV_{IMEP} due to CO₂ blending. Furthermore, the richening of air-fuel mixture leads to similar values of maximum temperatures with increased CO₂ percentages in the fuel blend. In general, addition of CO₂ should result in lower in-cylinder temperatures due to the higher specific heat capacity. However, the richening of air-fuel mixture due to NO_x control has a significant counter impact on the in-cylinder process. This strong impact of air-intake due to NO_x control was also found for hydrogen addition. CO₂ addition also showed higher values of exhaust temperatures at the point of exhaust valve opening. Overall, the modelling results showed that the positive effects of hydrogen on the in-cylinder process are more prominent than the negative effects of carbon dioxide for the same blending percentage.

After studying the effects of blending natural gas with individual components of anode-off gas, the AOG-NG MVEM simulations discussed in Chapter 6 help understand the impact of different fuel compositions (ISV) on engine performance and turbocharging. The MVEM simulation showed that there was a mismatch between the pressure before throttle and manifold pressure for 20H₂-NG fuel blend at 500 kWe. The mismatch is caused by the lower exhaust temperatures due to hydrogen addition leading to a reduced pressure before throttle in contrast to the increased manifold pressure caused by additional air requirements for same NO_x operation with hydrogen. Contrary to hydrogen, CO₂ addition required less amount of air to produce the same NO_x, thus, allowing a positive delta between the pressure before throttle and manifold pressure at 500 kWe. Thus, the MVEM shows that the test engine could run on a 20CO₂-NG fuel blend at 100 % load, however, it would reach its current turbocharging capacity on a 20H₂-NG fuel blend during engine measurements. Therefore, the turbocharging capacity of the engine would have to be increased to run with hydrogen at 500 kWe load.

Further on, the impact of ISVs such as current density, pre-reforming ratio, fuel utilization, heat integration and power splits on the integrated SOFC-ICE system have been covered in Chapter 7. Increase in current density led to an increase in the efficiency of the integrated power plant due to a larger load share of the SOFC when producing a fixed system power output. Next, with increasing pre-reforming ratio, the SOFC efficiency improved due to a small increase in its power output. However, the efficiency of the integrated AOG-NG engine reduced with increasing pre-reforming ratio due to operation at reduced loads. Furthermore, operation at high fuel utilizations showed improvements in SOFC efficiency, however, the engine efficiency dropped due to larger percentages of carbon dioxide in the anode-off gas. The impact of anode-off gas constituents on the dynamic response of the ICE has been covered in Chapter 7. Lastly, Chapter 8 provides a detailed understanding of static and dynamic back pressure (ISV) effects on marine engine performance when running against high

back pressure due to an underwater exhaust system.

6. *What is the optimal composition of anode-off gas based on engine performance, SOFC performance and SOFC-ICE integration?*

SOFC fuel utilization has a significant impact on anode-off gas composition. The 0-D SOFC model showed that increasing fuel utilization led to efficiency improvements, however, operation at high fuel utilization adversely affects the cell lifetime due to fuel starvation. At the same, operation at low fuel utilizations can significantly reduce SOFC efficiency. In this research, operation was found to be favourable at 75 % to 80 % fuel utilization as it ensures safe fuel cell operation, high SOFC efficiency and a good ratio of hydrogen and carbon dioxide in AOG-NG blend for improved engine operation. Thus, an optimal anode-off composition would correspond to fuel utilizations in the range of 75 % to 80 %. Chapter 7 presents the results for SOFC-ICE integration at different fuel utilizations and, thus, anode-off gas compositions.

7. *How does the integrated SOFC-ICE power pack compare against a conventional marine engine for power generation in terms of efficiency, emissions and power density (gravimetric and volumetric)?*

In the proposed integration approach, the SOFC is combined with an AOG-NG engine. The efficiency of this integrated AOG-NG engine was found to be higher than that of the standalone only natural gas (ONG) engine by a maximum of 3.55 % at 70 % fuel utilization while producing the same power output of 375 kWe. These improvements in performance of the AOG-NG engine contribute to enhanced performance of the integrated SOFC-ICE power pack.

The SOFC-ICE power split of 67-33 showed the highest efficiency improvement of about 8 %, while UHC and NO_x emissions reduced by about 43 % and 60 % in comparison to a conventional marine natural gas engine. Furthermore, carbon dioxide (CO₂) emissions reduced by 20.74 %. However, the 67-33 power split also accounted for space and weight increments of approximately two and a half times. For maritime applications, promising improvements in efficiency of 5.2 %, UHC and NO_x reductions of about 30 % and CO₂ reductions of about 12 % can be achieved from a 33-67 SOFC-ICE power split with comparatively much smaller increments in size and weight of 1.7 times compared to a conventional marine natural gas engine. This research shows that significant enhancements in efficiency and reductions in emissions can be attained by integrating the SOFC with a commercially existing engine technology.

Additionally, the 0-D SOFC model simulations showed that the SOFC took about 500 to 600 seconds to reach steady state (for a +2000 A m⁻² min⁻¹ ramp rate) and 600 seconds to reach the required load (for a +200 A m⁻² min⁻¹ ramp rate) during a load change from 250 to 375 kWe. Comparatively, the ICE achieved the same load change in about 14 seconds based on dynamic engine experiments. Thus, the study concluded that in the SOFC-ICE system proposed for maritime applications, a power split that favours the ICE would significantly improve the dynamic capabilities of the combined system and the possible sudden and large load changes can be met by the ICE.

8. *What are the quantitative effects of static back pressure on marine engine performance due to underwater exhaust system?*

The effects of steady-state back pressure have been analysed based on test-bench measurements performed on a pulse turbocharged diesel engine and model simulations. The back pressure study described in Chapter 8 found that air-excess ratio, exhaust receiver and exhaust valve temperature are the most critical engine parameters against high back pressure. The effect of static back pressure on fuel consumption was found to be less significant. Effects on air-excess ratio, exhaust receiver and valve temperatures were more pronounced at lower engine speeds (or loads along the propeller curve). Effects were inconsequential at high engine speeds, suggesting that engine performance at lower speeds needs more attention than that at higher speeds when exhausting underwater. The study also found that exhaust valve temperature and exhaust receiver temperature could be used to quantify thermal overloading of the exhaust valve and turbine blading, respectively. A method was presented that can be applied in practice by using a conceptual model of the smoke limit as well as thermal overloading to define acceptable limits of back pressure for an engine.

Simulation results showed that an engine with a constant pressure turbocharging system and a small valve overlap is able to sustain higher static back pressures compared to an engine with a large valve overlap. Thermal overloading was found at low speeds, thus, showing a need to temporarily switch to an exhaust above the water, when using an underwater exhaust system and constant pressure turbochargers. Interestingly, the research also found that a pulse turbocharged engine with a small valve overlap is better at handling high static back pressure than the modern, constant pressure turbocharged engines with the same valve overlap.

9. *What are the quantitative effects of dynamic back pressure on marine engine performance due to underwater exhaust system?*

In Chapter 8, to gain a qualitative and quantitative understanding of the engine performance against dynamic back pressure due to underwater exhaust systems, marine diesel engine performance was experimentally investigated against waves of varying amplitudes and wave periods based on real sea-state conditions. The experimental results showed that increasing wave amplitude of single and multiple back pressure waves increased exhaust receiver temperatures or thermal loading. Therefore, higher the sea-state higher will be the increment in exhaust receiver temperature. Adjacent to this, increasing wave period of back pressure waves also increased the exhaust receiver temperatures. Therefore, a smaller wave period is of less significance when operating with underwater exhaust systems possibly due to the finite response time of the governor against back pressure fluctuations. Thus, ship operations in a high sea-state and high wave period region could be of the highest significance when operating with underwater exhaust systems.

Interestingly, this research found that the effects of dynamic back pressure fluctuations were not as severe as those found during static back pressure measurements. Therefore, a marine engine may be able to handle much higher levels of dynamic back pressures when operating with underwater exhaust systems in higher sea-states. The

quick and continuous control of fuel flow by the governor and the air-intake controlled by the turbocharger response could play an important role in keeping the fuel penalty and exhaust receiver temperatures against dynamic back pressure below the values reached for a static back pressure of similar pressure amplitude. However, at a certain critical value of dynamic wave (pressure) amplitude and/or wave period the governor and turbocharger response may be unable to dampen the adverse effects of dynamic back pressure.

9.2. CONTRIBUTIONS OF THE THESIS

In this thesis, a combination of experiments and model simulations has been adopted to investigate SOFC-ICE integration for ships. This research provides novel experimentation knowledge of marine engine performance and enhanced understanding of SOFC performance in combination with a natural gas engine. A multitude of models have been developed to support the development of SOFC-ICE integration in addition to studying the impact of back pressure on marine engine performance due to underwater exhaust systems. In brief, the contributions of this thesis can be summarized as follows:

- In Chapter 2, a literature study covering a detailed discussion on the advantages and shortcomings of existing SOFC combined cycles has been presented. By discussing and analysing the shortcomings of the existing SOFC-ICE integration approach in literature, with respect to the necessary considerations for power generation onboard ships, a novel SOFC and AOG-NG Engine integration approach for maritime applications has been proposed. Parts of this literature study have been published in:
 - H.D. Sapra, J. Stam, J. Reurings, L. van Biert, W. van Sluijs, P. de Vos, K. Visser, A. P. Vellayani, H. Hopman, Integration of Solid Oxide Fuel Cell and Internal Combustion Engine for Maritime Applications, Applied Energy, 2020.
- In Chapter 3, a 0-D SOFC single cell-to-stack performance model has been presented. The 0-D model consists of a pre-reformer model, an equilibrium model for anode-off gas composition and an electrochemical model in addition to a mass and energy balance solver to compute cell voltage, anode-off gas composition, anode-off gas flow rates, polarization or current-voltage (i-V) curve, cell power, efficiency and temperature curves. The model has been used to study the impact of different SOFC control parameters or ISVs such as pre-reforming ratio, current density and fuel utilization on SOFC and system performance. Parts of this chapter have been published in:
 - H.D. Sapra, J. Stam, J. Reurings, L. van Biert, W. van Sluijs, P. de Vos, K. Visser, A. P. Vellayani, H. Hopman, Integration of Solid Oxide Fuel Cell and Internal Combustion Engine for Maritime Applications, Applied Energy, 2020.
- In Chapter 4, the experimental methodology and results for combusting different hydrogen-natural gas and carbon dioxide-natural gas blends in a SI, zero valve overlap, lean-burn and turbocharged marine engine have been presented. A comprehensive discussion covering the impact of H₂ and CO₂ addition on combustion stability, operating limits, efficiency and emissions of a marine natural gas engine has been provided. Parts of this chapter have been published in:

- H.D. Sapra, Y. Linden, W. van Sluijs, M. Godjevac, K. Visser, Experimental Investigations of Hydrogen-Natural Gas Engine for Maritime Applications, Proceedings of the ASME 2018 Internal Combustion Engine Fall Technical Conference, November, 2018.
 - H.D. Sapra, Y. Linden, W. van Sluijs, M. Godjevac, K. Visser, Experimental Investigations of Performance Variations in Marine Hydrogen-Natural Gas Engines, CIMAC World Congress, June, 2019. Awarded best CIMAC 2019 poster presentation.
 - H.D. Sapra, J. Stam, J. Reurings, L. van Biert, W. van Sluijs, P. de Vos, K. Visser, A. P. Vellayani, H. Hopman, Integration of Solid Oxide Fuel Cell and Internal Combustion Engine for Maritime Applications, Applied Energy, 2020.
- In Chapter 5, the effects of combusting blends of hydrogen-natural gas and carbon dioxide-natural gas in a marine lean-burn SI engine have been studied through combustion characterization modelling. A detailed comparison between the capabilities of Seiliger and Wiebe-based modelling approaches to characterize and capture the H₂-NG combustion process has been presented. The study showcases a detailed methodology to develop 0-D Seiliger and double Wiebe function-based combustion characterization models based on engine measurements to study and capture the combustion process for different fuel blends, engine loads and engine leaning. The chapter presents a single-zone, 0-D, thermodynamic heat release rate model that accounts for the impact of high amount of trapped residual gas found in the zero valve overlap test engine. Parts of this chapter have been published in:
 - H.D. Sapra, M. Godjevac, P. de Vos, W. van Sluijs, Y. Linden, K. Visser, Hydrogen-Natural Gas Combustion in a Marine Lean-Burn SI Engine: A Comparative Analysis of Seiliger and Double Wiebe Function-Based Zero-Dimensional Modelling, Energy Conversion and Management, 2020.
 - In Chapter 6, a methodology to capture and understand the variations in-cylinder process for an anode-off gas-natural gas fuel blend as deviations in Seiliger parameters for each individual anode-off gas constituent (H₂ and CO₂) has been presented. The study showcases the capabilities of the Seiliger-based modelling approach in combination with mean value engine modelling to accurately simulate the complete AOG-NG engine performance for different anode-off gas and natural gas fuel blends. The chapter provides a detailed description of the developed AOG-NG MVEM for SOFC-ICE integration. Furthermore, the impact of fuel compositions (ISV) on turbocharging and engine performance have been discussed in this chapter. Parts of this chapter have been published in:
 - H.D. Sapra, J. Stam, J. Reurings, L. van Biert, W. van Sluijs, P. de Vos, K. Visser, A. P. Vellayani, H. Hopman, Integration of Solid Oxide Fuel Cell and Internal Combustion Engine for Maritime Applications, Applied Energy, 2020.
 - In Chapter 7, an in-depth performance analysis has been presented by combing the 0-D SOFC model and the AOG-NG MVEM to investigate the potential of SOFC-ICE power plant for maritime applications. A combined system and component level investigation has been proposed to capture the complex interactions between the SOFC,

the integrated AOG-NG engine and the combined SOFC-ICE power plant. The impact of SOFC performance, AOG composition, ICE performance and load-sharing on system efficiency has been covered. A comparison between the SOFC-ICE power plant and a conventional marine natural gas engine has been presented with respect to efficiency, emissions and system size. Additionally, the chapter also presents a comparison between the load response of the SOFC and the ICE to discuss the dynamic capabilities from a maritime perspective while covering a discussion on the impact of AOG constituents on the load response of the marine NG engine. The chapter also provides a discussion on the unexplored potential of SOFC-ICE integration for future research. Parts of this chapter have been published in:

- H.D. Sapra, J. Stam, J. Reurings, L. van Biert, W. van Sluijs, P. de Vos, K. Visser, A. P. Vellayani, H. Hopman, Integration of Solid Oxide Fuel Cell and Internal Combustion Engine for Maritime Applications, *Applied Energy*, 2020.
- H.D. Sapra, J. Stam, L. van Biert, P. de Vos, K. Visser, M. Gert-Jan, Potential of Combined drive of Fuel cell And Internal Combustion Engine (COFAICE) for naval ships, *The International Naval Engineering Conference*, Online, October, 2020.
- In Chapter 8, a detailed understanding of static and dynamic back pressure (ISV) effects on marine engine performance, when running against high back pressure due to an underwater exhaust system has been provided. A methodology has been presented that can be applied in practice by using a conceptual model of the smoke limit as well as thermal overloading to define acceptable limits of back pressure for an engine. In this research, the application of an Ex-MVEM has been proposed to investigate the capabilities of different turbocharger configurations along with different engine valve overlap settings to tackle high back pressures.

To gain a qualitative and quantitative understanding of the engine performance against dynamic back pressure, experimental results detailing engine performance against waves of varying amplitudes and wave periods based on real sea-state conditions has been presented. This research shows that the effects of dynamic back pressure fluctuations may not be as severe as those found against static back pressure. Therefore, a marine engine may be able to handle much higher levels of dynamic back pressures when operating with underwater exhaust systems in higher sea-states. Parts of this chapter have been published in:

- H.D. Sapra, M. Godjevac, K. Visser, D. Stapersma, C. Dijkstra, Experimental and Simulation-Based Investigations of Marine Diesel Engine Performance Against Static Back Pressure, *Applied Energy*, 2017.
- H.D. Sapra, J. Singh, C. Dijkstra, P. de Vos, K. Visser, Experimental Investigations of Marine Diesel Engine Performance Against Dynamic Back Pressure at Varying Sea-States due to Underwater Exhaust Systems, *Proceedings of the ASME Internal Combustion Engine Fall Technical Conference*, October, 2019. Awarded the most valuable technical paper award in Track 1 - Large Bore Engines at the 2019 ASME ICE Fall Technical Conference

9.3. RECOMMENDATIONS FOR FUTURE RESEARCH

In this section, recommendations for future research are presented. The recommendations are aimed at further development of SOFC-ICE integration for ships and enhanced understanding of SOFC and engine performance through experimental and simulations-based investigations.

SOFC MODELLING

- The 0-D SOFC model presented in Chapter 3 was able to satisfactorily simulate the SOFC performance, however, the model showed deviations in cell performance prediction compared to the reference model. The deviations could be attributed to the difference in modelling approach of 0-D versus the 1-D model by Aguiar et al., model equations and assumptions. For improved accuracy in cell performance prediction, the 0-D SOFC model should be further calibrated and validated against experimental data. Additionally, heat transfer from the SOFC stack should be taken into consideration as it can impact cell performance.
- On comparing with literature, it was found that the 0-D SOFC model could be over-predicting the voltages by a small margin at high fuel utilizations. In other words, the drop in cell voltage due to increasing fuel utilization could be somewhat higher. Based on the earlier explanation, a higher drop in cell voltage at high fuel utilization will result in a lower power output and a lower improvement in cell efficiency. This possible shortcoming of the 0-D SOFC model and its impact on cell performance prediction should be further investigated in near future. Development of a higher level SOFC model with experimental validation could be adopted in future research to gain improved accuracy and more details pertaining to cell performance. Furthermore, a 1-D model is recommended to more accurately capture the temperature and voltage response while accounting for thermal gradients and stresses in SOFC load response.

ENGINE EXPERIMENTS

- Like hydrogen and unlike CO₂, carbon monoxide is a combustible product that will contribute to and support combustion. The volumetric lower heating value of CO is slightly higher than that of hydrogen. Therefore, the relatively smaller percentages of CO could also contribute to engine efficiency like hydrogen. Therefore, the effects of carbon monoxide from anode-off gas should be studied in future to account for the possible positive impact on SOFC-ICE integration.
- Engine performance with higher percentages of anode-off gas should be studied as there is more anode-off gas available for engine operation than the amount tested in this research.
- Comparing engine performance for alternative fuels like hydrogen at low air-excess ratios can indicate high improvements in engine efficiency while drastically increasing NO_x emissions beyond emission regulation limits. Therefore, for a clear discussion on the effects of alternative fuels and fuel blends, engine performance is recommended to be measured and compared at same NO_x emission values and not at same air-excess ratios.

COMBUSTION MODELLING AND AOG-NG MVEM

- The Seiliger and Wiebe modelling approaches presented in this research can be combined with a mean value open cycle model to produce combustion effects in sufficient detail while capturing total engine performance dynamics. Such Seiliger and Wiebe-based MVEMs can be employed to study controls, load variations, system integration, voyage simulations and even smart maintenance strategies for ships.
- In this dissertation, the Seiliger based approach is recommended due to its ability to accurately capture the variations in the combustion process at all the crucial points with low computation effort due to the discretized in-cylinder process.
- The presented combustion characterization methodology based on engine experiments could be applied to other alternative fuels and automotive engines.
- Improved parametric equations can be derived to compute Seiliger and Wiebe combustion parameters as a function of other input parameters such as spark-timing, air-excess ratio, manifold pressure, etc. using regression fitting. This could help develop generic and validated parametric equations that can be used to capture the combustion process and engine performance under varying test conditions. The parametrization process can be improved by testing with other fit equations and more fitting data, which could improve the parameterization of CO₂-NG combustion.
- In the AOG-NG MVEM, the isentropic compressor and turbine efficiency have been assumed to be constant. Under real operating conditions, these efficiencies change with charge pressure and impact the turbocharger performance. For further development of the AOG-NG MVEM, the impact of these efficiencies on turbocharging and AOG-NG engine performance should be investigated. In the current version of the AOG-NG MVEM, the pressure before throttle and manifold pressure are calculated separately. In future, these two pressures should be connected by modelling a throttle position such that a change in position of the throttle would change the manifold pressure relative to the pressure before the throttle. A throttle position model will be critical for investigating the dynamic response of the natural gas engine.
- Investigation into adaptations of different heat transfer correlations is recommended for future work to accurately understand and capture the impact of heat loss on the in-cylinder process due to combustion of only anode-off gas, alternative fuels and fuel blends.

SOFC-ICE INTEGRATION

- The developed 0-D SOFC model and mean value engine model should be adopted to study the transient capabilities of the integrated SOFC-ICE marine power pack. The MVEM can be also used to study control and load transients of marine SI natural gas engines. The dynamic response of the system and load-sharing should be further investigated based on a real case study while considering the operational load profiles of the ship. In addition to load response, a dedicated study should be performed to investigate the plant reliability, life-cycle and safety considerations.

- The heat integration and performance of the SOFC-ICE power plant presented in this dissertation could be optimized by employing anode-off gas (AOG) recirculation. Redirecting a controlled AOG percentage back into the SOFC can provide a direct supply of heat and steam for pre-reforming and preheating of incoming flows, thus, optimising the BoP. By implementing a bypass for the anode-off gas, the percentage of anode-off gas recirculated and the amount supplied to the engine can be controlled for further optimization. The potential of anode-off gas recirculation for SOFC-ICE integration should be investigated in future.
- Further research into a flexible fuel blend AOG-NG engine capable of operating on any blend of anode-off gas and natural gas is recommended as it could lead to unprecedented efficiency improvements at part load operation of the SOFC-ICE power plant. For the development of the flexible fuel blend AOG-NG engine, advanced combustion technologies such as spark-assisted (SAI) combustion could be interesting and should be considered for future research.
- By integrating the SOFC with a state-of-the-art NG engine, SOFC-ICE integration could allow operation at even higher efficiencies than those found in this research.
- Methanol and ammonia powered SOFC-ICE power plants should be researched in future due to their promise of very low emissions and high-efficiency operation.
- The research performed in this dissertation is the first step towards the development of SOFC-ICE integration for maritime applications. For successful implementation of the SOFC-ICE power pack, an operational test setup with an integrated SOFC and ICE should be developed. This will help in gaining an experimentally validated understanding of the system while providing insights into the challenges associated with building such a system.
- For a comprehensive understanding of the dynamic capabilities of the integrated SOFC-ICE system for marine power generation, a detailed and experimentally validated modelling study is recommended that captures the complex interactions between the SOFC, ICE and balance-of-plant components such as heat exchangers, blowers, pumps, etc.

BACK PRESSURE AND UNDERWATER EXHAUST SYSTEM

- The shape of the dynamic waveform at the turbine outlet due to an underwater exhaust system should be further investigated as it may depend on various parameters such as ship operations, exhaust system design and exhaust position. Furthermore, the impact on engine performance due to back pressure caused by position 1 and position 3 of the exhaust outlet, shown in Figure 8.26(a) of Chapter 8, should be investigated in future.
- The research on dynamic back pressure effects concluded that at a certain critical value of dynamic wave (pressure) amplitude and/or wave period the governor and turbocharger response may be unable to dampen the adverse effects of dynamic back pressure. These critical values of wave amplitude and wave period should be investigated further.

- If the underwater exhaust gas expulsion and lubrication indeed lower the ship resistance, as intended from the GasDrive project, the required power to be installed on-board a ship can be lowered, which will help in further reducing the fuel consumption and the space and weight requirements of the integrated SOFC-ICE system. For successful implementation of the GasDrive concept, it is crucial to investigate the performance of a natural gas engine against back pressure due to underwater exhaust systems in future.
- In the case of marine natural gas engines, the impact of back pressure on knock and misfire limits may be critical and should be investigated in future research. Additionally, finding engine back pressure limits based on emissions in addition to exhaust temperatures could be a very promising methodology for defining an acceptable back pressure ceiling for any engine. Lastly, further adoption of the AOG-NG MVEM and the Ex-MVEM in combination with experiments can help in gaining a comprehensive understanding of the static and dynamic back pressure effects on a marine natural gas engine.

A

SOFC GEOMETRICAL, PHYSICAL AND THERMODYNAMIC PROPERTIES

Table A.1: Geometrical properties data of single SOFC cell [1]

Properties	Symbol	Value	Unit
Active cell width	W	0.1	m
Active cell length	L	0.4	m
Channel height (air and fuel)	H	$1 * 10^{-3}$	m
Anode thickness	τ_{anode}	$500 * 10^{-6}$	m
Cathode thickness	τ_{cathode}	$50 * 10^{-6}$	m
Electrolyte thickness	$\tau_{\text{electrolyte}}$	$20 * 10^{-6}$	m

Table A.2: Physical properties data of single SOFC cell [1]

Properties	Symbol	Value	Unit
Specific heat PEN structure	$c_{p,\text{PEN}}$	500	$\text{Jkg}^{-1} \text{K}^{-1}$
Specific heat interconnect	$c_{p,\text{IC}}$	500	$\text{Jkg}^{-1} \text{K}^{-1}$
Electronic conductivity anode	σ_{anode}	$8 * 10^{-4}$	$\Omega^{-1} \text{m}^{-1}$
Electronic conductivity cathode	σ_{cathode}	$8.4 * 10^{-4}$	$\Omega^{-1} \text{m}^{-1}$
Electronic conductivity electrolyte	$\sigma_{\text{electrolyte}}$	$3340 \exp(-10300/T_{\text{PEN}})$	$\Omega^{-1} \text{m}^{-1}$
Emissivity PEN	ϵ_{PEN}	0.8	-
Emissivity interconnect	ϵ_{IC}	0.1	-
Diffusivity effective anode	$D_{\text{eff},\text{anode}}$	$3.66 * 10^{-5}$	$\text{m}^2 \text{s}^{-1}$
Diffusivity effective cathode	$D_{\text{eff},\text{cathode}}$	$1.37 * 10^{-5}$	$\text{m}^2 \text{s}^{-1}$

Table A.3: Electrode properties data of single SOFC cell [1]

Properties	Symbol	Value	Unit
Pre-exponential coefficient anode	k_a	$6.54 * 10^{11}$	$\Omega^{-1} m^{-2}$
Pre-exponential coefficient cathode	k_c	$2.35 * 10^{11}$	$\Omega^{-1} m^{-2}$
Activation energy anode	$E_{a,a}$	$140 * 10^3$	$J mol^{-1}$
Activation energy cathode	$E_{a,c}$	$137 * 10^3$	$J mol^{-1}$

Table A.4: Fit functions of molar specific enthalpy for temperature 700-1500 K [2]

Species	Fit function	Unit
CH ₄	$74.66 * T - 1.105 * 10^5$	$J mol^{-1}$
H ₂ O	$42.45 * T - 2.258 * 10^5$	$J mol^{-1}$
H ₂	$30.68 * T - 9911$	$J mol^{-1}$
CO	$33.57 * T - 1.223 * 10^5$	$J mol^{-1}$
CO ₂	$55.03 * T - 4.149 * 10^5$	$J mol^{-1}$
O ₂	$35.15 * T - 1.1235 * 10^4$	$J mol^{-1}$
N ₂	$33.12 * T - 1.154 * 10^4$	$J mol^{-1}$

REFERENCES

- [1] P. Aguiar, C.S. Adjiman, and N.P. Brandon. Anode-Supported Intermediate Temperature Direct Internal Reforming Solid Oxide Fuel Cell. I: Model-Based Steady-State Performance. *Journal of Power Sources*, 2004.
- [2] J.W. Reurings. A Modeling Study to Investigate Performance of SOFC-ICE Hybrid Systems for Marine Applications. Master's thesis, Delft University of Technology.

B

VARIABILITY IN PERFORMANCE MEASUREMENTS AND COMBUSTION MODELLING RESULTS

In this appendix, an uncertainty analysis is performed to study the variability in measurements under same testing conditions to allow for unbiased and representative analysis of engine performance data. For this purpose, the variability in SI marine engine performance measurements described in Chapter 4 is discussed. Furthermore, the variability in combustion modelling results due to deviation in in-cylinder pressure sensors is also analysed.

B.1. VARIABILITY IN PERFORMANCE MEASUREMENTS

To study the repeatability of measurements, three test cases of only natural gas (ONG) at 25 % load, 20H₂-NG blend at 50 % load and 05CO₂-NG blend at 75 % load were tested. For the ONG and 20H₂-NG test case, measurements were repeated three times at NO_x values of 200, 300, 400 and 500 mgN m⁻³ at 5 % reference oxygen. On the other hand, for the 05CO₂-NG test case, measurements were repeated only twice at NO_x values of 400, 500 and 1000 mgN m⁻³ at 5 % reference oxygen. Figure B.1 shows the spread of the repeated measurements of natural gas flowrate, manifold pressure and manifold temperature in addition to the mean value line and the +/-5 % line for the three test cases. Similarly, Figure B.2 shows the spread of the repeated measurements of exhaust oxygen, carbon monoxide and unburnt hydrocarbons relative to the mean value line and the +/-5 % line for the three test cases. In both the figures, the measurement set corresponding to green star markers corresponds to the measurements used for the performance analysis and modelling in this dissertation.

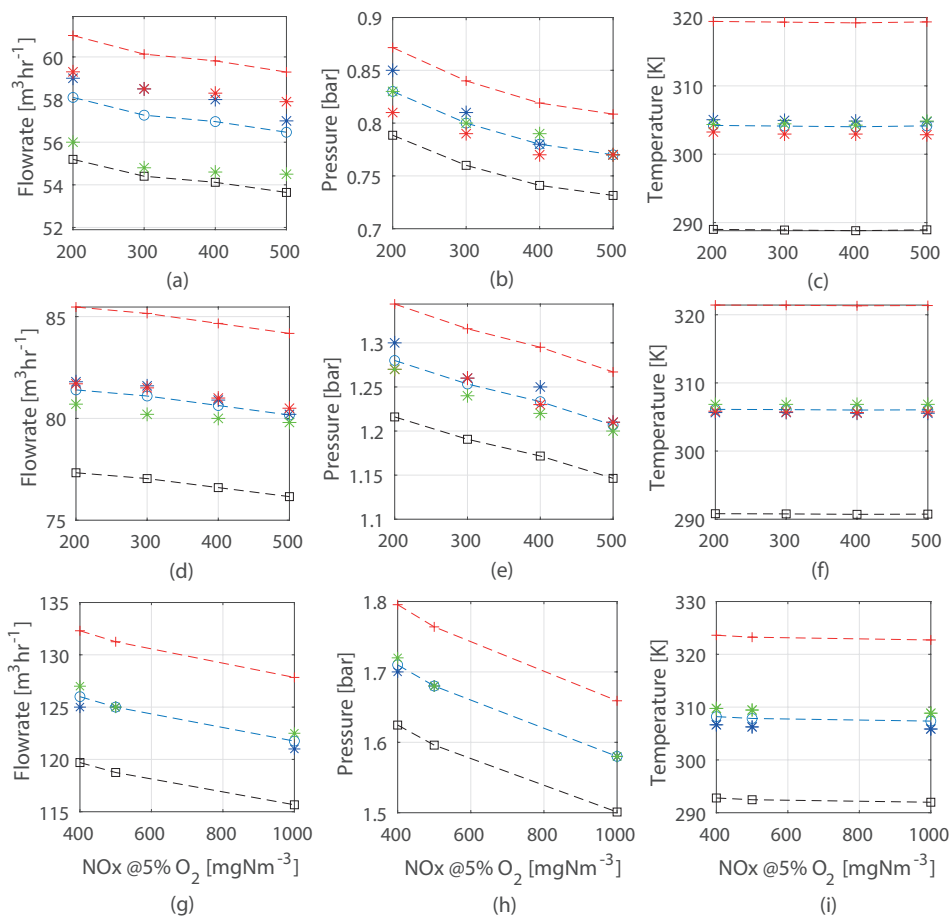


Figure B.1: Variability in repeated measurements of natural gas flowrate, manifold pressure and manifold temperature for the three test cases of ONG at 25% load (a-c), 20H₂-NG at 50% load (d-f) and 05CO₂-NG at 75% load (g-i) at different NOx emissions. Legend: (marker: o, linetype: dashed, colour: blue) represents mean value; (marker: plus, linetype: dashed, colour: red) represents +5% deviation from mean; (marker: square, linetype: dashed, colour: black) represents -5% deviation from mean; (marker: star, colour: blue) represents measurement set 1; (marker: star, colour: green) represents measurement set 2; (marker: star, colour: red) represents measurement set 3

In Figure B.1 (a), the measurement set 2 (green marker) was chosen for the engine performance analysis to avoid overestimation of improvements in engine efficiency due to hydrogen addition as this measurement set formed the benchmark ONG performance at 25% engine loading. As seen in Figure B.1, all measurements lied within the +/-5% deviation margin showing good repeatability. Similarly, the emission measurements in Figure B.2 also showed limited variability and are close to the mean values with the exception of UHC. Unburnt hydrocarbon emissions shown in Figure B.2(c), (f) and (i) exhibited relatively higher deviations, but close to the +/-5% margin.

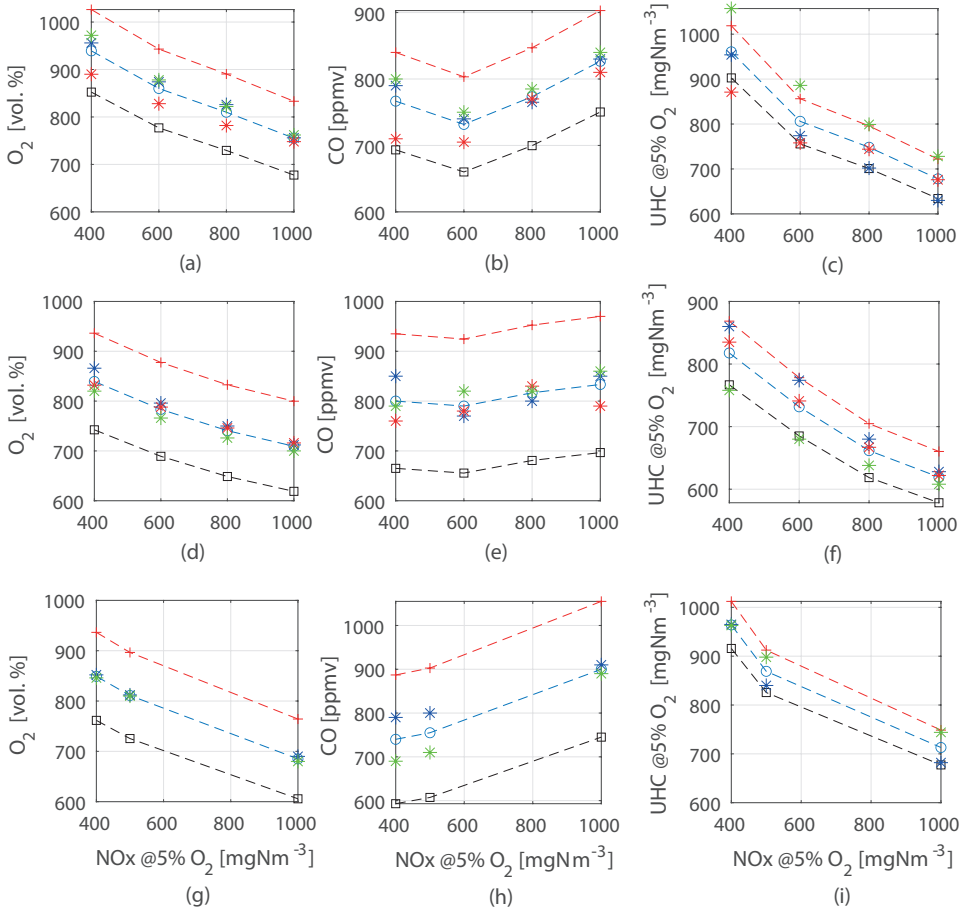


Figure B.2: Variability in repeated measurements of exhaust oxygen, carbon monoxide and unburnt hydrocarbons for the three test cases of ONG at 25% load (a-c), 20H₂-NG at 50% load (d-f) and 05CO₂-NG at 75% load (g-i) at different NO_x emissions. Legend: (marker: o, linetype: dashed, colour: blue) represents mean value; (marker: plus, linetype: dashed, colour: red) represents +5% deviation from mean; (marker: square, linetype: dashed, colour: black) represents -5% deviation from mean; (marker: star, colour: blue) represents measurement set 1; (marker: star, colour: green) represents measurement set 2; (marker: star, colour: red) represents measurement set 3

B.2. VARIABILITY IN COMBUSTION MODELLING RESULTS

The accuracy of the recorded pressure dictates the accuracy of the combustion process simulated by the models. The water-cooled piezoelectric in-cylinder pressure sensor (Kistler 7061B) has a maximum cumulative deviation of +/-3.04%. To understand the variability in combustion modelling results, the measured pressure signal for 10H₂-NG fuel blend and 500 mgNm⁻³ of NO_x at 75% load was shifted by +3.04% and -3.04%. These shifted signals were used as inputs for the combustion characterization models to understand the corresponding deviation in modelling results. The deviations in out-

puts of the combustion characterization models have been presented in Table B.1 for the pressure signal deviation of +/-3.04 %.

Table B.1: Percentage deviations in performance parameters simulated by the Seiliger and Wiebe combustion characterization models for a simulated deviation of +/-3.04 % in in-cylinder pressure measurements for 10H₂-NG fuel blend and 500 mgN m⁻³ NO_x values at 75 % engine load

	p _{max} [%]	T _{max} [%]	Work [%]	Q _{net} [%]	p ₆ [%]	T ₆ [%]
Seiliger +3.04 %	3.041	0.129	3.026	3.086	3.043	0.129
Wiebe +3.04 %	3.478	0.092	4.507	5.088	4.530	1.575
Seiliger -3.04 %	-3.041	-0.089	-3.031	-3.089	-3.044	-0.088
Wiebe -3.04 %	-3.143	-0.25	-3.112	-2.819	-2.679	0.286

As seen from Table B.1, the maximum deviation in modelling results was found to be less than or equal to about 5 % in the estimation of work and heat using the Wiebe combustion characterization model for a +3.04 % shift in in-cylinder pressure. The maximum deviations in work and heat were smaller in case of Seiliger modelling compared to the Wiebe modelling approach. Furthermore, the pressure values simulated by Seiliger and Wiebe deviated by approximately the same amount as the introduced deviation in pressure sensor measurement. Lastly, both modelling approaches produced deviations of 1.5 % or less in estimation of in-cylinder temperatures.

C

ADDITIONAL DETAILS OF HRR, SEILIGER AND WIEBE MODELLING

C.1. IMPACT OF TDC SHIFT ON NORMALIZED REACTION CO-ORDINATE

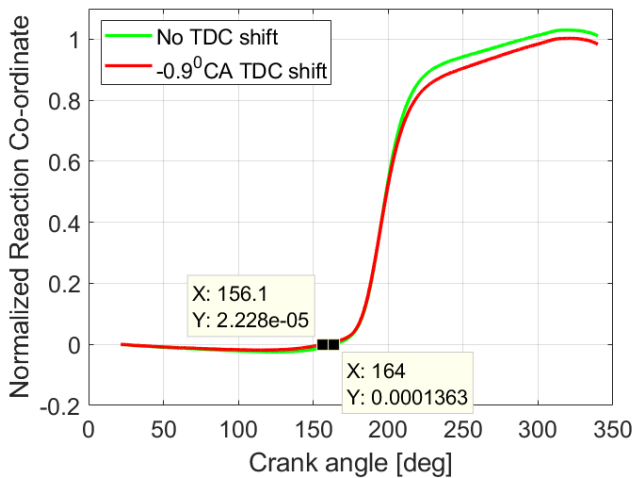


Figure C.1: Normalized reaction co-ordinate for 0H₂-NG fuel blend at 24°CA bTDC spark-timing, 375 kW_e engine loading and 500 mgN m⁻³ NO_x with no TDC shift (a) and -0.9°CA TDC shift

Table C.1: Parameters simulated by the Seiliger and Wiebe modelling approach. A: Available, NA: Not Available, AwHRR: Available with HRR model

Parameter	Seiliger	Wiebe
p_{\max}	A	A
T_{\max}	A	A
Work	A	A
Heat	A	A
p_6	A	A
T_6	A	A
CA10	NA	A
P@CA10	NA	A
CA50	NA	A
P@CA50	AwHRR	A
CA90	NA	A
P@CA90	AwHRR	A
CA(c)	NA	A
P@CA(c)	AwHRR	A
CA(dp/dt _{max})	NA	A
dp/dt _{max}	NA	A
T@CA10	NA	A
T@CA50	AwHRR	A
T@CA90	AwHRR	A
T@CA(c)	AwHRR	A

C.2. PARAMETERS SIMULATED BY THE SEILIGER AND WIEBE MODELLING APPROACH

In this research, p_{\max} , T_{\max} , work, net combustion heat, p_6 and T_6 modelling parameters are chosen for the purpose of comparison between the capabilities of two modelling approaches as these are vital parameters for simulation studies on system integration, controls and load variations. Other parameters such as pressure at CA10, CA50 and CA90 along with the maximum rate of pressure rise and their corresponding crank angles can be vital parameters for combustion characterization. However, it is vital to note that the choice of the modelling approach is dictated by the modelling objective, which is followed by three other factors, i.e., the level of detail, modelling accuracy and computational effort. The Seiliger modelling approach provides sufficient details of the in-cylinder and combustion process that can be accurately captured with variations in operating parameters such as load, leaning and fuel blends along with low computational effort. This makes the Seiliger modelling approach in combination with Mean Value Engine Models (MVEMs) ideal for studying system integration, voyage simulations, engine control, load variations and smart maintenance of ships. At the same time, it is vital to understand the inability of the Seiliger modelling approach in capturing crank angle resolved information without the HRR model as shown in Table C.1. As seen from Table C.1, p_{\max} , T_{\max} , work, net combustion heat, p_6 and T_6 are the common param-

eters that are directly available from both the modelling approaches. Therefore, these parameters can be used to compare the capabilities of the Seiliger and Wiebe modelling approach in capturing the H₂-NG in-cylinder and combustion process.

Crank angle based information such as CA10, CA50 and CA90 can be determined using the double Wiebe function. Additionally, the in-cylinder pressure values at CA10, CA50, CA90 and the maximum rate of pressure rise can be determined using the Wiebe modelling approach. On the other hand, CA10, CA50 and CA90 cannot be determined using Seiliger, since Seiliger is a 5-stage discretized in-cylinder model and not a crank angle based model. Table C.2 and C.2 together provide the error percentages between the double Wiebe function-based combustion characterization simulation and measured values of performance parameters for 20H₂-NG fuel blend and 500 mgN m⁻³ NO_x value at 75 % engine load.

Table C.2: Part 1: Error percentages between the Wiebe combustion characterization simulation and measured values of crank angle resolved parameters for 20H₂-NG fuel blend and 500 mgN m⁻³ NO_x values at 75 % engine load

	CA10	p@CA10	CA50	p@CA50	CA90	p@CA90
Measured	179.9	54.57	195.9	67.5	242	18.32
Wiebe	180.7	57.46	195.1	66.54	237.8	20.23
Error %	0.444	5.29	-0.408	-1.42	-1.74	10.45

Table C.3: Part 2: Error percentages between the Wiebe combustion characterization simulation and measured values of crank angle resolved parameters for 20H₂-NG fuel blend and 500 mgN m⁻³ NO_x values at 75 % engine load

	CA(dp/dt _{max})	dp/dt _{max}	T@CA10	T@CA50	T@CA90
Measured	184.9	1.254	879.6	1346	1235
Wiebe	175	1.272	926.8	1303	1244
Error %	5.354	1.435	5.36	-3.19	0.7234

As shown in Table C.2, the double Wiebe function can be used to compute crank angle resolved information with a maximum error of 10.45 % in the estimation of pressure at CA90. The error in estimation can be attributed to the difficulty in accurately capturing the end of combustion and also the difficulty in the accurate fitting of RCO as mentioned section 5.6.1 and section 5.5.2. Although by definition, Seiliger cannot provide values of crank angles corresponding to CA10, CA50 and CA90, error percentages can be computed for pressures and temperatures corresponding to CA10, CA50 and CA90 using Seiliger assuming the corresponding crank angle positions are known from the HRR model as shown in Table C.1. Table C.4 and C.5 together provide these error percentages.

Table C.4 shows that Seiliger produces large errors for pressure and temperature estimation at CA10 as the Seiliger process switches from stage 2 to 3 when CA10 occurs. On the other hand, Seiliger simulates pressures and temperatures at CA50 and CA90 with good accuracy as these points lie close to Seiliger stages. The Seiliger modelling approach is not capable of capturing the maximum rate of pressure rise as this value is infinity for the Seiliger modelling approach by definition. In the Seiliger process, the

Table C.4: Part 1: Error percentages between the Seiliger combustion characterization simulation and measured values of crank angle resolved parameters for 20H₂-NG fuel blend and 500 mgN m⁻³ NO_x values at 75 % engine load

	CA(c)	P@CA10	P@CA50	P@CA90	P@CA(c)
Measured	217.4	54.57	67.5	18.32	39.3
Seiliger	NA	67.84	67.84	18.12	40.24
Error %	NA	24.31	0.5	-1.09	0.865

Table C.5: Part 2: Error percentages between the Seiliger combustion characterization simulation and measured values of crank angle resolved parameters for 20H₂-NG fuel blend and 500 mgN m⁻³ NO_x values at 75 % engine load

	dp/dt _{max}	T@CA10	T@CA50	T@CA90	T@CA(c)
Measured	1.254	879.6	1346	1235	1430
Seiliger	NA	740.1	1359	1221	1467
Error %	NA	-15.85	0.96	-1.13	2.58

end of combustion corresponds to the end of the isothermal combustion stage, which is depicted by the Seiliger parameter 'c'. Table C.4 and Table C.5 provide the error in estimation of pressure and temperature by Seiliger compared to the measured values at point 'c'.

To summarize the above discussion, although the Wiebe modelling approach provides additional crank angle resolved information of the combustion process, the Seiliger modelling approach is capable of providing sufficient details of the H₂-NG in-cylinder and combustion process while accurately capturing the variations in the H₂-NG in-cylinder and combustion process for varying operating parameters with low computational effort. The variations in the combustion process are not well captured by the Wiebe modelling approach as explained in section 5.6.1 and section 5.6.2 of the chapter. Thus, both the Seiliger and Wiebe modelling approaches have their own advantages and limitations, which can dictate the choice of the modelling approach.

C.3. DERIVATION OF TRAPPED AIR-FRACTION

The derivation of trapped air mass fraction as a function of the residual gas mass fraction, air-excess ratio (λ) and the stoichiometric air-to-fuel ratio is as follows [1]:

The trapped air fraction ($x_{\text{air},t}$) can be written as a function of the trapped residual gas fraction ($x_{\text{rg},t}$) and trapped fuel fraction ($x_{\text{f},t}$),

$$x_{\text{air},t} = (1 - x_{\text{rg},t}) - x_{\text{f},t} \quad (\text{C.1})$$

where, $x_{\text{air},t} = \frac{m_{\text{air},t}}{m_t}$, $x_{\text{rg},t} = \frac{m_{\text{rg},t}}{m_t}$, $x_{\text{f},t} = \frac{m_{\text{f},t}}{m_t}$ and m_t is trapped mass in kg.

Equation C.1 can be written in the following manner,

$$\frac{m_{\text{air},t}}{m_t} = \left(1 - \frac{m_{\text{rg},t}}{m_t}\right) - \frac{m_{\text{f},t}}{m_t} \quad (\text{C.2})$$

Multiplying both sides of equation C.2 by the ratio of trapped air mass and trapped fuel

mass,

$$\frac{m_{air,t}}{m_t} \cdot \frac{m_{air,t}}{m_{f,t}} = \left(1 - \frac{m_{rg,t}}{m_t}\right) \cdot \frac{m_{air,t}}{m_{f,t}} - \frac{m_{f,t}}{m_t} \cdot \frac{m_{air,t}}{m_{f,t}} \quad (C.3)$$

Equation C.3 can be simplified by writing the term as a function of stoichiometric air-to-fuel ratio and air-excess ratio:

$$\frac{m_{air,t}}{m_{f,t}} = \frac{m_{air,min}}{m_{f,t}} \cdot \frac{m_{air,t}}{m_{air,min}} = \sigma \cdot \lambda \quad (C.4)$$

Substituting equation C.4 into equation C.3, and using the mass fraction definitions:

$$x_{air,t} \cdot \sigma \cdot \lambda = (1 - x_{rg,t}) \cdot \sigma \cdot \lambda - x_{air,t} \quad (C.5)$$

Rearranging equation C.5 gives,

$$x_{air,t} = \frac{(1 - x_{rg,t}) \cdot \sigma \cdot \lambda}{\sigma \cdot \lambda + 1} \quad (C.6)$$

C.4. DERIVATION OF TRAPPED MIXTURE TEMPERATURE FOR SI NG ENGINE WITH ZERO VALVE OVERLAP

In a conventional 4-stroke engine with a positive valve overlap, the trapped mass (m_t) is represented by equation C.7.

$$m_t = m_{ind} + m_{rg,t} + m_{ret} \quad (C.7)$$

where, ' m_{ind} ' is the air-fuel mass drawn into the cylinder during the induction stroke, ' $m_{rg,t}$ ' is the residual mass of combustion gas trapped from the previous cycle and m_{ret} is the part of scavenging mass retained after either the inlet or outlet valve closing.

In a natural gas engine with zero valve overlap, there is no scavenging and, therefore, retained mass in equation C.7 is zero. Thus, the total trapped mass becomes

$$m_t = m_{ind} + m_{rg,t} \quad (C.8)$$

Each mass term in equation C.8 is solved individually to calculate the trapped mixture temperature since the trapped temperature has a combined effect of the increased induction temperature and temperature due to mixing with the hot residual combustion gases trapped from the previous cycle. Starting with the total trapped and applying the ideal gas equation, we get:

$$m_t = \frac{p_t \cdot V_t}{R \cdot T_t} = \frac{p_t \cdot V_{IC}}{R \cdot T_t} \quad (C.9)$$

where, ' V_t ' is the trapped volume in m^3 and is equal to the cylinder volume at the moment of inlet valve closing (V_{IC}). The trapped volume is estimated from crank angle measurements [2]. Similarly, the induction mass is written as,

$$m_{ind} = \frac{p_t \cdot V_{ind}}{R \cdot T_{ind}} = \frac{p_t \cdot (V_{IC} - V_{IO})}{R \cdot T_{ind}} \quad (C.10)$$

where, ' p_t ' is the trapped pressure in Pa and is obtained from measurements, R is the gas constant in $\text{J kg}^{-1} \text{K}$, ' V_{ind} ' is the induction volume between inlet valve opening and closing measured in m^3 . In this engine with zero valve overlap, the inlet valve opens after the exhaust valve closes, thus, starting the induction stroke. This induction stroke ends with the closing of the inlet valve as shown in Table 4.1.

The cylinder volumes at the time of inlet valve closing and opening can be determined from geometrical formulations using the crank angle measurements. In equation C.10, the induction temperature (T_{ind}) is estimated in the following manner. During the induction stroke, as the mass enters the cylinder, its temperature will be higher than the temperature at inlet manifold due to heat-pick-up from the inlet duct walls [3]. Therefore, the induction temperature is determined from the measured manifold temperature by using equation C.11 [3],

$$T_{\text{ind}} = \epsilon_{\text{inl}} \cdot T_{\text{inl}} + (1 - \epsilon_{\text{inl}}) \cdot \text{MAT} \quad (\text{C.11})$$

where, ' ϵ_{inl} ' is the heat exchange effectiveness = 0.05 and ' T_{inl} ' is the inlet manifold duct wall temperature = 400 K [3].

After determining the trapped and induction mass, the residual mass in equation C.10 is derived. In the test engine with zero valve overlap, the exhaust blowdown process (exhaust stroke) begins with the opening of the exhaust valve and then ends with the closing of the exhaust valve. During the blowdown process, the mass in the cylinder expands to pressure and temperature equivalent to the pressure and temperature in the exhaust receiver manifold [3]. Thus, after the exhaust stroke or blowdown process, the pressure and the temperature of the mass still remaining inside the cylinder is equal to the blowdown pressure (p_{bld}) and blowdown temperature (T_{bld}). In the experiments performed for this study, the pressure in the exhaust receiver was measured, which is equivalent to the blowdown pressure. Assuming a polytropic blowdown process, the blowdown temperature can be computed from the measured blowdown pressure and the pressure at the moment of exhaust valve opening (p_{EO}).

$$T_{\text{bld}} = T_{\text{EO}} \cdot \left(\frac{p_{\text{bld}}}{p_{\text{EO}}} \right)^{\left(\frac{n_e - 1}{n_e} \right)} \quad (\text{C.12})$$

where, ' p_{EO} ' is the pressure at the moment of exhaust valve opening obtained from in-cylinder pressure measurements in Pa, ' n_e ' is the polytropic exponent, ' T_{EO} ' is the in-cylinder temperature in K at the moment of exhaust valve opening. It is calculated by applying the ideal gas equation at the moment of exhaust valve opening. At this point, the mass in the cylinder (m_{EO}) is equal to the trapped mass, since the in-cylinder mass is assumed to be constant without any crevice mass losses.

$$T_{\text{EO}} = \frac{p_{\text{EO}} \cdot V_{\text{EO}}}{R \cdot m_{\text{EO}}} \quad (\text{C.13})$$

After calculating the blowdown temperature, the trapped residual mass of combustion gas left after the blowdown process or at the point of exhaust valve closing is given by,

$$m_{\text{rg,t}} = \frac{p_{\text{bld}} \cdot V_{\text{EC}}}{R \cdot T_{\text{bld}}} \quad (\text{C.14})$$

where, ' V_{EC} ' is the cylinder volume in m^3 at the time of exhaust valve closing and is determined from geometrical formulations using the crank angle measurements.

To calculate the trapped temperature, equations C.9, C.10 and C.14 are substituted in equation C.8.

$$\frac{p_t \cdot V_{IC}}{R \cdot T_t} = \frac{p_t \cdot (V_{IC} - V_{IO})}{R \cdot T_{ind}} + \frac{p_{bld} \cdot V_{EC}}{R \cdot T_{bld}} \quad (C.15)$$

Although the gas constant is a function of the mixture composition, it changes minutely for trapped, induction and residual mass, therefore, it can be assumed constant. By simply rearranging the equation C.15, trapped mixture temperature is determined as a combination of the heat pick-up during induction and the high blowdown temperature of the residual combustion gas.

$$\frac{1}{T_t} = \frac{(V_{IC} - V_{IO})}{V_{IC} \cdot T_{ind}} + \frac{p_{bld} \cdot V_{EC}}{p_t \cdot V_{IC} \cdot T_{bld}} \quad (C.16)$$

C.5. VARIATIONS IN WIEBE SHAPE PARAMETERS

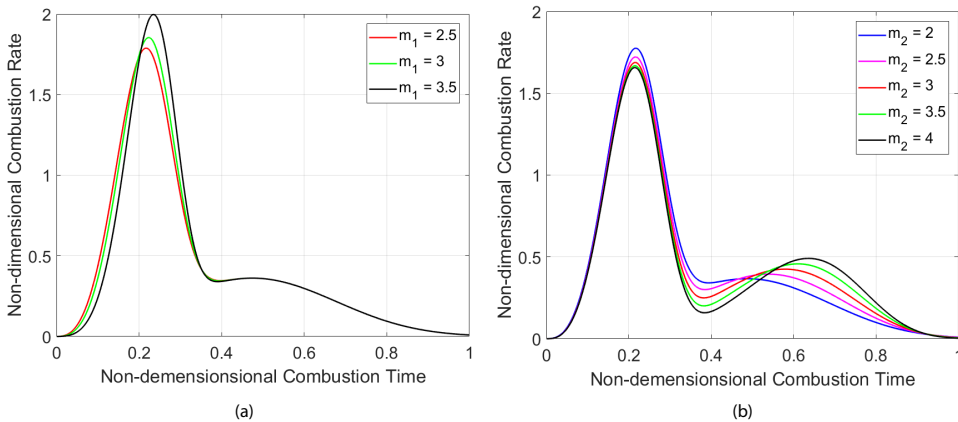


Figure C.2: Non-dimensional combustion rate for increasing value of m_2 (a) and m_2 (b) while other Wiebe combustion parameters are fixed at value found for $10H_2$ -NG fuel blend, 500 mgN m^{-3} NOx at 75 % engine load

Figure C.2(a) and Figure C.2(b) show the non-dimensional combustion or heat release rate for different values of m_1 and m_2 while the remaining Wiebe parameters are kept constant at values found for $10H_2$ -NG fuel blend and 500 mgN m^{-3} of NOx at 75 % engine load. This can help understand the expected variations in heat release as m_2 and m_2 change. In this analysis, each case of varying load, hydrogen percentage and engine leaning has been discussed separately.

LOAD

In [4], Ding used the double Wiebe function for diesel combustion with values of m_1 varying from 0.05 to 0.5. For this range of m_1 , the non-dimensional combustion rate increased with decreasing m_1 . For the H_2 -NG combustion studied in this research, the

value of m_1 varied from 2.5 to 3.5. As seen from Figure C.2(a), the non-dimensional combustion rate during the primary phase of combustion increases as m_1 varies from 2.5 to 3.5. However, variations in m_2 impact the heat release during the primary phase of combustion. An increase in value of m_2 means more heat is released in the late combustion phase and less is released during the primary combustion phase and vice versa. This impact of m_2 on the primary phase of combustion is evident in Figure C.2(b) and helps understand the heat release during load variations.

Based on the HRR model analysis, the decrease in engine load reduced the heat released during late combustion. The decrease in late combustion reduced the value of m_2 for lower loads, which increased the non-dimensional heat released during the primary phase of combustion as seen from Figure C.2(b). The increased normalized heat release in the primary phase of combustion was accompanied by an increased m_1 for lower loads. Therefore, m_1 decreased with increasing load as stated in section 5.6.2. However, this does not mean that the absolute heat release during the primary phase of combustion is higher for lower loads. The absolute value is a multiple of the non-dimensional heat release and the fuel mass, divided by combustion time [4]. Since the fuel mass is low at lower loads compared to the mass at higher loads, the absolute heat release is higher for higher loads even though the non-dimensional heat release is lower due to a lower value of m_1 and m_2 .

CASE 2: HYDROGEN PERCENTAGE

In this case, m_2 decreases with increasing hydrogen percentage as hydrogen reduces late combustion. A lower value of m_2 contributes to the heat release in the primary combustion phase as shown in Figure C.2(b). More non-dimensional heat is released in the primary combustion phase with hydrogen addition and an increased value of m_1 as seen in Figure C.2(a). However, this increment in m_1 was not found at all loads for increasing hydrogen percentages as shown in Figure 5.15(b) and explained in section 5.6.2.

CASE 3: ENGINE LEANING

During engine leaning to lower values of NO_x, more heat is released during the late combustion phase, which is depicted by increasing m_2 as seen in Figure 5.12(b). Higher the value of m_2 , higher the non-dimensional heat release in the last combustion phase and lower the heat released in the primary combustion phase, which is evident from Figure C.2(b). Thus, the increasing value of m_2 indicates deterioration of the combustion process. Additionally, engine leaning was accompanied by a decreased value of m_1 as seen in Table 5.7.

C.6. EFFECTS OF SPARK-TIMING ON THE IN-CYLINDER AND COMBUSTION PROCESS

To further discuss the capabilities of the Seiliger and Wiebe-based modelling approaches, the two models are employed to simulate the effects of changing the spark-timing from 18°CA to 21°CA to 24°CA bTDC for 10H₂-NG fuel blend and 500 mg N m⁻³ of NO_x at 75 % engine load. The methodology followed to study the effects of spark-timing variations is the same as that presented in chapter 5. The in-cylinder pressure and crank angle measurements for these 3 spark-timings were used to simulate the heat release process by

using the HRR model. In the next step, various outputs of the HRR model were used in the Wiebe and Seiliger-based combustion characterization models to capture the H₂-NG in-cylinder and combustion process for the varying spark-timings. Figure C.3 and Figure C.4 show the in-cylinder pressures and temperatures simulated by the Seiliger and Wiebe-based combustion characterization models for varying spark-timings.

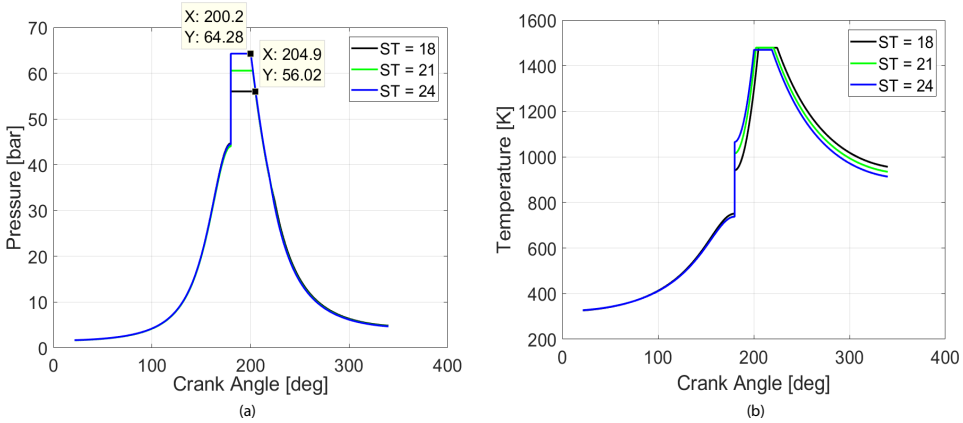


Figure C.3: In-cylinder pressure (a) and temperature (b) variations using the Seiliger characterization process for different spark-timings and 10H₂-NG fuel blend, 500 mg N m⁻³ NO_x at 75 % engine load

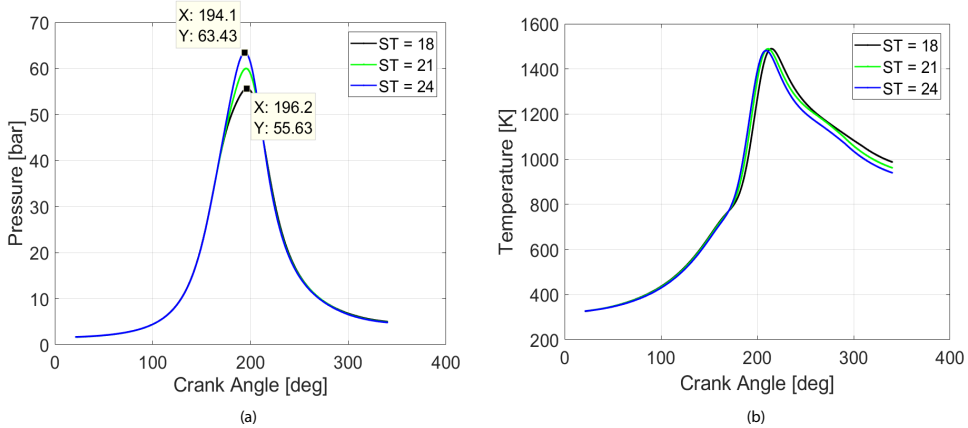


Figure C.4: In-cylinder pressure (a) and temperature (b) variations using the Wiebe characterization process for different spark-timings and 10H₂-NG fuel blend, 500 mg N m⁻³ NO_x at 75 % engine load

As seen from Figure C.3(a) and Figure C.4(a), both the Seiliger and Wiebe-based characterization models show that advancing spark-timing (ST) from 18°CA bTDC to 24°CA bTDC increases the peak pressures while shifting the point of maximum pressure towards TDC. By definition of Seiliger process, the Seiliger parameter ‘a’ increases with advanced ignition timing while the Seiliger parameter ‘b’ decreases, thus, moving the

point of maximum pressure to 20.2°CA for 24° ST and 24.9°CA aTDC for 18° ST. Similarly, the Wiebe modelling approach shows that the point of peak pressure lies at 14.1°CA bTDC for 24° ST while for 18° ST it shifts to 16.2°CA bTDC. The Wiebe characterization model also showed that CA50 shifted from 21.4°CA aTDC for 18° ST to 16.5°CA aTDC for 24° ST. The advancement of ignition timing also shifts the point of peak temperatures closer to TDC, while keeping all the maximum values close since the air-excess ratio was controlled to produce the same NO_x emission at each ignition timing. This impact on in-cylinder temperatures is simulated by both the modelling approaches. Furthermore, both the Seiliger and Wiebe models captured the decrease in temperatures at the point of exhaust valve opening with advanced ignition timing, which was also found during measurements. These results of varying the ignition timing match well with existing literature [5, 6].

In this manner, the effects of spark-timing on the in-cylinder and combustion process can be captured and studied by using the Seiliger and Wiebe modelling approach. In addition to load and hydrogen percentage, parametric equations can be also derived to compute Seiliger and Wiebe combustion parameters as a function of spark-timing to capture combustion process and engine performance under varying test conditions.

REFERENCES

- [1] S.M. Krol. Modelling and Performance Investigation of Anode-Off Gas Combustion in an IC Engine for Power Generation, 2018.
- [2] D. Stapersma. *Diesel Engines: A Fundamental Approach to Performance Analysis, Turbocharging, Combustion, Emissions and Heat Transfer Including Thermodynamical Principles. Vol. 3: Combustion*. Delft University of Technology, 2010.
- [3] D. Stapersma. *Diesel Engines: A Fundamental Approach to Performance Analysis, Turbocharging, Combustion, Emissions and Heat Transfer Including Thermodynamical Principles. Vol. 2: Turbocharging*. Delft University of Technology, 2010.
- [4] Y. Ding. *Characterising Combustion in Diesel Engines*. PhD thesis, Delft University of Technology, 2011.
- [5] J.A. Caton. Combustion Phasing for Maximum Efficiency for Conventional and High Efficiency Engines. *Energy Conversion and Management*, 2014.
- [6] S.N. Wildhaber. Impact of Combustion Phasing on Energy and Availability Distributions of an Internal Combustion Engine, 2011.

D

IN-CYLINDER PROCESS FOR COMPOSITION 2 AND 3

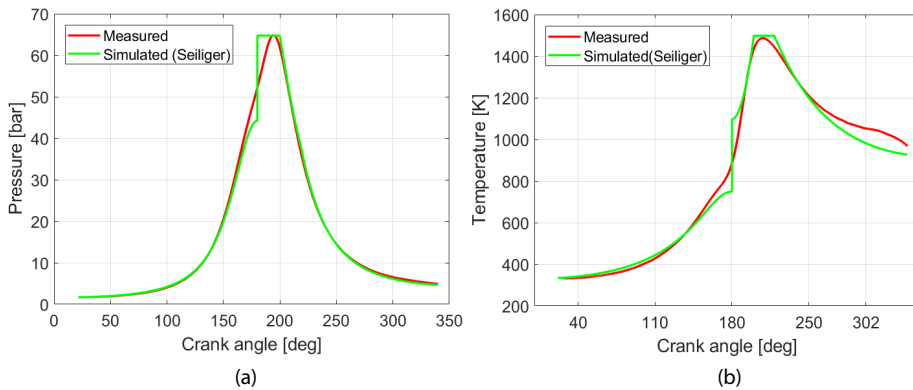


Figure D.1: Comparison between measured and simulated in-cylinder pressure (a) and temperature (b) using the Seiliger process modelling approach for 12.65 %H₂-12.65 %CO₂-74.7 %NG fuel blend at 75 % engine load

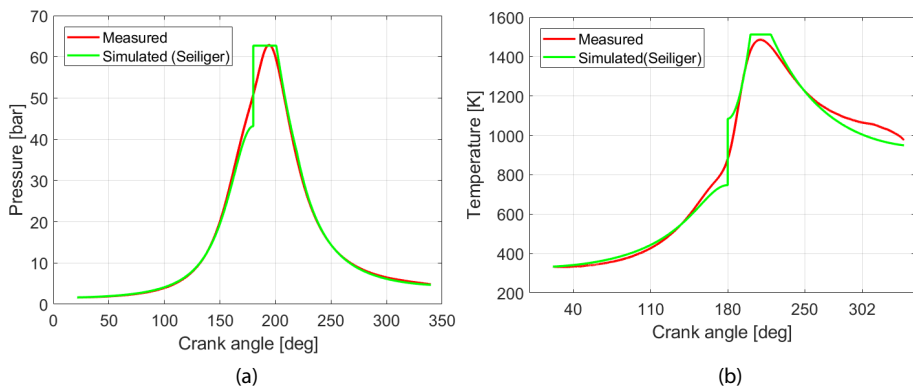


Figure D.2: Comparison between measured and simulated in-cylinder pressure (a) and temperature (b) using the Seiliger process modelling approach for 9.2 %H₂-17.5 %CO₂-73.3 %NG fuel blend at 75 % engine load

E

EXAMPLE EFFICIENCY CALCULATION FOR SOFC-ICE INTEGRATION

In this appendix, an example calculation for the efficiency of the integration SOFC-ICE system has been presented. The efficiency has been calculated for a 50-50 SOFC-ICE power split with a total power output of 750 kWe. The SOFC operates at a current density of 4750 Am^{-2} , fuel utilization of 80 % and pre-reforming of 0.3. The total numbers of cells is fixed at 11000. The integrated ICE operates on a 30-70 AOG-NG fuel comprising of 12.81 % hydrogen and 17.19 % carbon dioxide, by volume. This operating condition corresponds to the condition depicted with a vertical dashed line in Figure 7.3. The following step are followed to calculate the system efficiency:

Step 1: The efficiency of the SOFC is calculated by using equation E.1

$$\eta_{\text{SOFC}} = \frac{P_{\text{SOFC,AC}}}{\dot{N}_{\text{CH}_4}^{\text{in}} \cdot \text{LHV}_{\text{CH}_4}} \quad (\text{E.1})$$

where, ' $P_{\text{SOFC,AC}}$ ' is the AC stack power simulated by the model for the given operating conditions, which is equal to 373.8259 kWe. ' $\dot{N}_{\text{CH}_4}^{\text{in}}$ ' is the total molar flow rate of methane corresponding to the total number of cells, which is equal to 0.8448 mols^{-1} . ' LHV_{CH_4} ' is the lower heating value of CH_4 , which is equal to $802.6 \times 10^3 \text{ kJ mol}^{-1}$. Using these values the efficiency of the SOFC is calculated to be 55.14 %.

Step 2: The efficiency of the integrated ICE is calculated by the AOG-NG model using equation E.2.

$$\eta_{\text{I-ICE}} = \frac{P_{\text{ICE}}}{\dot{m}_{\text{fuel}} \cdot \text{LHV}_{\text{fuel}} - \dot{m}_{\text{H}_2} \cdot \text{LHV}_{\text{H}_2}} \quad (\text{E.2})$$

where, ' P_{ICE} ' is the brake power output of the ICE, which was 376.17 kWe. ' \dot{m}_{fuel} ' is the total AOG-NG fuel flow rate entering the ICE, which is equal to $152.026 \text{ kg h}^{-1}$ or 0.0422 kgs^{-1} for the given operating conditions. ' \dot{m}_{H_2} ' is the flow rate of hydrogen from

the SOFC used in the 30-70 AOG-NG blend consumed in the ICE, which is equal to 1.6253 kg h^{-1} or $4.5896 \times 10^{-4} \text{ kg s}^{-1}$. 'LHV_{fuel}' and 'LHV_{H₂}' are equal to 26.01 MJ kg^{-1} and $127.53 \text{ MJ kg}^{-1}$, which are the lower heating values of the 30-70 AOG-NG blend and hydrogen, respectively, calculated by the AOG-NG MVEM. Using these values and equation E.2, the efficiency of the integrated engine was calculated to be 36.24%. This efficiency value corresponds to the efficiency of the integrated ICE, which excludes the incoming energy contribution of hydrogen since it is obtained from the SOFC and, thus, accounted for in the SOFC efficiency calculation. If the incoming energy of hydrogen is taken into account in the efficiency calculation, then the efficiency of the standalone ICE operating on the same 30-70 AOG-NG blend is 34.27%. Therefore, the efficiency of the integrated AOG-NG ICE is higher than that of the standalone ICE operating on the same 30-70 AOG-NG blend by about 2%. At the same time, the efficiency of the integrated AOG-NG ICE is higher than that of the standalone ICE operating on only NG at 375 kWe by about 2.56%. Thus, hydrogen addition from AOG caused a 0.6% efficiency improvement solely due to better combustion.

Step 3: Based on the estimated efficiencies of the SOFC and integrated AOG-NG ICE, the efficiency of the SOFC-ICE system is calculated by applying equations E.3.

$$\eta_{\text{SOFC-ICE}} = \frac{P_{\text{SOFC-ICE}}}{EC_{\text{SOFC}} + EC_{\text{I-ICE}}} \quad (\text{E.3})$$

where, 'P_{SOFC-ICE}' is the total power output of the system, which is equal to 750 kWe. 'EC_{SOFC}' represents the incoming energy contribution of the SOFC while 'EC_{I-ICE}' represents the incoming energy contribution of the integrated engine. These two values are calculated by dividing the individual power outputs of each component by its corresponding efficiency computed using equations E.1 and E.2. In this manner, EC_{SOFC} was computed to be 678.036 kW while EC_{I-ICE} was computed to be 1039.8705 kW. Based on these values the efficiency of the integrated SOFC-ICE system for the given operating conditions is estimated to be 43.657%, which can be seen in Figure 7.3.

SAMENVATTING

Zelfs tijdens de COVID-19 pandemie is de scheepvaartsector doorggegaan met het wereldwijd vervoeren van vitale vracht, zoals voedselvoorraden, medicijnen en medische apparatuur. Schepen zijn onmisbaar voor de wereldhandel, de economie en de wereldwijde gezondheidszorg. De toename van de vraag naar wereldhandel zorgt er bovendien voor dat, in combinatie met de opkomst van containerisatie en intelligente procesautomatisering, de internationale scheepvaart voortdurend groeit. Gedreven door economie en technologie, zullen toekomstige schepen naar verwachting groter en intelligenter zijn, terwijl er tegelijkertijd ook dringend behoefte is aan “groenere” schepen met minder impact op het milieu, aangezien huidige, moderne schepen nog altijd doorgaans goedkope en vervuilende brandstoffen gebruiken in relatief conventionele dieselmotoren.

Schepen zijn momenteel voor een almaar stijgend aandeel verantwoordelijk voor de totale uitstoot van broeikasgassen en andere schadelijke emissies zoals stikstofoxiden (NO_x), zwaveloxiden (SO_x) en fijnstof (PM), met als gevolg ernstige gezondheidsrisico's en zelfs vroegtijdige sterfgevallen als gevolg van luchtverontreiniging. Daarom zijn aanzienlijke verbeteringen in energie-efficiëntie en vermindering van de emissies van schepen naar lucht essentieel. Om deze verbeteringen te bewerkstelligen, heeft de International Maritime Organisation (IMO) strikte voorschriften opgesteld voor de uitstoot van luchtverontreinigende stoffen door schepen, met als doel de totale jaarlijkse uitstoot van broeikasgassen door schepen voor 2050 met tenminste 50 % te verminderen ten opzichte van de uitstoot van broeikasgassen door schepen in 2008. Aan deze emissievoorschriften is moeilijk te voldoen met de huidige scheepsdieselmotoren die werken op conventionele scheepsbrandstoffen zoals HFO (Heavy Fuel Oil), MDO (Marine Diesel Oil) en MGO (Marine Gas Oil). Daarom doet de maritieme technisch-wetenschappelijke gemeenschap, samen met de maritieme industrie, onderzoek naar alternatieve brandstoffen en aandrijfsystemen die de energie-efficiëntie helpen verbeteren en de uitstoot verminderen.

In dit proefschrift worden mogelijke alternatieve scheepsbrandstoffen beoordeeld op hun productiecapaciteit, brandstofkosten, opslag, veiligheid (toxiciteit), technische haalbaarheid op korte termijn en milieu-impact. Op basis van de analyse wordt aardgas (NG), in ieder geval op korte termijn, aangewezen als een zeer goede keuze voor een maritieme brandstof. Dit geldt zeker als de uitstoot van methaan of andere onverbrande koolwaterstoffen (UHC) kan worden beperkt. Daarom onderzoekt dit proefschrift de mogelijkheden van systeemintegratie voor verbeterde energieopwekking aan boord van NG-aangedreven schepen als onderdeel van het GasDrive-project. GasDrive is een nieuw concept voor energievoorziening aan boord van schepen dat een seriële integratie voorstelt van een Solid-Oxide brandstofcel (SOFC) en een interne verbrandingsmotor (ICE) met onderwateruitlaatsysteem (UWE) om een hoog systeemrendement te bereiken met zeer lage emissies. Het afvoeren van uitlaatgassen onder water helpt om nul directe emissies naar de atmosfeer mogelijk te maken (emissies zijn indirect nog steeds aanwezig), terwijl

tegelijkertijd de mogelijkheid ontstaat van weerstandsvermindering via uitlaatgassmering van de scheepsrump. Dit onderzoek onderzoekt de haalbaarheid en het potentieel van dit nieuwe, geïntegreerde SOFC-ICE power plant concept voor maritieme toepassingen. Naast de SOFC-ICE integratie, is een ander doel van dit onderzoek om inzicht te verschaffen in de effecten van hoge statische en dynamische tegendruk op de prestaties van scheepsmotoren als gevolg van onderwateruitlaatsystemen. GasDrive, en het onderzoek dat in dit proefschrift wordt gepresenteerd naar “energy converters” op aardgas, heeft tot doel de weg vrij te maken voor de volgende generatie van uiterst efficiënte energiecentrales aan boord van schepen die werken op alternatieve scheepsbrandstoffen.

In dit onderzoek laat het overzicht van bestaande literatuur over gecombineerde SOFC-cycli zien dat SOFC-ICE integratie momenteel voornamelijk gericht is op de toepassing van geavanceerde verbrandingstechnologieën in motoren die werken als bodemcycli, hetgeen leidt tot een typische SOFC-ICE vermogensverdeling van respectievelijk ongeveer 85-15%. Hoewel dit een veelbelovende benadering kan zijn voor systemen aan land om een maximaal rendement te bereiken, kan deze integratieaanpak moeilijk te overwinnen uitdagingen voor schepen opleveren, zoals beperkte capaciteit voor dynamische belasting en onevenredig grote ruimte- en gewichtsvereisten van maritieme energiecentrales. Daarnaast is het potentieel van SOFC-ICE integratie voor energieopwekking aan boord van schepen en andere maritieme installaties überhaupt nog niet goed onderzocht. Bijgevolg stelt het huidige werk een nieuwe benadering voor van SOFC-ICE integratie voor maritieme toepassingen, die nog altijd een relatief hoog-efficiënte energieopwekking mogelijk maakt: het SOFC anode-off gas (AOG) wordt gemengd met aardgas (NG) en verbrand in een conventionele, commercieel beschikbare vonkontstekking (SI) motor voor gecombineerde energieopwekking. Het doel van dit onderzoek is om de impact van SOFC-ICE integratie en onderwateruitlaat op de motorprestaties te onderzoeken en de werking van het geïntegreerde SOFC-ICE systeem voor maritieme toepassingen te kwantificeren om haalbaarheid, verbeteringen in energie-efficiëntie en emissiereducties aan te tonen in vergelijking met conventionele NG-scheepsmotoren.

Om de SOFC-prestaties te simuleren en de overeenkomstige anode-off-gasstroomsnelheden en –samenstellingen te bepalen, is een nul-dimensionale (0-D) cell-to-stack modelleringsbenadering ontwikkeld. Het ontwikkelde model is geverifieerd met resultaten uit de literatuur. Met de bekende anode-off-gassamenstelling zijn de effecten van anode-off-gasverbranding experimenteel bestudeerd op een turbocharged, maritieme vonkontstoken NG-motor. Dit experimentele onderzoek wordt gebruikt om een methodologie verder te ontwikkelen om verbrandingsmodellen in de cilinder te bouwen die de effecten van anode-off gasverbranding kunnen vastleggen. Het verbrandingsmodel in de cilinder dat in staat is om anode-off-gaseffecten te simuleren, is gecombineerd met een Mean Value Engine (motor) Model (MVEM) om het geïntegreerde SOFC-ICE systeem te analyseren. De experimenten, het ontwikkelde MVEM en het 0-D SOFC-model worden gebruikt om de effecten van geïntegreerde systeemvariabelen, zoals SOFC-stroomdichtheid, SOFC-brandstofverbruik, brandstofsamenstelling voor de motor, verschillende SOFC-ICE vermogensverdelingen, etc., op SOFC-ICE integratie in kaart te brengen met betrekking tot haalbaarheid, energie-efficiëntie en emissies. Net als bij de SOFC-ICE-integratie, worden de effecten van statische en dynamische tegendruk (ook een geïntegreerde systeemvariabele), als gevolg van onderwateruitlaatsystemen, op de prestaties van scheepsmo-

toren onderzocht door motorexperimenten te combineren met een uitgebreid motor-model.

De belangrijkste bevindingen van het proefschrift zijn dat een efficiëntieverbetering van ongeveer 8 % kan worden behaald bij een 67-33 % vermogensverdeling tussen de SOFC en de ICE respectievelijk, terwijl een totaal vermogen wordt geproduceerd van 750 kWe. Tegelijkertijd kunnen de UHC- (methaan) en NO_x-emissies met ongeveer 43 % en 60 % respectievelijk worden vermindert in vergelijking met een conventionele aardgas-motor voor schepen. Bovendien kan de uitstoot van kooldioxide (CO₂) worden vermindert met 20.74 %. Echter, de 67-33 power split levert ook een ruimte- en gewichtstoename van ongeveer twee-en-een-half keer op. Voor meer realistische (kleiner, lichter) en beter dynamisch belastbare maritieme toepassingen van het SOFC-ICE systeem, kunnen veelbelovende verbeteringen in efficiëntie van 5.2 %, UHC- en NO_x-reducties van ongeveer 30 % en CO₂ reducties van ongeveer 12 % worden bereikt, met een 33-67 % SOFC-ICE vermogensverdeling. Deze systemen resulteren in relatief veel kleinere toenames in grootte en gewicht van 1,7 keer in vergelijking met een conventionele aardgas-motor voor schepen. Dit onderzoek toont aan dat aanzienlijke verbeteringen in efficiëntie en emissiereducties kunnen worden bereikt door de SOFC te integreren met commercieel bestaande motortechnologie. Geïntegreerde SOFC-ICE systemen hebben verder nog onontgonnen potentieel voor ongekende efficiëntieverbeteringen bij deellastbedrijf voor maritieme energieopwekking. Verder concludeert de studie dat in het voorgestelde SOFC-ICE systeem voor maritieme toepassingen een vermogensverdeling ten gunste van de ICE de dynamische belastbaarheid van het gecombineerde systeem aanzienlijk doen verbeteren waardoor de mogelijke, en regelmatig voorkomende, plotselinge en grote belastingwisselingen kunnen worden opgebracht door de ICE.

Naast SOFC-ICE integratie, richtte dit doctoraal onderzoek zich ook op de effecten van statische en dynamische tegendruk als gevolg van onderwateruitlaatsystemen op de prestaties van scheepsmotoren. Met behulp van de experimenteel gevalideerde en meer gedetailleerde MVEM worden de rookgrens van de motor en de thermische overbelasting onderzocht om de grenzen van aanvaardbare tegendrukken voor een motor te bepalen. Bovendien laten de MVEM-simulatie-resultaten zien dat een combinatie van een puls-turbocompressorsysteem en een kleine klepoverlap de capaciteiten van motoren voor het omgaan met tegendruk aanzienlijk kan verbeteren. Interessant is dat uit dit onderzoek blijkt dat de effecten van dynamische tegendrukfluctuaties niet zo ernstig zijn als die die gevonden zijn tijdens statische tegendrukmetingen. Daarom kan een scheepsmotor mogelijk veel hogere niveaus van dynamische tegendruk aan bij het werken met onderwateruitlaatsystemen in hoge golven. Als de onderwater-uitlaatgassensmering inderdaad de scheepsweerstand verlaagt, zoals bedoeld vanuit het GasDrive-project, kan het benodigde vermogen dat aan boord van een schip moet worden geïnstalleerd worden verlaagd, hetgeen zal helpen om het brandstofverbruik en de ruimte- en gewichtseisen van het geïntegreerde SOFC-ICE systeem nog verder te verminderen.

ACKNOWLEDGEMENTS

For a long time, before initiating this PhD, I never imagined that I would have the patience and aptitude to pursue and submit a doctoral dissertation. However, today, as I compile this final section of my thesis, I am overwhelmed by a sense of achievement and immense gratitude for every individual who has made this possible for me.

Let me initiate by expressing my sincerest appreciation for my promotors and daily supervisor, prof. ir. Hans Hopman, dr. Peter de Vos and Rear Admiral (ME, ret) ir. Klaas Visser, without whom this research and dissertation would not be complete and fruitful. Prof. Hopman, thank you very much for all your guidance, wisdom and the opportunity to pursue this research. Your unrelenting support has been exceptionally gratifying and motivating during my PhD, especially, during the final stretch of my research.

For you, Peter, I feel that my words will fall short in expressing the profound admiration I have for you. I can undoubtedly say that I have learned something new from every discussion and enjoyed every conversation with you. Thank you very much for patiently listening and educating me during our frequent and multiple-hour-long discussions. My heartfelt appreciation for translating the summary in Dutch. Also, maybe a little late, but please accept my immense gratitude for teaching me Fundamentals of Marine Engineering over skype after I fractured my foot on the fourth day of coming to the Netherlands. I believe that this is the course that sparked my imagination and passion for maritime, so thank you for that and everything else.

To dear Rear Admiral Visser, I am eternally grateful to you for this wonderful journey and showcasing great confidence in me even when I faltered. I am always inspired by your energy and passion for pushing the boundaries of research. I will be blessed if I have half your energy and wisdom when I have the same earth experience as you do. I wish to thank you for introducing me to teaching by giving me the opportunity to give lectures and supervise master students under your guidance. Thanks to you, I have found my passion for education and research. Adjacent to this, I would also like to take the opportunity to thank you and Mam for your continuous kind wishes and thoughts for Apoorvi and me.

Next, I wish to dearly thank dr. Milinko Godjevac for his support and guidance. Our discussions really helped me structure the scope of my research, improve my work and improve my academic writing skills. I truly cherish our scientific and personal conversations. Also, thank you prof. dr. Aravind for teaching me fuel cell fundamentals and systems. The knowledge I gained by following your course was very helpful in my PhD research.

During this PhD journey, it has been my pleasure to work with fellow GasDrive researcher and friend, dr. Lindert van Biert. Lindert, thank you for the amazing collaboration, for helping me in my struggle of improving my academic writing skills, and for always reminding me that less is more. I also want to thank my fellow PhD and friend, Jelle Stam, for very interesting discussions on fuel cell experiments and fundamentals, excel-

lent cooperation and making GasDrive fun and productive. Dear Jelle, I have learned a lot about fuel cells from you and Lindert, for which I am immensely grateful to you both. Parallel to this, I wish to express my appreciation for dr. Ali Haseltalab for bringing his expertise of controls to GasDrive. Ali, my friend, I want to thank you for the enlightening talks on education, politics and culture. You are wise beyond your years. Next, I want to thank Celia Wei and Pim Bullee for the amazing collaboration and research. I will miss our lively discussions during the project meetings. GasDrive would be incomplete without you and your contributions. I would also like to express my immense appreciation for prof. dr. Rudy Negenborn for his guidance and organization of the GasDrive project.

To dr. Rinze Geertsma, it has been a great joy of my life to have you as my colleague and friend. Your energy is inspiring and infectious. I am grateful to you for your invaluable comments in improving my work and my research articles. My first research article would be incomplete without the supervision and critical remarks of prof. Douwe Stapersma. Thank you for introducing me to the process of scientific research and academic writing during the initial stages of my PhD. Next, I wish to thank Roelf van Till for being an amazing office mate. Thank you for the delightful conversations and for creating a very productive and comfortable office environment.

The GasDrive project would not be a success without the contribution and support of Pon Power, Damen, Defence Material Organization, Royal IHC, Boskalis, Feadship, Oceanco and Wärtsilä. I want to thank Wim van Sluijs, Joost Schapendonk, Chris Dijkstra, Marcel Roberscheuten, Arie v. Oord and Youri Linden for allowing me and assisting me in performing engine experiments at Pon Power and the Netherlands Defence Academy. This work would be incomplete with your support. I also wish to thank our industrial partners, Benny Mestemaker, Gert-Jan Meijn, Evy De Maeyer, Pieter van Loon, Fabien Vispoel, Isaac Barendregt, Joost Wijnads, Teus van Beek and Michel Janssen, and the academic members, prof. dr. Rob Lammertink of University of Twente and prof dr. Tinka Murk and dr. Edwin Foekema of Wageningen University & Research, for their crucial guidance and contributions during the user committee meetings.

During my PhD, I have had the immense pleasure of sharing my knowledge and learning from excellent MSc. and BSc. students during their graduation projects. Thank you Byungjoo Lee, Steven Krol, Jeroen Reurings, Jaswinder Singh, Ruben Tol, Jurian Bosklopper, Xiao Sen Zheng, Maurice Vermeulen, Tim Lelieveld, Maarten Adams and Luuk Jacobse for your efforts and for enriching this research. My PhD journey would be incomplete without the support of my other M&TT department colleagues. First and foremost, thank you, Faisal, Marc, Lode, Udai, Nikos, Congbiao and Pranav for the delightful, serious, hilarious and informative coffee break conversations and dinner outings. I loved the breadth and depth of our conversations. Thank you to Arthur, Jeroen, Henk, Robert, Austin and Harleigh for the wonderful and warm working environment. I also want to thank my fellow PhDs, Alina, Carmen, Johan, Brenno, Hamid, Javad, Sietske, Nicole, Joan, Rie, Jurrit, and Koen for the great times we shared. A big thanks to Dineke, Gracia, Anouk, Monique, Patty and Pauline for their relentless and fantastic efforts in helping me with all the administrative work and for ensuring the smooth functioning of the department. I am truly grateful to you.

This journey would not have come to fruition without my friends, housemates and family. Thank you Rishab and Avinash for the beautiful evenings at home and the de-

licious meals. I want to thank my parents Dershan Lal Sapra and Raj Sapra for all their love, support and encouragement. To my dear Maa, thank you for being so strong and for your unconditional love. I love talking to you every morning when I walk from home to work, it helps me start my day on a beautiful note. Thank you, Papa, for inspiring me to pursue a PhD and for proofreading my every article, proposal and my thesis. You are the best adviser and friend I can ask for. I also wish to thank my father-in-law, Viney Chaudhri, for being a true inspiration and for sharing his love of science with me. Dear Paa, I really love our talks about science, spirituality, life and education. Thank you so much for your love and wisdom. To, my dearest brother, Yash, and my sister-in-law, Apoorva, thank you so much always for being there for me and all of us. Your love and support give me the strength to keep going, no matter what. Next, I want to thank my adorable niece, Tia, for she is a bundle of joy and a source of energy that defies the first law of thermodynamics. I am truly amazed by your intelligence and creativity, and I look forward to learning more about black holes from you.

And now, to the most important person, my dearest wife, Apoorvi, you are my most incredible source of support, love and inspiration. I am eternally grateful to you for standing by me through thick and thin, and for always believing in me, and for motivating me to do better every day. I am always inspired by your intellect, resilience and passion for science. With your patience and understanding, you have made our journey absolutely beautiful and joyful. I am looking forward to being together with you. Thank you for everything, for I could not have done any of this without you. Thank you for being YOU.

Harsh Darshan Sapra, Delft, November 2020

CURRICULUM VITÆ

Harsh Darshan SAPRA

22-12-1989 Born in Pune, India.

EDUCATION

2005 Secondary School Certificate (Mathematics Science)
St. Joseph's Boys High School, Pune, India

2005–2007 Higher Secondary Certificate (Mathematics Science)
Wadia College, Pune, India

2007–2011 Bachelor of Science (Mechanical Engineering)
University of Pune, Pune, India

2013–2015 Master of Science (Mechanical Engineering, Mechanical Systems & Integration)
Delft University of Technology, Delft, Netherlands

2016–2020 Doctor of Philosophy (Energy Systems)
Delft University of Technology, Delft, Netherlands

AWARDS

2019 Best CIMAC World Congress 2019 technical poster presentation

2020 Best IMAREST Benelux seminar talk of 2019

2020 Second prize at the OceansX One Hackathon

2020 The most valuable technical paper award in Track 1 - Large Bore Engines
at the 2019 ASME ICE Fall Technical Conference

LIST OF PUBLICATIONS

8. **H.D. Sapra**, J. Stam, L. van Biert, P. de Vos, K. Visser, M. Gert-Jan *Potential of COmbined drive of Fuel cell And Internal Combustion Engine (COFAICE) for naval ships*, The International Naval Engineering Conference, Online, October 2020.
7. J. Bosklopper, **H.D. Sapra**, R. van de Ketterij, W. van Sluijs, C. Bekdemir, P. de Vos, K. Visser *Experimental Study on a Retrofitted Marine Size Spark-ignition Engine Running on Port-injected 100 % Methanol*, The International Naval Engineering Conference, Online, October 2020.
6. **H.D. Sapra**, J. Stam, J. Reurings, L. van Biert, W. van Sluijs, P. de Vos, K. Visser, A. P. Velayani, H. Hopman *Integration of Solid Oxide Fuel Cell and Internal Combustion Engine for Maritime Applications*, Applied Energy, October 2020.
5. **H.D. Sapra**, M. Godjevac, P. de Vos, W. van Sluijs, Y. Linden, K. Visser *Hydrogen-Natural Gas Combustion in a Marine Lean-Burn SI Engine: A Comparative Analysis of Seiliger and Double Wiebe Function-Based Zero-Dimensional Modelling*, Energy Conversion and Management, February 2020.
4. **H.D. Sapra**, J. Singh, C. Dijkstra, P. de Vos, K. Visser *Experimental Investigations of Marine Diesel Engine Performance Against Dynamic Back Pressure at Varying Sea-States Due to Underwater Exhaust Systems*, Proceedings of the ASME 2019 Internal Combustion Engine Fall Technical Conference, Chicago, October 2019 .
3. **H.D. Sapra**, Y. Linden, W. van Sluijs, M. Godjevac, K. Visser *Experimental Investigations of Performance Variations in Marine Hydrogen-Natural Gas Engines*, CIMAC World Congress, Vancouver, Canada, June 2019.
2. **H.D. Sapra**, Y. Linden, W. van Sluijs, M. Godjevac, K. Visser *Experimental Investigations of Hydrogen-Natural Gas Engine for Maritime Applications*, Proceedings of the ASME 2018 Internal Combustion Engine Fall Technical Conference, San Diego, November 2018.
1. **H.D. Sapra**, M. Godjevac, K. Visser, D. Stapersma, C. Dijkstra *Experimental and Simulation-based Investigations of Marine Diesel Engine Performance Against Static Back Pressure*, Applied Energy, July 2017.

